NASA Conference Publication 2215
Part 1

Large Space Systems Technology - 1981

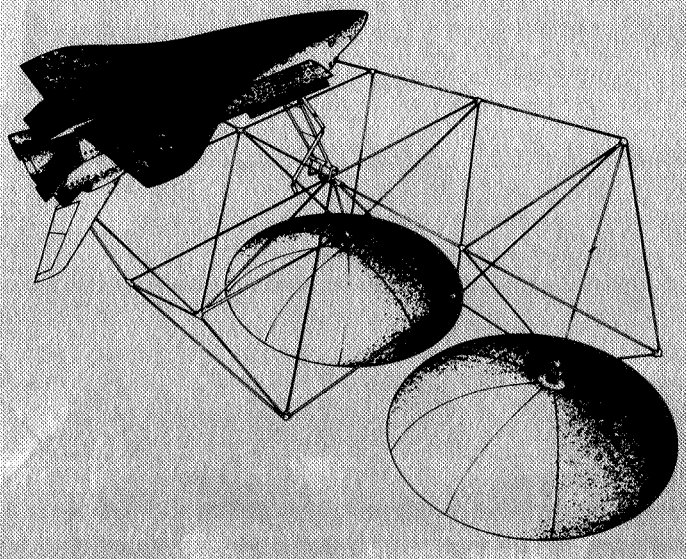

Third Annual Technical Review
held at NASA Langley Research Center
Hampton, Virginia
November 16-19, 1981

NASA

NASA Conference Publication 2215
Part 1

Large Space Systems Technology - 1981

Compiled by
William J. Boyer
NASA Langley Research Center
Hampton, Virginia

Third Annual Technical Review
held at NASA Langley Research Center
Hampton, Virginia
November 16-19, 1981

NASA
National Aeronautics
and Space Administration

Scientific and Technical
Information Branch

1982

The use of trade names or manufacturers' names in this publication does not constitute endorsement, either expressed or implied, by the National Aeronautics and Space Administration.

PREFACE

This publication is a compilation of the papers presented at the Third Annual Large Space Systems Technology (LSST) Technical Review conducted at NASA Langley Research Center on November 16-19, 1981. The Review provided personnel of government, university, and industry with an opportunity to exchange information, to assess the present status of technology developments in the Large Space Systems Program, and to influence the course of development of new technology for large space systems.

The papers describe technological or developmental efforts that were accomplished during Fiscal Year 1981 in support of the LSST Program and were prepared by those in government, university, and industry who performed the work. These papers were divided into four major areas of interest: (1) technology pertinent to large antenna systems, (2) technology related to the control of large space systems, (3) basic technology concerning structures, materials, and analyses, and (4) flight technology experiments.

This publication is divided into two parts. Part 1 contains information on program status; structures, materials, and analyses; and control of large space systems. Part 2 covers large antenna systems and flight technology experiments.

This compilation provides the participants and their organizations with the papers presented at the Review in a referenceable format. Also, users of large space systems technology can follow the development progress with this document along with proceedings of previous and future LSST Technical Reviews. (See NASA CP-2168, 1981.) The LSST Program Office, Langley Research Center, which hosted the Review, provides this information as an aid in measuring performance and in planning future tasks.

This publication was expedited and enhanced through the efforts of the staff of the Research Information and Applications Division, Langley Research Center.

William J. Boyer
Manager, LSST Program Office
NASA Langley Research Center

CONTENTS

CONTROLS

PART 2*

ANTENNAS

---

*Part 2 is presented under a separate cover.

FLIGHT TECHNOLOGY EXPERIMENTS

THIRD ANNUAL TECHNICAL REVIEW ATTENDEES

NASA Headquarters
Washington, DC

R. F. Carlisle
J. B. Dahlgren
D. E. England
F. D. Kochendorfer
W. T. Tumulty, Jr.
S. L. Venneri

NASA Langley Research Center
Hampton, VA

Dr. D. P. Hearth
P. F. Holloway
R. C. Goetz
H. T. Wright
Dr. M. F. Card
Dr. G. D. Walberg
W. M. Moore
I. Akpan (ODU)
J. L. Allen, Jr.
E. S. Armstrong
D. Babb
Dr. M. C. Bailey
H. T. Banks (ICASE)
F. B. Beck
W. K. Belvin
H. J. C. Blume
D. E. Bowles
W. J. Boyer
Dr. R. A. Breckenridge
G. M. Buck
H. G. Bush
D. H. Butler
T. G. Campbell
B. A. Childers
Dr. C. R. Cockrell
C. W. Coffee, Jr.
M. Cooper (GWU)
P. L. Daniel (ICASE)
R. B. Davis
L. J. DeRyder, Jr.
R. Dompka (GWU)
J. T. Dorsey (GWU)
R. S. Dunning
R. W. Faison
J. T. Farmer
M. Ferebee
Dr. W. B. Fichter
Dr. L. B. Garrett
J. W. Goslee
W. L. Grantham

NASA Langley Research Center
Hampton, VA (Continued)

W. H. Greene
H. A. Hamer
B. R. Hanks
W. L. Heard, Jr.
B. B. Hefner, Jr.
R. B. Holt
W. R. Hook
Dr. G. C. Horner
Dr. J. M. Housner
Dr. E. K. Huckins, III
Dr. W. F. Hunter
Dr. K. Ito (ICASE)
S. M. Joshi (ViRA Inc.)
E. Kamaratos (CNC)
Dr. S. J. Katzberg
L. S. Keafer, Jr.
C. R. Keckler
B. M. Kendall
F. Kopriver III
B. A. Langford, Jr.
E. B. Lightner
Dr. E. R. Long, Jr.
S. A. T. Long
U. M. Lovelace
J. Mahaney (ODU)
Dr. M. M. Mikulas, Jr.
R. Miserentino
Dr. R. C. Montgomery
Dr. I. Najfeld (ICASE)
J. F. Newcomb
J. E. Pennington
L. W. Peterman, Jr.
Dr. L. D. Pinson
M. D. Rhode
R. A. Russell
E. P. Sandberg
C. G. Saunders, Jr.
A. A. Schy
Dr. J. D. Shaughnessy
J. S. Short
Dr. J. J. Singh
L. W. Taylor, Jr.
Dr. R. G. Teglas (ICASE)
Dr. D. R. Tenney
Dr. E. A. Thornton (ODU)
Dr. S. S. Tompkins
R. T. Voland
J. E. Walz
L. Weisstein
J. P. Williams

NASA Langley Research Center
Hampton, VA (Continued)

R. E. Williger
Dr. J. W. Wilson
R. L. Wright
J. W. Young
W. R. Young
E. Zisk

NASA Ames Research Center
Moffett Field, CA

L. G. Lemke
T. R. Pochari

NASA Goddard Space Flight Center
Greenbelt, MD

L. R. Dod
H. P. Frisch
E. W. Travis
J. P. Young

Jet Propulsion Laboratory
Pasadena, CA

C. M. Berdahl
W. A. Edmiston
R. S. Edmunds
M. El-Raheb
R. E. Freeland
Dr. A. Gupta
Dr. E. Heer
W. A. Imbriale
G. C. Lagomarsini
Dr. R. Levy
Dr. Y. H. Lin
J. M. McLauchlan
G. Rodriguez
D. B. Schaechter
Dr. J. G. Smith
Dr. R. R. Stephenson
S. Szirmay
A. F. Tolivar
Dr. S. J. Wang
Dr. W. J. Weber III

NASA L. B. Johnson Space Center
Houston, TX

L. M. Jenkins
W. A. Lewton
F. T. Pearce

NASA Lewis Research Center
Cleveland, OH

B. E. LeRoy

NASA Marshall Space Flight Center
Huntsville, AL

Dr. J. Blair
E. C. Hamilton
R. Jewell
J. D. Micheal
R. W. Schock
J. W. Stokes, Jr.
Dr. H. B. Waites

Aerospace Corporation
Los Angeles, CA

M. Aswani
J. E. Bennett

Bolling Air Force Base
BAFB, DC

A. K. Amos
D. R. Urlich

Astro Research Corporation
Carpinteria, CA 93013

Dr. J. M. Hedgepeth
R. Samuels

Ball Aerospace Corporation
Boulder, CO

I. Sreenivasiah

Barnes Engineering Company
Stamford, CT

P. Armstrong
S. C. Spielberger
K. A. Ward

Bendix Corporation
Teterboro, NJ

F. D. Chichester

Boeing Aerospace Company
Seattle, WA

C. T. Golden
J. A. Lackey
E. E. Spear
Dr. R. G. Vos

Boeing Company
Hampton, VA

W. E. Parker

Brunswick Corporation
Costa Mesa, CA

C. B. Kurz
S. R. Langer
M. F. Steele

C. S. Draper Laboratory
Cambridge, MA

Dr. E. Fogel
J. G. Lin
C. M. Satter
Dr. K. Soosaar

Communications Research Center
Ontario, Canada

F. Vigneron
D. G. Zimcik

COMSAT Laboratories
Clarksburg, MD

D. N. Srinivas

Air Force Rocket Propulsion Laboratory
Edwards Air Force Base, CA

R. Preston

General Dynamics Convair
San Diego, CA

J. G. Bodle
D. L. Browning
R. V. Halstenberg
L. R. Norris

General Electric Company
Philadelphia, PA

H. Edighoffer
P. Foldes
R. B. Wiley
Dr. C. Zweben

General Research Corporation
Santa Barbara, CA

R. R. Chase

Grumman Aerospace Corporation
Bethpage, NY

F. Austin
C. J. Goodwin
L. H. Hemmerdinger
J. L. Schultz

Harris Corporation
Washington, DC

H. J. Andrews

Harris Corporation
Melbourne, FL

W. F. Croswell
T. A. Gutwein
J. W. Shipley
M. R. Sullivan
Dr. B. C. Tankersley

Headquarters Space Division (AFSC)
Los Angeles, CA

Lt. S. G. Hancock

Honeywell, Incorporated
Minneapolis, MN

T. B. Cunningham
C. W. Farnham
A. K. Hammell

Honeywell, Incorporated
McLean, VA

W. T. Herring

Howard University
Washington, DC

Dr. P. M. Bainum
R. Krishna
V. K. Kumar
A. S. S. R. Reddy

Hydraulic Research TEXTRON
Irvine, CA

Dr. J. F. Garibotti

Integrated Systems Incorporated
Palo Alto, CA

M. G. Lyons

Kentron International
Hampton, VA

E. P. Brien
R. E. Calleson
D. P. Giesy
J. K. Jensen
R. W. LeMessurier
J. E. Phelps
R. E. Wallsom
R. F. Walsh

Lockheed Palo Alto Research Laboratory
Palo Alto, CA

Dr. J. A. Breakwell
Dr. K. C. Park

Lockheed Missiles and Space Company
Sunnyvale, CA

K. Forsberg
N. F. Garcia
Dr. J. Y. L. Ho
K. F. Johansen
R. M. Vernon
R. D. Winquist
A. A. Woods, Jr.

Martin Marietta Corporation
Denver, CO

A. L. Brook
J. V. Coyner, Jr.
C. E. Farrell
A. E. Fehr
J. N. Juang
J. Herbert
G. Lang
D. Rudolph
F. R. Schwartzberg
D. A. Strange
W. H. Tobey

Martin Marietta Corporation
Hampton, VA

F. K. Mattson

Massachusetts Institute of Technology
Cambridge, MA

D. L. Akin
M. L. Bowden

McDonnell Douglas Technical Services
Houston, TX

A. Hotz

Naval Electronics Systems Command
Arlington, VA

R. DuPuy

Naval Research Laboratory
Washington, DC

R. E. Lindberg, Jr.

OAO Corporation
Greenbelt, MD

R. Sellappan

OCSE - Rome Air Development Center
Rome, NY

R. W. Carman

Ohio State University
Columbus, OH

M. Bragg
G. Gregorek

Princeton University
Princeton, NJ

C. Weeks

Rockwell International
Downey, CA

H. S. Greenberg
J. Wokurka

Rockwell International
Hampton, VA

E. G. Snyder, Jr.

Sigma Data Services Corporation
Rockville, MD

R. Miezis

SPAR Aerospace Limited
Ontario, Canada

J. S. C. Yuan

System Planning Corporation
Arlington, VA

R. B. Baird

Teledyne-Brown Engineering
Huntsville, AL

W. Goldberg

TRW
Redondo Beach, CA

J. T. Bennett
B. Bruce
Dr. R. Gluck
Dr. R. S. Neiswander
R. H. Van Vooren

University of Idaho
Moscow, ID

Dr. R. F. Gibson

University of Toronto Institute for
Aerospace Studies (UTIAS)
Ontario, Canada

G. B. Sincarsin

U.S. Air Force Academy, CO

W. P. Witt III

Virginia Associated Research Campus (VARC)
of the College of William and Mary
Newport News, VA

A. Kyser

Vought Corporation
Dallas, TX

R. L. Cox
J. J. Pacey

W. C. Hayes Associates, Incorporated
Leesburg, VA

W. C. Hayes

MATURING LSST ROLE IN NASA PLANNING

Richard F. Carlisle
NASA Headquarters
Washington, D.C.

Large Space Systems Technology - 1981
Third Annual Technical Review
November 16-19, 1981

TRANSITION IN PROGRAMS

The LSST program has made a transition from a structures-based program to a systems program as shown in figure 1. Systems analysis for both platforms and antennas has formally been adopted to identify technology development requirements of subsystems and to act as a focal point for integrating subsystem technologies and evaluating their effects on overall system performances and subsystem interaction. Land Mobile Satellite Service (LMSS) work, that was completed this year, showed the need for additional feed technology and identified the need for distributed control to meet system communications requirements.

Both antennas and platforms of the large space-system class will require, as an initial step, advanced system identification along with distributed control to meet systems performance requirements. Modular control is the correlary technology for systems undergoing large configuration changes during construction and assembly operations. These initial steps will build the technology base that will lead to self-diagnosing and compensating systems with adaptive control.

The LSST antenna program has focused on point-design deployable mesh antennas since its inception. The technology is well along, and, this year, ground testing will dominate the effort. As the ground development phase approaches completion about 1983, system flight testing will be required to complete the technology development.

As the deployable program matures, technologies associated with advanced configurations will be investigated. This past year, for instance, antenna system work has progressed with truss and modular configurations and membrane reflectors with promising results. (Details of the studies are presented elsewhere in this document.)

Past platform activities have included application studies (science and applications, GEO communications, and solar-powered satellite). Current platform technology will focus on the generic aspects of platform systems which have commonality across applications, advanced power, and manned platforms. A ground program for deployable platforms has been initiated that will utilize ground testing for advanced technology development. Any residual technology voids at the completion of the ground program will be resolved with flight testing. Future advanced platform technology will investigate erectable and fabricated concepts.

Assembly analysis work in the neutral buoyance facility at the Marshall Space Flight Center (MSFC) has progressed to the point where space testing is required to correlate orbital assembly operations with ground simulations. The Structural Assembly Deployment Experiment (SADE) is a flight experiment that will validate the man-machine assembly analysis algorithm and provide the space-to-ground correlation.

- LSST
  - STRUCTURES ⟶ SYSTEMS
    - SYSTEMS ANALYSIS (ANTENNA/PLATFORM)
      - SYSTEM PERFORMANCE
      - SUBSYSTEM INTERACTION

      } LMSS: STRUCTURE, THERMAL CONTROL, RF
    - CONTROL
      - ADVANCED SYSTEM IDENTIFICATION
      - DISTRIBUTED
      - MODULAR

      } (ANTENNA/PLATFORM)
- ANTENNAS
  - DEPLOYABLES (MESH) ⟶ TRUSS/MODULAR (MEMBRANE)
    - GROUND DEVELOPMENT
      - FLIGHT TEST
- PLATFORMS
  - APPLICATION STUDIES
    - PLATFORM SYSTEM ANALYSIS ⟶ GENERIC, ADV. POWER, S.O.C.
    - DEPLOYABLE PLATFORM GROUND PROGRAM ⟶ ERECTABLE FABRICATED
      - (FLIGHT TEST - TBD)
  - ASSEMBLY ANALYSIS
    - S.A.D.E.

Figure 1

1982 LSST PROGRAM

Figure 2 shows the distribution of the FY 1982 LSST program elements to the centers. Primary focus for antennas is at the Langley Research Center (LARC) and for platforms at MSFC.

	LARC	JPL	MSFC	JSC	GSFC	LERC
ANTENNAS						
ANT. SYST. ANAL.	X					
HOOP COLUMN	X					
WRAP RIB		X				
ELEC. STAT. MEM.	X					
ELEC. MAG. ANAL.	X					
PLATFORMS						
PLAT.SYST. ANAL.			X			
DEPLOY. PLAT.			X			
ASS'Y. ANAL.			X			
ASS'Y. TECH.				X		
ASS'Y. EXPT.			X			
LSS TECHNOLOGY						
CONTROL/STAB.	X	X	X			
DOCK/BERTH				X		
IAC					X	
ARAMIS			X			
M-SAT						X
PROPUL/STR.						X

Figure 2

CURRENT PLANS

Figure 3 shows current planning for antennas and platforms. Antennas and platform systems analysis will be continuing efforts that will receive more emphasis in FY 1982. The deployable antenna ground program (hoop column and wrap rib) will continue in FY 1982 and start phasing down about the end of FY 1983. Initial planning for an antenna system flight experiment will start in FY 1982 and build up through FY 1983 in preparation for a flight in the late FY 1987 time frame.

The deployable platform ground program is a 6-year effort that started in FY 1981. It will continue to grow this year with component testing starting in FY 1983 and with deployable structures, utilities, etc., starting later in the program.

The assembly experiment (SADE) will complete experiment definition in FY 1982 and start final experiment hardware design in preparation for a FY 1985 launch.

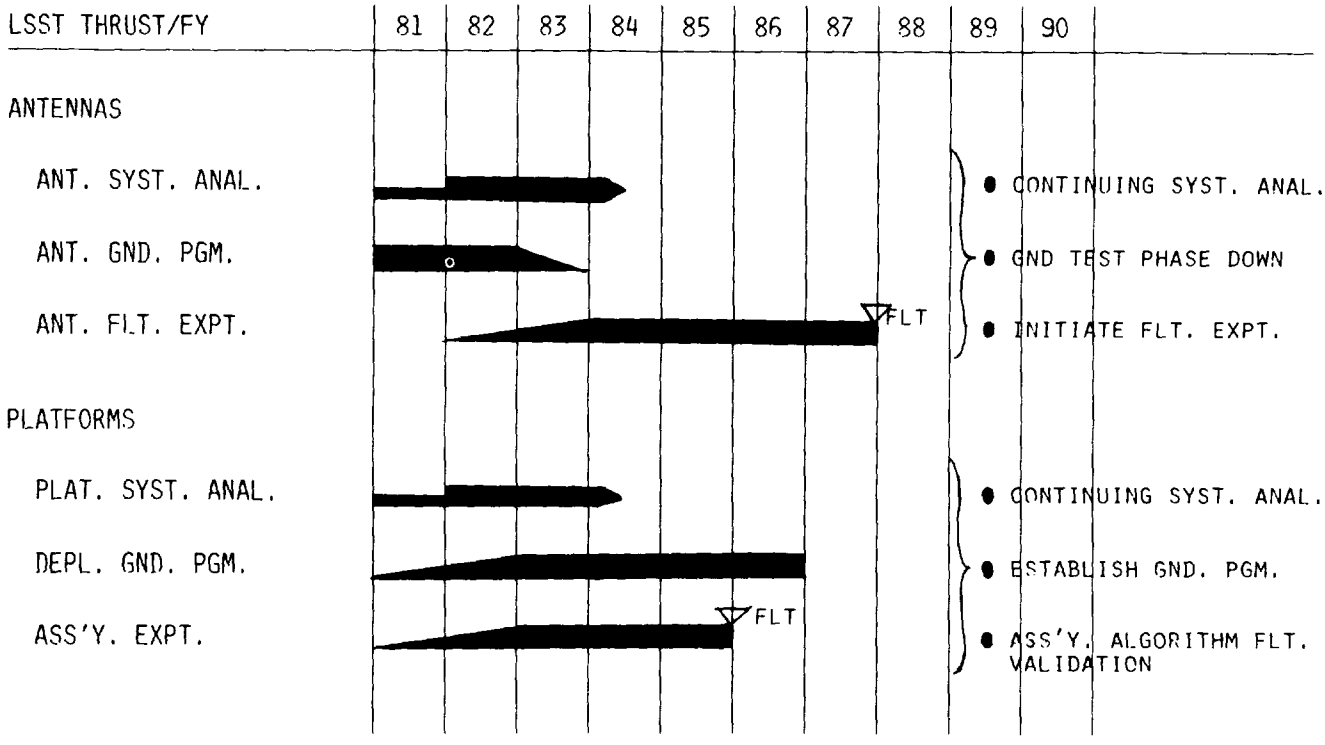

Figure 3

PRELIMINARY SCHEDULE FOR SPACE-STATION TECHNOLOGY DEVELOPMENT

Figure 4 shows preliminary planning and associated milestones for space-station technology development. With a phase C/D start in FY 1986, there are 4 years to allow technology to be developed that will significantly advance space-station capabilities.

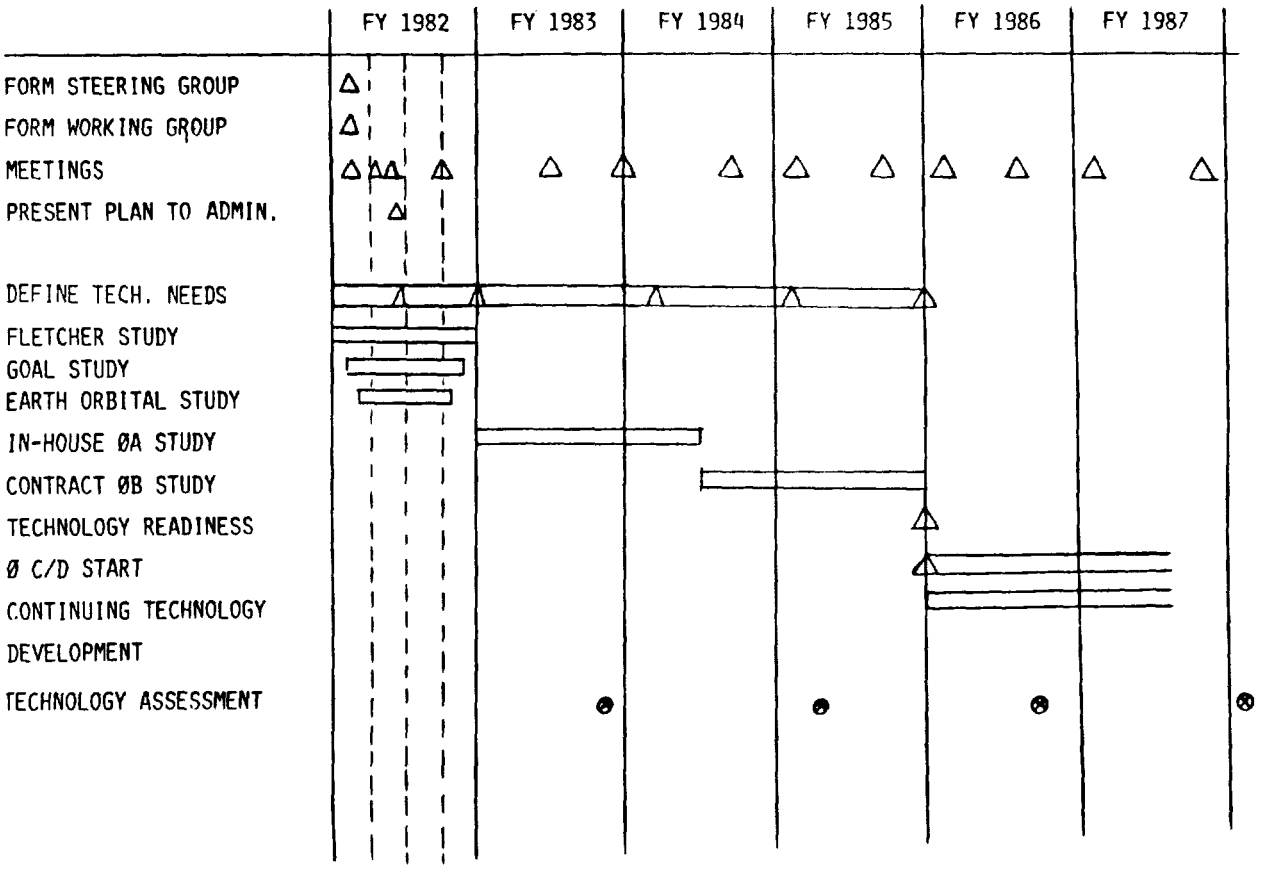

Figure 4

TECHNOLOGY FOR SPACE STATION

If we look at technology required for a space station and compare it with the LSST program, we find considerable similarity as shown in figure 5. Many of the technologies being worked on for antennas and platforms are required for the space station. In addition, the timing is about right. The antenna ground program will have been completed and the deployable platform program will be well underway. The SADE experiment will have flown and primary antenna flight-experiment hardware elements will have been fabricated and will be in ground simulation and test.

- STATION IS A LARGE SPACE SYSTEM
- TIME FOR TECHNOLOGY DEVELOPMENT
- ALREADY-WORKING APPLICABLE TECHNOLOGY
- FITS CURRENT LSS PROGRAM
- SPACE STATION REPRESENTS EXPANSION OF LSST

Figure 5

APPLICATIONS APPROACH

The point design approach typically groups missions by LSS class (e.g., antennas, platforms, etc.) to determine strawman requirements for the design. Another approach extracts requirements that are common to all or to a majority of missions within each class. When common requirements are extracted across LSS classes, generic LSS technology elements can be identified.

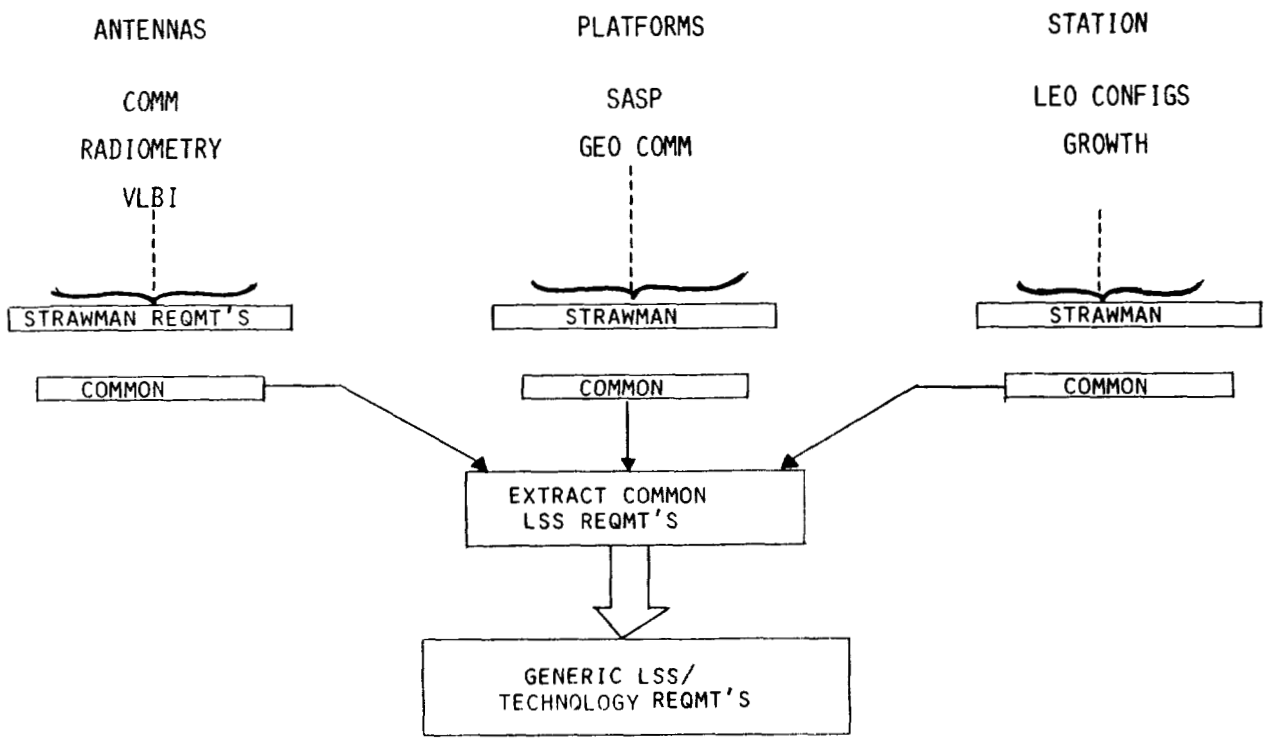

Figure 6

LSS CHARACTERISTICS

Common technology issues for antennas, platforms, and space stations can collectively be referred to as LSS characteristics. Figure 7 identifies major technology elements that are common to all (most) large space systems. Technology development directed toward these characteristics will provide maximum leverage for large space systems.

- LARGE CONFIGURATION CHANGES
  - STOWED/DEPLOYED
  - ASSEMBLED
- COMPLEX STRUCTURES
  - VERY LOW FREQUENCY, DENSE MODES
  - DAMPING UNCERTAINTIES & NON-LINEARITIES
- ADVANCED CONTROL SYSTEMS
  - DISTRIBUTED
  - ADAPTIVE
- HIGHLY INTERACTIVE SUBSYSTEMS
  - STRUCTURE DYNAMICS
  - THERMAL
  - CONTROL

Figure 7

CONCLUSIONS

Discipline and system technology must be worked together, in an integrated fashion, for maximum benefit to LSST as shown in figure 8. System performance can be affected not only by individual discipline performance but also by discipline interactions. Integrated system studies and trades assess individual and combined subsystem effects on overall performance and establish technology requirements and drivers within and between subsystems. Current technology programs that include ground development and testing will still leave technology voids. Space testing is required to overcome ground-test effects, and an integrated system is required to assess system performance and subsystem interaction.

An antenna is chosen as the representative large space system for flight testing because it exhibits characteristics common to most large systems and is the most mature LSS configuration. As an integrated systems experiment, system and discipline technology and interaction can be validated simultaneously. In addition, common technology issues applicable not only to antennas but also to platforms and space stations can be validated.

- DISCIPLINES OUTPUT LSS APPLICABLE GENERIC TECHNOLOGY
- LSST SUPPORTS SYSTEMS TECHNOLOGY/APPLICATIONS
- LSST REQUIRES INTEGRATED SYSTEMS TO COMPLETE TECHNOLOGY DEVELOPMENT
- ANTENNA FLIGHT EXPERIMENT SATISFIES
  - SYSTEM PERFORMANCE
  - SUBSYSTEM INTERACTION (STRUCTURE/CONTROL/THERMAL/RF)
- SYSTEMS TECHNOLOGY FROM ONE APPLICATION APPLIES TO OTHERS
  - ANTENNA
    - STRUCTURE DYNAMICS/SYSTEM IDENTIFICATION
    - DISTRIBUTED CONTROL
    - SUBSYSTEM INTERACTION

} PLATFORMS STATION

Figure 8

LSST: BEYOND THE GROUND PROGRAM

William T. Tumulty
NASA Headquarters
Washington, D.C.

Large Space Systems Technology - 1981
Third Annual Technical Review
November 16 - 19, 1981

COVER SHEET OF ORIGINAL PLAN

The large space-systems technology program was formally initiated in FY 1979 as a 5-year effort. Figure 1 shows the cover sheet of the original technical plan.

NASA
National Aeronautics and Space Administration

Large Space Systems Technology

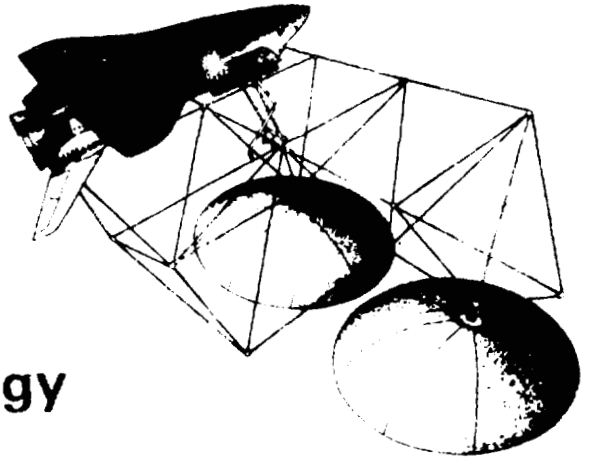

TECHNICAL PLAN (FY-79 - FY-83)

LSST Program Office
Langley Research Center
Hampton, Virginia 23665

Figure 1

LARGE ANTENNA-SYSTEM TECHNOLOGY DEVELOPMENT PLAN

The task elements of the original development plan are ongoing today as shown in figure 2. Of particular interest are the hoop column and wrap rib antenna efforts. These antenna technology developments were planned with analytical and ground-test activities to output a comprehensive data base in the FY 1983 time frame. This information was to be used to assess technology status at ground-program completion and define additional flight testing to complete technology development.

With antenna ground-development hardware being completed in FY 1981, and test and evaluation occupying most of FY 1982, the program has significantly matured. The original scheduling is pretty much on track too, with phase down expected to start in FY 1983. This, coupled with a firm understanding of ground-test limitations and associated technology voids, necessitates planning for subsequent flight experimentation.

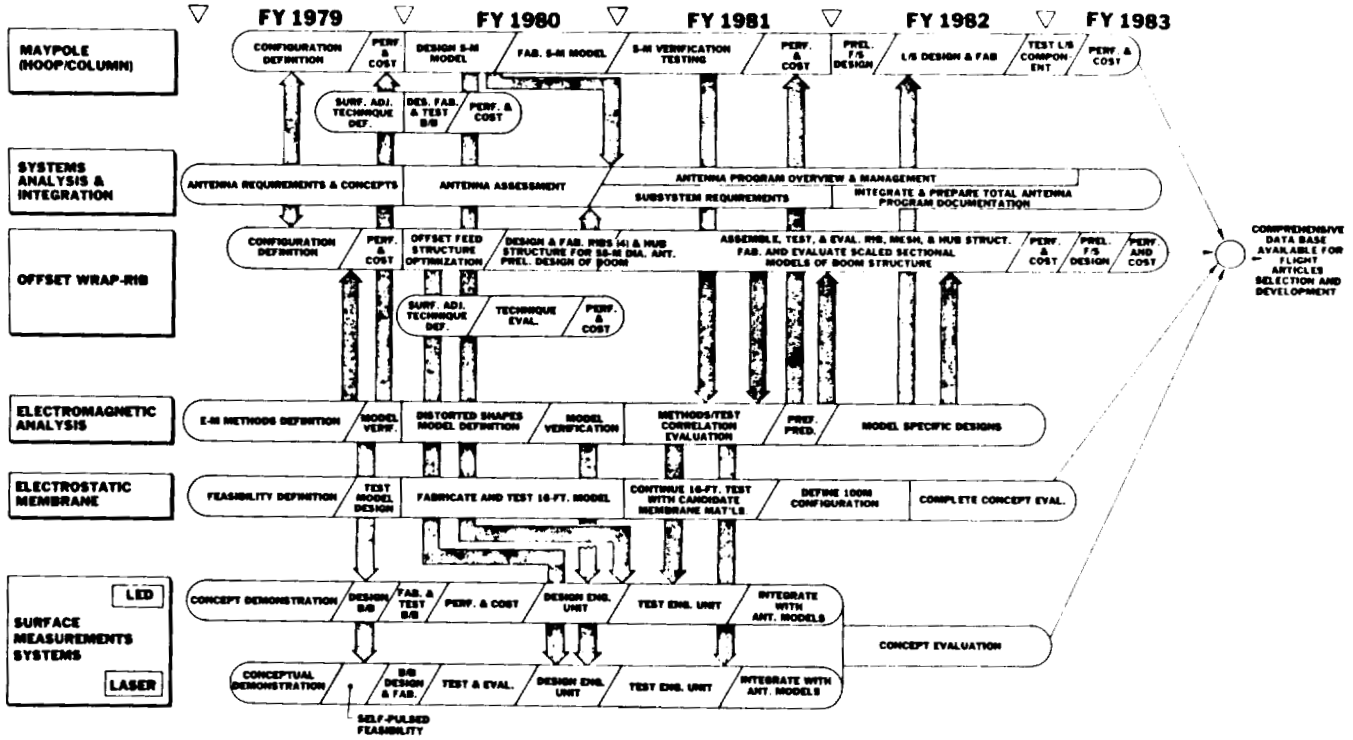

Figure 2

CURRENT LSST GROUND PROGRAM

The current antenna ground program that is funded by LSST is depicted in figure 3. (Complimentary discipline technology programs in dynamics, control, and RF that support these efforts are not shown.)

The ground-development hardware is being utilized to assess mesh management and surface characterization, deployment/kinematics, structural characterization and effects of RF performance due to surface distortion, and aperture blockage.

	HOOP COLUMN (1984)	WRAP RIB (1983)
MESH MANAGEMENT	50 M SURFACE ADJUST. MODEL	55M SURF. ADJUST.
DEPLOYMENT	15M MODEL WITH SURFACE	55M MODEL WITH 4 RIB, 3 GORE, HUB
FEED MAST		STRUCTURAL MODEL
RF	BREADBOARD PILLOW & CABLE EFFECTS	

Figure 3

TECHNOLOGY VALIDATION AND TRANSFER

Technology transfer implies validation of analytical tools, ability to predict and understand interactions between subsystems, and finally the ability to predict and achieve system performance confidently with minimal risk. To accomplish this, simulation and test activities with both hardware and software elements are required as seen in figure 4. Within the limitations of ground testing, simulations are updated and software and analytical tools are validated.

Subsequent flight testing is required when the ground environment restricts the validation process. Hardware commonality between ground and flight programs eliminates uncertainties associated with different sets of hardware and yields a cost benefit.

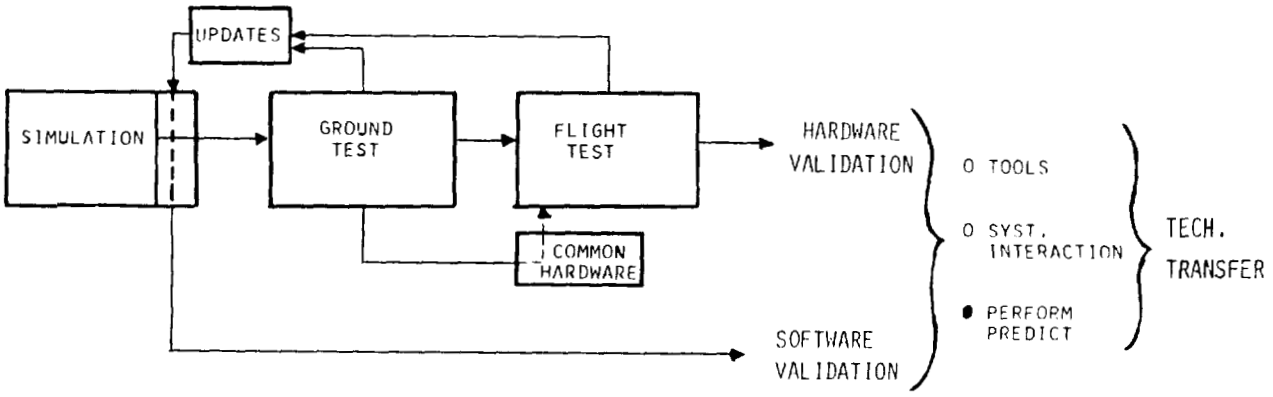

Figure 4

REVIEW OBJECTIVES

In February 1981, an LSST Antenna Review was convened at LaRC to review program status and identify additional ground and required flight activities required to complete deployable antenna technology development. The objectives are stated in figure 5.

- EXAMINE THE DEVELOPMENT LOGIC FOR THE GROUND-BASED LSST HOOP/ COLUMN AND OFFSET WRAP-RIB ANTENNA PROGRAMS
- IDENTIFY ADDITIONAL WORK THAT NEEDS TO BE UNDERTAKEN TO BRING CONCEPTS TO A SYSTEMS TECHNOLOGY READINESS STATE
- IDENTIFY NEED FOR GROUND-TEST TECHNIQUES AND FACILITIES
- IDENTIFY NEED FOR FLIGHT VALIDATION INCLUDING SPECIALIZED INSTRUMENTATION
- FORMULATE TECHNICAL PLANS AND RESOURCES REQUIRED TO COMPLETE THE TECHNOLOGY DEVELOPMENT FOR THESE CONCEPTS

Figure 5

REVIEW COMMITTEE CONCLUSIONS

The review committee was composed of system and discipline technologists and included participation by the structures/dynamics, controls, thermal, and RF subsystems from the NASA Centers. As shown in figure 6, they concluded that flight testing was required to fill residual technology voids at the completion of the ground programs in order to complete technology development and validate the simulation process. They also concluded that a flight-experiment system was required to assess system and subsystem performance and effects of discipline interactions.

FLIGHT TESTING REQUIRED TO:

- FILL GROUND-TEST VOIDS
  - DAMPING EFFECTS
  - 1 G EFFECTS
  - DYNAMICS/CONTROL INTERACTION
  - RF/FEED/REFLECTOR INTERACTIONS
- CORRELATE GROUND TO FLIGHT
  - VALIDATE SIMULATION

SYSTEM FLIGHT EXPERIMENT TO PROVIDE:

- SYSTEM TEST
- DISCIPLINE INTERACTIONS - STRUCT/THERMAL/CONTROL/RF
- RF PERFORMANCE
- SYSTEM PERFORMANCE
- LOW-RISK TECHNOLOGY VALIDATION

Figure 6

STRUCTURE DYNAMICS

Structural characteristics and analytical and ground-test uncertainties make structure dynamics (see fig. 7) a high-risk technology element. Zero-g flight testing is required to characterize the structural plant adequately for the structure and control subsystems and to validate the technology of systems identification.

- VERY LOW FREQUENCY DENSE MODES
- PRECISE KNOWLEDGE OF FREQUENCIES AND SHAPES REQUIRED
- ANALYSIS RELIABLE FOR $\sim$ 1ST 20 MODES
  - NEED CHARACTERIZATION OF $\sim$ 1ST 100 MODES
- LSS NON-LINEARITIES VERSUS LINEAR SYSTEMS ANALYSIS
- ABILITY TO MEASURE AND SPECIFY DAMPING
- GROUND-TEST UNCERTAINTIES
  - 1-G EFFECTS
  - TEST CONFIGURATION (COMPONENT AND SCALED)
  - BOUNDARY CONDITIONS
  - AERODYNAMIC ENVIRONMENT EFFECTS

SYSTEMS IDENTIFICATION

Figure 7

CONTROLS

Deployable antenna control requirements include precision control of the reflector surface and feed-mast motion compensation as shown in figure 8. Since the dynamics of the dish structure, feed mast, and mesh are highly interactive and the structure and control subsystems are so intimately related, a complete system including all of the structural elements and a control system is required for flight testing. In addition, in order to achieve system performance, both the hoop column and wrap-rib configurations require distributed control with actuators at the reflector hub and mast tip.

- GROUND-BASED TESTS VALIDATE THEORY
- FLIGHT EXPERIMENT TO DEMONSTRATE:

STRUCTURAL INTERACTION ↕ MESH

- MODAL DAMPING/VIBRATION SUPPRESSION
- FEED MOTION COMPENSATION
- PRECISION SURFACE/SHAPE CONTROL

REQUIRES A STRUCTURAL SYSTEM

- DISH STRUCTURE
- FEED MAST
- MESH

- WANT GROUND-DYNAMICS STRUCTURE TEST PRECEEDING FLIGHT EXPERIMENT
- FLIGHT EXPERIMENT REQUIRES MULTIPLE DISTRIBUTED SENSORS
- FLIGHT EXPERIMENT REQUIRES ACTUATORS AT FEED & DISH FOR MODAL/ VIBRATION SUPPRESSION

MINIMUM DISTRIBUTED CONTROL

Figure 8

SYSTEM FLIGHT-TEST REQUIREMENTS

Figure 9 identifies discipline validation requirements to be satisfied by the antenna-system flight test. The system test will also assess discipline interactions and total system performance. Note that structure dynamics, systems identification, and distributed control are technology issues that can be satisfied by an antenna flight experiment that is applicable to large space systems across the board.

- RF PERFORMANCE VALIDATION
  - SURFACE ACCURACY
  - FEED ALIGNMENT
  - FEED PERFORMANCE
  - ELECTROMAGNETIC SYSTEM PERFORMANCE
- POINTING AND CONTROL VALIDATION
  - DYNAMIC MODELING
  - PARAMETER IDENTIFICATION
- DEPLOYMENT DYNAMICS VALIDATION
  - KINEMATICS
  - LOADS
  - RELIABILITY
  - CONTOUR ACCURACY
  - MULTI-ELEMENT INTERACTION

Figure 9

RELATED ISSUES

Other issues that affect planning for the antenna flight test are highlighted in figure 10. Due to the complexity of the antenna system, an in-depth assessment of interactions with the Shuttle and its capability must be made. An instrumentation and data-collection system that satisfies integrated system and subsystem requirements is needed. The flight test must address technologies that relate to the maximum number of applications. Finally, the experiment must choose a configuration that maximizes technology benefit for reasonable cost.

- SHUTTLE CAPABILITY/EXPERIMENT INTERACTION
- INSTRUMENTATION AND DATA COLLECTION
- AFFORDABILITY
- APPLICATIONS
- CONFIGURATION

Figure 10

MISSION REQUIREMENTS OF ANTENNA FLIGHT TEST

Technology is being developed for future mission applications as shown in figure 11. The antenna flight experiment must be configured to advance technology that captures as many mission requirements as possible. Cost will be the factor that limits the number and resolution to which these requirements can be met.

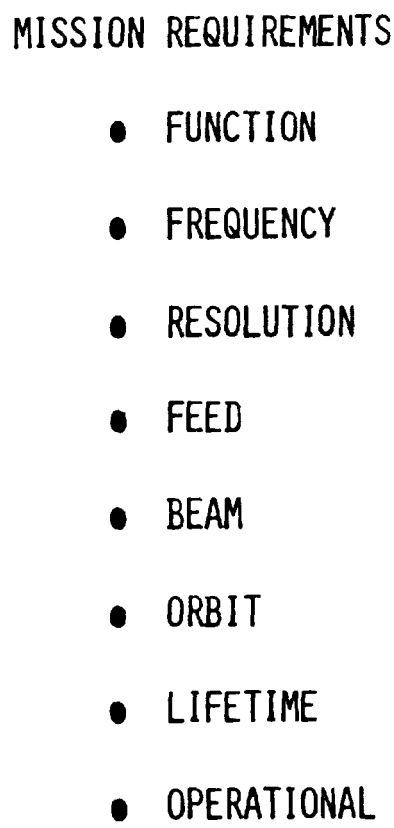

Figure 11

CANDIDATE CONFIGURATIONS OF ANTENNA FLIGHT TEST

The antenna flight experiment must be a configuration that best satisfies technology objectives and maximizes technology advancement for the least cost. Listed in figure 12 are candidate configurations that must be assessed against these criteria to determine the optimum flight-experiment configuration.

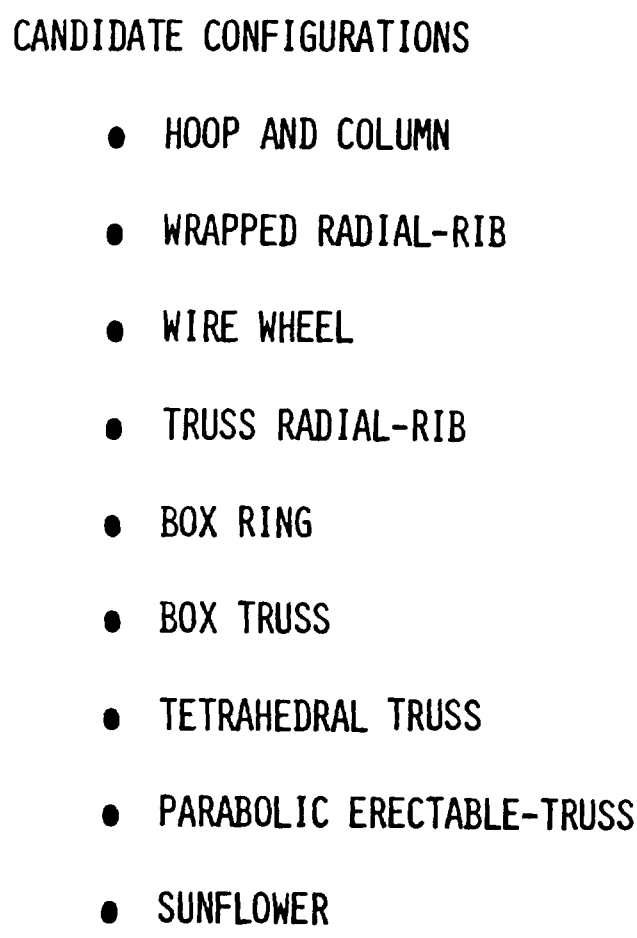

Figure 12

PREPARATION FOR ANTENNA FLIGHT TEST

Planning for the antenna flight test in the FY 1987 time frame is being initiated this year as shown in figure 13. FY 1982 activities will focus on preparations for the phase B procurement which is to start in mid FY 1983. In phase B flight-experiment selection criteria (see fig. 14) will be developed and procurement documentation prepared. The competition will be open to all concepts with a configuration being selected for maximum technology benefit with the widest mission applicability. A single contractor will be chosen for phases B and C/D to coparticipate in the experiment development with NASA in-house technologists. Phase B funding will be appropriated by the Spacecraft Systems Office (OAST, NASA Headquarters) and phase C/D funding with new start budgetary allocations beginning in FY 1985. Initial ground hardware designed and fabricated during phase B will roll over into the phase C/D program as protoflight hardware to accelerate the C/D start and eliminate hardware replication costs.

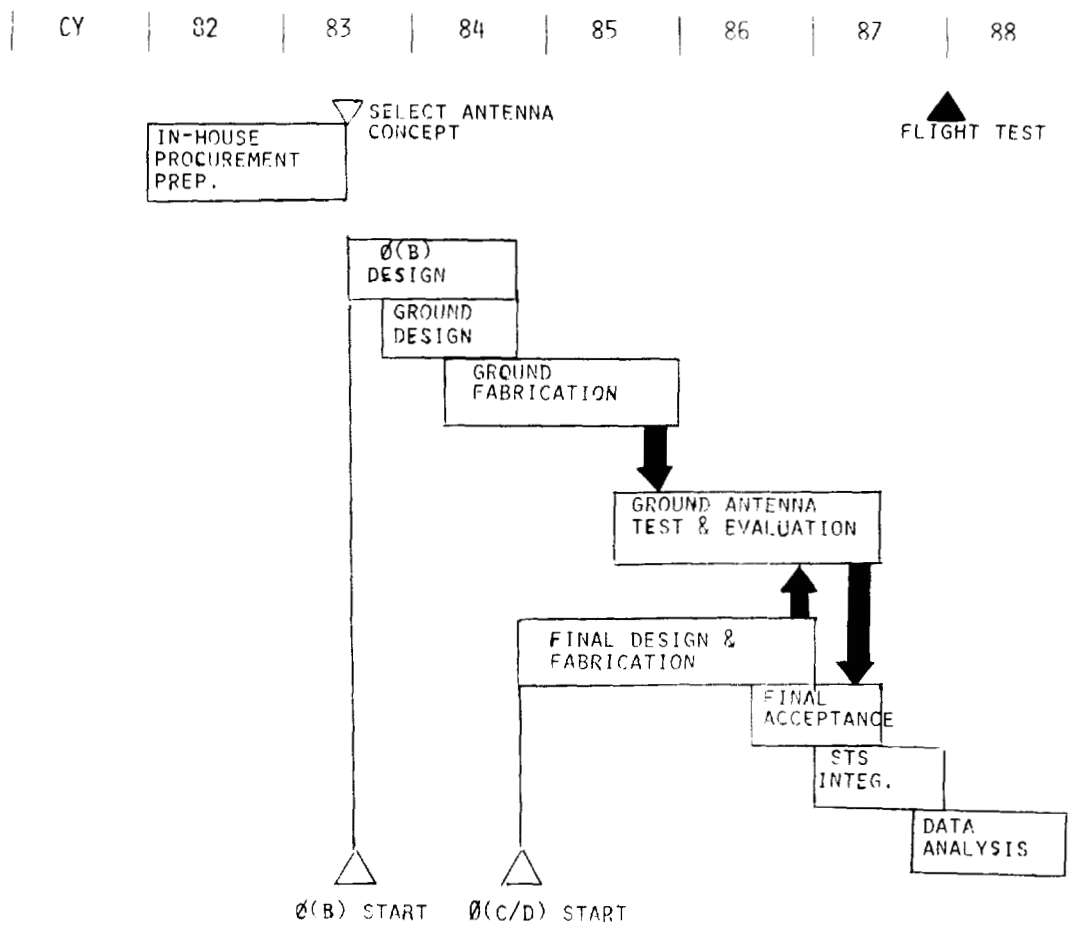

Figure 13

- DEVELOP SELECTION CRITERIA
- OPEN-CONCEPT COMPETITION
- CHOOSE CONFIGURATION FOR MAXIMUM TECHNOLOGY BENEFIT CONSIDERING: MISSION APPLICABILITY/AFFORDABILITY
- EXPERIMENT DEVELOPMENT:
  - IN-HOUSE NASA
  - INDUSTRY
- SINGLE CONTRACTOR - PHASE B, C, D
- FUNDING:
  - RSS - THROUGH Ø(B)
  - BALANCE BUDGETARY

Figure 14

THE EFFECTS OF ELECTRON AND GAMMA RADIATION ON EPOXY-BASED MATERIALS

R. E. FORNES, J. D. MEMORY, R. D. GILBERT
NORTH CAROLINA STATE UNIVERSITY
RALEIGH, NORTH CAROLINA

AND

E. R. LONG, JR.
MATERIALS DIVISION
NASA LANGLEY RESEARCH CENTER
HAMPTON, VIRGINIA

LARGE SPACE SYSTEMS TECHNOLOGY - 1981
THIRD ANNUAL TECHNICAL REVIEW
NOVEMBER 16-19, 1981

Radiation effects on epoxy-based materials are being studied at North Carolina State University under a grant (NSG-1562) from the Materials Division of the NASA Langley Research Center. The research is conducted by members of the School of Textiles, Department of Textile Chemistry and Department of Fiber and Polymer Science, and the School of Physical Sciences and Applied Mathematics, Department of Physics and Department of Chemistry. The objectives of this work are to evaluate the effects of radiation on the mechanical properties of epoxy-based structural materials and to measure the fundamental radiation-generated events which cause the changes in mechanical properties. The approach to these objectives is the exposure of specimens of graphite/epoxy composites and epoxy resins to electron and gamma radiation, followed by mechanical property and fundamental measurements. This report will present a portion of the data which has been gathered to date.

OBJECTIVE

EVALUATION OF THE EFFECTS OF RADIATION ON THE MECHANICAL PROPERTIES OF EPOXY-BASED STRUCTURAL MATERIALS.

MEASUREMENT OF THE FUNDAMENTAL, RADIATION-GENERATED EVENTS WHICH CAUSE THE CHANGES IN MECHANICAL PROPERTIES.

APPROACH

EXPOSURE OF SPECIMENS OF GRAPHITE EPOXY COMPOSITE AND EPOXY RESIN TO ELECTRON AND GAMMA RADIATION.

MEASUREMENT OF CHANGES IN THE VALUES OF MECHANICAL AND FUNDAMENTAL PROPERTIES.

Figure 1

RADIATION EFFECTS ON FLEXURAL PROPERTIES OF A GRAPHITE/EPOXY COMPOSITE

The flexural properties of miniature (25 mm x 13 mm x 0.51 mm) unidirectional specimens of T300/5208 composite for electron radiation exposures in vacuum for doses up to and including 8×10^9 rads are shown in figures 2a and 2b. The specimens were fabricated at Langley Research Center from prepreg material. The fiber direction was in the direction of specimen length (longitudinal), so the flexural properties were fiber-dominated. Each datum point is the mean of ten specimens. The 95 percent confidence-of-fit bands for the mean are also shown. The strength appears to slightly increase with dose, approximately four percent at 8×10^9 rads, while the modulus appears unaffected. However, the size of the confidence band is sufficiently large that the location of the mean is uncertain to the extent that larger, perhaps significant, changes in flexural properties with radiation could have occurred. The appreciable uncertainty in the location of the mean does suggest that an additional emphasis on quality control of specimen preparation and/or testing procedures may be necessary.

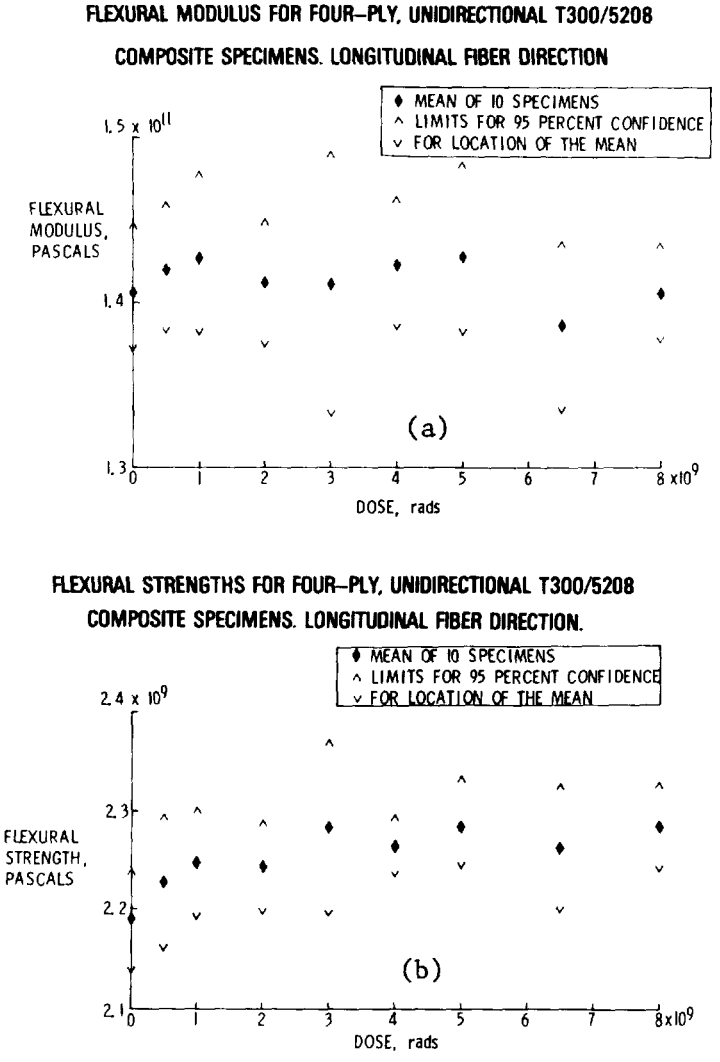

Figure 2

RADIATION EFFECTS ON FLEXURAL PROPERTIES OF A GRAPHITE/POLYIMIDE COMPOSITE

Similar exposures to electron radiation have been made on flexural unidirectional C6000/PMR15 composite specimens, with a longitudinal fiber orientation. The effects on flexural properties were very similar to those just shown for the graphite/epoxy composite material. In figures 3a and 3b, flexural data for specimens of the C6000/PMR15 composite with a transverse fiber orientation are shown for radiation doses also up to and including 8 x 10^9 rads. The specimens were fabricated at Langley Research Center from neat resin and tows of graphite fiber. For the transverse fiber direction, the means suggest no change in either modulus or strength. But, again the uncertainty in the location of the mean may have masked a more appreciable, perhaps significant, change due to the radiation. Transverse-oriented fiber, unidirectional flexural specimens of the graphite/epoxy composite will be studied in the future. Specimen preparation and testing procedures will be an important consideration while planning and conducting these tests.

FLEXURAL MODULI FOR FOUR-PLY, UNIDIRECTIONAL C6000/PMR15 COMPOSITE SPECIMENS. TRANSVERSE FIBER DIRECTION.

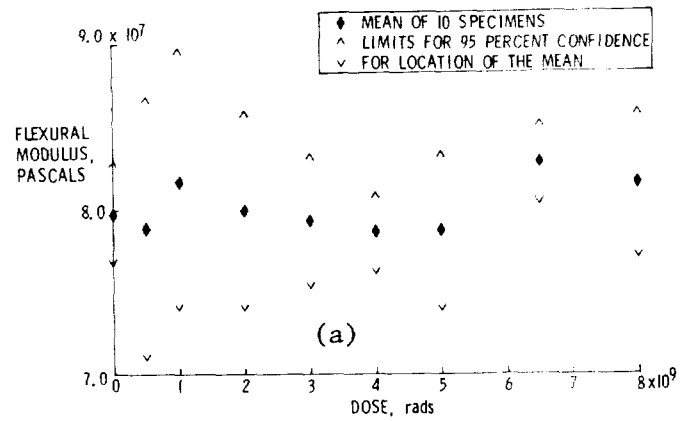

FLEXURAL STRENGTHS FOR FOUR-PLY, UNIDIRECTIONAL C6000/PMR15 COMPOSITE SPECIMENS. TRANSVERSE FIBER DIRECTION

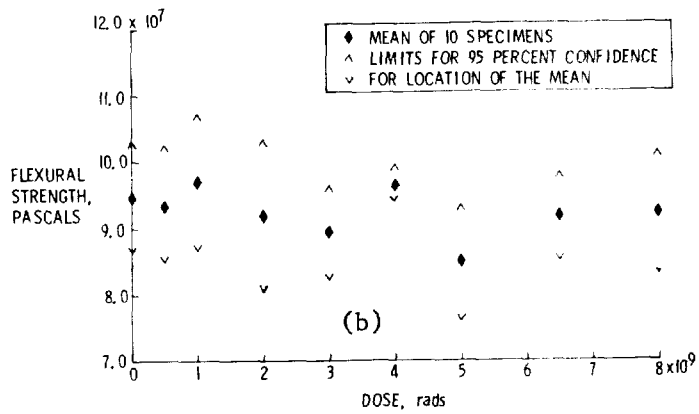

Figure 3

SCANNING ELECTRON MICROSCOPY OF FIBER/RESIN COMPOSITES

Photographs from scanning electron microscopic analysis of the failure edge of a flexural specimen are shown in figure 4a for T300/5208 and in figure 4b for C6000/PMR15. Neither pair of photographs shows a difference in the failure mode at the fiber-resin interface due to radiation exposure. Since the fiber-resin interaction is more mechanical interlocking than chemical interaction, the lack of change in the failure mode had, to a certain extent, been anticipated.

SCANNING ELECTRON PHOTOGRAPHS OF THE FAILURE EDGE OF FLEXURAL SPECIMENS OF GRAPHITE/EPOXY COMPOSITE.

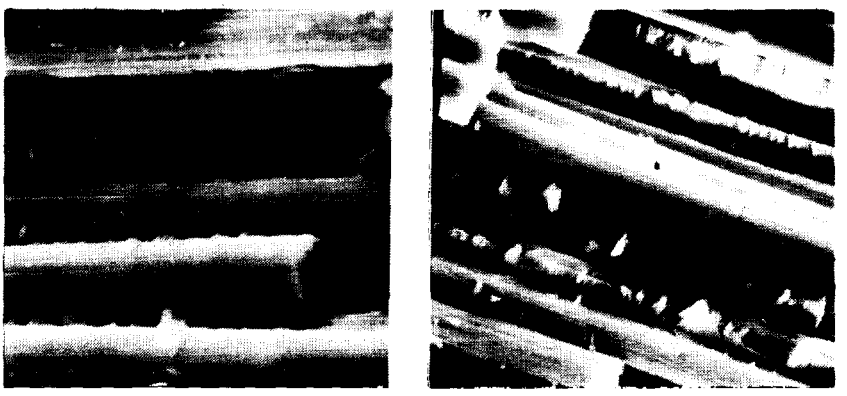

DOSE = 0 rads (a) DOSE = 8×10^9 rads

SCANNING ELECTRON PHOTOGRAPHS OF THE FAILURE EDGE OF FLEXURAL SPECIMENS OF GRAPHITE/POLYIMIDE COMPOSITE

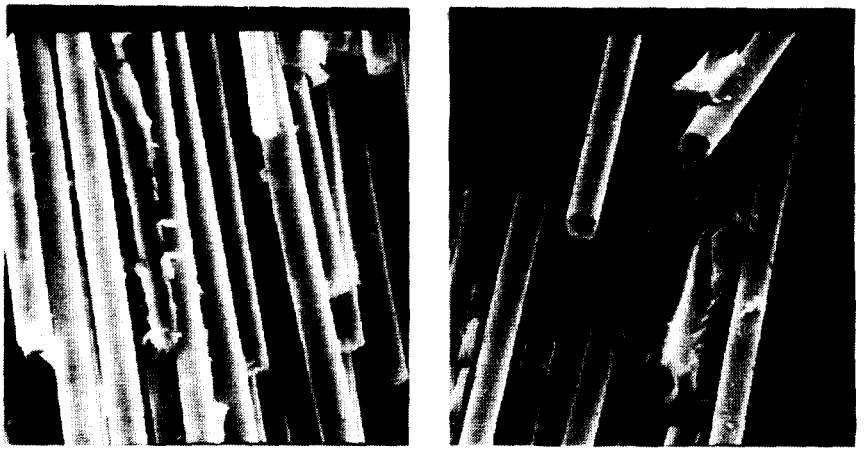

DOSE = 0 rads (b) DOSE = 5×10^9 rads

Figure 4

X-RAY DIFFRACTION ANALYSIS OF GRAPHITE/EPOXY COMPOSITE

Figure 5a is a pair of X-ray diffraction photographs of T300/5208 composite with no radiation exposure and with a radiation dose of 8×10^9 rads. There is no change in either the diffuse scatter due to the resin or the broad diffusion peak along the equator due to the graphite fiber. Therefore, the radiation did not affect the crystallinity, either of the amorphous resin or of the graphite fiber which originally consisted of either very small-size crystalline structure or numerous defects. A lack of change in crystallinity confirms that atomic displacement is not one of the effects of electron radiation. Figure 5b is a microdensitometric trace of the photographs. The amplitudes of the traces confirm that no differences exist.

WIDE ANGLE X-RAY PHOTOGRAPHS OF T300/5208 COMPOSITE WITH AND WITHOUT EXPOSURE TO ELECTRON RADIATION.

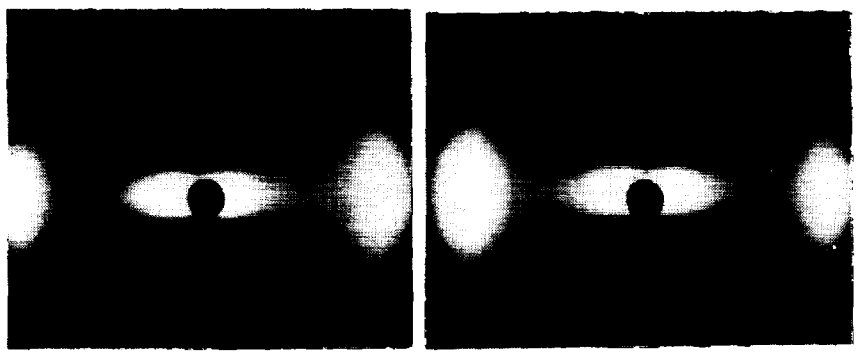

DOSE = 0 rads (a) DOSE = 8×10^9 rads

MICRODENSITOMETER TRACES OF WIDE ANGLE X-RAY PHOTOGRAPHS OF T300/5208

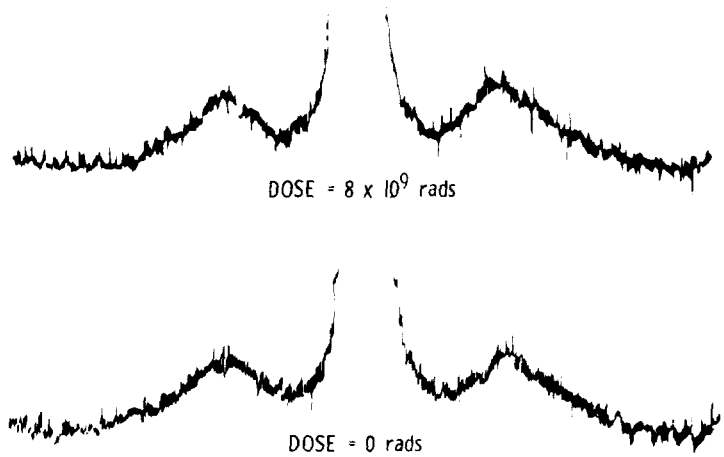

(b)

Figure 5

ELECTRON SPIN RESONANCE SPECTROSCOPIC ANALYSIS OF RADIATION EFFECTS

The major effect of radiation upon polymeric materials is the creation of chemical radicals, which are groups with unpaired electrons in molecular orbitals. The presences of these unpaired electrons in a specimen are measured by electron spin resonance (or electron paramagnetic resonance) spectroscopy. The specimen is simultaneously subjected to a fixed frequency signal and a sweeping magnetic field. At a particular combination of signal and field, characteristic of the electron's environment, the unpaired electron's spin is flipped and a net absorption of energy is detected. Usually, the absorption is detected in its first derivative form, as shown in figure 6a for tetraglycidyl diamino diphenyl methane, TGDDM, which has been cured with diamino diphenyl sulphone, DDS. The signal of diphenylpicrylhydrazyl, DPPH, is also shown because it is included with the specimen for calibration purposes. The epoxy's signal shown in figure 6a is due to radiation-generated radicals, the number of which varies with dose. The signal magnitude, position, and structure vary with radiation dose as shown in figure 6b.

ELECTRON SPIN RESONANCE SPECTRA OF ELECTRON-IRRADIATED EPOXY

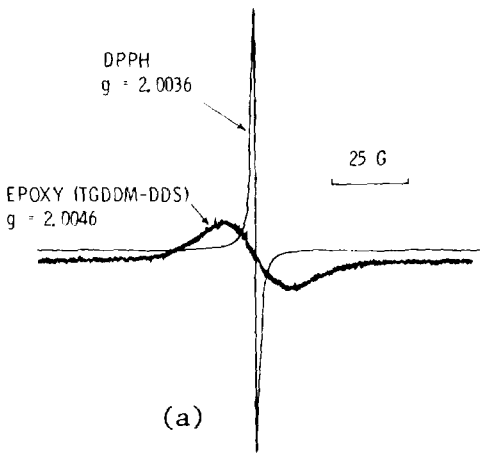

ELECTRON SPIN RESONANCE OF ELECTRON-IRRADIATED EPOXY (TGDDM-DDS)

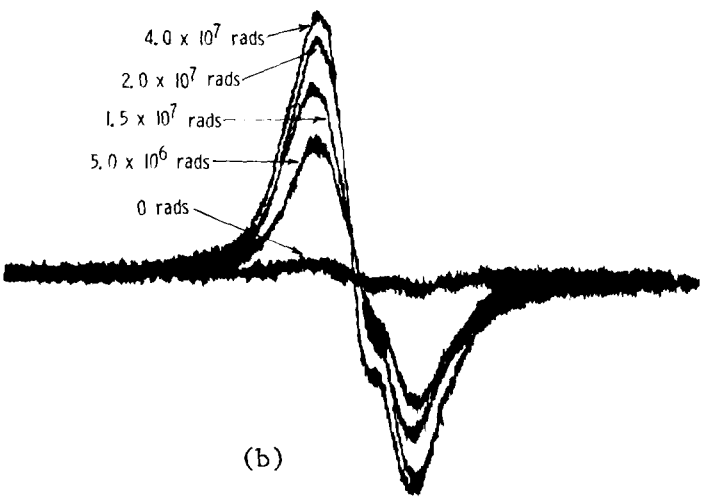

Figure 6

ELECTRON RADIATION-GENERATED RADICAL CONCENTRATIONS AND DECAYS IN EPOXY RESINS

The variation of radical concentration in the cured epoxy resin TGDDM-DDS with dose after room temperature exposures to electron radiation is shown in figure 7a. For 1.3×10^8 rads, the radical concentration at the end of exposure is approximately 1.9×10^{18} spins/g, or one spin for every 55 molecules. Figure 7b shows the decay in radical concentration at room temperature with time after exposure. Two radical distributions are present, as suggested by the sharp change in the slopes of the curves in figure 7b, one with a half-life on the order of twelve minutes and another with a much longer half-life. Consequently, the total number of spins per gram which occurred over a long exposure period was much larger than the value at the end of exposure and may have amounted to only several molecules per spin. The current literature suggests that each spin would probably, in the end, generate a cross-link or chain scission. In contrast, based upon the mechanical data discussed earlier, the radicals within this epoxy may have decayed in a process of self-healing. But, we must also point out that the EPR data, because of the large radical concentration, can be suggesting a review of the techniques used for the measurements of mechanical properties.

INITIAL RADICAL CONCENTRATIONS IN EPOXY RESIN AFTER ELECTRON IRRADIATION

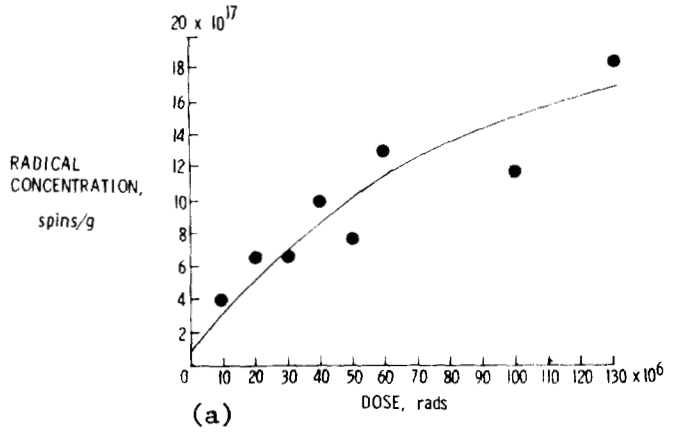

ROOM-TEMPERATURE DECAY OF ELECTRON-RADIATION-GENERATED RADICALS IN EPOXY RESIN

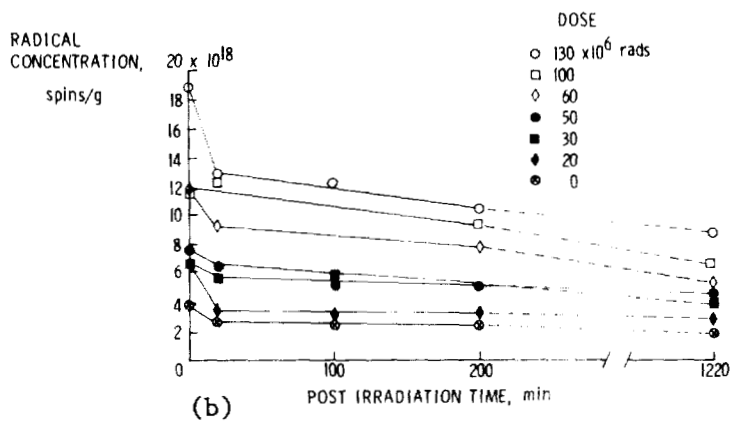

Figure 7

GAMMA RADIATION-GENERATED RADICAL CONCENTRATIONS AND DECAY IN EPOXY RESIN

Radical concentrations in epoxy resin for a range of doses from gamma radiation are shown in figure 8a. The concentrations up to the maximum dose studied, 6 x 10^7 rads, are approximately twice that for electron radiation. The higher density may be due to the fact that the gamma exposures were conducted at cryogenic temperatures; hence, short-lived species were trapped. This appears, to an extent, to be the case from the decay data shown in figure 8b. Presently, three radical distributions, each with different half-lives, are believed to be within these decay data. The concentration at end of exposure and the decay during exposure suggest, as in the case of the electron radiation, that the total spin formation was sufficient to cause changes in mechanical properties, unless self-healing was the dominant process. Additional studies using EPR for the study of epoxy resin after electron and gamma radiation will be conducted to measure radical densities at higher doses and related to the mechanical data, both for this and other epoxy systems.

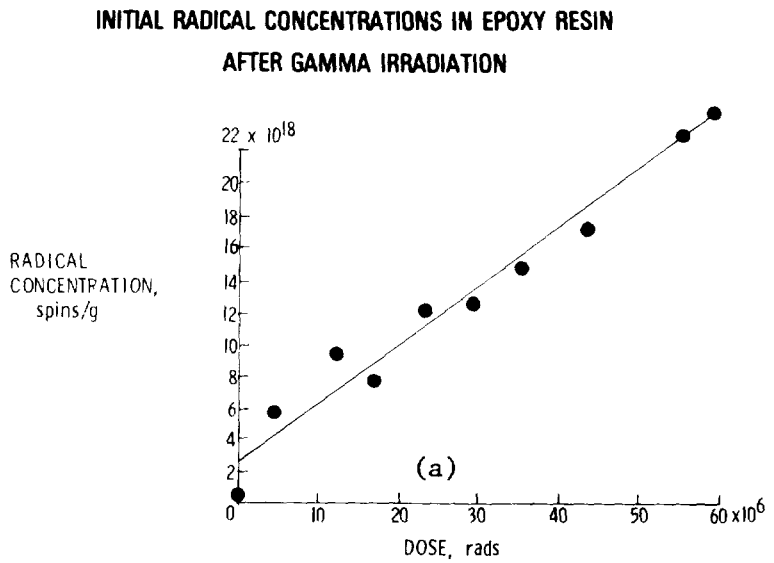

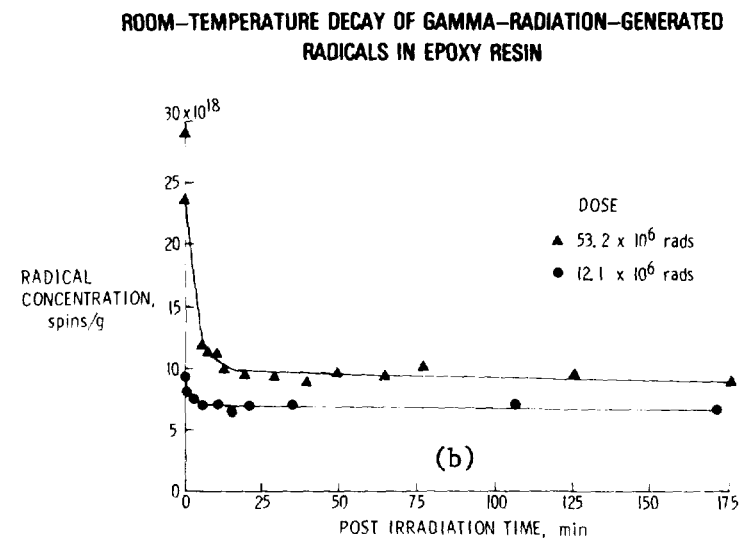

Figure 8

SUMMARY

The study at North Carolina State University has, to date, shown little or no change in flexural properties of miniature specimens of a graphite/epoxy composite due to exposure to electron and to gamma radiation. (A study of just the flexural properties of specimens of a graphite/polyimide composite also showed little or no change due to exposure to radiation.) In addition, no change in failure mode at the fiber-resin interface and in the crystallinity of the fiber and the resin has been found. The absence of changes at the fiber-resin interface and in the crystallinities was expected. However, the observation of only a small change in flexural properties was a pleasant surprise. Some doubt in the observation of stable flexural properties is cast, though, by electron paramagnetic resonance spectra of a relatively large number of radiation-generated radicals. The latter generally lead to a change in cross-linking and in chain-scissioning which should alter mechanical properties. Consequently, the measurements of flexural properties will continue, both for the epoxy discussed in this report and for simpler epoxy systems. Also, fundamental analysis will be conducted for the higher doses used in the mechanical property studies. EPR and other fundamental methods will be used to better understand the chemical changes and mechanisms caused by the radiation.

SUMMARY

RESULTS

1. - NO MAJOR CHANGES IN FLEXURAL PROPERTIES OF SPECIMENS OF A GRAPHITE EPOXY COMPOSITE FOR RADIATION DOSES UP TO 5×10^9 rads.

2. - NO CHANGES IN THE FAILURE MODE AT THE FIBER-RESIN INTERFACE OR IN THE CRYSTALLINITY OF THE FIBER OR THE RESIN FOR RADIATION DOSES UP TO 5×10^9 rads.

3. - A HIGH CONCENTRATION OF RADIATION-GENERATED RADICALS WITH MULTIPLE DECAY CONSTANTS FOR DOSES UP TO 130 Mrads.

FUTURE WORK

1. - CONTINUED STUDY OF FLEXURAL PROPERTIES OF EPOXY-BASED MATERIALS FOR SEVERAL EPOXY SYSTEMS.

2. - FUNDAMENTAL ANALYSIS FOR CHARACTERIZATION OF RADIATION EFFECTS ON THE CHEMICAL STRUCTURE OF EPOXY RESINS

Figure 9

BASIC PHYSICAL AND CHEMICAL PROCESSES IN SPACE RADIATION EFFECTS ON POLYMERS

E. Kamaratos
Department of Chemistry
Christopher Newport College
Newport News, VA 23606

J. W. Wilson
NASA Langley Research Center
Hampton, VA 23665

C. K. Chang
Department of Chemistry
Christopher Newport College
Newport News, VA 23606

Y. J. Xu
Department of Physics
Old Dominion University
Norfolk, VA 23508

Large Space Systems Technology - 1981
Third Annual Technical Review
November 16-19, 1981

SPACE RADIATION PHYSICS AND CHEMISTRY

Space ionizing radiation-induced changes in a structural material are initiated by energetic charged particle impact which transfers kinetic energy of the particle via its coulomb field into electronic excitation energy of the material. In complex molecules, the electronic energy is usually shared among various vibrational modes through potential surface crossing phenomena which depend intimately on the molecular structure (ref. 1). Radicals produced through bond rupture are usually placed on a highly repulsive potential surface which may subsequently lead to reactions not accessible at thermal energies in the early phases. The time progression proceeds under conditions of near thermal equilibrium after <1 nsec and reactions are akin to the more usual chemical processes (ref. 2). In the solid state, long lived radicals result from their lack of mobility and chemical activity ends only after long time periods which depend on the temperature. It is natural for laboratory studies to begin with final chemical products to infer events leading to their production. It is more natural from a physicist's point of view to consider the initial impact and energy handling processes. In the future we should meet in the middle of the diagram with some understanding of the radiation degradation of polymers. In the present report we are interested mainly in the energy absorption and the immediately following events.

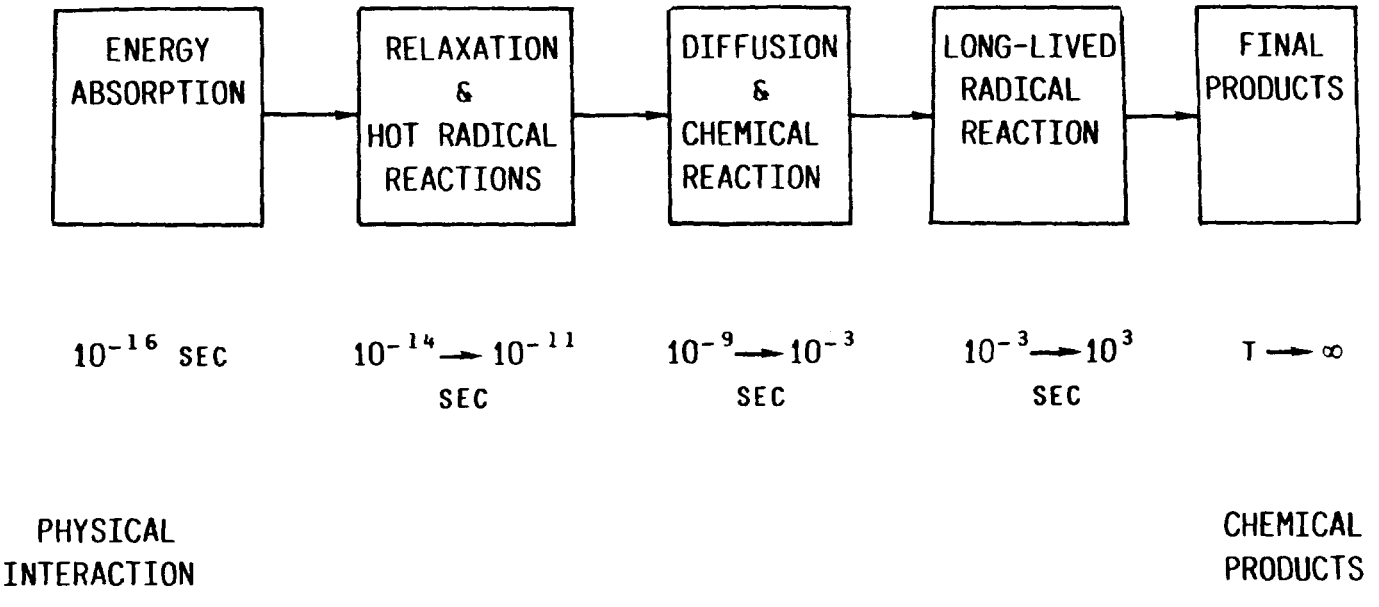

ENERGY ABSORPTION

There are three major questions concerning the energy absorption event. First we should consider how the energy is imparted to the molecule followed by the second question of how the energy was handled by the system leading to the final collision products. These final collision products are the chemically active species which lead to the ultimate change in the material. Of nearly equal importance to what is produced is the third question relating to the spatial distribution of various product types in relation to the charged particle trajectory. We shall consider these questions in more detail.

ENERGY ABSORPTION

A) INTO WHAT MOLECULAR MODES OF THE POLYMER IS THE ENERGY DEPOSITED?

B) WHAT ARE THE CORRESPONDING COLLISION PRODUCTS?

C) WHAT IS THE SPATIAL DISTRIBUTION OF THESE COLLISION PRODUCTS?

COLLISIONAL ENERGY LOSS IN POLYMERS

The energy transferred per unit distance traveled by a passing charged particle to molecules as derived by Bethe (ref. 3) is shown. That the passing coulomb field appears as a field of virtual photons is evidenced by the strong dependence of the stopping power on the optical dipole oscillator strengths, f_n, and the corresponding excitation enery levels, E_n. As chemical bonds are altered, there is a shift in the excitation energies, E_n, and a shift in oscillator strengths as well (ref. 4), consequently the energy deposit depends on the specific molecular structure. The energy deposit, dE, over a distance, dx, of the trajectory is spread laterally from the particle path according to cylindrical symmetry. Ehrenfest's theorem requires the interaction time to be short compared to the oscillator's period and empirically the photon transfer probability to a level E_n is given (ref. 5) by P_n. Clearly the most energetic molecular states are excited near the particle path and the lateral extent of excitation expands with increasing particle velocity. Note that the high energy ionization processes (i.e. large E_n) lie nearest the particle path but the energetic secondary electrons migrate far from the initial particle trajectory (ref. 6). A fundamental quantity is the mean excitation energy, I, which is related to dipole oscillator strengths, f_n, and energy levels, E_n, as shown. This quantity will be studied for effects due to chemical bonding.

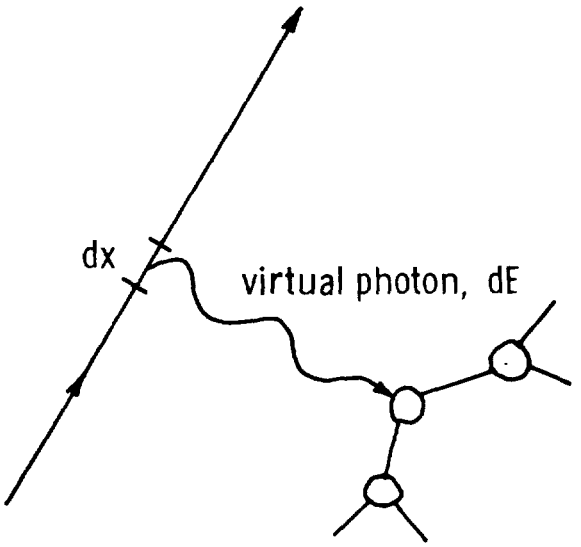

STOPPING POWER

$$\frac{DE}{DX} = \left[\frac{4\pi N Z_1^2 E^4}{MV^2}\right] \sum_N F_N \ell N \left[\frac{2MV^2}{E_N}\right]$$

LATERAL EXTENT

$$P_N = \text{EXP}\left[-\left(\frac{E_N}{3HV}\right) R\right]$$

FUNDAMENTAL QUANTITY

$$Z \ell N(I) = \sum_N F_N \ell N(E_N)$$

LOCAL PLASMA MODEL FOR POLYMERS

The calculation of excitation energies and oscillator strengths of polymers is beyond present day computational ability. Considerable simplification can be made through replacement of the molecule by an equivalent spatial dependent plasma (ref. 7). The stopping power is now expressed in terms of the local plasma density, $\rho(r)$, and the corresponding plasma frequency, ω_p. The lateral extent of the energy deposit, P_p, and the mean excitation energy, I, are now also given in terms of the local plasma model. To effectively use this model for molecular calculations, means of simple approximation to the electron density of the molecule must be found. For this purpose we used the Gordon-Kim electron gas model (ref. 8) of molecular bonds for the estimation of chemical bond effects (refs. 9-10). The main value of the local plasma model is it's utter simplicity. The accuracy of the local plasma model is tested here by applying the relation between the mean excitation energy, I, and the local plasma density as a fundamental quantity to ionizing radiation interaction.

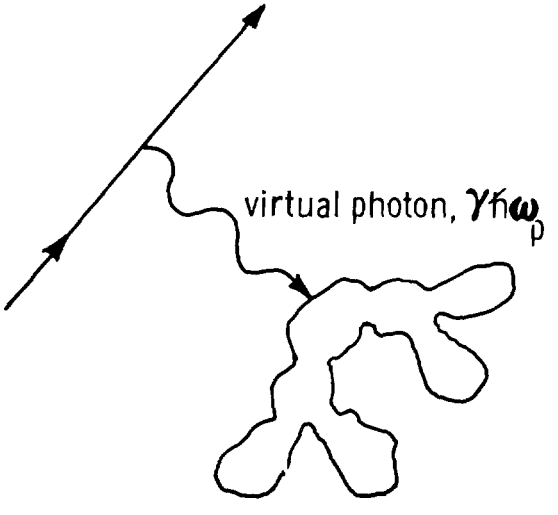

STOPPING POWER

$$\frac{DE}{DX} = \left[\frac{4\pi NZ_1^2 E^4}{MV^2}\right] \int \rho(R)\, \ell N \left[\frac{2MV}{\gamma H \omega_p}\right] D^3R$$

$$\omega_p = \sqrt{4\pi E^2 \rho(R)/M}$$

LATERAL EXTENT

$$P_p \sim EXP\left[-\left(\frac{\gamma H \omega_p}{3HV}\right) R\right]$$

FUNDAMENTAL QUANTITY

$$Z\, \ell N(I) = \int \rho(R)\, \ell N\, (\gamma H \omega P)\, D^3R$$

CHEMICAL BOND EFFECTS ON MEAN EXCITATION ENERGIES

The mean excitation energies of several molecules related to the polymer problem have been calculated according to the local plasma approximation. The values labeled "atomic" are those obtained using the Bragg rule (ref. 11), in which chemical bond effects are neglected, with the accurate atomic values of Inokuti and coworkers (ref. 12). The present theoretical results are shown for comparison. In addition, experimental results are also shown for which the merit of the present theory is clearly displayed. We conclude from these comparisons that the local plasma model gives an adequate representation of particle impact with the polymer, although the coupling between the electronic mode excited and the remaining vibrational-rotational modes of the polymer are yet undetermined. In search of empirical evidence of the polymer's reaction to the impact we have examined specific fragmentation data from mass spectroscopy.

$$I = \exp\left[Z^{-1} \int \rho(R) \ln\left(\gamma H \omega_p\right) D^3R\right]$$

	Atomic	Present Theory	Experimental
CH_4	35.1	44.7	42.8
$(CH_2)_x$	43.5	55.0	53.4
C_6H_6	50.6	60.6	61.4±1.9
H_2	15.0	18.9	18.5±0.5
Graphite	62.0	76.1	78.5±1.5

STRUCTURE OF AN EPOXY POLYMER

A repeating unit is shown in the structure of an epoxy resin produced by curing tetraglycidyl methylenedianiline with diamino diphenyl sulfone (ref. 13). This resin is one of the resins that are reported to be under investigation for possible use in composite materials for applications ranging from Army materiel to aircraft and space structures. An interesting characteristic of this polymer is the presence of several tertiary amino functional groups in the repeating unit that impart certain chemical properties to the polymer like, e.g., those of a weak base. These chemical properties may lead to degradation of the mechanical properties, in addition to increase in weight, on chemical reaction (e.g., with CO_2 and atmospheric pollutants). The association and subsequent reaction of the amino groups with molecules of water may have an effect on the NMR line observed with the soaked polymer that was recently ascribed to a state of the water molecules "perhaps hydrogen bonded to the polymer" (ref. 14). In addition to the amino functional group there are two additional functional groups in the repeating unit: the -OH (hydroxyl) and the $-SO_2$ (sulfonyl) functional groups. The presence of functional groups may also be important in the determination of transients formed after the transfer of energy from ionizing radiation to a polymer. Since electrons penetrate into matter deepest and are the primary constituents of the space ionizing radiation, and since all ionizing radiation in space leads to the formation of secondary electrons on interaction with matter, it is of general interest to investigate the effect of electron impact on molecules first. From this viewpoint it is of interest to study the role of functional groups in electron impact fragmentation of molecules. Because of the predominant production of positive ions (usually, but not always, by orders of magnitude) over that of negative ions on electron-impact and the larger availability of mass spectra for positive ions, this investigation started with positive ions first. However, the possibility of an important role for negative ions should not be discounted.

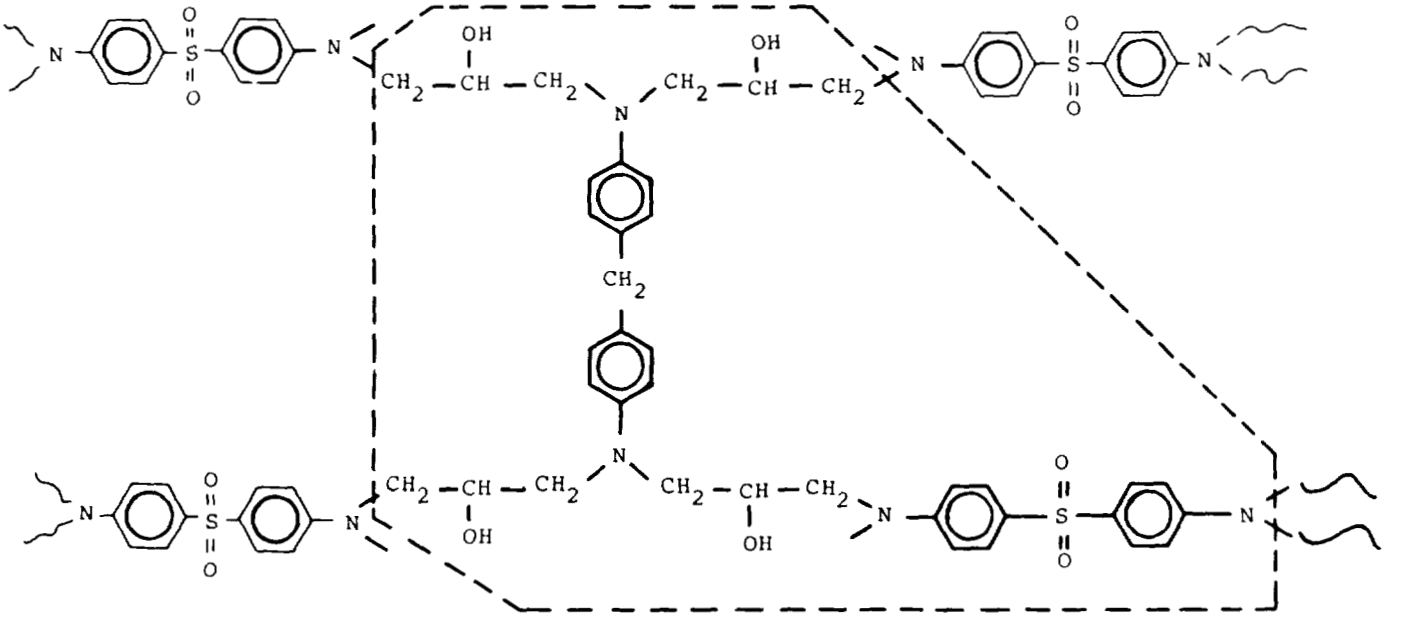

ELECTRON-IMPACT MASS SPECTRA OF MOLECULES WITH AN AMINO GROUP

Mass spectra of some molecules that contain amino functional groups are shown (ref. 15). It has been observed experimentally that among several chemical functional groups, including the hydroxyl and amino groups, that are present as substituents in aliphatic chemical compounds the amino functional group influences the chemical bond scission and ionization on electron impact the most strongly (refs. 16-17). The extent of substitution on the amino group itself appears to increase the influence of the amino group on the dissociative ionization. The dominant bond scission is that between α and β carbon atoms in hydrocarbon chains, leading to the formation of imonium ions. In aromatic amines with no α and β carbon atoms in aliphatic groups the parent ion or the alkyl substituted amino group ion may be formed predominantly.

93 C_6H_7N 62-53-3
Benzenamine

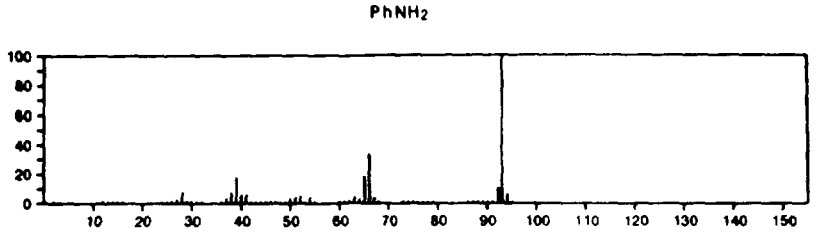

149 $C_{10}H_{15}N$ 91-66-7
Benzenamine, *N*,*N*-diethyl-

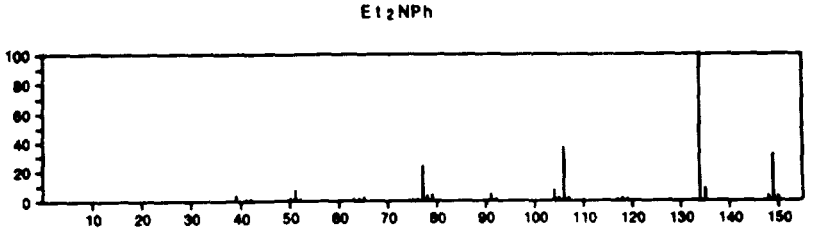

177 $C_{12}H_{19}N$ 53927-61-0
Benzenamine, *N*-(2,2-dimethylpropyl)-*N*-methyl-

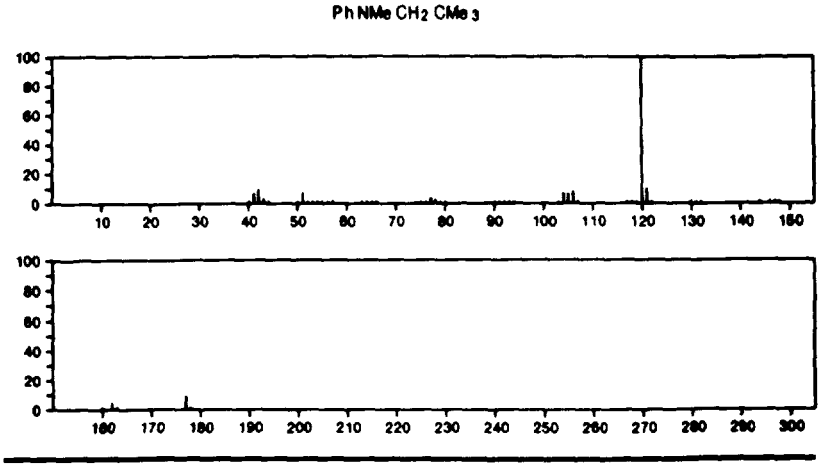

ELECTRON-IMPACT MASS SPECTRA OF LARGE MOLECULES WITH AMINO GROUPS

Structural formulae and electron-impact mass spectra are shown for additional molecules that have amino functional groups as their substituents and, in addition, appear to be constituents to some extent of the repeating unit in the structure of the polymer. The fragmentation pattern on electron-impact of these and other compounds to be investigated may lead to the identification of some of the sites of bond scission and of ions and radicals that may be formed under the action of ionizing radiation on the polymer.

198 $C_{13}H_{14}N_2$ **101-77-9**

Benzenamine, 4,4'-methylenebis-

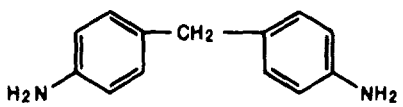

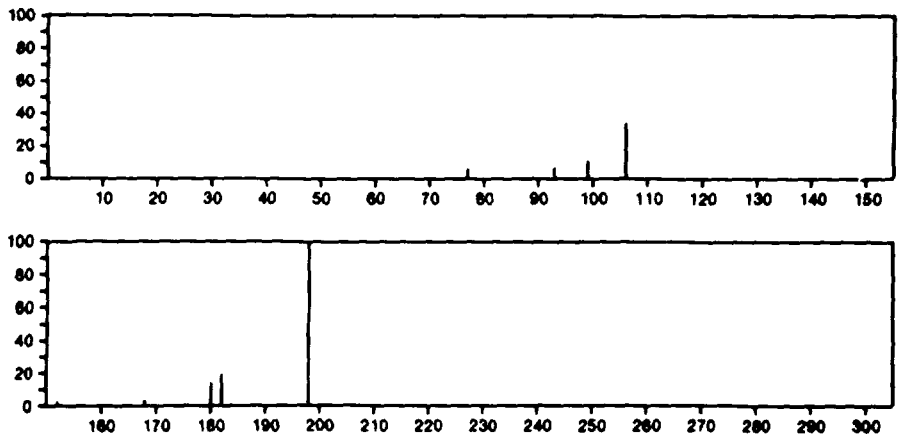

268 $C_{17}H_{20}N_2O$ **90-94-8**

Methanone, bis[4-(dimethylamino)phenyl]-

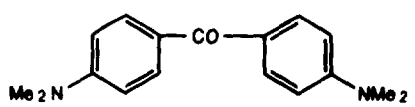

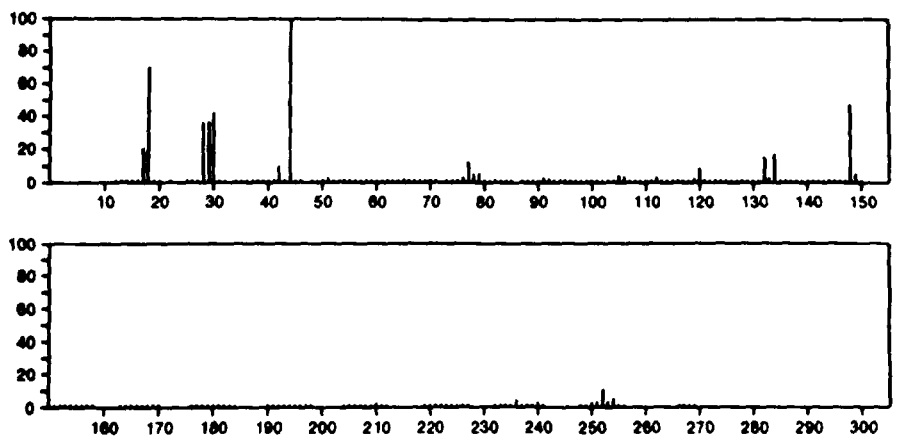

ELECTRON-IMPACT MASS SPECTRA OF MOLECULES WITH A HYDROXYL GROUP

The electron-impact mass spectra of several molecules that contain the hydroxyl functional group are shown. The hydroxyl group in aliphatic compounds appears to favor ionization and scission of the bond between α and β carbon atoms with respect to the hydroxyl group, although much less dominantly compared to the amino group.

198 $C_{14}H_{14}O$ **614-29-9**

Benzeneethanol, α-phenyl-

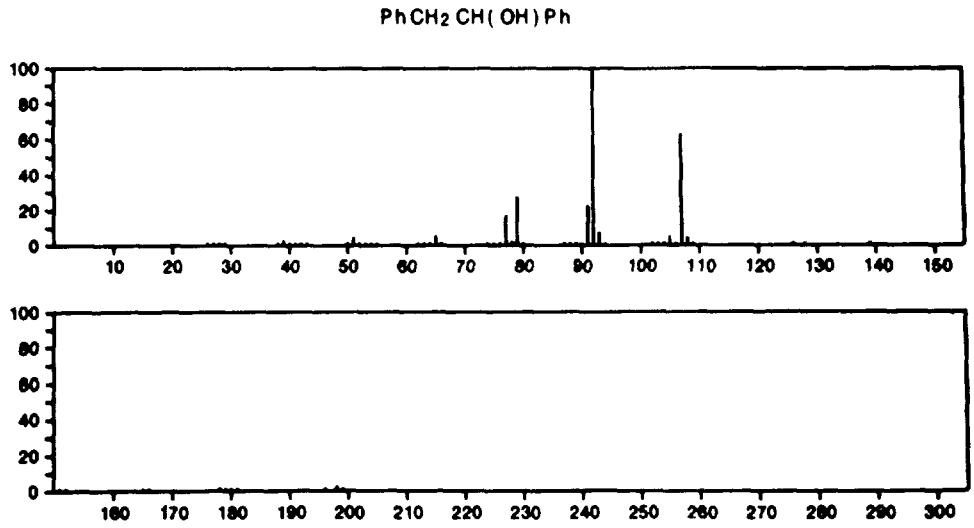

192 $C_{13}H_{20}O$ **7661-43-0**

Phenethyl alcohol, α-butyl-β-methyl-

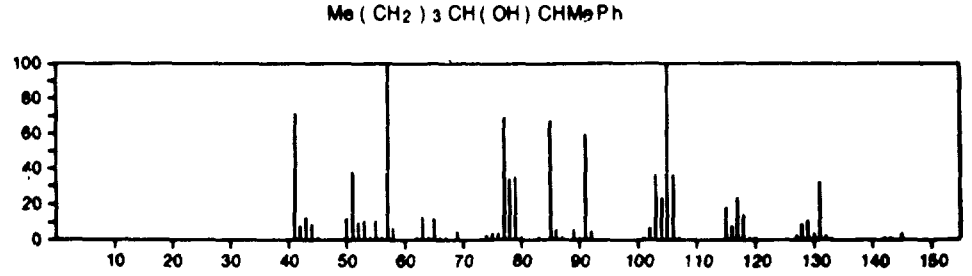

ELECTRON-IMPACT MASS SPECTRA OF MOLECULES WITH BOTH A HYDROXL AND AN AMINO GROUP

When both an amino group and a hydroxyl group are present in a molecule, the amino group appears to form a more abundant, if not the most abundant, fragment ion on electron-impact, namely the $=C=NH^+$ (imonium ion) compared to the $=C=OH^+$ (oxonium ion), the ion from the hydroxyl group.

75 C_3H_9NO 78-91-1
1-Propanol, 2-amino-

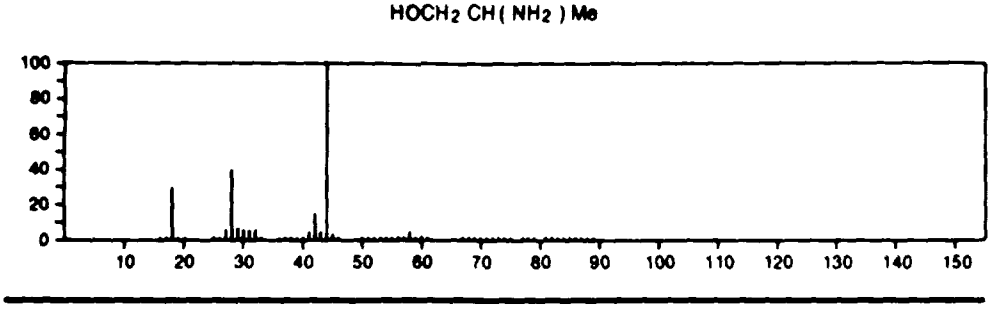

75 C_3H_9NO 78-96-6
2-Propanol, 1-amino-

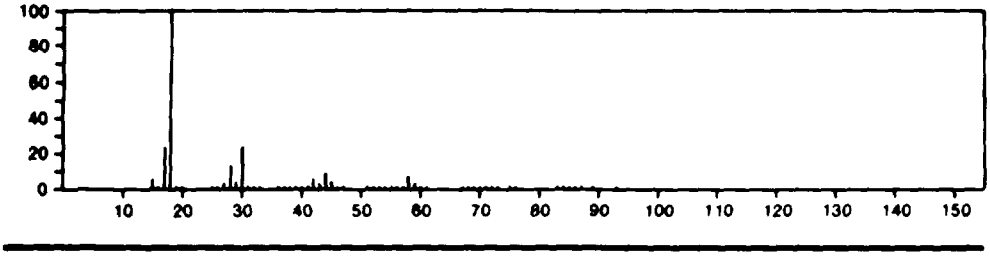

75 C_3H_9NO 156-87-6
1-Propanol, 3-amino-

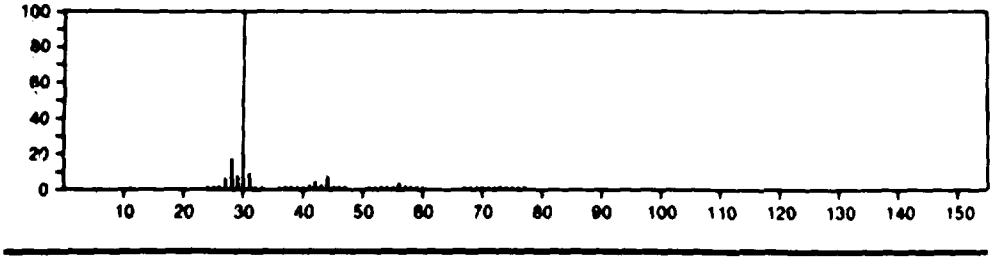

ELECTRON-IMPACT MASS SPECTRA OF MOLECULES WITH A SULFONYL GROUP

The electron-impact mass spectra of certain molecules that contain the $-SO_2-$ functional group are also shown. Ions formed by scission of C-S and S-O bonds appear to form in addition to the parent ion. The nature of the substituents influences the dissociative ionization involved.

248 $C_{12}H_{12}N_2O_2S$ **80-08-0**

Benzenamine, 4,4'-sulfonylbis-

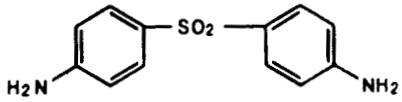

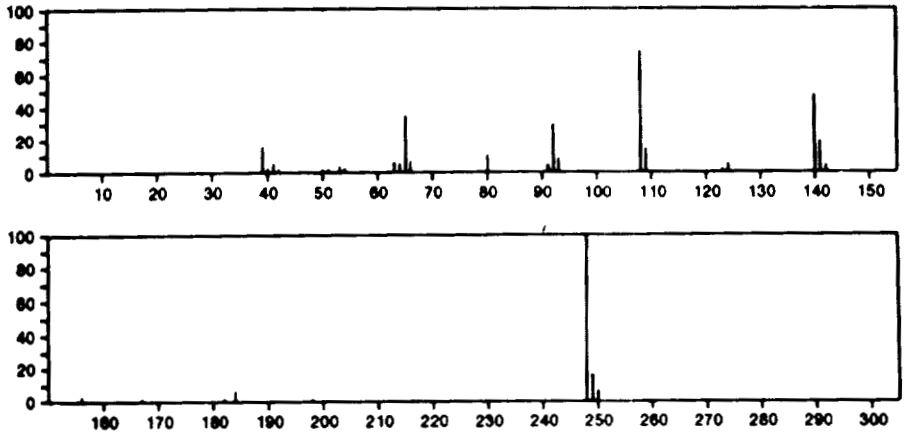

218 $C_{12}H_{10}O_2S$ **127-63-9**

Benzene, 1,1'-sulfonylbis-

PhSO2Ph

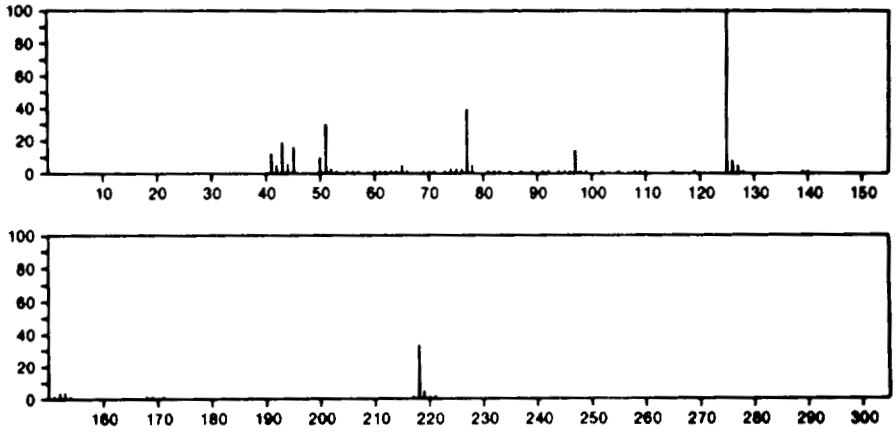

SITES OF MAJOR DISSOCIATIVE IONIZATION ON THE POLYMER ACCORDING TO ELECTRON-IMPACT MASS SPECTRA

Sites of possible major ionization and bond scission are shown on a repeating unit of the polymer formed by curing tetraglycidyl methylene-dianiline with diamino diphenyl sulfone. The determination of possible sites is based on electron-impact mass spectrometric evidence.

SITES OF MAJOR DISSOCIATIVE IONIZATION ACCORDING TO ELECTON-IMPACT MASS SPECTRA

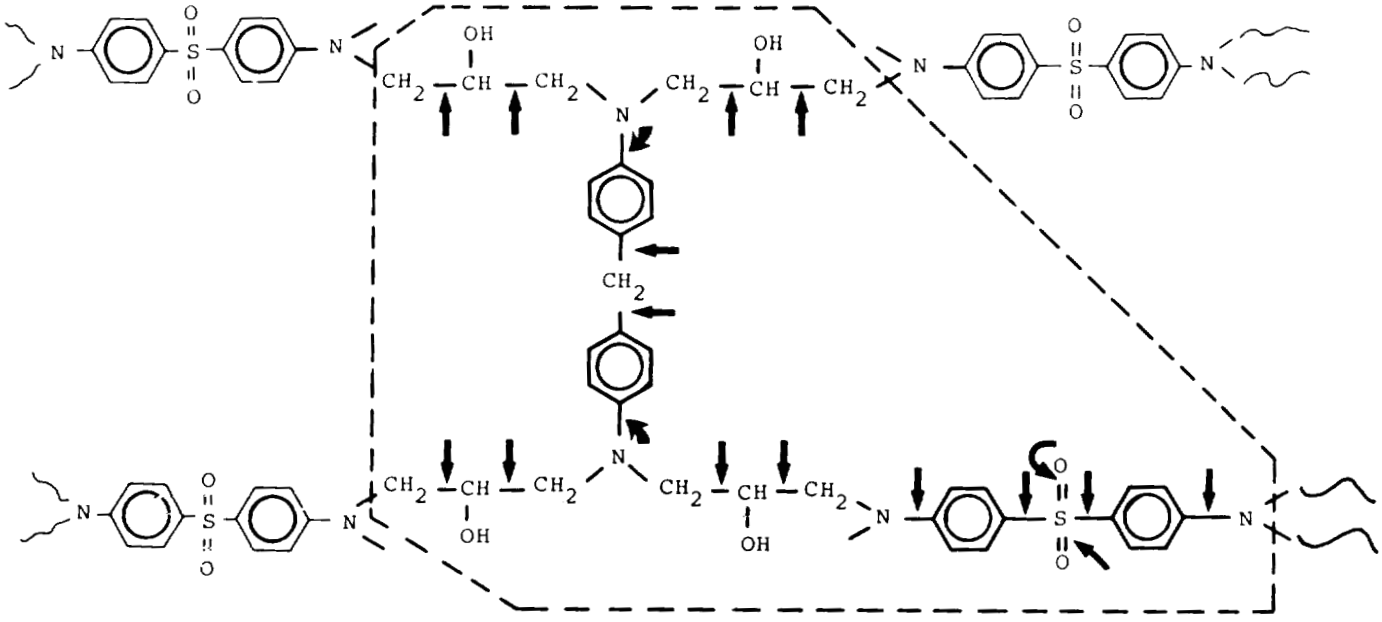

LONGITUDINAL ENERGY ABSORPTION FOR PROTONS PENETRATING INTO THE POLYMER AND A COMPOSITE MATERIAL OF THE POLYMER

The density of chemically active species is of utmost importance in determining the chemical products within an activated region since they affect the rates of various competing chemical reactions. We shall now consider the spatial inhomogeneity of the initial energy deposit. The energy absorption as a function of penetration depth is shown for monoenergetic protons of three energy levels. It has been calculated according to the stopping power of Anderson and Ziegler (ref. 18). The energy deposit per unit volume is quite high due to the proton's low speed and limits the penetration to short distances (note that the penetration depth is expressed in units of areal density which is the distance of penetration times the material density). Penetration depths and energy deposit in this graph for low energy protons should be compared with electron data of the following graph.

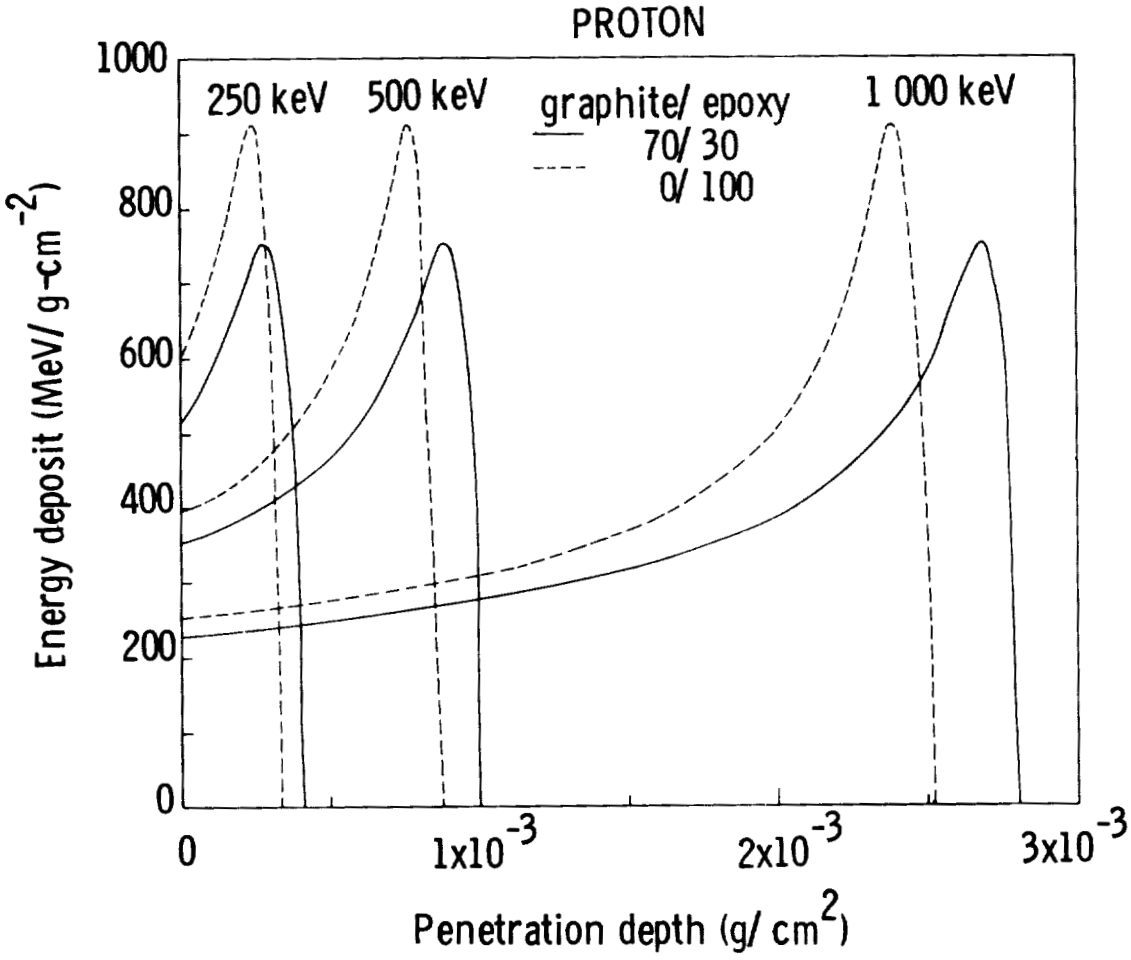

LONGITUDINAL ENERGY ABSORPTION FOR PASSAGE OF ELECTRONS THROUGH THE POLYMER AND A COMPOSITE MATERIAL OF THE POLYMER

The energy absorption for electrons is more dispersed in the material as a result of the electron's smaller mass and higher velocity. Shown here is the distribution of energy deposit as a function of penetration depth calculated according to the electron transmission coefficient and average transmitted energy (ref. 19). The declining peak values as a function of depth results from the increased multiple scattering of the electrons randomizing their direction of travel at larger depths. Such effects are of principal importance in defining dose profiles within the material.

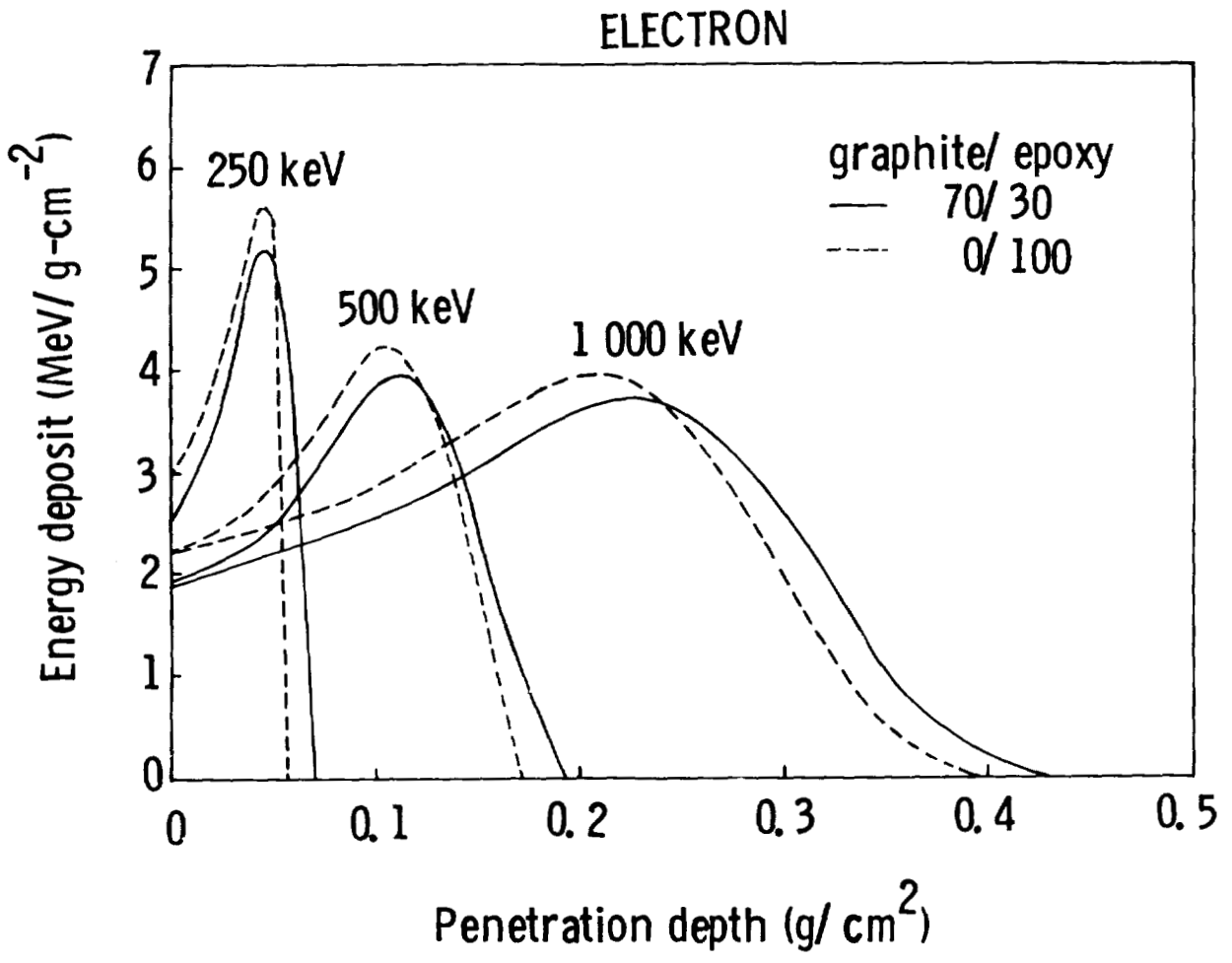

EXCITATION AND IONIZATION DENSITY NEAR A 100-KeV-PARTICLE PATH

The lateral dispersion of the energy deposit extends over two energy absorption regions, the core and the penumbra. In the core, the energy transferred from a passing charged particle to a material shows radial dependence that depends on the mechanism of the coulombic interaction considered. One process involves the coulombic interaction between the charged particle and the electron of one individual atom or molecule, in which case the radial dependence of the energy transferred is given approximately (ref. 5a) by equation (1). Another process involves the collective longitudinal excitation of valence electrons of the atoms or molecules in the condensed phase, in which case the radial dependence is given approximately (ref. 5b) by equation (2) (for singly charged projectiles)

$$P_n \approx \exp(-E_n r/3hv) \tag{1}$$

$$\rho(r) \approx \exp(-2\omega_p r/v)/r^2 \tag{2}$$

Clearly, the highest energy transfers are restricted to small radial distances. Even so the highest energy transfers result in energetic secondary electrons which generally travel far from their sites of production and deposit their energy far from the trajectory of the original passing particle forming a penumbra of energy deposited outside the core region. The core and penumbra of 100 KeV protons and electrons are shown clearly in the graph. The core region of the proton is limited to a few atomic distances by the proton's low velocity while the electron core to about 6 nm according to equation (1). The proton-produced penumbra is limited by the secondary electron mass to proton mass ratio, which limits the energy transferred to secondary electrons. The electron produced penumbra extends far off the graph to the right. There are great differences between the excitation densities achieved by the passage of the two particles. Without doubt, rapid recombination will characterize the chemistry in the proton's core region. A more detailed analysis is required to better define the chemistry of these various regions of exposure.

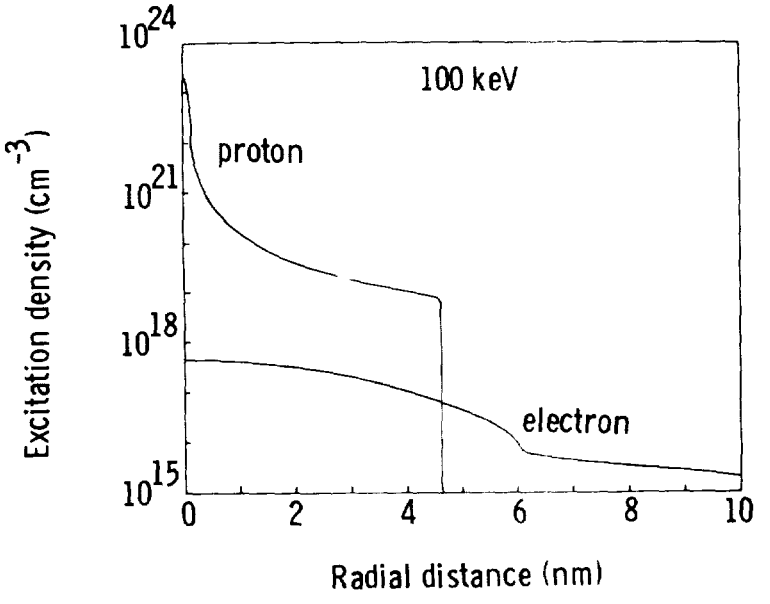

EXCITATION AND IONIZATION DENSITY NEAR A 1000-KeV-PARTICLE PATH

At higher particle energy the same features are apparent in the track structure but the radial distances are expanded. The proton core region still appears on the graph but the electron core extends to the right of the present graph. Qualitatively, we anticipate the proton core chemistry to be radically different from the remainder of the exposed regions. The chemical change in any solid material will be limited to a small cylindrical region around the individual particle trajectory. Early in the exposure these cylindrical regions will not overlap and their evolution will develop independently of one another. Late in the exposure of highly irradiated material the chemistry of later tracks will generally be altered by the prior change of the material caused by a previous track.

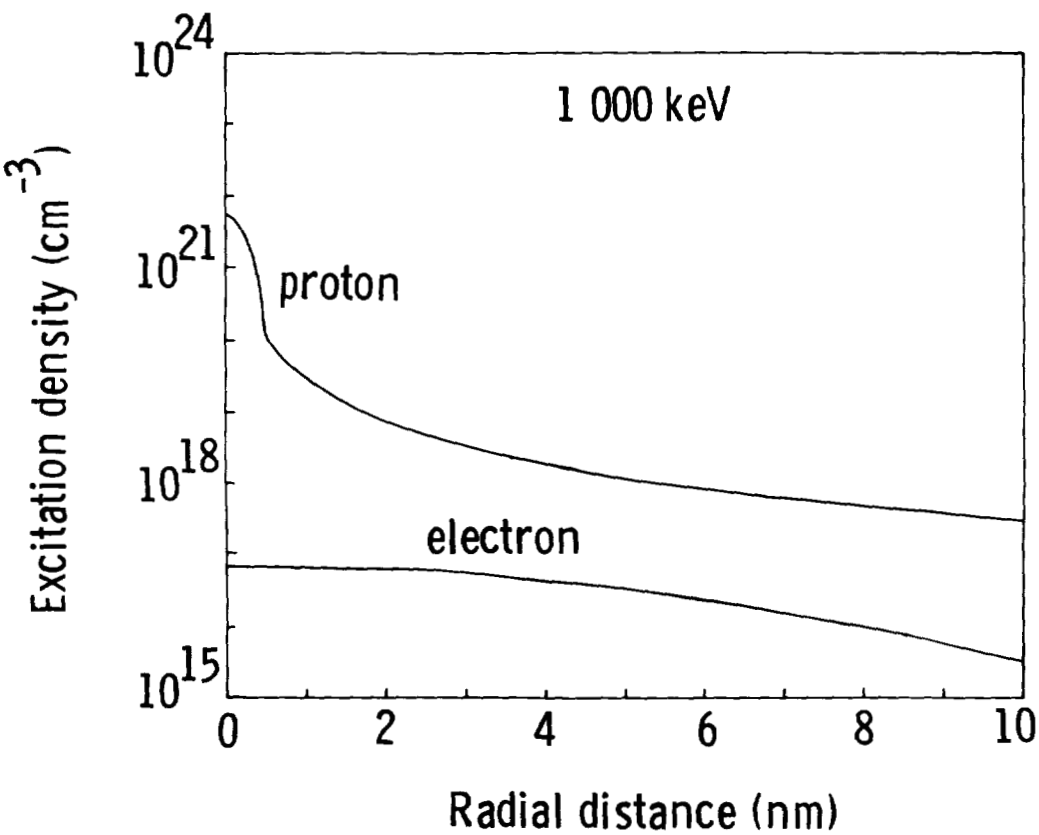

GEOSTATIONARY DOSE IN ORGANIC COMPOSITES SHOWING GEOMETRIC AND MODEL UNCERTAINTIES

The accumulated 30 year dose for geostationary orbit is shown in the graph. It is represented by exposure of $\approx 10^{11}$ rad at ≈ 0.5 μ depths due to low energy protons and $\approx 5 \times 10^{9}$ rad at ≈ 50 μ due to electrons. At these values, each portion of material receives energy by the near passage of several particles. Two effects could result from such multiple track exposure: (a) if sufficiently close in time, then chemically active species of the two trajectories may alter the chemical end product; (b) even if long times elapsed between the passage of the two particles then the second passes through previously altered material. Of interest is the number of traversals which overlap within a given time interval for an accelerated test of the 30-year geostationary exposure.

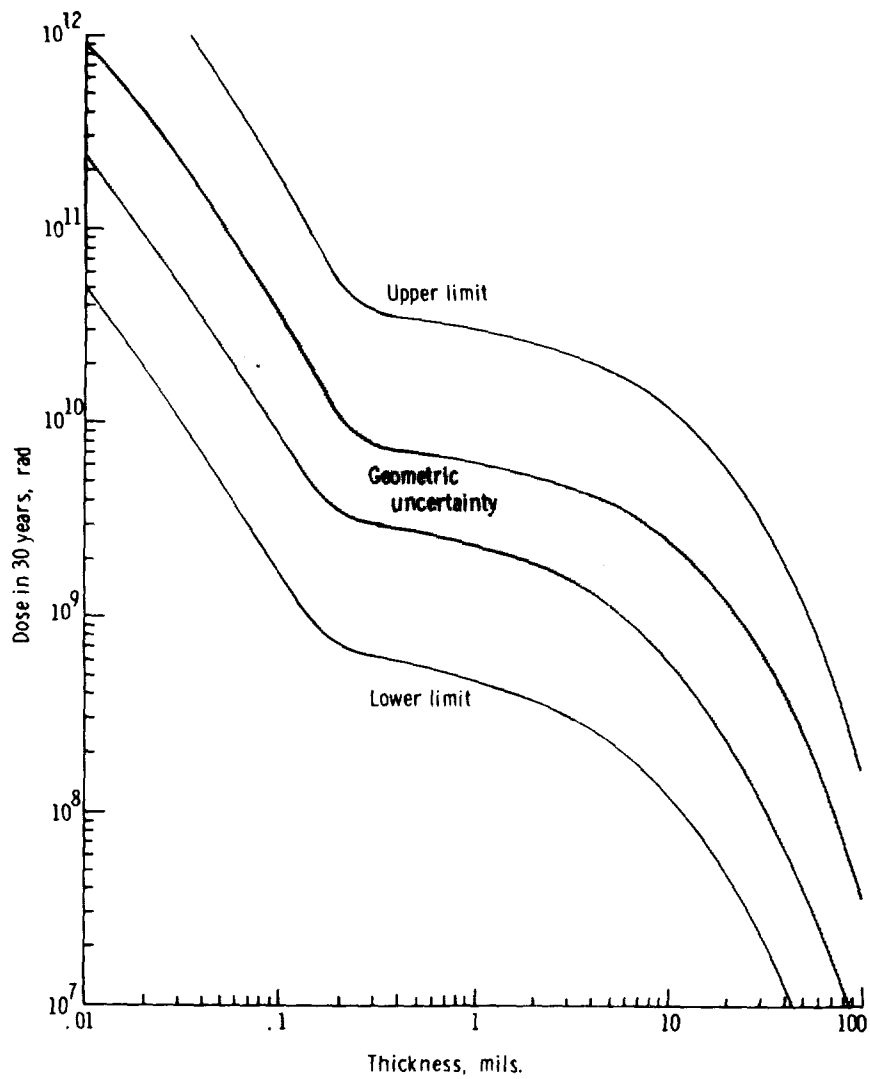

PROBABILITY OF OVERLAP OF TWO-PARTICLE TRACKS WITHIN TIME Δt (30-YEAR GEOSTATIONARY EXPOSURE ACCELERATED BY 10^4)

The probability of overlap of two particle tracks within a time interval Δt is shown for an accelerated test at 30 year geostationary exposure levels. The test is assumed completed in one day (24 hours). It is seen that the more active chemical species ($\Delta t \approx 1$ μsec) will rarely be affected by such events. A small effect is expected for the slow chemical processes ($\Delta t \approx 1$ msec) in the penumbra region of the electron exposure. Effects on long lived radicals ($\Delta t = 1$ sec) are likely in nearly all regions. Most of the exposure is seen to take place in previously disturbed material ($\Delta t \approx 1$ day). What is clear from these figures is that material changes result from the combined effects of spatially compact individual particle tracks.

	PROTON		ELECTRON	
ΔT	CORE	PENUMBRA	CORE	PENUMBRA
1 μSEC	3×10^{-11}	3×10^{-8}	5×10^{-7}	2×10^{-5}
1 MSEC	3×10^{-8}	3×10^{-5}	5×10^{-4}	2×10^{-2}
1 SEC	3×10^{-5}	3×10^{-2}	5×10^{-1}	≈ 1
1 DAY	≈ 1	≈ 1	≈ 1	≈ 1

SUMMARY AND CONCLUSIONS

- A useful model of charged particle impact with the polymer has been presented.
- Principal paths of molecular relaxation have been identified.
- The radiation-induced changes will be confined to local regions about individual particle tracks.
- The main additional effects of accelerated testing may result from effects because of possible higher temperatures and long-lived free radicals.
- Chemically active source terms are now reasonably defined. Attention must now be given to subsequent processes.

References

1. a. Rosenstock, H. M.; Wallenstein, M. B.; Wahrhaftig, A. L.; and Eyring, H.: Absolute Rate Theory for Isolated Systems and the Mass Spectra of Polyatomic Molecules. Proc. Natl. Acad. Sci. U.S., vol. 38, 1952, pp. 667-678. b. Rosenstock, H. M.: Theory of Mass Spectra. A General Review. Adv. Mass Spectrom, vol. 4, 1968, pp. 523-545.

2. Kupperman, A.: Diffusion Model of the Radiation Chemistry of Aqueous Solutions. Radiation Research, North-Holland Pub., 1967, pp. 212-234.

3. Bethe, Hans A.: Zur Theorie der Durchgangs schneller Korpurskular-strahlen durch Materie. Ann. Physik, vol. 5, 1930, pp. 325-400.

4. Platzman, Robert J.: Influences of Details of Electronic Binding on Penetration Phenomena, and the Penetration of Energetic Charged Particles through Liquid Water. Symposium on Radiobiology; The Basic Aspects of Radiation Effects on Living Systems (Oberlin College, June 14-18, 1950), 1952, pp. 139-173.

5. a. Wilson, John W.: Solar-Pumped Gas Laser Development. NASA TM 81894, December 1980. b. Ritchie, R. H.; and Brandt, Werner: Primary Processes and Track Effects in Irradiated Media. Radiation Research; Biomedical, Chemical and Physical Perspectives. Academic Press, Inc., 1975, pp. 315-324.

6. Katz, R.; Ackerson, B.; Homayoonfar, M.; and Sharma, S. C.: Inactivation of Cells by Heavy Ion Bombardment. Radiation Res., vol. 47, 1971, pp. 402-424.

7. Lindhard, J.; and Scharff, M.: Recent Developments in the Theory of Stopping Power. Principles of the Statistical Method. Penetration of Charged Particles in Matter (Conference at Gatlinburg, Tennessee, September 15-18, 1958.). NAS-NRC Publ. 752, 1960, pp. 49-55.

8. Gordon, R. G.; and Kim, Y. S.: Theory for the Forces Between Closed-Shell Atoms and Molecules. J. Chem. Phys., vol. 56, 1972, pp. 3122-3133.

9. Wilson, John W.; and Kamaratos, Efstathios: Mean Excitation Energy for Molecules of Hydrogen and Carbon. Phys. Lett., vol. 85A, 1981, pp. 27-29.

10. Wilson, J. W.; Chang, C. K.; Xu, Y. J.; and Kamaratos, E.: Ionic Bond Effects on Mean Excitation Energy for Stopping Power. To be published in J. Appl. Phys., Feb. 1982.

11. Bragg, W. H.; and Kleeman, R.: On the α Particle of Radium and their Loss of Range in passing through various atoms and molecules. Philos. Mag., vol. 10, 1095, pp. 318-340.

12. Dehmer, J. L.; Inokuti, M.; and Saxon, R. P.: Systematics of moments of dipole oscillator-strength distributions for atoms of the first and second row. Phys. Rev., vol. 12A, 1975, pp. 102-121.

13. Long, E. R., Jr.: Electron and Proton Absorption Calculations for a Graphite/Epoxy Composite Model. NASA Technical Paper 1568. November 1979, p. 16.

14. Lawing, D.; Fornes, R. E.; Gilbert, R. D.; and Memory, J. D.: Temperature dependence of broadline NMR spectra of water-soaked, epoxy graphite composites. J. Appl. Phys., vol. 52, 1981, pp. 5906-5907; and references therein.

15. Heller, S. R.; and Milne, G. W. A. (eds.): EPA/NIH Mass Spectral Data Base; 1980 Cumulative Indexes. NSRDS-NBS 63, Suppl. 1.

16. Remberg, G.; Remberg, E.; Spiteller-Friedmann, M.; and Spiteller, G.: Massenspektren Schwach Angeregter Moleküle. 4. Mitteilung. Org. Mass Spectrom., vol. 1, 1968, pp. 87-113.

17. Remberg, G.; and Spiteller, G.: Über den Einfluss von Substituenten auf die primären Abbaureaktionen aliphatischer Verbindungen im Massenspectrometer. Chem. Ber., vol. 103, 1970, pp. 3640-3660.

18. Anderson, H. H.; and Ziegler, J. F.: The Stopping and Ranges of Ions in Matter. Vol. 3. Hydrogen Stopping Powers and Ranges in All Elements. Pergamon Press, 1977.

19. Mar, B. W.: An Electron Shielding Analysis for Space Vehicles. Nucl. Sci. and Eng., vol. 24, 1966, pp. 193-199.

Pulsed Radiolysis of Model Aromatic Polymers and Epoxy Based Matrix Materials

Amitava Gupta, Jovan Moacanin,
Ranty Liang and Dan Coulter

Energy and Materials Research Section

Jet Propulsion Laboratory
California Institute of Technology
Pasadena, California 91109

Abstract - Models of primary processes leading to deactivation of energy deposited by a pulse of high energy electrons have been derived for epoxy matrix materials and poly[1-vinyl naphthalene]. The basic conclusion is that recombination of initially formed charged states is complete within 1 nanosecond, and subsequent degradation chemistry is controlled by the reactivity of these excited states. Excited states in both systems form complexes with ground state molecules. These excimers or exciplexes have their characteristic emissive and absorptive properties and may decay to form separated pairs of ground state molecules, cross over to the triplet manifold or emit fluorescence. ESR studies and chemical analyses subsequent to pulse radiolysis have been performed in order to estimate bond cleavage probabilities and net reaction rates. The energy deactivation models which have been proposed to interpret these data have led to the development of radiation stabilization criteria for these systems.

Introduction - Reliable prediction of chemical and mechanical stability of large space structures over periods of up to thirty years requires that a fundamental understanding of damage mechanisms be built into models for prediction of long term damage for each candidate material and the corresponding system. Methodology of predictive model development involves adoption of a dual approach in which engineering testing on hardware is complemented by mechanistic modeling of the effect of radiation stresses on the materials and subsequent validation of these models by means of accelerated tests. This material science approach allows better definition of engineering tests and test facilities and may also be used to interpret engineering test data in terms of changes in chemical structure of the material causing a specific failure mode. Development of mechanistic models requires an understanding of the primary processes which occur on impact of the energetic species (in our work, 600-KeV electrons) on the material. These primary processes control the subsequent cascade of energy deactivation paths some of which involve bond cleavage and consequent chemical change. Primary processes can be inferred from an investigation of the net chemical change; however, it is necessary to use time resolved techniques in order to directly observe them and study their mechanisms. In this work, the excitation source is a nanosecond pulsed electron beam, which allows time resolution down to 1-2 nsec. Time and spectrally resolved fluorescence and transient absorption have been recorded on a model aromatic-polymer poly[1-vinyl naphthalene] and a typical epoxy matrix material, namely the tetraglycidyl 4,4'-diaminodiphenyl methane-diaminodiphyenyl sulfone (TGDDM-DDS) system. Chemical analysis has been performed on P1VN subsequent to pulsed excitation and ESR studies have been performed on the epoxy resin as a function of curing and the number of beam pulses incident on the

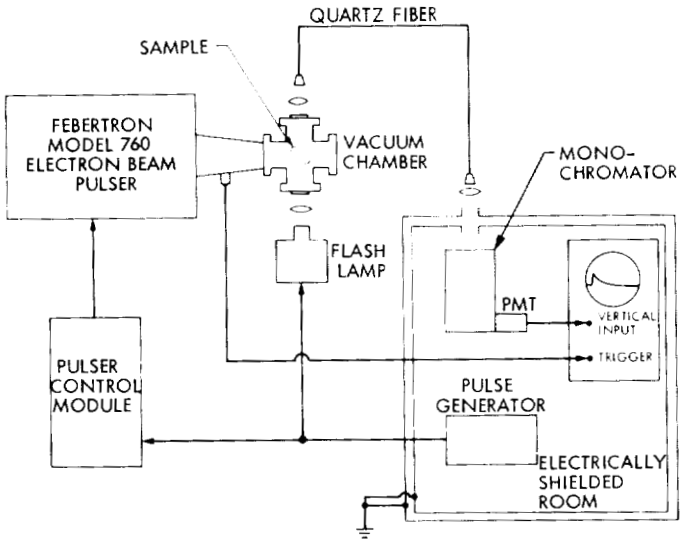

Fig. 1. Schematic diagram of JPL pulse radiolysis laboratory.

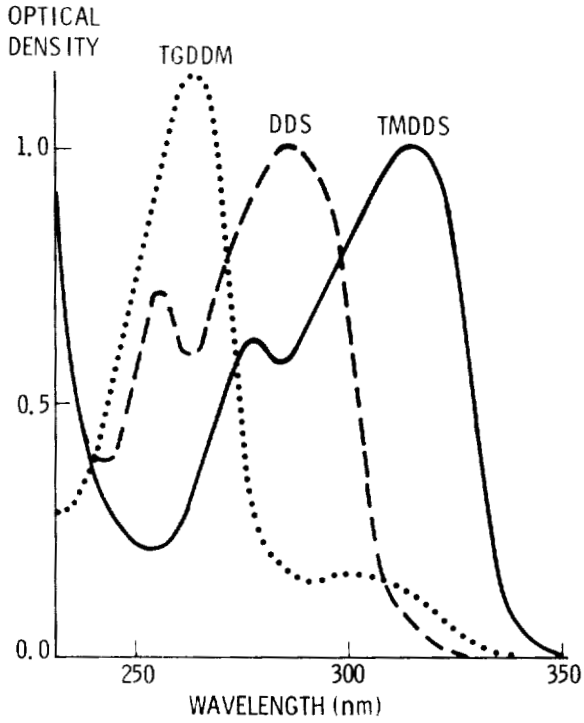

Fig. 2. UV absorption spectra of TGDDM (.013g/l), DDS (.013g/l) and TMDDS (.011g/l) in CH_2Cl_2.

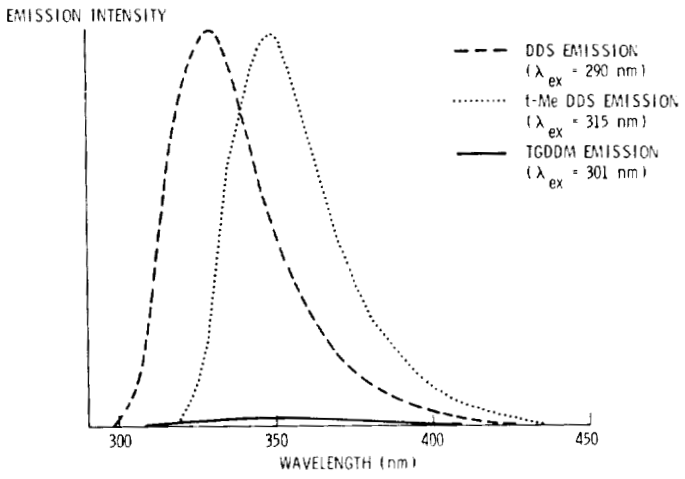

Fig. 3a. Photoexcited emission spectra of TGDDM (.013g/l), DDS (.013g/l) and TMDDS (.011g/l) in CH_2Cl_2.

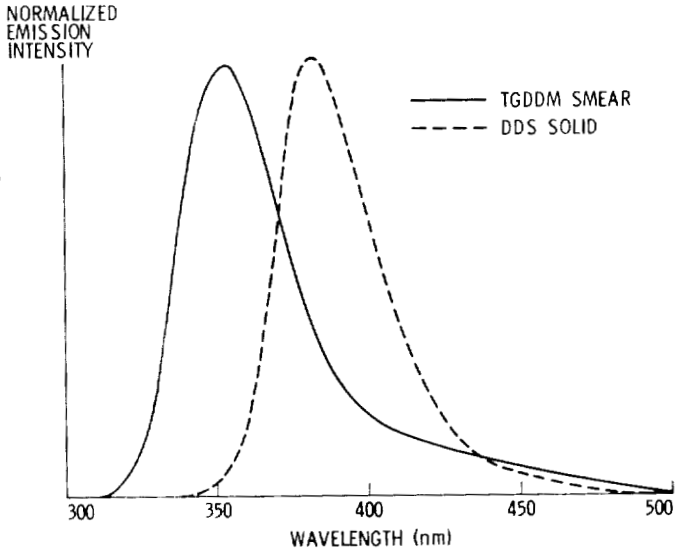

Fig. 3b. Photoexcited emission spectra of TGDDM smear (λex = 301 nm) and solid DDS (λex = 290 nm).

material. In this paper, we report the status of degradation modeling on the epoxy system. An account of the work on P1VN has been published and will not be discussed here.

Experimental Methods and Results - The source of excitation is a Febertron (Hewlett-Packard) which generates 3-ns pulses (FWHM) of 600-KeV electrons with approximately 10 joules per pulse. Solid samples were placed in an evacuated sample chamber. Fluorescence was collected by a quartz lens and was transmitted via a fiber optics assembly to a 1/4-m monochromator. The spectrally resolved emission was then monitored by a 1P-28 phototube, the output of which was displayed on a Tektronix fast-rise scope. Transient absorption measurements were carried out by using a xenon flash lamp (2-μs pulses) as a probe beam incident on the sample approximately 20° to the e-beam. After passing through the e-beam excited volume, the probe beam was collected and transmitted via the fiber optics assembly, spectrally resolved and analyzed as before. Figure 1 shows the experimental set up. Pure (neat) samples of TGDDM, DDS, their mixtures, and cured specimens were studied by this technique. DDS was exhaustively methylated to form NN'tetramethyl diaminodiphenyl sulfone (TMDDS). A recrystallized sample of TMDDS was characterized by IR and NMR spectroscopy and also by elemental analysis. TMDDS may be used as a model for DDS after it has became part of the fully cross-linked network. Under actual conditions a more realistic model will be some weighted statistical mixture of TMDDS, Tri-M DDS and DMDDS, when Tri-M DDS and DMDDS are the trimethylated and dimethylated analogs of TMDDS. Synthesis of these model compound is in progress. To obtain cured specimens, mixtures of TGDDM and DDS in appropriate mole ratios were heated in a vacuum oven at 175°C for five hours, and pumped overnight to remove any volatile matter. Optically excited fluorescence spectra of these samples were recorded on a Perkin-Elmer MPF-3A spectrofluorimeter.

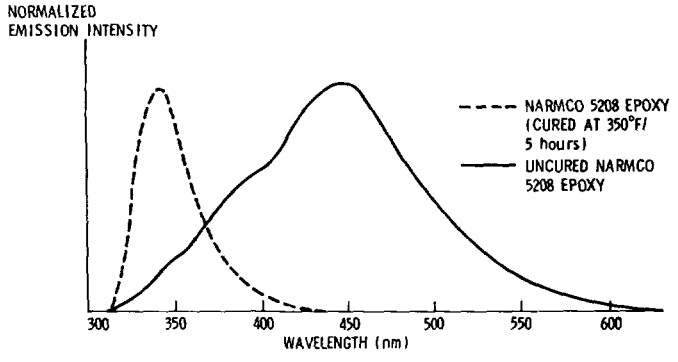

Fig. 4. Photoexcited emission spectra of cured and uncured NARMCO 5208 epoxy formulation (λex = 301 nm).

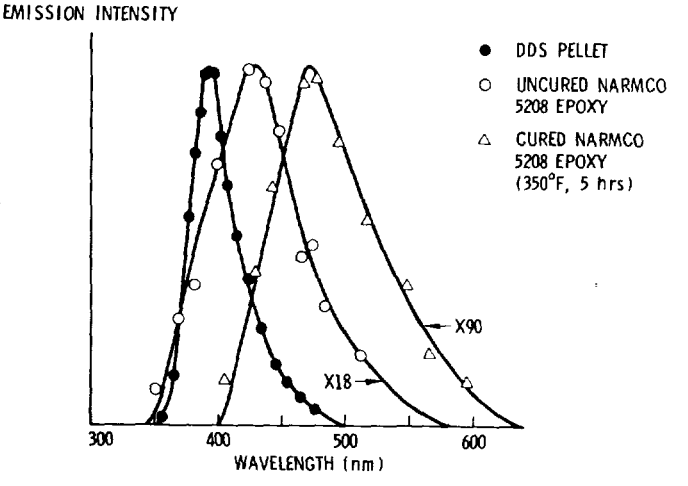

Fig. 5 Prompt emission spectra of solid DDS, cured and uncured NARMCO 5208 epoxy formulation following pulsed electron beam excitation.

Fluorescence spectra were also recorded on dilute solutions of the pure materials and their mixtures in CH_2Cl_2. Figure 2 shows absorption spectra of TGDDM, DDS and TMDDS in dilute solution. Figure 3a shows the emission spectra of DDS, TMDDS and TGDDM in dilute CH_2Cl_2 solution while Figure 3b shows the same spectra taken on TGDDM and DDS in neat form. Figure 4 shows the emission spectra of the uncured mixture and the resin cured at 180°C (350F) for 5 hours. Figure 5 shows emission spectra taken at 0-5-ns delay following pulsed e-beam excitation on DDS, uncured mixture and the cured resin. Figure 6 shows typical time profiles for the uncured mixture as a function of wavelength. Table 1 gives fluorescence decay lifetimes measured on these systems.

Discussion - Since the emission intensity from TGDDM is 80-150 times weaker than that from DDS or TMDDS, it is expected that the emission of the mixture (cured or uncured) will be dominated by TMDDS or DDS fluorescence. Comparison of emission spectra of DDS in dilute solution with the spectrum of neat DDS shows that it is considerably red shifted in neat DDS. While the same effect is also observed in case of TGDDM, it is not nearly as large. This result has been attributed to formation of excited state complexes or excimers in these systems in which an excited molecule interacts with a neighboring molecule in the ground state in approximate parallel configuration with the excited molecule. Interaction between molecules of the same species forms excimers, while interaction between two different species forms exciplexes. Excimers are not efficiently formed within the excited state lifetime of DDS in dilute solution, since the formation of excimers is a bimolecular process and requires multiple diffusive encounters. Excimer formation is found to be not nearly as important in case of TGDDM as it is for DDS. The uncured mixture should then show evidence of formation of two excimers as well as a heterogeneous complex, the exciplex between DDS and TGDDM. The emission envelope of the uncured mixture (Figure 3b) does indeed have three segments approximately corresponding to emissions

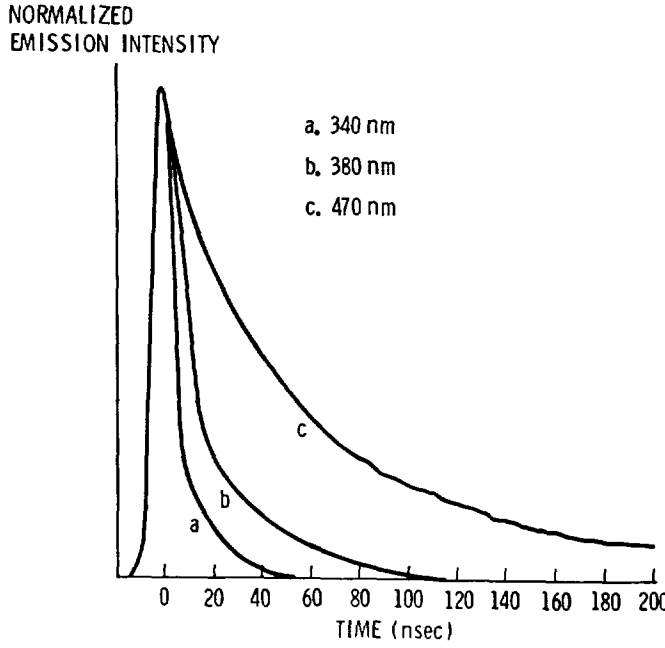

Fig. 6. Time-resolved emission from uncured NARMCO 5208 epoxy formulation following 3-nsec pulsed electron beam excitation.

Table 1. Fluorescence Decay Times Following Pulse Radiolysis

SYSTEM	λ(nm)	τ_{FAST} (nsec)	τ_{SLOW} (nsec)
TGDDM	350	≤ 5	-
	450	-	10-20
DDS	350-450	≤ 5	10-15
UNCURED NARMCO 5208	340	≤ 5	10-20
	470	18-22	85-100
CURED NARMCO 5208 (350°F, 5 hrs)	470	≤ 5	MULTI-EXPONENTIAL

from these three species. However, diffusive encounters of two molecules or substantial, rapid molecular rotation is eliminated on network formation, and hence only a trace amount of excimer formation is expected in cured specimens, when the exciting photon happens to be incident on a methylated DDS molecule in a preformed, configuration position with a TGDDM or another methylated DDS molecule. Hence the emission spectrum of the cured system is blue shifted and largely resembles a combination of emission spectra from methylated DDS molecules. Scheme 1 may be proposed to interpret the optical excitation data,

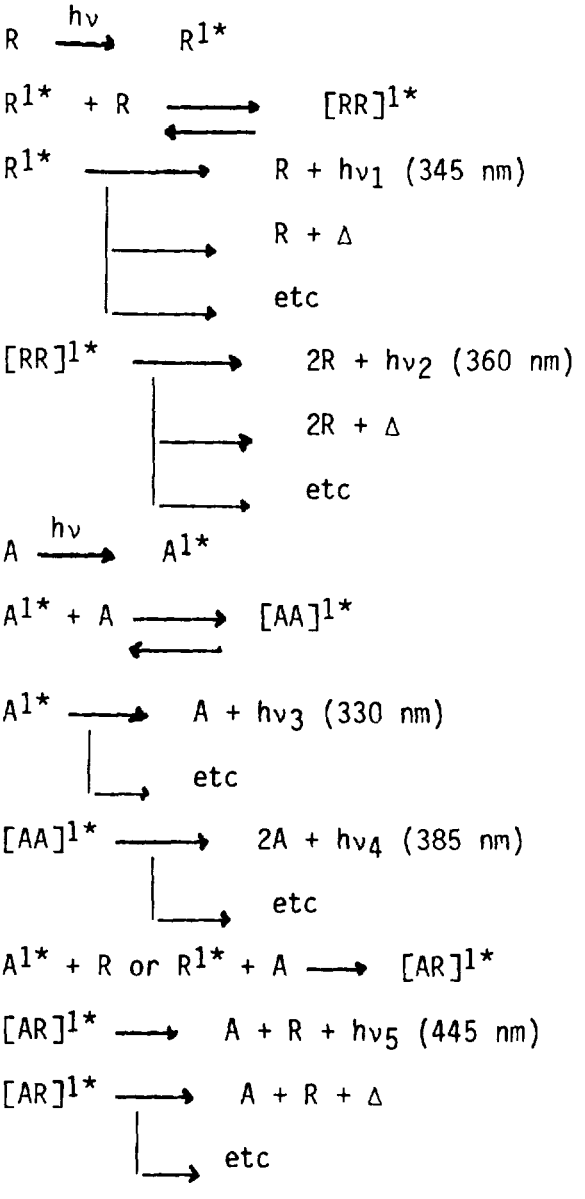

Scheme 1

where A is DDS and R is TGDDM scheme 1. In scheme 1, $[AA]^{1*}$ is the DDS excimer, $[RR]^{1*}$ is the TGDDM excimer, while $[AR]^{1*}$ is the exciplex. These excited state complexes have no ground state counterpart, since there is no ground state complex formation in this system, as determined by monitoring electronic spectra as a function of concentration. In other words, the excimers and the exciplex have potential

of concentration. In other words, the excimers and the exciplex have potential minima in the excited state but no such minimum in the ground electronic state. The nature of electronic interaction leading to stabilization of $[AR]^{1*}$ is not understood clearly, but it seems that there is a considerable degree of charge transfer, allowing mixing of higher excited states of A and R in $[AR]^{1*}$. Under favorable conditions, $[AR]^{1*}$ may be dissociated to form radical cations and anions. This experiment is in progress, and if successful, will produce useful insight into the nature of bonding in $[AR]^{1*}$ and hence its reactivity and lifetime.

The primary products of e-beam excitation are radical cations and anions. Recombination takes place through the back transfer of an electron from the anion to the cation. Within the spur, the ions are nearest neighbors and recombination is ultrafast, being essentially complete in less than 10 ps. Outside of the spur, recombination requires migration or hopping of the electrons from the anion until it encounters a cation. Normally this recombination would lead to the formation of excited states such as R^{1*} or A^{1*}. However in that case, the emission spectra following pulse radiolysis would be identical to that observed on optical excitation, except for perhaps a measurable time delay in the onset of fluorescence following pulse radiolysis. This is found to be the case for TGDDM, DDS and the uncured mixture, but the emission spectrum of the cured resin is considerably red shifted following e-beam excitation. This red shift may be rationalized as being due to direct formation of exciplexes when adjacent ionic species interact and seek to recombine within the rigid network, particularly since the exciplex is expected to incorporate a considerable degree of charge separation. Hence Scheme 2 may be proposed to interpret pulse radiolysis data:

$$R \xrightarrow{e^-} R^{+\cdot} + R^{-\cdot}$$

$$R^{+\cdot} + R^{-\cdot} \longrightarrow R^{1*} + R$$

$$R^{1*} \longrightarrow \text{etc}$$

$$A \xrightarrow{e^-} A^{+\cdot} + A^{-\cdot}$$

$$A^{1*} \longrightarrow \text{etc}$$

$$A^{-\cdot} + R^{+\cdot} \longrightarrow [AR]^{1*} \longrightarrow \text{etc}$$

Scheme 2

Fluorescence decay of uncured mixtures is found to have three single exponential decay components (Table 1). The fast component ($\tau \simeq 5$ ns) increases in amplitude at shorter wavelengths (300-390 nm) and is assigned to the TGDDM monomers (R^{1*}). There is a slow component of variable lifetime ($\tau \simeq 70$-90 ns) occuring at longer wavelengths (400-500 nm) which may be assigned to the exciplex (RA^{1*}). A third component having a lifetime of 10-25 ns, occurs at intermediate wavelengths and is tentatively assigned to the DDS excimer AA^{1*}.

The mechanism of excimer and exciplex formation from A^{1*} and R^{1*} as observed on optical excitation or directly from A^- and R^+ as observed on pulse radiolysis on the cured system, requires the postulation of fast migration of excited states and electrons, since diffusive encounter rates even in uncured materials are not sufficiently fast to explain the observed rate of onset of excimer and exciplex fluorescence. Preliminary estimation of these hopping frequencies put them at or above

fluorescence. Preliminary estimation of these hopping requencies put them at or above 10^{10} sec^{-1}. Such fast hopping processes allow the possibility of quenching or trapping the excitation energy as well as charges by placing quenchers or acceptors in the matrix. Less than 2 mole percent of quencher concentration is sufficient. Then the matrix can be depleted of its excitation energy before bond cleavage can take place. In preliminary experiments > 90% quenching of energy in P1VN was demonstrated by using 1 mole percent of anthracene traps. Additives for radiation stabilization may be developed according to these quenching criteria. For the TGDDM-DDS system, the initial additive being tested is TMDDS, which is compatible to the network, does not change its chemistry, and acts as a shallow trap of excitation and electrons.

THE EFFECTS OF MICROCRACKING ON THE THERMAL EXPANSION OF GRAPHITE-EPOXY COMPOSITES

D. E. BOWLES
NASA LANGLEY RESEARCH CENTER
HAMPTON, VIRGINIA

LARGE SPACE SYSTEMS TECHNOLOGY - 1981
THIRD ANNUAL TECHNICAL REVIEW
NOVEMBER 16-19, 1981

DIMENSIONAL STABILITY OF SPACE STRUCTURES

The performance characteristics of many large space structures are dependent upon their dimensional stability. One example of this is a space communications antenna, as shown in figure 1, in which small dimensional changes may cause a defocusing of the antenna and a corresponding loss in efficiency. The materials to be used in these structures include graphite cables, organic matrix composites, and metal-matrix composites. Composites are selected because of their inherent dimensional stability (high stiffness, low CTE) and their light weight. The primary factors controlling the dimensional stability of these materials are listed in the figure. For organic-matrix composites, microcracking is one of these primary factors. Permanent changes in the thermoelastic properties and/or permanent residual strains can result from this type of damage. The present research was concerned with the effect microcracking has on the thermal expansion of graphite-epoxy composites.

DIMENSIONAL STABILITY OF SPACE STRUCTURES

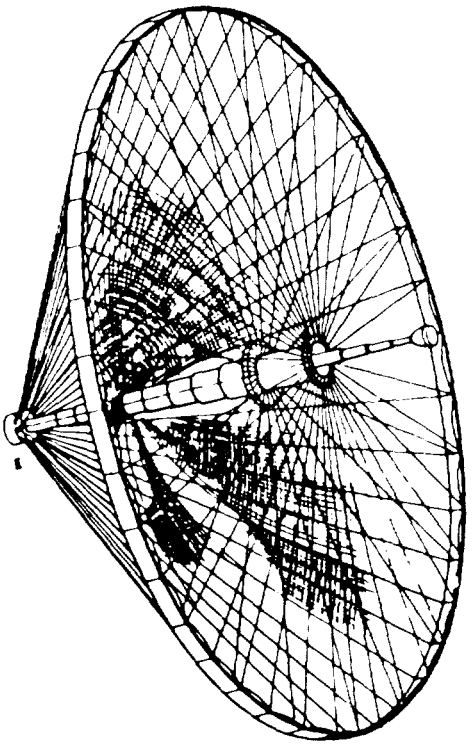

HOOP/COLUMN ANTENNA

FACTORS CONTROLLING DIMENSIONAL STABILITY

- CABLES
  - THERMAL CYCLING
  - MECHANICAL LOADING
- ORGANIC MATRIX COMPOSITES
  - MOISTURE DESORPTION
  - THERMAL CYCLING
  - MECHANICAL LOADING
  - MICROYIELDING (CAUSED BY MATRIX MICROCRACKING)
  - RADIATION
- METAL MATRIX COMPOSITES
  - THERMAL CYCLING
  - MECHANICAL LOADING

Figure 1

MICROCRACKING IN COMPOSITES

Microcracks in organic-matrix composites are small cracks in the matrix material which extend parallel to the fiber direction. They occur when the internal stresses exceed the transverse strength of an individual lamina. The two primary causes of microcracking are mechanical and thermal loads.

A limited amount of research has been conducted concerning the causes and effects of microcracking in composites. Repeated thermal cycling has been shown to cause microcracking in graphite-epoxy laminates which causes the CTE to approach that of the unidirectional material (ref. 1). A typical example of this thermal microcracking is shown in figure 2. Research has also shown that residual strains, due to microcracking, of up to 20 με may develop in graphite-epoxy during the first cooling cycle to 130 K (ref. 2). What has been lacking in past research is a quantitative relationship between the amount of microcracking and changes in CTE. This was the main focus of the current research.

MICROCRACKING DUE TO THERMAL CYCLING IN GRAPHITE-EPOXY

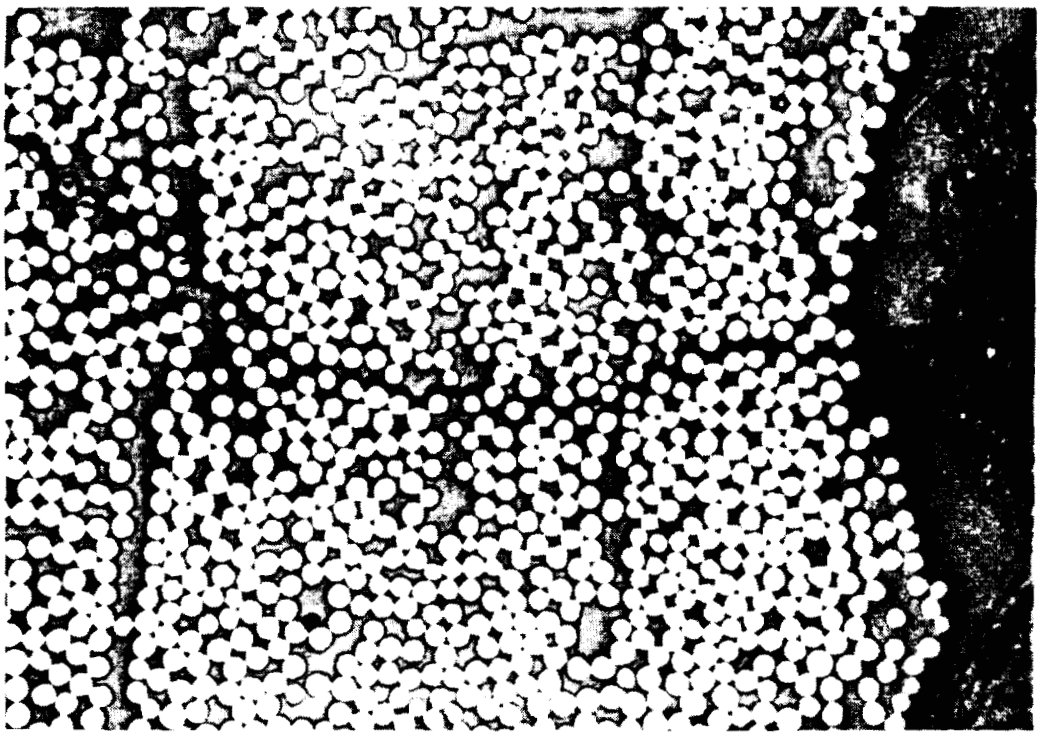

(REF. 1) ⊢75 μm⊣

Figure 2

RESEARCH OBJECTIVE AND APPROACH

The objective of this research was to study the effect of microcracking on the CTE of graphite-epoxy. To accomplish this objective, the approach outlined in figure 3 was used. Specimens from two quasi-isotropic ($[0/\pm45/90]_s$ and $[0/90/\pm45]_s$) laminate configurations were mechanically loaded in static tension to produce varying amounts of microcracking in selected plies. The loading direction was perpendicular to the 90° plies. Mechanical loading was selected as the method for producing microcracks in the specimens because the amount of damage could be easily controlled. The amount of microcracking was characterized by computing an average crack density in the damaged plies. CTE measurements were then made on the damaged specimens to correlate CTE values with crack density. An analysis was also proposed and implemented to model the effect.

RESEARCH PROGRAM

OBJECTIVE -
- STUDY THE EFFECT OF TRANSVERSE MATRIX MICROCRACKING ON THE CTE OF GRAPHITE-EPOXY

APPROACH -
- PRODUCE VARYING AMOUNTS OF MICROCRACKING WITH STATIC TENSION TESTS ON TWO QUASI-ISOTROPIC LAMINATES ($[0/\pm45/90]_S$ AND $[0/90/\pm45]_S$)
- CHARACTERIZE THE AMOUNT OF DAMAGE IN TERMS OF CRACK DENSITY
- CORRELATE THE AMOUNT OF MICROCRACKING WITH THE CHANGE IN CTE
- PROPOSE ANALYSIS TO MODEL THE EFFECT

Figure 3

MECHANICALLY INDUCED MICROCRACKING

A photomicrograph of a typical microcracking pattern in one of the mechanically loaded specimens is shown in figure 4. For this particular specimen, cracks formed in the central 90° plies as well as the adjacent 45° plies. Loading was at 73% of ultimate in a direction perpendicular to the 90° plies. Microcrack patterns were recorded while under load using an edge replication technique. From previous research, it was found that microcracks formed in this fashion did extend through the entire width (25 mm) of the specimen and therefore, damage viewed along the edge was representative of the entire specimen. Crack densities were computed by observing the edge replica in a standard microfiche card reader and counting the number of cracks in a particular ply over a 25 mm length. Loads varied from 0 to 82% of ultimate to produce specimens with crack densities ranging from 0 to 2.0 cracks per mm.

TYPICAL MICROCRACKING DUE TO MECHANICAL LOADING

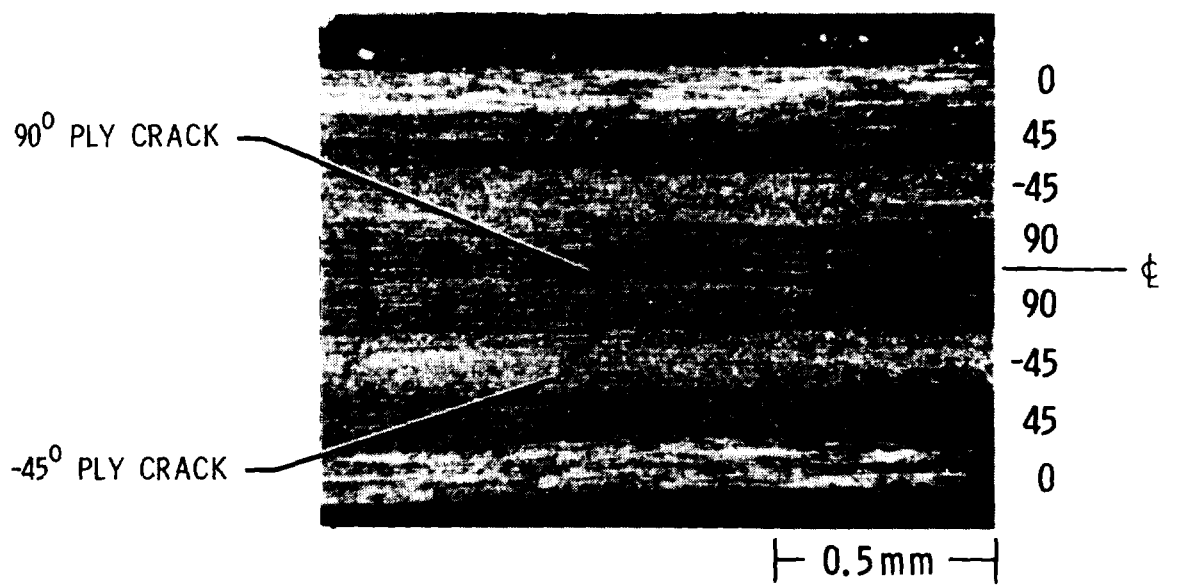

Figure 4

CTE MEASUREMENTS

CTE measurements were made using a moire interferometry technique, the details of which may be found in reference 3. A schematic diagram of the experimental arrangement is shown in figure 5. This is an optical interference technique in which thermal strain values are determined by computing the change in the number of interference fringes over a 25-mm gage length between any two temperatures. Thermal strain measurements were taken for each specimen between room temperature and 422 K. All specimens were conditioned at 422 K for 18 hours prior to testing to remove any moisture.

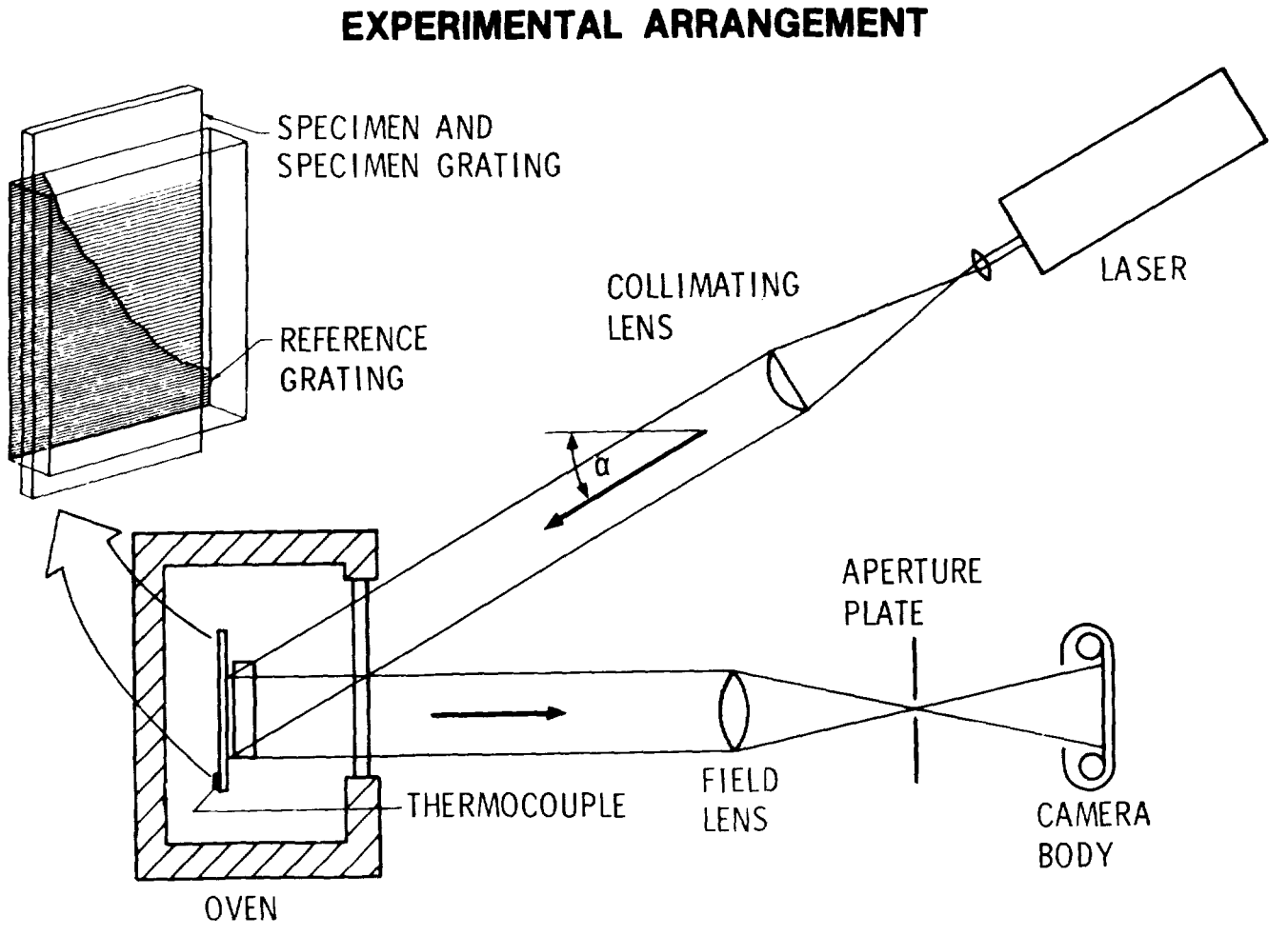

Figure 5

TYPICAL THERMAL EXPANSION DATA

A typical thermal expansion curve is shown in figure 6. These data represent both heating and cooling data for one cycle between 300 and 422 K. No differences were observed between heating and cooling or from cycle to cycle. CTE values are not directly obtained from the measurements but are computed from the slope of the $\Delta L/L$ versus temperature curve. All of the specimens exhibited a slightly nonlinear thermal strain response. A 2nd order least-squares polynomial was found to fit the data and an average CTE was computed for the entire temperature range by computing the slope at the average temperature (360 K). This average CTE value will be used in all subsequent discussions.

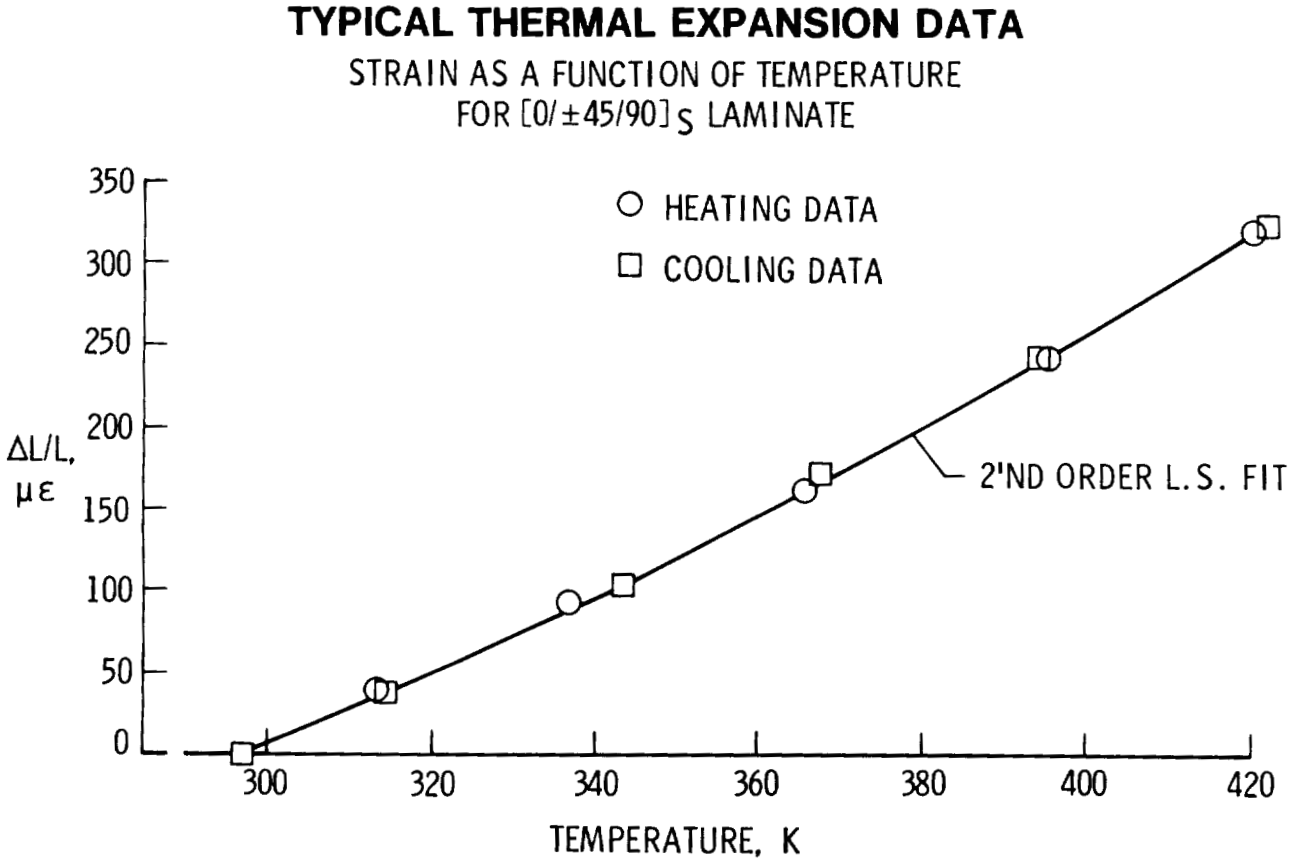

Figure 6

EXPERIMENTAL RESULTS

The results of CTE measurements plotted as a function of crack density in the 90° plies are shown in figure 7. An explanation for the scatter in CTE values for the $[0/90/\pm45]_s$ laminate at zero crack density is that only the data point with the largest CTE truly represents zero crack density since it had no load applied. The other two data points represent specimens that had loads applied. Although no cracks were visible, some small amount of damage was thought to exist. Maximum reductions in CTE of 21 and 25% occurred in specimens with crack densities of 1.10 and 2.05 mm^{-1}, respectively. These two specimens had been loaded to 73 and 82% of ultimate, respectively, with some microcracks forming in the adjacent 45° plies as well as the 90° plies.

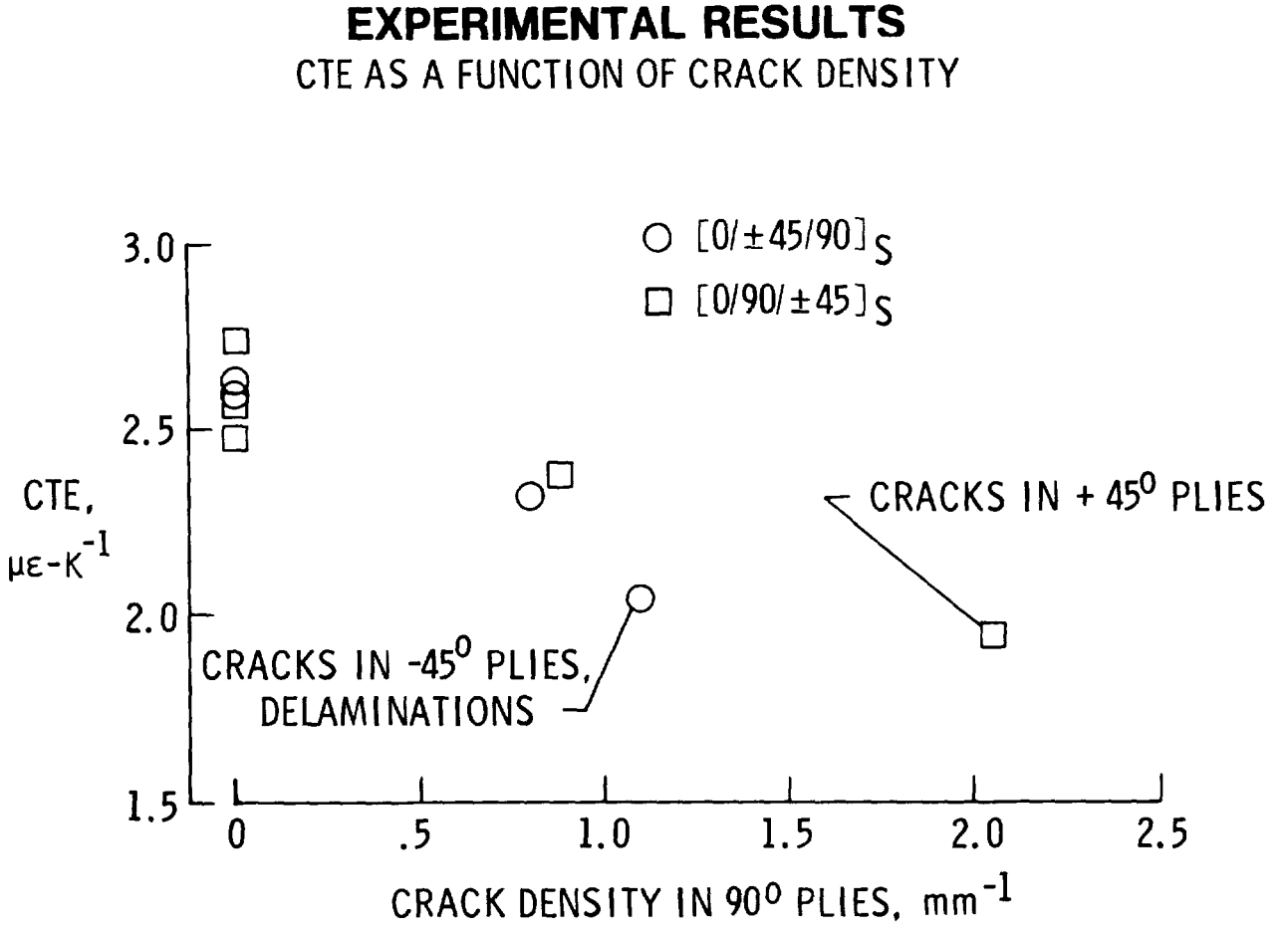

Figure 7

LAMINATE ANALYSIS

Laminate analysis is a useful tool for predicting the inplane CTE of composite laminates. It has been suggested (ref. 2) that laminate analysis may also be suitable for predicting the CTE of composites when microcracks are present, if appropriate modifications are made. These modifications include reducing the transverse stiffness, E_2, the transverse CTE, α_2, and the shear modulus, G_{12}, of the cracked plies. These reduced values are then used as input parameters to the laminate analysis. The effect of reducing E_2 by various amounts on the laminate CTE of a quasi-isotropic configuration is shown in figure 8. If E_2 is reduced by 100% in all plies, the laminate CTE approaches the value for the unidirectional ([0]) laminate in the fiber direction. A similar effect on the laminate CTE would result if α_2 were reduced from its original value. For this particular laminate configuration, $[0/\pm45/90]_s$, a reduction in G_{12} has negligible effect on CTE.

LAMINATE ANALYSIS TO INCLUDE EFFECT OF MICROCRACKING

LAMINATE CTE AS A FUNCTION OF LAMINA TRANSVERSE STIFFNESS, E_2, FOR $[0/\pm45/90]_S$ LAMINATE

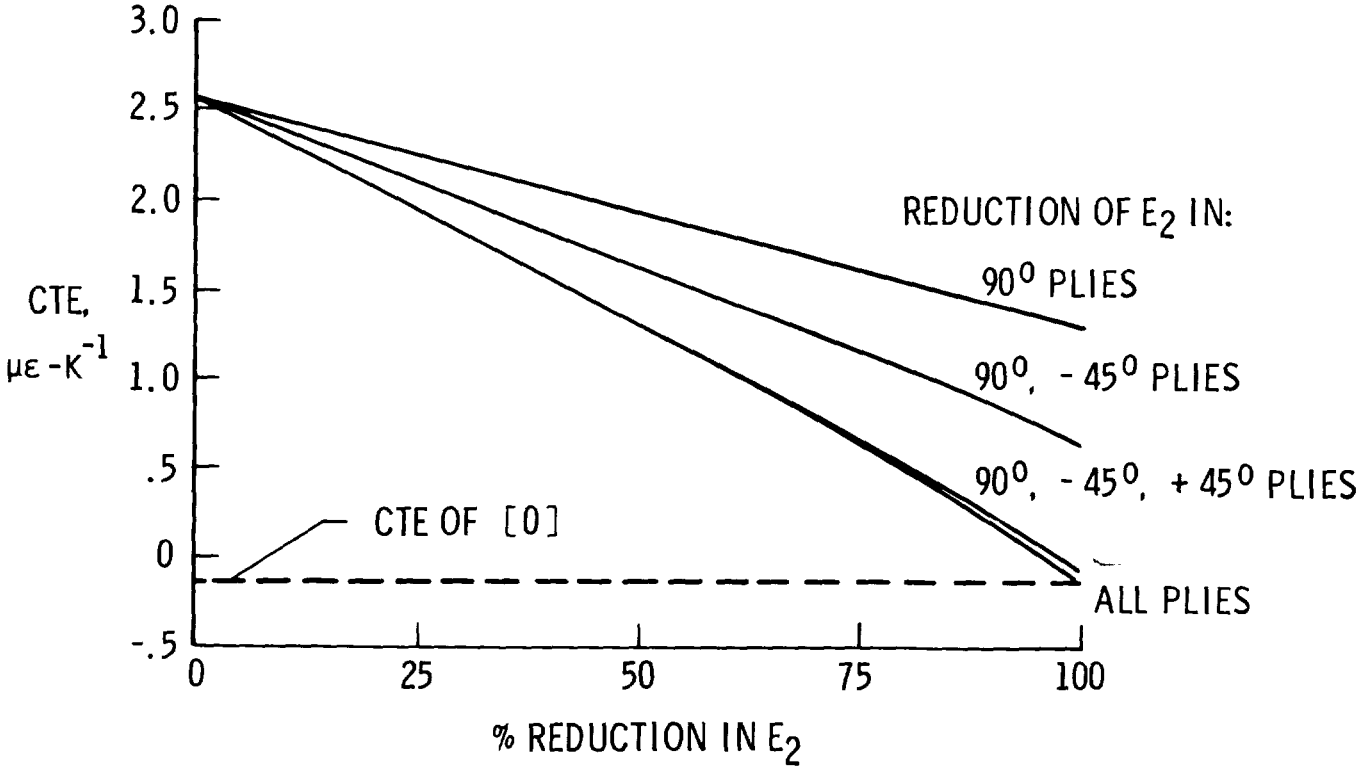

Figure 8

RELATIONSHIP BETWEEN CRACK DENSITY AND REDUCTION IN LAMINA PROPERTIES

The relationship between crack density and reduction in lamina properties must be known in order to use laminate analysis to predict the effect of microcracking on the CTE. Lockheed under NASA contract NAS1-16406 (ref. 4) has been studying the effect of microcracking and delamination on laminate stiffness reduction. In the course of their research, they developed a relationship between crack density and the reduction in lamina transverse stiffness, E_2. A finite element analysis was used to first determine the effect of crack density on laminate stiffness reduction. Then simple laminate analysis was used to determine the amount of reduction in lamina stiffness needed to account for the reduction in laminate stiffness. From these two analyses, the relationship between crack density and reduction in lamina E_2 was determined. A plot of this relationship is shown in figure 9. For the maximum crack densities produced in the current research, the reduction in E_2 was approximately 35%.

MASTER CURVE FOR REDUCTION IN LAMINA VALUES OF E_2

REDUCTION IN E_2 AS A FUNCTION OF CRACK DENSITY

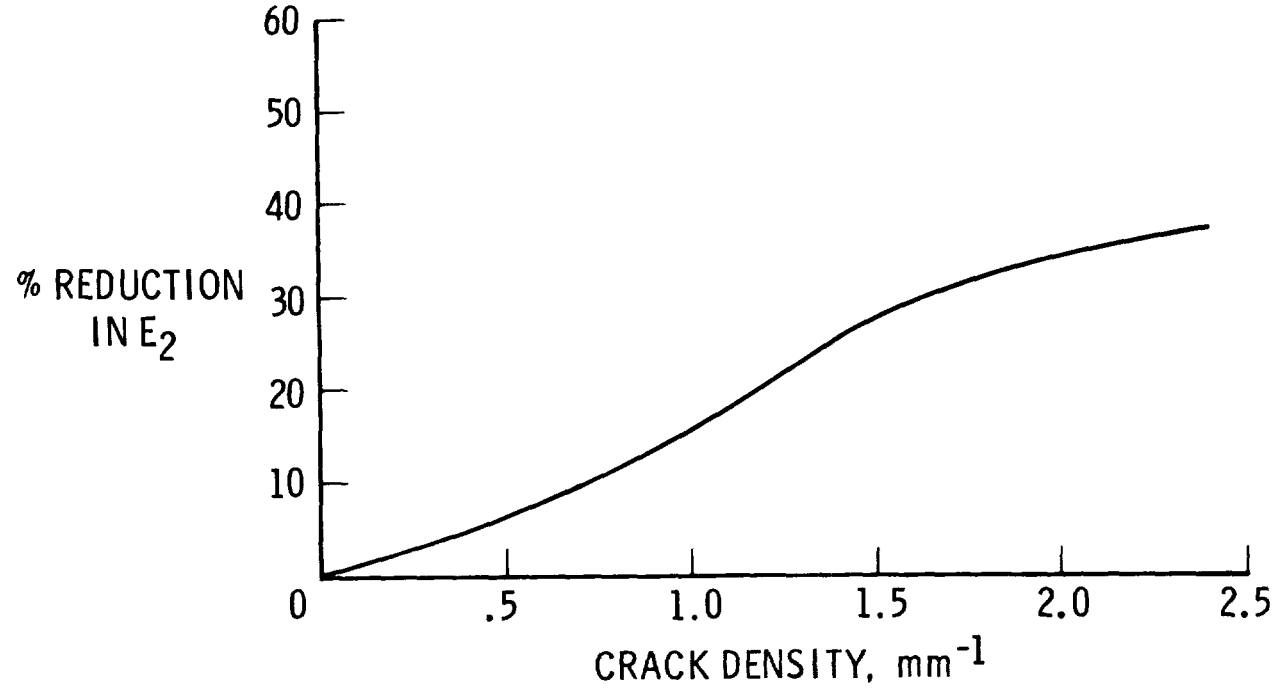

Figure 9

COMPARISON OF EXPERIMENTAL RESULTS AND ANALYTICAL PREDICTIONS

A comparison of the experimental data with the analytical predictions based on the approach previously described is shown in figure 10. The predictions for zero crack density agree well with the measured values. Two different schemes were used to account for microcracks. The first consisted of reducing only E_2 of the cracked plies. In the second, both E_2 and α_2 of the cracked plies were reduced. The correlation between crack density and the amount of reduction in E_2 to be used in the laminate analysis was determined from the plot in figure 9. For the scheme where both E_2 and α_2 were reduced, the amount of reduction in each property was assumed to be the same. The dashed lines, shown in the plot below at crack densities of 1.10 and 2.05 mm^{-1}, are the predictions including the effect of cracks in the 45^o plies. In general, there is good agreement between the prediction using reduced values of both E_2 and α_2 and the experimental results.

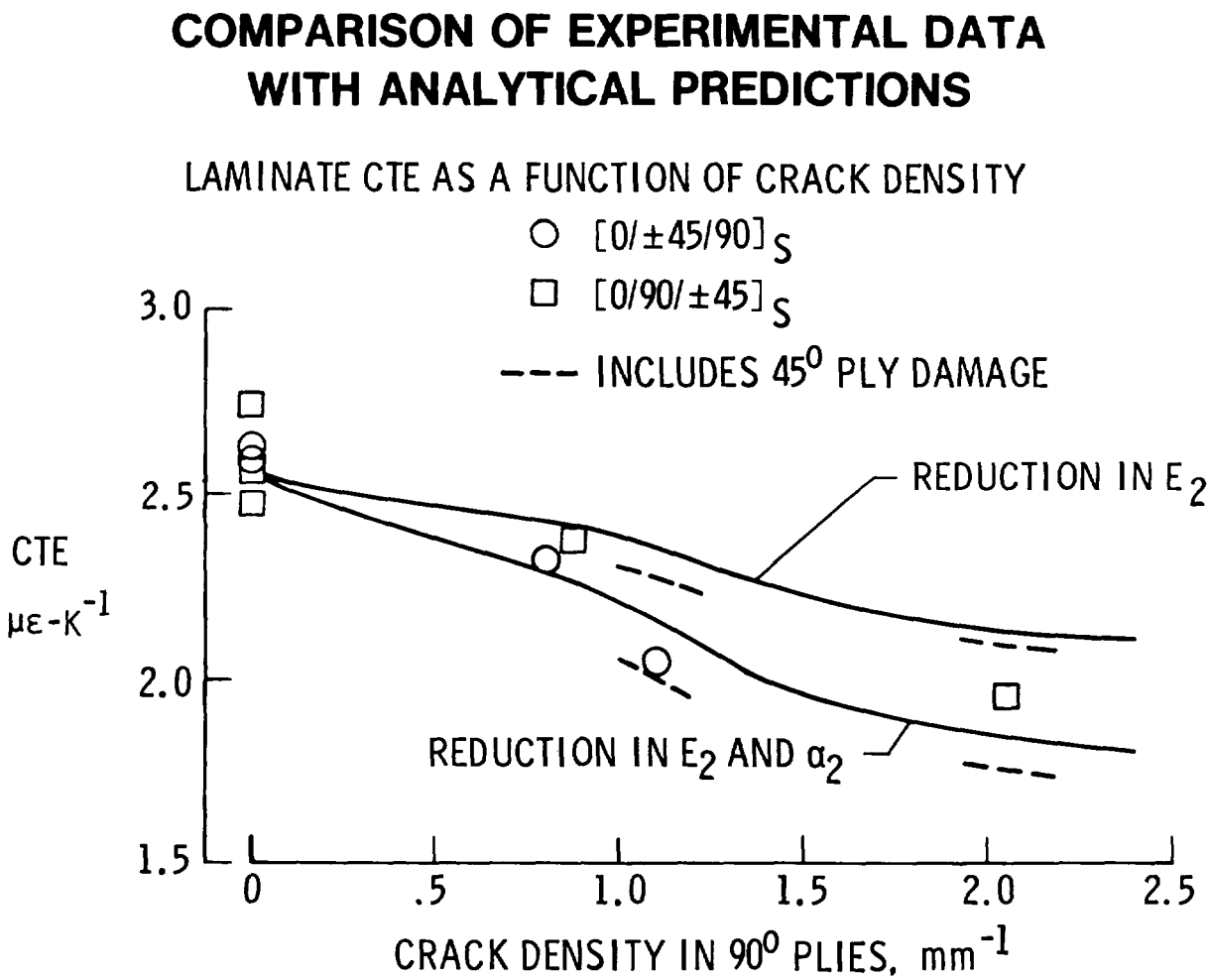

Figure 10

CONCLUSIONS AND FUTURE WORK

The results of this research indicate that microcracking does affect the CTE of composite laminates. The amount of reduction in CTE was a function of the crack density. A maximum reduction of approximately 25% occurred in a quasi-isotropic specimen with a crack density of 2.05 mm^{-1} in the 90° plies. Also laminate analysis with appropriate reductions in E_2 and α_2 of the damaged plies appears to be capable of modeling the observed change. These conclusions are summarized in figure 11.

Future work will include characterizing the amount of microcracking due to thermal loads (i.e. thermal cycling) and measuring the effect on CTE, both above and below room temperature. Work will also continue in improving the modeling capability to predict CTE degradation due to damage formation.

CONCLUSIONS

- MICROCRACKING DOES AFFECT THE CTE OF THE COMPOSITES TESTED
- EXPERIMENTAL DATA SHOWS THAT THE CHANGE IN CTE IS A FUNCTION OF CRACK DENSITY
- LAMINATE ANALYSIS WITH A REDUCTION IN E_2 AND α_2 OF THE DAMAGED PLIES APPEARS TO BE CAPABLE OF MODELING THIS OBSERVED CHANGE

FUTURE WORK

- STUDY THE EFFECT OF MICROCRACKING ON THE CTE BELOW ROOM TEMPERATURE
- IMPROVE ANALYSIS TO RELATE THE AMOUNT OF MICROCRACKING TO CHANGES IN LAMINA THERMOELASTIC PROPERTIES AND LAMINATE CTE
- STUDY THE EFFECT OF THERMALLY INDUCED MICROCRACKING ON CHANGES IN CTE

Figure 11

REFERENCES

1. Camahort, J. L.; Rennhack, E. H.; and Coons, W. C.: Effects of Thermal Cycling Environment on Graphite/Epoxy Composites. ASTM STP 602, 1976.

2. Eselun, S. A.; Neubert, H. D.; and Wolff, E. G.: Microcracking Effects on Dimensional Stability. 24th National SAMPE Conf., San Francisco, CA, May 8-10, 1979.

3. Bowles, D. E.; Post, D.; Herakovich, C. T.; and Tenney, D. R.: Moire Interferometry for Thermal Expansion of Composites. Experimental Mechanics, vol. 21, no. 12, Dec. 1981.

4. O'Brien, T. K.; Ryder, J. T.; and Crossman, F. W.: Stiffness, Strength, Fatigue Life Relationships for Composite Laminates. Seventh Annual Mechanics of Composites Review, Dayton, OH, Oct. 28-30, 1981.

THERMAL EXPANSION OF GRAPHITE-EPOXY

BETWEEN 116 K AND 366 K

JOHN S. SHORT AND MICHAEL W. HYER
VIRGINIA POLYTECHNIC INSTITUTE AND STATE UNIVERSITY
BLACKSBURG, VA

AND

DAVID E. BOWLES AND STEPHEN S. TOMPKINS
NASA LANGLEY RESEARCH CENTER
HAMPTON, VIRGINA

LARGE SPACE SYSTEMS TECHNOLOGY - 1981
THIRD ANNUAL TECHNICAL REVIEW
NOVEMBER 16-19, 1981

STUDY OBJECTIVES

The dimensional stability of materials used in large space structures must be established at both low and high temperatures. The Moire interferometer system, ref. 1, developed and currently used at the NASA Langley Research Center is limited to making thermal expansion measurements above room temperature. The objective of the present study was to develop and demonstrate an interferometer technique to measure small thermal strains associated with graphite-epoxy (Gr/Ep) composites over the temperature range of 116 K to 366 K. A series of tests was conducted to determine the effects of variability within a set of specimens on the thermal strain of Gr/Ep. Since specimen edge effects may be important for quasi-isotropic laminates, the effects of specimen width on thermal strain were investigated. All work was sponsored by NASA under Cooperative Agreement NCCI-15.

- DEVELOP A DEVICE TO MEASURE THE SMALL THERMAL STRAINS ASSOCIATED WITH Gr/Ep AND OTHER LOW EXPANSION MATERIALS BETWEEN 116 K AND 366 K
- CONDUCT A TEST PROGRAM TO:
  - DEMONSTRATE RANGE AND RESOLUTION OF THE DEVICE
  - DETERMINE VARIABILITY WITHIN A SAMPLE OF Gr/Ep SPECIMENS
  - COMPARE THERMAL RESPONSE OF 0.6 cm AND 2.5 cm WIDE Gr/Ep SPECIMENS

Figure 1

MEASUREMENT OF SMALL THERMAL STRAINS

The composite laminates used in structures where dimensional stability is critical will have coefficients of thermal expansion approaching zero. Therefore, any dilatometer used to characterize the dimensional stability of these composites must detect strains on the order of one microstrain (1 $\mu\varepsilon$).

In the present study, a laser Priest interferometer was chosen as a practical approach to meet the measurement and testing requirements. A comparison of the features of the Priest interferometer with the ideal measuring device is shown in figure 2. For the Priest interferometer, measurement resolution is $\lambda/10$ (λ is the wavelength of the laser); flat, rectangular specimens are cut to length; specimen ends are rounded to provide two-point contact only; and thermal strain is measured with respect to a reference.

MEASUREMENT OF SMALL THERMAL STRAINS

- IS CRITICAL TO AN EXPERIMENTAL PROGRAM FOR DIMENSIONAL STABILITY RESEARCH
- MEANS DETECTING STRAINS ON THE ORDER OF 1 $\mu\varepsilon$
- REQUIRES A MEASURING DEVICE WITH FEATURES SUCH AS:

IDEAL	PRIEST INTERFEROMETER
INFINITE RESOLUTION	$\lambda/10$ RESOLUTION
CONTACTLESS	TWO POINT CONTACT
UNRESTRICTED SPECIMEN GEOMETRY	FLAT, RECTANGULAR SPECIMEN
	SPECIMEN CUT TO LENGTH
NO SPECIMEN PREPARATION	REFERENCE TO NBS STANDARD
ABSOLUTE STRAIN MEASUREMENT	

Figure 2

PRIEST INTERFEROMETER

A Priest interferometer measures the displacement of an unknown specimen relative to two parallel rods of a known reference material. A schematic of the laser, Priest interferometer developed in this study is shown in figure 3. The interferometer was enclosed in a chamber in which the temperature of circulating air was controlled by a resistance heater and liquid nitrogen. A helium neon laser illuminated the interferometer through a window in the top of the chamber. The fringe pattern was recorded by a camera.

The specimen displacement with respect to the reference rods is proportional to the inclination, θ, of the top optical flat. For two nearly parallel optical flats, $\theta = n\lambda/2L_g$ where n is the number of fringes across the gauge length, L_g, and λ is the laser wavelength. A change in the relative displacement of the specimen from one temperature to the next, is equal to $(n-n_o)\lambda/2$ where n and n_o are the number of fringes at the new and old temperatures, respectively. The relative thermal strain, ε_r, is obtained by dividing the displacement by the specimen length, L_s. The total absolute specimen strain is obtained by adding ε_r to the known displacement of the reference rods, ε_q.

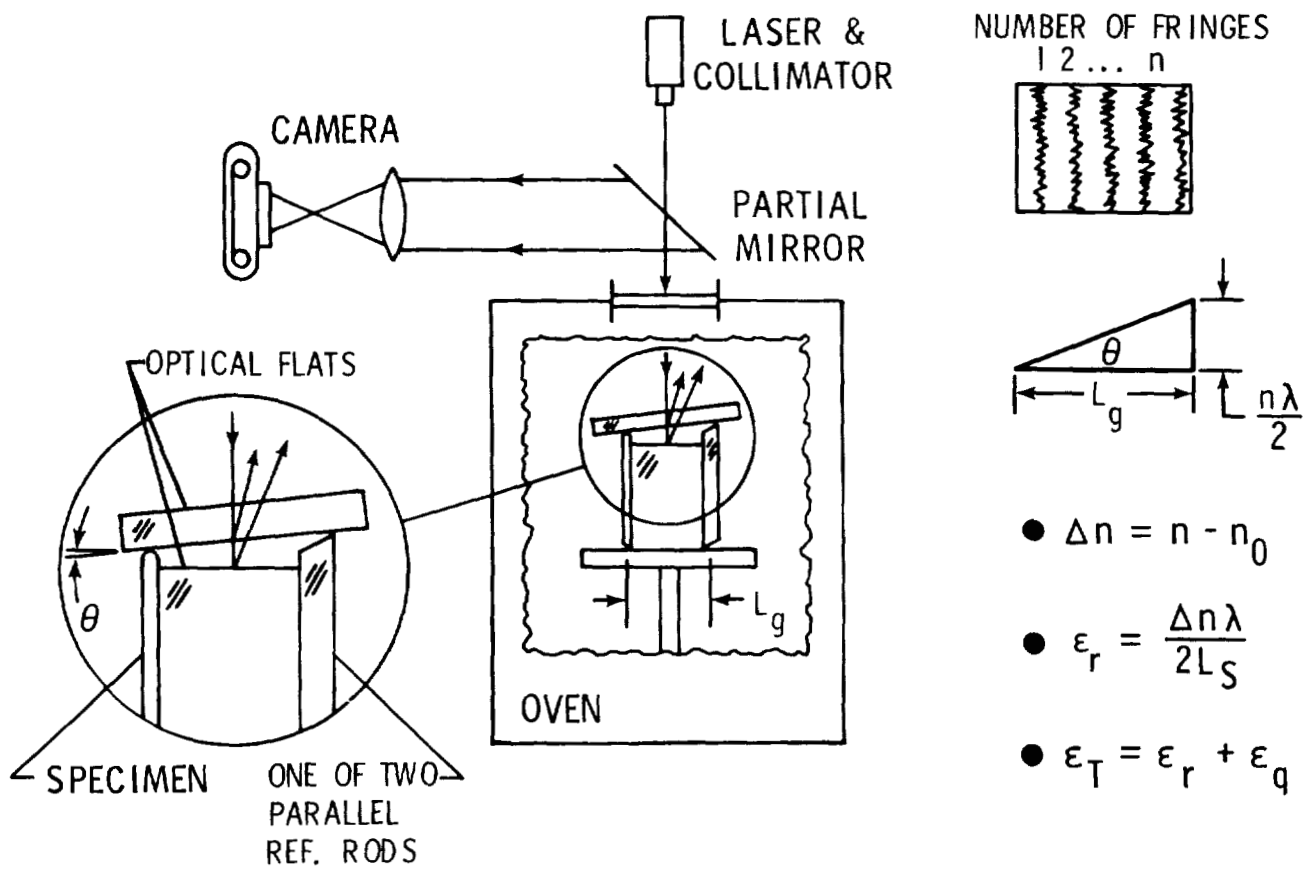

Figure 3

TYPICAL FRINGE PATTERNS

Typical fringe patterns at two different temperatures are shown in figure 4 with sample calculations for the thermal strain. The relative specimen strain, ε_r, was calculated with the equation from figure 3. The total absolute specimen strain was obtained by adding ε_r = 37 με to the strain of the reference rods, ε_q = 13 με. The strain of the reference rods was obtained from manufacturer's calibration data.

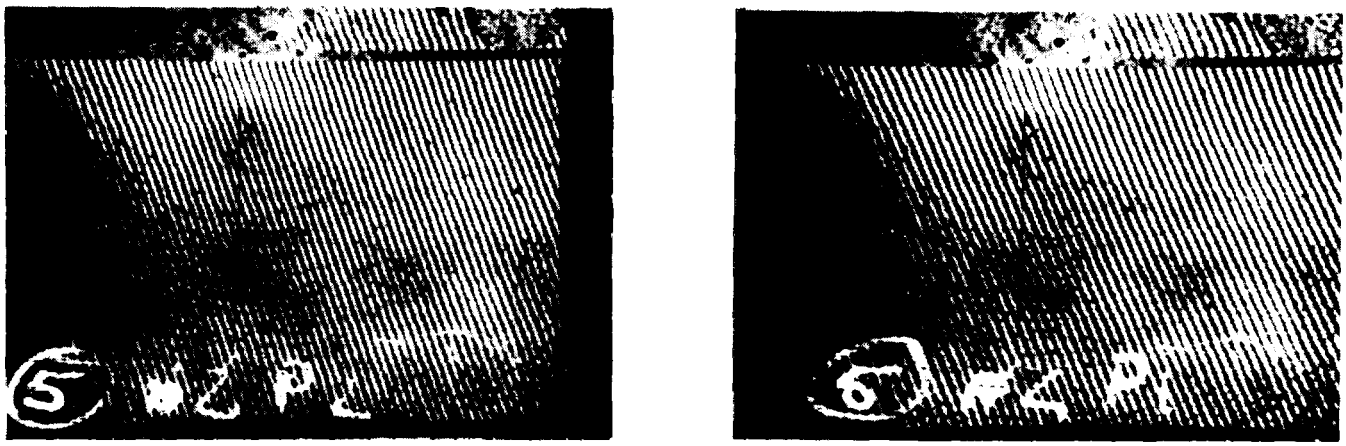

$n_0 = 55,\ T = 300\ K$

$n = 64,\ T = 325\ K$

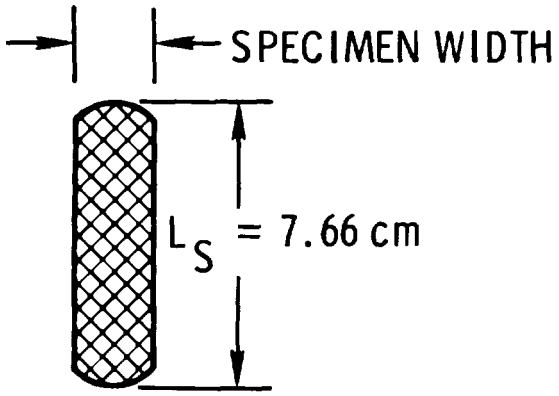

$$\varepsilon_r = \frac{(64-55)\,(63\times 10^{-6}\ \text{cm})}{2(7.66\ \text{cm})} = 37\,\mu\varepsilon$$

$$\varepsilon_T = 37 + 13 = 50\,\mu\varepsilon$$

Figure 4

TEST PROGRAM

The test program used in this study is shown in figure 5. The range and resolution of the Priest interferometer were determined with molybdenum and composite specimens. The effects of material variability on the thermal strain within a set of specimens taken from the same panel were determined with composite specimens. The effects of specimen width on thermal expansion were also determined with composite materials. Specimens widths of 0.6 cm and 2.5 cm were selected since these two are commonly used, respectively, with dilatometers and in mechanical tests.

Each specimen was thermally cycled three times from room temperature to 366 K, cooled to 116 K, and reheated to room temperature. Expansion data were taken at 28 K increments after equilibrium had been reached at predetermined temperatures. The composite specimens were dried at 395 K to constant weight prior to testing.

- DEMONSTRATE RANGE AND RESOLUTION OF APPARATUS

  $[0_8]$ T300/5208, Gr/Ep, MOLYBDENUM TESTS

- DETERMINE VARIABILITY OF Gr/Ep SPECIMENS

  CYCLING OF 2.5 cm WIDE SPECIMENS

  COMPARISON OF "IDENTICAL" SPECIMENS

- CONDUCT A COMPARATIVE STUDY OF WIDTH EFFECT

  COMPARISON OF RESULTS FROM TESTS ON 2.5 cm AND 0.6 cm WIDE Gr/Ep SPECIMENS

I. D.	SPECIMEN TYPE	# OF TESTS
M	2.5 cm MOLY	3
①	2.5 cm $[0/\pm 45/90]_S$	3
②	"	6
③	"	3
④	"	3
⑤	0.6 cm $[0/\pm 45/90]_S$	3
⑥	"	3
⑦	2.5 cm $[0_8]$	3

Figure 5

RANGE AND RESOLUTION

The operating range and resolution of the Priest interferometer were assessed with a molybdenum specimen and an 8-ply unidirectional graphite-epoxy specimen. Over the temperature range of 116 K to 366 K, the thermal strain can be resolved to within about 1με over a total strain range of as much as 1500 με.

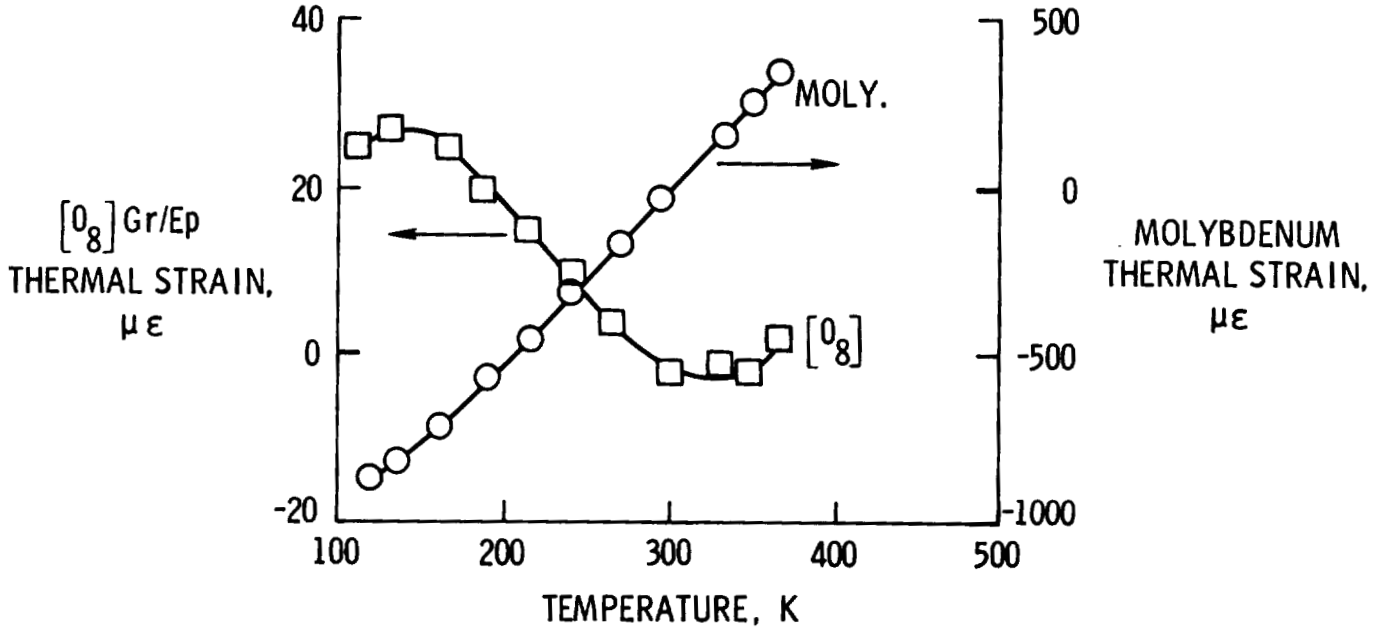

Figure 6

CYCLING REPEATABILITY

Figure 7 shows the thermal strain during each of three thermal cycles on the same quasi-isotropic, graphite-epoxy specimen. Each cycle resulted in essentially the same thermal strain. The data do not indicate any residual strain or hysteresis which has been reported for graphite-epoxy by other investigators. The absence of hysteresis in this study may be a result of stress relaxation which may have occurred during aging at room temperature.

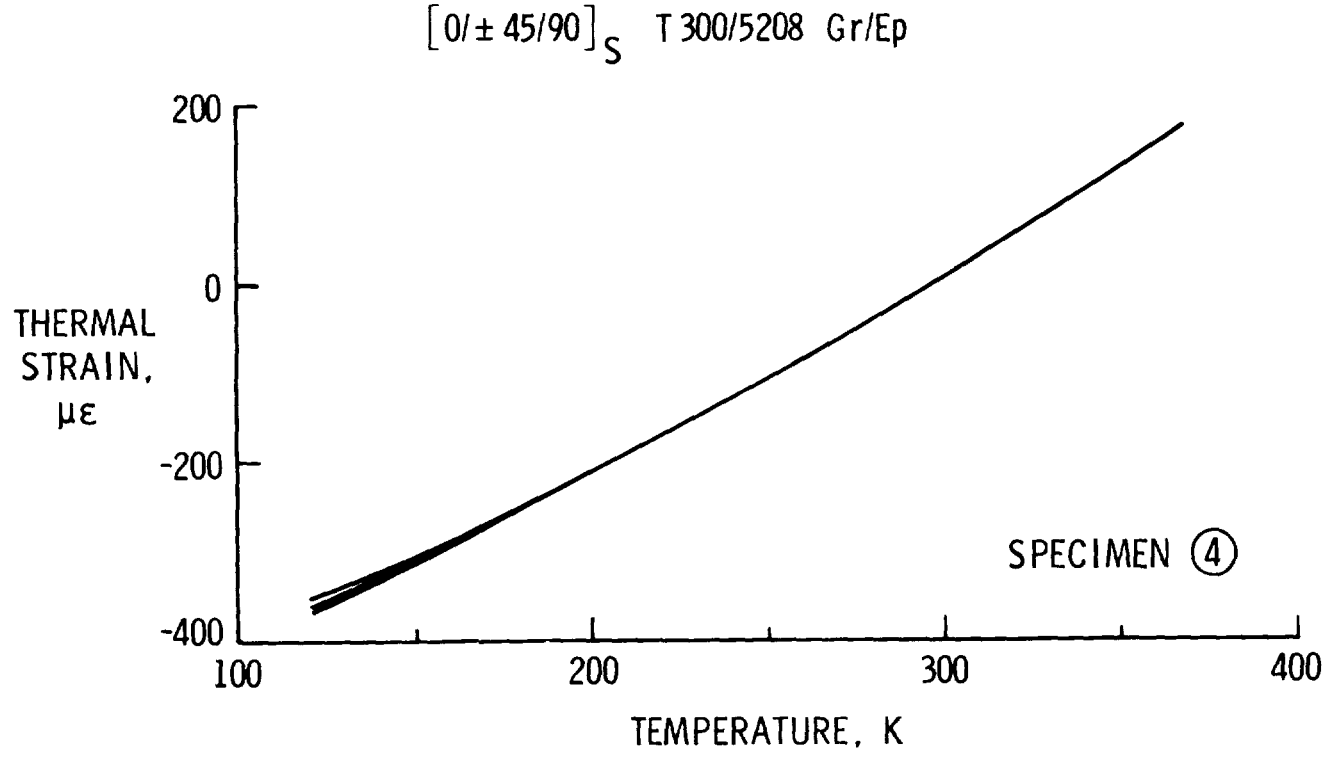

Figure 7

SPECIMEN VARIABILITY

The thermal strains of three quasi-isotropic composite specimens cut from the same panel are compared in figure 8 to evaluate the effects of specimen variability on thermal response. Each curve represents the average thermal strain for three thermal cycles. There were no significant differences in the response of two specimens. The thermal strain of a third specimen differed from the other two by about 10% and 20% at the high and low temperatures, respectively.

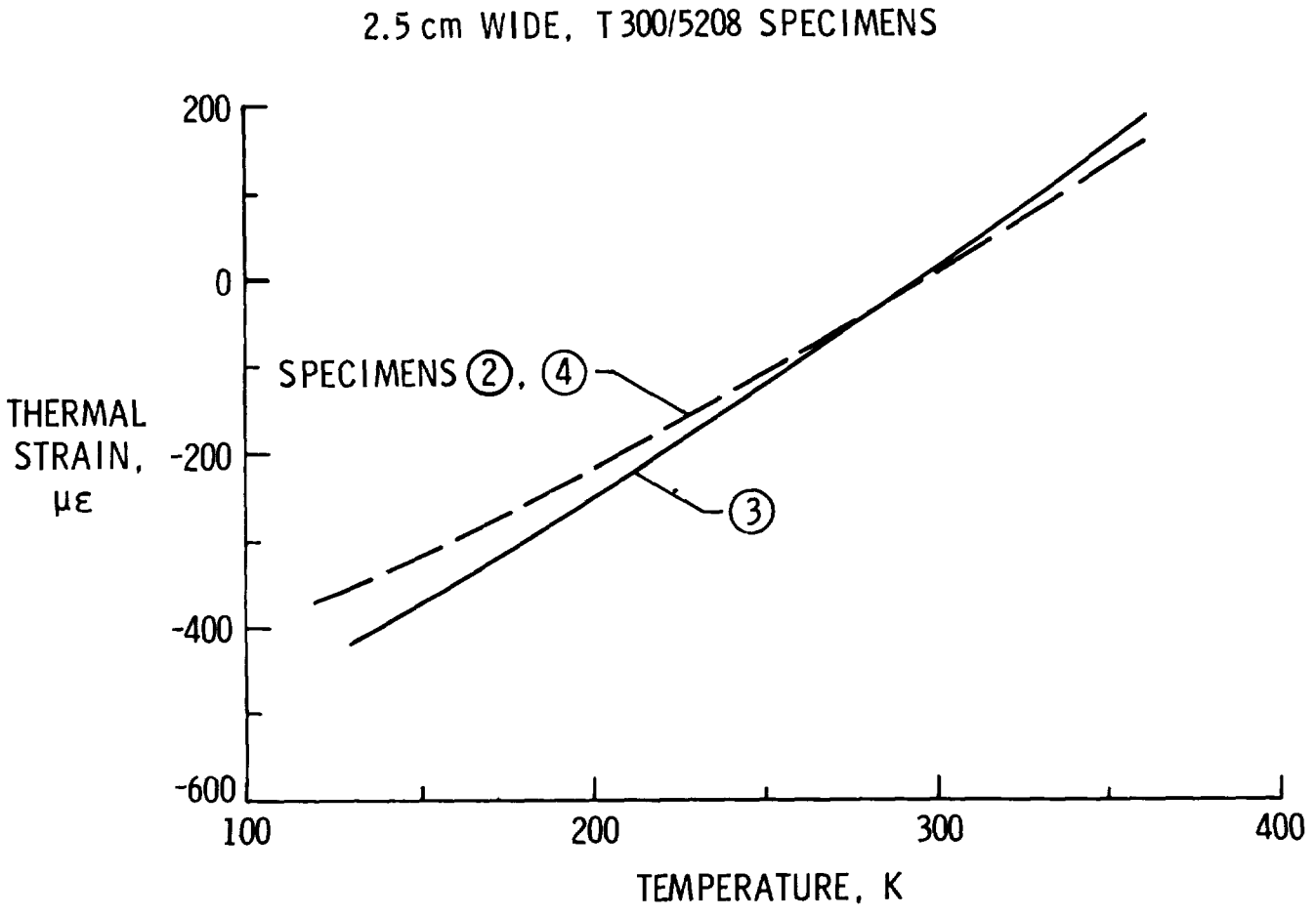

Figure 8

SPECIMEN WIDTH EFFECT

The thermal responses of specimens 0.6 cm and 2.5 cm wide are compared in figure 9. The dashed lines show the data scatter band for the 2.5 cm wide specimens (figure 8). The response of one of two 0.6 cm wide specimens falls within the scatter band for the 2.5 cm wide specimen. The response at elevated temperature of the second 0.6 cm wide specimen also fell within the scatter band. However, at low temperatures the response of this specimen was very different from the 2.5 cm wide specimen. Therefore, there appears to be a significant width effect at low temperatures. Since only two 0.6 cm wide specimens were tested, the results are inconclusive.

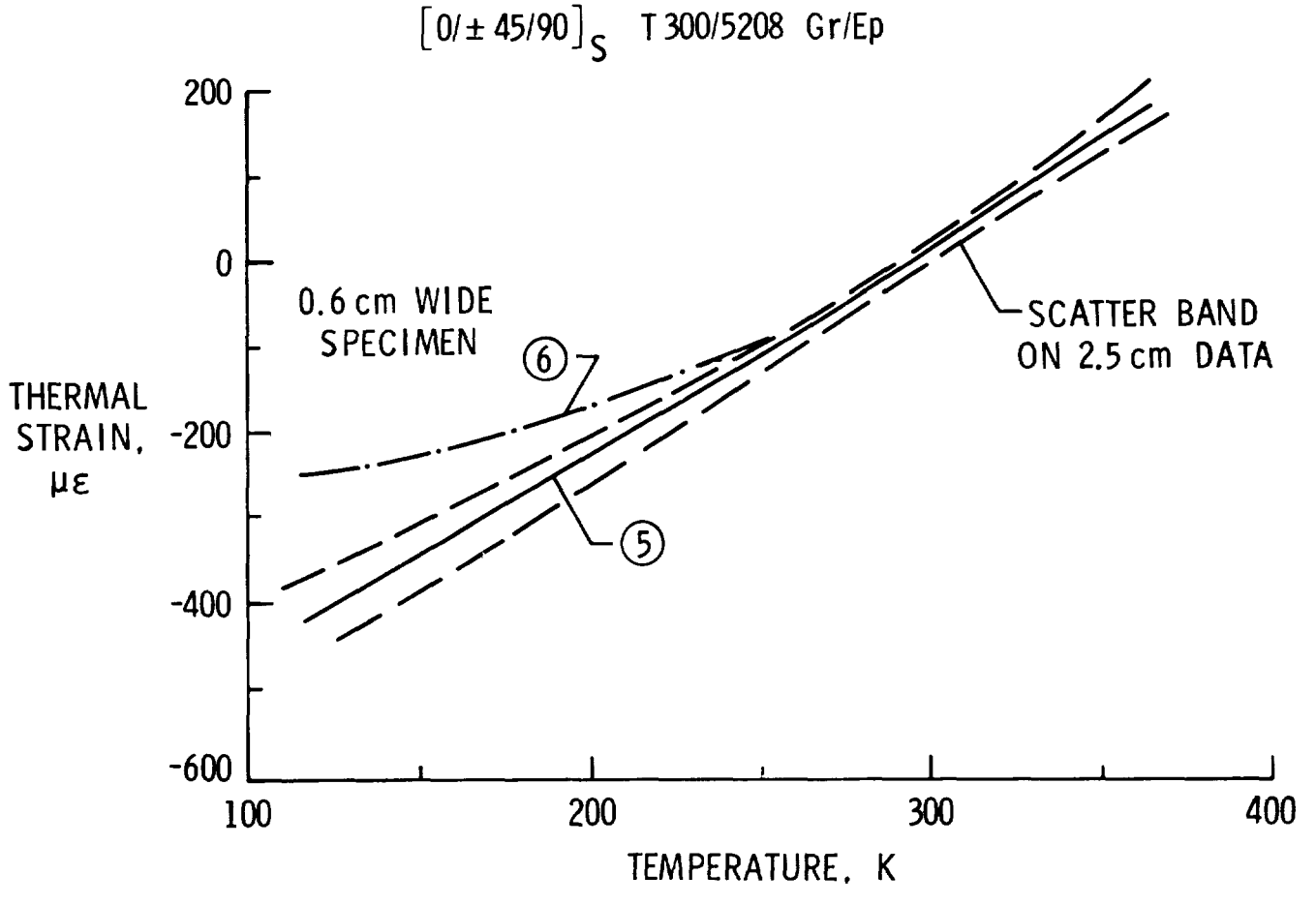

Figure 9

COEFFICIENT OF THERMAL EXPANSION

The coefficients of thermal expansion (CTE) determined in this study for two different laminate configurations at two temperatures are shown in the table. For the unidirectional laminate, the CTE varies significantly over the temperature range. For the isotropic laminate, the CTE is about constant over the temperature range. The values of CTE are similar to those reported by other investigators.

T 300/5208 Gr/Ep LAMINATE

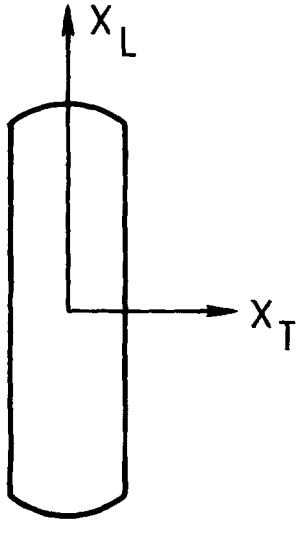

LAYUP	α_L AT 200 K	α_L AT 350 K
$[0_8]$	$-0.13 \frac{\mu\varepsilon}{K}$	$0.17 \frac{\mu\varepsilon}{K}$
$[0/\pm 45/90]_S$	$2.0 \frac{\mu\varepsilon}{K}$	$2.5 \frac{\mu\varepsilon}{K}$

Figure 10

SUMMARY

A Priest laser interferometer has been developed to measure the thermal strain of composite laminates. The salient features of this interferometer are that (1) it operates between 116 K and 366 K, (2) it is easy to operate, (3) minimum specimen preparation is required, (4) coefficients of thermal expansion in the range 0-5 με/K can be measured, and (5) the resolution of thermal strain is on the order of 1 με. The thermal response of quasi-isotropic, T300/5208, graphite-epoxy composite material was studied with this interferometer. This study showed that (1) for the material tested, thermal cycling effects are negligible, (2) variability of thermal response from specimen to specimen may become significant at cryogenic temperatures, and (3) the thermal response of 0.6 cm and 2.5 cm wide specimens are the same above room temperature.

REFERENCE

1. Bowles, D. E.; Post, D.; Herakovich, C. T.; and Tenney, D. R.: Moire Interferometry for Thermal Expansion of Composites. Experimental Mechanics, vol. 21, no. 12, Dec. 1981.

FINITE ELEMENT THERMAL-STRUCTURAL MODELING OF ORBITING TRUSS STRUCTURES

Earl A. Thornton, Associate Professor
Jack Mahaney, Undergraduate Research Assistant
Pramote Dechaumphai, Graduate Research Assistant

Mechanical Engineering and Mechanics Department
Old Dominion University
Norfolk, Virginia 23508

Large Space Systems Technology - 1981
Third Annual Technical Review
Langley Research Center

November 1981

INTRODUCTION

The flights of Columbia have given added impetus to large space structures research. In the next few years large orbiting structures will be deployed or constructed in orbit. One structural concept under development at the NASA-Langley Research Center is the tetrahedral truss. The large size of these trusses and stringent operational requirements for allowable deformations have placed emphasis on effective analysis methods. The purpose of this paper is to describe an integrated finite element (FE) thermal-structural approach for accurate and efficient modeling of large space structures.

The paper will first describe differences between the conventional FE approach as implemented in large programs and an integrated FE approach currently under development (refs. 1-3). Considerations for thermal modeling of truss members will be discussed next, and three thermal truss finite elements will be presented. The performance of these elements will then be evaluated for typical truss members neglecting joint effects. Finally, a simple truss with metallic joints and composite members will be studied to evaluate the effectiveness of the approach for realistic truss designs.

- MOTIVATION
  - SIZE OF STRUCTURES
  - ACCURATE PREDICTION OF HEAT LOADS AND TEMPERATURE
  - CONTROL OF DEFORMATION
- PURPOSE
  - DESCRIBE INTEGRATED FINITE ELEMENT (FE) THERMAL-STRUCTURAL MODELING OF LARGE SPACE TRUSSES
- SCOPE
  - CHARACTERISTICS OF INTEGRATED APPROACH
  - ORBITING STRUCTURES THERMAL MODELING
  - DESCRIPTION AND COMPARISON OF FINITE ELEMENTS
  - CONDUCTANCE EFFECTS ON TEMPERATURES
  - JOINT EFFECTS ON TEMPERATURES AND DEFORMATIONS

CONVENTIONAL THERMAL-STRUCTURAL TRUSS ANALYSIS

In orbit, a truss member experiences a nonlinear temperature distribution due to the combined heat transfer modes. Typically, there are significant temperature gradients near the joints and interior temperatures may be higher or lower than the joint temperatures. To represent this temperature distribution, several conventional two node finite elements based on a linear temperature variation are required. Additionally, different thermal-structural models are required since a single conventional two-node element can be used for the structural analysis. Since most programs compute only nodal temperatures, T_i, integration of the member temperature distribution is required between analyses to obtain the equivalent nodal forces for the structural analysis. Thus, use of conventional finite element programs such as NASTRAN and SPAR for thermal-structural analysis of orbiting trusses leads to different thermal-structural models and requires extra data processing between the thermal and structural analyses.

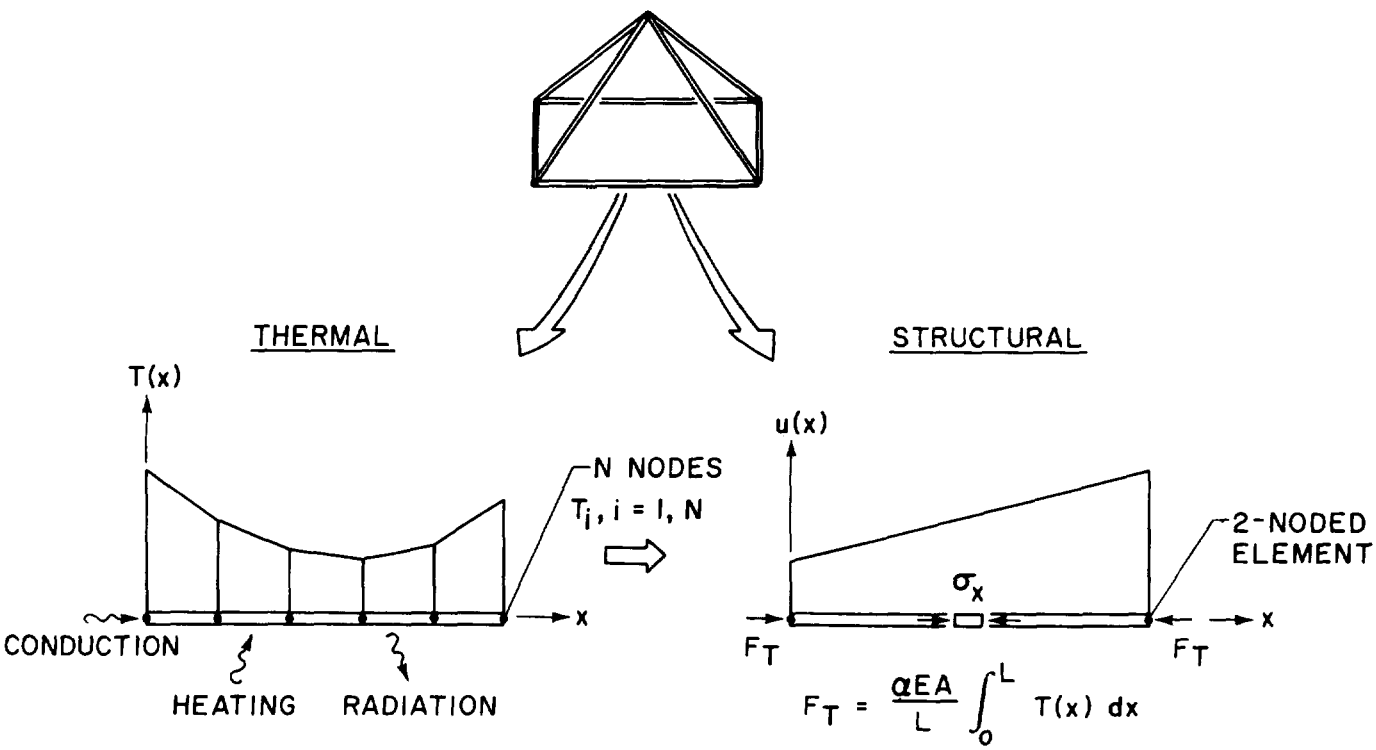

- DIFFERENT THERMAL-STRUCTURAL MODELS
- T(x) INTEGRATION REQUIRED BETWEEN ANALYSES

INTEGRATED THERMAL-STRUCTURAL TRUSS ANALYSIS

The purpose of the integrated thermal-structural analysis approach is to improve the accuracy and efficiency of the combined analyses. Improvement in accuracy (for comparable number of unknowns) is obtained by using improved thermal elements to represent member nonlinear temperature distributions. The improved thermal elements are formulated with two nodes to permit a common discretization for thermal and structural models. Later figures will show that the type of thermal element required depends on the thermal properties of the member. After temperatures are computed, the member temperature distribution is integrated within the thermal analysis program and transferred directly to the structural program. Thus the thermal and structural models use a common discretization with no data processing required between analyses. Observe that although a common discretization (i.e. common nodes and element connections) is used, the mathematical formulation of the thermal and structural elements are different. This is an important distinction between the conventional and integrated approaches, and the different formulation of the elements in the integrated approach is the basis for improvement in accuracy and efficiency.

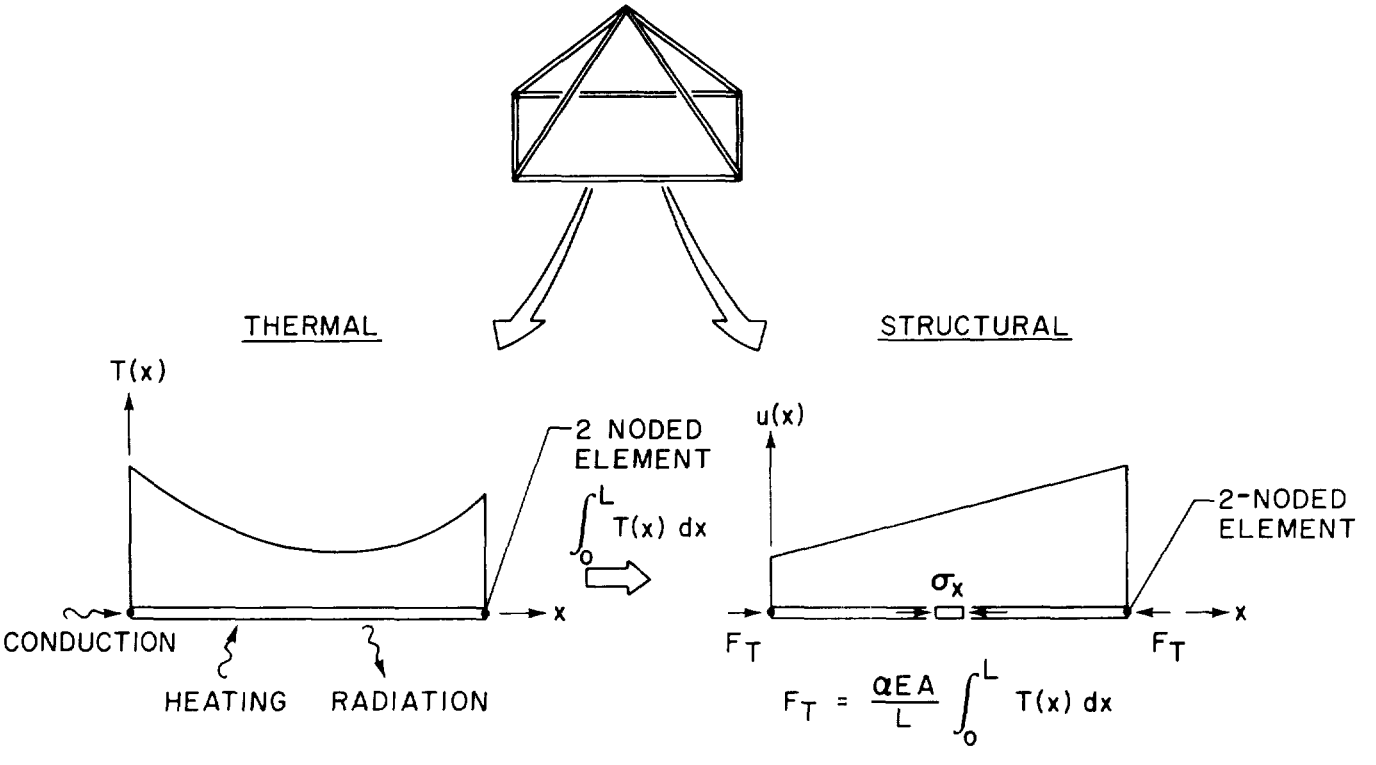

- SAME DISCRETIZATION
- NO DATA PROCESSING REQUIRED BETWEEN ANALYSES

ORBITING STRUCTURES THERMAL MODELING

A truss member experiences conduction heat transfer combined with emitted radiation and radiation heating from both nearby truss members and other satellite components. In this study of fundamental concepts of thermal-structural modeling, a number of simplifying assumptions are made. Radiation exchanges between members are neglected because computational experience (ref. 4) has shown that the member-to-member radiation heat exchanges in a truss are negligible in comparison to the incident heating and emitted radiation. Although member-to-surface radiation exchanges may be important, they are not considered. In general, both material and surface properties are temperature dependent and vary throughout an orbit, but, herein, member properties are assumed constant. Member-to-member shadowing effects may also be significant, but they are not considered. Temperature gradients through the member thickness are likewise neglected so that the temperature is assumed to vary only along the member length. The basic heat transfer problem is inherently nonlinear because of the emitted radiation and transient because of the strong time-dependence of the heat loads. Heat load computations are described briefly in Reference 3.

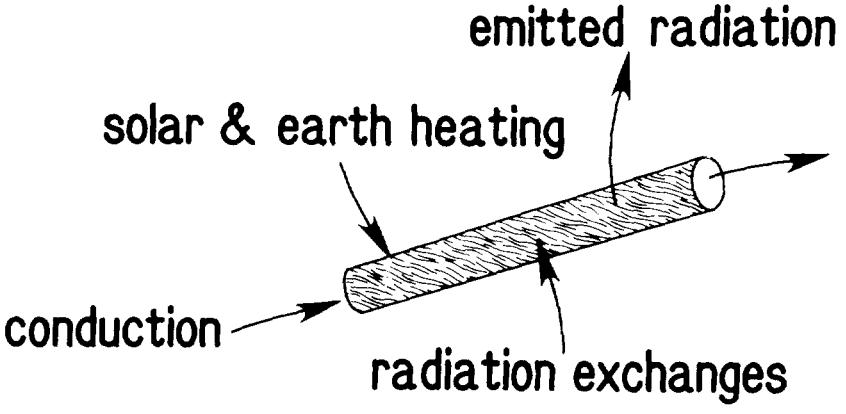

- Considerations
  - –conduction combined with radiation
  - –nonlinear, transient
  - –member–to–member radiation exchanges
  - –member–to–surface radiation exchanges
  - –temperature dependence of material and surface properties

ROD ELEMENT THERMAL MODELS

Three thermal models of a truss member are considered: (1) a conventional two node element with a linear temperature distribution, (2) a nodeless variable higher order element with a quadratic temperature distribution, and (3) an isothermal element. The first two elements are useful in modeling members with significant member temperature gradients due to conduction, and the last element is useful for modeling members with negligible conduction. The isothermal element is similar to traditional lumped heat transfer models and does not transfer heat via conduction between adjacent members as with the first two elements. Thus with isothermal elements, the solution of simultaneous equations is avoided, and the transient response of each member is computed separately.

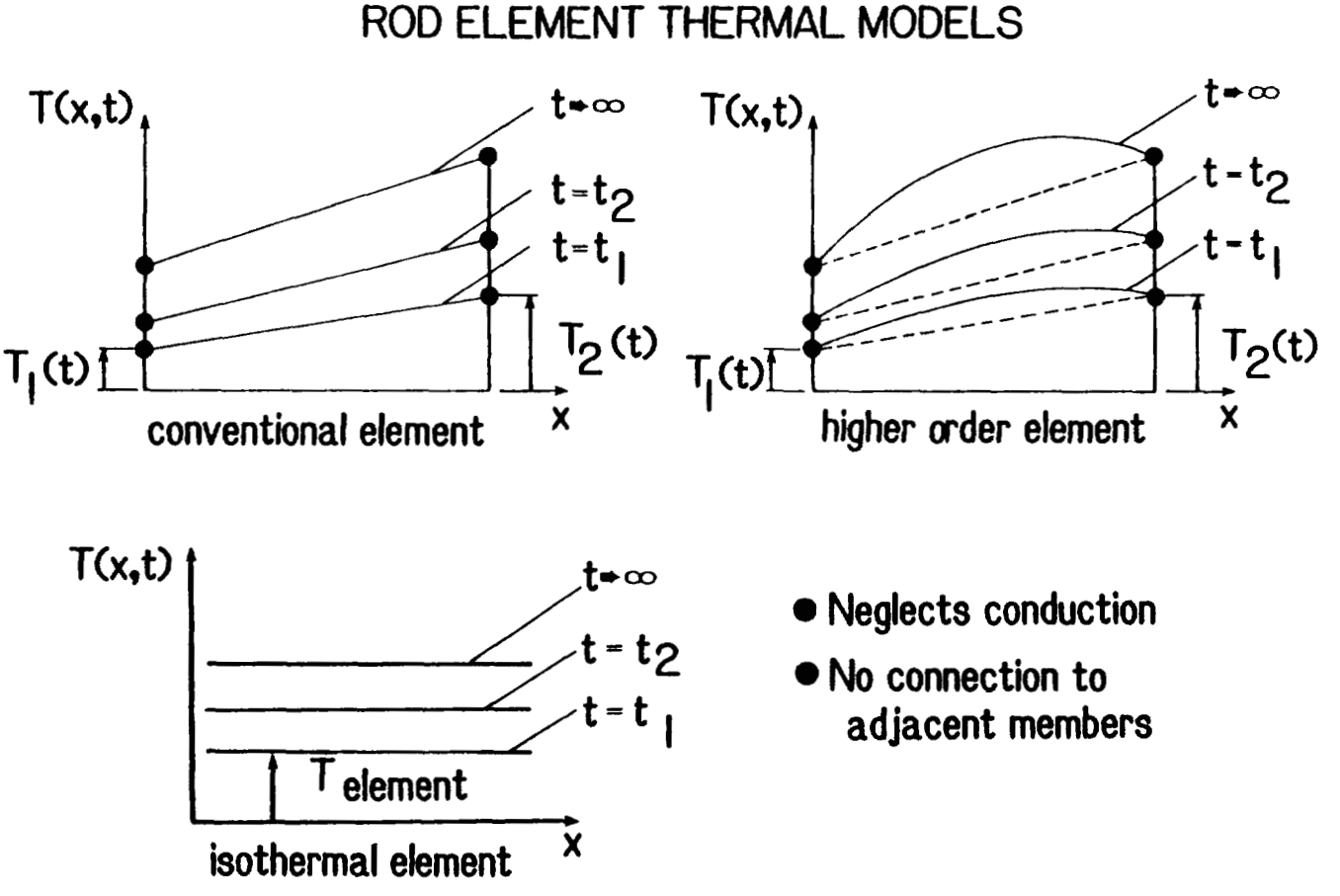

EFFECTS STUDIED

To evaluate the three thermal finite elements, studies were made to determine: (1) the effect of thermal conductance on temperature distributions, and (2) the effects of metallic joints on temperatures and displacements for composite members. The studies were performed by first computing detailed temperature distributions for a three-member truss with a refined model of conventional elements. Then, the performance of each thermal element was evaluated by comparing one element per member solutions with the refined model results.

A truss member temperature distribution depends on the member conductance kA/L where k is the thermal conductivity, A is the cross-sectional area and L is the member length. Two cases of conductance are considered: high conductance, which is characteristic of metallic members, and low conductance, which is characteristic of composite members. In this study member joints are neglected.

In the second study, modeling of composite members with metallic joints was considered. Both the thermal and deformation response are computed, and an approximate method for including metallic joint effects in simple finite element models is presented.

- THERMAL CONDUCTANCE (kA/L) ON TEMPERATURES
  - NEGLECT JOINTS
  - HIGH CONDUCTANCE MEMBERS (METALLICS)
  - LOW CONDUCTANCE MEMBERS (COMPOSITES)

- METALLIC JOINTS WITH COMPOSITE MEMBERS
  - TEMPERATURE RESPONSE
  - DEFORMATIONS
  - APPROXIMATE ANALYSIS APPROACH

HIGH CONDUCTANCE TRUSS MEMBER TEMPERATURE DISTRIBUTIONS

The simple three-member truss shown is subject to different heating rates and undergoes steady-state heat transfer. Each member of the truss was first modeled with eight conventional elements, and the computed temperatures (shown as the solid line) serves as the reference "exact" solution for the evaluation. Member conductance was based on all aluminum members. The truss was then analyzed with: (1) one conventional element per member, (2) one higher-order nodeless variable element per member, and (3) one isothermal element per member.

The figure shows that one conventional element per member predicts the nodal temperatures quite well but either under- or overestimates interior member temperatures. Since member forces depend on the integration of member temperature distributions, use of a single conventional element per member introduces serious errors in the structural analysis and is not recommended. The isothermal element predicts neither accurate nodal temperature nor average member temperatures and is clearly inadequate. The single nodeless variable element per member does an excellent job of predicting the nodal and member interior temperatures and is the superior element for this high conductance case.

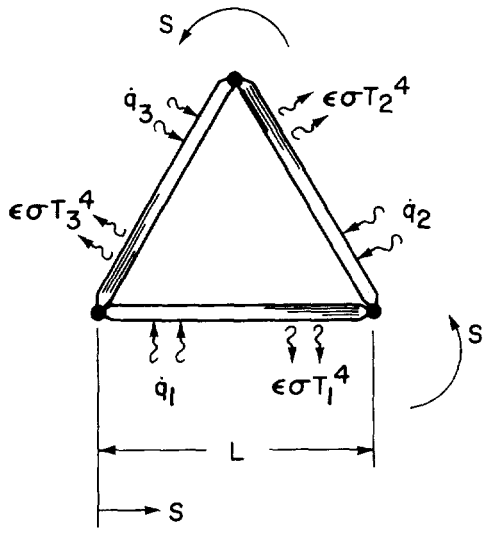

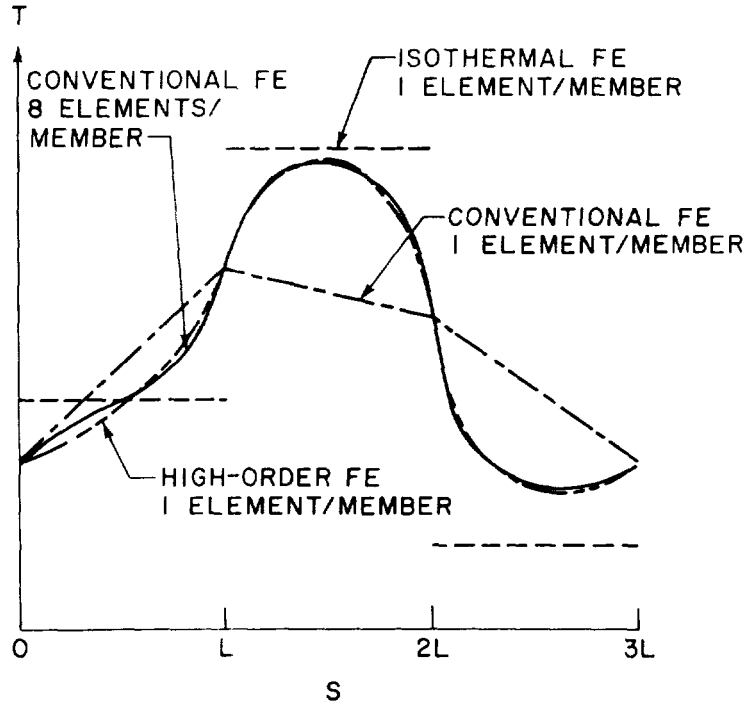

LOW CONDUCTANCE TRUSS MEMBER TEMPERATURE DISTRIBUTIONS

The three-member truss in the previous figure was re-analyzed with a conductance based on all graphite-epoxy members.

The "exact" solution based on eight conventional elements per member shows extremely sharp temperature gradients near the joints but nearly uniform temperature over most of the member length. A single conventional element predicts correct nodal temperatures, but incorrectly predicts the temperature distribution within an element. The isothermal element, however, does an excellent job of predicting the nearly uniform member temperatures. The higher-order element did better than the single conventional element but tended to under- or overestimate member interior temperatures.

For computation of the structural response, the results from the isothermal elements are superior for this low conductivity material since the average member temperature is predicted quite well. Use of these elements gives improved structural accuracy and also allows smaller, uncoupled thermal models with significant computational advantages.

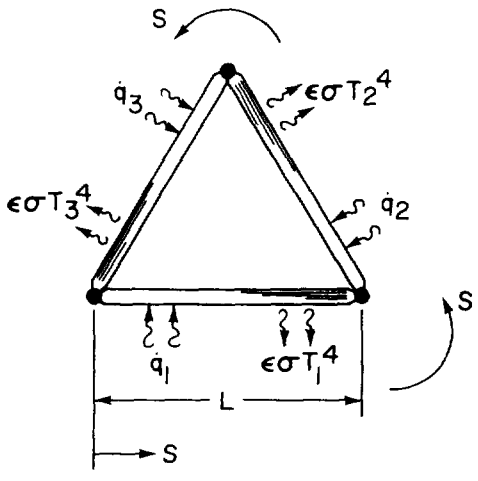

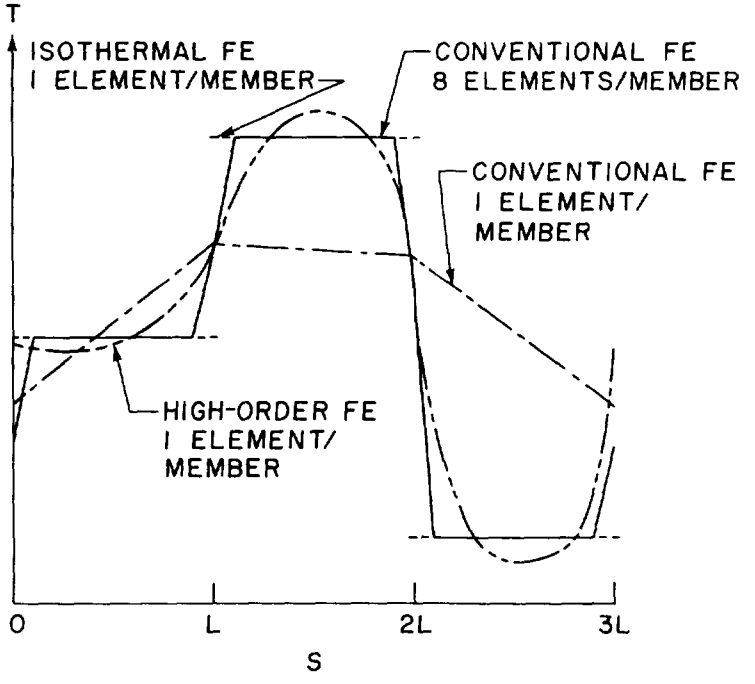

THREE-MEMBER ORBITING TRUSS USED IN JOINT EFFECTS STUDY

The previous figure showed that one isothermal element per member was capable of predicting member temperatures of graphite-epoxy members. To investigate the effects of metallic joints, a three-member truss based on the LRC octetruss, ref. 5, was analyzed. Each member consists of two truncated cones made of graphite-epoxy tubes connected with aluminum joints and is 5.42 meters (213 inches) long from end to end. The transient thermal-structural response was computed for the truss in a geo-synchronous orbit in the ecliptic plane. The truss is earth-facing, but the truss plane is oriented obliquely so that each member receives different solar heating.

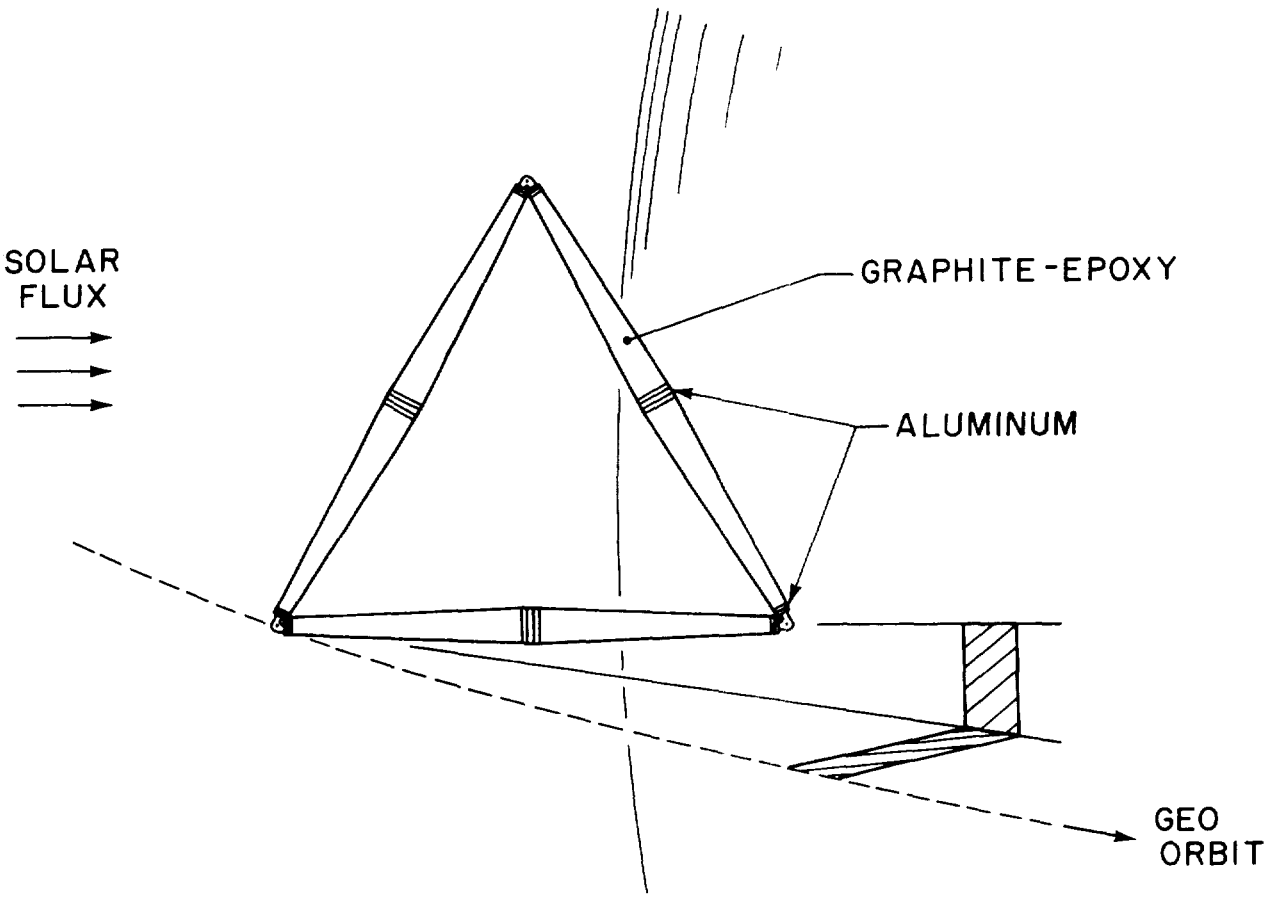

TRUSS TEMPERATURE DISTRIBUTIONS AT TYPICAL ORBIT POSITION

The truss is shown receiving solar heating at a typical orbit position prior to entering the earth's shadow. Truss temperatures were computed using a detailed model of twenty-one conventional elements per member taking into account the different thermal properties of the aluminum and graphite-epoxy members and varying cross-sectional area. Temperatures were also computed with one isothermal element per member neglecting the joints.

For this typical orbit with direct solar heating, joint effects are small. Member temperatures are nearly uniform except the joints have slightly higher temperatures due to different surface properties. All temperatures are very close to radiation equilibrium; surface absorptiveness and emittance control the temperatures. Member temperatures are predicted quite well by a single isothermal element per member.

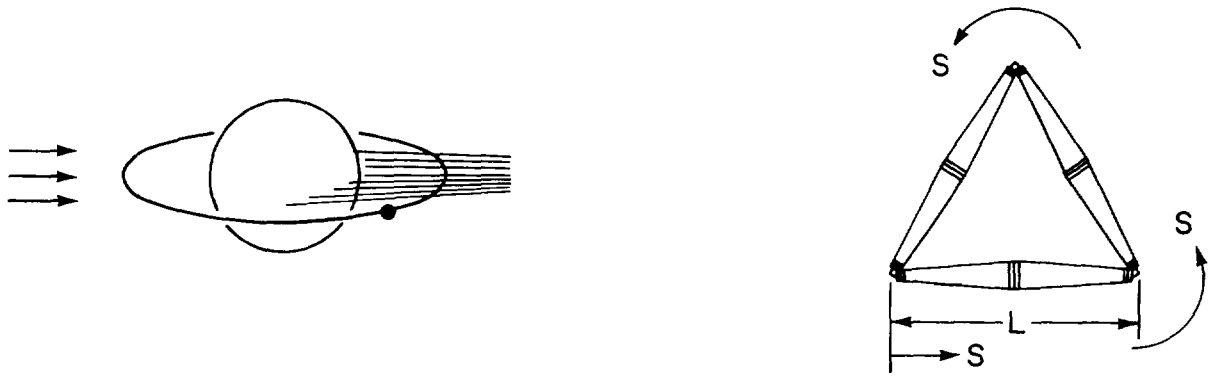

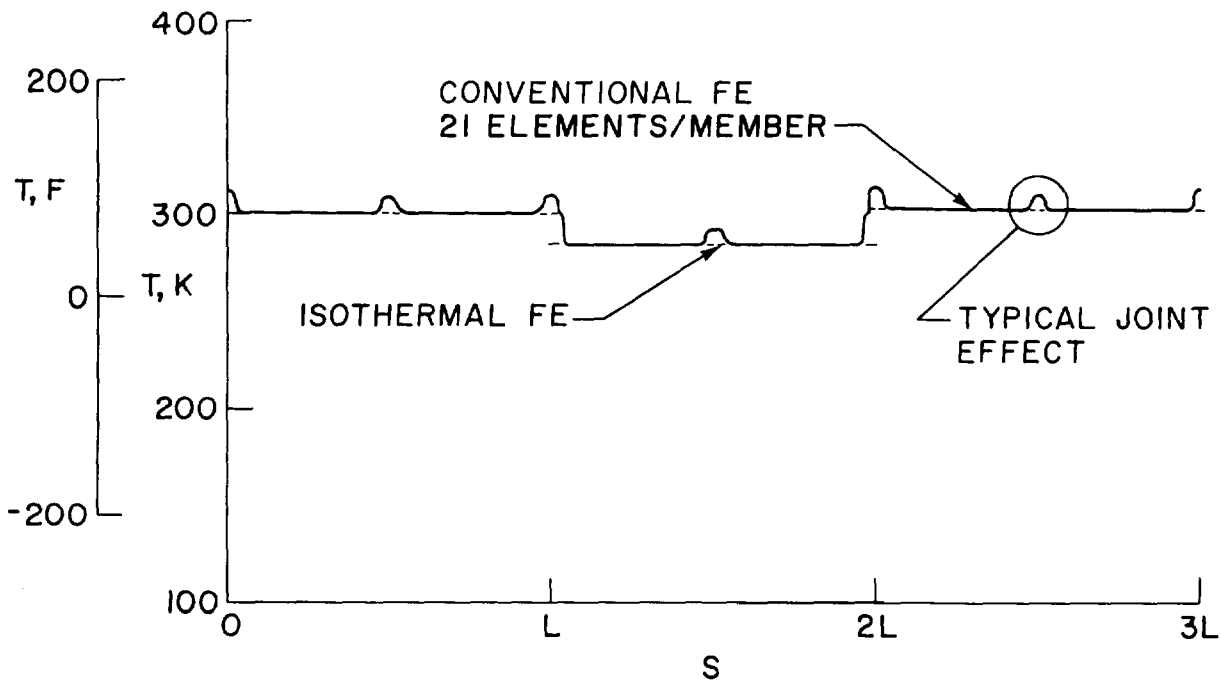

TRUSS TEMPERATURE DISTRIBUTIONS IN EARTH SHADOW

Once the truss enters the earth shadow, there is a rapid drop in temperatures since the only incident heating is due to earth emission, which is quite small. The composite member temperatures drop quite rapidly, but the joint temperatures fall more slowly due to their larger thermal capacitance which controls the transient thermal response. Thermal capacitance is defined as ρcV where ρ is the density, c is the specific heat, and V is volume.

Member temperatures are equal due to the small earth heating and are predicted accurately by the isothermal elements.

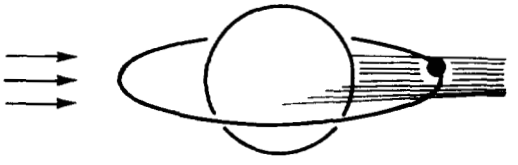

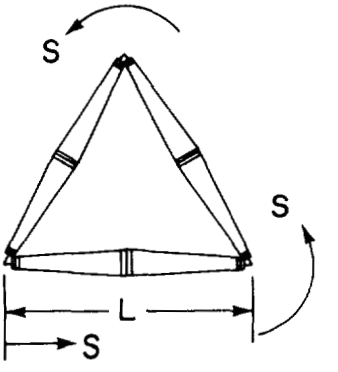

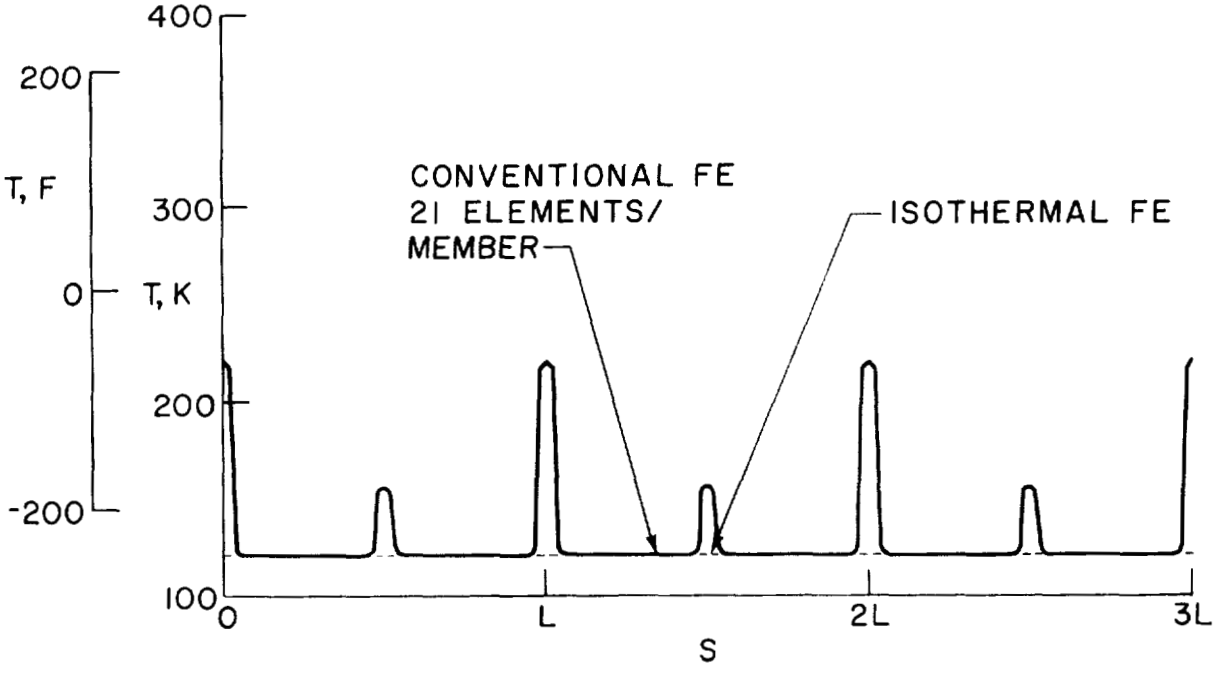

TRUSS MEMBER AXIAL DISPLACEMENT ORBITAL HISTORY

The axial displacement history of a typical truss member is shown during a geosynchronous orbit period. Deformations are based on a noon position reference temperature when the member receives large solar heating. The member first contracts and then expands slightly during the first twelve hours of the orbit as the incident heat drops and then rises with changing member orientation. The member lies in an oblique earth-facing plane and receives maximum solar heating at t = 11 hours when the small thermal expansion occurs. During earth shadow transit there is a rapid contraction of the truss, and it experiences its maximum distortion.

The structural response based on the isothermal element temperature history and a single structural element with only the graphite-epoxy coefficient of expansion tends to underestimate the structural deformations. The next figure shows the variation of the axial displacement along the member length at time t = t_1 on the graph below.

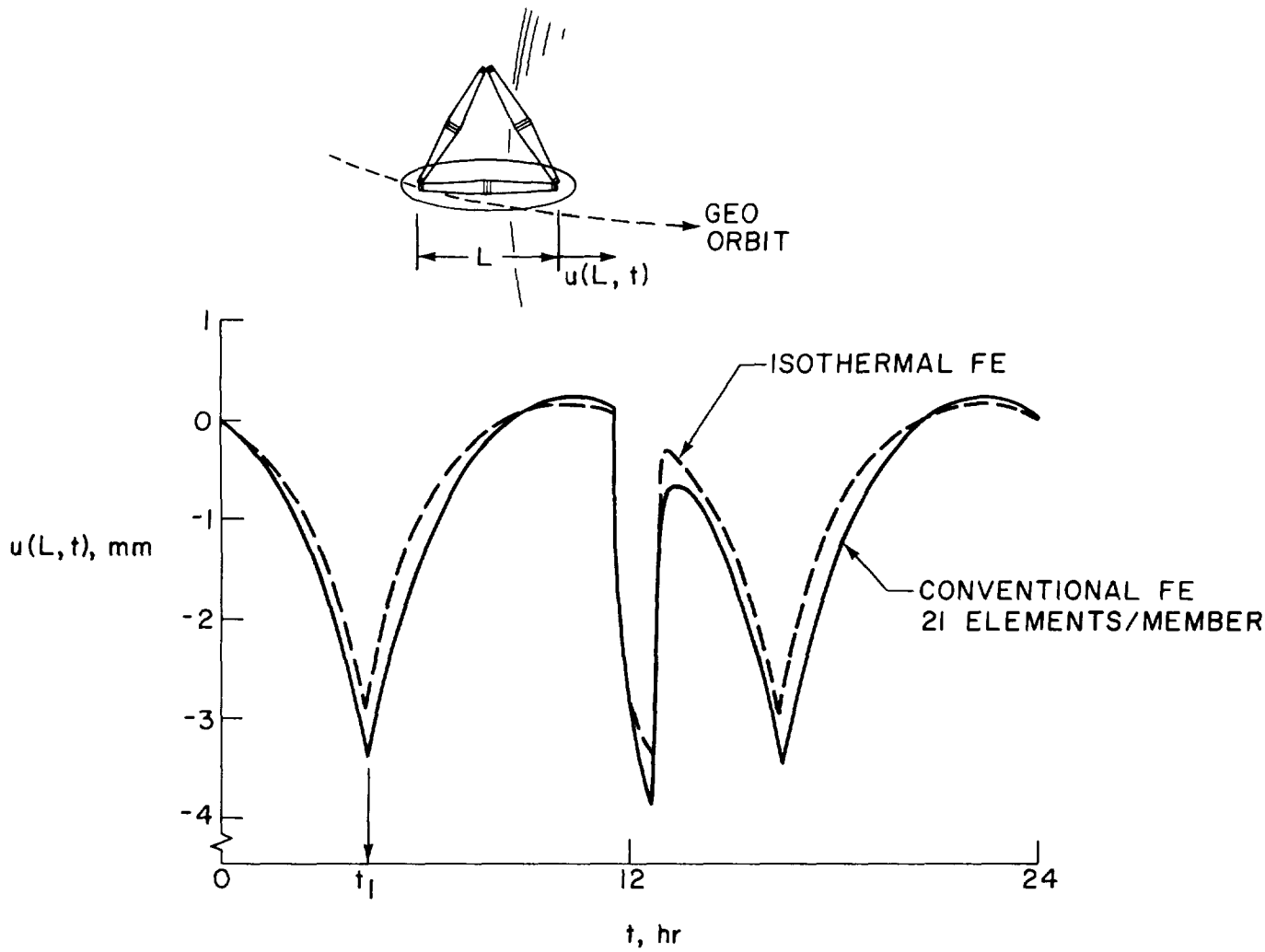

TRUSS MEMBER AXIAL DISPLACEMENT DISTRIBUTIONS

The details of the axial displacement variation along member length is shown at time $t = t_1$. The conventional twenty-one element solution shows the relatively larger distortions experienced by the member at the three aluminum joints due to their higher thermal expansion coefficients. As mentioned previously, a single structural element with only the graphite-epoxy coefficient of expansion underestimates the deformation since it neglects the aluminum joints; maximum member contraction is underestimated by 18 percent.

To compensate for the aluminum joints, another isothermal analysis was performed with equivalent member capacitances and thermal expansion coefficients based on weighted averages of member aluminum and graphite-epoxy properties. This analysis overestimated the member contraction by 8 percent.

There are significant computational savings to be gained by using one isothermal element and one structural element per truss member. In a large truss with hundreds of members, the one element per member approach is probably the only tractable solution method. The above study shows, however, that aluminum joints can have significant effects on deformations. Additional study is needed to define clearly the role of joint effects of deformations of large trusses.

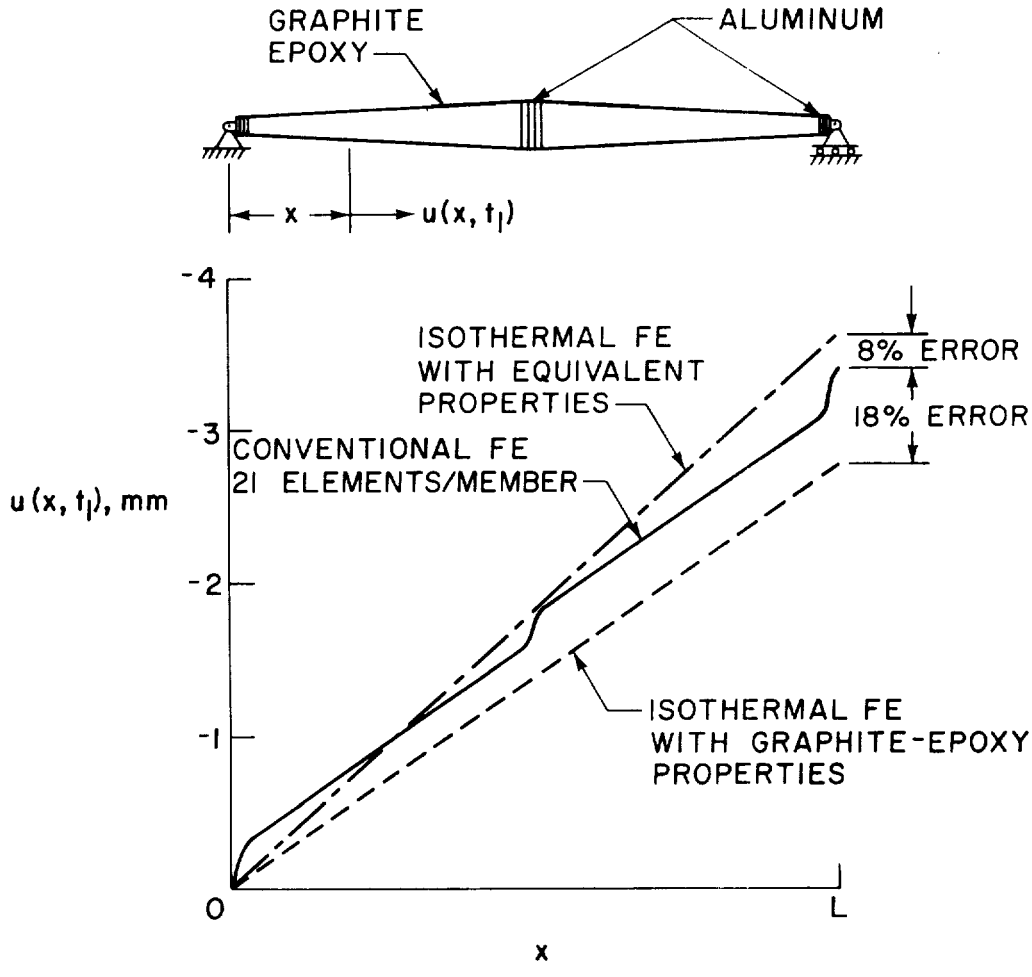

CONCLUDING REMARKS

This paper demonstrates the characteristics of an integrated thermal-structural analysis approach which employs a geometric model with a common discretization for all analyses. It uses improved thermal elements and the results from the thermal analysis directly in the structural analysis without any intervening data processing.

Comparative calculations for three thermal elements show that a higher-order element works best for high conductivity materials and that an isothermal element works best for low-thermal conductivity materials. These elements give a good representation of member temperatures and yield the best member forces. Conventional two-node elements available in NASTRAN and SPAR predict temperatures well in a refined mesh with several elements per member, but they would not be effective in large truss analysis due to prohibitive computational costs. Analyses with isothermal elements would be preferable for trusses with composite members since member temperatures can be computed efficiently and accurately.

A study of the effects of aluminum joints on the thermal deformations of a simple, plane truss with composite members showed that joint effects may be significant. When aluminum joints were neglected, member deformations were underestimated by 18 percent. Further study is needed to assess the role of joint effects on the deformation of large trusses.

ACKNOWLEDGEMENT

This paper was based upon research supported by the NASA-Langley Research Center under grant NSG 1321. Allan R. Wieting, Head of the Aerothermal Loads Branch, is technical monitor.

- CHARACTERISTICS OF INTEGRATED APPROACH
  - GEOMETRIC MODEL WITH COMMON DISCRETIZATION
  - IMPROVED THERMAL ELEMENTS
  - STRUCTURALLY INTEGRATED THERMAL RESULTS
- THREE TRUSS THERMAL ELEMENTS DESCRIBED FOR CONDUCTION COMBINED WITH RADIATION
- ISOTHERMAL ELEMENT BEST FOR LOW CONDUCTIVITY MATERIAL
  - GOOD REPRESENTATION OF MEMBER TEMPERATURES
  - BEST MEMBER FORCE
- CONVENTIONAL THERMAL ELEMENTS IN NASTRAN AND SPAR NOT EFFECTIVE
- METALLIC JOINT EFFECTS SIGNIFICANT AND REQUIRE FURTHER STUDY
- INTEGRATED FINITE ELEMENT APPROACH ATTRACTIVE FOR ORBITING STRUCTURES ANALYSIS

REFERENCES

1. Thornton, Earl A.; Dechaumphai, Pramote; and Wieting, Allan R.: Integrated Thermal-Structural Finite Element Analysis. Proceedings of the AIAA/ASME/ASCE/AHS 21st Structures, Structural Dynamics and Materials Conference, May 12-14, 1980. Seattle, Washington, pp. 957-999, AIAA Paper No. 80-0717.

2. Thornton, Earl A.; Dechaumphai, Pramote; Wieting, Allan R.; and Tamma, Kumar K.: Integrated Transient Thermal-Structural Finite Element Analysis. Proceedings of the AIAA/ASME/ASCE/AHS 22nd Structures, Structural Dynamics and Materials Conference, April 6-8, 1981. Atlanta, Georgia, pp. 16-32, AIAA Paper No. 81-0480.

3. Mahaney, Jack; Thornton, Earl A.; and Dechaumphai, Pramote: Integrated Thermal-Structural Analysis of Large Space Structures. Symposium of Computational Aspects of Heat Transfer in Structures held at NASA Langley Research Center, November 3-5, 1981. (To be published as a NASA CP.)

4. Chambers, B. C.; Jensen, C. L.; Coyner, J. V.: An Accurate and Efficient Method for Thermal-Thermo-elastic Performance Analysis of Large Space Structures. AIAA 16th Thermophysics Conference, June 23-25, 1980, Palo Alto, California. AIAA Paper No. 81-1178.

5. Card, M. F.; Bush, H. G.; Heard, W. L., Jr.; Mikulas, M. M., Jr.: Efficient Concepts for Large Erectable Space Structures. Large Space Systems Technology, An Industry/Government Seminar held at NASA-Langley Research Center, Hampton, Virginia, January 17-19, 1978. NASA CP 2035, pp. 627-656.

VIBRATION AND BUCKLING STUDIES OF PRETENSIONED STRUCTURES

By

W. Keith Belvin

Structures and Dynamics Division

NASA Langley Research Center

Hampton, Virginia 23665

Large Space Systems Technology

1981

Third Annual Technical Review

November 16-19, 1981

INTRODUCTION

Many proposed large space structures make use of the low mass and deployability of pretensioned structures to achieve efficient designs. These structures use tension elements (cables, rods and membranes) to provide stiffness and stability to structural systems. To understand the fundamental structural characteristics of pretensioned structures, analyses and tests of some simple configurations have been performed. The buckling and vibration behavior of a pretensioned stayed column have been studied in detail.

Fig. 1 shows several areas which have been identified as needs in pretensioned structure research. The first four will be discussed with the aid of data obtained during analyses and tests of the stayed column. Deployment will not be discussed.

- ANALYTICAL MODELING AND VERIFICATION
- EFFECTS OF FABRICATION IMPERFECTIONS
- OPTIMUM PRESTRESS LEVEL
- EFFECTS AND ANALYSIS OF NONLINEARITIES
- CONTROLLED SEQUENTIAL DEPLOYMENT

Figure 1

Pretensioned Stayed Column

The test article, shown in Fig. 2, consists of 24 cables or stays attached to a central tube. The column length is 5.2 m and the mass, including joints and fittings, is 0.504 kg. Three (3) stay planes consisting of eight (8) stays and one radial spoke are used to provide isotropic stiffness. Lateral stiffness provided to the central tube by the stays was designed to insure Euler buckling in individual bays. Imperfection analysis was used to determine the prestress level required to prevent stay slackening due to static compressive loading.

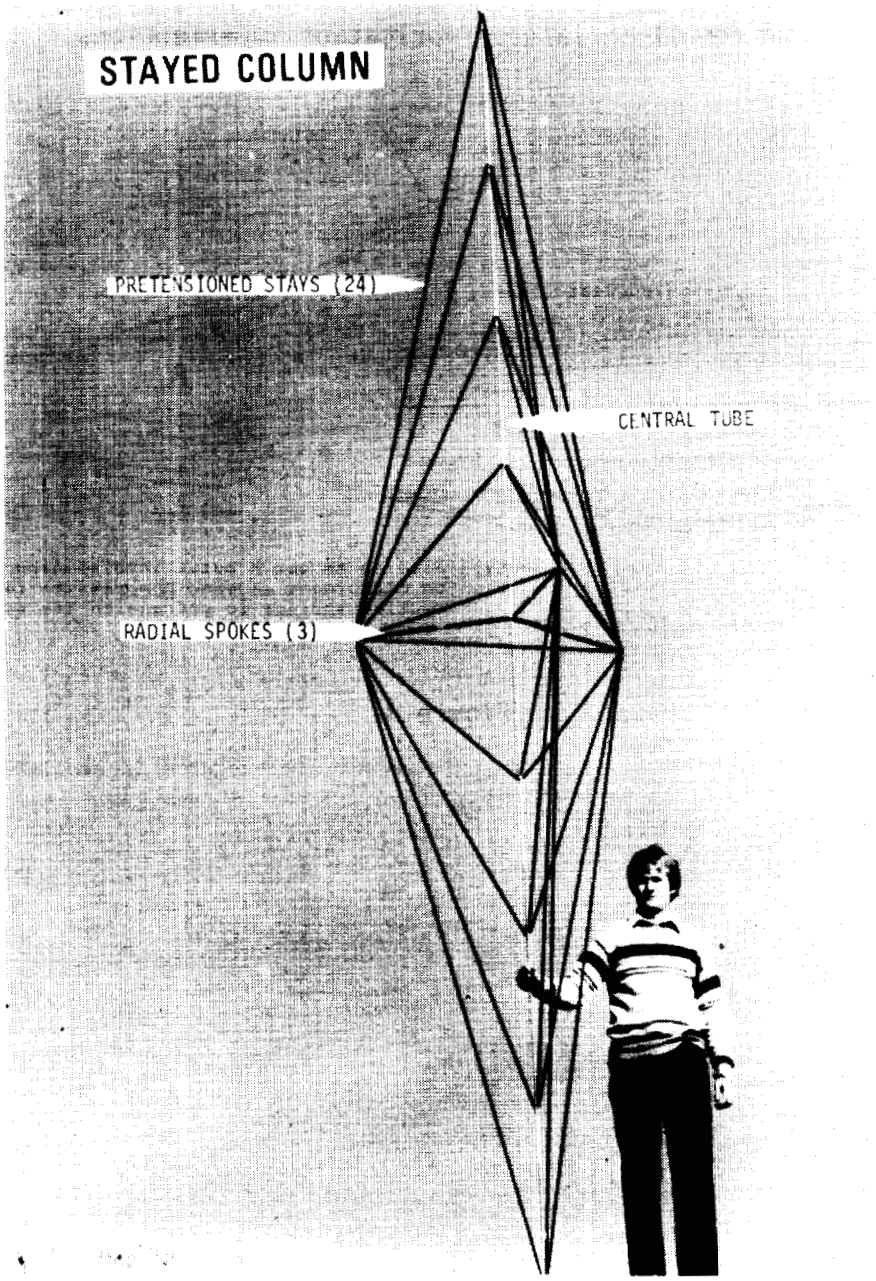

Figure 2

Constant-Force Spring Capsules Used to Reduce Imperfections

To provide axial stiffness, the stays must be in tension at all times. The pretension force for each set of stays is provided by a constant force spring capsule as shown in Figure 3. This capsule uses the Euler load of three buckled stainless steel strips to maintain the sum of the axial components of tension in the three stays to be constant. If the central tube bending stiffness is negligible, the spring capsule will absorb errors in stay length and distribute an equal force to each stay. However, the central tube bending stiffness is not negligible in most cases and prevents the force from being evenly distributed. Nevertheless, the use of a spring capsule to pretension the stays reduces the effects of fabrication imperfections by allowing the stays to move along the central tube axis. Rigidly attaching the stays to the central tube would preclude axial motion and result in larger fabrication imperfections.

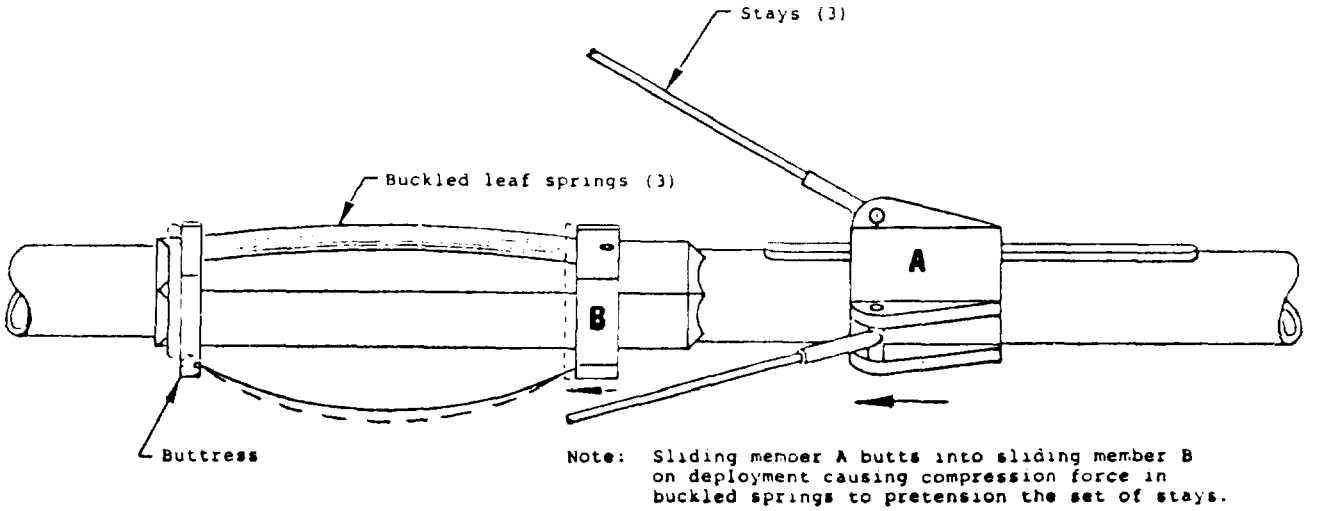

Figure 3

Buckling and Vibration Test Fixture

All buckling and vibration tests of the stayed column were performed in the test fixture shown in Fig. 4. Non-contacting proximity probes were used to measure static and dynamic deflections. Static axial load was applied to the column by adding weight to the load pan. Only the lateral vibrational characteristics of the column were analyzed. Consequently, the electrodynamic shaker was always oriented perpendicular to the column axis. Vibration tests were performed with and without axial load.

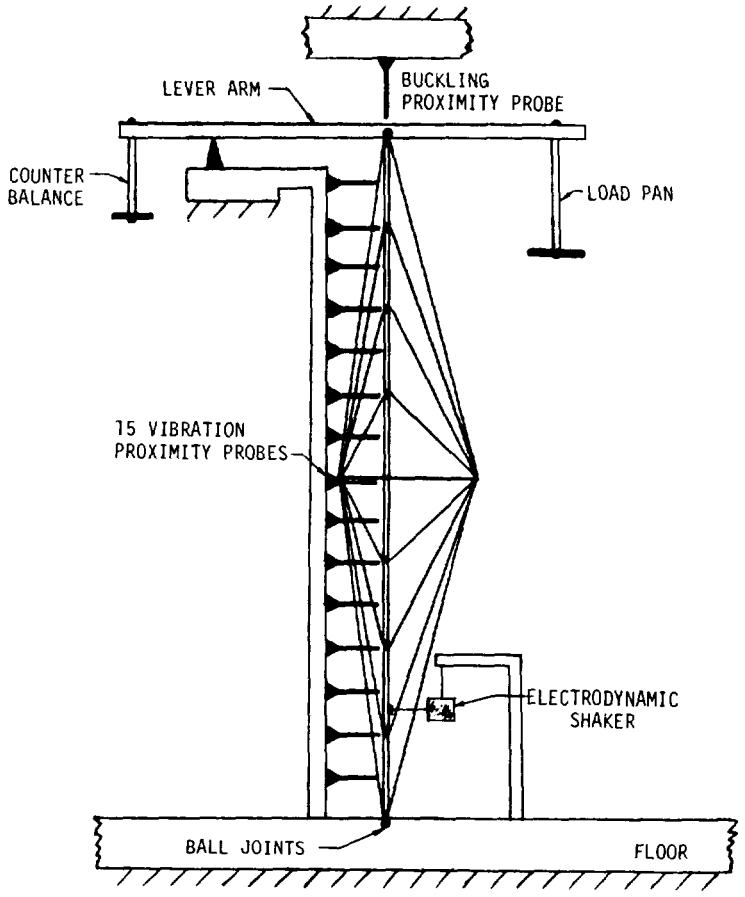

Figure 4

Buckling Behavior and Analyses

As mentioned earlier, the column was designed to produce Euler buckling between bays. The mode shape, shown in Figure 5, was computed by finite element analysis and shows indeed that the design results in such a mode. The initial precompression is highest in the center bays and can be noticed by larger deflections in these bays. Two finite element analyses were used to analyze the buckling load: Model 1 used linear stiffness terms and model 2 used "exact" transcendental stiffness terms. Both analyses agreed within 2 percent of the observed buckling load of 277.4 N. The use of spring capsules permits a highly determinate load path with taut stays and permits accurate calculations of buckling loads.

ANALYTICAL AND EXPERIMENTAL BIFURCATION BUCKLING LOAD

	BUCKLING LOAD, N
MODEL 1	280.67
MODEL 2	277.22
EXPERIMENTAL	277.4

MODE SHAPE

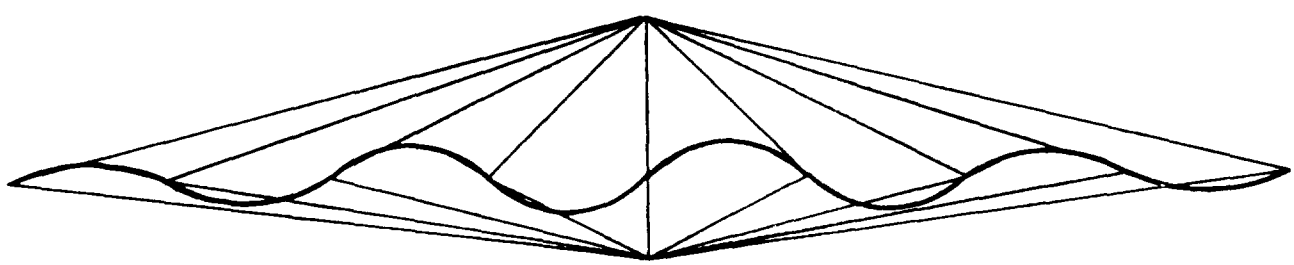

Figure 5

Unusual Post Buckling Behavior Observed

The end shortening that occurs after buckling results in slackening of the stays. When the stays become slack, they no longer provide the lateral stiffness required to form nodes in the central tube. Stay slackening results in the central tube buckling in an overall bending mode. Since the buckling load of the slack stay mode is much less than the load associated with the taut stay mode, the column exhibits a post buckling restoring force of approximately 1/64 the original buckling load. Figure 6 shows a graphical representation of the stayed column's load deflection path in the post buckling region . To return to the original shape the column compressive load must be reduced below the slack stay buckling load. This behavior will require the designer to insure a safe margin between the design operating load and the buckling load.

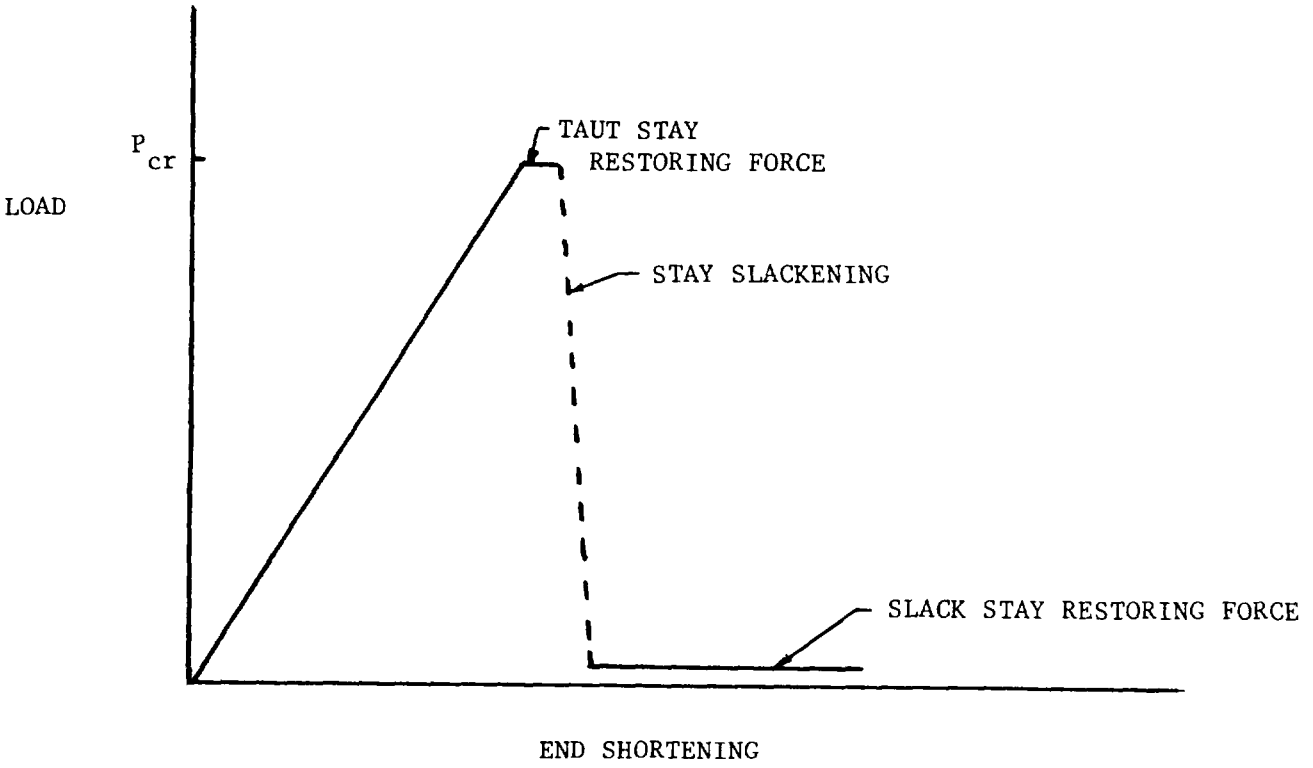

Figure 6

Frequency Spectrum

Response of the column to dynamic excitation is difficult to analyze due to the large number of natural frequencies or high modal density of the structure. Figure 7 shows the quadature component of displacement at the 15 proximity probe locations indicated in Figure 4. A frequency sweep using sinusoidal excitation was performed to access the number of natural frequencies from 10 to 60 Hz. Whereas only three modes dominated by central tube deflections were found, a large number of lateral stay resonances occur because fabrication imperfections introduce different tension levels in each stay. Many localized modes of vibration occur in the structure as noted by almost random distribution of peaks. The large number of localized modes may be advantageous since energy may be dissipated in local responses rather than global type modes.

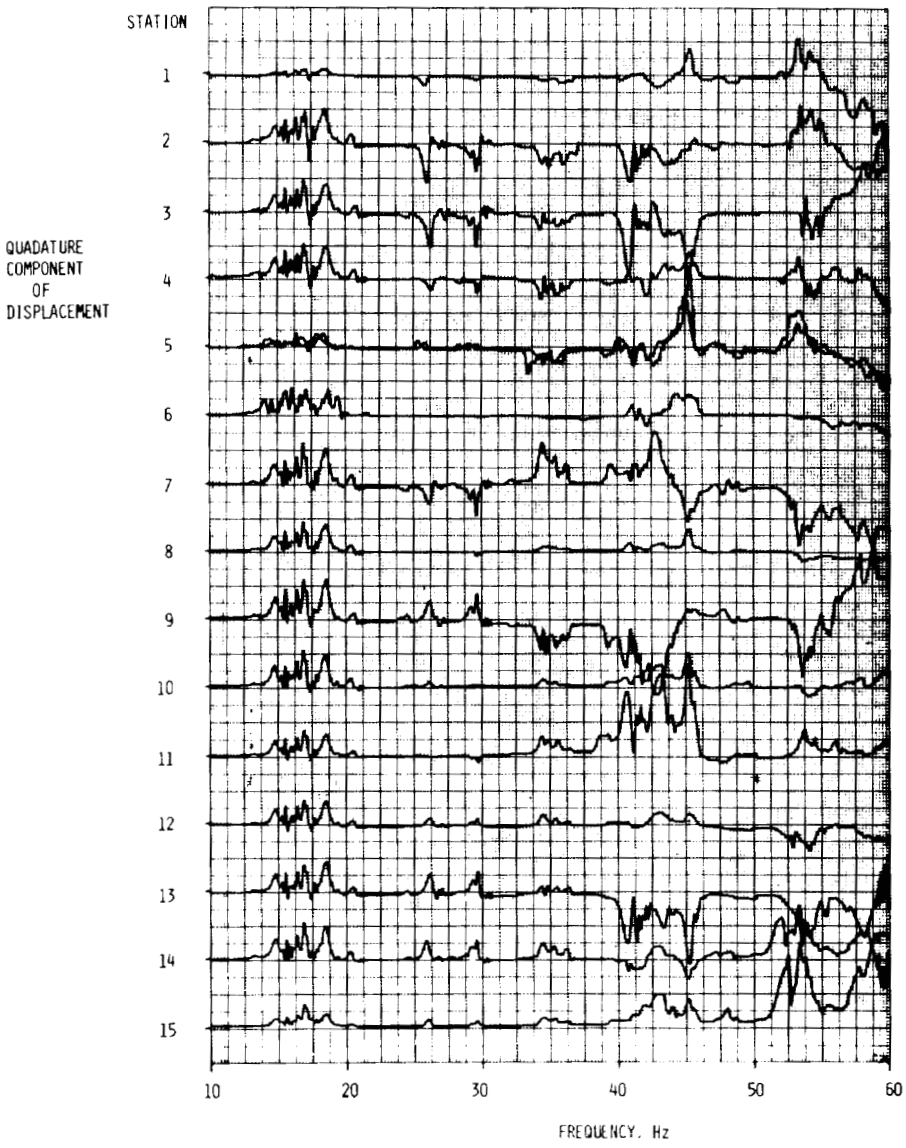

Figure 7

Fabrication Imperfection Effects on Stay Frequencies

As mentioned earlier, fabrication imperfections can introduce different tension levels in individual stays. The stayed column was designed assuming one stay would be too short by εl_n and the two opposite stays too long by εl_n. (Where ε is a measure of fabrication tolerances, $1.16 \times 10\text{-}4^{m}/_{m}$ for this design, and l_n is the stay length of the n^{th} set.) These imperfections resulted in the design tension levels shown in Fig. 8. Calculated stay frequencies based on the design tension level and measured stay frequencies for the first lateral mode of vibration are also shown in Fig. 8. These data show the deviation in frequency of individual stays created by fabrication imperfections. Since imperfections occur randomly, and the imperfections were not measured, the actual fabrication tolerance (ε) has not been determined.

	STAY FORCE, N
N=1	2.4
N=2	1.9
N=3	5.2
N=4	10.6

C A B STAY PLANE	MEASURED FREQUENCY, Hz A	B	C	CALCULATED A B C
TOP HALF				
N=4	17.7	14.6	15.6	17.25
N=3	13.9	17.2	17.0	15.68
N=2	19.8	18.1	15.4	13.46
N=1	29.8	22.8	31.2	23.91
BOTTOM HALF				
N=1	25.6	22.3	31.1	23.91
N=2	15.1	15.0	14.7	13.46
N=3	15.9	16.9	16.1	15.68
N=4	16.7	16.4	15.2	17.25

Figure 8

Verification of Dynamic Models

Verification of the stayed column dynamic models was performed by measuring the frequency and shapes of the central tube vibration modes. Two dynamic models were used to predict the central tube modes: Model 1 used linear finite elements with single element representation of the stays and model 2 used a transcendental frequency determinant which accounts for the lateral inertia of the stays. Correlation between analysis and test data of the first three modes is shown in Figure 9. The experimental data is difficult to analyze because of modal coupling between stay and central tube resonances. Nevertheless, both analyses predict the central tube modes with reasonable accuracy. Model 1 and Model 2 predict approximately the same frequency since the stays only represent 8 percent of the total column mass. When the stay mass is not small compared to the effective member mass it is connected to, lateral cable inertia should not be neglected. This inertia can reduce the effective stiffness of the structure and lead to unconservative designs if neglected.

	MODE 1	MODE 2	MODE 3
		FREQUENCY, Hz	
MODEL 1	19.45	36.71	54.64
MODEL 2	19.63	36.09	54.21
EXPERIMENTAL	19.9	34.1	56.5

MODE SHAPES

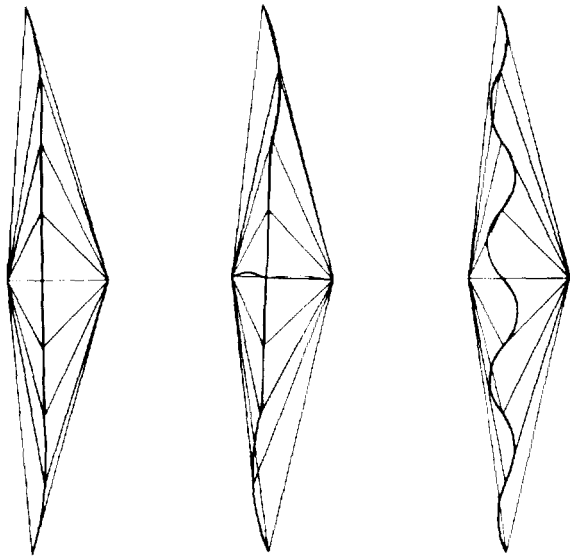

Figure 9

Nonlinear Vibration-Load Interaction

An important characteristic of any structure is the behavior the structure exhibits under load. The previous figure showed the vibration modes of the central tube with no load. Figure 10 shows the change in frequency of these modes that occurs when a static compressive load is applied to the column. All three modes are reduced in frequency with increasing compressive load. However, the third mode, which has the same mode shape as the buckling mode, is most affected by the compressive load. The data points of Figure 10 were obtained experimentally in order to verify the analysis. At loads below 50 percent of the buckling load the data agree with analysis reasonably well. Above 50 percent of the buckling load nonlinear oscillations occurred. This nonlinear behavior is attributed to isolated stay slackening resulting from beam-column interaction. In a dynamic environment, vibration-load interaction may produce premature collapse of the column due to stay slackening. Consequently, the dynamic environment should be considered in designing the prestress level.

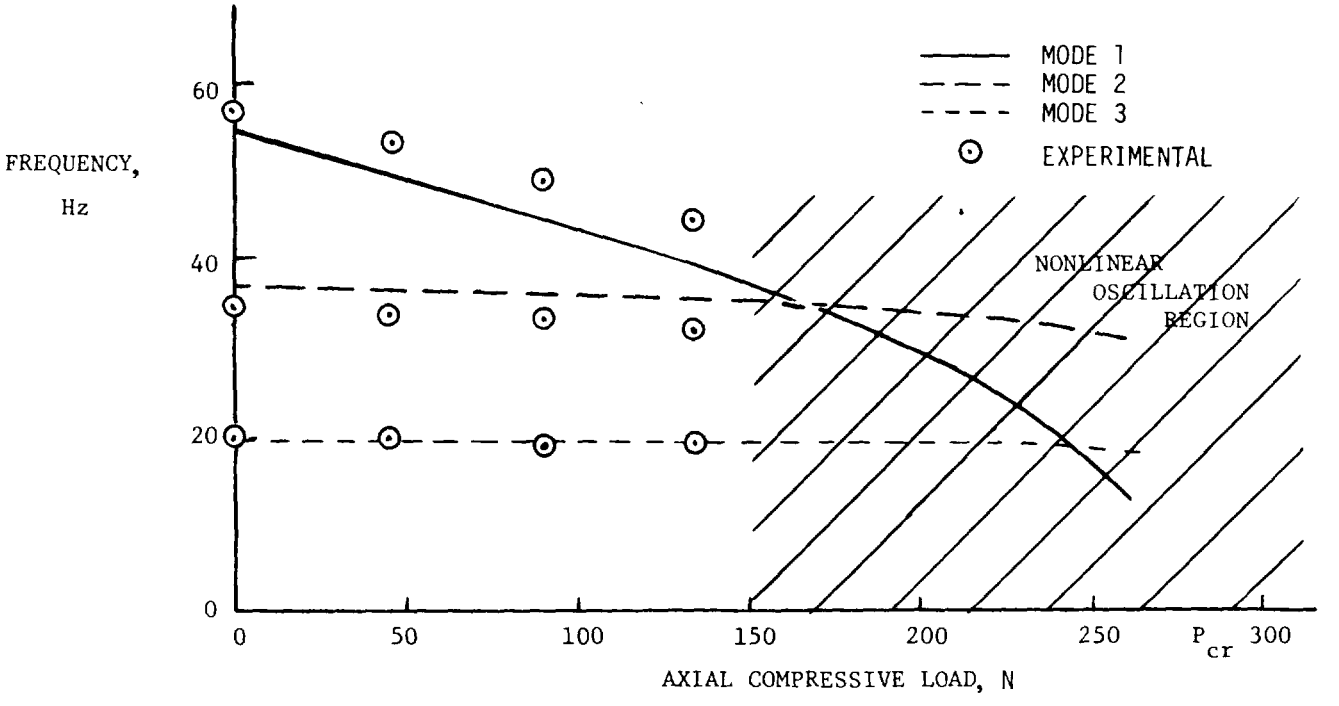

Figure 10

Effects of Prestress

To prevent stay slackening, the stays are pretensioned during deployment. These pretension forces create precompression in the central tube and spokes. The effect of prestress on the buckling and vibration characteristics of the column was studied by analyzing the column at various prestress levels. Figure 11 shows the change in buckling load with stay pretension and also the change in frequency of the first three central tube modes. Increasing pretension increases precompression in the central tube and thus lowers the buckling load proportionately. A reduction in the frequency of the central tube vibration modes also occurs with increasing pretension. The reduced buckling load and reduced frequencies of vibration are usually considered undesirable characteristics. Consequently, prestress levels are designed to minimize these effects. However, designs based on minimizing stay tension are less conservative since stay slackening is more likely to occur.

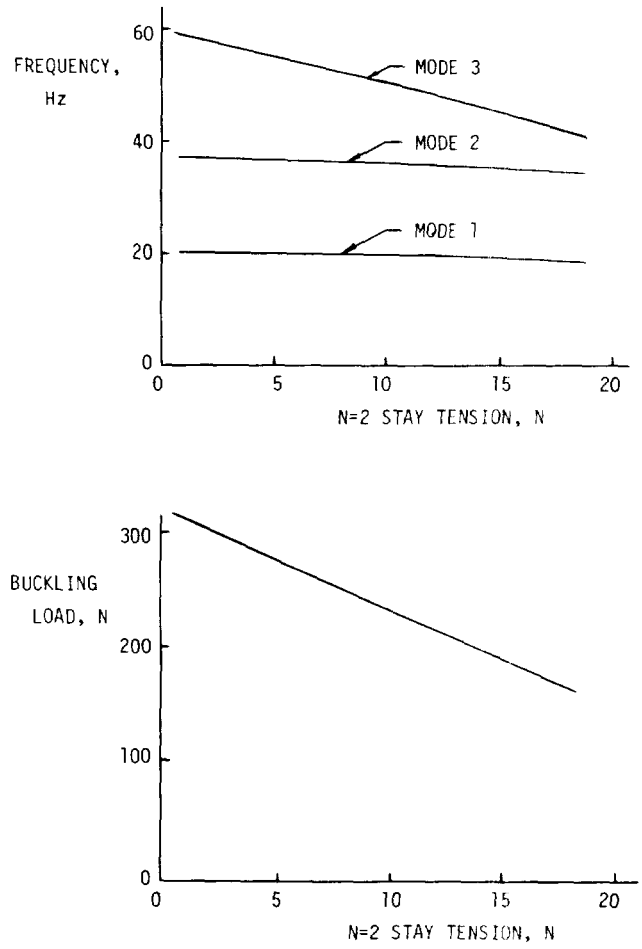

Figure 11

Summary

Results of analyses and tests of a simple pretensioned structure have been presented. Linear finite element analysis correlated well with experimental small amplitude vibration data. The bifurcation buckling load was also predicted accurately. Postbuckling behavior of the column was unusual and results in a post buckling restoring force of only 1/64 the bifurcation buckling load. Interaction between lateral accelerations and compressive load creates isolated stay slackening at loads above 50 percent of the buckling load. Figure 12 shows several generalized conclusions regarding pretension structures. More research will be required to fully understand their impact on the use of pretensioned structures as large space structures.

- EXPERIMENTAL VERIFICATION OF ANALYTICAL MODELS IS DIFFICULT
- IMPERFECTIONS CREATE UNKNOWN TENSIONS IN INDIVIDUAL STAYS
- DYNAMIC LOADING MUST BE CONSIDERED IN SIZING PRESTRESS LEVELS
- STAY SLACKENING MAY PRODUCE SIGNIFICANT NONLINEARITIES

Figure 12

VIBRATION DAMPING CHARACTERISTICS OF GRAPHITE/EPOXY COMPOSITES FOR LARGE SPACE STRUCTURES

R. F. Gibson
Engineering Science Department
and
Mechanical Engineering Department
University of Idaho
Moscow, Idaho 83843

Large Space Systems Technology - 1981
Third Annual Technical Review
November 16-19, 1981
NASA Langley Research Center
Hampton, Virginia

INTRODUCTION

Characterization of the vibration damping properties of fiber reinforced composites is important for several reasons. If the dynamic behavior of composite material components is to be estimated during the design stage, it is necessary to know something about the damping in the materials. Indeed, one of the advantages of fiber reinforced composites over conventional structural metals is their enhanced damping characteristics. Another advantage is the potential for designing materials which have predetermined damping, strength and stiffness properties. It is also known that damping is sensitive to microstructural detail, so that the potential exists for using damping measurements to study such things as microstructural damage and fiber-matrix bond integrity. A logical extension of such studies would be the development of non-destructive damping measurement techniques for use in quality control and in-service inspection of composite components.

Previous work by researchers at NASA Langley has resulted in the development of nestable tapered columns and tetrahedral truss elements for orbital assembly of large space structures (refs. 1 and 2). In order to satisfy constraints on Space Shuttle payloads and on deflections of the assembled structures due to physical loading and solar heating, a $[90/0_3/90]$ graphite fiber reinforced epoxy laminate has been selected as the material to be used in the columns. Although the design of the columns has been based primarily on static loading, it is now desirable to investigate the dynamic behavior as well. Dynamic response of such components is governed by their stiffness, mass and damping properties. On earth, such a structure would be subjected to significant damping due to aerodynamic drag and/or acoustic radiation. In the vacuum of space, however, vibrational energy must be dissipated by either internal damping in the structural material, by friction in the connecting joints, or by active control (refs. 3 and 4). The intent of this investigation was to measure the internal damping and dynamic stiffness of the graphite/epoxy composite material used in the columns, and to study the relationships between dynamic properties derived from tests of small specimens and those of full-scale columns. Such relationships are important because, if it can be shown that small specimens are representative of full-scale components, the effects of loading and environmental conditions can be assessed more readily by testing small specimens.

Based on previous experience with structural vibrations of truss networks and experiments with small models, it is expected that transient vibration of a large space structure will cause both extensional and flexural vibrations of the column elements. Extensional vibrations of the columns would occur primarily at the lowest natural frequency of the structure, which is expected to be well below 1 Hz. The dominant flexural modes have been found to occur in the range 10 - 1000 Hz. Accordingly, the techniques used to measure material damping involve both extensional and flexural vibration in the appropriate frequency ranges.

Flexural damping was measured by using a forced vibration technique developed and used previously by the author (refs. 5 and 6). The technique is based on resonant flexural vibration of shaker excited double cantilever specimens.

Extensional damping was measured by subjecting similar specimens to low frequency sinusoidal oscillation in a servohydraulic tensile testing machine while plotting load versus extensional strain. The size of the resulting hysteresis loop is directly related to the damping in the material. The reason for using such a technique is that the vibration exciters such as those used in the flexural damping tests will not operate at the low frequencies required for extensional vibration testing.

DESCRIPTION OF MATERIALS

The current version of the basic graphite/epoxy nestable column element is a tapered tube 2.6 m (102 in.) long with a 0.635 mm (0.025 in.) thick $[90/0_3/90]$ laminated wall. The large end of the tube has a diameter of 102 mm (4 in.) while the small end has a diameter of 51 mm (2 in.). The 90° plies are of 0.127 mm (0.005 in.) thick T-300 fiber/epoxy, while the 0° plies are 0.127 mm (0.005 in.) thick VSB-32 pitch fiber/epoxy. Two types of epoxies have been used. Early tubes were made using prepreg tape with Hexcel F-263 (or equivalent) epoxy resin, while current tubes are made using a dry fiber resin impregnation procedure with Hysol ADX-16/Epotuf 37-619 resin. The aim of this investigation was to test small flat samples of both types of composites and both types of resins. Resin data is needed for the micromechanics analysis of the composite in terms of constituent material properties (ref. 6). At this writing, only the graphite/F-263 composites and the ADX-16 neat resin samples have been fabricated and tested. All specimens were fabricated by Lockheed Missiles and Space Company, Sunnyvale, California (ref. 7). Test specimens 300 mm long x 25 mm wide x 0.635 mm thick were cut from cured 300 mm x 300 mm panels. Neat resin samples were typically 300 mm x 25 mm x 2.5 mm.

EXTENSIONAL VIBRATION

Global motions of large space structures are expected to occur at extremely low frequencies (< 1 Hz). These motions will generate corresponding low frequency extensional oscillations of the column elements. This type of deformation was simulated on small strain-gaged specimens (Fig. 1) by using a MTS servohydraulic tensile testing machine, and damping was found from the resulting load-strain (or stress-strain) hysteresis loops, on an x-y plotter. Loading was applied through

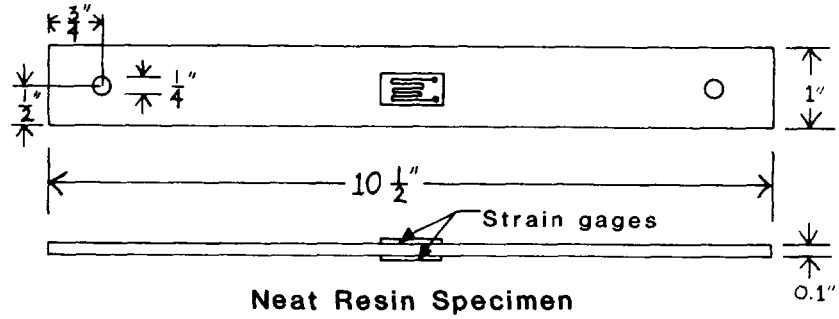

Neat Resin Specimen

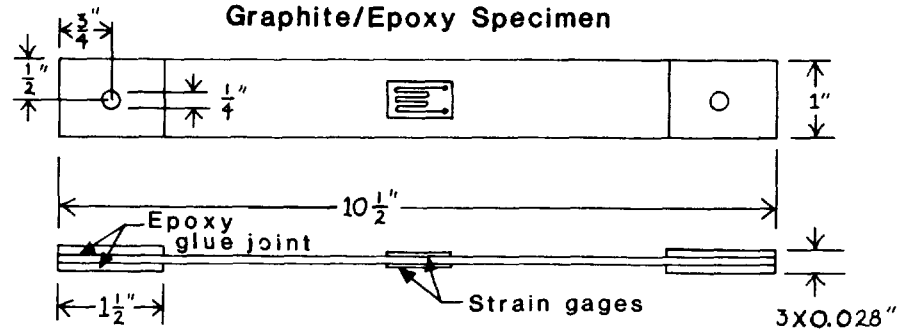

Graphite/Epoxy Specimen

Figure 1

6.35 mm (0.25 in.) diameter steel clevis pins which were inserted through the holes in the ends of the specimens, as shown in Fig. 1. Clevis type loading fixtures were used rather than flat friction grips in order to minimize parasitic energy losses due to clamping friction. A tensile mean stress was applied so that the specimen-loading fixture assembly was always in tension and possible nonlinearities associated with load reversal were avoided. The amplitude of the alternating load was 60-80% of the mean load. The two active gages on each specimen were wired into the bridge circuit on opposite sides, so that bending strains were cancelled out and the resulting bridge output was twice the extensional strain.

Data from the measured hysteresis loops was converted to damping in terms of the loss factor, or loss coefficient (refs. 8 and 9). The loss factor is defined as

$$\eta = \frac{D}{2\pi U} \tag{1}$$

where D = energy dissipated per cycle

U = energy stored at maximum vibratory displacement

For a single-degree-of-freedom model (which is generally acceptable for lightly damped systems near resonance) the loss factor is related to other damping definitions as follows:

$$\eta = \frac{E''}{E'} = \frac{\delta}{\pi} = \frac{\Delta f}{f_o} = \frac{1}{Q} = 2\frac{c}{c_{cr}} \tag{2}$$

where

E'' = loss modulus

E' = storage modulus

δ = logarithmic decrement

Δf = bandwidth of the 3 db down or half-power points

f_o = undamped natural frequency

Q = quality factor

$\frac{c}{c_{cr}}$ = damping ratio

Referring to Fig. 2, the energy dissipated per cycle is simply the area enclosed by the elliptical hysteresis loop

$$D = \pi cd = \pi\left(\frac{a}{2}\cos\theta\right)d \tag{3}$$

The energy stored at maximum displacement may be approximated by the triangular area

$$U = \frac{1}{2}\left(\frac{b}{2}\right) d\cos\theta \tag{4}$$

Note that U is the energy associated with the vibration only, not the total area under the curve (i.e., the energy due to the mean stress is not included). According to Eq. (1) the loss factor is then

$$\eta = \frac{D}{2\pi U} = \frac{\pi ad\cos\theta}{2(2\pi)\left(\frac{1}{2}\right)\left(\frac{b}{2}\right)d\cos\theta} = \frac{a}{b} \tag{5}$$

Specimens were subjected to several cycles of loading to stabilize the hysteresis loops; then the load cell output was plotted versus the strain gage bridge output on an x-y recorder and the dimensions a and b were used to find the loss factor, η, according to Eq. (5). Although the MTS controller has a frequency range of 0.01-100 Hz, the HP 7045A x-y plotter introduced its own phase lag at frequencies above approximately 0.1 Hz. This was checked by plotting load versus load for various frequencies. The resulting plot was a straight line (indicating no phase lag) for 0.01 - 0.1 Hz, but a narrow ellipse of steadily increasing size for frequencies above 0.1 Hz. Thus, with the equipment used, the frequency range for the damping measurements was limited to 0.01 - 0.1 Hz.

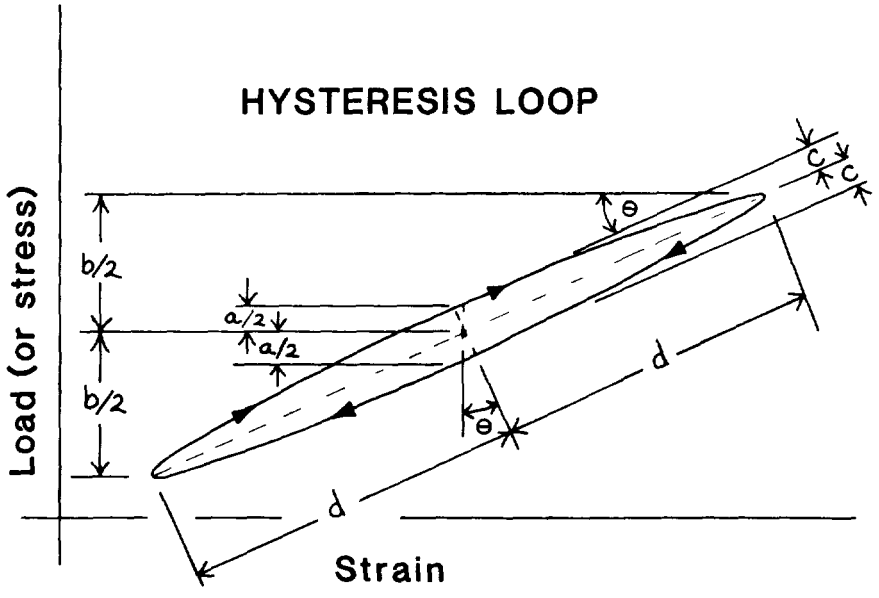

Figure 2

Loss factor data for the previously described materials are shown in Figs. 3 and 4, along with data from flexural vibration tests (to be described in the next section). It was expected that damping would approach zero as the frequency

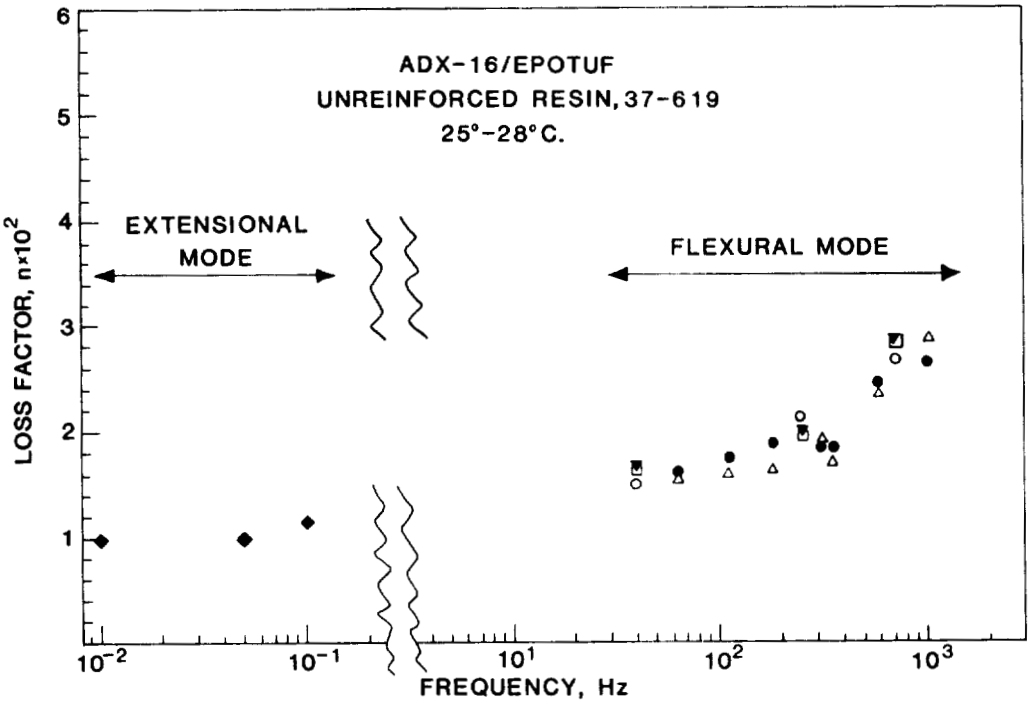

Figure 3

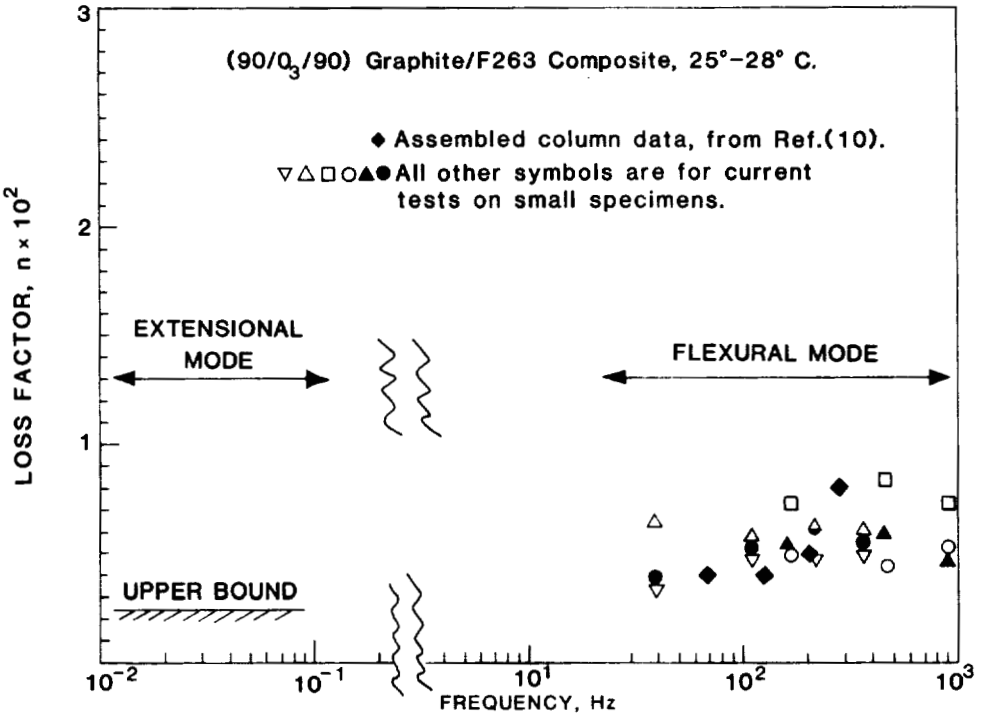

Figure 4

approaches zero, but the rate of decrease appears to be very low. Neat resin damping is greater than composite damping, as expected from micromechanics analysis (i.e., most of the energy dissipation occurs in the resin, and the fibers contribute little damping). Since the neat resin is essentially isotropic, the extensional damping is consistent with flexural damping, as it should be. The composite is anisotropic, however, and the flexural damping depends on the laminate stacking sequence, whereas the extensional damping should not (e.g., a high damping layer is more effective on the outer surface than on the neutral axis in flexure). Thus, the flexural damping for the $[90/0_3/90]$ layup should be greater than the extensional damping. Only the upper bound is shown for the composite extensional damping, because the hysteresis loop was very "noisy." This was due to the fact that the composite extensional modulus was much higher (and the resulting strains were much lower) than those for the neat resin, so the strain signals for the composite samples were more susceptible to electrical noise.

FLEXURAL VIBRATION

Flexural vibrations of column elements are expected to occur in the intermediate frequency range 10-1000 Hz. Experiments with small structural models under transient excitation show that flexural vibrations of the columns continue long after the global motion of the structure has been damped out. Thus, flexural damping is needed in order to minimize flexural fatigue problems.

Flexural damping of the previously described specimens was found by using a forced vibration, resonant dwell technique (ref. 5). As shown in Figs. 5 and 6, the specimen is mounted in a double cantilever arrangement on an electrodynamic shaker. Damping is found by measuring the ratio of base amplitude to tip amplitude at resonance. Unlike other techniques, this method allows precise control over both frequency and amplitude, so that the effects of these parameters can be studied. Considerable effort has been made to minimize parasitic losses in the apparatus which could cause errors in measured damping. For example, the balanced double cantilever arrangement serves to minimize frictional losses at the specimen clamping surfaces, and the specimen is tested at very low amplitude to minimize aerodynamic damping.

It is shown in ref. 5 that the loss factor is related to the resonant amplitude ratio of the cantilever specimen by

$$\eta = C_r \frac{a_b}{a_t} \tag{6}$$

where C_r = dimensionless coefficient which depends on resonant mode number, r

a_b = resonant amplitude at base of specimen (x=0)

a_t = resonant amplitude at tip of specimen (x=L)

If the base acceleration and the displacement at some arbitrary point, x_o, are measured, it is shown in ref. 5 that Eq. (6) reduces to

$$\eta = \frac{C_r \phi_r(x_o) \ddot{a}(o)}{\phi_r(L) \omega_r^2 a(x_o)} \tag{7}$$

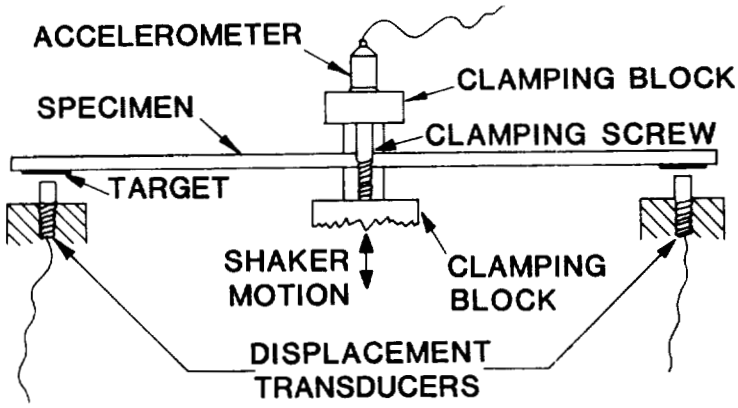

Figure 5

Figure 6

where $\phi_r(x_o)$, $\phi_r(L)$ = mode shape function evaluated at $x = x_o$ and $x = L$, respectively

$\ddot{a}(o)$ = base acceleration amplitude ($x = 0$)

ω_r = resonant frequency of rth mode

$a(x_o)$ = displacement amplitude at $x = x_o$

The present apparatus differed from the one reported in ref. 5, in that tracking filters were used for both the accelerometer and displacement probe signals, and data was generated in digital form by using a digital RMS voltmeter and a computer-printer system.

Flexural loss factors are shown in Figs. 3 and 4, along with previously described extensional data. Specimens of several lengths were tested at frequencies up through the fifth mode. Beyond the fifth mode, the displacement probe signals dropped to the noise level, making the data questionable. The rate of increase in the loss factor with increasing frequency is not as great for the composite as for the neat resin, although it should be pointed out that the resin tested is not the same as the resin in the composite tested. It is hoped that testing of the F263 resin and the ADX-16 composite at a future date will shed further light on this matter. Along with small specimen data in Fig. 4, some limited data (unpublished) for assembled full-scale columns are shown. S. A. Leadbetter (Structural Mechanics Branch, Langley Research Center) obtained this data in 1976 by using the Kennedy-Pancu method on free-free columns vibrated in flexure with an electrodynamic exciter. Due to nonlinear behavior in the connecting joint, no column damping values were found for the first mode, and the data plotted in Fig. 4 is for modes 2-5. Comparison of small specimen loss factors with column loss factors in Fig. 4 shows that there is no significant difference. It is believed that the graphite/F263 composite is representative of the early model columns tested by Leadbetter. Thus, it appears that for the frequencies and amplitudes used in these tests, the material damping is much greater than the joint damping. This contradicts the widely held notion (based on accumulated experience with metallic structures) that joint damping is more important than material damping. Additional data on both columns and small specimens is needed before definite conclusions can be drawn, however.

CONCLUSIONS

Limited data on extensional and flexural damping of small specimens of graphite/epoxy and unreinforced epoxy resin have been obtained. The experimental techniques and data reduction techniques have been described, and the limitations explained. Damping was found to vary slowly and continuously over the frequency range 0.01 - 1000 Hz, and no drastic transitions were observed. Composite damping was found to be less than neat resin damping, as expected from micromechanics theory. Comparison of small specimen damping values with assembled column damping values seems to indicate that, for these materials, material damping is more important than joint damping. Additional tests of current model columns and current specimens with the ADX-16 resin are needed before definite conclusions can be drawn, however. Additional extensional testing is also needed in order to examine frequency and amplitude effects beyond the limited range reported here. The data reported here was limited not by the test apparatus, but by signal conditioning and data acquisition. It is believed that filtering of the strain gage signals and the use of digital storage with slow playback will make it possible to extend the frequency and amplitude ranges significantly.

ACKNOWLEDGEMENTS

This work was carried out during the summer of 1981 under a NASA/ASEE summer faculty fellowship program at NASA Langley Research Center. The author is especially grateful to Dr. Garnett Horner and his colleagues in the Structural Dynamics Branch.

REFERENCES

1. Bush, H.G., Mikulas, M.M., and Heard, W.L. Jr.: Some Design Considerations for Large Space Structures. AIAA Journal, 16 (4), April 1978, 352-359.

2. Bush, H.G., and Mikulas, M.M.: A Nestable Tapered Column Concept for Large Space Structures. NASA TMX -73927, 1976.

3. Trudell, R.W., Curley, R.C., and Rogers, L.C.: Passive Damping in Large Precision Space Structures, Proceedings of 21st Structures, Structural Dynamics and Materials Conference, Seattle, Washington, May 1980, Paper No. 80-0677.

4. Structural Dynamics and Control of Large Space Structures, NASA Conference Publication 2187, June 1981

5. Gibson, R.F., Yau, A., and Riegner, D.A.: An Improved Forced Vibration Technique for Measurement of Material Damping, Proceedings of SESA 1981 Spring Meeting, Dearborn, Michigan, June 1981.

6. Gibson, R.F., and Yau, A.: Complex Moduli of Chopped Fiber and Continuous Fiber Composites: Comparison of Measurements with Estimated Bounds, J. of Composite Materials, 14, April 1980, 155-167.

7. Fabrication of Damping Test Specimens, LMSC Report No. D757128, September 1981, Lockheed Missiles and Space Company, Sunnyvale, California.

8. Lazan, B.J.: Damping of Materials and Members in Structural Mechanics, Pergamon Press, 1968.

9. Ungar, E.E., and Kerwin, E.M., Jr.: Loss Factors of Viscoelastic Systems in Terms of Energy Concepts. J. Acoustical Society of America, 34, (7), July 1962, 954-957.

THE POTENTIAL OF NONPERIODIC TRUSS STRUCTURES FOR SPACE APPLICATIONS

K. C. Park, Staff Scientist
Applied Mechanics Laboratory
Lockheed Palo Alto Research Laboratory
3251 Hanover Street
Palo Alto, California 94304

and

J. M. Winget, Graduate Student
Division of Engineering
California Institute of Technology
Pasadena, California 91125

Large Space Systems Technology - 1981
Third Annual Technical Review
November 16-19, 1981

DYNAMIC CONSIDERATIONS FOR SPACE STRUCTURES

The design and analysis of large space structures for dynamic loads require the considerations of: wave propagation, transient response and steady-state vibration problems. The desirable intrinsic structural characteristics to these problems are good dispersive properties, rapid decay of the transients and an optimum distribution of frequency spectrum, respectively. The truss lattices proposed so far for constructing large space platforms are based on either tetrahedrons or octetruss elements. Although they are easy to construct and their equivalent continuum models can be developed as periodic structures, the space platforms made of such periodic lattices can have two major drawbacks of the three dynamics considerations. First, periodic structures can be considered to be well tuned. Therefore, they do not possess good wave dispersion characteristics. Second, if the dimensions of the platform are fixed then the frequency spectrum of the structure is also fixed, thus leaving no room for frequency modifications other than through redesign and/or effective vibration control devices.

OBJECTIVE OF PRESENT STUDY

- TAILOR LATTICE-TRUSS STRUCTURES TO IMPROVE CONTROLLABILITY OF DYNAMIC RESPONSES
- INVESTIGATE WHAT CAN BE DONE TO IMPROVE DYNAMIC PERFORMANCE OF STRUCTURES

DYNAMIC CONSIDERATIONS FOR SPACE STRUCTURES

- GOOD WAVE DISPERSION
- RAPID DECAY OF THE TRANSIENTS
- DESIRED FREQUENCY SPECTRUM & MODE SHAPES
- ADAPTABILITY TO PASSIVE & ACTIVE CONTROL

PERIODIC LATTICE-TRUSS STUCTURES

ADVANTAGE	DISADVANTAGE
EASY TO CONTRUCT & ASSEMBLE	TUNED STRUCTURE: POOR WAVE DISPERSION
EQUIVALENT CONTINUUM MODEL	FIXED FREQUENCY SPECTRUM WITHOUT RE-DESIGN

NONPERIODIC LATTICES FOR IMPROVED DYNAMIC PERFORMANCE

The observations from the preceding section motivate us to seek means for improving wave dispersion properties and for introducing detuning provisions within the structures. This calls for the adoption of nonperiodic lattice structures. In addition, one would like to have room for rearrangements of internal lattice members so that the desired frequency spectrum can be realized to a maximum extent. This paper explores an alternative approach for the construction of large space platforms by adopting nonperiodic lattice configurations. This is in the hope of improving the two aforementioned dynamic characteristics, viz., wave dispersion and controllable frequency spectrum, by the internal rearrangements of the nonperiodic lattices without changes in material properties and dimensions of the lattice members.

TWO TECHNIQUES FOR ALTERING DYNAMIC CHARACTERISTICS OF A GIVEN STRUCTURE

- FIXED-MATERIAL/VARYING LATTICE ARRANGEMENTS (TECHNIQUE ADOPTED HERE)
- FIXED-LATTICE ARRANGEMENT/VARYING MEMBER PROPERTIES

WHY IRREGULAR LATTICE TRUSSES FOR SPACE STRUCTURES

- DETUNE THE STRUCTURES TO IMPROVE WAVE DISPERSIVE PROPERTIES
- TAILOR THE LATTICE GEOMETRY (OR MEMBER PROPERTIES) TO IMPROVE FREQUENCY SPECTRUM AND MODE SHAPES FOR EASIER VIBRATION CONTROL
- FROM CONTINUUM POINT OF VIEW, WE WISH TO EXPLOIT ANISOTROPY TO IMPROVE DYNAMIC PERFORMANCE OF LARGE SPACE STRUCTURES

It is noted that stable lattices consist basically of triangles and/or quadrangles. In the search of stable nonperiodic lattice truss platforms it is highly desirable to make the top and bottom surfaces of irregular tri- and/or quadrangular patterns while all the vertical connecting members are identical. The simplest possible nonperiodic lattice configurations that meet these requirements turn out to be the ones shown in Figures 1 and 2. In this paper they will be called dipenta-dodecahedron(or DPD-hedron) and pentatriangular-octahedron (or PTO-hedron), respectively. The DPD-hedron and PTO-hedron are the two building-block lattices used to form nonperiodic lattice truss platforms. Figure 3 shows five different internal arrangements of the DPD-hedron by utilizing four stabilizing members on the two pentagonal top and bottom surfaces. Similarly, three distinct internal arrangements are possible for the PTO-hedron. A platform segment made of the two lattices is shown in Figure 4. Note that in order to emphasize the freedom to arrange the stabilizing members as desired they have been omitted from Fig. 4. Incidently, the two lattices can, if properly reshaped, be used to construct spherical, cylindrical and parabolic surfaces.

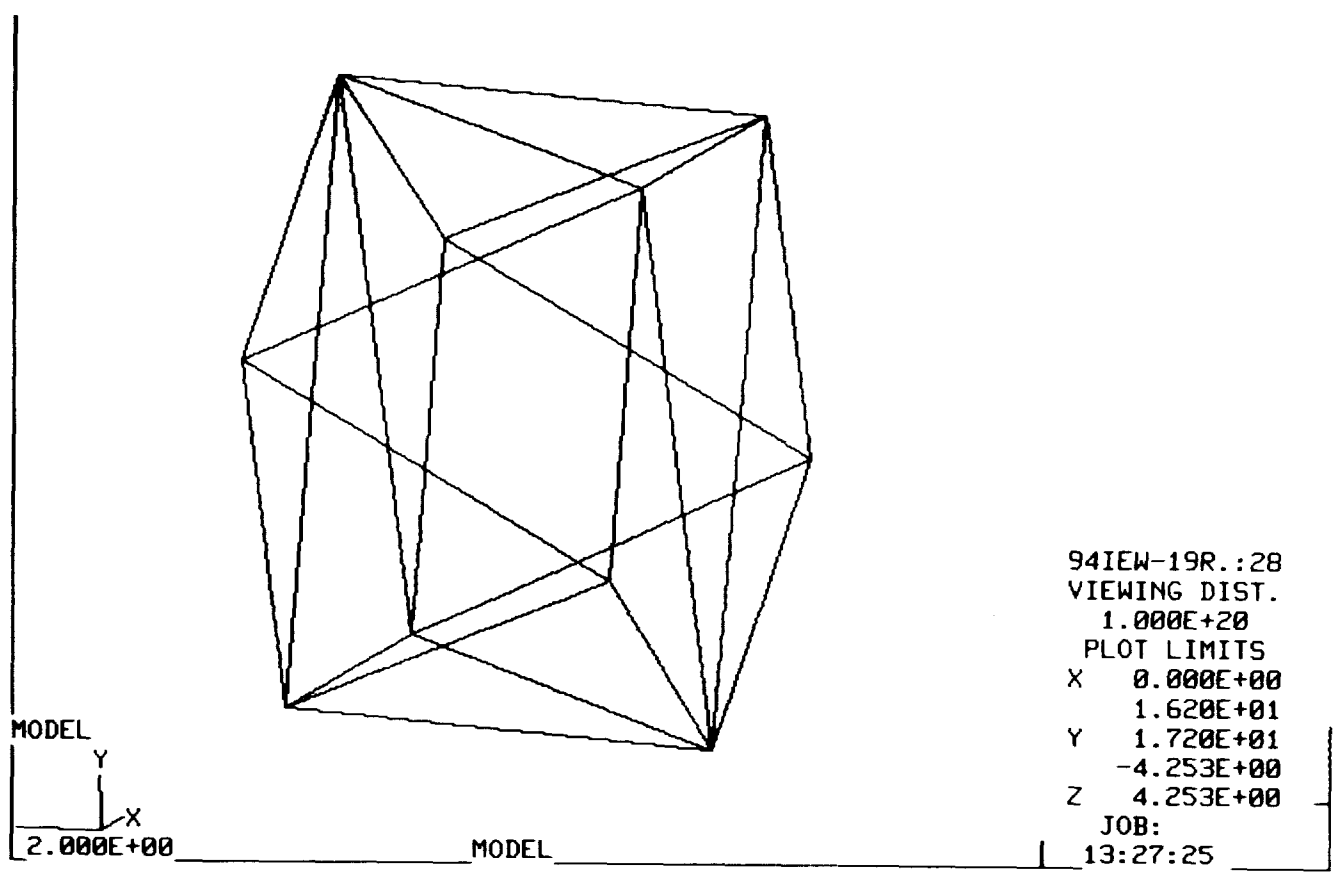

FIG. 1 DPD-HEDRON

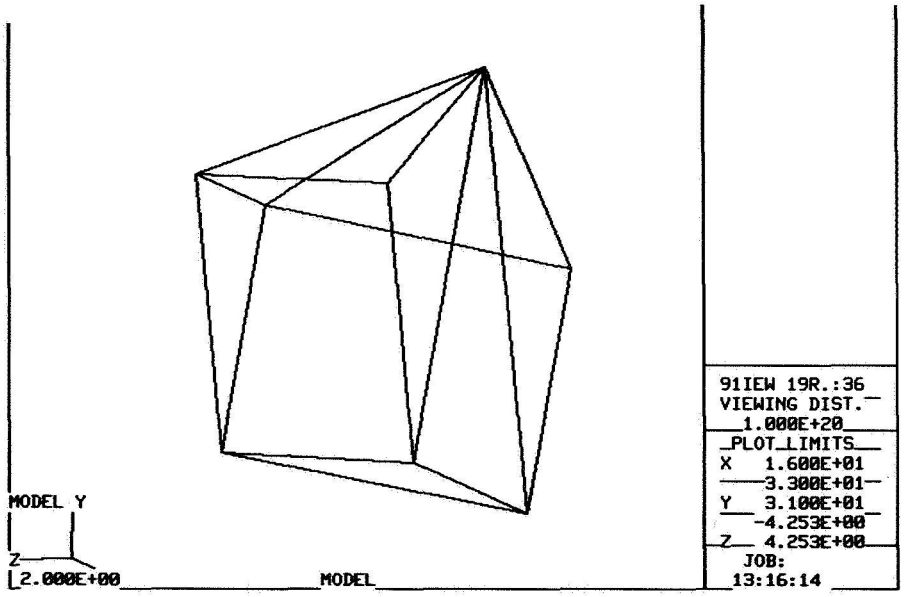

FIG. 2 PTO-HEDRON

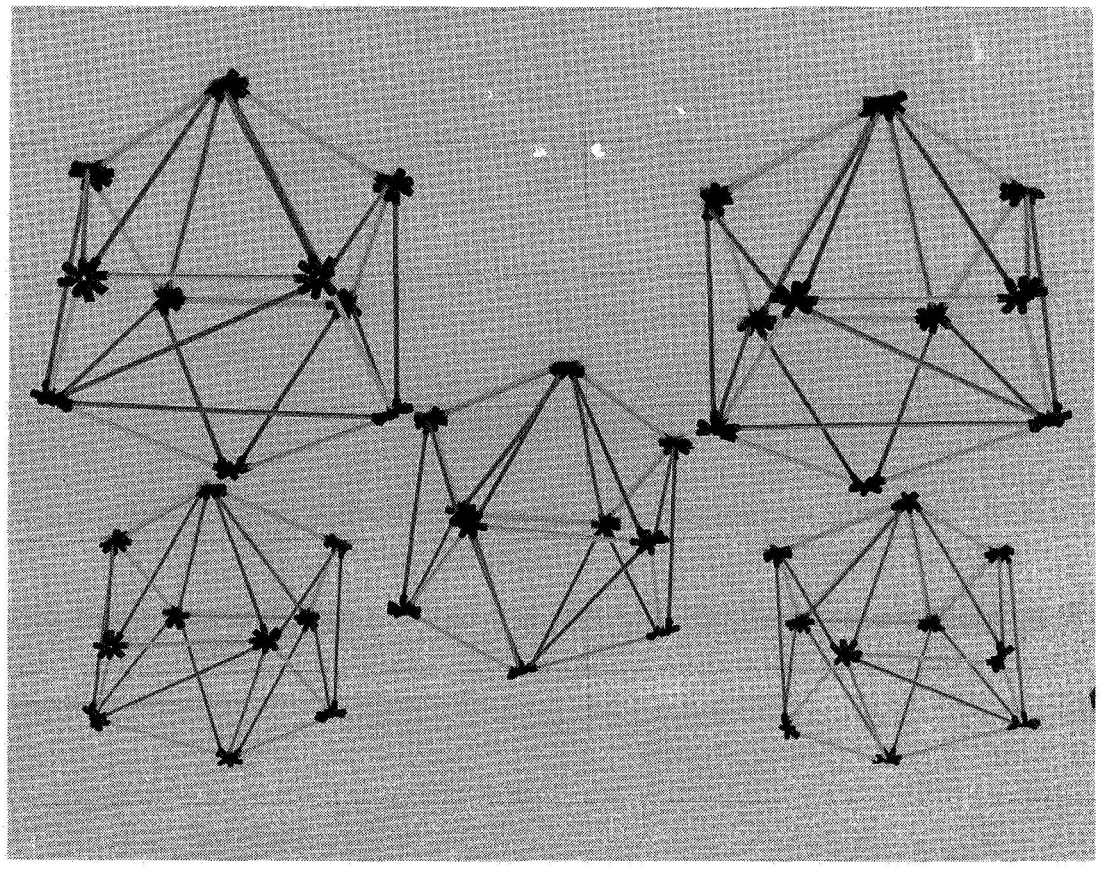

Fig. 3 Five different internal arrangements of DPD-hedron

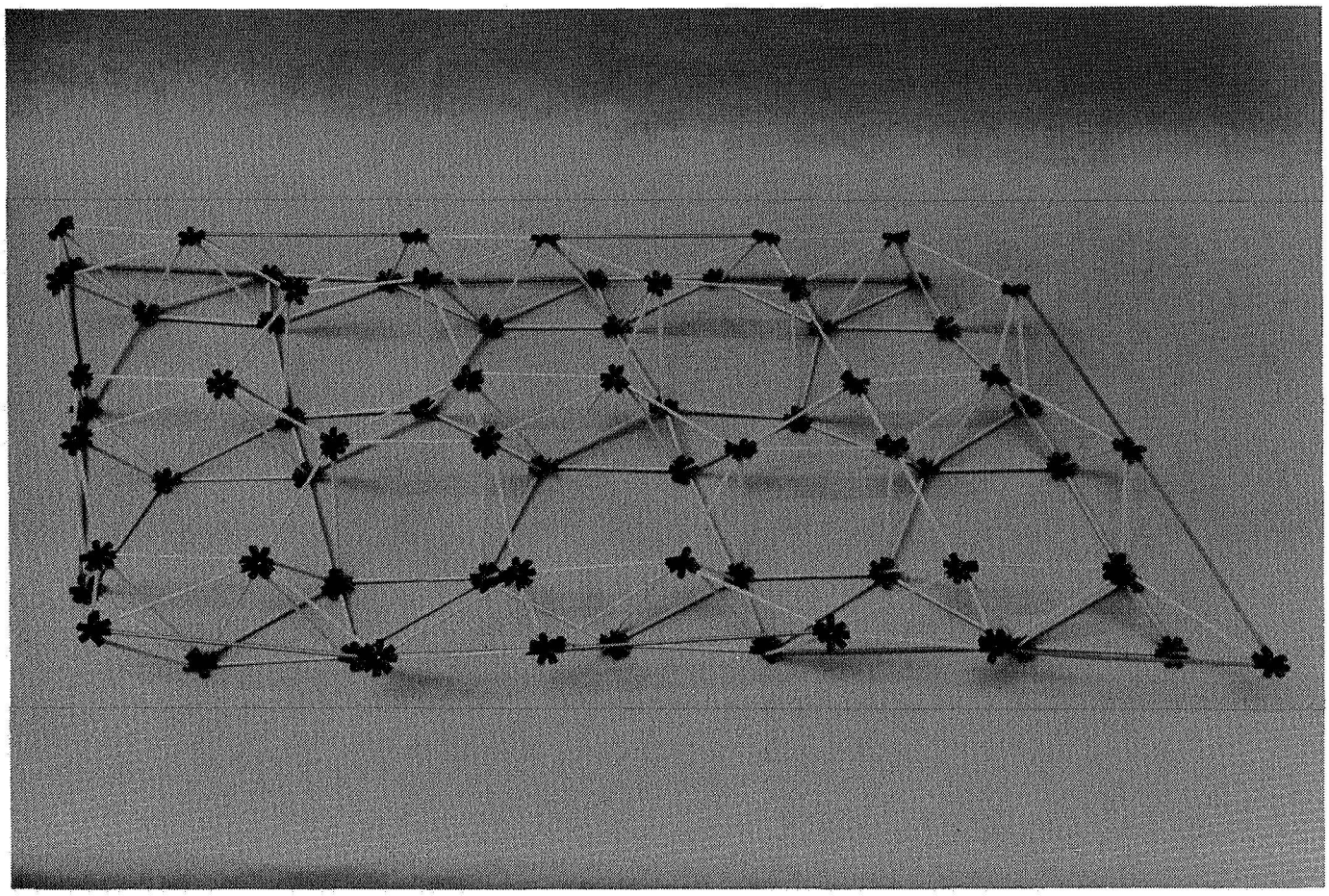

Fig. 4 Flat platform made of DPD and PTO-hedrons (diagonal members are absent)

DYNAMICS OF NONPERIODIC TRUSS BEAMS

In order to assess the dynamic characteristics of truss structures made of the nonperiodic lattices, a cantilever truss beam as shown in Figure 5 was analyzed for vibrations. In addition, three additional lattice configurations were also constructed along with two beams made of tetrahedrons (Fig. 6). Figure 7 shows the relative frequency variations of the six cantilever truss beams for their first mode. To make the comparison meaningful, the beam length, the number of lattice joints and the total weight were chosen to be identical within 2 percent differences. Note from Figure 7 that the frequencies of the four nonperiodic truss beams vary over 60 percent while those of the two beams of tetrahedron lattices vary only about 13 percent. Such wide frequency variations of the proposed nonperiodic truss beams indicate that the introduction of nonperiodic lattices could be effectively used to improve the controllability of steady-state vibration as well as improved wave dispersion characteristics.

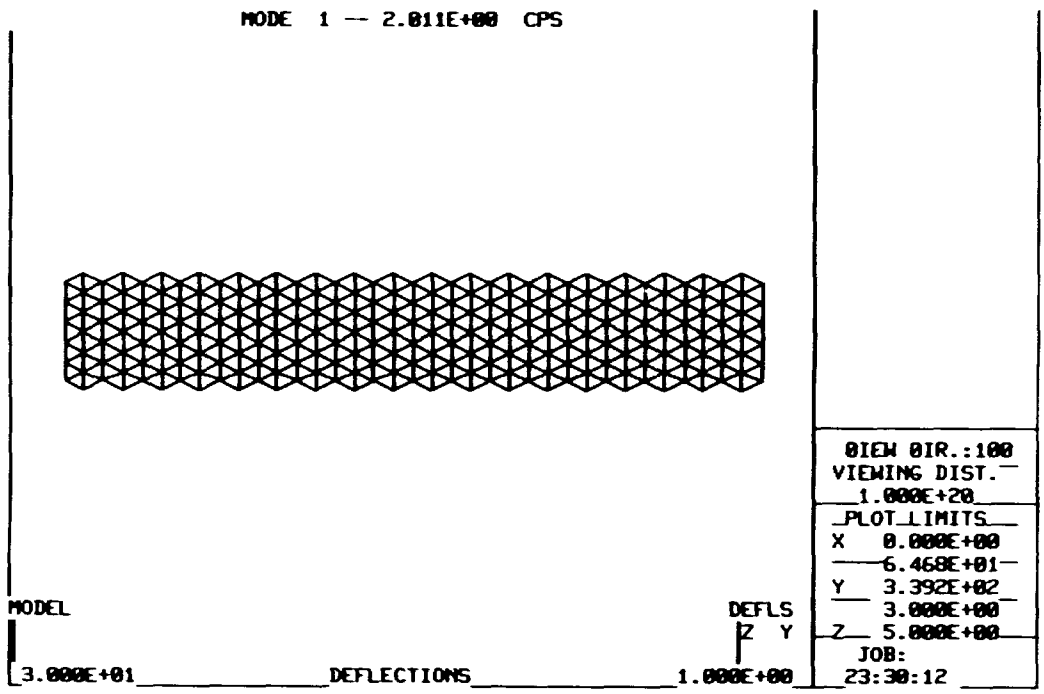

FIG. 5 TOP SURFACE OF VERTICALLY ARRANGED TETRAHEDRON TRUSS BEAM

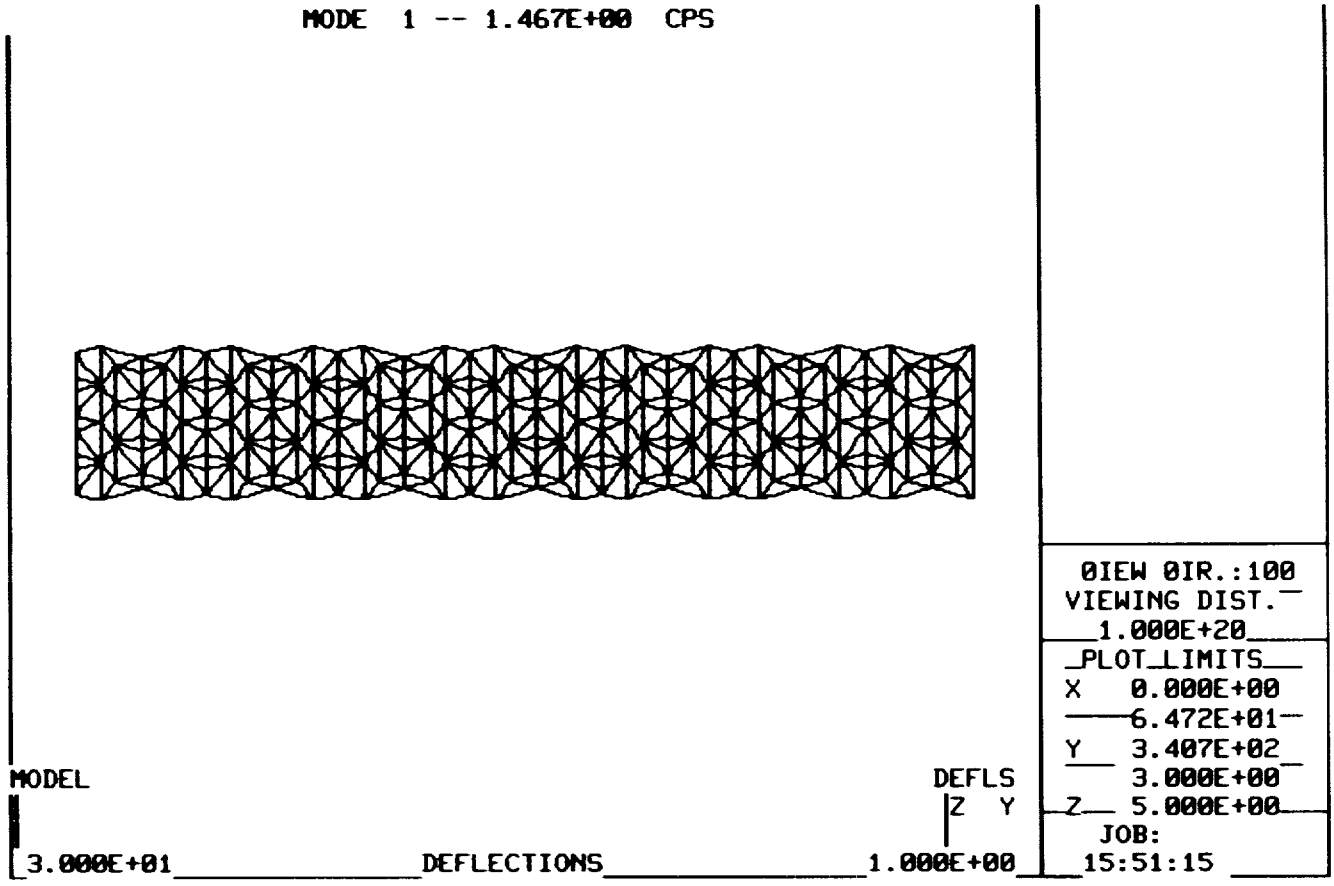

Fig. 6 Top surface of nonperiodic lattice; type 2 truss beams

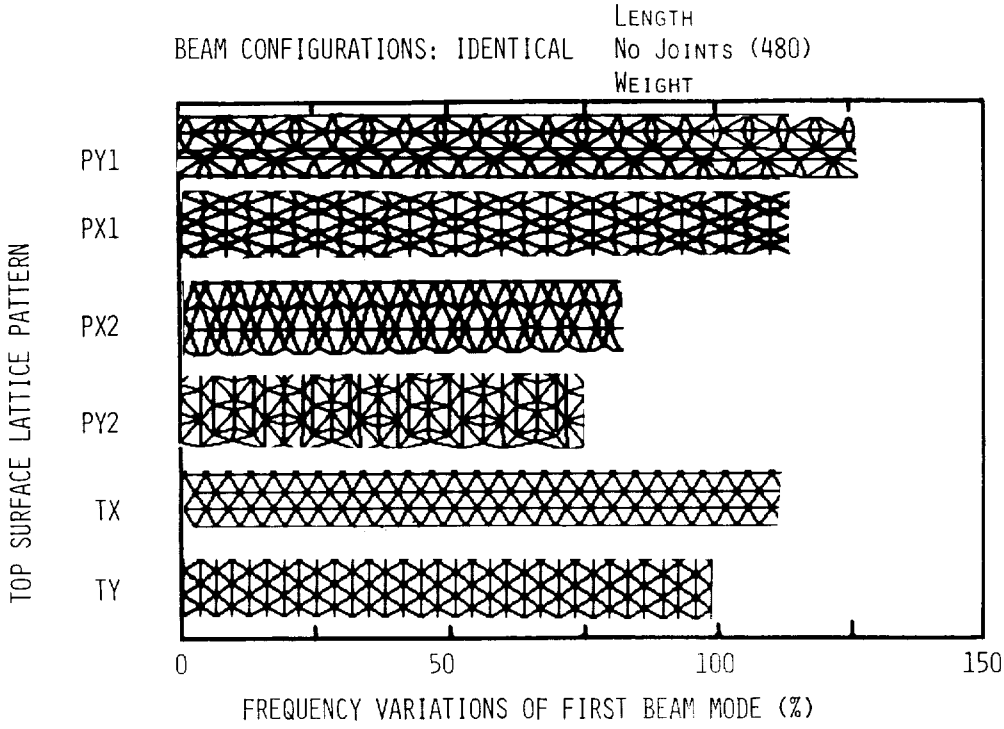

FIG. 7 RELATIVE FREQUENCY OF SIX LATTICE TRUSS BEAMS

VIBRATION OF FREE-FREE TRUSS PLATES

Free-free vibration analysis of an octetruss plate as shown in Fig. 8 was performed as a benchmark problem and the vibration nodal lines for the first five modes are determined as indicated in Fig. 8. In order to examine the effect of different lattice patterns, several arrangements were constructed. Two of the present lattice arrangements are shown in Figs. 9 and 10 along with their vibration nodal lines. Note the significant changes in the vibration nodal patterns. As for frequency magnitudes, the present lattice arrangements give about 15 ~ 25 % frequency variations.

FREE-FREE VIBRATION OF TRUSS PLATES

	TETRAHEDRON	PRESENT LATTICES
• ASPECT RATIO	1.0002	1.0723
• WEIGHT RATIO	1.000	1.03
• MEMBER LENGTH	1.078	1.000
• NO. OF JOINTS	628	631
• NO. OF ELEMENTS	2646	2463
• NO. OF EQUATIONS	3762	3780
• AREA RATIO	1.000	1.0106

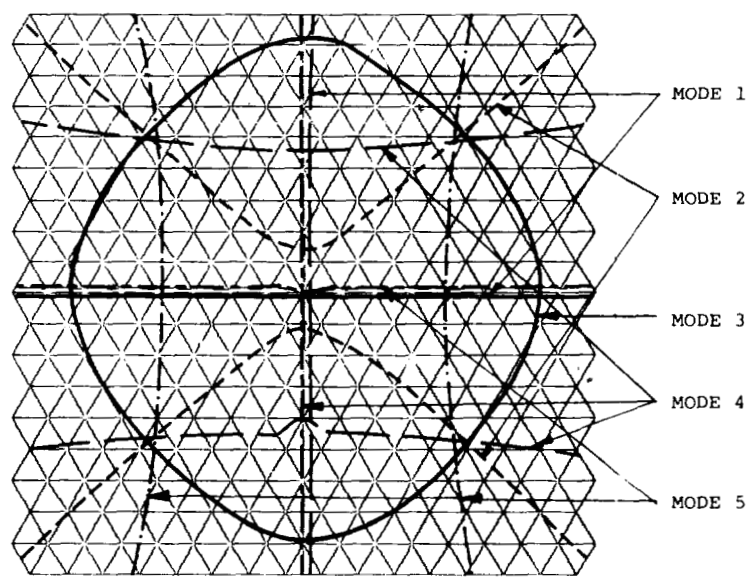

Fig. 8 Vibration Nodal Lines of Free-Free Octetruss Plate

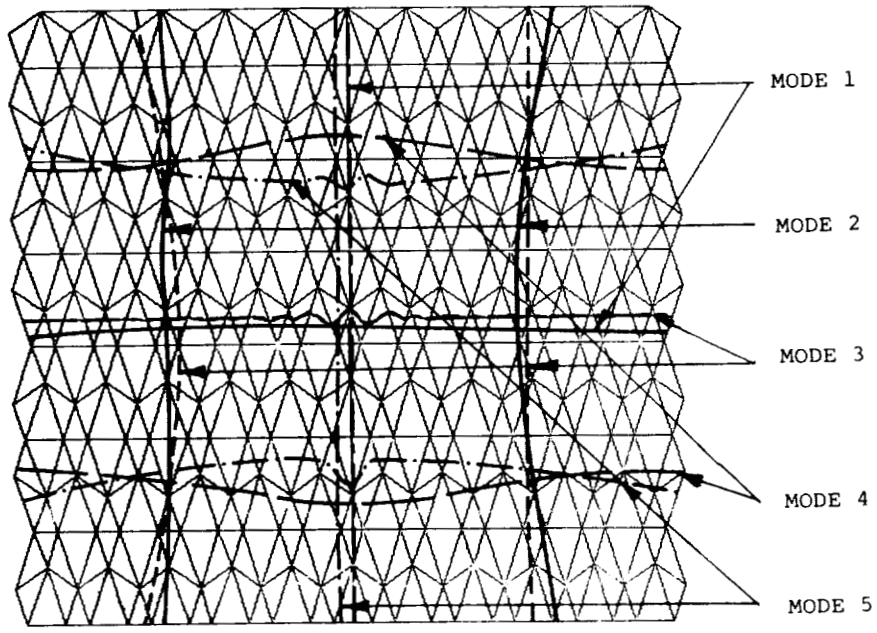

Fig. 9 Vibration Nodal Lines of Free-Free Irregular Truss Plate

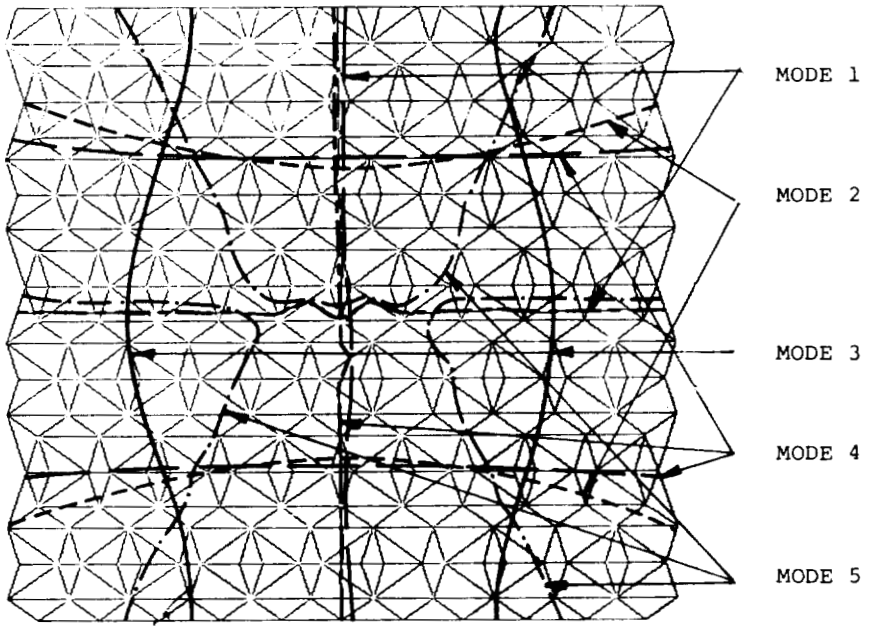

Fig. 10 Vibration Nodal Lines of Free-Free Irregular Truss Plate

SUMMARY

- NONPERIODIC (OR IRREGULAR) LATTICE-TRUSS STRUCTURES CAN IMPROVE WAVE DISPERSION PROPERTIES
- FOR BEAM BENDING, NONPERIODIC (PRESENT) LATTICES CAN VARY ABOUT 65% OF THE FUNDAMENTAL FREQUENCY
- FOR FREE-FREE PLATE, NONPERIODIC LATTICES CAN ALTER THE MODE SHAPES AS DESIRED. IN PARTICULAR MAY BE ABLE TO COME UP WITH AN OPTIMUM MODE SHAPES FOR PASSIVE AND ACTIVE CONTROL-POINT LOCATIONS
- FOR FREE-FREE PLATE, A SELECTED FREQUENCY RANGE CAN BE VARIED ABOUT 15 - 25%

FUTURE STUDY

- CONDUCT TRANSIENT ANALYSIS TO ASSESS THE EFFECTIVENESS OF INTRODUCING IRREGULAR (OR ANISOTROPIC) PATTERNS TO LARGE SPACE PLATFORMS
- DEVELOP DESIGN (PRELIMINARY) TECHNIQUES FOR ALTERING DYNAMIC CHARACTERISTICS FOR GIVEN DESIGN REQUIREMENTS
- INVESTIGATE THE FEASIBILITY OF INTRODUCING DEN-HARTOG TYPE VIBRATION CONTROLLER EITHER BY UTILIZING VERTICAL STIFFENERS OR PLACING ADDITIONAL UNLINKED STRUCTURAL MEMBERS

IAC LEVEL "0" PROGRAM DEVELOPMENT

R. G. Vos
Boeing Aerospace Company
Seattle, Washington

Large Space Systems Technology - 1981
Third Annual Technical Review
November 16-19, 1981

SUMMARY AND CURRENT STATUS

This paper describes activities and software resulting from NASA Contract NAS5-25767, "Integrated Analysis Capability (IAC) for Large Space Systems." This contract is part of the NASA LSST program supporting effort, with direction by the Goddard Space Flight Center (J. P. Young, Technical Monitor).

The Phase I IAC contract effort produced a pilot computer code and a general development plan. That work was reported on at the previous (1980) LSST Technical Review. The ongoing Phase II effort is scheduled to produce an initial operational capability, designated as IAC Level 1, by the end of CY 82.

In the present paper, the first four figures deal with the current IAC status and some planned technical requirements and objectives. The remainder of the paper reports on the development of an intermediate prototype capability, accomplished during FY 81 and designated as IAC Level "0".

The current status of the IAC development activity is summarized in Figure 1. The listed prototype software and documentation have been delivered, and details have been planned for development of the Level 1 operational system. The planned end product IAC is required to support LSST design analysis and performance evaluation, with emphasis on the coupling of required technical disciplines. A recently formalized requirement is for the long-term IAC to effectively provide two distinct features: 1) a specific set of analysis modules (thermal, structural, controls, antenna radiation performance and instrument optical performance) that will function together with the IAC supporting software in an integrated and user friendly manner and 2) a general framework whereby new analysis modules can readily be incorporated into IAC or be allowed to communicate with it.

- Ongoing Phase II Contract
- Prototype software delivered
  - Technical modules – MSC NASTRAN®, DISCOS, TRASYS, SINDA, ORACLS
  - Solution paths – standalone, thermal/structural, structural/control, thermal/structural/control
  - Executive/data management/graphics/module interfaces
- Draft documentation delivered
  - User manual for prototype system
  - Functional specs document
- Details planned for operational system

Figure 1

IAC REQUIRED CAPABILITIES

Much of the required technical capability of IAC can be described as being part of one or more distinct "solution paths." Each path is actually a class of solutions, which consists of a number of selectable options and variations, rather than a rigidly predefined and automated process. An engineer-in-the-loop mode of operation is therefore possible and, in fact, emphasized. Currently, five such solution paths, as shown in Figure 2, have been defined. The solid lines of paths I to IV indicate capabilities which have been implemented and are available for use and evaluation within the current prototype software package. The standalone (uncoupled) operation of each technology or major technical module is defined to be Solution Path I. Paths II through V involve an increasing degree of interdisciplinary coupling and corresponding greater complexity. Solution Path II provides thermal deformations via the coupling of a thermal analyzer such as SINDA or NASTRAN with a structural analyzer such as NASTRAN or SPAR. A prototype modeling integration module (MIMIC) has been implemented during FY 81 to handle data flow between the generally incompatible thermal and structural models. Path III accomplishes a structural/control analysis, in either the frequency or time domain, by providing required modal data from a structural analyzer to the DISCOS system dynamics module. Solution Path IV has been implemented during FY 81. It provides a time domain thermal/structural/control analysis, including a time varying but quasi-static thermal loading, i.e., thermal loads are unaffected by the dynamic motions. Finally, Path V is to provide a fully coupled analysis in the frequency domain and is directed at problems such as thermal flutter of long spacecraft members.

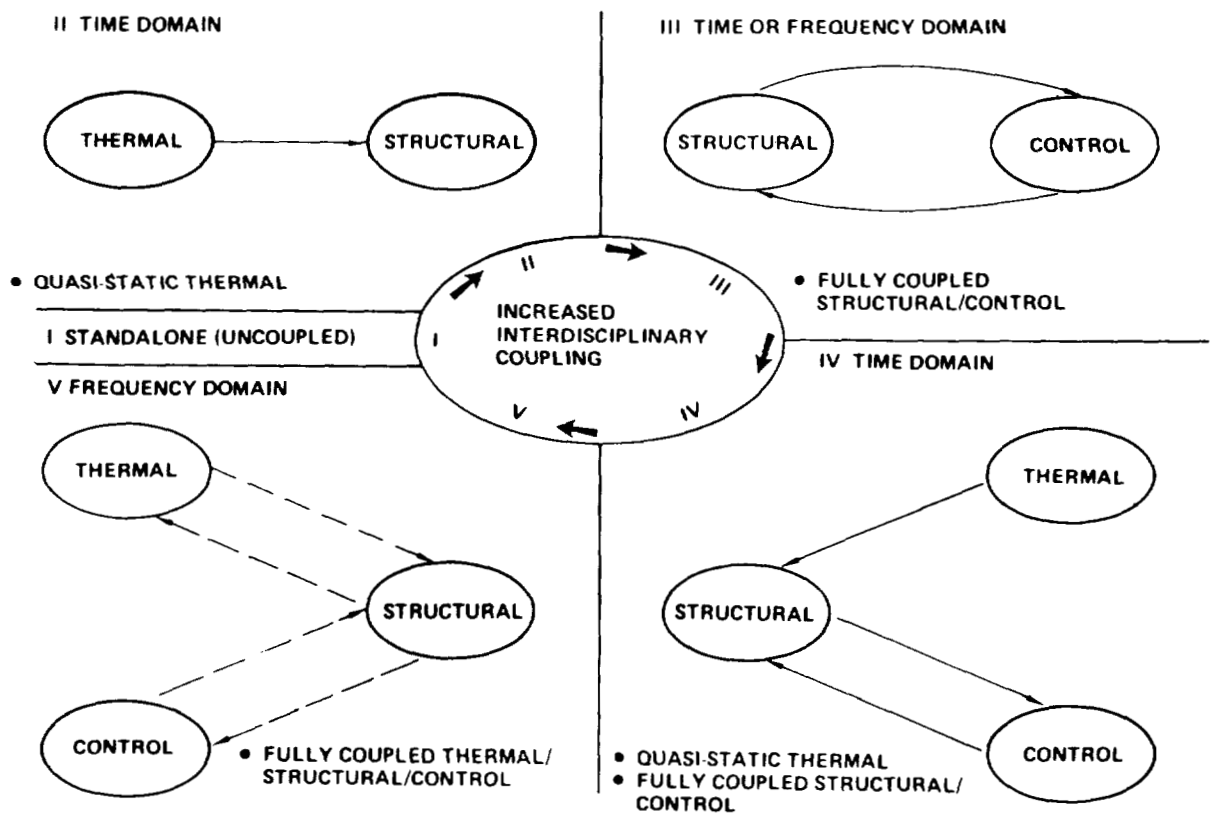

Figure 2

IAC SELECTED TECHNICAL MODULES

The technical modules currently defined for implementation within IAC are shown in Figure 3. These modules are classified into four technical groups - system dynamics, structural, thermal and controls. The solid lines indicate capabilities which have been incorporated into the prototype software system, while dashed lines indicate planned capabilities which have not yet been implemented. DISCOS (Dynamic Interaction Simulation of COntrols and Structures) is a primary computational backbone of the IAC system. The selected thermal and structural modules are generally well known within the technical community. ORACLS (Optimal Regulator Algorithms for the Control of Linear Systems) is a package of selected subroutines which emphasizes modern control theory design. SAMSAN (SAMpled System ANalysis capability) is a similar package which emphasizes classical control methods and is currently under development at GSFC. The MODEL controls program will consist of several special-purpose interactive or batch versions, which in general create FORTRAN code to numerically solve a set of user defined differential equations.

It will be readily apparent to those familiar with the designated structural and thermal modules that there is some duplication of capability, e.g., NASTRAN/SPAR and SINDA/NASTRAN. This is due in part to a Phase I study and conclusion that both finite difference and finite element thermal codes should be available within IAC. More importantly, it is the result of a conscious effort to provide alternate technical modules within several areas of IAC in order to support as wide an existing user community as practical. The list of IAC technical modules will continue to grow as additional user groups define LSST requirements and as technology and data-coupling are implemented in areas such as antenna radiation and instrument optical performance.

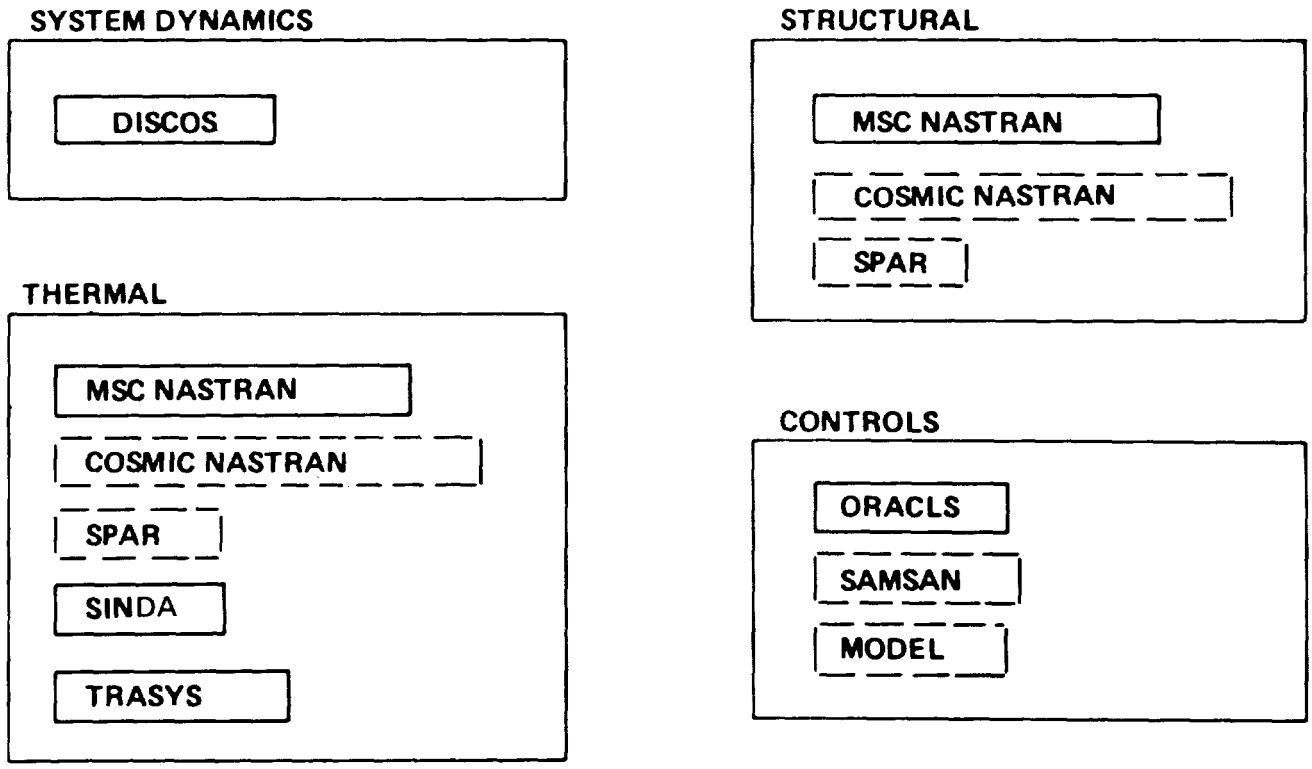

Figure 3

IAC SYSTEM INTEGRATION PHILOSOPHY

The solution paths already discussed define basic technical requirements of the IAC system. The selected technical modules provide major components for supporting the individual technologies represented within these paths, and required interdisciplinary couplings are largely being implemented via new interface software which bridges between the different technologies and mathematical modeling techniques.

At the overall system level, Figure 4 summarizes the philosophy for integration of the entire IAC package. Key characteristics required of IAC are shown on the right, and corresponding components of the supporting software and hardware are given on the left. First, the computational complexities inherent in most LSS problems led to an early decision that IAC must operate in an engineer-in-the-loop fashion, rather than in a highly automated "button pushing" mode of operation. A specialized executive program is used to make all capabilities available to the engineer, in a modular but consistent and engineer friendly manner. Second, in order to accomplish in-depth analyses with the selected technical modules, in a reasonably efficient and natural manner, a file oriented data management system has been developed. In order to provide effective user access to data, some enhancements to the file oriented system, relative to data identification and display, have been implemented. For the same reason, considerable emphasis is being given to interactive graphics. The IAC target host computers are state-of-the-art machines with significant virtual memory capability. At the present time such machines are largely in the super-minicomputer class, but new mainframes can be expected to increasingly satisfy this target requirement. The DEC VAX 11/780 super-minicomputer is being used for the current IAC development.

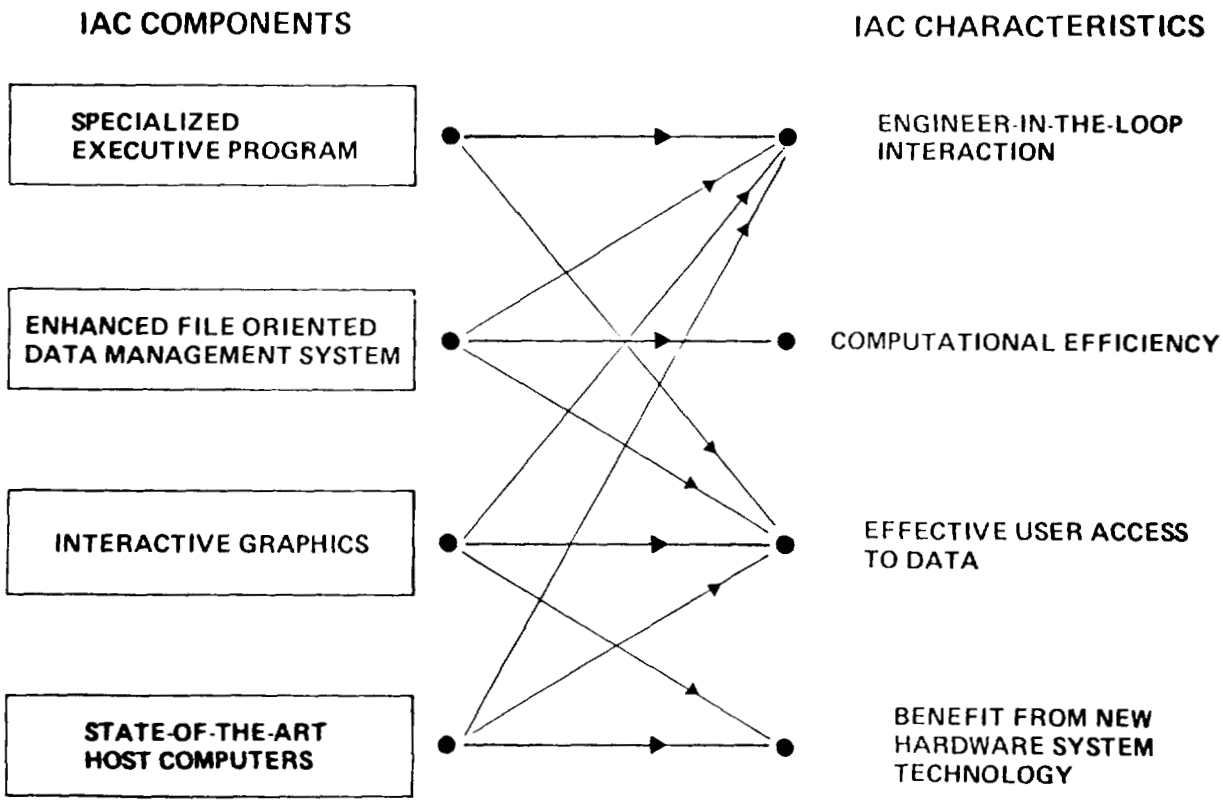

Figure 4

COMPLETED LEVEL 0 ARCHITECTURE

A schematic of the Level 0 (prototype) architecture is shown in Figure 5. The executive provides the user with a common interface to all of the diverse technical modules and to the IAC supporting software. The executive software includes a command interpreter, module driver, and data handling and graphics display capabilities. The software is programmed in FORTRAN '77, and the graphic capabilities are based on the DI-3000 SIGGRAPH Core standard support package. The executive provides for access to, and communication between, three types of data storage areas: (1) a file oriented database; (2) a user-specific virtual memory workspace; and (3) the host file system. The major technical modules currently implemented within IAC are DISCOS, MSC NASTRAN, ORACLS, SINDA, and TRASYS. The interface modules INDA, etc. provide required data-flow linkages between IAC and the technical modules. The MIMIC interface module is a prototype mesh variable transformation capability designed to aid the user in handling modeling incompatibilities, e.g., between thermal and structural analyses in IAC solution Paths II and IV.

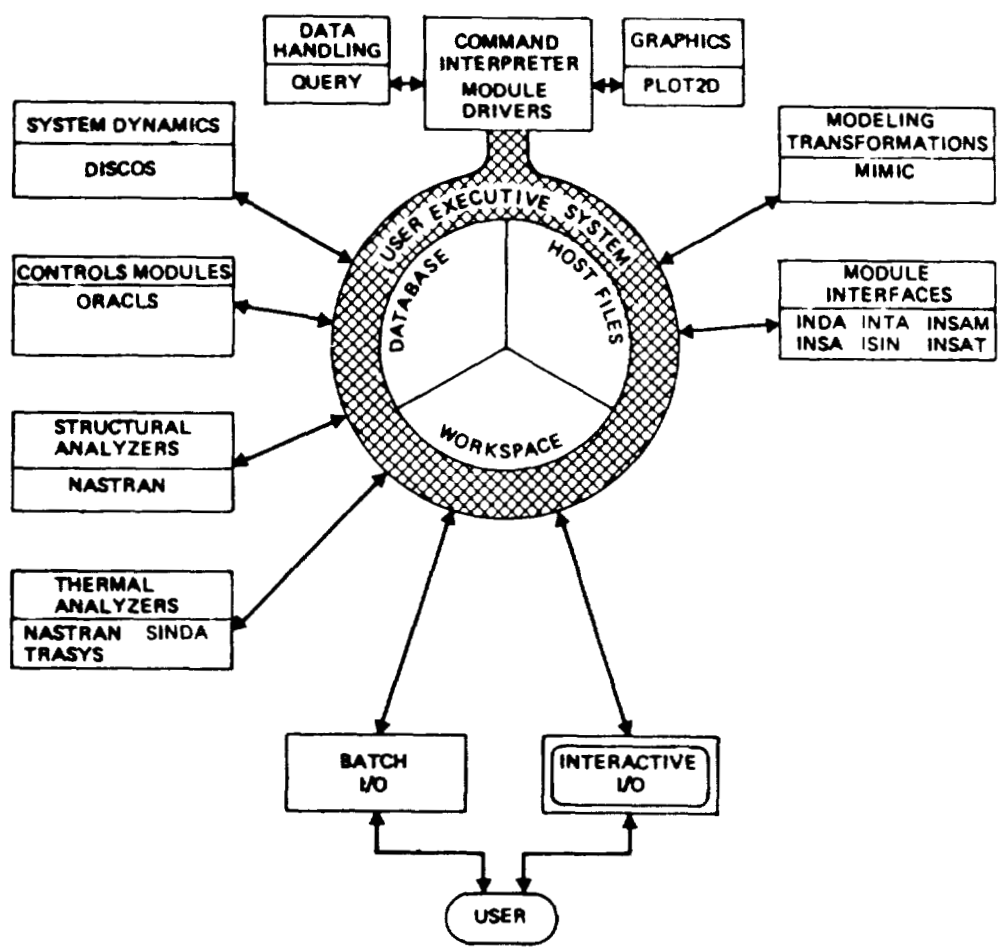

Figure 5

EXECUTIVE JOB FLOW

The executive integrates other components of the system into a unified package, and provides the primary interface between IAC and the user. A schematic of executive functions is shown in Figure 6. The emphasis is on interactive operation; however, modules are often executed in essentially a batch mode. The user accomplishes the mainstream of his tasks within the IAC "primary job." Within this job he/she may request the executive to execute a module, with user specified parameters. He/she may also request that a sequence of commands (including module executions) be initiated as a separate "secondary job," in a batch mode concurrently with the primary job. In addition, the user may execute many direct commands, e.g., relating to help information, data handling or graphics tasks. Certain direct commands cause the execution of lower level executive routines, which may then be driven by user tutorials or menus. In order to fully utilize the host operating system features, a capability has also been developed to execute any host (computer operating system) command, or sequence of host commands, from within the IAC executive. The broken connecting links in the figure denote temporary transfers of control between IAC and the host operating system.

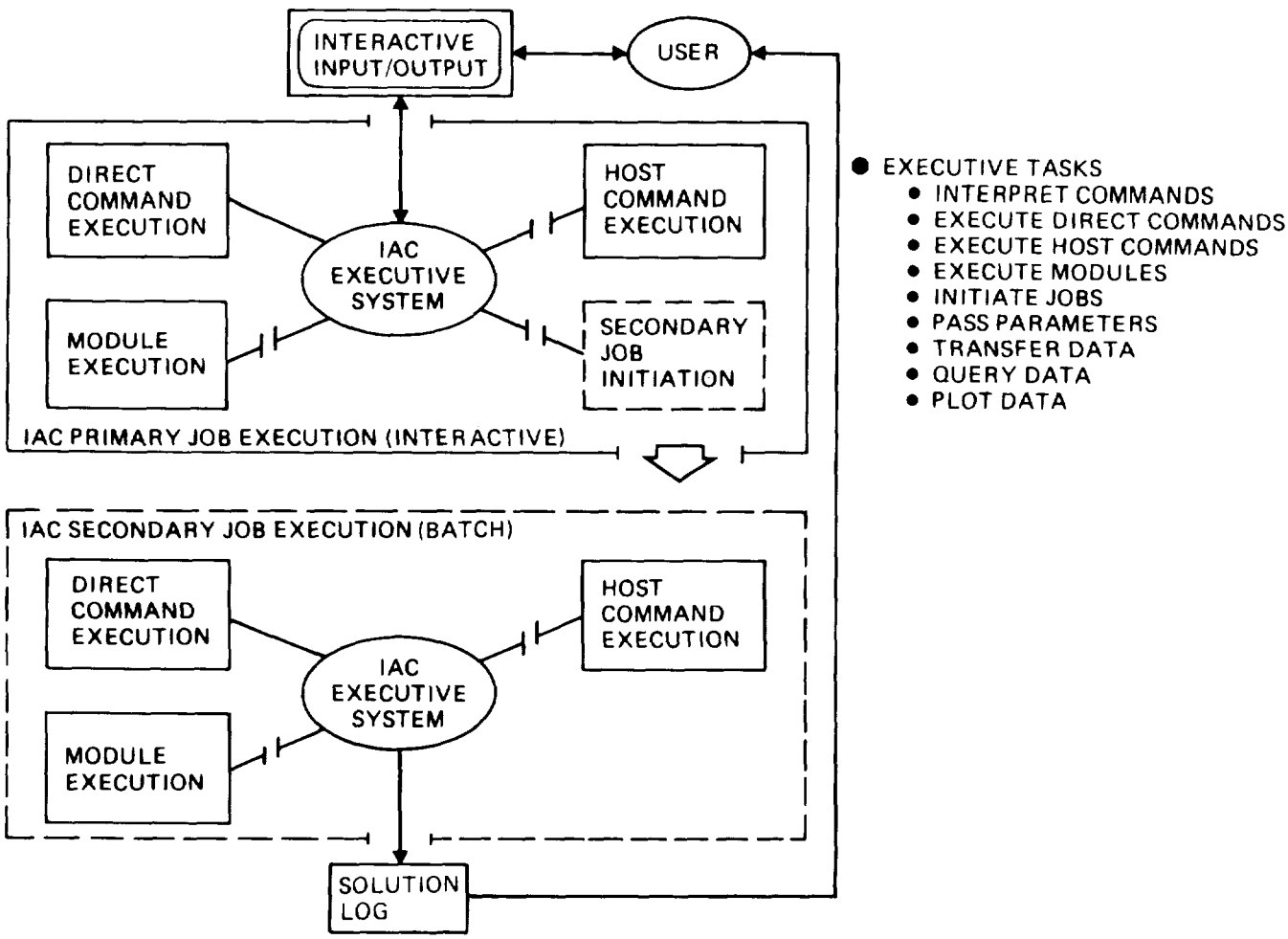

Figure 6

DATA HANDLING

IAC provides a variety of data handling tools which support data computation, manipulation and evaluation. Figure 7 lists some typical processes which are supported by these tools.

The IAC data handling system has been designed with a primary emphasis on computational efficiency (in generation and use of new bulk analysis results) and a secondary emphasis on informational type query (for processing and display of existing items of information). The host file system is utilized to a large degree to provide an efficient and natural interface to many of the IAC computational modules. The database and associated data structures facilitate communication by providing standard data organizations and formats. The virtual memory workspace provided by the IAC executive allows for detailed user query of data.

IAC currently provides three types of data structures - array, relation, and TOC (table of contents). These data structures may contain integer, real, double precision, and/or text type data. An IAC array consists of a general matrix (arbitrary order and index dimensions), and optional labeling data associated with each index. A typical array of node/time/temperature data is illustrated in Figure 7. Such arrays can be used to communicate between different modules (e.g., provide thermal analyzer results as loadings to a static deformation analyzer). They also permit user query, e.g., display of temperature ranges for a given set of nodes, or plotting of temperature versus position for selected times and nodes. A relation is a 2-dimensional table, where each column has an associated name and each row represents a particular occurrence of values. A TOC is a special form of relation, which catalogs the characteristics of other data structures.

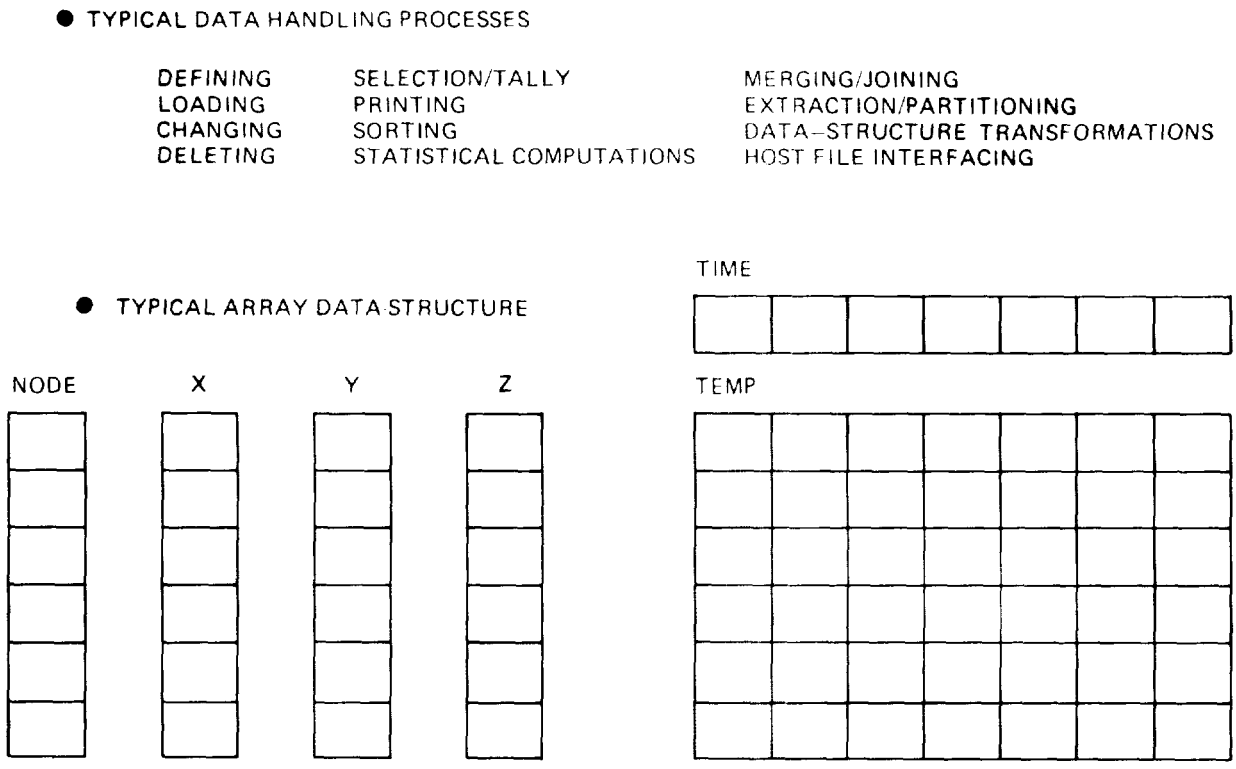

Figure 7

GRAPHICS DATA DISPLAY

It is useful to classify graphics applications within a system such as IAC into the areas of geometry, math models, graphs, and field descriptions. The Level 0 development has produced a general graphing capability, by which relationships between variables in an IAC database or workspace may be displayed. Geometry and math-model graphics applications can be handled by a variety of available but usually installation dependent packages for CAD and model generation/display (e.g., NASCAD, AD-2000, SUPERTAB, PATRAN). IAC will be capable of interfacing with such packages. IAC will also utilize, wherever possible, the available graphics capabilities of individual technical modules. Field description refers to the display of analytical field variables (e.g., temperature, stress) as a function of time, geometrical or math-model associated position, etc. Recent advancements in color raster graphics hardware are especially applicable to field description type displays.

Figure 8 shows a schematic of the current IAC graphing capability for display of X-Y curves, bar graphs, correlation tables, etc. Data is selected from the database or workspace by the user via a tutorial prompting routine, and a card image plot file is created. The plot file is a complete and device-independent numerical representation of a graph. The plot file provides a useful interface between the raw data and the pictorial display; the plot file can also be directly created or modified by the host editor, and stored or retrieved via the user's host file directory. The actual CRT graph display is generated from the plot file, via a DI-3000 based interactive plotting package. DI-3000 is an ACM SIGGRAPH Core standard graphics support package, which IAC has utilized in its graphics software development.

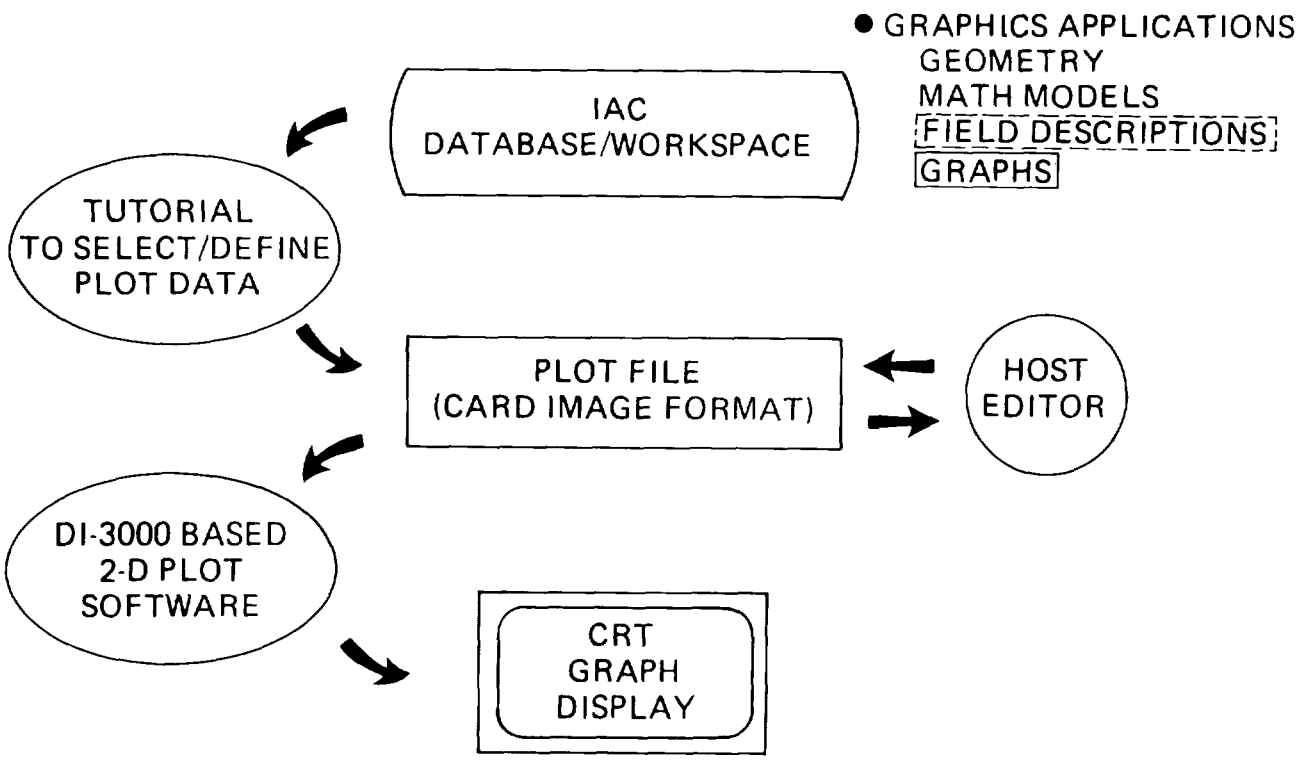

Figure 8

TECHNICAL MODULE ACCOMPLISHMENTS

The FY 81 accomplishments related to technical modules are summarized in Figure 9. The new MSC NASTRAN Version 61 was implemented within IAC. This required modification of several IAC/NASTRAN interface modules because of some NASTRAN upward incompatibilities in solution procedures and DMAP modules. The DISCOS program was enhanced to include effects of time varying quasi-static thermal and mechanical loadings (IAC thermal/structural/control solution path). The TRASYS radiation analyzer was implemented, with some streamlining in the user/JCL interface and in the handling of TRASYS scratch files. The associated graphics module TRASPLOT was also implemented within IAC. The SINDA module (including the SINFLO fluid flow capability) was implemented with some modifications similar to those for TRASYS. The ORACLS software package was converted from the CDC to VAX host computer, consistent with FORTRAN '77 language syntax. The IAC/ORACLS implementation provides for execution of both standard and user-defined driver programs for selected groups of ORACLS routines. A particular standard driver has been developed for design of a continuous or discrete regulator.

As stated earlier, one of the long-term IAC objectives is to provide a general framework which simplifies the incorporation of new modules into the system. This objective can best be met by an evolutionary process, and some initial results have been achieved during the Level 0 development. A general table-driven set of module execution software has been developed, which reduces the executive code required to implement a new module. Some improved techniques have been devised for handling module scratch storage and output listing file requirements. Standard JCL procedures have been developed, which have general applicability to many FORTRAN '77 oriented modules.

- MSC NASTRAN
  - New version 61 implemented
- DISCOS
  - Mods to include quasi-static thermal loadings
- TRASYS
  - Computational module TRASYS implemented
  - Graphics module TRASPLOT implemented
- SINDA
  - Computational module SINDA implemented
- ORACLS
  - Conversion from CDC to VAX
  - Provision for both standard and user-defined drivers
  - Driver developed for continuous or discrete regulator
- Techniques to simplify incorporation of new modules

Figure 9

DATA-FLOW ACCOMPLISHMENTS

A primary task of IAC is to integrate (or interface) various existing technologies and capabilities, via establishment of appropriate data flow between them. The FY 81 accomplishments related to data flow are summarized in Figure 10.

Interface modules have been developed or extended for NASTRAN thermal, dynamics and statics solutions. These modules accomplish the transfer of data between NASTRAN and the IAC database, and in some cases provide automated generation for portions of a NASTRAN input file. DISCOS is capable of obtaining input data arrays directly from the IAC database. The Level 0 development has provided the capability for DISCOS to obtain time varying modal thermal displacement data from the database. The IAC/ORACLS implementation emphasizes direct communication with the database and utilizes many of the IAC data handling tools for matrix definition, manipulation and display. The Level 0 development has provided the capability for ORACLS to transfer arbitrary matrices to and from the IAC database. A SINDA interface module has been developed to transfer particular output results to the database. A subroutine has been added to TRASYS which allows radiation results to be created in NASTRAN consistent input format. A mesh-point interpolator (MIMIC) has been implemented which aids in transforming field variables from one math model to another. The interfaces necessary to support the IAC thermal/structural/control solution path have been completed.

Looking to the future, there will undoubtedly be some useful technical modules which do not execute within IAC or communicate with an IAC database. Therefore, some prototype IAC tools have been developed to provide general data flow between module formatted host files and an IAC database.

- IAC module interfaces
  - NASTRAN THERMAL
  - NASTRAN DYNAMICS (normal modes)
  - NASTRAN STATICS
  - DISCOS
  - ORACLS
  - SINDA
  - TRASYS/NASTRAN
- Non-IAC module interfaces
  - Host-file/IAC-database transformation capabilities
- Modeling integration
  - MIMIC (mesh point interpolator) implemented
- Solution Path IV (thermal/structural/control) completed

Figure 10

THERMAL/STRUCTURAL/CONTROL SOLUTION PATH DEVELOPMENT

The IAC thermal/structural/control solution path was accomplished during FY 81. It provides a time-domain system dynamics analysis, including the effects of time-varying but quasi-static thermal loads (dynamic changes in configuration are assumed not to affect the thermal loading). Four major technical modules are involved in this solution path-- transient thermal, dynamic normal modes, static deformation, and system dynamics (including controls effects).

Operation of the last part of this solution path is illustrated in Figure 11, including only NASTRAN and DISCOS as the last two above mentioned technical modules. (Required data from the transient thermal and the normal modes analyses are assumed to be already existing in the database.) As shown, the user supplies a NASTRAN statics partial input file, containing a nodal-based math model. Interface software is then executed which creates an enhanced input file, using mode shapes and transient nodal temperatures from the database. This process automatically generates NASTRAN thermal load sets, and converts the model from a nodal to a modal basis via an approach similar to static condensation. The NASTRAN statics analyzer is then executed and the computed time-varying modal thermal displacements are stored in the database. Nodal displacements can also be made available for user evaluation and display. A DISCOS time-domain analysis is finally performed, using the modal thermal displacements as quasi-static loadings along with mode shapes and modal characteristics also in the database.

It should be noted that although this solution path is primarily oriented toward quasi-static thermal loadings, it is equally applicable to quasi-static mechanical loadings since general time varying modal displacement loadings are passed to the system dynamics analyzer.

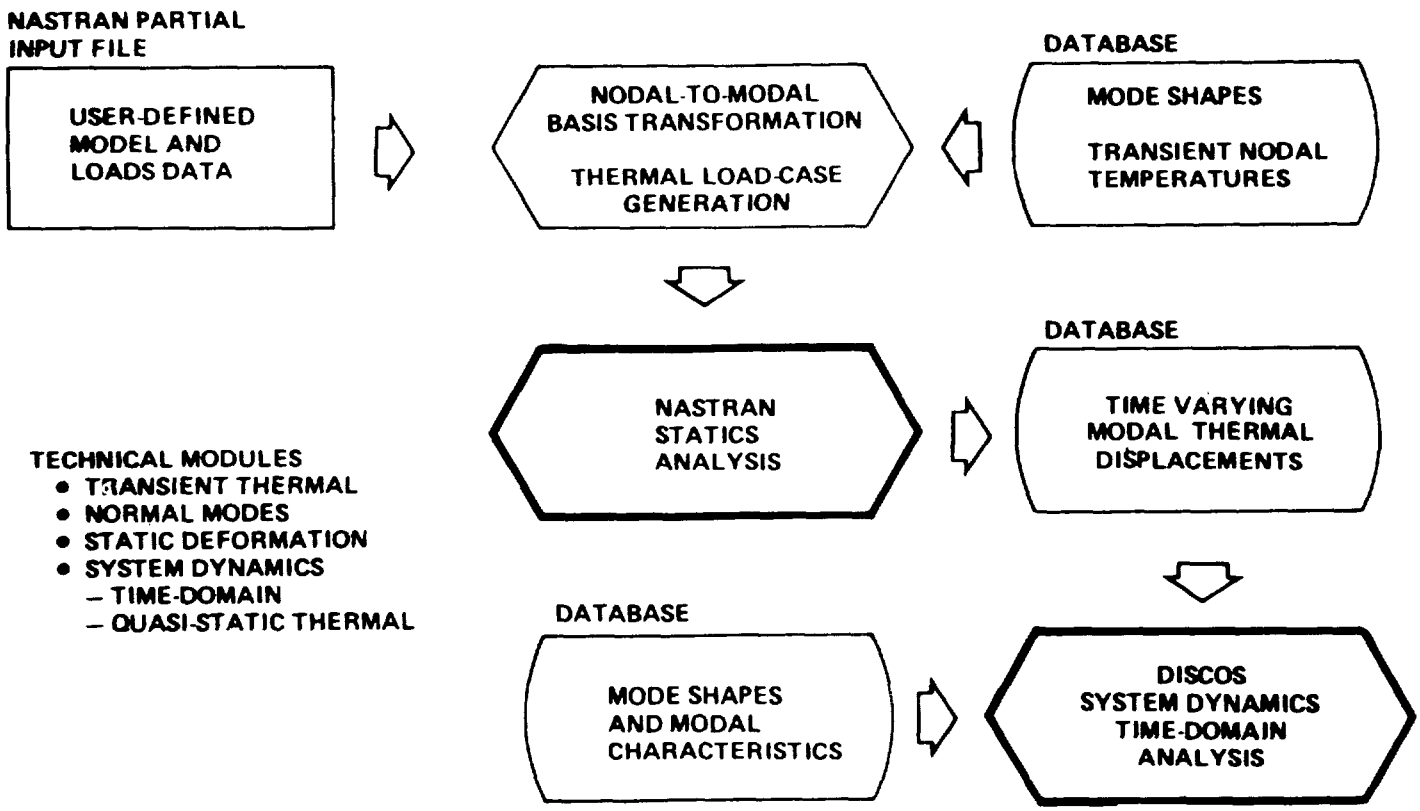

Figure 11

PLANNED LEVEL 1 ARCHITECTURE

Part of the FY 81 activity has involved the planning of details for the initial operational (Level 1) software to be completed during CY 82. The planned Level 1 architecture is described in figure 12.

Limited evaluation and testing performed thus far on the Level 0 software indicates that it will provide a solid foundation for developing the operational system. However, it must be recognized that Level 0 IAC is only a prototype product, and considerable vital work remains to be done during FY 82 in providing a generally usable capability. This work includes advancement of the module data-flow links (Solution Paths II to IV) to large-problem operational status, completion of critical supporting capabilities in the executive and data handling areas, implementation of additional modules, code debugging, and further documentation of the system.

The list of available IAC technical modules will be expanded through a joint effort by Boeing and NASA GSFC, with the implementation of the SPAR structural and thermal capabilities and the controls modules SAMSAN and MODEL. Some additional capabilities will be added to ORACLS and DISCOS, including improved data communication with other controls programs. The RIM (Relational Information Management) module will be implemented within IAC. This will make available the RIM query processing capabilities and also provide for a link to available IPAD (Integrated Programs for Aerospace Design) software.

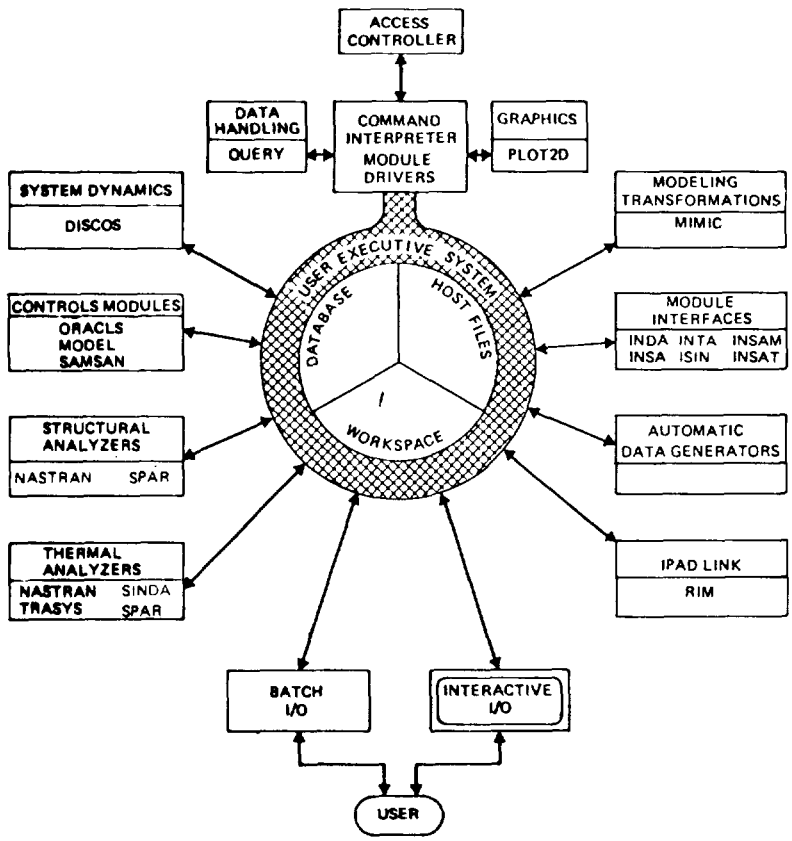

Figure 12

IAC CONTROL SYSTEM ANALYSIS DEVELOPMENT

HAROLD P. FRISCH

GODDARD SPACE FLIGHT CENTER
GREENBELT, MARYLAND

LARGE SPACE SYSTEMS TECHNOLOGY--1981
THIRD ANNUAL TECHNICAL REVIEW
LANGLEY RESEARCH CENTER
HAMPTON, VA 23665
NOVEMBER 16-19, 1981

MODEL (MULTIOPTIMAL DIFFERENTIAL EQUATION LANGUAGE) PROGRAM

The MultiOptimal Differential Equation Language provides a means for generating numerical solutions to systems of differential equations using a digital computer. The notation of this language is similar to that usually used in describing physical systems by differential equations. Thus, the learning process is simplified, programming becomes easier, and debugging is more readily accomplished. Programs written in the MultiOptimal Differential Equation Language are machine translated into FORTRAN 4 code which is optimal in several respects.

The interactive version of MODEL makes use of interactive system routines so that the user may observe the solution as it is being generated and interact with the program in a manner similar to that associated with analog simulation.

The DISCOS-Control version of the MODEL simulation language is used to describe the control system for a plant which is modelled by the DISCOS program. DISCOS plant variables may be referenced in the control system description and all the sensor signals, coupling torques (e.g., motors), momentum devices (e.g., flywheels) and external loads (jets, magnetics, etc.) are automatically linked to the DISCOS plant model.

All MODEL development work is being done at NASA GSFC by Benjamin G. Zimmerman. This in-house work is proceeding on schedule; however, associated documentation is not yet ready for general release.

A FAMILY OF PROGRAMS WHICH OUTPUT OPTIMALLY WRITTEN FORTRAN PROGRAMS AND SUBROUTINES FOR DYNAMICS ANALYSIS

INPUT: NON-LINEAR ORDINARY DIFFERENTIAL EQUATIONS (ODE'S) IN STANDARD MATHEMATICAL NOTATION

--- FOR EXAMPLE ---

DERIVED EQUATIONS	INPUT TO MODEL
$\dddot{y} = A\,\dot{y} + D\,x^3$	Y''' = A*Y' + D*X**3
$\dot{x} = E\,\tan(x\ddot{y})$	X' = E*TAN(X*Y')
	END

THE MODEL FAMILY OF PROGRAMS

MODEL is not a new program at NASA/GSFC; various versions of it have been in use since 1971. These versions however interfaced only with hardware used by the Guidance and Control Branch at GSFC. The IAC program has provided the impetus to not only rewrite the program in a more machine portable form but to also create a family of MODEL programs. This family of programs will significantly expand analysis capabilities via use of a simulation language program.

MODEL-I is in effect the MODEL program that has been used for project support work by the G&C Branch since 1971. It is now considered to be fully checked out and bug free.

MODEL-C is a response to users that desire a more user friendly interface between the equations which define control system dynamics and the DISCOS program. It is now possible to use MODEL-I for standalone controls analysis and then to use the MODEL-I input file as input to MODEL-C to obtain subroutine CONTRL for a coupled controls structure interaction analysis via DISCOS.

MODEL-S is nearing the final completion stage. It is designed to allow the user to readily input sampled data control equations. While MODEL-I can and has been used for sampled data controls analysis, users had to set up zero order holds and digital computational delays as logic functions. With MODEL-S, users will be capable of defining sampled data controllers in a much more user friendly manner.

MODEL-I	INPUT:	NON-LINEAR TIME DOMAIN ODE'S
	OUTPUT:	FORTRAN PROGRAM FOR "TRUE" INTERACTIVE TIME DOMAIN ANALYSIS
MODEL-C	INPUT:	NON-LINEAR ODE'S WHICH DEFINE CONTROL SYSTEM DYNAMICS FOR THE DISCOS PROGRAM
	OUTPUT:	FORTRAN SUBROUTINE COMPATIBLE WITH DISCOS CONTROL SYSTEM DEFINITION NEEDS
MODEL-S	INPUT:	NON-LINEAR SAMPLED DATA CONTROL SYSTEM EQUATIONS; NON-LINEAR ODE'S, ZERO ORDER HOLDS AND DIGITAL COMPUTATIONAL DELAYS
	OUTPUT:	FORTRAN PROGRAM FOR "TRUE" INTERACTIVE TIME DOMAIN ANALYSIS

TRIVIAL DEMONSTRATION PROBLEM

The admittedly trivial demonstration problem is presented to dramatize the simplicity of setting up the input data required by any of the MODEL family of programs. Line 1 defines which of the MODEL family is to be used, on line 2 the equation which defines the system is written and on line 3 an END statement is provided.

Users need not specify input parameter values for K, D, W or any initial condition. MODEL will provide default values for all. The user is free to override them when input data is read into the MODEL written program. Furthermore if no output selection commands are given, MODEL outputs all time varying state variables to the lineprinter. "True" interactive plot and analysis capabilities are available by insertion of one more line of input data.

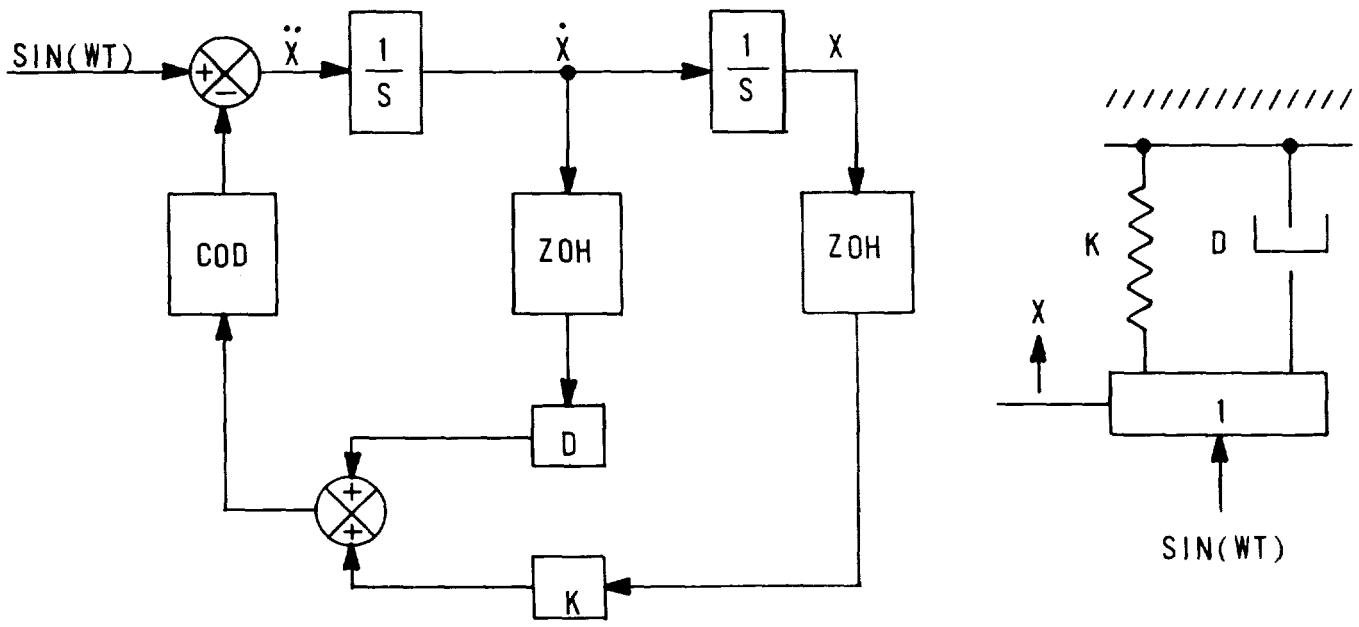

ZOH ZERO ORDER HOLD
COD (DIGITAL) COMPUTATIONAL DELAY

MODEL PROGRAM INPUT

```
MODEL-I    //[CONTINUOUS SYSTEM]
X'' =  SIN(W*T) - K*X - D*X'
END
MODEL-S    //[SAMPLED DATA SYSTEM]
X'' =  SIN(W*T) - COD(K*ZOH(X) + D*ZOH(X'))
END
```

DISCOS

A DIGITAL PROGRAM FOR THE DYNAMIC INTERACTION SIMULATION
OF CONTROL AND STRUCTURE

The prime emphasis with respect to DISCOS (ref 1) over the past year has been in responding to the desires of several users for a more user friendly input data interface.

It is currently possible to enter all standard DISCOS input data via keyboard response to tutorial prompts, generated by the DISCOS tutorial input program written by Joan Sanborn at GSFC.

With respect to the "user supplied subroutines" for DISCOS, it has been demonstrated at GSFC that this need can to a major extent be eliminated. The breadboard demonstration program which proved this ability is currently being incorporated into DISCOS.

In the process of converting DISCOS from the IBM computer to the VAX, a documentation program was written. ALL DISCOS program documentation is now contained within the source code. The documentation program is capable of recognizing delimiters within the source code and generating the full DISCOS REFERENCE GUIDE. Up to date documentation is now always available to DISCOS users via a rerun of the documentation program.

****** NEW CAPABILITIES ******

TUTORIAL PROGRAM TO SET UP INPUT DATA

DISCOS TO MODEL-C INTERFACE

DISCOS/VAX CREATED FROM DISCOS/IBM (COSMIC STANDARD)

PROGRAM TO WRITE DISCOS REFERENCE GUIDE

Controls analysts have access to a vast array of published algorithms to solve an equally large spectrum of controls related computational problems. Unfortunately the subroutines which implement the algorithms do not always readily interface with each other, and furthermore they are frequently less applicable than their creators imply in accompanying documentation (ref 2).

SAMSAN is an attempt to collect together in one self-consistent library a complete set of computational algorithms which are applicable for large order classical controls analysis. The SAMSAN library is biased toward numerical accuracy; computational speed is important but accuracy is given higher priority. An attempt is made to include only those algorithms which are backed up by rigorous numerical error analysis and are applicable for large order control system analysis, i.e., order less than about 200.

The limit of about 200 is arrived at from practical computational speed considerations and more importantly from the fact that most iterative algorithms associated with non-symmetric matrices yield results which are exact for some matrix A+E where E is viewed as error in knowledge of A. Furthermore if the associated computing problem is well-conditioned the norm of E is usually given as:

$$NORM(E) < K * N^{P} * 2^{-B} * NORM(A)$$

WHERE

K is about equal to 10.0
N is the order of the non-symmetric matrix "A"
P is about equal to 2.0
B is about equal to 52 (DOUBLE PRECISION ON IBM)

In application when N exceeds about 200 and "A" contains a fair spread in numeric magnitudes, the norm of E gets disturbingly large.

A COLLECTION OF NUMERICALLY SUPERIOR ALGORITHMS

FOR SAMPLED DATA CONTROL SYSTEM ANALYSIS

WHY?

A SELF-CONSISTENT SET OF NUMERICALLY RELIABLE ALGORITHMS

FOR LARGE ORDER CONTROL SYSTEM ANALYSIS DOES NOT EXIST

MANY STANDARD CONTROLS ANALYSIS METHODS ARE BASED UPON THE

NEED TO SET UP AND SOLVE AN ILL-CONDITIONED COMPUTING PROBLEM

ILL-CONDITIONED COMPUTING PROBLEMS

The most common function appearing in classical controls analysis literature is the polynomial in power series form. Unfortunately if one desires to analyze large order control system problems via use of polynomials in power series form, one will almost assuredly encounter numerical computation problems. This fact is one of the most important results of numerical error analysis. It is also one of the most consistently ignored facts in frequency domain analysis.

The symmetric matrices arrived at in structures analysis are guaranteed to have a linearly independent eigenvector for every eigenvalue. This fact leads to the ability to generate reduced order dynamic models via modal analysis.

The non-symmetric matrices of controls and structures-controls analysis do not necessarily and usually do not have a full set of linearly independent eigenvectors. This fact prohibits a complete decoupling of the system equations via eigen analysis. Theoretically the best that can be done is to almost decouple the equations by reducing the associated matrix to Jordan canonical form. This cannot be done using floating point arithmetic. Furthermore if one unsuspectingly requests all eigenvectors for a matrix which does not have a full set, the net result will be either a singular or a near singular eigenvector matrix and hence one useless for modal analysis.

MODERATE DEGREE POLYNOMIALS IN POWER SERIES FORMAT, (N .GE. 15)

$$A_N S^N + \ldots + A_2 S^2 + A_1 S + A_0$$

COMPUTATION OF POLYNOMIAL ROOTS

EVALUATION OF POLYNOMIAL NEAR A ROOT

NON-SYMMETRIC MATRICES

INVERSION OF NEAR SINGULAR EIGENVECTOR MATRICES

REDUCTION OF MATRIX TO JORDAN CANONICAL FORM

**** NEW CAPABILITIES ****

The most common origin of high degree polynomials in controls analysis is from the expansion of determinants of polynomials in either the Laplace variable "S" or the Z-transform variable "Z". Brute force expansion and combination of like power terms leads naturally to power series polynomials.

SAMSAN has an algorithm which will determine all eigenvalues of a matrix of low to moderate degree polynomials. By using this algorithm it is possible to obtain polynomials associated with determinantal expressions in factor polynomial form, a more desirable form from the standpoint of numerical analysis (ref 3).

SAMSAN contains the algorithms associated with the program BLOCK IT distributed by COSMIC. These algorithms enable one to reduce a non-symmetric matrix to block diagonal form via a real non-singular transformation matrix. The net result is that SAMSAN users have the ability to almost decouple a full set of system equations and obtain reduced order models via a quasi-modal analysis method.

Frequency domain analysis methods have been a mainstay of controls design methods for the past several decades. Surprisingly, algorithms for generating frequency response data are not widely distributed.

SAMSAN users have a full frequency response computation capability. Frequency response in the "S", "Z" or "W" domain is available via algorithms with advanced stepping logic.

COMPUTE ALL EIGENVALUES OF A MATRIX OF LOW DEGREE POLYNOMIALS

COMPUTE THE REAL NON-SINGULAR TRANSFORMATION MATRIX WHICH WILL REDUCE A REAL NON-SYMMETRIC MATRIX TO BLOCK DIAGONAL FORM

FOR TRANSFER FUNCTIONS DEFINED AS POLYNOMIAL RATIOS IN EITHER THE "S", OR "Z" DOMAIN, COMPUTE BODE, NICHOLS, NYQUIST & ROOT LOCUS FREQUENCY RESPONSE DATA IN EITHER "S", "Z" OR "W" DOMAIN

REFERENCES

1. Bodley, C.S., Devers, A.D., Park, A.C., and Frisch, H.P., "A Digital Computer Program for the Dynamic Interaction Simulation of Controls and Structure (DISCOS)." NASA Technical Paper 1219, Vols 1 and 2, May 1978.

2. Frisch, H.P., "Pitfalls and Guidelines for the Numerical Evaluation of Moderate-Order System Frequency Response." NASA Technical Paper 1814, June 1981.

3. Frisch, H.P., "Reduced Order Feedback Control Equations for Linear Time and Frequency Domain Analysis." NASA Technical Paper 1818, June 1981.

LARGE ADVANCED SPACE SYSTEMS (LASS)

COMPUTER-AIDED DESIGN PROGRAM ADDITIONS

C. E. Farrell
Martin Marietta Corporation
Denver, Colorado

Large Space Systems Technology - 1981
Third Annual Technical Review
November 16-19, 1981

INTRODUCTION

LSS preliminary and conceptual design requires extensive iterative analysis because of the effects of structural, thermal, and control intercoupling. Langley Research Center is developing a computer aided design program that will permit integrating and interfacing of required large space system (LSS) analyses. The primary objective of this program is the implementation of modeling techniques and analysis algorithms that permit interactive design and trade-off studies of LSS concepts. This paper presents an overview of the status of the program and the capabilities added through performance of contract NAS1-16447 by the Denver Division of Martin Marietta Aerospace. This contract was sponsored by the LRC Systems and Experiments Branch. Contract officer was U.M. Lovelace with computer-aided design activity monitored by Dr. L. B. Garrett.

LARGE ADVANCED SPACE SYSTEM (LASS) DESIGN COMPUTER PROGRAM

Figure 1 shows the capabilities of the Langley Systems and Experiments Branch Large Advanced Space Systems (LASS) computer-aided design program before performance by Martin Marietta of Task 3 of Contract NAS1-16447. The LASS program initially was implemented on a CDC main frame. It is an analysis tool to be used in preliminary and conceptual design of LSS. The analysis modules shown use algorithms that will permit interactive analysis. Thus they each take only a few seconds of computer time for execution. Besides instantaneous outputs they also combine to create dynamic analysis program inputs for off-line (or batch) structural analysis.

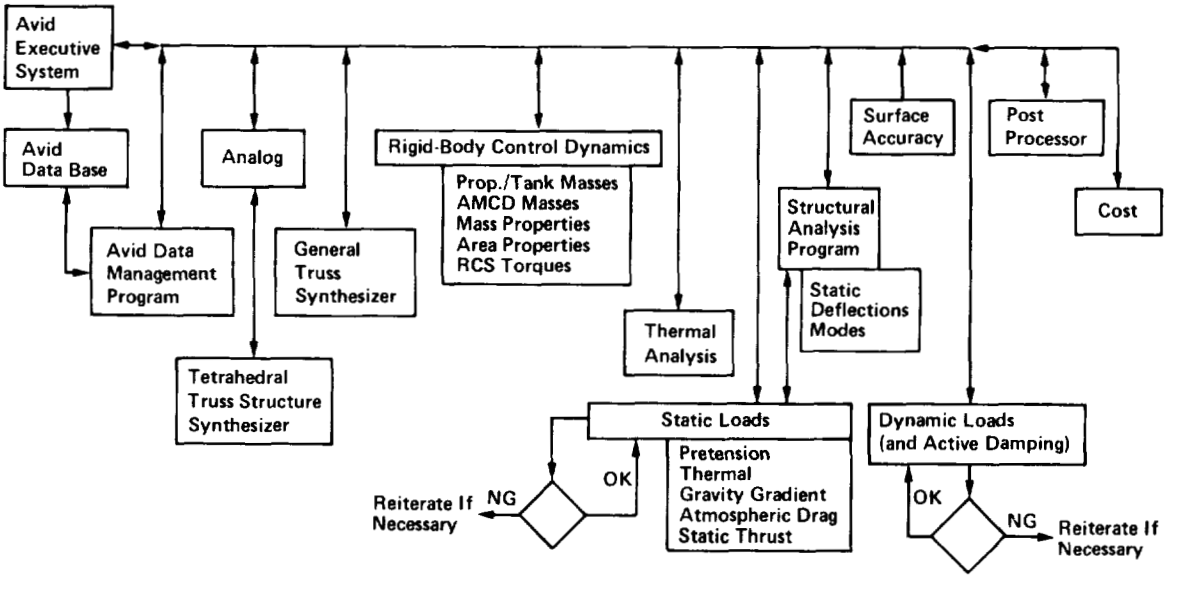

Figure 1

LASS WITH EXPANDED CAPABILITY

Figure 2 details the capabilities of the LASS program upon completion of the contract. Eight new software modules were added to the program. The existing rigid body controls module was modified to include solar pressure effects. The new model generator modules and appendage synthesizer module are integrated (interfaced) to permit interactive definition and generation of LSS concepts. The mass properties module permits interactive specification of discrete masses and their locations. The other new or modified modules permit interactive analysis of orbital transfer requirements, antenna primary beam gain, and attitude control requirements. In its present configuration, the program is best used with a graphics terminal compatible with a Tektronix model 4014 although other standard terminals may be used. Extensive outputs are automatically written onto files for off-line printing.

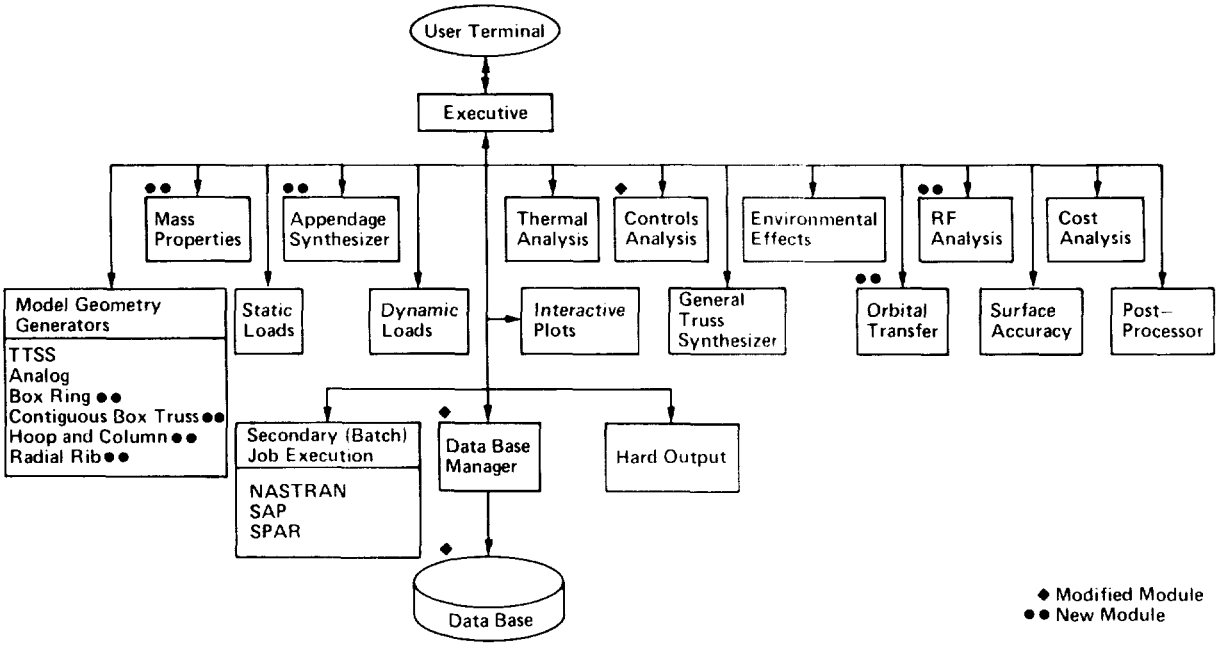

Figure 2

AUTOMATED MODEL GENERATOR INPUT/OUTPUT

Each new automated model generator module provides the user with the ability to interactively specify the configuration inputs to permit automatic modeling of a LSS structure. The truss model generators create only the reflective surface support model, while the hoop-column and radial rib modules have options to include center feed masts, stays, and hoop elements. Figure 3 shows the general types of parameters that must be input for model generation and the outputs that result. Each model generator creates geometry, element, and property model data in NASTRAN format. A LRC-developed post processor reformats this data for SAP structural analysis program execution. The output files are used and may be modified upon subsequent execution of the Appendage Synthesizer Module and/or Mass Properties Module to permit rapid and efficient creation and analysis of different LSS concepts.

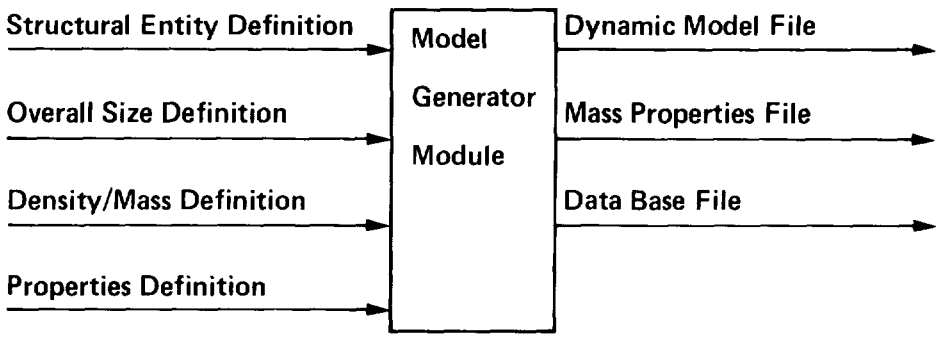

Figure 3

APPENDAGE SYNTHESIZER MODULE INPUT/OUTPUT

The Appendage Synthesizer Module provides the capability of interactively specifying and modeling the structural elements and masses associated with the feed beam and feed support masts. Figure 4 shows the input parameters to be specified by an interactive user for creating models of these appendages and for updating the dynamic model and mass property matrices files to reflect the appendages' addition to the structure. There are six automated mast element model generators included in the module. A user may select the type of element and he is then prompted to specify the appropriate mass parameters. This module provides the capability of comparing effects of different types of feed configurations with the same or different base structures.

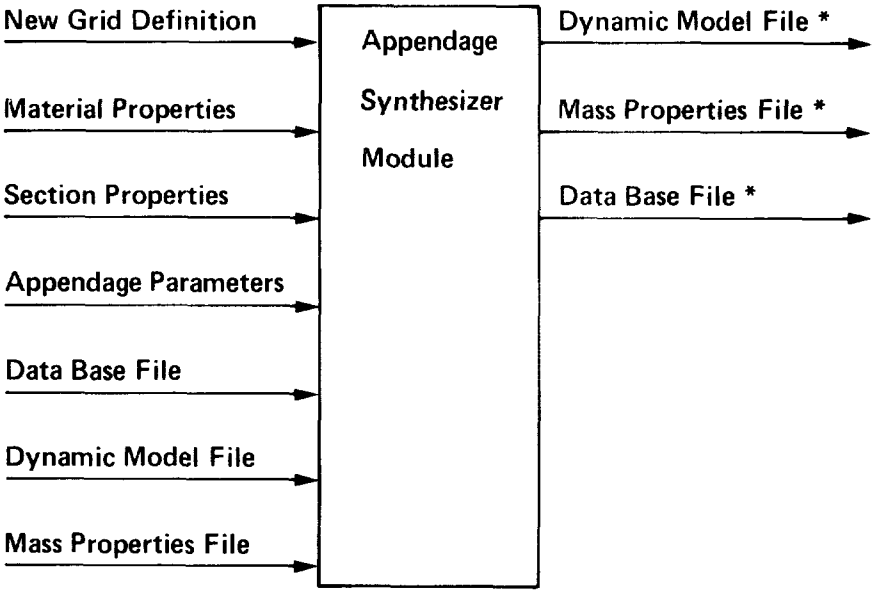

* New or Modified

Figure 4

MASS PROPERTIES MODULE INPUT/OUTPUT

The final stage in LASS modeling of a complete LSS spacecraft involves the Mass Properties Module. The module permits modification of concentrated masses at model grid points and thus provides the capability of analyzing effects of placing auxiliary equipment at different locations on the LSS. This module also performs the calculations required to determine total dry S/C mass, center of mass coordinates, and inertias. In addition, a mass breakdown is output identifying the contribution to total mass of the various structural elements in the particular model. Figure 5 shows the general input and output capabilities of this module. The module data base contains configuration information (e.g. the type of basic structure). The mass properties matrices contain node, connectivity, and property data in unformatted form. These data may be used to calculate overall areas needed for force and torque calculations in the controls analysis module.

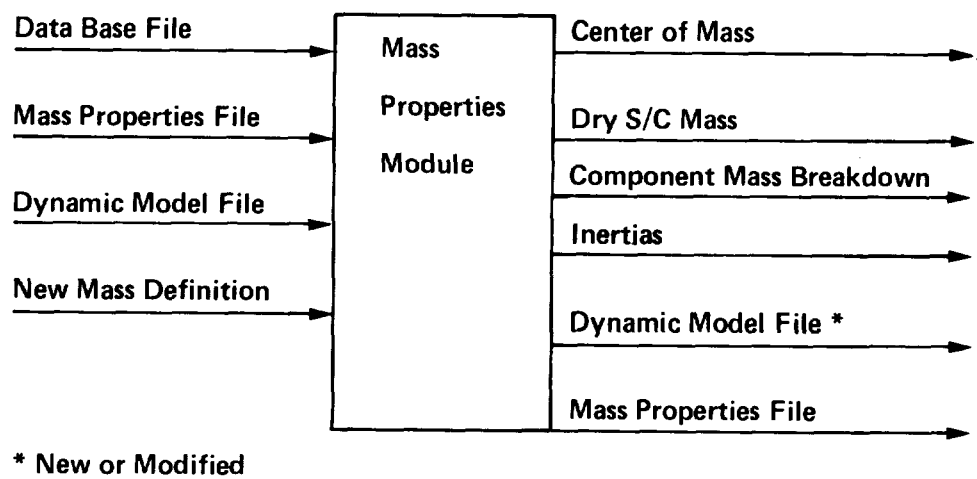

Figure 5

RCD MODULE INPUT/OUTPUT

Upon completion of model generation the user can perform one of the interactive analyses or can choose to perform a batch executable analysis using NASTRAN or SAP. The interactive analyses added during the contract include orbital transfer and rf analysis plus the ability to determine attitude control system requirements that result from solar flux, aero drag, and gravity gradient. The orbital transfer model might be used first in order to determine wet spacecraft mass and to then recalculate the mass properties. This would lead to rigid body controls (RCD) analysis using the RCD Module. Figure 6 shows the input/output characteristics of this module. Internal to the module are the calculations to determine perturbing forces and torques and resultant momentum and force buildup. The input data shown is carried in a data base file created through execution of the modules described previously or by interactive input. Orbit definition may be modified to permit analysis of a concept at different orbits. Another mode is analysis of control requirements for several competing structural concepts.

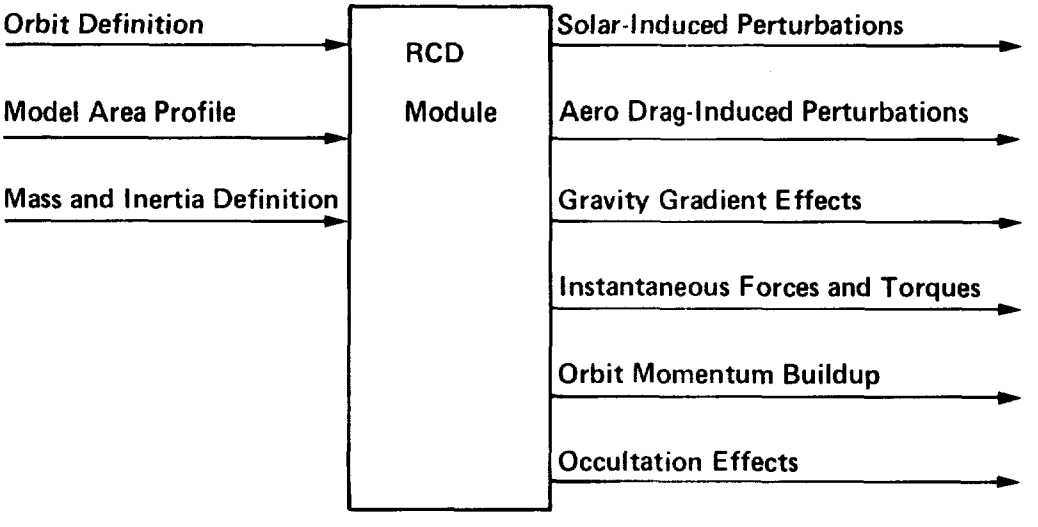

Figure 6

LASS USER SCENARIO

Figure 7 shows a scenario representative of the operations that might occur when the LASS program is used for LSS conceptual design. The feedback path from the "Iterate" decision block shows that a user may go to any module in the program. This is a key feature of the interactive capability of LASS. At the exit from any module the user can execute any other module or reexecute the current one. The "user friendly" executive of LASS readily permits its use by personnel who are not currently motivated to use available software tools. Its iterative, integrated analysis capability makes it attractive as a systems analysis tool that provides quantitative evaluation of competing concepts. The fast response of an interactive environment lends itself to increased creativity in that more concepts may be created and analyzed than in a "batch" operating mode.

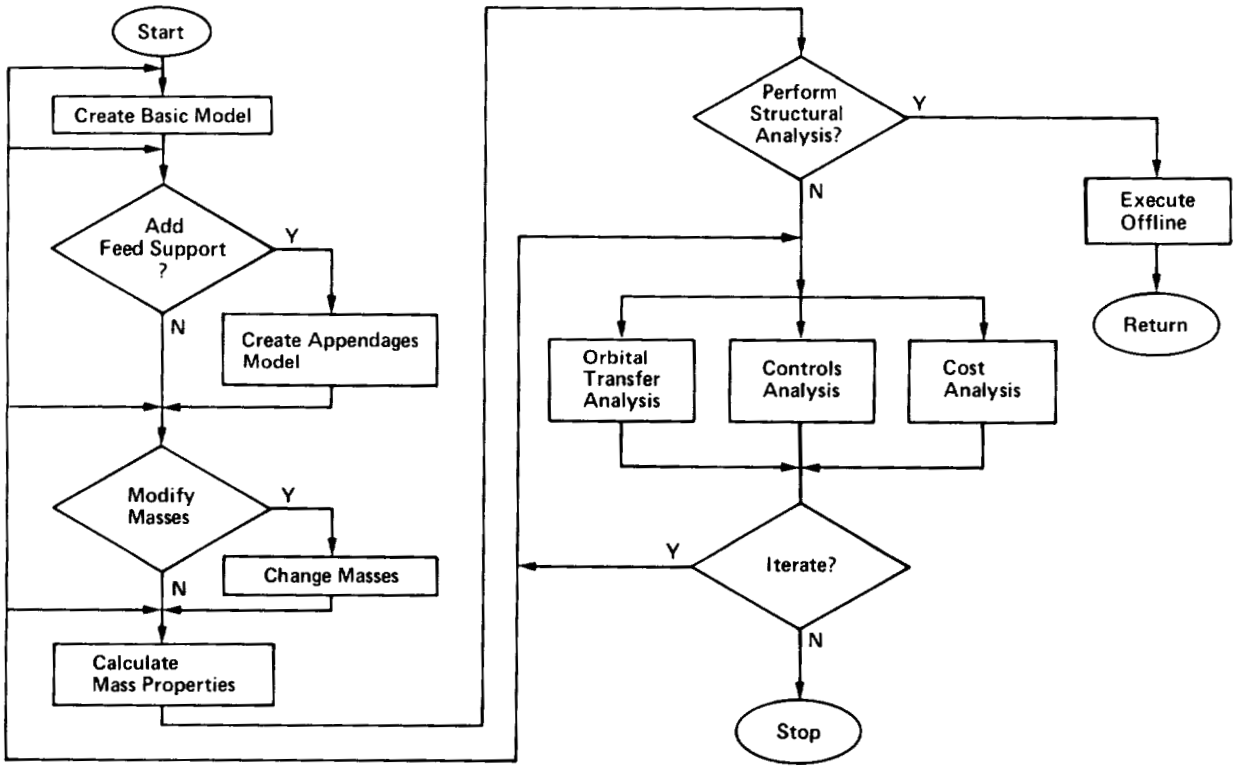

Figure 7

SEQUENTIAL DEPLOYMENT OF TRUSS STRUCTURES

John M. Hedgepeth
Astro Research Corporation
Carpinteria, California

Large Space Systems Technology - 1981
Third Annual Technical Review
16-19 November 1981

DESIGN CONCEPTS FOR LARGE ANTENNA REFLECTOR STRUCTURES

During the past year, Astro has been working on the design and analysis of truss-type reflector structures using expandable mesh as an rf reflecting surface. This work, which is supported by a contract from Langley Research Center, is motivated by the excellent accuracy and stiffness performance indicated by previous analyses of these types of structures.

In order to achieve the objective, a number of ground rules were established which are aimed at simplifying the mechanization of the truss configuration. Most of these ground rules are being used in our work on spaceflight hardware systems. They have proven to be very helpful in keeping the development, fabrication, and test costs of deployable structures under control. The only new one arising from the current application is that of mesh attachment. It is desired to fasten the mesh directly to the surface struts of the truss and avoid intricate systems of shaping wires, tie-downs, or harnesses.

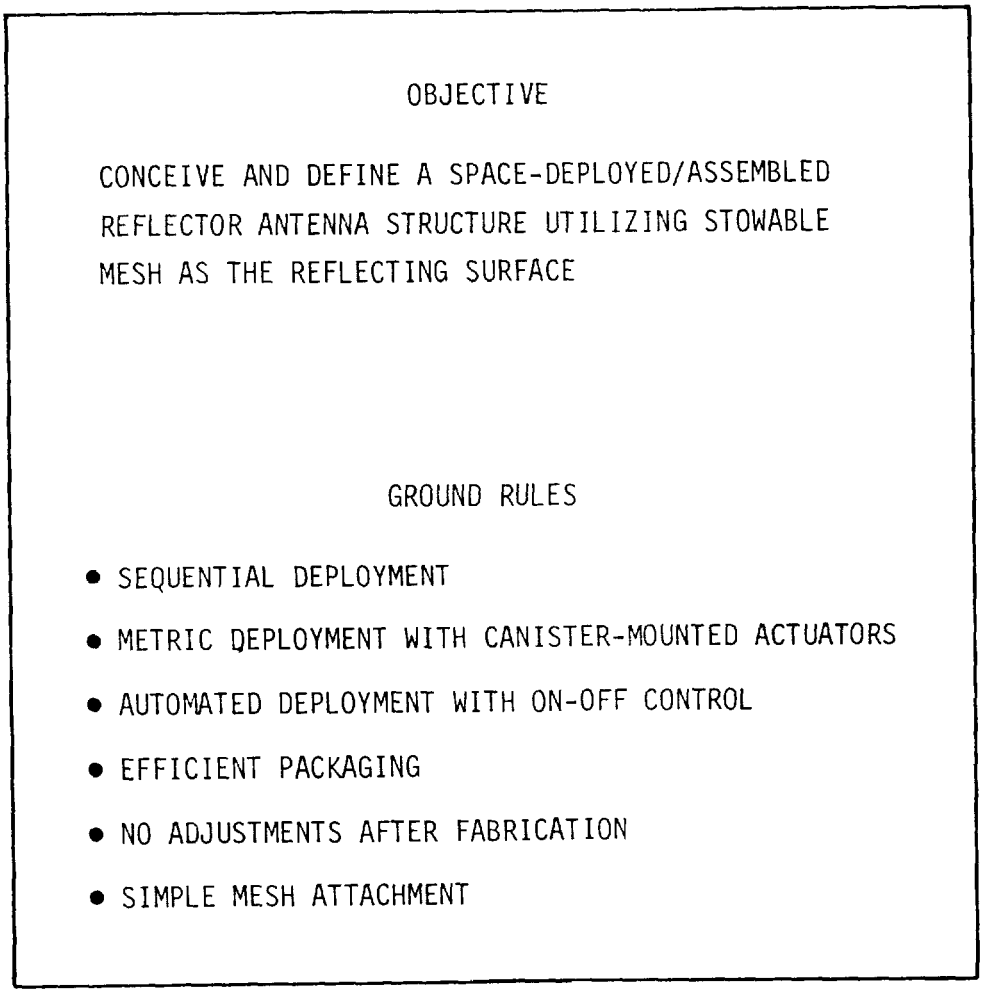

Figure 1

TETRAHEDRAL TRUSS STRUCTURE

The geometry investigated most intensively has been the triangular tetrahedral truss shown here. A square-type truss having the same topology has also been investigated.

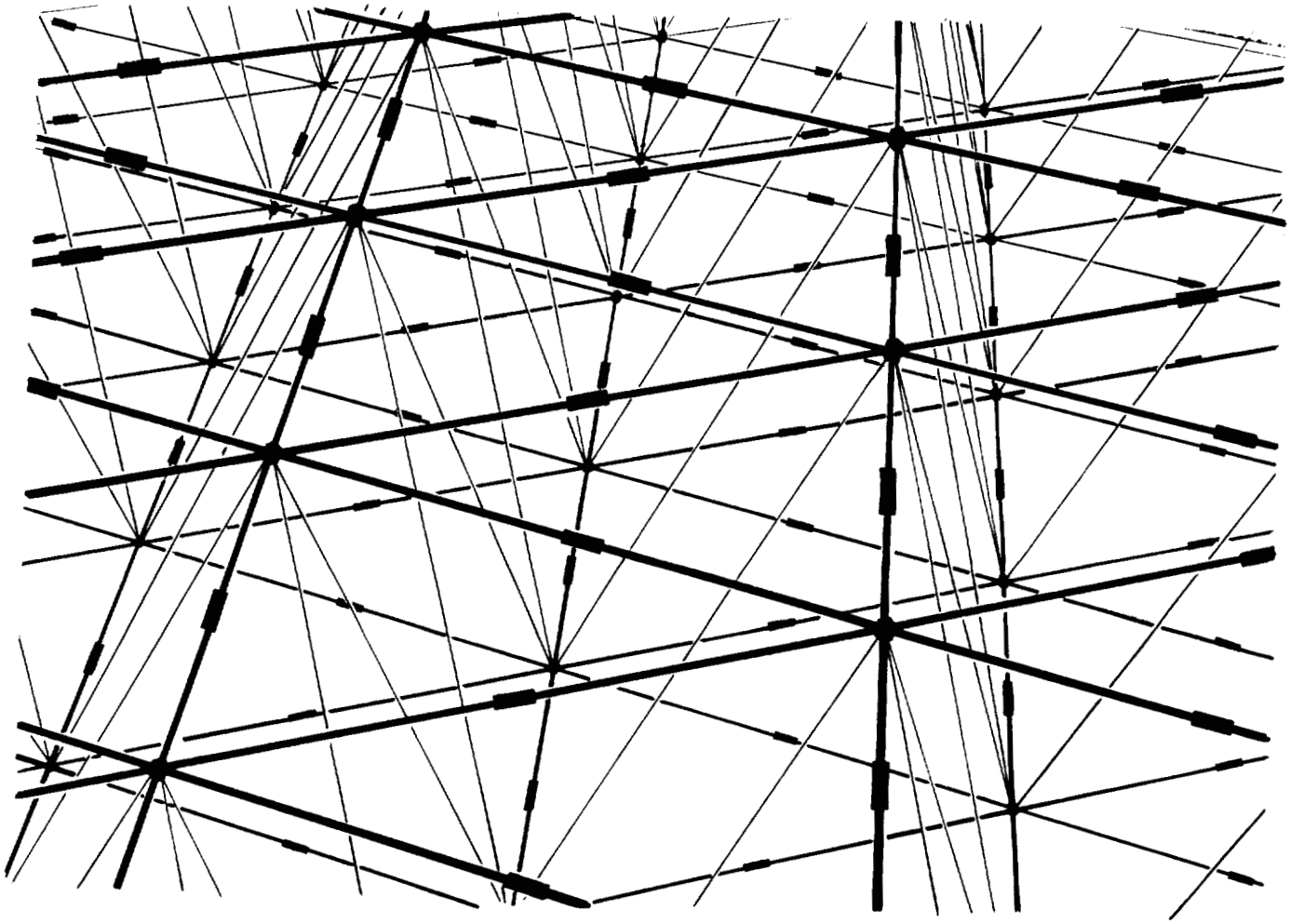

Figure 2

TETRAHEDRAL TRUSS NOMENCLATURE

The tetrahedral truss is composed of surface struts and core members. In the particular deployable form invented in this contract, the entire truss is viewed as being made up of a number of parallel truss "ribs" connected to each other by interrib struts and members as shown on this figure.

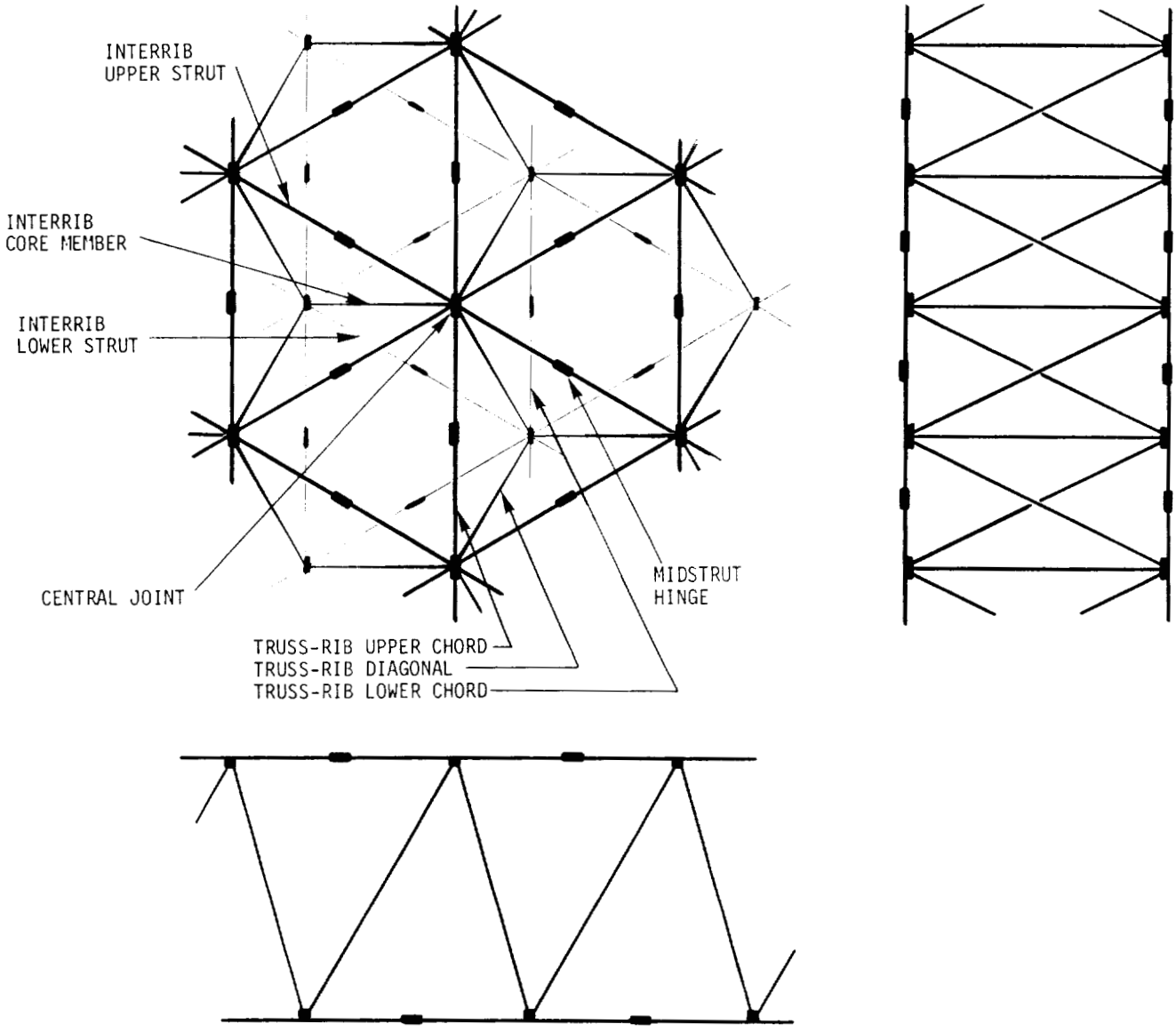

Figure 3

PARTIALLY DEPLOYED STRUCTURE

In this new concept of deployment, the truss ribs are deployed first along their length, and then the interrib members are deployed. This sketch shows five deployed truss ribs still packaged together with fully deployed structure on either side. These fully deployed trusses have high stiffness and the truss ribs sandwiched between them are well-controlled simply by controlling the positions of the two fully deployed portions. The positioning of the fully deployed portions is accomplished by deployment mechanisms at the two boundaries of the structure.

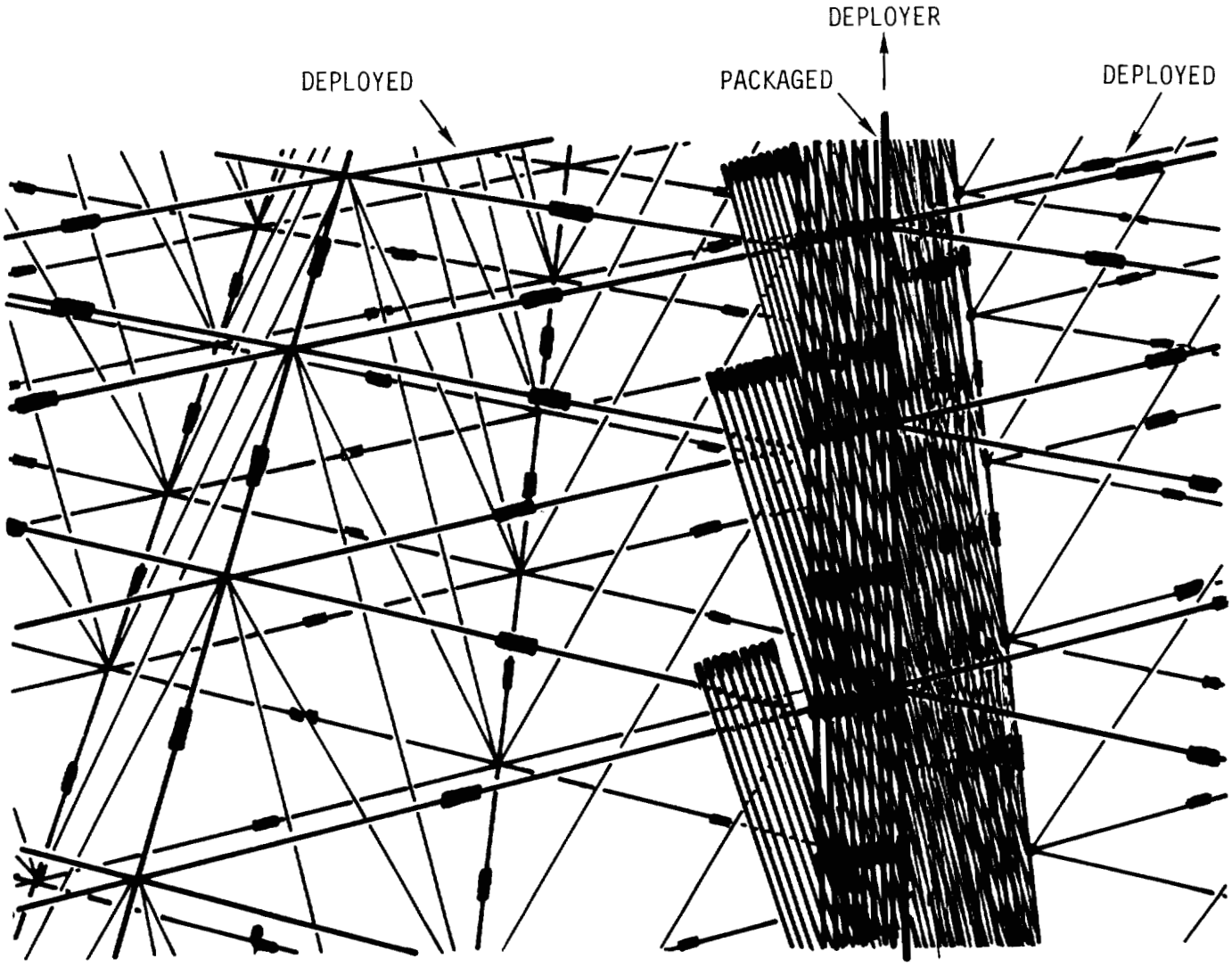

Figure 4

MID-DEPLOYMENT

The deployment mechanisms are indicated in this figure by the small half circles. Appropriate actuators will grasp the fully deployed portions, move them apart, and allow the required amount of fully packaged truss to leave the deployment mechanism.

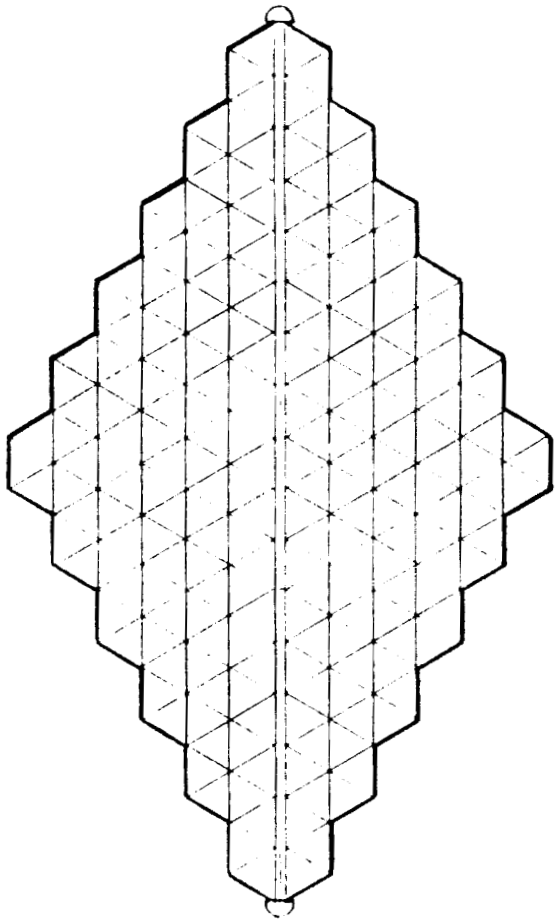

Figure 5

TRUSS RIB WITH INTERRIB ELEMENTS

A fully deployed single truss rib with its associated interrib elements is shown in this figure. Of course, the rib itself packages neatly by allowing midstrut joints to fold outwards allowing the diagonals to lie alongside each other. The difference between the present packaging method and the "standard method," which involves synchronous deployment, is the manner in which the interrib elements are packaged.

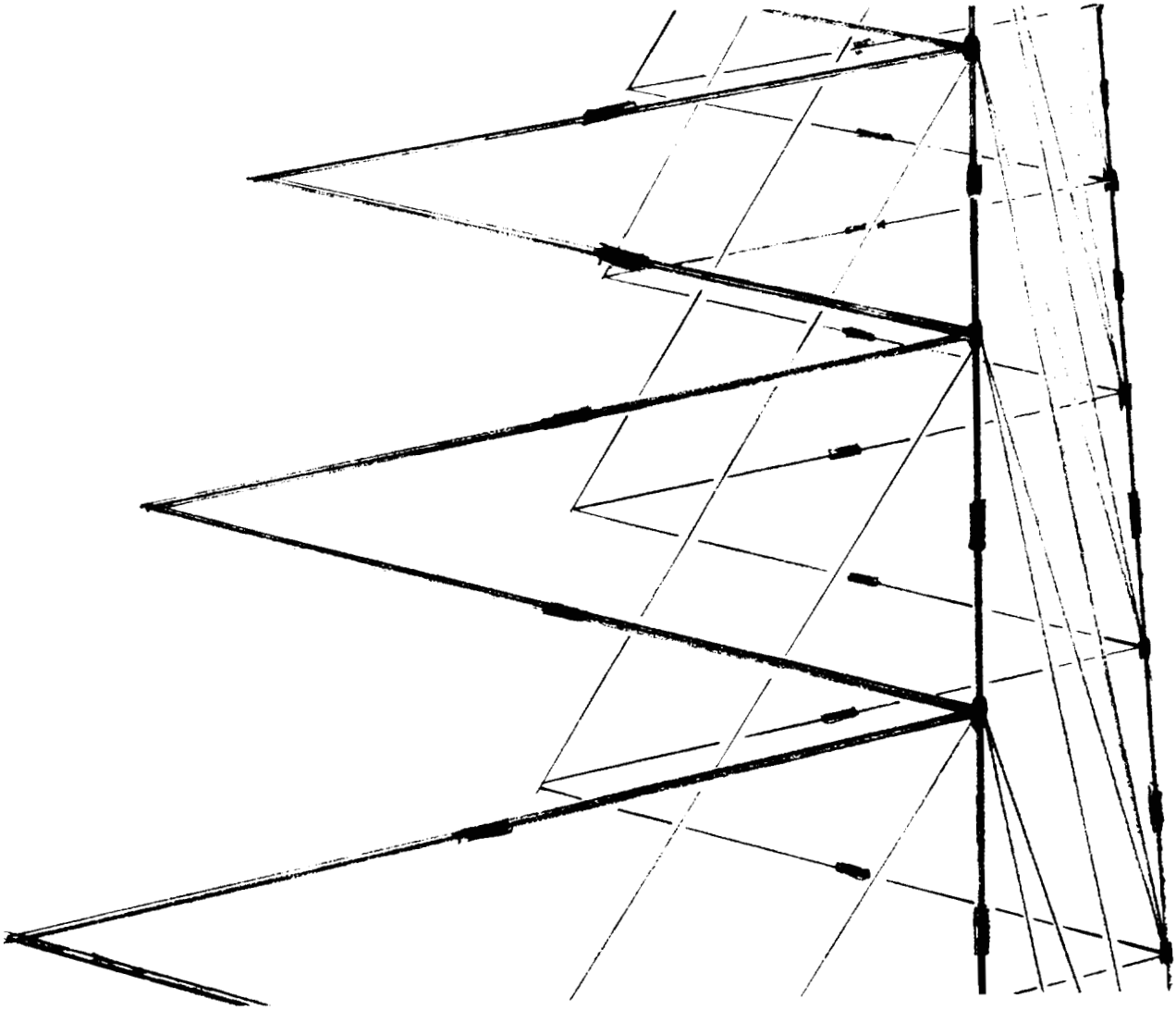

Figure 6

SECOND-STAGE DEPLOYMENT

This sketch shows the deployment of the interrib elements. Note that only one of the interrib struts on each surface is folded outward. The other surface strut folds over against the appropriate truss chord. It is this action which allows sequential deployment.

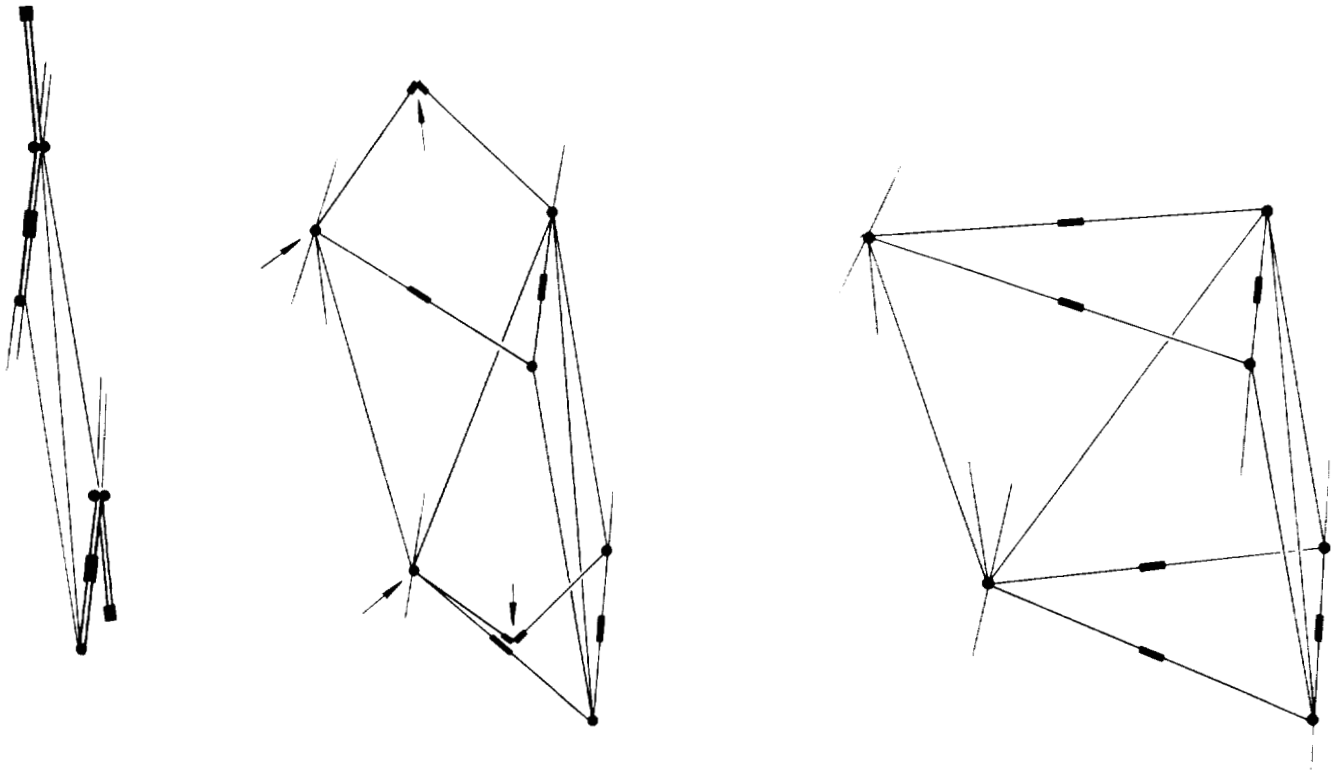

(a) STOWED (b) PARTIALLY DEPLOYED (c) DEPLOYED

Figure 7

CENTRAL JOINT

The previously described type of deployment requires specially designed joints. The central joint at which nine members intersect is a particularly tough design problem. After a considerable amount of effort, we have been able to design the joint shown here which has all the proper articulations and incorporates buttresses as necessary to stabilize the joint when fully deployed. Note that all motions are single hinge-type rotations.

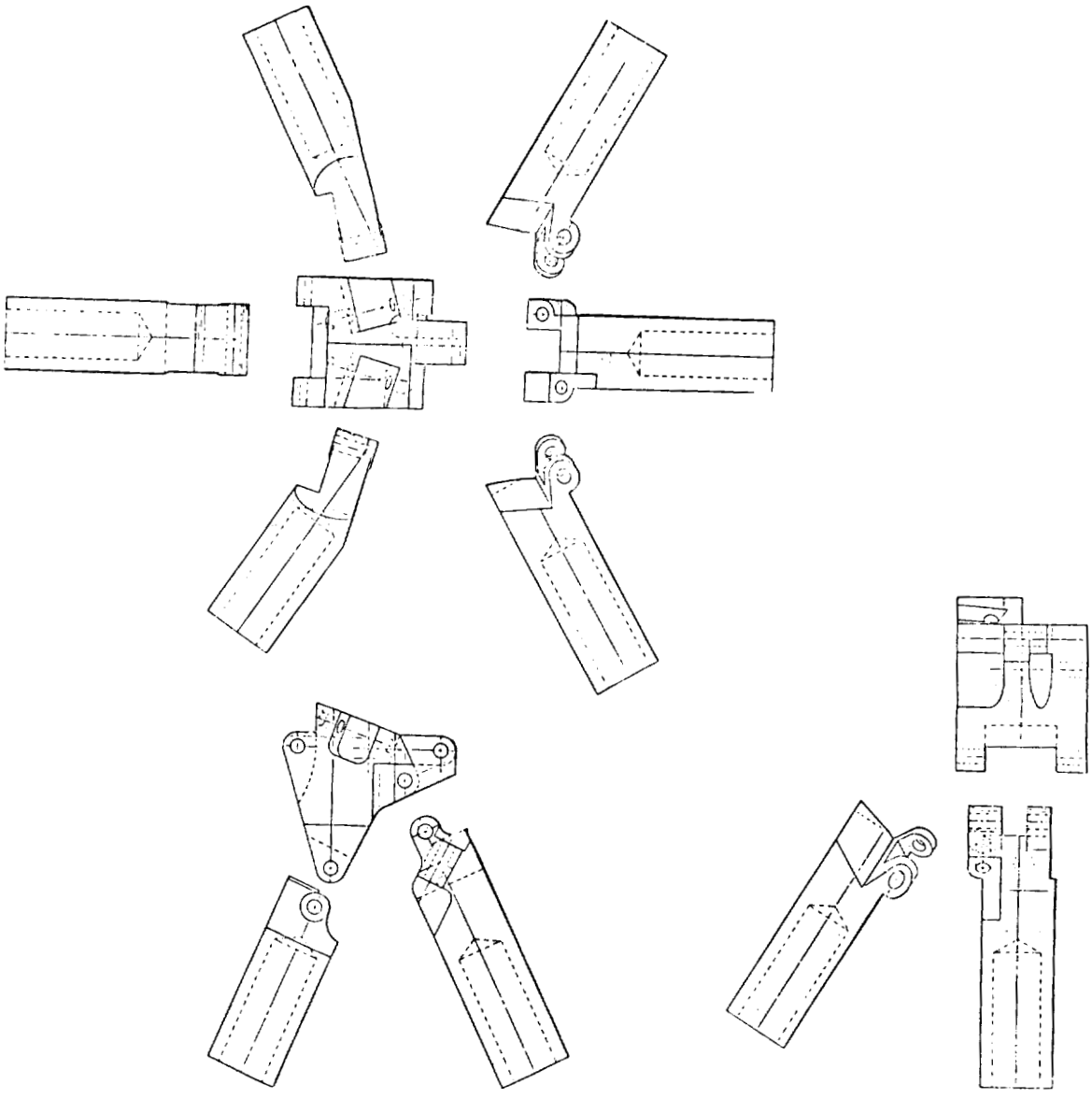

Figure 8

NINE-MEMBER CENTRAL JOINT

The first example of the nine-member central joint in hardware form is shown in the photographs here. The various stages of deployment of this joint are shown.

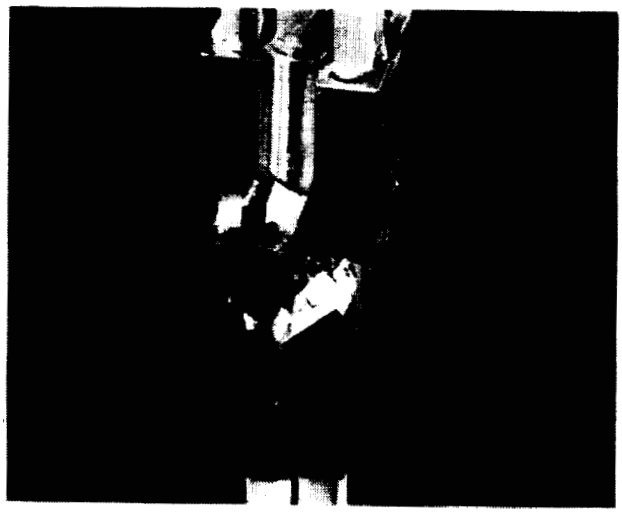

(a) STOWED

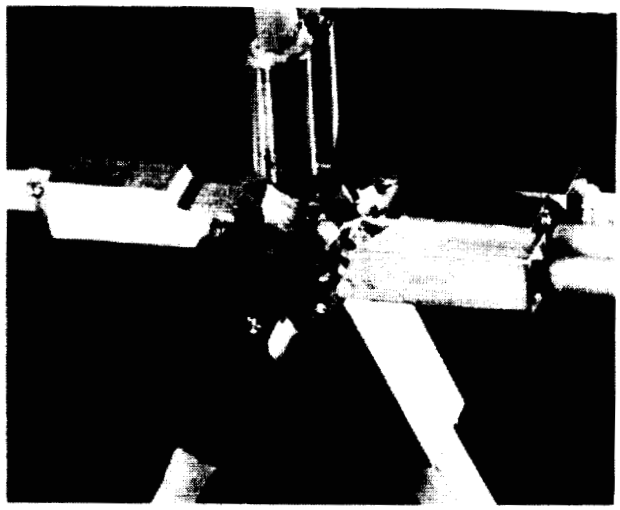

(b) FIRST-STAGE DEPLOYMENT

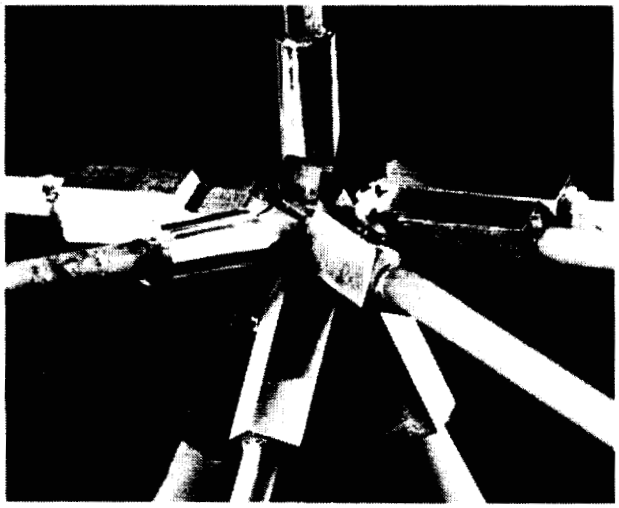

(c) ONE-SIDE SECOND-STAGE DEPLOYMENT

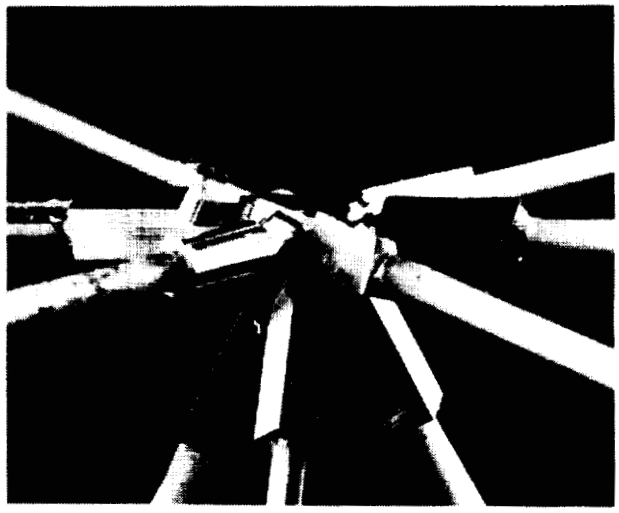

(d) FULLY DEPLOYED

Figure 9

MIDSTRUT HINGE

The midstrut hinge is a refinement of a design which has already been flight proven on the Seasat Synthetic Aperture Radar Extendible Support Structure. The main problem solved here was to squeeze the packaged hinge into a cross-sectional area no larger than the members to which it is attached.

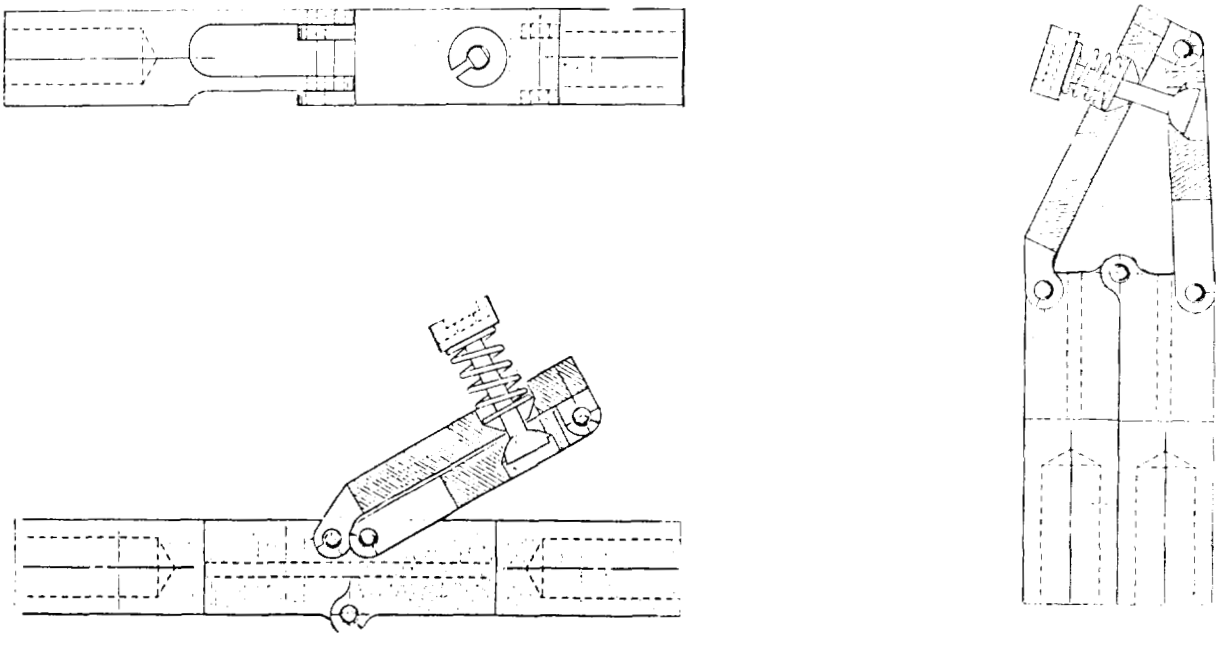

Figure 10

PACKAGING EFFICIENCY

Each of the nine-member joints package into a triangular cluster shown here. The ratio of deployed-to-stowed dimensions is determined by tightly packaging these clusters together. Note that for a circular deployed structure the package is smaller in the direction perpendicular to the rib than it is in the direction parallel to the rib. These packaging ratios are correct for flat truss surfaces. For doubly curved truss surfaces, there may be a necessary increase in package size caused by the requirement to adjust member lengths so as to achieve the designed geometry both deployed and packaged. The amount of increased package size has been studied for a spherical truss surface. Several different strategies of laying out the structure on the spherical surface have been studied, and one has been selected which minimizes the penalty in package size.

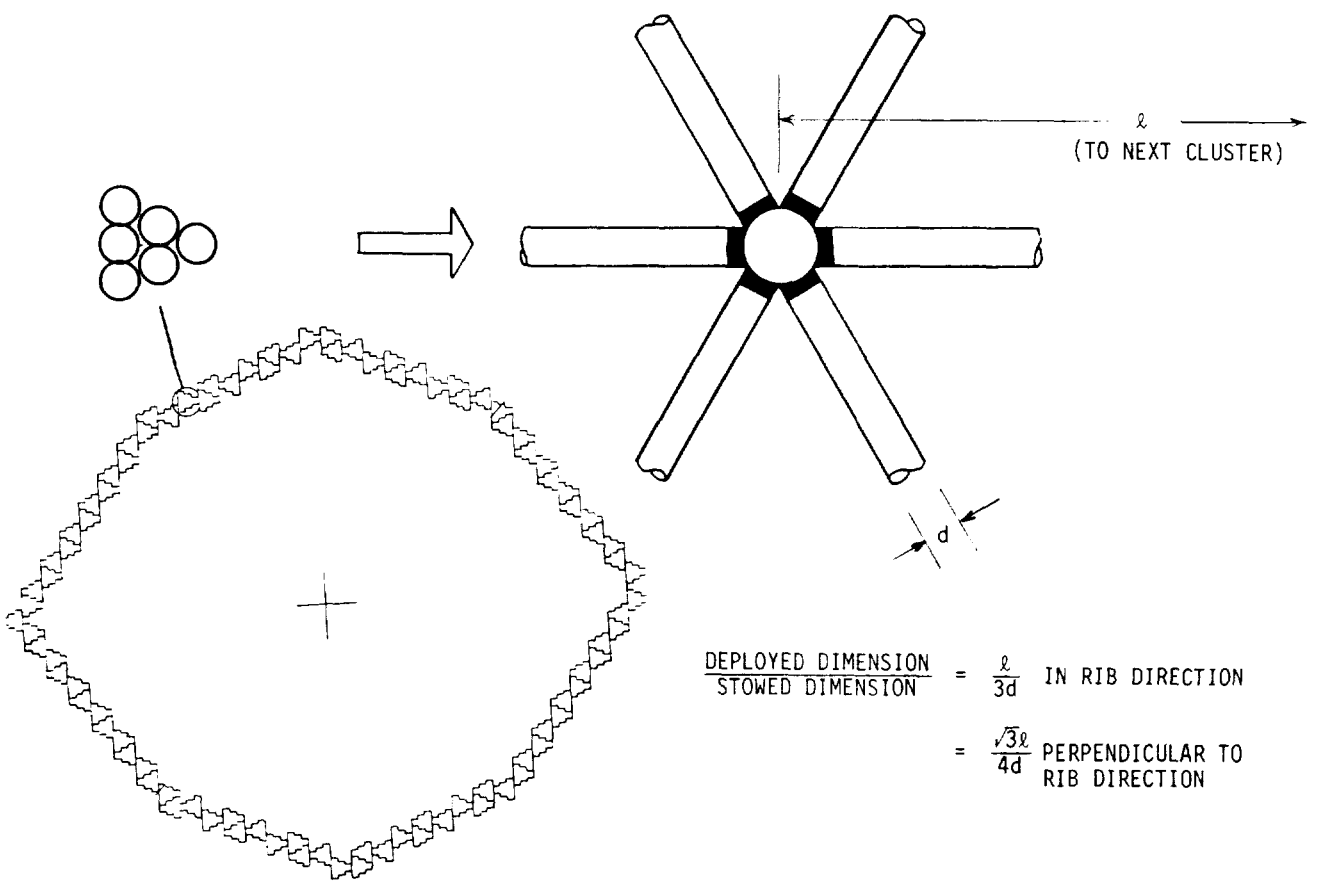

Figure 11

PACKAGED SIZE FOR SPHERICAL SURFACE

The package size along and perpendicular to the truss rib directions for a spherical surface are shown here. The package size is nondimensionalized with respect to the theoretical values in the truss rib direction for zero curvature. The abscissa is the ratio of focal length to diameter. The smaller the value of F/D, the more curved the surface is. With the particular strategy used, the increase in package size due to curvature along the truss rib is gradual and is caused by the fact that the size of the surface triangles tends to get smaller as the surface slope increases. In the cross-rib direction, the geometry dictates inequalities in the deployed and packaged lengths of the interrib core members. These length inequalities are adjusted by appropriately moving the hinge locations. As long as this relocation allows the hinge to stay within a member, no packaging penalty is incurred. However, for slender members at low enough F/D, the hinges must go outside of the member and therefore start dominating the package size. Thus, for a very slender member there may be significant penalty due to curvature. However, for a slenderness of say 100, very little penalty would be expected.

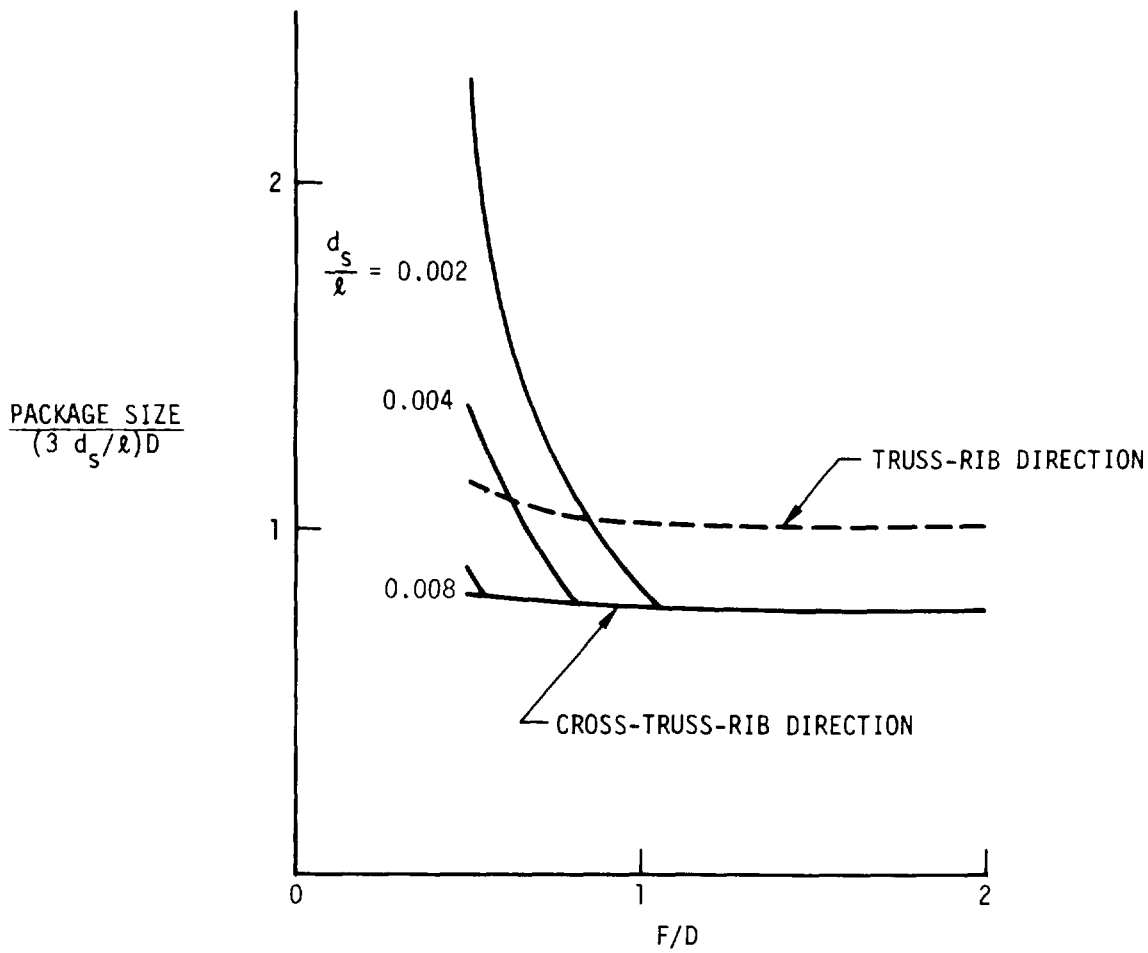

Figure 12

The accomplishments to date, the work planned next year, and what we recommend for the following year are shown here. It is the long-range intent of the effort to make the sequential deployable truss antenna available to potential users.

PROGRAM SCHEDULE

ACCOMPLISHMENTS	PLANNED 1982	RECOMMENDED 1983
SEQUENTIAL DEPLOYMENT CONCEPT, GENERALIZED EXAMPLES	CONSTRUCT MEDIUM-SCALE DEPLOYABLE MODEL (1-m STRUT LENGTH) FROM 1/2-INCH-DIAMETER GRAPHITE-COMPOSITE TUBING SUITABLE FOR TESTING	AUGMENT MEDIUM-SCALE MODEL TO INCLUDE TRUSS RIM AND MORE BAYS
GENERALIZED TETRAHEDRAL TRUSS TRIANGLE TO SQUARE	DETERMINE GEOMETRY FOR PARABOLOIDAL SURFACE	INTEGRATE SIMULATED MESH WITH MODEL
DESIGN FOR MESH FACETING ACCURACY	DETERMINE METHODS FOR INTEGRATING REFLECTOR MESH WITH STRUCTURE	DETAIL DESIGN AND FABRICATE OPERATING DEPLOYER AND INTEGRATE WITH AUGMENTED MEDIUM-SCALE MODEL
HINGE-GEOMETRY ANALYSIS	DESIGN HINGE GEOMETRY FOR TRUSS-RIM POINTS	BUILD A FULL-LENGTH DEPLOYABLE TRUSS SEGMENT WITH CURVED-SURFACE GEOMETRY
CONCEPT DEMONSTRATION MODEL	DESIGN DEPLOYER (PRELIMINARY)	PERFORM SUPPORTING ANALYSIS
PACKAGE SIZE AND WEIGHT ANALYSIS	BUILD DEPLOYER VISUALIZATION MODEL	
SHELL VIBRATION ANALYSIS	PERFORM SUPPORTING ANALYSIS	
HIGH-FIDELITY MODEL DESIGN AND CONSTRUCTION		
GEOMETRICAL DETERMINATION FOR SPHERICAL SURFACES		

Table 1

MOBILE WORK STATION CONCEPT FOR ASSEMBLY OF LARGE SPACE STRUCTURES (ZERO-GRAVITY SIMULATION TESTS)

Walter L. Heard, Jr., and Harold G. Bush
NASA, Langley Research Center

Richard E. Wallsom and J. Kermit Jensen
Kentron International, Inc.

Large Space Systems Technology--1981
Third Annual Technical Review
November 16-19, 1981

LARGE SPACE TRUSS STRUCTURE

Previous studies have identified truss structure such as illustrated in Fig. 1 as a prime candidate for low-mass, large-area spacecraft. Both deployable and erectable trusses have received considerable attention for this purpose, and both have their unique advantages and disadvantages. Deployable trusses which are intended to be preassembled on earth, packaged by folding for transportation to orbit in the Space Shuttle, and unfolded on-orbit can become structurally complex and are difficult to package efficiently. Erectable structures, on the other hand, which are intended to be assembled piece by piece on-orbit, are characterized by high packaging efficiency and relative structural simplicity. They, however, require development and demonstration of rapid on-orbit assembly methods employing quick-attachment joining techniques before advantage of such benefits can be realized. The Mobile Work Station concept presented herein is a Langley Research Center version that is intended to enhance astronaut assembly of truss structure that is either too large or complex to fold for efficient Shuttle delivery to orbit.

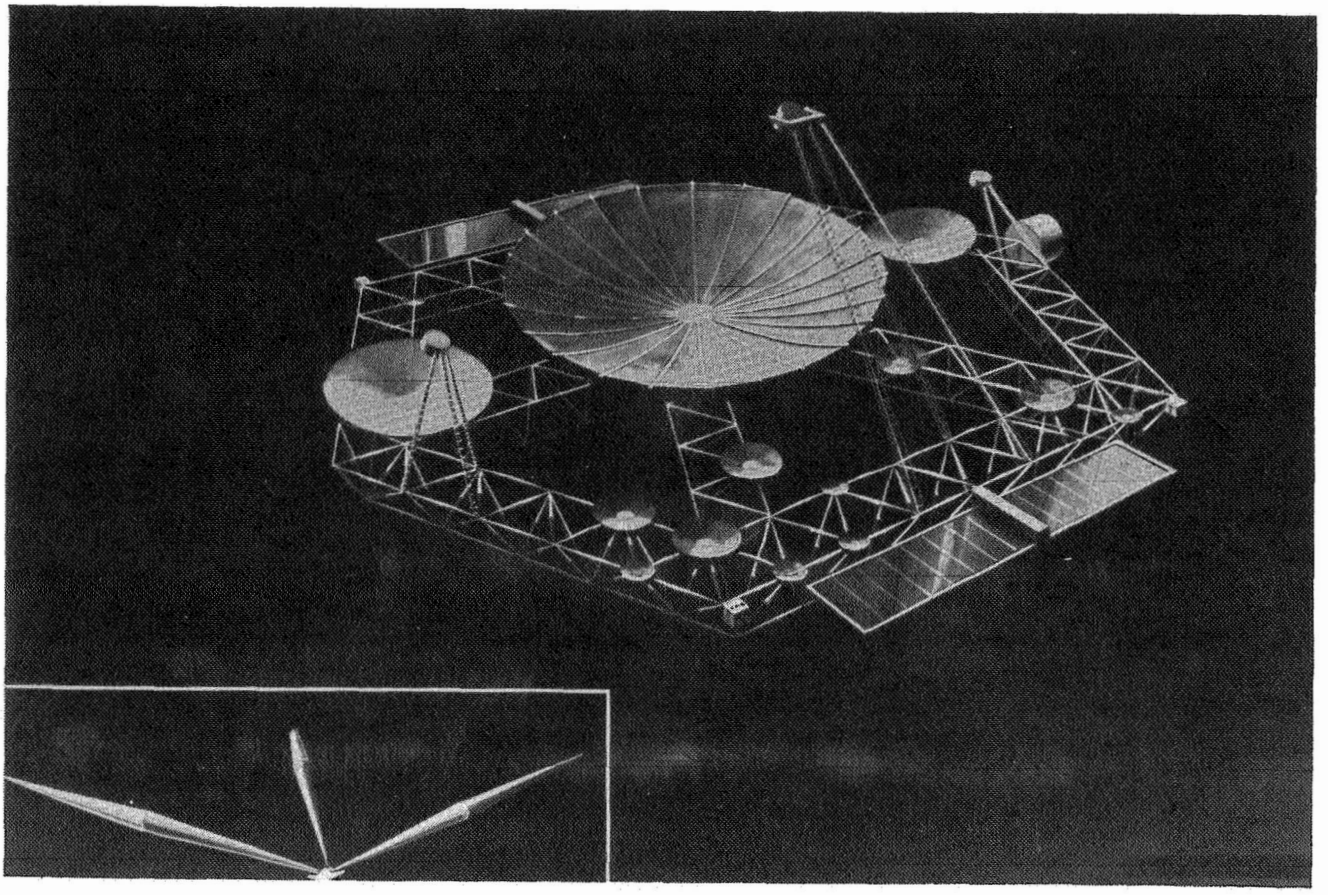

Figure 1

FEATURES OF ERECTABLE SPACE STRUCTURE

Two important features of erectable space structure (ref. 1) are presented in Fig. 2. The first is that minimum-mass erectable designs, based on stiffness requirements, are approximately equal in mass to deployable designs. Thus, mass-wise, there is no advantage of one concept over the other. However, it is also shown in reference 1 that erectable structures featuring nestable struts are superior to deployables from a packaging standpoint. This packaging advantage offers a potential economic payoff in terms of reduced Shuttle delivery flights provided efficient on-orbit methods of assembly for erectable structure are available.

- **MINIMUM-MASS DESIGNS EQUAL IN MASS TO DEPLOYABLES**
- **ERECTABLE STRUCTURES SUPERIOR TO DEPLOYABLES FOR PACKAGING**

Figure 2

MODEL OF MOBILE WORK STATION

Fig. 3 is a photograph of a model of the Mobile Work Station that was used to study the problem. The Mobile Work Station consists of four pairs of major components: (1) work platforms, (2) elevator towers, (3) conveyor rails, and (4) trolley beds. These components are shown attached to the Shuttle cargo bay and supporting a tetrahedral truss beam which represents a large space structure being assembled. The Mobile Work Station concept requires two pressure-suited astronauts to make the structural connections. Each astronaut works from one of the moveable platforms located on each side of the structure being assembled. The astronauts are secured by foot restraints in the work platforms at all times during the assembly and are moved within a prescribed plane as required. The platforms can move up and down on the towers, and the towers can move left and right on the trolley beds. This allows the astronauts to concentrate on assembling the structure without expending great amounts of energy manually moving themselves and material. Upon completion of periodic stages of assembly, the truss is conveyed along the conveyor rails away from the work area to make room for additional structure to be assembled. For all tests a beam-like truss similar to that shown in Fig. 3 was assembled using 5.4-m-long nestable struts. Although the Mobile Work Station is shown attached to the Shuttle, it could also be attached to a Space Operations Center or it could even be a free flyer. This concept is simply a space version of an assembly line. Construction tasks are repetitive; many, if not all struts can be identical, and quick-attachment joints eliminate the need for tools.

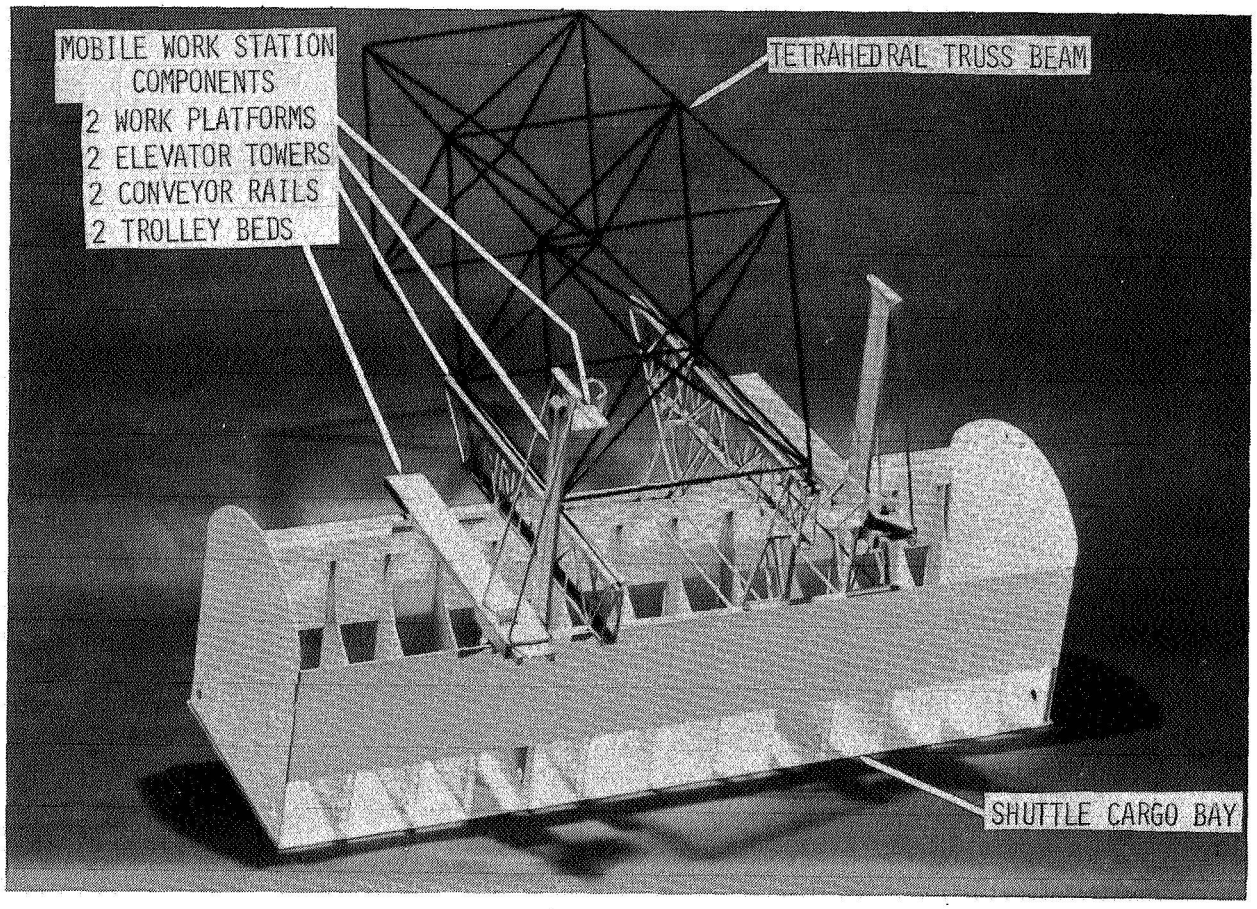

Figure 3

MOBILE WORK STATION

Fig. 4 is a photograph of the Mobile Work Station actual hardware. It weighs about 1360 kg. Much of this weight and volume of structure was required to support the two test subjects in an upright position while performing the 1-g assembly operations and to meet the requirements of underwater operation. A space version of the concept would have an entirely different configuration than the one shown in Fig. 4 because it would not have these restrictions and would be made lighter and less voluminous.

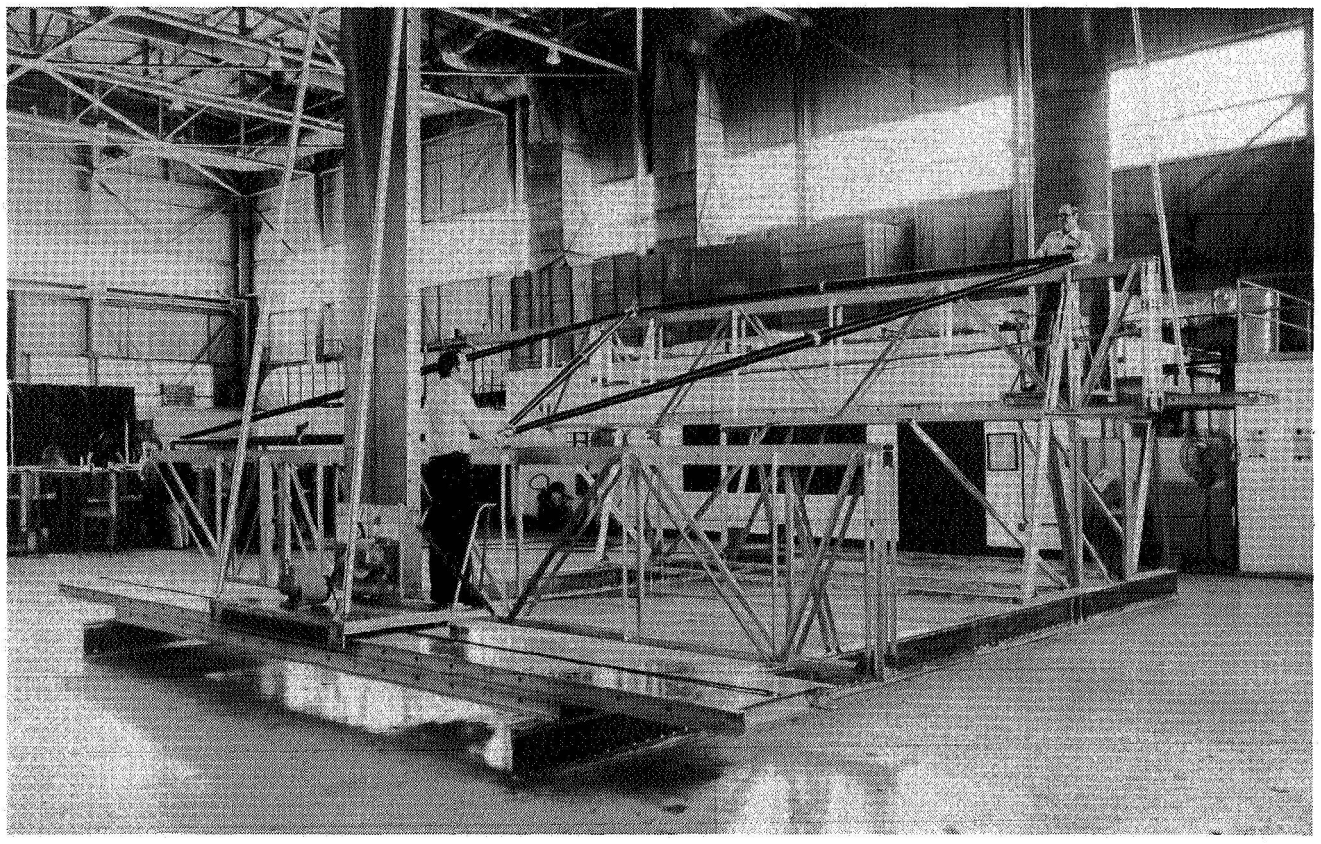

Figure 4

MOBILE WORK STATION 1-G ASSEMBLY TEST

Fig. 5 shows the Mobile Work Station 1-g assembly test in progress. The two test subjects are installing a transverse strut. The movement of the platforms as well as the conveyor is powered by air motors which are operated by a third subject at a console using "joy stick" controllers. The air motors and control console are not representative of flight hardware, but were used for economy reasons and to facilitate underwater operation in the neutral buoyancy tests. All of the hoses shown in the figure are air lines and would not be present in an actual flight version.

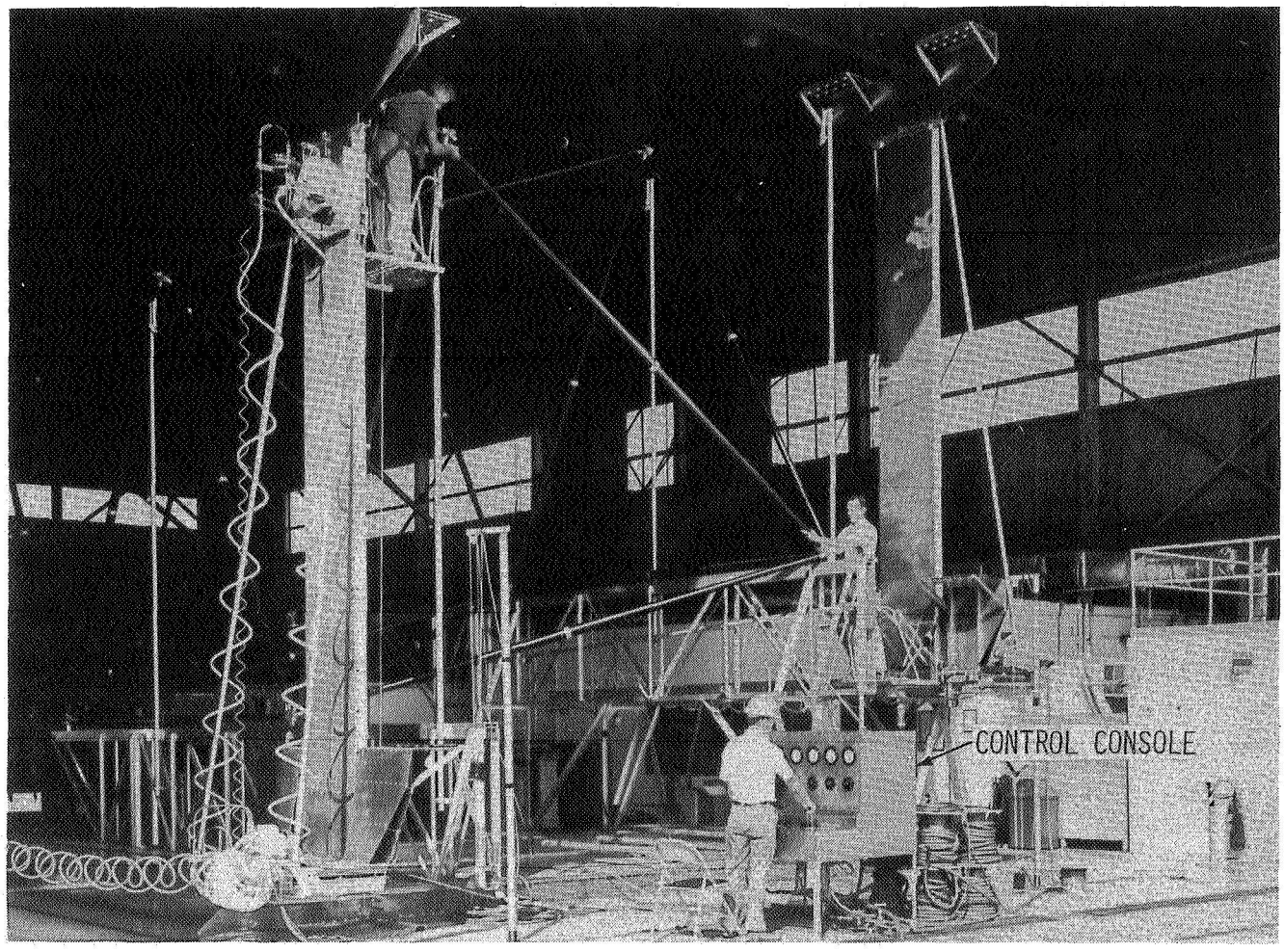

Figure 5

MOBILE WORK STATION O-G TEST SETUP

Fig. 6 shows the Mobile Work Station simulated O-g test setup in Marshall Space Flight Center's Neutral Buoyancy Facility. The struts were stored in racks on each side of the test subjects. Each subject had 19 struts within reach, all of of which were neutrally buoyant as were both test subjects.

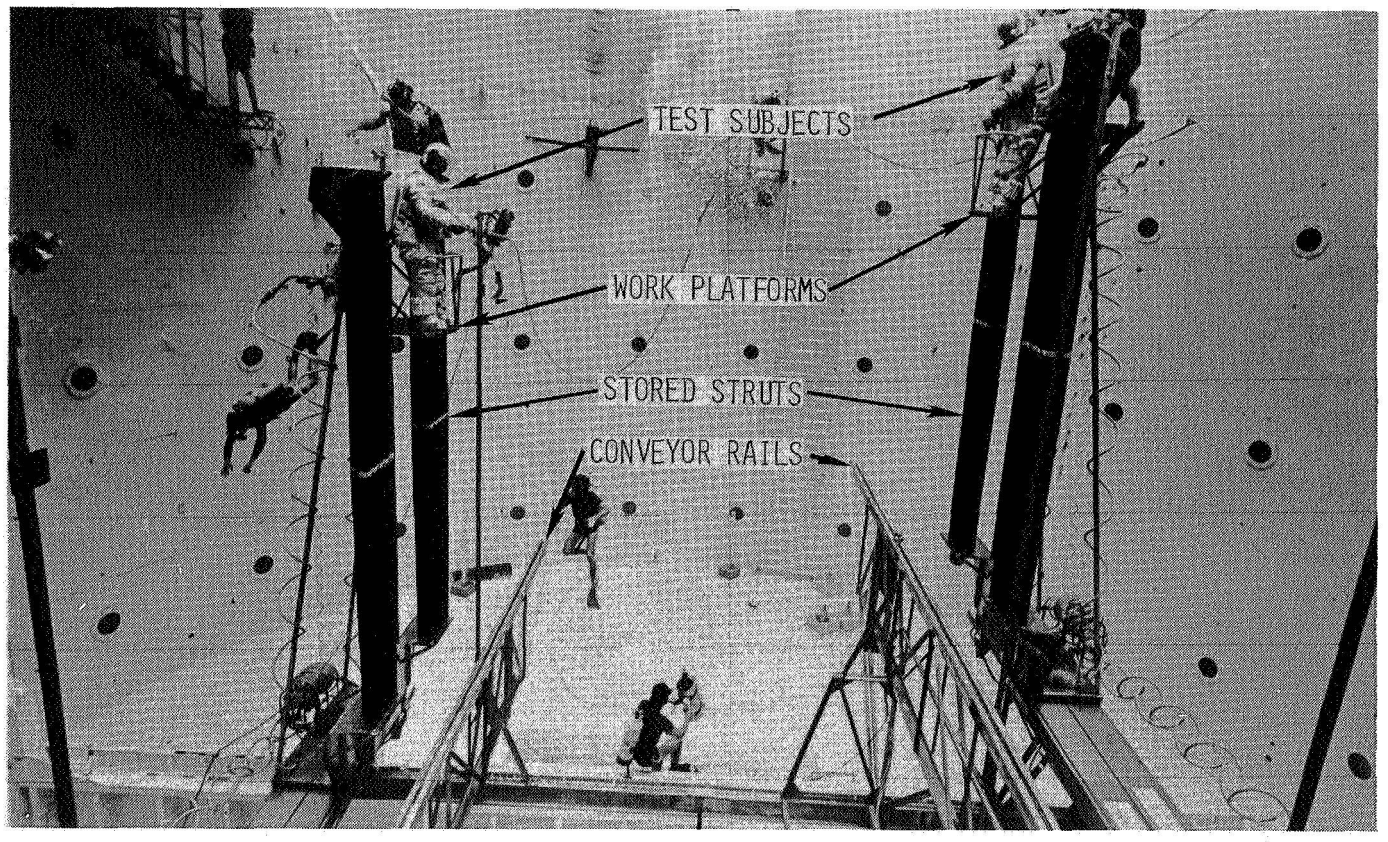

Figure 6

MOBILE WORK STATION O-G TEST SETUP

Fig. 6 shows the Mobile Work Station simulated O-g test setup in Marshall Space Flight Center's Neutral Buoyancy Facility. The struts were stored in racks on each side of the test subjects. Each subject had 19 struts within reach, all of of which were neutrally buoyant as were both test subjects.

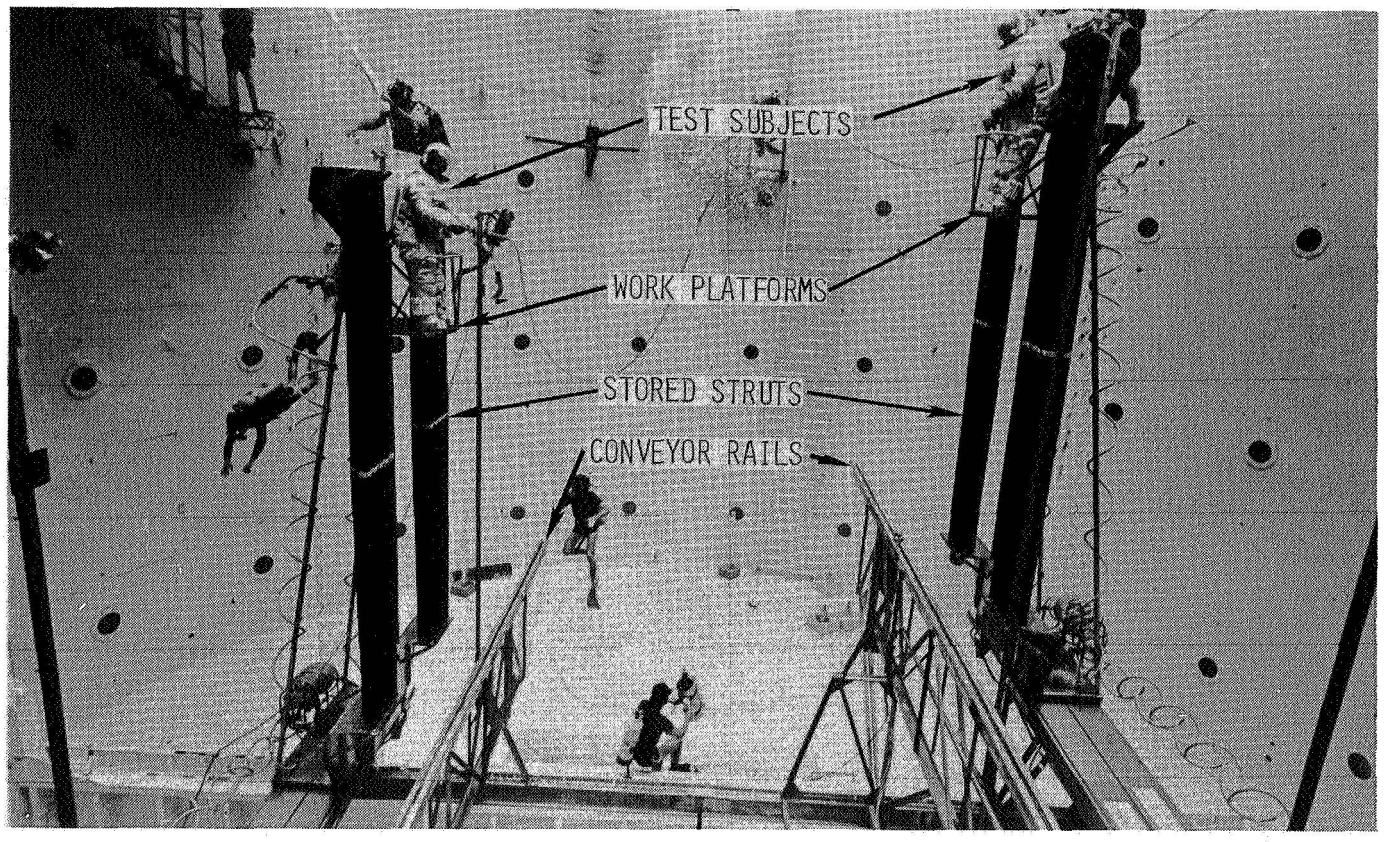

Figure 6

38-STRUT TRUSS ASSEMBLY IN MOBILE WORK STATION

Fig. 7 shows the truss completely assembled. The final structure was approximately 16.5 m in length and 4.5 m each side. It consisted of 38 struts. The assembly procedure was predetermined and was followed precisely through use of a third test subject located at a control console outside the tank. This third subject was in voice contact with the test subjects and controlled the location of the work platforms with the aid of video monitors. Only the struts spanning the truss width could be installed by both subjects simultaneously as shown in Fig. 7. The horizontal and diagonal struts on each side of the truss required installation by one test subject alone. This task was not difficult in the neutral buoyancy environment. Weightlessness allowed the test subject to connect only one end of the strut at a time, and since no climbing on the structure was required, the strut remained in place while the test subject was translated to connect the opposite end. Preset precision lengths of the interchangeable struts permitted this redundant structure to go together with relative ease.

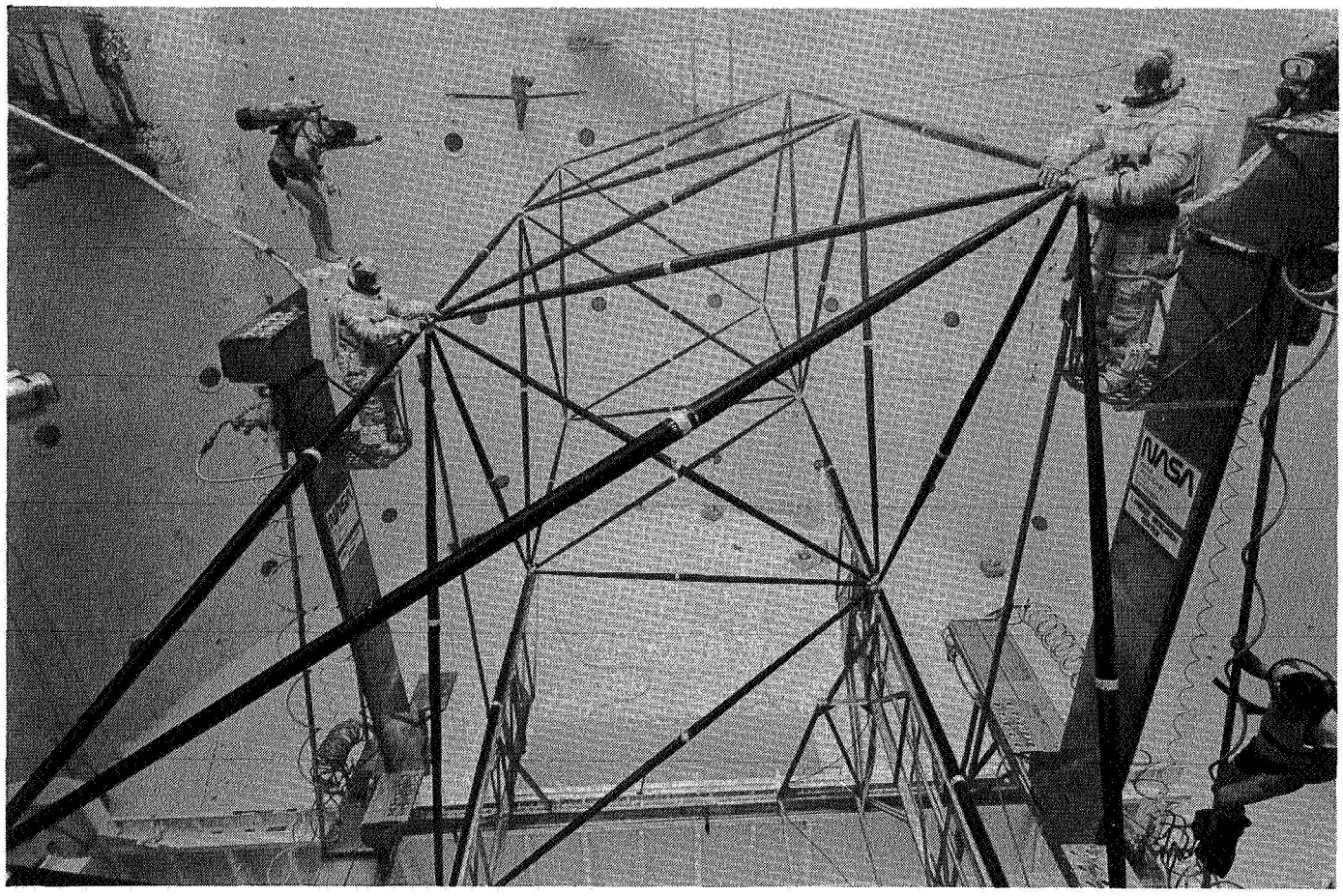

Figure 7

ASSEMBLY RATES

Assembly rates using the Mobile Work Station in three ground test environments are shown in Fig. 8. Also shown is a projected assembly rate that represents an estimate for space operation of the Mobile Work Station. The 1-g assembly in street clothes and air took an average of 24 seonds per strut. Maneuvering the struts in air is more realistic of space operation than in water based on drag effects; however, the test subjects were not impeded by pressure suits for these tests. The effects of gravity were of little consequence because the struts were so light--only about 1.6 kg apiece. The assembly performed in neutral buoyancy in SCUBA averaged 39 seconds per strut. Thus, water drag added about 15 seconds per strut to the assembly rate in air. Finally, the neutral buoyancy and pressure suit test yielded an average of 53 seconds per strut. Thus, the pressure suit encumberance added another 14 seconds per strut to the neutral buoyancy assembly rate obtained in SCUBA. An assembly rate for space operation can be approximated by either subtracting the 15 seconds per strut which is apparently the result of water drag from the 53 seconds per strut assembly rate, or by adding the 14 seconds per strut which is apparently the result of pressure-suit restrictions to the 24 seconds per strut assembly rate. In either case, the projected space assembly rate appears to be about 38 seconds per strut.

	TEST ENVIRONMENT	ASSEMBLY RATE SEC/STRUT
TEST	1-G, STREET CLOTHES, AIR	24
TEST	0-G, SCUBA, WATER	39
TEST	0-G, PRESSURE SUIT, WATER	53
PROJECTED	0-G, PRESSURE SUIT, SPACE	38

Figure 8

COMPARISON OF ON-ORBIT ASSEMBLY METHODS

A comparison of other on-orbit assembly methods with the Mobile Work Station data is given in Fig. 9. The on-orbit assembly time in days is plotted against assembly rate in struts per day for various size, hexagonal, tetrahedral truss platforms of maximum span D. Curves are plotted for D of 200, 400, 600, and 800 meters. Also shown by the dashed line is the present, five-day, on-orbit operational limit of the Space Shuttle. The shaded vertical bars represent assembly rates assuming 8-hour days for: (1) all manual, EVA assembly based on data obtained from neutral buoyancy assembly tests of a six strut tetrahedral truss structure (ref.2), (2) the Mobile Work Station data presented herein, and (3) automatic machine assembly rates derived from theoretical timelines assuming 24-hour-per-day operation (ref. 3). It is shown in Fig. 9 that the Mobile Work Station assembly rate is approximately a factor of five faster than manual assembly and approaches predictions for automatic assembly. It should be noted, however, that manual assembly requires manual translation which increases as the size of the structure increases. With the Mobile Work Station, astronaut translation requirements depend only on the length of the struts and not the size of the structure. Thus, long translation times are eliminated and extravehicular time is devoted primarily to structural assembly.

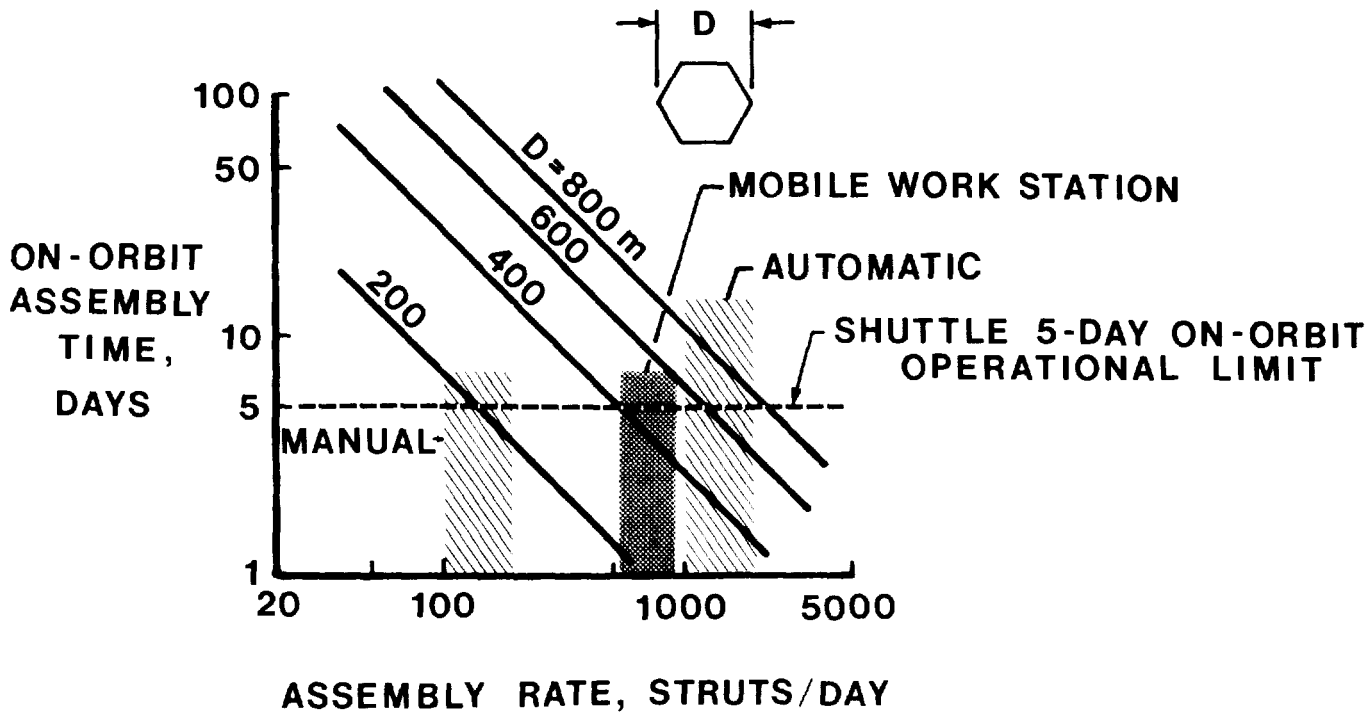

Figure 9

CONCLUDING REMARKS

The potential of augmented astronaut assembly can be illustrated by applying the result of this test program to a "barebones" assembly of the truss structure shown in Fig. 1. If this structure were assembled from the same nestable struts that were used in the Mobile Work Station assembly tests, the spacecraft would be 55 meters in diameter and consist of about 500 struts. The struts could be packaged in less than 1/2 % of the Shuttle cargo-bay volume and would take up approximately 3 % of the mass lift capability. They could be assembled in approximately four hours. Thus it appears that this rather simple but rapid on-orbit assembly concept for erectable structures is not only feasible, but could be used to significant economic advantage by permitting the superior packaging feature of erectable structures to be exploited and thereby reduce expensive Shuttle delivery flights.

REFERENCES

1. Heard, Walter L., Jr.; Bush, Harold G.; and Walz, Joseph E.: Structural Sizing Considerations for Large Space Structures. NASA CP-2168, Nov. 1980.

2. Bement, Laurence J.; Bush, Harold G.; Heard, Walter L., Jr.; and Stokes, Jack W., Jr.: EVA Assembly of a Large Space Structure Element. NASA TP-1872, June 1981.

3. Vernon, R. M.: Automated Installation of Large Platform Utilities. NASA CP-2168, Nov. 1980.

ORBITER BASED CONSTRUCTION EQUIPMENT

C. J. Goodwin
Grumman Aerospace Corporation
Bethpage, New York

Large Space Systems Technology - 1981
Third Annual Technical Review
November 16-19, 1981

HANDLING AND POSITIONING AID IN USE

Many orbiter based activities need equipment to hold a payload steady while it is being worked on. This work may be construction, updating, repair, services, check-out, or refurling operations in preparation for return to Earth. The Handling and Positioning Aid (HPA) shown here is intended for use as general purpose equipment. It is initially conceived as being simple to operate, relatively stiff, and having the capability of holding the items to be worked on clear of the cargo bay, within the view field of the aft flight deck and within the envelope of the RMS. The basic HPA has a turntable at its tip, which can rotate the work-piece for easy access. It can support an EVA work platform with a large envelope - adjustable both for position along the HPA and for distance from it. The HPA base, which spans the cargo bay from longeron to keel to longeron, which spans ness and strength to support the shoulder. It can be ground adjusted to many stations along the length of the orbiter cargo bay.

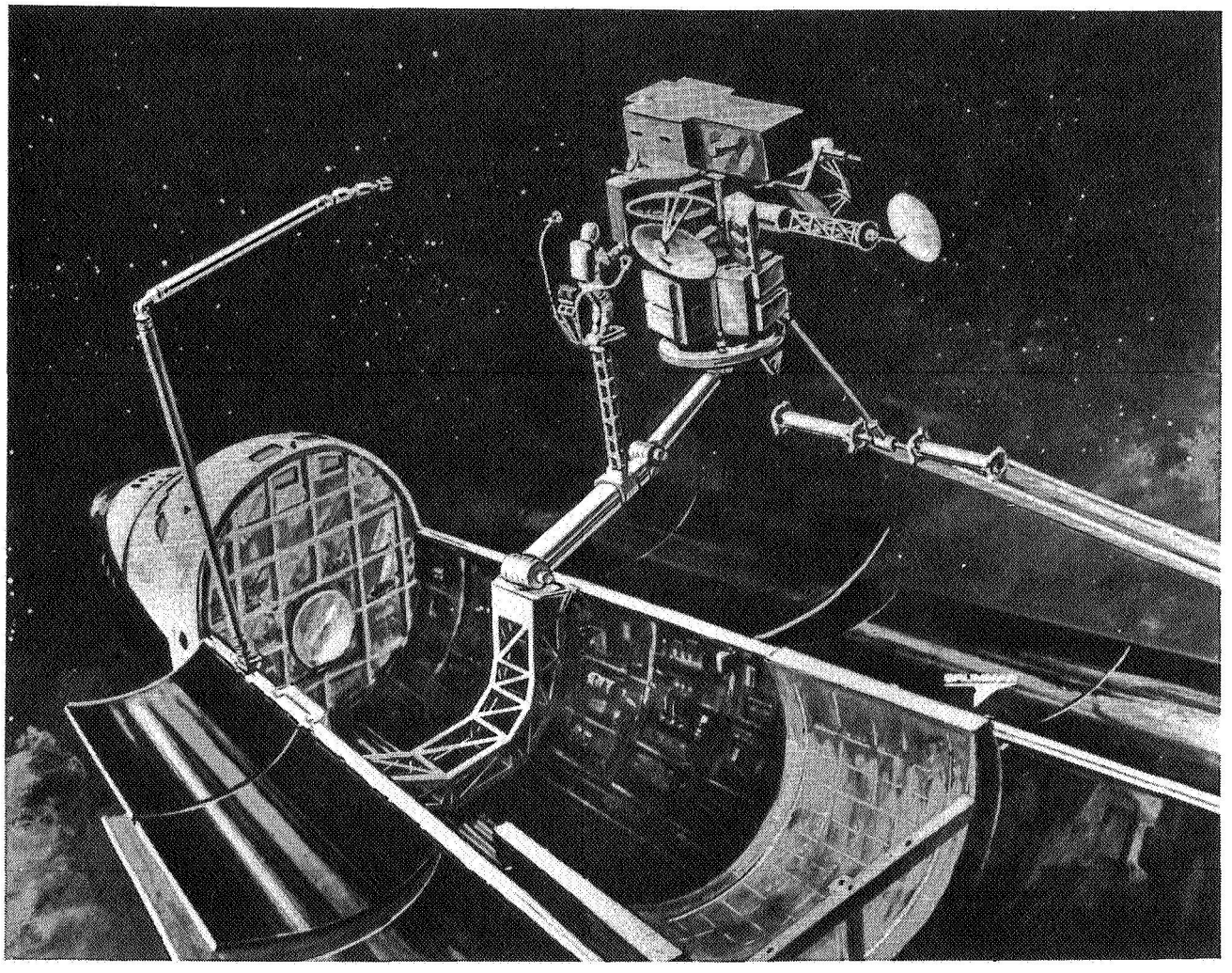

HPA REQUIREMENTS SUMMARY - TWO CATEGORIES

From an analysis of ten reference missions, we have determined that two types of HPA mobility are needed: a tilt table, which simply swings out of the cargo bay, pivoting about an athwartships "y" axis, and an articulated arm with the general features of the previous illustration. These two types of HPA differ in their reach, degrees of freedom, location within the bay, stiffness requirements, and the amount of cargo they might be called upon to support during shuttle ascent and descent.

This paper will discuss some of the more detailed requirements, particularly as they apply to the articulated arm version.

MOBILITY	TILT TABLE	ARTICULATED ARM
• REACH DOF ANGULAR RANGE	NA 1 OR 2 90 TO ±180°	4.5 – 5.5 m 3 TO 5 130 TO ±180°
• LOCATION VARIES	MID TO AFT BAY	FORWARD TO MID BAY
• ARM STIFFNESS	1.8×10^6 Nm/RAD	@1.15×10^7 N.m^2 EFFECTIVE EI
• CARGO SUPPORT	2000/4000 kg	0 TO 10 000 kg
• BERTHING DEVICE	SINGLE STANDARD?	SOME STANDARDIZATION BUT NOT COMPLETE
• SPACECRAFT INTERFACES – POWER – DATA	AUTOMATIC CONNECT & DISCONNECT. REQUIRED.	
– FLUID	NA	MANUAL CONNECT & DISCONNECT. FEASIBLE
• WORK ZONE PREFERENCE	• WITHIN THE VIEW PYRAMIDS • INSIDE THE 80% RMS RADIUS	

HPA MODULAR CONCEPT

The full HPA concept has tilt table versions and an articulated arm version. Each mounts various end effectors to suit the different missions. To simplify change of configuration on the ground and to minimize costs, a modular approach is used.

A base frame mounts the HPA to the orbiter and supports the active parts of the system. For inboard operations, movement of the berthing fixture from stowed to operational position is achieved by mounting a tilt table to the base frame. In one version, the table is a ring supported off the base frame by auxiliary struts. The berthing capability is, in fact, incorporated in this ring and is positioned for operations when the table/ring is tilted from its stowed position. An alternative version of the tilt table has a fulcrum spanning the base frame. The center of the fulcrum mounts a berthing spider which goes from stowed to operational position by rotating the fulcrum. Either tilt table version can be mounted to the base frame.

For an outboard HPA, a two piece articulating arm is mounted to the same base frame. Although commonality of arm piece length is an objective, each can be varied at ground assembly if a particular mission demands it. The tip of the outboard arm piece accommodates the berthing fixture required for the mission.

The base frame may, on occasion, be used without either tilt table or articulated arm, as a cargo support - spanning around the lower part of the cargo bay. In this way, modular components can be ground assembled to provide the various HPA configurations.

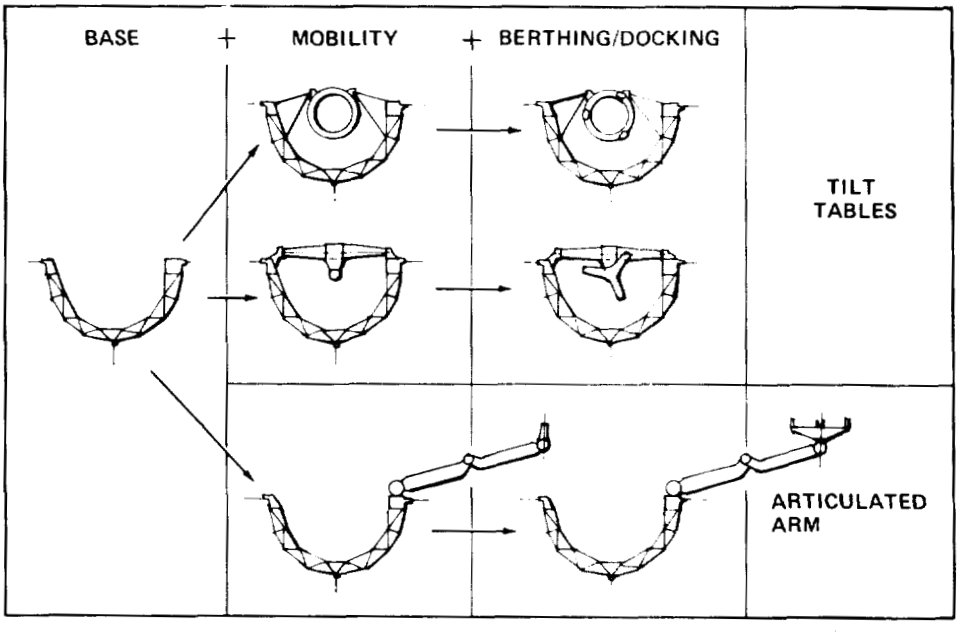

CONTROL COMPLEXITY - ARTICULATED ARM

Routine operation of the articulated arm comprises, typically, unstowing the arm, positioning the tip in a predetermined position, rotating the tip, moving to some other position, etc., and finally, restowing the arm. After each movement, there is usually one fairly long period - (hours, a whole shift) - while work is performed on the payload and the arm remains still. The five degrees of freedom afford access to anywhere in a 5.5 m radius hemisphere. The one-joint-at-a time control mode allows the control system to be kept simple. Even though the control speed is slow, the basic arm movements do not consume many minutes each. To keep arm checkout simple, sufficient power is supplied to allow for ground operations.

The HPA may be required to play an active role in payload berthing. Present analysis shows that the five degrees of freedom will be adequate for this function, if three of the joints can be coupled in the lunge mode (see sketch). This coordinated linear movement does not require any significant increase in control complexity.

ROUTINE OPERATIONS

- **5 DEGREES OF FREEDOM ~ SHOULDER 2, ELBOW 1, WRIST 2**
- **CONTROL FROM AFT FLIGHT DECK ~ ONE JOINT AT A TIME**
- **CONTROL RATES ~ 1 DEG PER SECOND, MAX ~ 1/3 DEG PER SECOND MIN**
- **POWER FOR GROUND CHECK-OUT WITHOUT SPECIAL EQUIPMENT**

ADDITIONAL CAPABILITY FOR ACTIVE BERTHING ROLE

- **THE LUNGE MODE SIMULTANEOUS OPERATION OF SHOULDER & WRIST AT ONE SPEED & ELBOW AT TWICE THAT SPEED PROVIDES LINEAR MOTIONS**

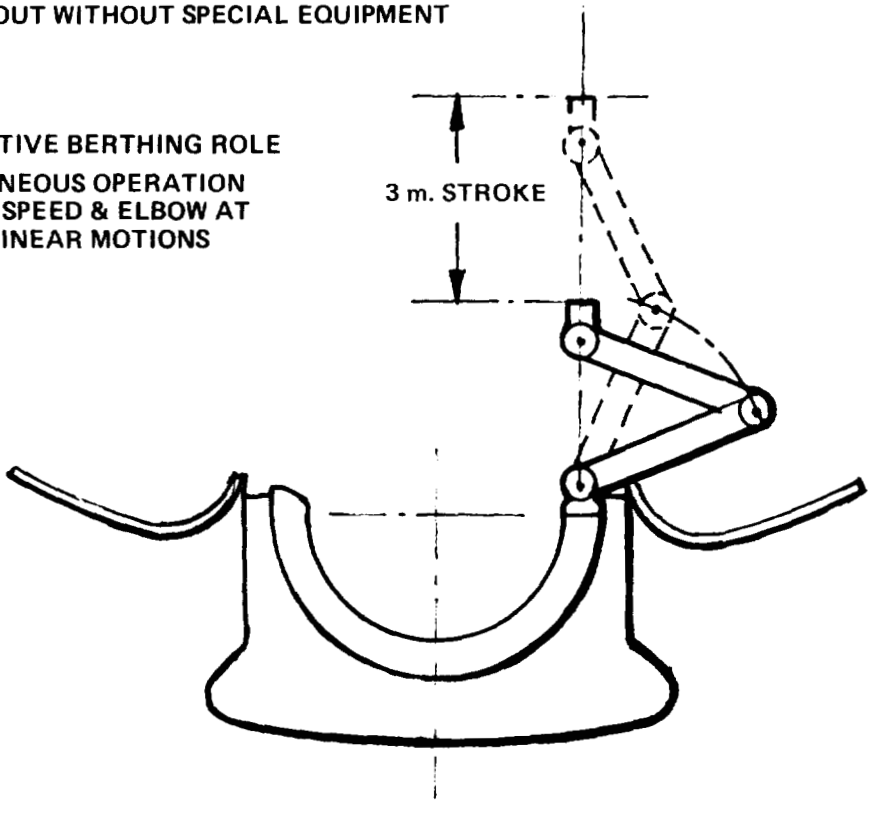

THE EFFECT OF HPA ARM STIFFNESS ON COUPLED BODY FREQUENCY - SPACECRAFT WEIGHT & SIZE VARIED PARAMETRICALLY

This chart provides some insight into the fundamental frequency of a sizeable payload and an Orbiter coupled together by a medium length arm mounted 12 m (40 ft.) from the Orbiter cg, as shown on the upper right.

Before considering the parametric variables, various frequency boundaries should be noted. The Orbiter Prime Reaction Control Subsystem (PRCS) provides "easy" control down to a frequency of 2 cycles per second; by software modifications, control authority could be extended down to about 0.3 cps. The Vernier Reaction Control Subsystem (VRCS) can currently control down to 0.1 cps and again, by modification, its capability could be extended down to 0.02 cps.

Besides spacecraft weight - the horizontal ordinate - there are two parameters treated in the plot: (1) Effective arm stiffness, with a lower value of EI = 1.2×10^7 N-m^2 (4×10^9 lb-in^2) and a higher value four times as high. The lower value results in a relatively modest structural weight - the higher value borders on the unacceptable. (2) Spacecraft size; expressed in terms of h, the offset between the arm pick-up and the spacecraft cg and r, the spacecraft radius of gyration. These quantities are to some extent interchangeable. Three sets of h and r values have been chosen typical of a small satellite, a medium sized space structure, and a large space platform. The arm length of 5.6 m (18.3 ft) is chosen to suit a spectrum of representative payloads.

The three frequency bands reflecting these spacecraft sizes and arm stiffness values cut across the RCS boundaries as a function of spacecraft weight. Upon study of this plot we have selected the lesser effective arm stiffness for the following reasons.

- It is lighter
- The VRCS is likely to be the system of choice during service and construction activities, which will permit handling a structure of about 50,000 kg without RCS modification.
- Any large space platform to which the Orbiter is attached may have a CMG/Inertia Wheel control which would make the use of the VRCS moot.

As a point of interest, the performance of the RMS supporting a small satellite is shown in the lower left corner of the plot.

THE EFFECT OF HPA ARM STIFFNESS ON COUPLED BODY FREQUENCY – SPACECRAFT WEIGHT & SIZE VARIED PARAMETRICALLY

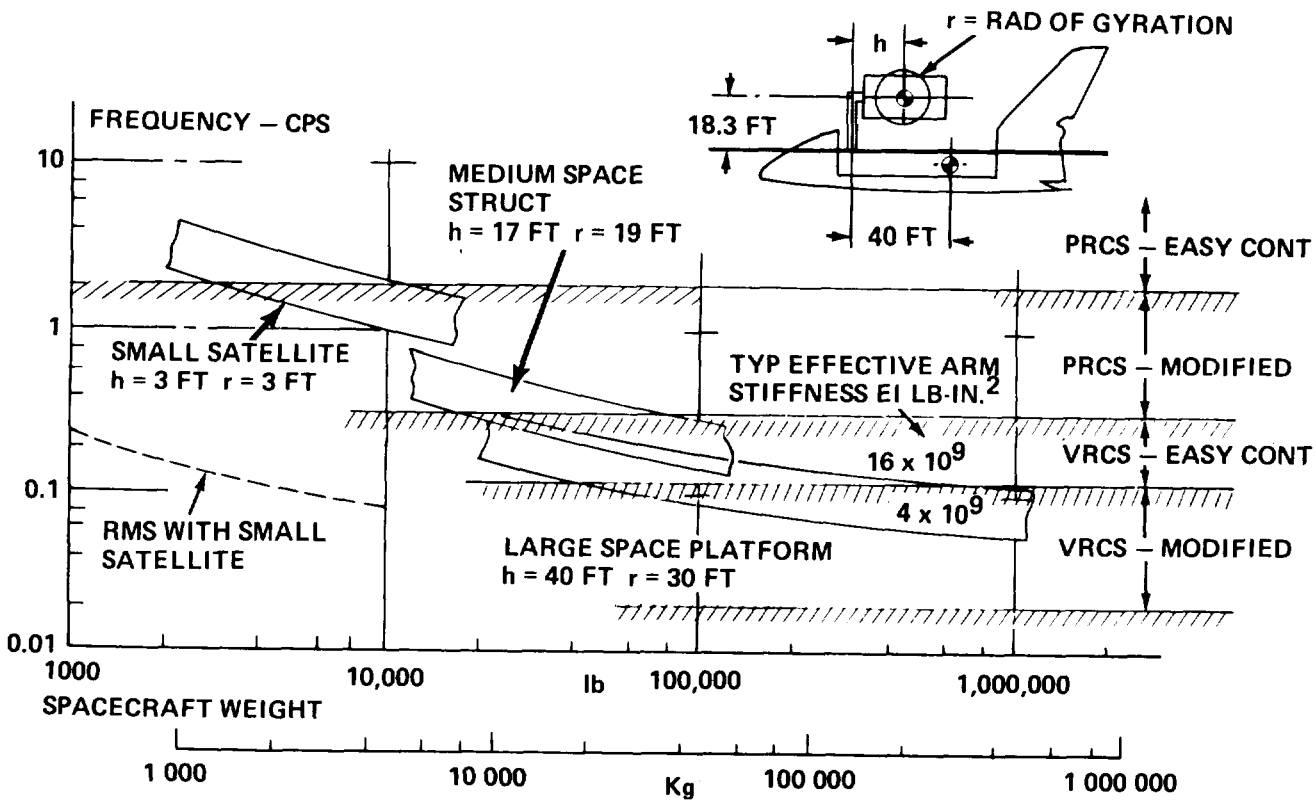

PRELIMINARY OPTIMIZATION OF ARTICULATED ARM FOR STIFFNESS WITH MINIMUM WEIGHT

This chart shows an arm designed to produce an effective stiffness between its shoulder joint and tip (inclusive) of 1.2 x 10^7 N-m^2 (4 x 10^9 lb-$in.^2$) EI.

As shown by the plot of stiffness distribution, the shoulder and elbow gears are the weak links in providing high stiffness. The gear boxes are very heavy for the stiffness they provide. They represent only 6% of the total structural length, but account for 40% of the weight.

The table at the top left hand corner of the chart shows the contribution of each element to the tip deflection.

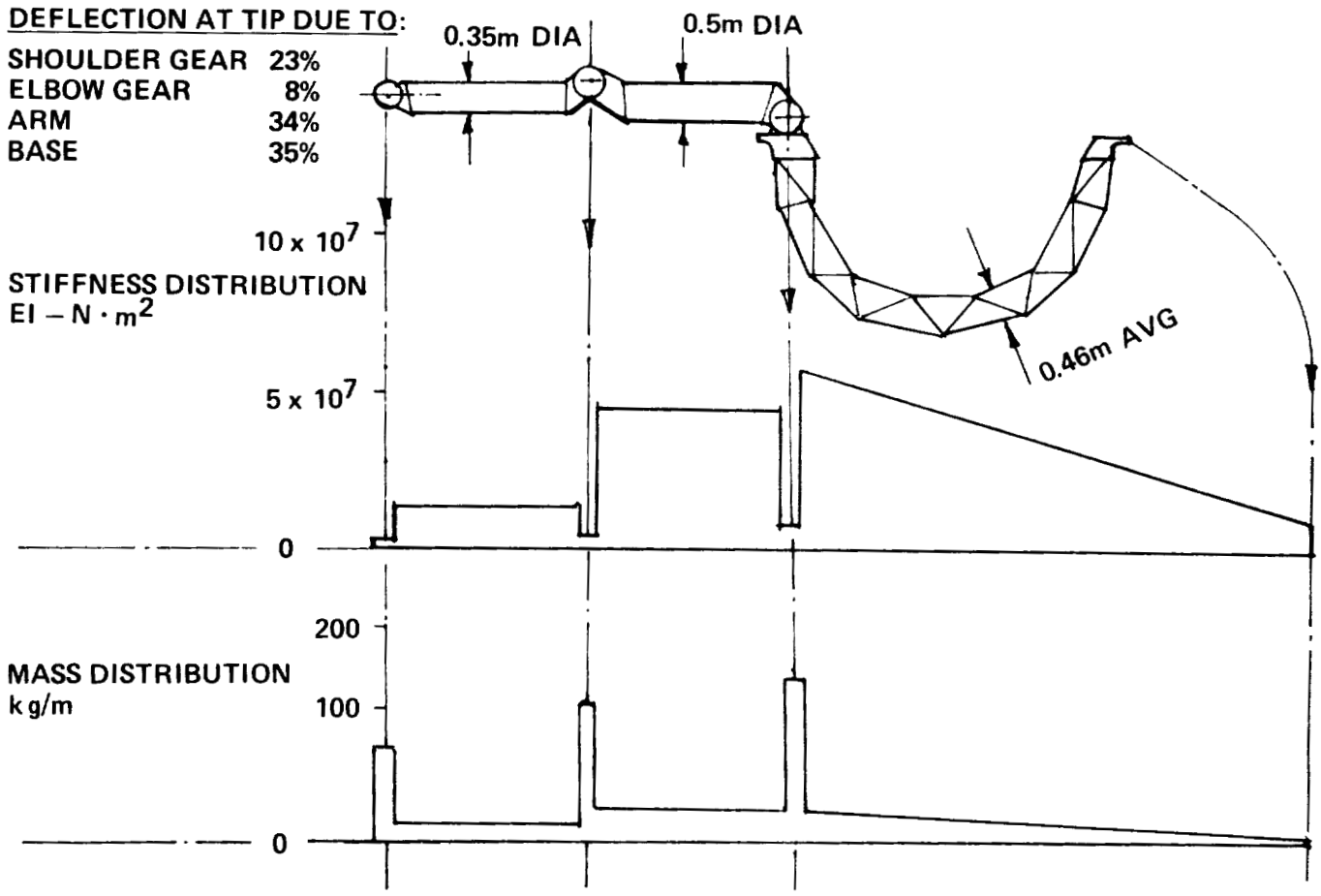

BERTHING AND DOCKING FIXTURES - FIRST APPRAISAL

The chart illustrates three berthing fixtures that could be used with a tilt table and four berthing/docking fixtures to be used with an articulated arm. Also shown is our first appraisal of which reference mission will use which fixture.

Considering first the five tilt table users, four are initially listed as employing the open center version, which is borrowed from the MMS/FSS hardware. The fifth, the Geostationary Platform, requires a tilt table with latches spaced to pick up on an Orbit Transfer Vehicle of nearly 4.6 m (15-ft.) diameter. This is mission dedicated equipment and does not suit any other reference mission.

Three missions employing an articulated arm use a center bearing spider fixture, possibly having more than one size. The SOC mission is shown twice. In one case the reference mission is assumed to involve docking, and, in another case, berthing. In both cases the fixture includes a center hole for the passage of shirtsleeved astronauts. It should be noted that the SOC (berthing) mission fixture will quite possibly be mounted not on an HPA but on the so-called Orbiter Docking Tunnel. In this event it should not, properly speaking, appear on this chart.

In endeavoring to reduce the number of fixtures it was noted that the four tilt table missions initially shown as using the open-center turntable do not make significant use of the hole in the middle. They could therefore interface with a spider turntable of the same latch pitch circle diameter (1.8m). Further examination of the Large Space Structure (LSS) mission shows that its interface device can also be adjusted to use the 1.8-m diameter size spider.

Seven of the nine reference missions shown would then use an essentially common spider structure, some in a tilt table version, some on an articulated arm.

The two logical exceptions to this standardization initiative are the large diameter interface for an OTV and the "hole-in-the center" astronaut interface for the SOC whether berthing or docking.

BERTHING AND DOCKING FIXTURES — STANDARDIZATION?

	BERTHING			DOCKING
	OPEN CENTER	SPIDER	SPIDER	OPEN CENTER
TILT TABLE • LATCH PITCH CIRCLE DIA • REP MISSIONS	 1.8 m ST →● UARS →● INTELSAT →● OAO →●	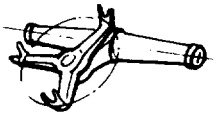 1 – 1.8 m	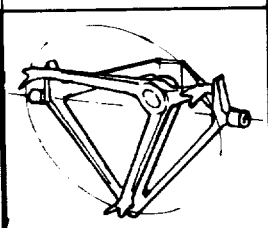 4.2 m GEO PLATFORM (MISSION PECULIAR OTV INTERFACE)	
ARTICULATED ARM • LATCH PITCH CIRCLE DIA • REP MISSIONS	 1.3 m SOC BERTH (MAY ATTACH TO DOCKING TUNNEL NOT. HPA)	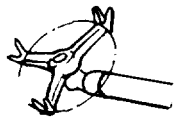 1 – 1.8 m • ORB SERV RTFM • 25 kw PWR MOD •	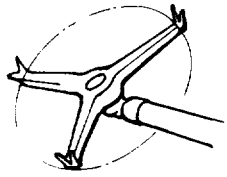 3.3 m LSSD	 1.5 m SOC (DOCK)

SUPPORT EQUIPMENT

Items of support equipment identified during analysis of the reference missions are listed. Certain items are shown to be required repeatedly, even in this limited sample of future missions. The items indicated in the final column will have measureable impact on the use of the cargo bay volume; therefore, stowage provisions and locations should be selected carefully. It may be possible to provide stowage for many of the commonly used pieces of equipment within the framework of the HPA base structure.

	REFERENCE PAYLOADS										
EQUIPMENT	GEO PLATFORM	DEPLOY PLATFORM	LSSD	SOC	ST	UARS	INACT OAO	INTELSAT	25 kw PM	PEP	CARGO BAY STOWAGE IMPACT
HPA	√	√	√	√	√	√	√	√	√	√	•
RMS	√	√	√	√	√	√	√	√	√	√	
UMBILICAL – FLUID									√		
– DATA			√		√				√	√	
– POWER			√		√				√	√	
BERTHING/DOCKING DEVICE	√		√	√		√	√		√	√	•
SPECIAL TOOLS	√	√	√	√		√	√		√	√	
PROXIMITY OPS MODULE		√					√				•
CARGO BAY STORAGE		√	√		√	√	√				•
SPECIAL END EFFECTOR			√	√			√				
OCP/MFR		√	√			√			√		•
MODULE REPLACEMENT AIDS					√					√	
STARBOARD RMS			√								
WORK PLATFORM		√	√		√	√	√				

STANDARDIZATION & INTEGRATED STOWAGE

OVERALL PROGRAM STATUS

To place the HPA in its proper time context, the overall program and its status are shown.

There are two types of hardware: the flight article and a ground development test article. In phase 1, which is just drawing to a close, an initial look at flight article concepts has been followed by design of the ground test article. Phase 2 will see this test article manufactured, after which simulation at Bethpage and at NASA JSC will commence.

If all goes according to plan, flight article activity will resume when simulation results start to accumulate.

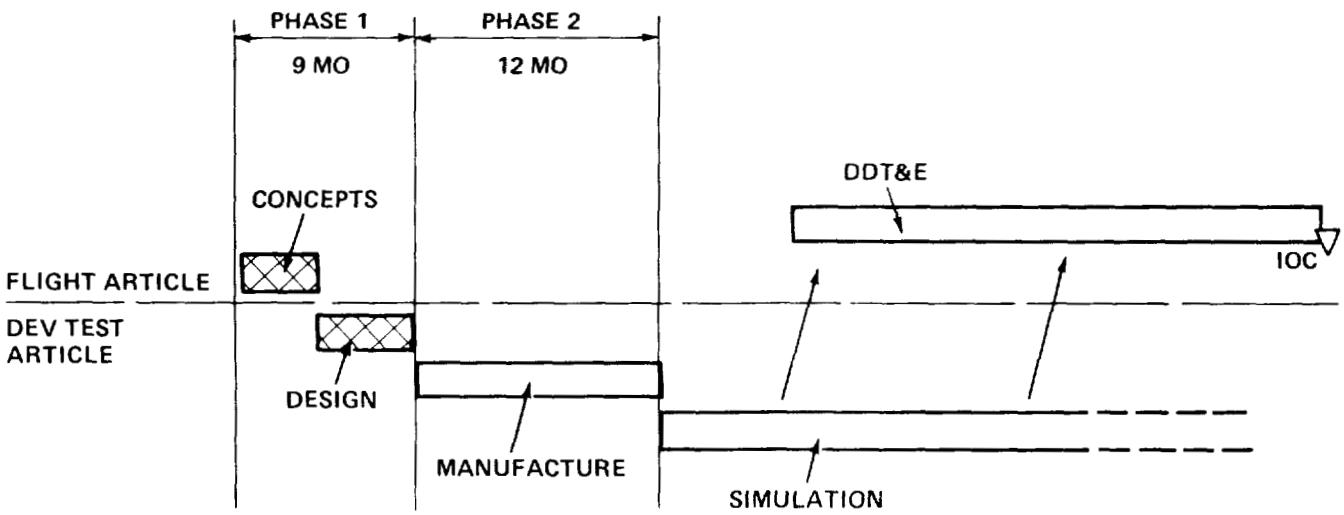

PHASE 1 OBJECTIVES:

FOR ORBITER BASED CONSTRUCTION & SERVICE SUPPORT EQUIPMENT:

- **DEFINE TECHNOLOGY ADVANCEMENTS NEEDED**
- **DEVELOP HANDLING & POSITIONING AID CONCEPTS**
- **PREPARE PRELIMINARY DESIGN OF DEVELOPMENT TEST ARTICLE**

PHASE 2 OBJECTIVE:

- **BUILD DEV TEST ARTICLE ON TIME AND WITHIN BUDGET**

HPA CHARACTERISTICS

In summary, the HPA provides a wide choice of work station positions, both immediately above the orbiter cargo bay and beyond. It can act in a primary docking role and, if required, can assist actively in the berthing process.

The HPA is intended to be stiff; it can, therefore, be robust. In addition, its control philosophy is simple. For these reasons we believe it can be made inherently reliable.

Finally, it is modular to provide several configurations to serve many missions.

ACTIVITIES

- **WORK STATION**
  - **INBOARD**
  - **OUTBOARD**
- **ASSIST WITH BERTHING?**
- **PRIMARY DOCKING DEVICE**

FEATURES

- **STIFF/ROBUST**
- **SIMPLE**
- **RELIABLE**
- **MODULAR**

DEPLOYABLE PLATFORM SYSTEMS DEVELOPMENT

R. E. Jewell
NASA
George C. Marshall Space Flight Center
Huntsville, Alabama

Large Space Systems Technology - 1981
Third Annual Technical Review
November 16-19, 1981

FUNCTIONAL PLAN

The flow chart shows the interaction between the different aspects of platform systems technology. In order to perform technology in the different discipline areas, shown below the dashed line, generic platform systems must be established and used as reference in defining and executing technology work in the discipline areas shown. Specific outputs of the activity are indicated to the right of the chart.

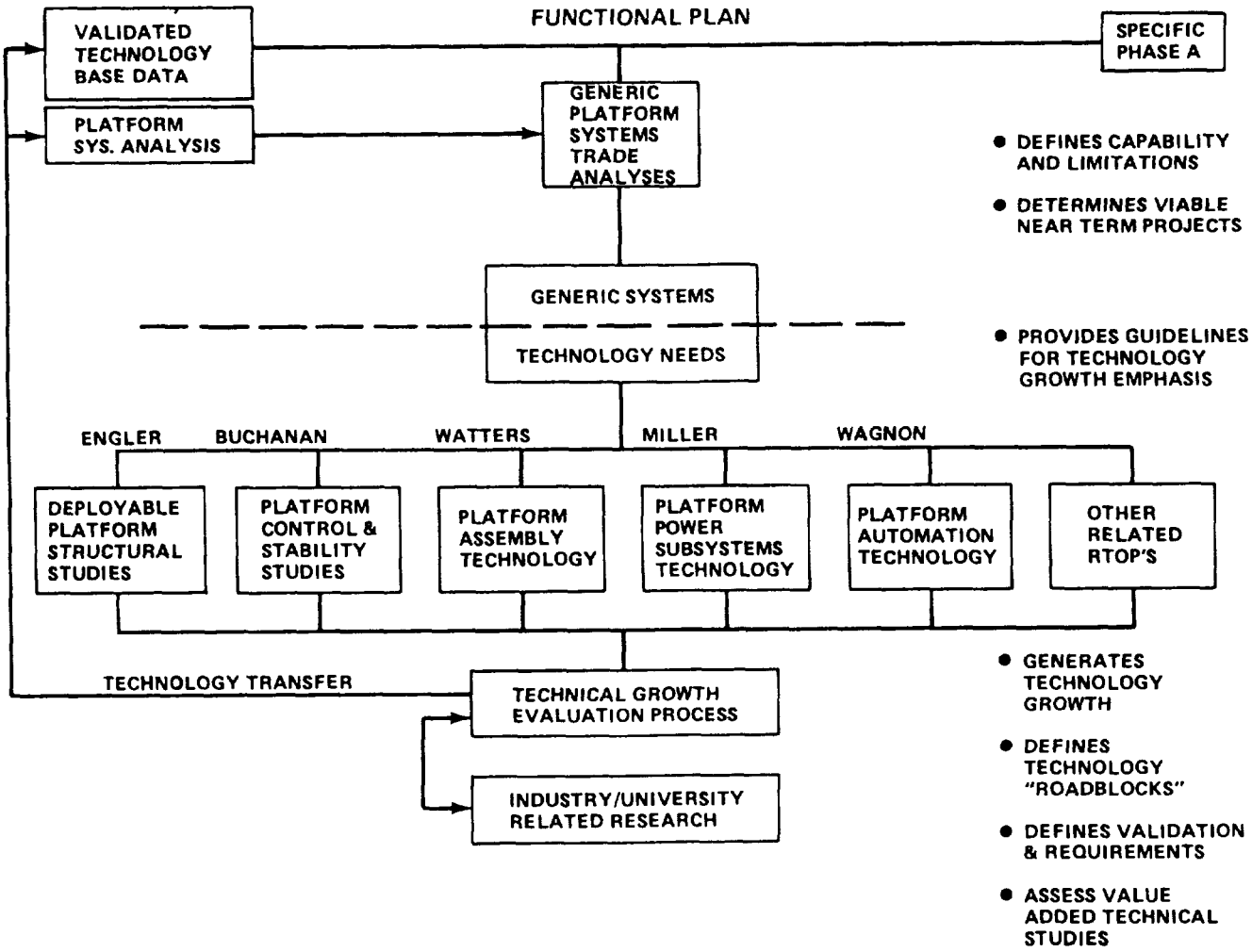

LONG RANGE OBJECTIVE

The long range objective is to achieve technology readiness for one or more deployable platform systems by 1986. All technology areas required for deployable platform structures will be identified and worked.

APPROACH

A two-phase program is planned to insure attainment of the development objective. In Phase I, engineering studies are performed to identify various deployable platform structures concepts, and based on established selection criteria, one or two viable concepts are chosen for a follow-on concept design effort. Generic platform design requirements are used in this effort. Phase II will expand the technology work into hardware verification of the selected deployable structure concept(s). In an incremental program, an orderly progression from component to subsystem development and finally to an overall system verification will take place. Flight experiments required to augment the ground test will be identified during this program phase.

LONG RANGE OBJECTIVE

- DEVELOP TO TECHNOLOGY READINESS ONE OR MORE DEPLOYABLE PLATFORM SYSTEM CONCEPTS BY 1986

APPROACH

- EXECUTE TWO PHASED PROGRAM TO INSURE ATTAINMENT OF DEVELOPMENT OBJECTIVE

PHASE I ENGINEERING STUDY ACTIVITY

- CONCEPT DEVELOPMENT AND SELECTION
- CONCEPT DESIGN

PHASE II HARDWARE DEVELOPMENT, TEST AND EVALUATION

- COMPONENTS AND SUBSYSTEMS
- SYSTEMS
- FLIGHT EXPERIMENT DEFINITION

OVERALL STUDY GUIDELINES

The goal of the Deployable Platform System Technology program is to perform an integrated program with demonstrated technology readiness in 1986 through test proven hardware on the system level. In order to achieve versatility, point design of the system is avoided, and a generic platform, incorporating features of presently conceived platforms (LEO and GEO), is utilized. Other applied major guidelines include the adaptation of a building block approach with self-contained automatic deployed modules and minimum EVA for assembly and maintenance. The basic launch vehicle is assumed to be the Space Shuttle (STS).

- FY 1986 TECHNOLOGY READINESS
  - TEST PROVEN HARDWARE
- COMPLETE SYSTEM - NOT JUST A STRUCTURE
- GENERIC - NOT A BASEPOINT DESIGN
- VERSATILITY
  - CAN BE USED TO BUILD PLATFORMS OF DIFFERENT CONFIGURATIONS
  - "BUILDING BLOCK" APPROACH - SELF-CONTAINED MODULES
- DISTINCTION BETWEEN LEO AND GEO DESIGNS
- ADAPTABLE FOR A WIDE RANGE OF PAYLOADS
- AUTOMATIC DEPLOYMENT
  - MINIMUM EVA
- BASED ON STS CAPABILITIES

MAJOR TECHNICAL CONCERNS

A listing of major technical concerns, which will be addressed in the technology program, is shown. Special emphasis will be given to the areas indicated.

- ✓ DEPLOYMENT METHODS
- STRUCTURAL CONCEPTS
- ✓ UTILITIES INTEGRATION
- STRUCTURAL PERFORMANCE
- ✓ COMPATIBILITY WITH ENVIRONMENTS
- DESIGN FLEXIBILITY
- CONTROL SYSTEM HARDWARE INTEGRATION
- CONTROL SYSTEM/STRUCTURAL SYSTEM INTERACTION
- ✓ PACKAGING EFFICIENCY
- DEPLOYMENT ASSEMBLY
- POWER AND THERMAL SYSTEM INTEGRATION
- PROPULSION SYSTEM INTERACTION & INTEGRATION
- ✓ SPACECRAFT OPERATIONS AND SERVICING
- ✓ PAYLOAD INTEGRATION
- MATERIAL SELECTION
- COST TRADES

DEPLOYABLE PLATFORM SYSTEMS, PHASE I

This schematic depicts the study flow for the first phase of the technology program. No hardware tests are planned during this segment of the effort which is performed in two parts.

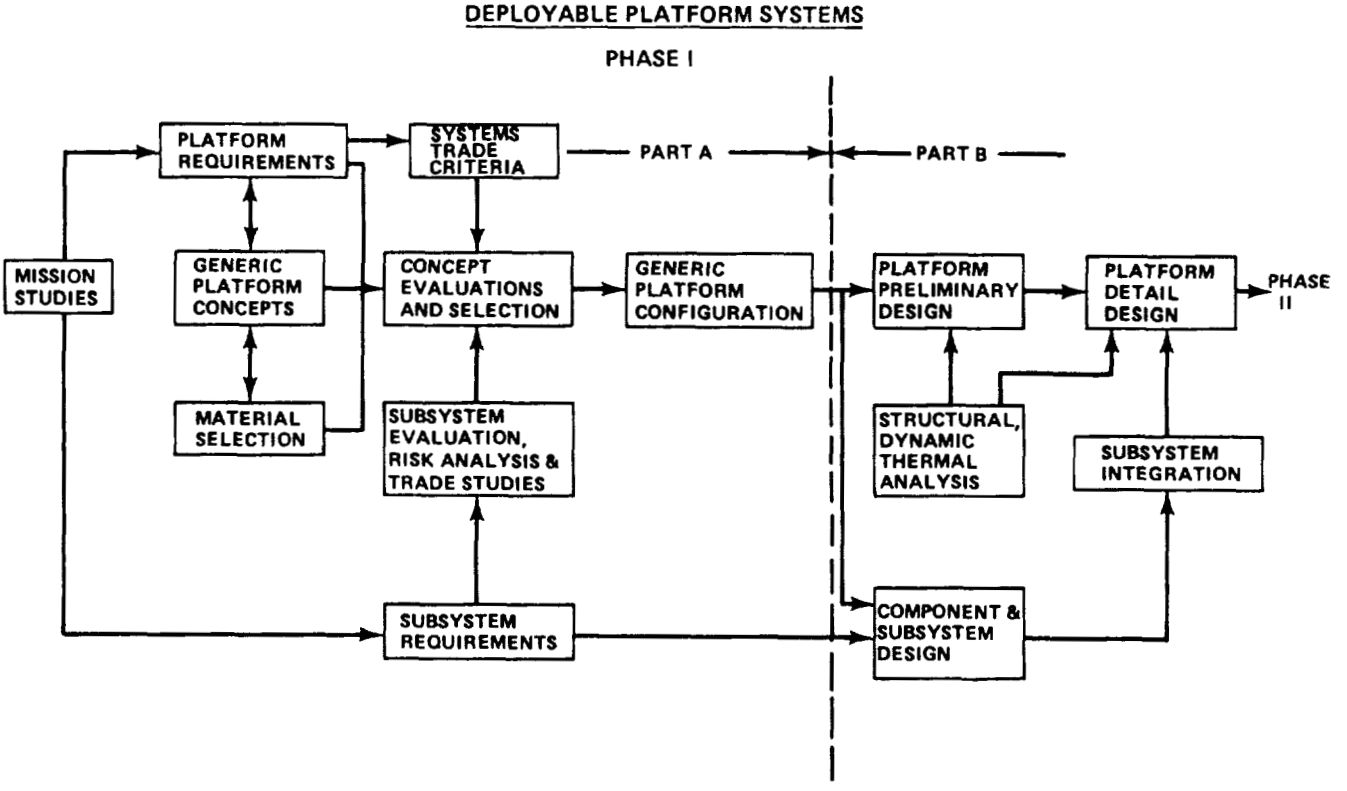

GENERIC DEPLOYABLE PLATFORM REQUIREMENTS

A matrix of requirements will be established to direct the design of the generic spacecraft configuration and the development of concepts for the platform design. Information will be extracted from the MSFC summary document of the three focus missions. Other sources of requirements are JSC 0770, Vol. XIV, Space Shuttle System Payload Accommodations, and CR-160861, Shuttle Considerations for the Design of Large Space Structures. The matrix will distinguish between LEO and GEO requirements, where pertinent, and will include structural strength and stiffness; payloads masses and sizes; materials environments and temperatures; utilities quantity, sizes, and function; orbiter integration; space operations functions and mission equipment, such as TT&C, solar arrays, batteries, and control system components.

GENERIC DEPLOYABLE PLATFORM REQUIREMENTS

STRUCTURAL

- **SUITABLE FOR EITHER AREA OR LINEAR PLATFORM**
- **STRUCTURAL ELEMENT SIZE:**
- **STRUCTURAL FREQUENCY**
- **STRENGTH OF BEAM**
- **STIFFNESS OF BEAM**
- **MATERIAL**

DEPLOYMENT/STOWAGE/RETRACTION

- **MUST DEPLOY AUTOMATICALLY**
- **SHOULD BE ABLE TO RETRACT**
- **PACKAGING RATIO 10 TO 30:1 (DEPLOYED/STOWED)**
- **MUST OBSERVE SHUTTLE ORBITER PAYLOAD BAY CONSTRAINTS**

UTILITY INTEGRATION AND INTERFACES

- **POWER RANGE**
- **DATA RATE**
- **THERMAL CONTROL**
- **UTILITIES CABLES, AND LINES, MUST BE FULLY INTEGRATED INTO THE DEPLOYED TRUSS WORK**
- **UNIVERSAL INTERFACE HARDWARE ADAPTER CAPABILITY AS A GOAL**

GENERIC PLATFORM REQUIREMENTS (CONT'D)

SUBSYSTEM INTEGRATION

- POWER SYSTEM SOLAR ARRAYS : AUTOMATICALLY DEPLOYED
- PROPULSION SYSTEM : ALTITUDE/ATTITUDE CONTROL/REBOOST
- THERMAL CONTROL : AUTOMATICALLY DEPLOYED OR MOUNTED ON DEPLOYED STRUCTURE

PAYLOAD INTEGRATION

- PAYLOAD MASS AND POSITION SENSITIVITY
- ACCESSABILITY/SERVICEABILITY REQ'TS

OPERATIONS AND SERVICING

- PLATFORM MUST BE COMPATIBLE WITH ORBITER DOCKING AND BERTHING METHODS AND HARDWARE

MISSION

- PRIMARY ORBIT : LOW EARTH ORBIT (400 TO 600 km) WITH GEOSYNCHRONOUS ACCESS.
- ORBITAL MANEUVERS : ALTITUDE CHANGES ORBIT REBOOST
- 30 YEAR LIFE : LONG TERM ENV. EFFECTS, MATERIALS & SUBSYSTEMS

MATURED STRUCTURAL CONCEPTS

Applicable structural concepts will be compiled for structures system selection. Both new and mature concepts, as shown, will be investigated.

CONCEPT	DEVELOPMENT STATUS	MATERIALS
① CONTINUOUS LONGERON MAST 	SPACE-PROVEN, WITH INSTALLATION OF SMALL ELECTRICAL LINES	FUTURE USE OF LOW CTE COULD BE PROBLEM
② ARTICULATED LONGERON MAST	DEMONSTRATION MODELS WITHOUT PREINSTALLED UTILITIES	FUTURE DESIGN COULD USE LOW CTE MATERIALS
③ EXTENDIBLE SUPPORT STRUCTURE FOR SEASAT 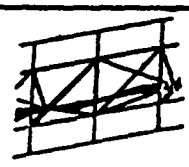	SPACE-PROVEN, BUT WITHOUT UTILITIES INSTALLATION—5 FT x 35 FT LONG	TITANIUM, BUT CAN BE LOW CTE
④ DIAMOND-SHAPED BEAM 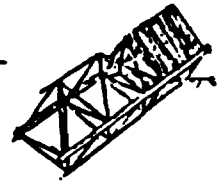	DEMONSTRATED AUTOMATIC DEPLOYMENT OF FIVE-BAY STRUCTURE—SMALL UTILITIES INCLUDED—MODEL 5 x 7.5 FT CROSS-SECTION	LOW CTE MATERIAL WITH ALUMINUM FITTINGS
⑤ DOUBLE-CELL, DOUBLE-FOLD TRUSS 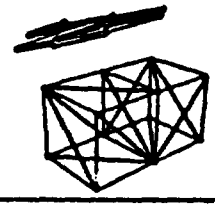	DEMONSTRATED DEPLOYMENT IN MSFC BUOYANCY TANK WITH 4 WIRE BUNDLES—EXTERNALLY APPLIED FORCES—SIZE, 3 M x 3 M x 6 M LONG	ALUMINUM, BUT CAN EMPLOY LOW CTE MATERIALS
⑥ BOX TRUSS WITH X-BRACING 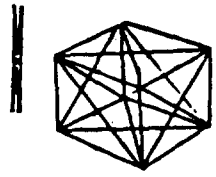	DEMONSTRATION MODEL WITHOUT UTILITIES	LOW CTE MATERIAL

ADDITIONAL DEPLOYABLE STRUCTURES CONCEPTS

Applicable structural concepts will be compiled for structures system selection. Both new and mature concepts, as shown, will be investigated.

Type	Deployed	Partially Deployed	Packaged
(1) Warren Truss – Transverse Fold	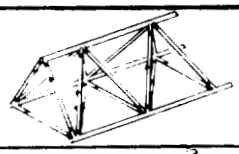	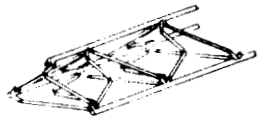	
(2) Cable Cross-Braced – Transverse Fold	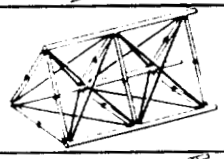	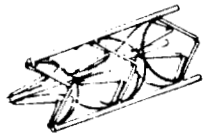	
(3) Cable Cross-Braced – Transverse and Longitudinal Fold	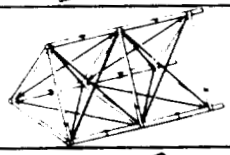	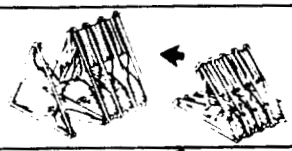	
(4) K Brace – Longitudinal Fold	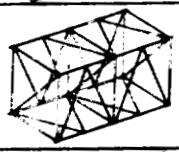	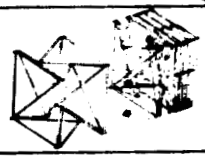	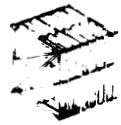
(5) K Brace – Longitudinal Fold	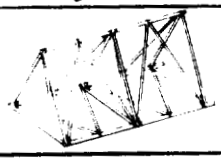		

UTILITIES INTEGRATED WITH STRUCTURE

The overall spacecraft design will be broken down into separate design areas, and several concepts will be developed for each area. The areas which will be developed are:

- Folding/deployable structural trusses--including the existing diamond truss and double-cell, double-fold.
- Deployable methods and mechanisms.
- Installation, attachment, and deployment of utilities.
- Expansion/contraction in fluid lines.
- Interfaces between structure and modules (payloads, control module, RCS, etc.).
- Interfaces between utilities and modules.

A typical design problem, integrated utilities, is depicted in this picture.

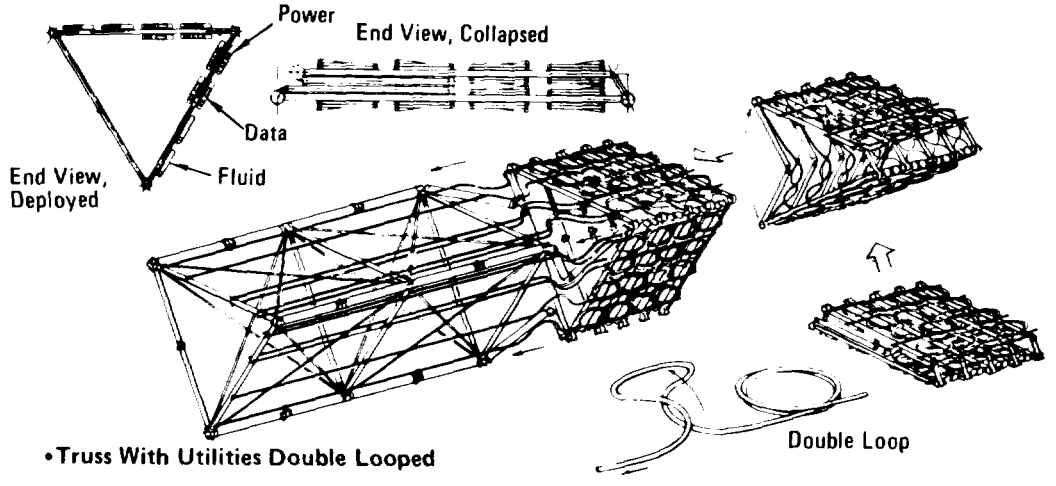

ELEMENTS OF DEPLOYABLE PLATFORM SYSTEM

A generic linear and area shaped deployable spacecraft configuration will be developed from the requirement established. The purpose of the spacecraft configurations is not to freeze the design, but to help understand and solve the localized problems which will be encountered, i.e., to see the forest in addition to seeing the trees. The spacecraft configuration will be configured to support the reference payload group (selected from the three focus missions) for LEO or GEO applications. The drawing of the generic deployable spacecraft configuration shows the following typical elements:

- Structure
- Control module
- Propulsion system
- RCS--distributed thrusters
- Solar array
- Electric power distribution
- Docking/berthing provisions
- Payloads--the reference payload group
- Radiators
- Interfaces between structure and modules/payload/RCS
- Module-to-module interface
- Fluid line routing

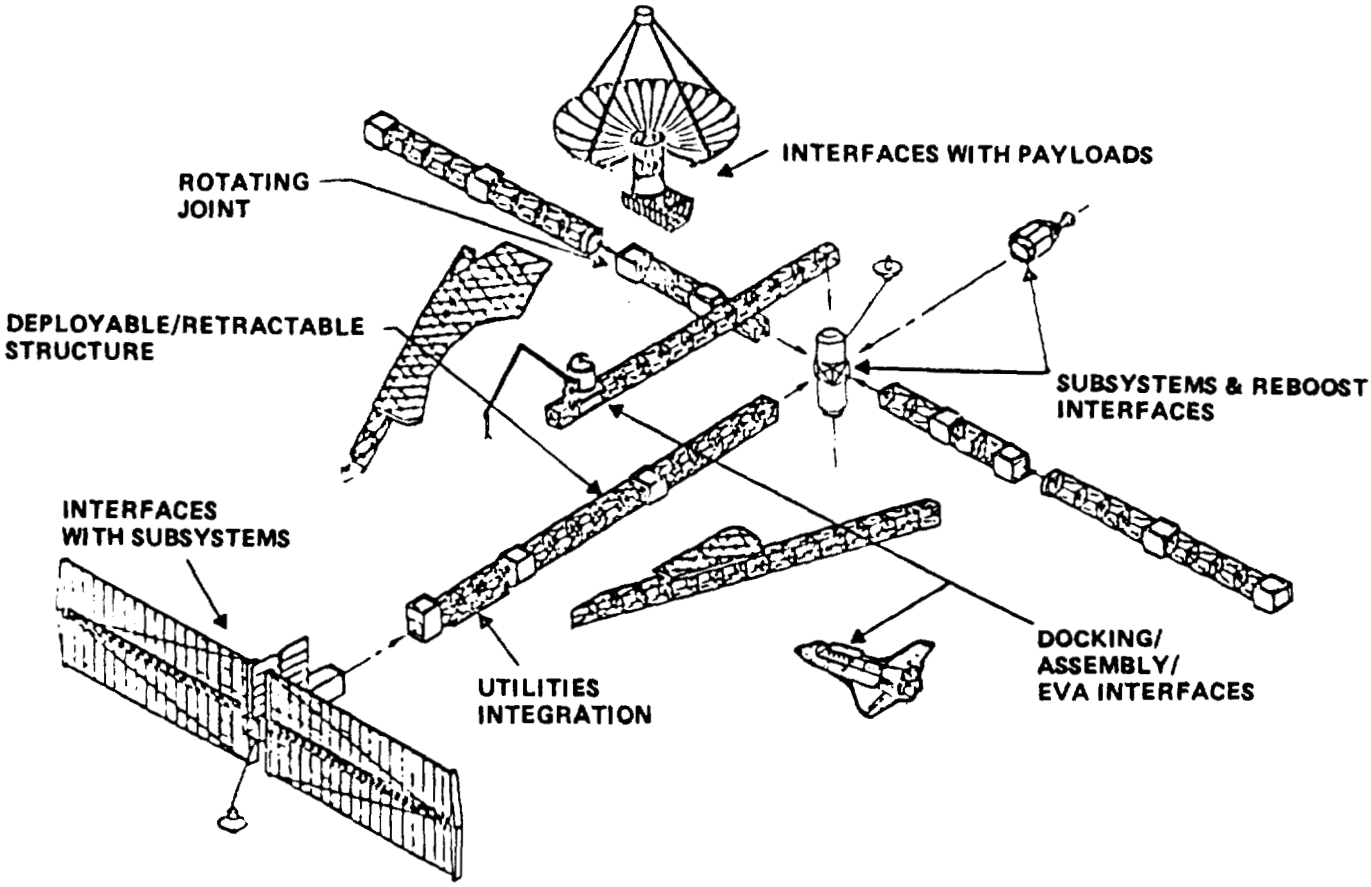

SYSTEM LEVEL CONCEPT DEVELOPMENT TRADES

The concepts for separate components or subsystems will be screened and then matched to each other to form integrated platform systems. For example, each foldable truss will be matched with the type deployment mechanism to which it is best suited. Similarly, the various concepts of utilities installation will be matched with structures and deployment methods. The objective is to produce integrated systems, each capable of deploying a structural truss complete with (as far as possible) all of the utilities, plus interfaces and interconnects for payloads and modules. The emphasis is placed on the system, not individual pieces or subsystems. A subsystem, however ingenious it may be, will be discarded if it cannot perform its role as part of the integrated system. An integrated system forms the basis of a series of building blocks which can be assembled to construct deployable platforms of various configurations. The integrated process will be supported by analyses in all of the pertinent areas:

- Deployment methods/mechanisms--external mechanisms, strain energy.
- Structures--strength, stiffness, member shape and size, attachments.
- Utilities installation--cable bend radii, flexing, fatigue.
- Materials--aluminum, composites, structures, utilities.

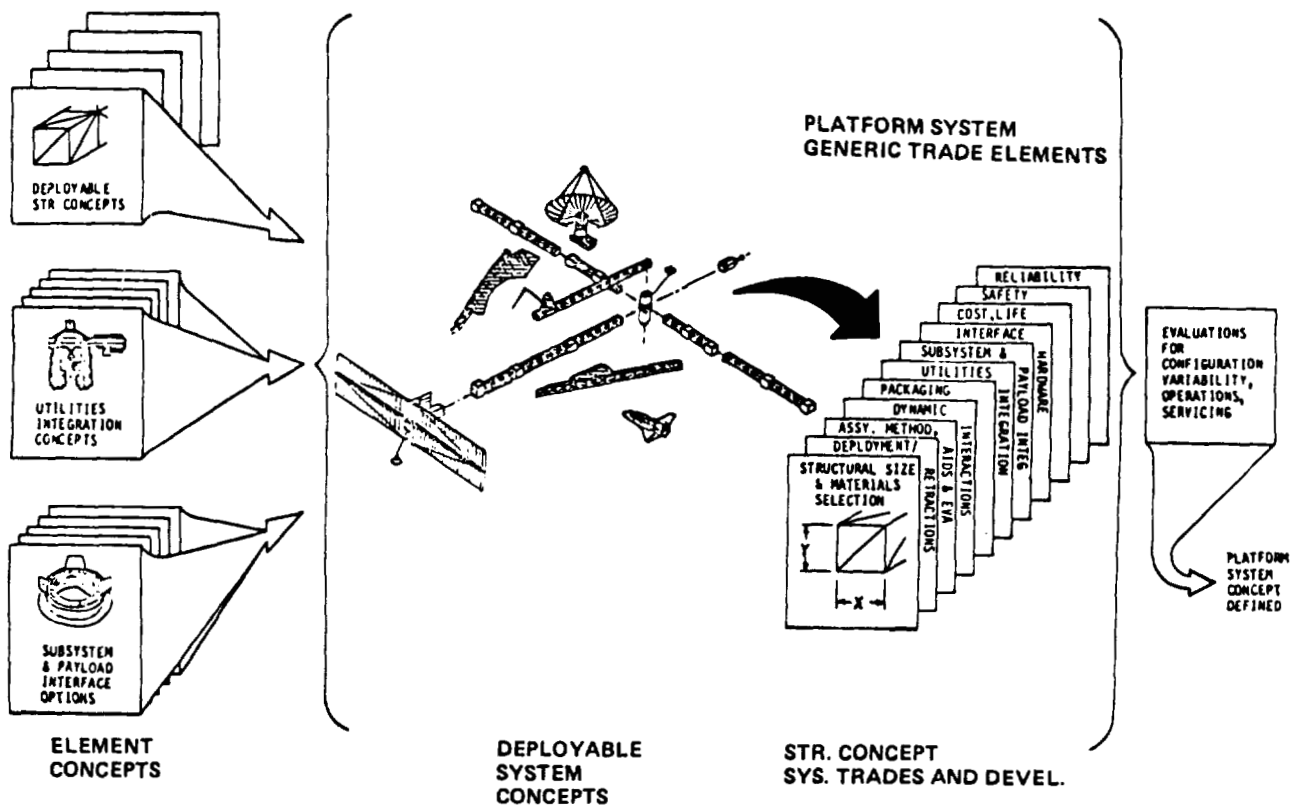

SYSTEM LEVEL CONCEPT DEVELOPMENT TRADES (Cont'd)

The criteria for selection of a deployable platform system will encompass basic structure performance, subsystem accommodation, space assembly operations, orbiter integration implications, and development cost. With these categories, the specific criteria will be developed; for example, such structures performance criteria as thermal stability, weight, packaging efficiency, etc. For each set of criteria, the methodology to be used in the screening process involving a combination of numerical data (where feasible) and engineering judgments to apply a point rating scheme and summary comparisons will be developed. For each type of criteria, a written definition of what constitutes acceptable numerical or qualitative limits will be prepared. Detailed engineering data from the concept characteristics matrix will be combined to form a set of overall ratings, based on the selection criteria. The sum of possible points and total costs for each concept will then be compared on summary screening charts, and one or two structural concepts selected for design and analysis to complete Phase I of the Technology program.

DEPLOYABLE PLATFORM SYSTEM TECHNOLOGY SCHEDULE

The schedule shows the overall program consisting of two phases. Phase I was discussed in detail. Phase II effort will deal in component, subsystem, and system development. Extensive hardware design, fabrication, and validation effort is planned to achieve the demonstrated technology readiness by 1986.

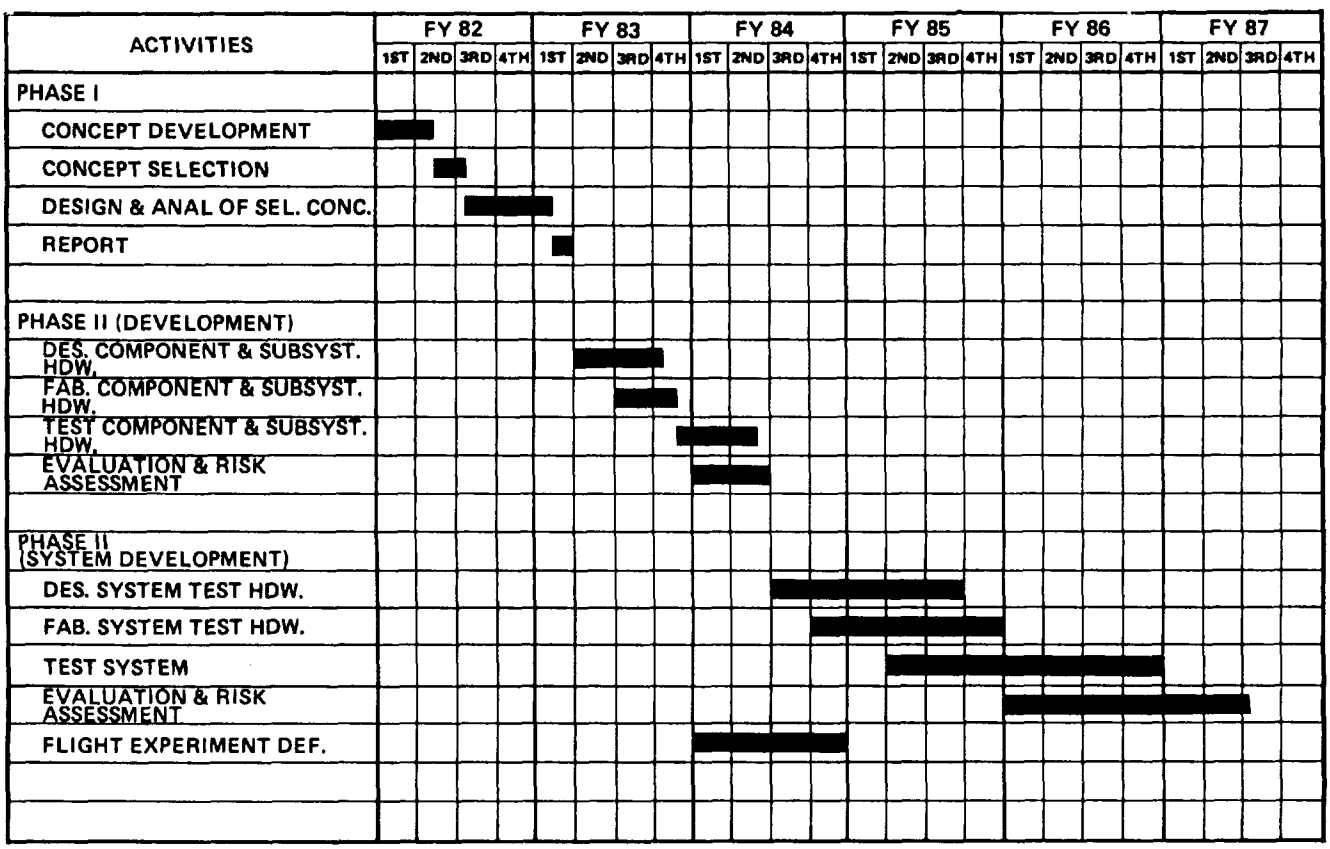

TECHNOLOGICAL NEEDS OF ADVANCED EARTH-OBSERVATION SPACECRAFT

A. L. Brook
Martin Marietta Corporation
Denver, Colorado

Large Space Systems Technology - 1981
Third Annual Technical Review
November 16-19, 1981

Because this paper was not available at time of publication, only slides are presented.

EOS Study Objective

Provide Design and Analysis Data on
Microwave Radiometer Satellites, Augmented
with Additional Earth Surface and
Atmospheric Observation Sensors.

EOS Study Outline

- Analyze Mission Scenarios
  Develop Sensor Sets

- Develop Conceptual Spacecraft Designs
  Perform Spacecraft Analyses

- Evaluate and Rank EOS Concepts
  Identify Compropises/Advantages for Multidiscipline EOS

- Perform Parametric Subsystem Analyses
  Identify New Technology Requirements

- Expand LaRC Integrated Analysis Program

EOS — Systems to be Considered

- Microwave Radiometer Satellite (MRS)
  - 50 - 200 m Diameter
  - 700 km Altitude

- MRS Plus Supplementary Instruments for
  - Earth Observations, or
  - Ocean Observations, or
  - Atmospheric Observations, or
  - Combinations of the Above

120 Meter x 60 Meter Radiometer

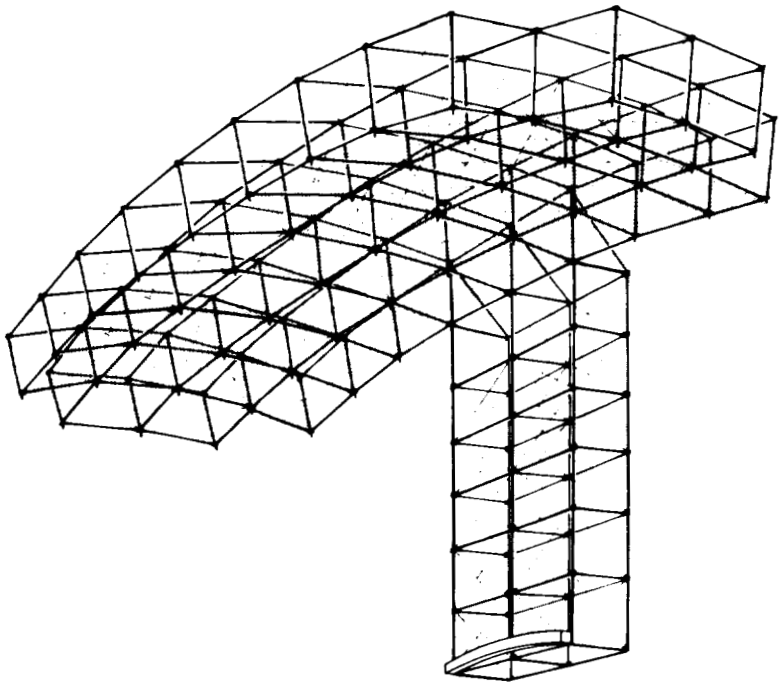

120 Meter by 60 Meter Radiometer Design Parametric

Size

- 8 Bay by 4 Bay Reflector
- 8 Bay by 2 Bay Feed Mast
- 15 Meter Boxes

Member Sizes

- Surface 8.9 cm (3.5 in.) Diameter by 0.089 cm (0.035 in.)
- Verticals 6.35 cm (2.5 in.) Square by 0.089 cm (0.035 in.)

Weight

- (6900 lb) 3130 Kg Reflector, Feed, and Mesh
- (1000 lb) 454 Kg Feed Mass Allocation

Dynamics - First Five Fundamental Frequencies

1) 1.23 Hz
2) 1.46 Hz
3) 1.78 Hz
4) 4.21 Hz
5) 4.41 Hz

Typical Measurement Requirements for MRS

Measurand	Range	Resolution, km	Repeat, days	Observable at, GHz
Soil Moisture	5-40%, 10-25-cm Depth	1-10	1-3	1-10
Water Surface Temperature	270-310°K	1-10	1-3	1-8
Water Roughness (Wind)	0-60 m/s	1	3-7	1-37
Salinity	0-40 PPT	1-10	1-3	1-2
Water Pollution (Oil Slicks)	0-1-cm Thickness	1	1	1-10
Probable Operating Frequency: 1-5 GHz				

Typical Supplementary Observations

Earth Surface

Resource Identification and Mapping
Land Mass Imaging
Geological Feature Identification

Atmosphere

Composition
Dynamics
Energy Transfer

Ocean

Color
Currents
Wave State
Ice

Spectra

Ultraviolet
Visible
Infrared
L/X-Band SAR

Remote-Sensing Spectral Distribution

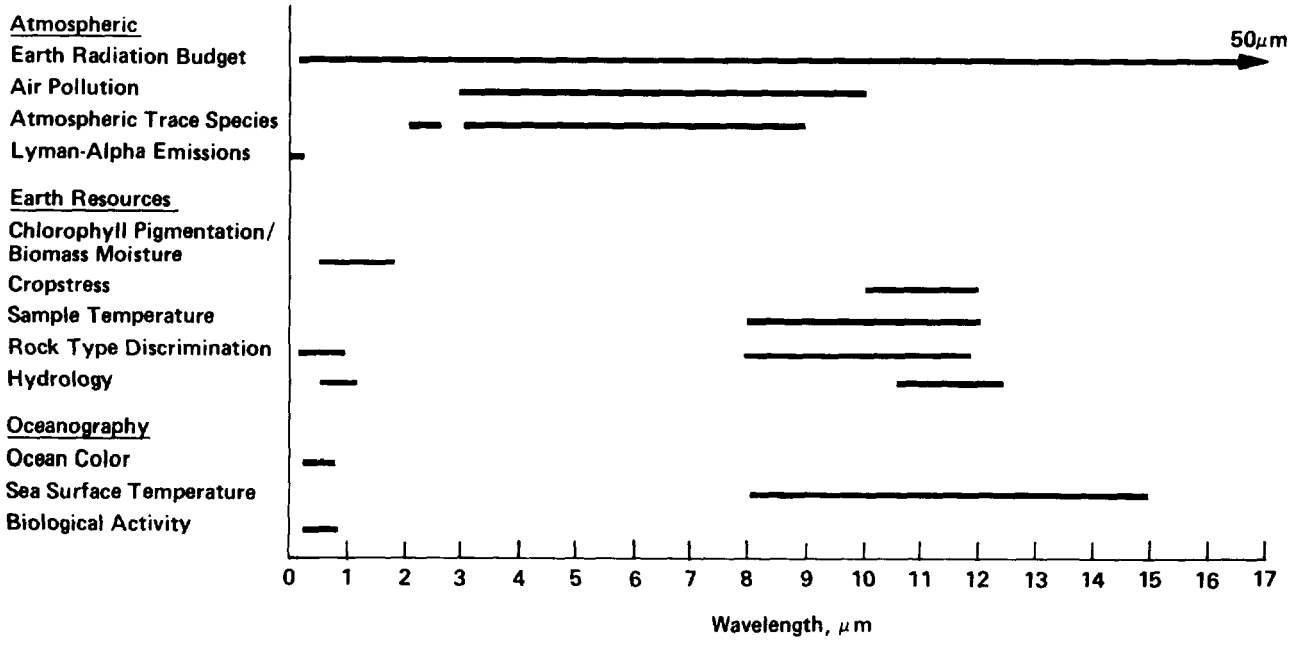

Typical Instrument Characteristics

Mass:	10-500 kg (2/3 in 50-250 kg Range)
Altitude:	700 km Okay for Most, (SARs are Large at 700 km)
Orbit Inclination:	60 deg Okay for Most, Some Require 98 deg
Pointing Accuracy:	$\pm$0.1 deg for All
Pointing Stability:	$\pm$30 arc-s for All
Unobstructed LOS Access:	NADIR $\pm$90 deg along and across Track
Average Power:	500 w/Instrument Except for SAR (Several kW) LIDAR (2.6 kW), All 28 Vdc
Data Rates:	1 kbps - 120 Mbps per Instrument Real Time, Near Real Time

LSS CONTROL TECHNOLOGY

A.F. Tolivar
Jet Propulsion Laboratory
Pasadena, California

Large Space Systems Technology - 1981
Third Annual Technical Review
November 16-19, 1981

LSST CONTROLS TECHNOLOGY DEVELOPMENT

The objective of LSS Controls is to define and develop the necessary control technologies required by a variety of future large platform and antenna missions.

The plan shows technology developments in three main areas. The top part of chart shows the SYNTHESIS tasks which support the definition, development and evaluation of control systems for classes of platform and antenna applications, leading to the selection and evaluation of preferred mechanization.

The center of the chart shows the ADVANCED TECHNOLOGY DEVELOPMENT tasks which develop the fundamental technology needed to achieve precise attitude, pointing, and shape control required by LSS, as well as the associated hardware concepts.

The TECHNOLOGY VALIDATION tasks address the verification of control technology through ground demonstrations of control technology and the definition of flight experiments required for verification and for establishing technology readiness.

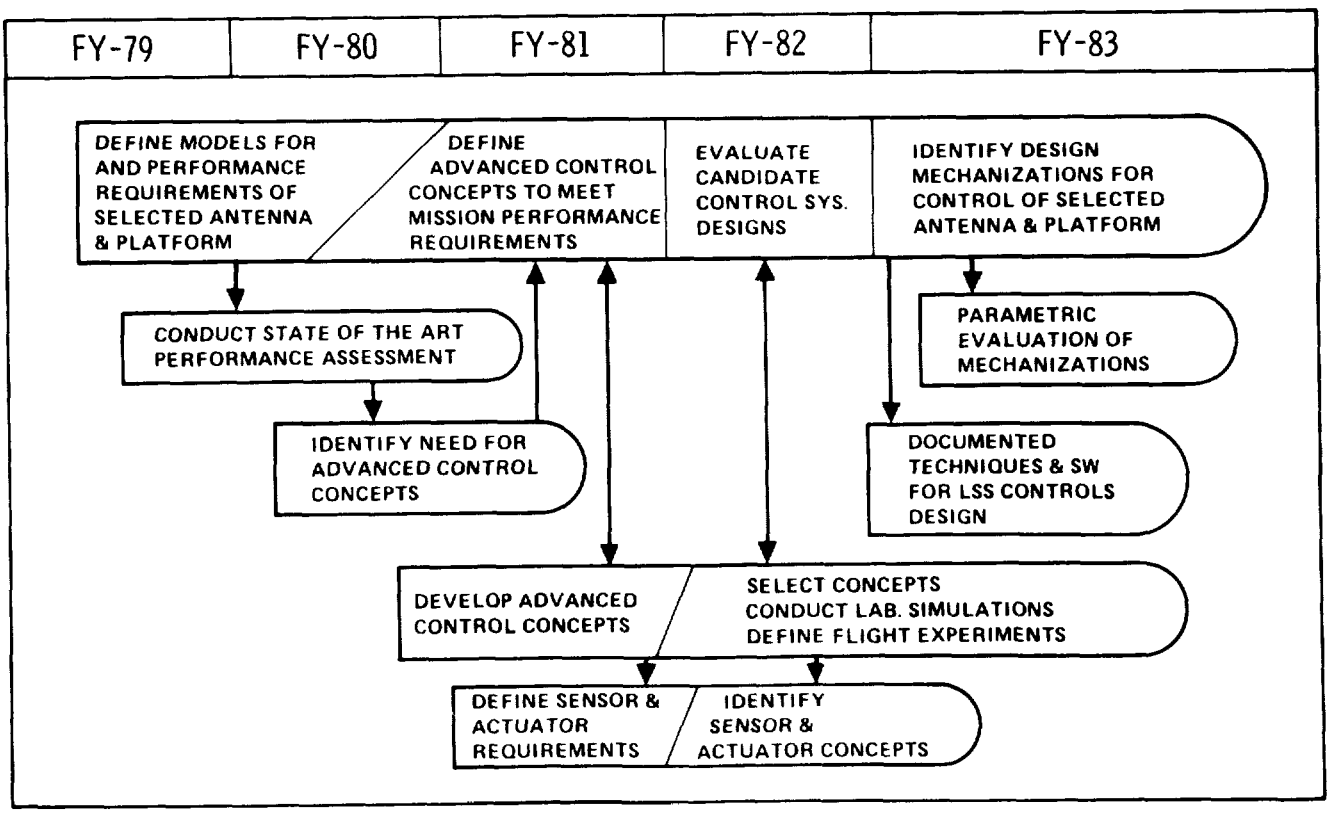

JPL LSS CONTROLS PROGRAM ELEMENTS

The LSS Controls program at JPL addresses the synthesis tasks for large antennas and platforms, as well as the Technology Development and Validation areas. In this presentation I will summarize briefly the overall LSS Controls program at JPL. The following four speakers, Y.H. Lin, J.M. McLauchlan, R.S. Edmunds, and D.B. Schaechter, will follow with detailed reports on Antenna Control, Shape and Vibration Sensors, Platform Control, and Advanced Control Technology and Validation, respectively.

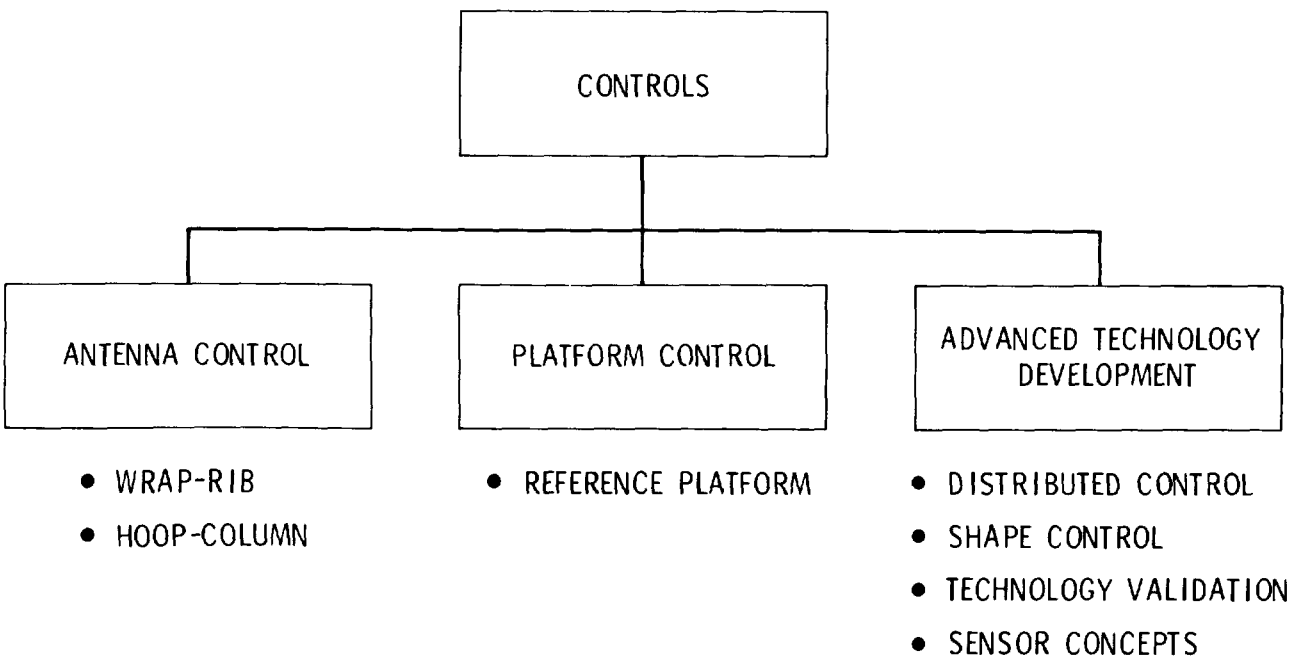

FY'81 ACCOMPLISHMENTS - ANTENNA AND PLATFORM CONTROL

(1) Updated control requirements and dynamic models to reflect the latest configurations for platforms and antennas (3-dimensional platform models with 4 payloads, 64m Hoop-Column antenna, and a 55m Wrap-Rib antenna).

(2) Defined and developed a hierarchy of control systems needed to meet the performance requirements of various classes of missions. This hierarchy constitutes an inventory of control technology which provides specific control solutions of varying complexity depending upon the specific mission requirements.

(3) A study was completed to define the control subsystem for the Land Mobile Satellite Service (LMSS) mission. The specific LMSS disturbance environment and control requirements were defined and preliminary control subsystems were developed for both the single-aperture offset-fed wrap rib and the quad-aperture hoop column implementations. The subsystems defined included control concepts as well as detailed equipment lists (type, dimensions, weight, power, etc.). This study is covered in detail in a separate paper (also included in these proceedings in the section on antennas) entitled "Attitude Control Subsystem Study for the LMSS Spacecraft".

(4) A key accomplishment in the platform and antenna control area has been the quantitative assessment and identification of sensor and actuator requirements, performance regime achievable, the sensitivity of that performance to system (structure/control) uncertainties, and the identification of key technology drivers.

- UPDATED DYNAMIC MODELS AND CONTROL REQUIREMENTS
- DEFINED AND DEVELOPED ADVANCED CONTROL CONCEPTS TO MEET MISSION PERFORMANCE REQUIREMENTS
- DEFINED CONTROL SUBSYSTEM MECHANIZATION FOR THE LMSS COMMUNICATIONS MISSION
- QUANTITATIVE ASSESSMENT OF
  - SENSOR AND ACTUATOR REQUIREMENTS
  - PERFORMANCE REGIME
  - SENSITIVITY TO CONTROL/STRUCTURAL UNCERTAINTIES
  - TECHNOLOGY DRIVERS

FY'81 ACCOMPLISHMENTS - CONTROL TECHNOLOGY

(1) Techniques have been developed for computing the sensitivity matrix of the far-field electric fields of antennas with respect to feed displacements. This sensitivity matrix is being used to account for RF considerations in the design of RF-performance-optimum control systems.

(2) Continued development of the experimental facility has resulted in a detailed finite-element model of the flexible beam and in accurate calibration of the sensor and actuator scale factors. Interactive software has been developed and added to the facility, thus allowing very fast implementation of control laws. A laser/retroreflector system has been incorporated to visualize the motion of the beam.

(3) Static shape estimation and control has been demonstrated experimentally on the beam facility. The method has been also demonstrated through computer simulation of a 55-meter wrap-rib reflector using 18 sensors and 18 actuators distributed circularly around the reflector.

(4) An active distributed control approach has been developed which exhibits reduced sensitivity to model errors. The concept has been demonstrated experimentally.

- DEVELOPED ANALYSIS KNOW-HOW TO DETERMINE ANTENNA CONTROLLER DESIGNS BASED ON RF PERFORMANCE
- EXPERIMENTAL FACILITY DEVELOPMENT
- STATIC SHAPE ESTIMATION AND CONTROL
  - LABORATORY DEMONSTRATION
  - APPLICATION TO 55M REFLECTOR
- ACTIVE DISTRIBUTED CONTROL ANALYSIS AND LABORATORY DEMONSTRATION

FY'82 TASK SUMMARY - CONTROL TECHNOLOGY

A major theme of the FY'82 work will be the development of control systems which can either adapt to changing or uncertain models or be insensitive to the model errors. Specific tasks are:

(1) Develop expanded algorithms for distributed control and for system identification required for off-line and real-time knowledge of the flexible spacecraft dynamics.

(2) Investigate the sensitivity of the shape determination and control system to actuator/sensor type, number and location.

(3) Compute the sensitivity of the far field of an antenna to reflector shape deformations. Develop control-design approach to optimize RF performance.

(4) Experimental verification of precise shape control with poorly known dynamics and application to multidimensional plate-like structures.

- DEVELOP EXPANDED IDENTIFICATION ALGORITHMS FOR MODAL DETERMINATION AND DISTRIBUTED CONTROL
- ESTABLISH SHAPE DETERMINATION AND CONTROL PERFORMANCE SENSITIVITY TO ACTUATOR/SENSOR TYPE, NUMBER AND LOCATION
- COMPUTE RF SENSITIVITY TO DISH DISTORTION AND DEVELOP CONTROL DESIGNS TO OPTIMIZE RF PERFORMANCE
- EXPERIMENTAL VALIDATION OF PRECISE SHAPE CONTROL WITH POORLY KNOWN DYNAMICS

FY'82 TASK SUMMARY - ANTENNA AND PLATFORM CONTROL

(1) A variety of platform and payload configurations will be examined covering both manned and unmanned applications. Study will include the effects of platform and pointing mount stiffness on payload controller performance as well as the effects of man/shuttle disturbances.

(2) The large antenna control task will complete the evaluation of additional system drivers and establish performance levels and sensitivity to truncation errors as well as software and hardware constraints, nonlinearities, etc.

(3) A task will be initiated to define a control flight experiment. This task will address the definition of control experiment goals and requirements, the development of mechanization approaches and the identification of instrumentation requirements.

- EXAMINE SENSITIVITY OF CONTROLLER PERFORMANCE TO DISTURBANCES CAUSED BY MAN/SHUTTLE INTERFACE

- COMPLETE EVALUATION OF SYSTEM DRIVERS AND ESTABLISH PERFORMANCE OF ADVANCED CONTROL SYSTEMS FOR LARGE ANTENNA MISSION CONCEPTS

- DEFINE FLIGHT EXPERIMENT CONTROL GOALS AND REQUIREMENTS, DEVELOP MECHANIZATION APPROACHES AND INSTRUMENTATION REQUIREMENTS

CONTROL OF LARGE SPACE ANTENNAS: WRAP-RIB - HOOP/COLUMN

Yu-Hwan Lin
Jet Propulsion Laboratory
Pasadena, California

Large Space Systems Technology - 1981
Third Annual Technical Review
November 16-19, 1981

OUTLINE

This part of the presentation addresses the control work at JPL for large space antenna systems. Included in the discussions are the wrap-rib and hoop/column antenna concepts.

This presentation can be outlined (fig. 1) as follows: First, a brief description will be given for the LSST focus missions calling for the deployment of either wrap-rib or hoop/column antennas. Then, for either antenna concept, control problems will be described, control options discussed, quantitative results presented. System drivers for either antenna concept will be identified. Finally, this presentation will be concluded along with a brief description of the planned work for the upcoming year.

- FOCUS MISSIONS
- CONTROL PROBLEMS
- CONTROL OPTIONS
- RESULTS AND SYSTEM DRIVERS
- PLANNED WORK

Figure 1

LSST ANTENNA FOCUS MISSIONS

The LSST antenna focus missions (fig. 2) such as communications and radiometry call for antennas ranging in size from 10 to 100 meters, operating frequency of the order of GHz, antenna line-of-sight (LOS) pointing accuracy in the neighborhood of 0.04^{o}, and antenna surface accuracy of about 1/40 to 1/20 of a wavelength.

	SIZE (m)	FREQUENCY (GHz)	POINTING ACCURACY (DEG)	SURFACE ACCURACY (mm)	FEED	ORBIT (km)	LIFE (YRS)
COMMUNICATIONS	30-100	0.4-2.5	0.035	6-36	OFFSET	GEO	10
RADIOMETRY	10-100	1-11	0.05-0.025	0.5-6	OFFSET OR ON-AXIS	300-600	10

Figure 2

LMSS ACCURACY REQUIREMENTS

10 Years Operational Phase

A specific mission example is the Land Mobile Satellite System or LMSS which is a communications concept intended to provide telephone service to mobile users in the Continental United States. This concept calls for a single shuttle launch in the midnineties and the deployment of a large antenna in geostationary orbit. Technology readiness is to be flight demonstrated by the late eighties.

In order for the LMSS to provide adequate communication service, system accuracy requirements must be satisfied as shown in figure 3. It is noted that most accuracy requirements for the control subsystem are fractions of system requirements. For example, LOS pointing must be controlled to less than 0.03°, LOS stability must be controlled to less than 0.02°, and dish surface accuracy must be less than 6 mm.

Two antenna configurations being considered for the LMSS mission are shown in figures 4 and 5: the hoop/column and the wrap-rib configurations.

	SYSTEM	CONTROL
POINTING* (AFTER CALIBRATION/ COMPENSATION FOR THERMAL OFFSETS, ETC.)	$\pm 0.10^0$	$\pm 0.03^0$
STABILITY*	$\pm 0.03^0$	$\pm 0.02^0$
DISH SURFACE ACCURACY, RMS	12 mm	6 mm
SOLAR ARRAY POINTING	$\pm 1^0$	$\pm 1^0$

*ILLUSTRATION OF POINTING AND STABILITY ERRORS:

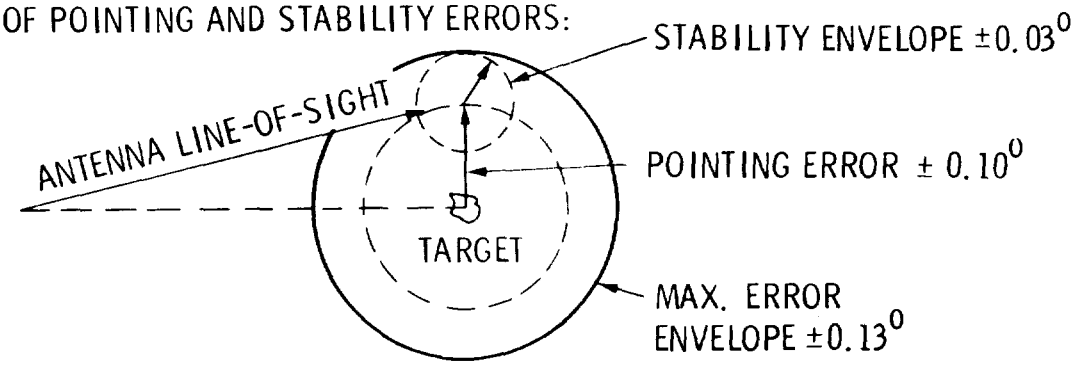

Figure 3

HOOP/COLUMN LMSS

CONFIGURATION AND MASS PROPERTIES

The hoop/column concept (fig. 4) has the following fundamental elements: a 122-meter diameter hoop (the plane of which is perpendicular to the viewgraph), and an 88-meter telescoping mast (or column). The antenna feed system is located at one end and a bus structure is located at the other end of the mast. The antenna reflector is about 118 meters in diameter, and there are a large number of stringers supporting the hoop or maintaining the shape of the reflector mesh.

Total weight of the system is about 10,000 lb, half of which is concentrated at the antenna feed area. The other half of the system weight is almost equally distributed among the hoop, the mast, and the bus.

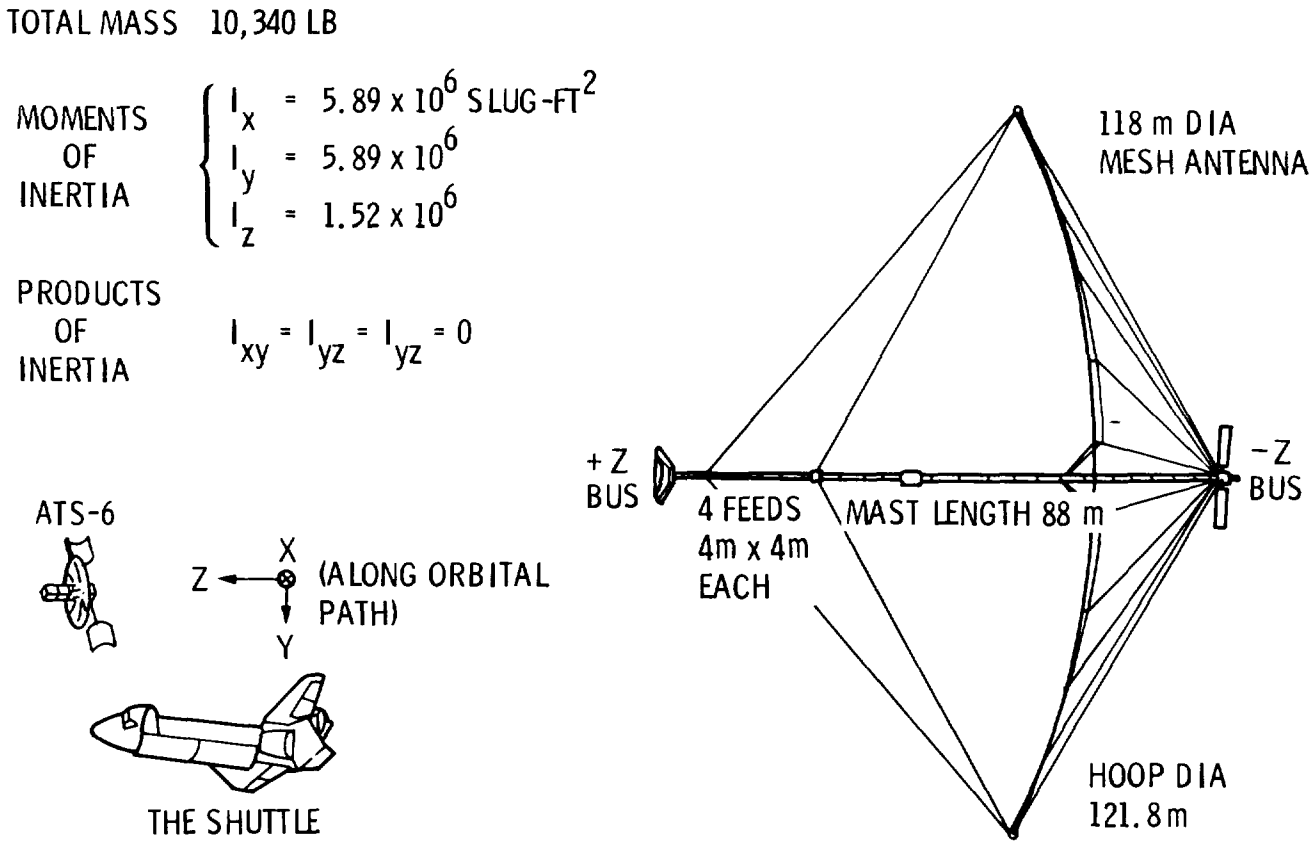

Figure 4

WRAP-RIB LMSS

CONFIGURATION AND MASS PROPERTIES

The wrap-rib concept (fig. 5) has a 55-meter diameter dish to the right and a feed array mounted on the spacecraft bus which is about 80 meters to the left of the dish. The dish and the bus are connected by the boom structure. The short boom is about 33 meters long and the long boom measures about 80 meters. Total weight of the system is about 9700 lb, 80% of which is concentrated at the bus area, and the other 20% at the dish.

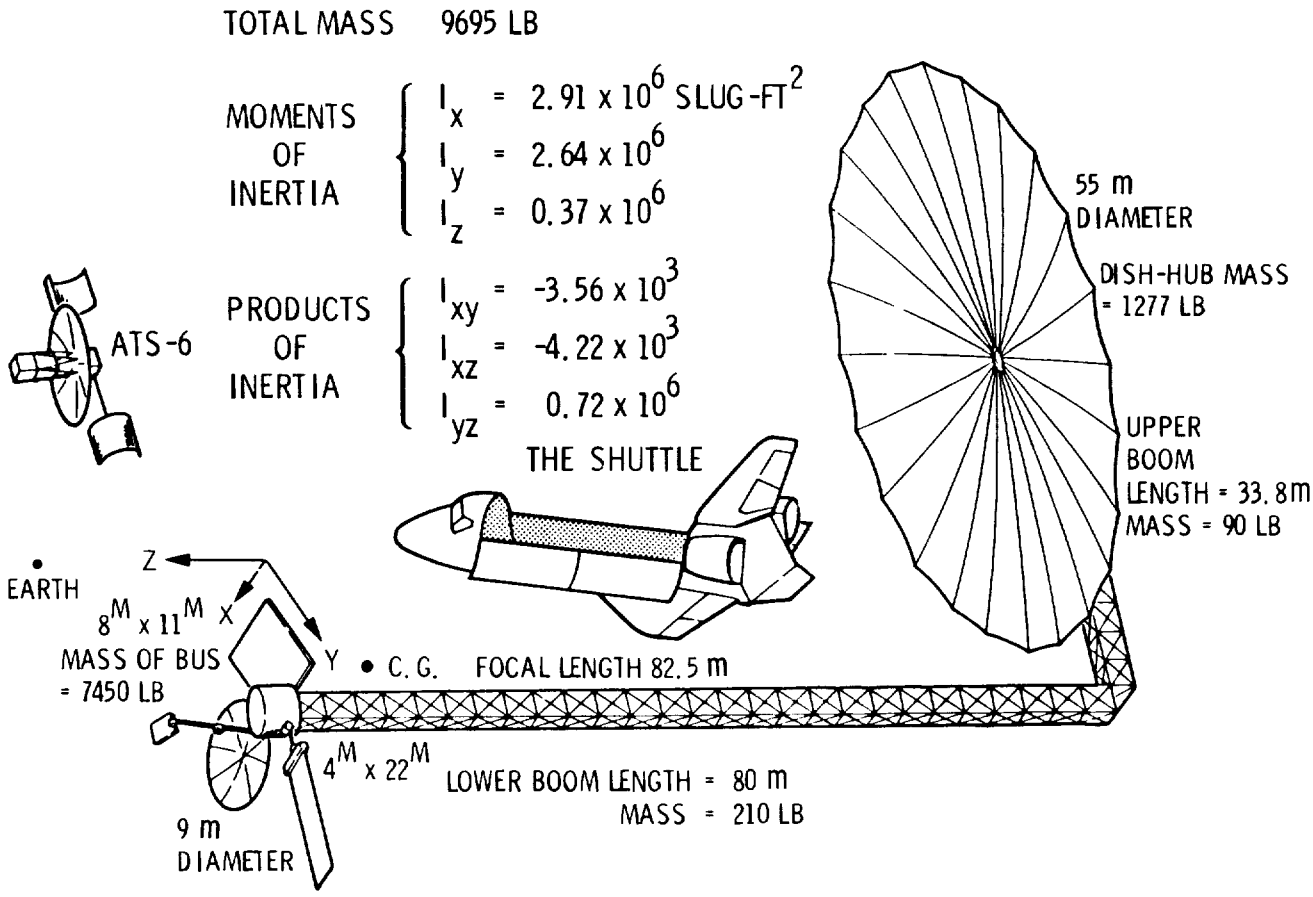

Figure 5

OBJECTIVES

The long range objective is to develop control technology for missions such as LMSS requiring large space antenna systems.

Specific objectives (fig. 6) are to identify control problems and system drivers, to develop control solutions, to establish control performance regime achievable, and to recommend system trade options.

First consider the control of the hoop/column antenna systems.

- IDENTIFY SYSTEM DRIVERS
- DEVELOP CONTROL TECHNOLOGY
- ESTABLISH SYSTEM PERFORMANCE REGIME
- PERFORM SYSTEM TRADES

Figure 6

CONTROL DESIGN DRIVERS

(HOOP/COLUMN)

In addition to attitude control, there are other important control requirements (fig. 7) as discussed in the following:

The feed and the dish are physically separated but are connected by the flexible mast. Their relative stability must be maintained, or dish pointing error and antenna defocus error can result.

The dish itself is also flexible. Its vibration or deformation can cause dish surface error, resulting in RF gain loss.

Consider the Z-axis inertia given in figure 4. Except the mass of the hoop, other system mass is largely concentrated along the mast or the Z-axis. Therefore 80% of the Z-axis inertia is contributed by the hoop. But the stiffness associated with hoop rotation is relatively small. As a result, the frequency associated with the rotation of the hoop may be low, which can cause control/structure dynamics interactions.

Furthermore, consider a situation where dynamic coupling can occur. Suppose a control action is applied at the bus as shown, to correct errors associated with the antenna feed positions. As indicated the distortion of the dish, the mast and the hoop can result.

All these problems can be compounded by the model uncertainty problem, which refers to the dynamic discrepancy that always exists between the on-board controller model and the real structure. Later on reasons for this discrepancy will be given and the resulting problem will be quantified.

- MAINTAIN STABILITY AND ACCURATE RF POINTING BY MINIMIZING
  - ATTITUDE ERRORS
  - FEED DISPLACEMENT
  - DISH DEFORMATION
  - HOOP ROTATION
- ACHIEVE PRECISION CONTROL IN THE PRESENCE OF
  - MODEL UNCERTAINTY
  - DYNAMIC COUPLING

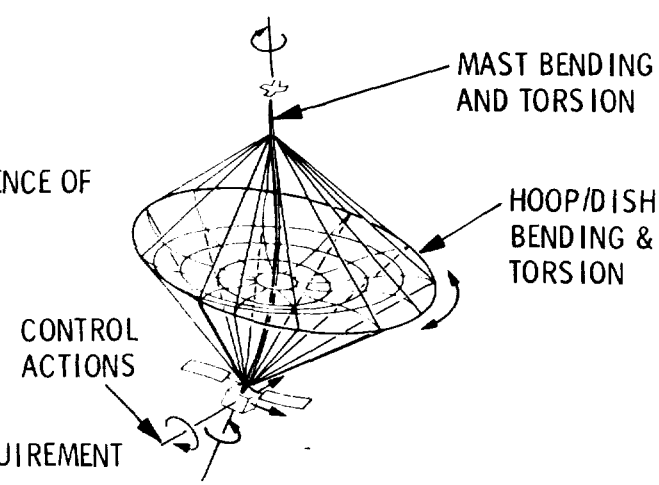

LMSS CONTROL REQUIREMENT

	SYSTEM	CONTROL SUBSYSTEM
POINTING ACCURACY	0.10^0	0.03^0
STABILITY	0.03^0	0.02^0
SURFACE ACCURACY	12 mm	6 mm

Figure 7

CONTROL HIERARCHY

(HOOP/COLUMN)

There are a number of control options for the hoop/column antenna systems. Applicability of each option depends on factors such as mission objectives, system accuracy requirements, disturbance environment, and cost and risk involved.

As described earlier, fundamental elements of the hoop/column system are the bus, the feed, and the hoop. (See fig. 1.) It is thus reasonable to first consider a lumped controller located at either the bus or the feed. When the controller is located at the bus, it is referred to as the bust controller. Similarly, when the controller is located at the feed, it is referred to as the feed controller.

Both the bus and the feed controllers are referred to as single-site controllers. Either controller is assumed to have attitude sensing and torque actuation capabilities like current spacecraft attitude controllers.

A natural extension of the single-site controller is the two-site controller, which calls for attitude sensing and torque actuation at the bus and at the feed.

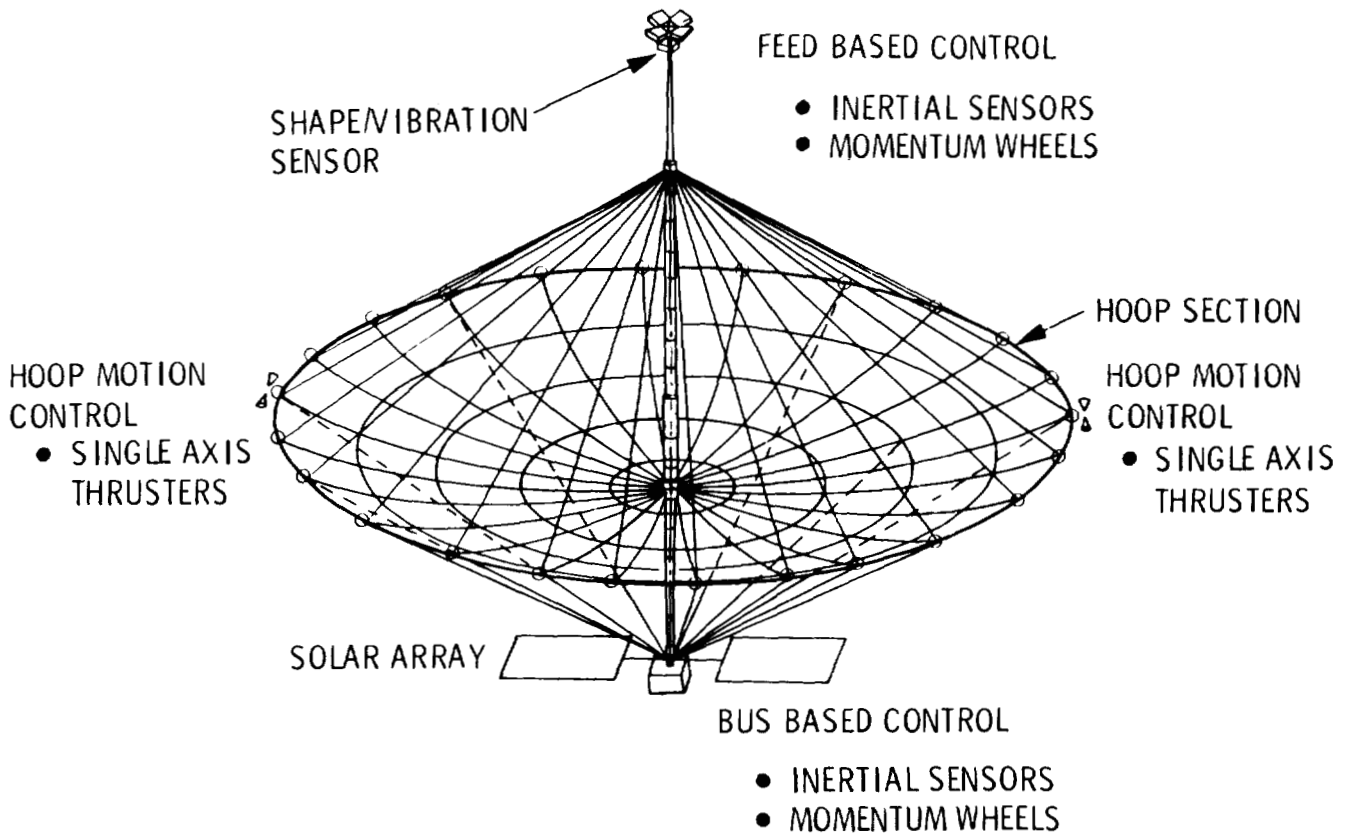

Figure 8

CONTROL HIERARCHY - Continued

(HOOP/COLUMN)

The third system is the two-site controller plus hoop motion sensing and hoop rotation control. Hoop motion sensing can be performed with either inertial or optical sensors. Hoop rotation control can be achieved with single axis thrusters.

The fourth system is the third system plus static or dynamic dish shape control with existing control stringers. This system may be required for missions of very high performance.

Single-site and two-site controllers represent current technology and they were considered for the hoop/column systems. Their results will be presented shortly. The third and fourth systems represent reasonable extrapolations of current technology and are under study. (See fig. 9.)

1. SINGLE-SITE CONTROL WITH INERTIAL SENSORS AND ACTUATORS AT SPACECRAFT BUS OR FEED

2. TWO-SITE CONTROL WITH SENSORS AND ACTUATORS AT BOTH BUS AND FEED

3. FEED-DISH-HOOP MOTION CONTROL WITH HOOP ACTUATORS AND SENSOR

4. "3" + SURFACE SHAPE CONTROL

Figure 9

CONTROL/DYNAMICS SIMULATION SYSTEM

(HOOP/COLUMN)

In order to evaluate control performance, a simulation software program was developed, and its block diagram is shown in figure 10.

It consists of 3 major blocks, one of which is the control system representing either single-site or two-site controllers as discussed earlier. The second block represents the structural model for the hoop/column antenna system. The parameters of the antenna model can be changed and the resulting performance is computed and recorded in the performance evaluation block. Various performance parameters can be obtained.

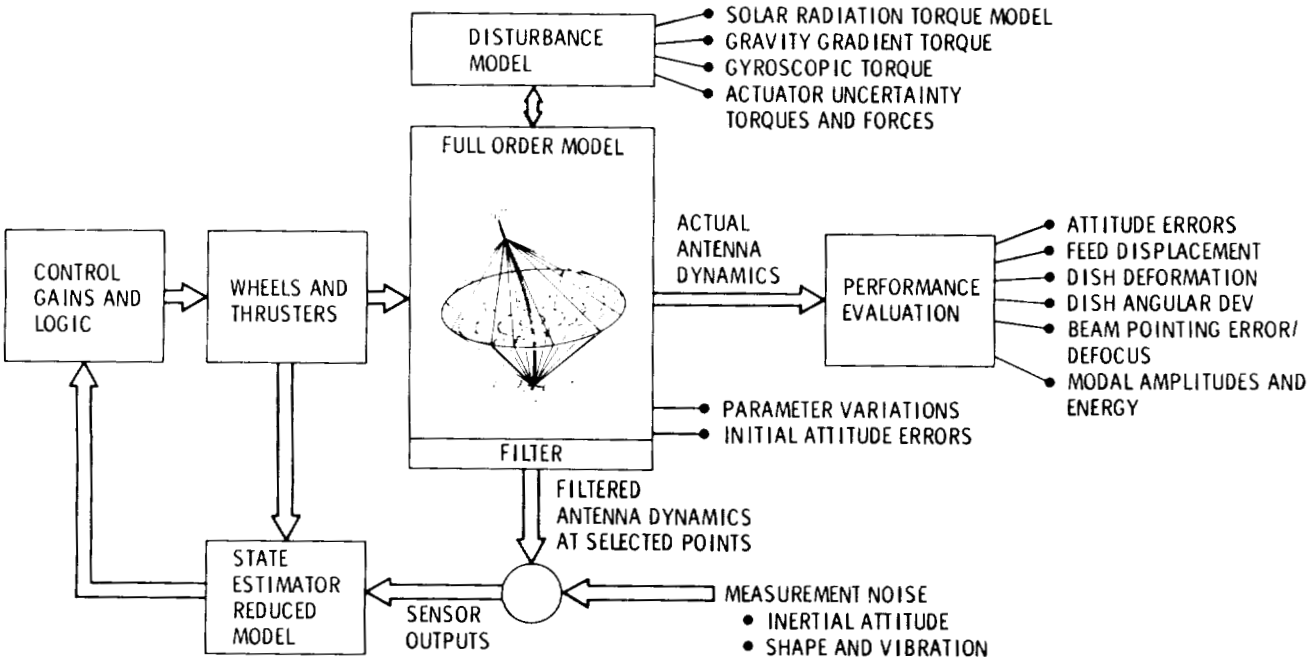

Figure 10

64-m DIAMETER HOOP/COLUMN ANTENNA

CHARACTERISTICS

The best available model for the hoop/column antenna system is the 64-m diameter model developed by the Harris Corporation and is shown in figure 11. It was therefore integrated in the control simulation program.

- MODAL FREQUENCIES

NO.	FREQ, HZ	DESCRIPTIONS
7	0.10	1ST MAST TORSION
8	0.43	1ST MAST ROLL BENDING
9	0.43	1ST MAST PITCH BENDING
10	0.58	2ND MAST TORSION
11	1.07	3RD MAST TORSION
12	1.83	2ND MAST/DISH ROLL BDG
13	1.90	2ND MAST/DISH PITCH BDG
14	3.20	DISH WARPING
15	3.28	DISH WARPING
16	3.36	DISH WARP MAST BENDING
17	3.37	DISH WARP MAST BENDING
18	4.43	DISH WARP MAST BENDING

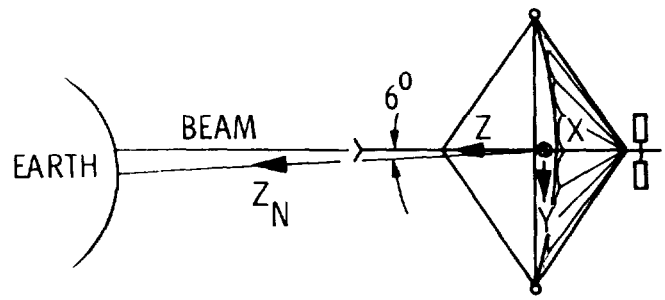

- 64-mD ANTENNA
- QUAD-APERTURE

- MASS PROPERTY
  - MASS: 2790 kg
  - MOMENT OF INERTIA
    1.42×10^6 kg-m^2
    1.42×10^6
    2.73×10^5
  - BALANCED CONFIGURATION

- MAX DISTURBANCE TORQUES
  - GRAVITY GRADIENT 1.89×10^{-3} N-m
  - GYROSCOPIC 6.30×10^{-4}
  - SOLAR PRESSURE 6.23×10^{-3}

Figure 11

122-m DIAMETER HOOP/COLUMN CONFIGURATION

LMSS POINT DESIGN

An ongoing effort at Harris aims to develop a 122-m diameter model to represent the LMSS design. Modal frequencies for the 122-m model as currently estimated by the Harris Corporation are shown in figure 12. The 122-m model development is expected to be completed in January and the resulting model will be integrated into the control simulation program.

- ESTIMATED MODAL FREQUENCIES

NO.	FREQ, HZ	DESCRIPTIONS
7	0.35	MAST TORSION
8	0.18	ROLL BENDING
9	0.18	PITCH BENDING
10	0.31	MAST TORSION
11	0.56	MAST TORSION
12	0.95	MAST/DISH ROLL BENDING
13	0.99	MAST/DISH PITCH BENDING
14	1.68	DISH WARPING
15	1.71	DISH WARPING
16	1.76	DISH WARPING MAST BENDING
17	1.77	DISH WARPING MAST BENDING
18	2.42	DISH WARPING MAST BENDING

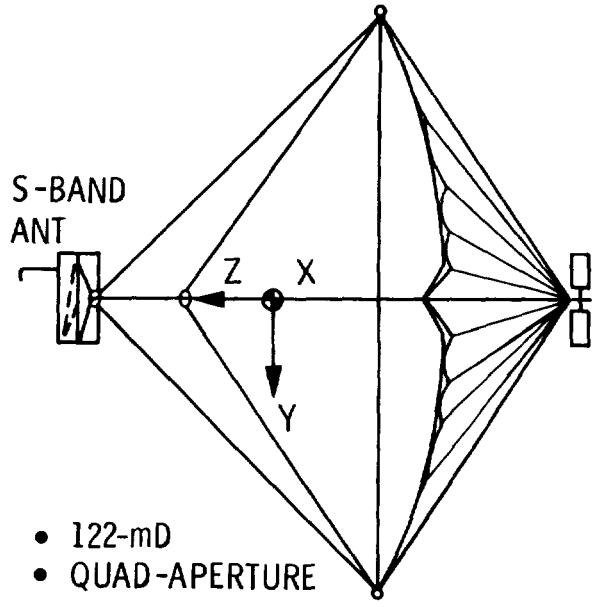

- MASS PROPERTY
  - MASS: 4218 kg (9279 LB)
  - MOMENT OF INERTIA
    7.53×10^6 kg-m^2
    7.56×10^6
    1.49×10^6
  - BALANCED CONFIGURATION

- MAX DISTURBANCE TORQUES
  - GRAVITY GRADIENT 1.0×10^{-2} N-m
  - GYROSCOPIC 3.3×10^{-3}
  - SOLAR PRESSURE 2.48×10^{-2}

Figure 12

MODELING PROBLEMS

(HOOP/COLUMN)

With antenna models selected and control systems designed, control performance of the hoop/column antenna system can be evaluated. However, control performance evaluation will not be complete, if model uncertainty is not considered. Again, model uncertainty here refers to the dynamics discrepancy that always exists between on-board controller model and the real large space system. Figure 13 illustrates that large space systems are characterized by nonlinearities, infinite degrees of freedom, flexibility, parameter changes, etc. Due to practical limitations, the best model available is often represented by a linear finite-element model of very high dimension. Even if the on-board controller can implement this very best model of very high dimension, there still exists a dynamic discrepancy between the on-board controller model and the real large space system. Therefore in control performance evaluation, model uncertainty is considered a significant control system design driver.

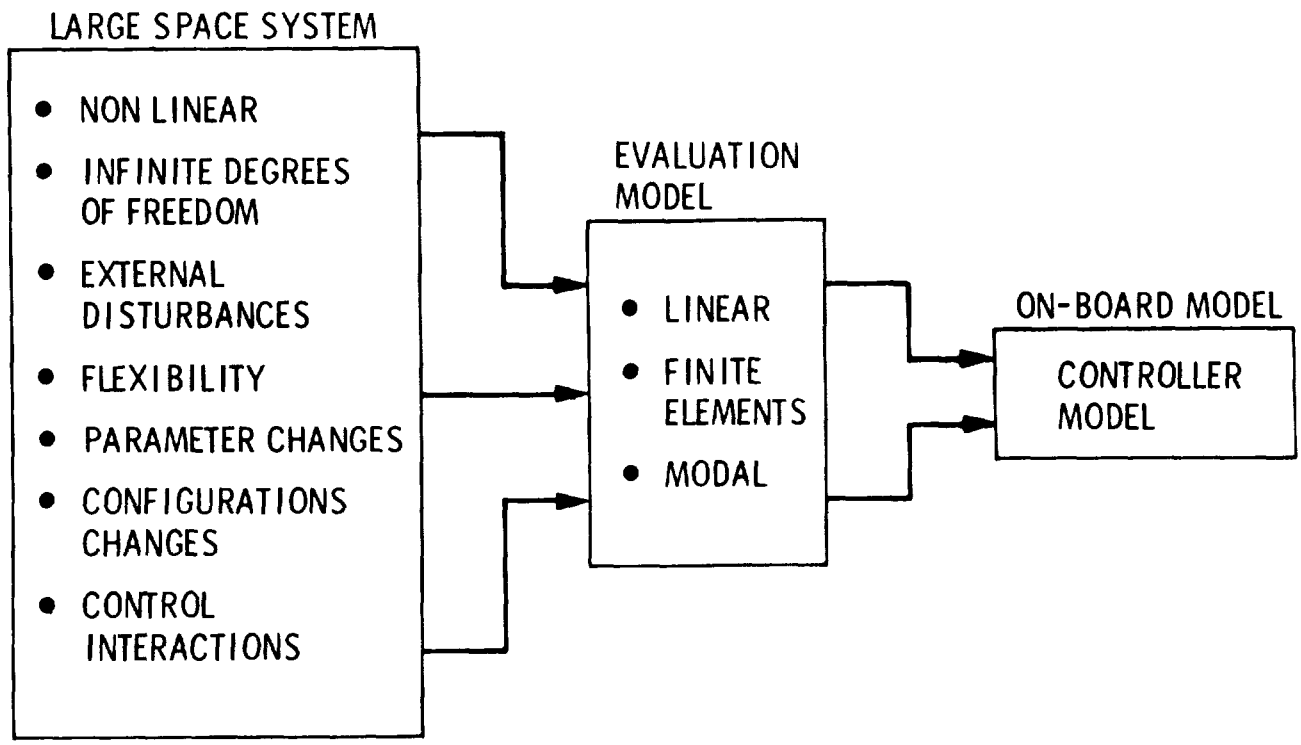

- LARGE STRUCTURES ARE INFINITE-DIMENSIONAL SYSTEMS THAT CANNOT BE COMPLETELY MODELED

Figure 13

CONTROL SENSITIVITY SUBJECT TO PARAMETER ERRORS

(HOOP/COLUMN)

For the hoop/column antenna, figure 14 illustrates that significant changes in control performance can occur when the modal frequencies of the actual hoop/column antenna system are different from those of the on-board controller model. First consider the feed controller. Suppose in this case the dish surface error is 1 mm, when the actual system frequency is the same as the design frequency. As the actual system frequency differs from the design frequency, the dish surface error may increase or decrease. But, as the actual system frequency is reduced by more than 20% or increased beyond 30%, the feed controller becomes unstable.

For the bus controller, the result indicates that the performance is relatively better than that of the feed controller. But the system becomes unstable when the actual system frequency is reduced by 20% or increased by 17%.

Figure 14 further illustrates that the two-site controller with attitude sensing and torque actuation at both the bus and the feed can perform better and can be more robust than the other two controllers. This means that the model undertainty problem can be reduced by different control designs.

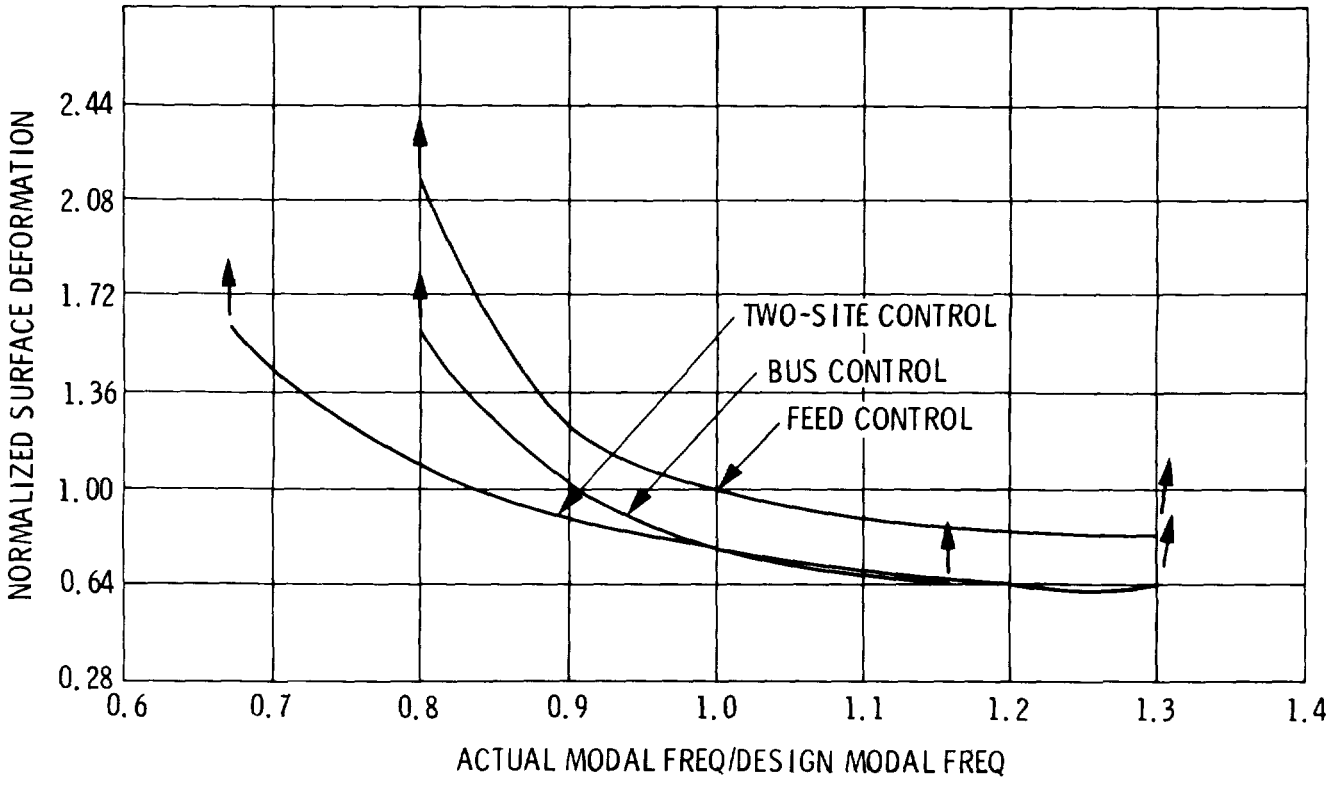

Figure 14

TWO-SITE CONTROL PERFORMANCE SENSITIVITY

TO PARAMETER ERRORS

(HOOP/COLUMN)

The other antenna performance parameters exhibit similar results as the actual system frequency differs from the design frequency. For example, in the case of the two-site controller, the bus pointing, in general, is better than the feed pointing until the control system becomes unstable. The feed/dish relative displacement error exhibits similar results as indicated in figure 15.

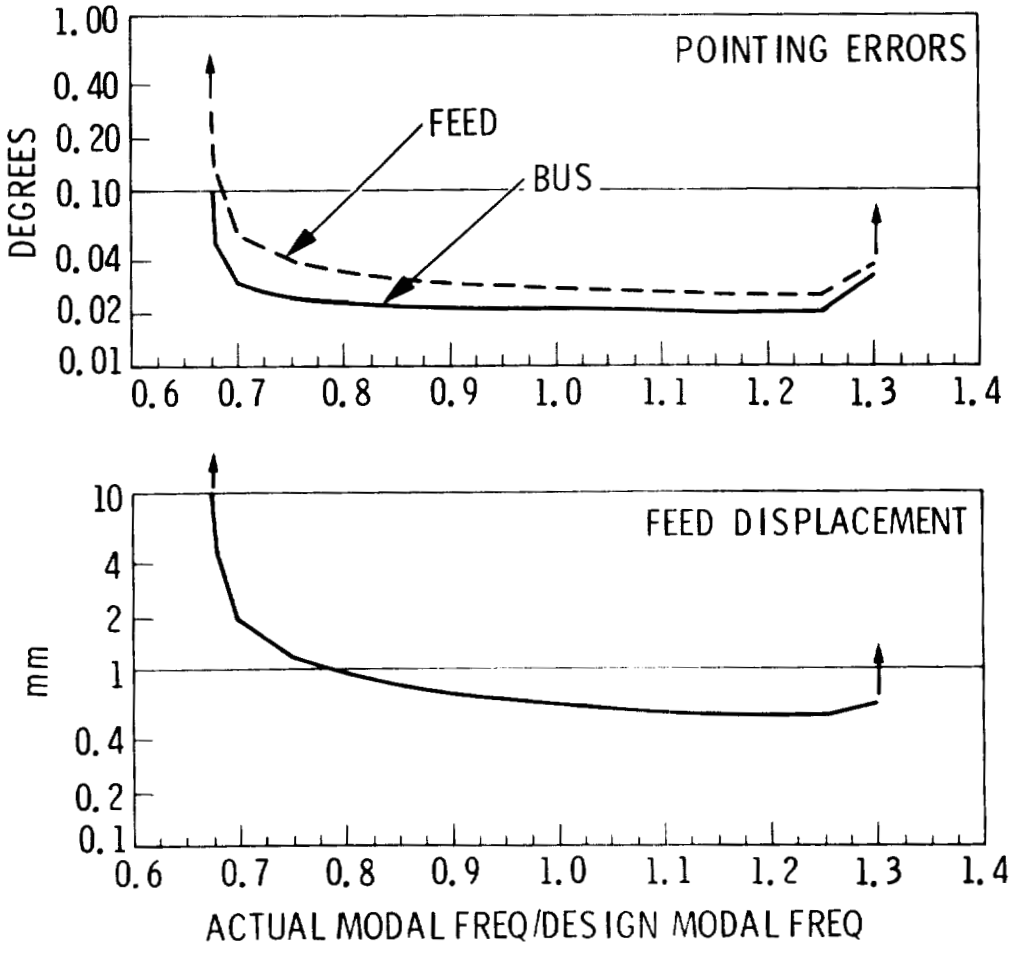

Figure 15

IDENTIFICATION OF CRITICAL MODAL PARAMETERS

(HOOP/COLUMN)

Results of figures 14 and 15 are summarized in the bottom of figure 16 as the category of all modes. For example, the feed control and the bust control both become unstable as the actual system frequencies of all modes are reduced by 20%. Similarly, two-site control remains stable in the region of 0.67 to 1.3 as before.

However, if only frequencies of torsional modes or if only frequencies of bending modes change, different results occur. Figure 16 indicates that as far as the stability is concerned, the accuracy of torsional frequencies is more important than that of the bending frequencies.

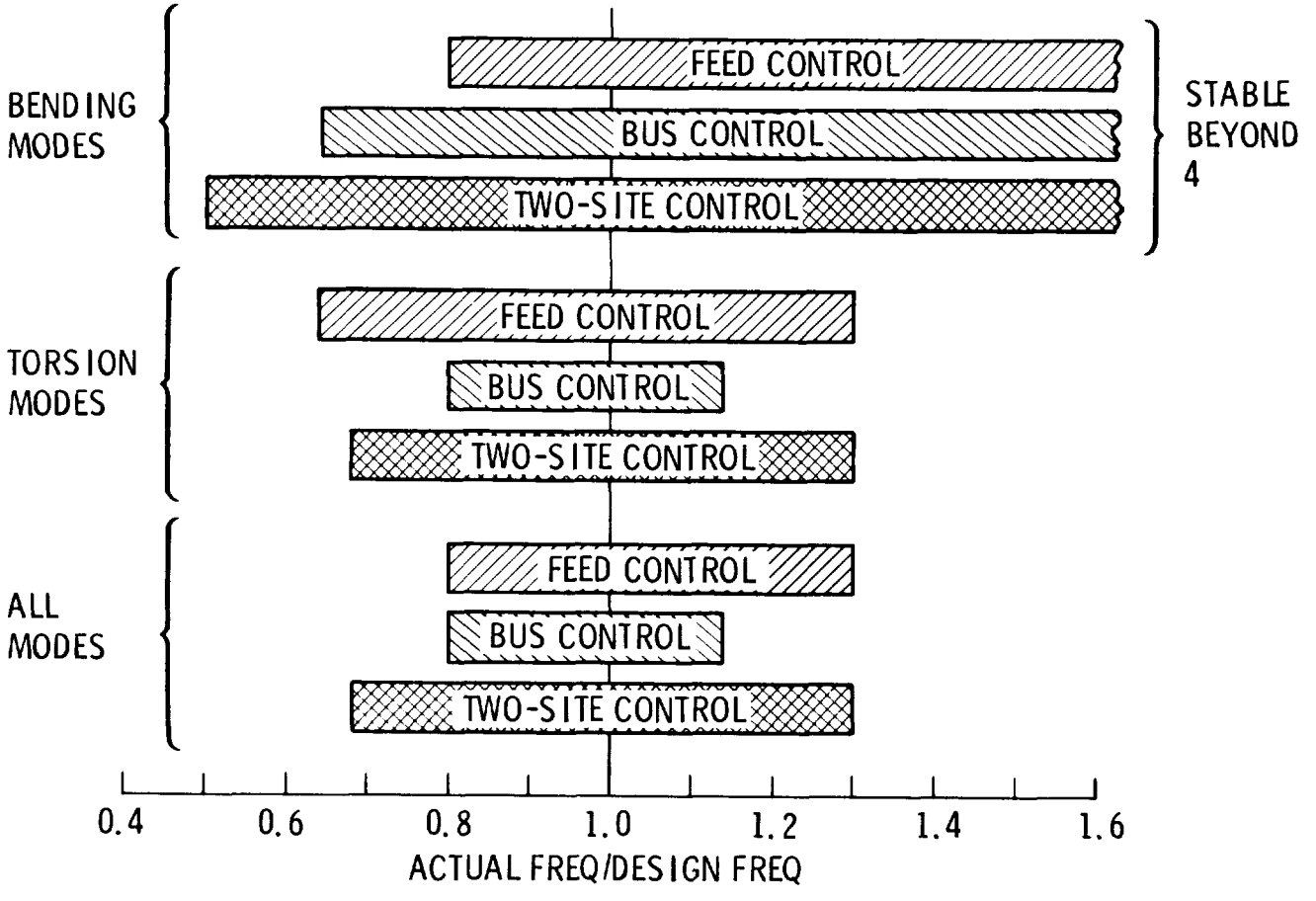

Figure 16

SUMMARY

(HOOP/COLUMN)

- The system drivers are summarized in figure 17 and are the following:

  1. Inevitable uncertainties or dynamics discrepancy that always exists between controller design model and the real structure; this can cause system instability

  2. Low structural frequencies associated with hoop/mast torsions; these modes determine system stability margins

- Two-site control system is more robust than single-site controllers in the presence of system frequency uncertainties

  As the two-site control system concept is applied to the LMSS design, it results in reasonable hardware requirements, the details of which will be reported as part of the LMSS study presentation contained elsewhere within this review.

- Finally, it appears that identification of critical modes can allow a control system to achieve its best performance. However, identification of critical modes must be performed while the large space antenna system is being controlled. The reason is that some modes may be critical to one type of controllers but not critical to others.

- SYSTEM DRIVERS
  - UNCERTAINTIES IN CONTROL/STRUCTURAL INTERACTIONS
  - LOW STRUCTURAL FREQUENCIES
    - HOOP
    - MAST
- TWO-SITE CONTROL SYSTEM
  - MORE ROBUST THAN SINGLE-SITE CONTROLLERS
  - RESULTING IN REASONABLE HARDWARE REQUIREMENTS AS APPLIED TO THE LMSS MISSION
- IDENTIFICATION OF CRITICAL MODES INSURES BEST CONTROL PERFORMANCE

Figure 17

CONTROL PROBLEMS

(WRAP-RIB)

Next, consider the control of wrap-rib antenna systems (fig. 18).

The task is to control the wrap-rib system (fig. 5) to meeting accuracy requirements shown in figure 3. First control problem is associated with the imbalanced configuration of the wrap-rib antenna system. The imbalanced configuration is evidenced by the fact that 80% of system mass is concentrated at the bus area and 20% at the dish area. Therefore, the axis of minimal inertia is 17° off from the local vertical which is the Z-axis in figure 5. This results in a large constant gravity gradient torque on the system with magnitude of 1.14×10^{-2} ft-lb.

Another difficulty caused by the imbalanced configuration is that it results in a large cross product of inertia. This inertia causes significant dynamic coupling between two attitude axes.

For wrap-rib antenna systems, feed and dish are also physically separated but connected with the flexible boom structure. Their relative motions can cause dish pointing and antenna defocus errors.

- IMBALANCED CONFIGURATION
  - LARGE CROSS PRODUCT OF INERTIA
  - COUPLING BETWEEN CONTROL AXES
- FEED/DISH RELATIVE MOTIONS
  - DISH POINTING ERRORS
  - DEFOCUS ERRORS
- DISH VIBRATIONS
  - RF GAIN LOSS
  - COUPLING WITH FEED MOTIONS
- LOW FREQUENCIES OF BOOM
  - CONTROL/STRUCTURE INTERACTIONS
- STRUCTURAL UNCERTAINTIES/MODEL ERRORS
  - ERROR IN BOOM FREQUENCIES

Figure 18

FEED MOTION AND BOOM DISTORTION

(WRAP-RIB)

The 55-m diameter dish is also a flexible structure. Its vibrations will have two distinct impacts on system performance. First, its vibrations can cause dish surface errors, resulting in RF gain loss. Second, its vibrations can couple with dynamics of other parts of the system as illustrated by figure 19. Consider a torsional motion of the dish. It can cause the short boom to bend and twist. The elbow of the boom is translated. As a result, the long boom is bending and the feed/bus is therefore experiencing attitude errors.

Next, all models to date indicate that lowest vibration frequencies of the system are associated with the boom structure. The low frequencies of the boom can cause control/structure interactions, resulting in performance degradation. This problem is further compounded by the model uncertainty problem discussed earlier. Consequently, low frequencies of the boom with uncertain values can cause serious problems such as system instability.

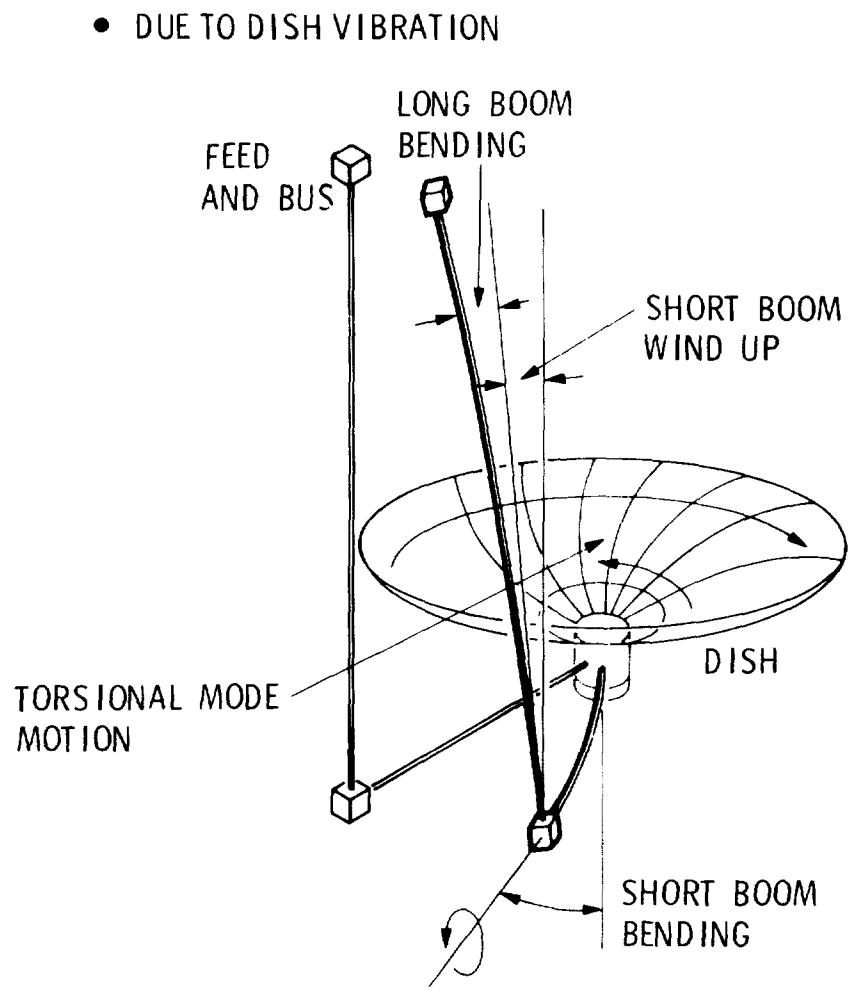

Figure 19

CONTROL SYSTEM HIERARCHY

(WRAP-RIB)

The control system hierarchy is summarized in figure 20.

Control System 1 is typical of the current attitude controllers for 3-axis spacecraft stabilization. Attitude sensors and actuators are lumped together and mounted on the bus of the antenna system. Flexible dynamics associated with the boom and the dish may only be inferred from attitude sensor outputs.

Control System 2 represents a departure from system 1 in that it calls for an optical sensor at the bus to perform multipoint distributed sensing of the dish. The reason for having this sensor is to obtain information about flexible dynamics of the boom and the dish directly. Since the information about feed/dish relative motion is measured and available, it is possible to control this motion with reduced performance sensitivity to uncertainties associated with boom dynamics. However, the control is still performed at the bus.

Control System 3 represents system 2 plus extra control authority at the hub of the dish to stabilize boom motions. The reason is that it is difficult to control boom motions such as the short boom twist with a controller at the bus that is 80 meters away. This is exactly what happens as will be illustrated in detail.

Control System 4 may be reasonable for missions with even more stringent requirements. For LMSS, however, Systems 1, 2, and 3 were considered and their results will be presented.

1: LUMPED CONTROLLER AT SPACECRAFT BUS

2: "1" + MULTIPOINT SENSING OF DISH

3: "2" + CONTROLLER AT HUB OF DISH

4: "3" + DISTRIBUTED CONTROL OF DISH AND BOOM

Figure 20

ILLUSTRATION OF CONTROL HIERARCHY

(WRAP-RIB)

The control hierarchy is illustrated by figure 21.

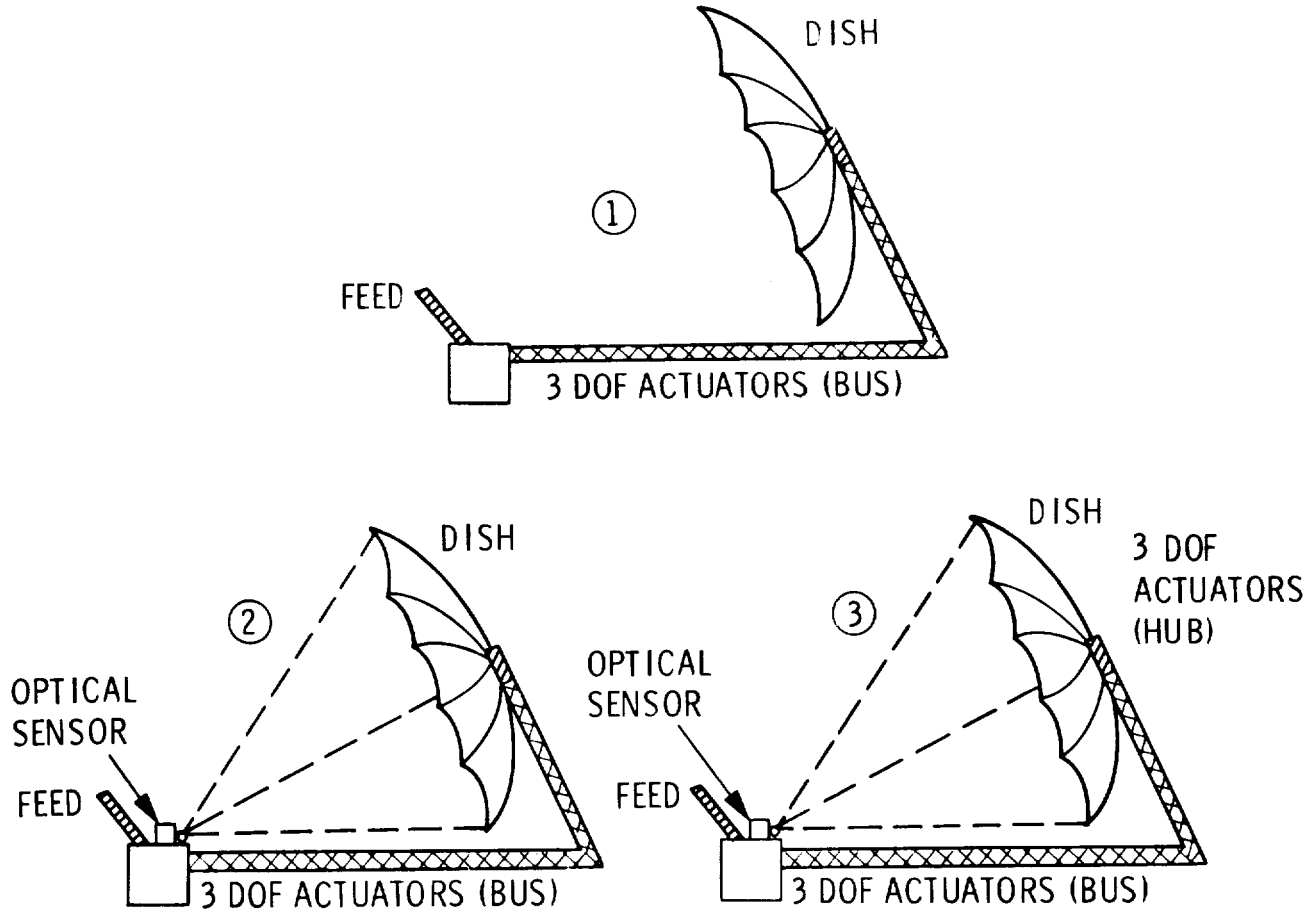

Figure 21

THE FINITE-ELEMENT STRUCTURAL MODEL

(WRAP-RIB)

Before presenting results of these control systems, a description is given here for the antenna models on which control performance is evaluated.

Part of the model development work has been geared to capture the characteristics of the LMSS as much as possible. Therefore, a finite-element model (fig. 22) was developed to represent the wrap-rib configuration of the LMSS. The details of this work are contained in the presentations by R. Freeland and M. El-Raheb of JPL (refs. 1 and 2). It is noted that lowest system vibration frequencies in this model involve boom distortions as indicated in modes 1, 2, and 3. In particular, the first flex mode is associated with the short boom twist with a frequency of about 0.087 Hz.

FLEX MODE	FREQ (Hz)	DESCRIPTION
1	0.0872	SHORT BOOM TORSION
2	0.1473	DISH TORSION, LONG BOOM TWIST
3	0.1965	DISH TORSION, LONG BOOM BENDING
4	0.2062	DISH BENDING
5	0.2201	DISH BENDING, LONG BOOM BENDING
6	0.2906	DISH TORSION
7	0.6644	DISH ROTATION, LONG BOOM BENDING

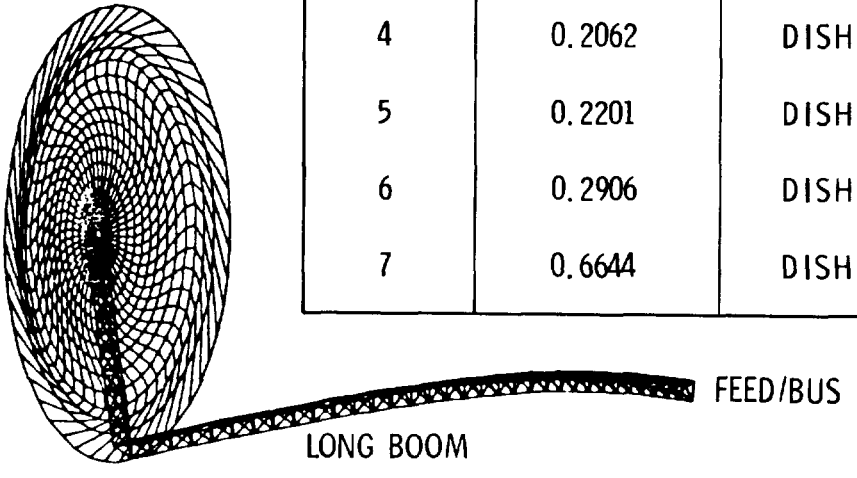

Figure 22

PARAMETRIC MODELS FOR CONTROL STUDIES

(WRAP-RIB)

To undertake control studies for the antenna system, parametric models (fig. 23) of the wrap-rib antenna system were also developed. It is noted that in the nominal case where there are no parameter errors, the mode frequencies and mode shapes of the parametric model are very close to those in the finite-element model. However, the development of parametric models is intended to have the following advantages. It allows easy and inexpensive change in model parameters, such as modal damping, boom stiffness, and mass of dish, bus, or feed, so that it can predict changes in system behavior as a result of model parameter change. It also permits simulation of different control concepts such as distributed sensing of dish and actuations at bus, at hub, or at both locations. Therefore, this capability is vital to control designs and sensitivity analyses.

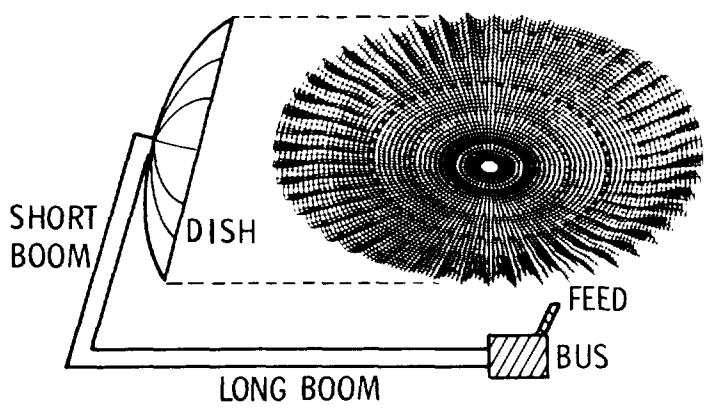

MODE	NOMINAL FREQ (Hz)	DESCRIPTION
1	0.0874	SHORT BOOM TORSION
2	0.1493	DISH TORSION, LONG BOOM TWIST
3	0.1826	DISH TORSION, LONG BOOM BENDING
4	0.2117	DISH BENDING
5	0.2285	DISH BENDING, LONG BOOM BENDING
6	0.4250	DISH TORSION
7	0.7575	DISH ROTATION, LONG BOOM BENDING

- VERY GOOD MATCH WITH THE F. E. MODEL IN THE NOMINAL CASE
- VERY EASY TO CHANGE MODEL PARAMETERS
- VERY EASY TO SIMULATE DIFFERENT CONTROL MECHANIZATION CONCEPTS
- NECESSARY FOR CONTROL DESIGNS AND SENSITIVITY ANALYSES

Figure 23

AUTOMATION OF CONTROL DESIGN AND SENSITIVITY ANALYSIS

(WRAP-RIB)

To perform control and sensitivity analysis requires handling a large amount of data. To eliminate major manual operations and human errors, a software program was developed. Similar to the one for hoop/column studies this program consists of three major elements (fig. 24), one of which is the antenna model with parameters at selected values. The second block is the control and estimation element which simulates mechanizations of control systems 1, 2 and 3 as described earlier. The last element consists of all subroutines for computing antenna performance parameters such as dish surface RMS errors, dish pointing errors, and feed/dish relative displacements.

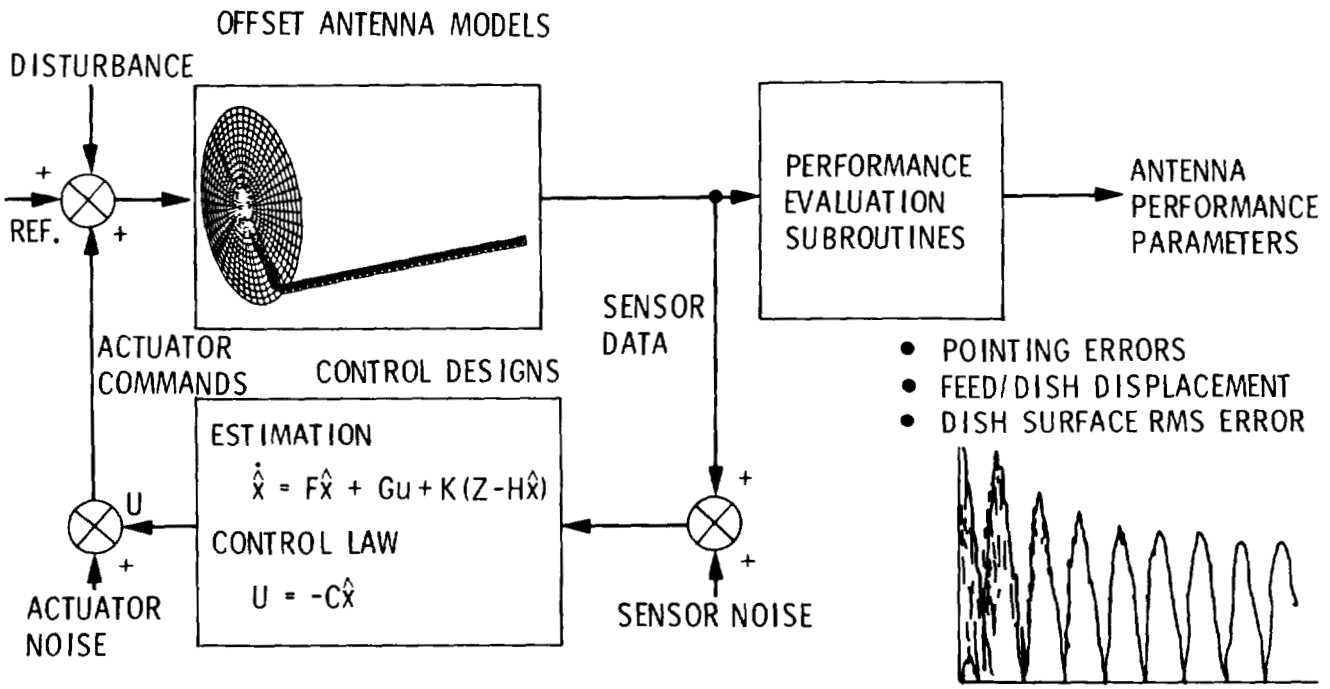

Figure 24

ANTENNA CONTROLLER DESIGNS BASED ON RF PERFORMANCE

(WRAP-RIB)

This simulation program (fig. 25) is currently being updated to include an RF model for the prediction of RF performance such as RF gain, sidelobe levels, and RF pointing. The purpose of the RF model is to permit antenna control designs based on RF performance, which should be the ultimate parameter to be optimized.

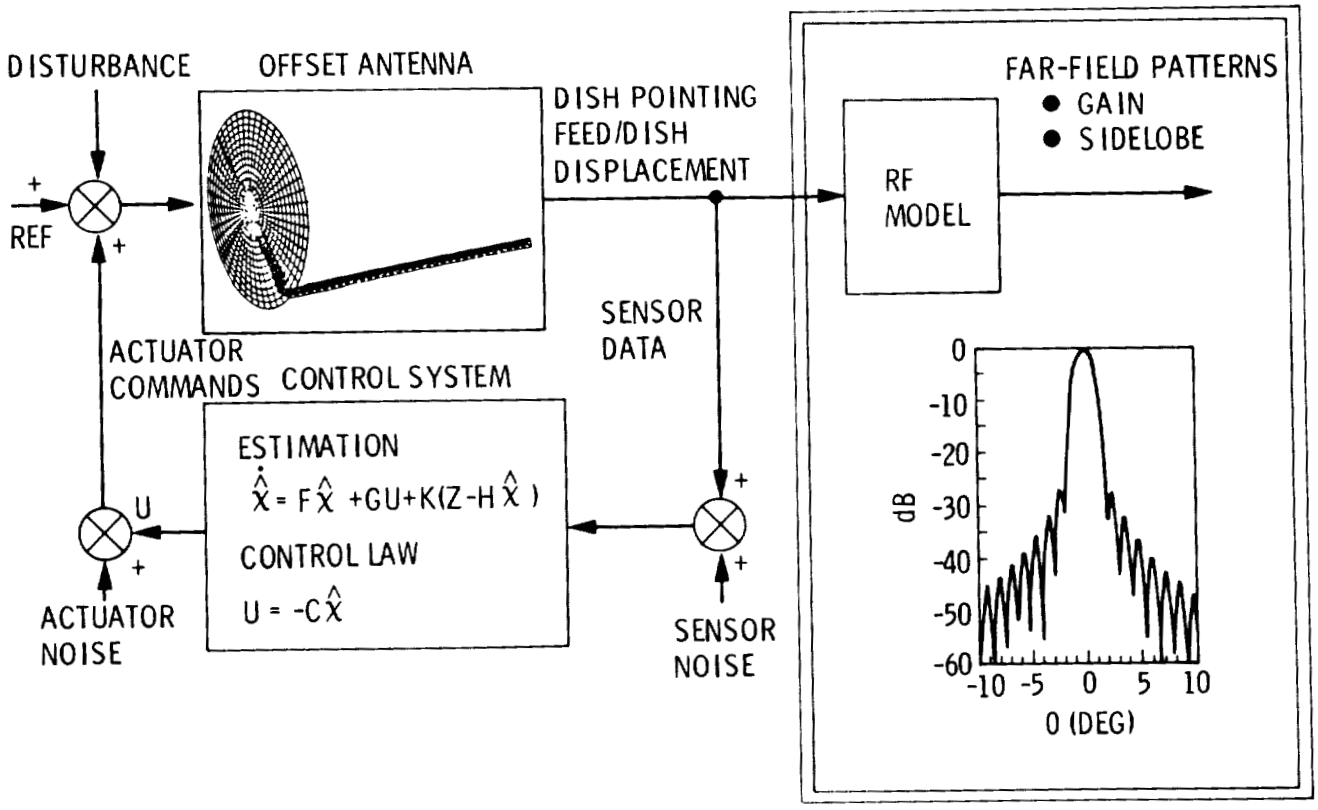

Figure 25

DISH LINE-OF-SIGHT STABILITY

(WRAP-RIB)

Consider the first case where actual boom frequencies are the same as the boom frequencies used in the control designs. Figure 26(a) shows the dish LOS stability error as a result of having 1 newton-meter sinusoidal disturbance torque applied to the antenna. For example, in cases where the disturbing sinusoidal torque has the same frequency as the first vibration frequency of the antenna at 0.55 rad/sec, the dish LOS error will be 0.03° for control system 1, 0.015° for control system 2, and 0.002° for control system 3. This means that having capabilities of optical sensing and extra control at dish hub, system 3 is able to bring peak errors down by an order of magnitude and distribute the errors in a harmless manner.

In addition, system 3 provides performance more stable and robust than the other two systems as actual boom frequencies decrease. This is illustrated in figures 26(b) and (c). As actual boom frequencies decrease to 62.5% of the design frequencies, the peak LOS errors for system 3 is about 2.5 times better than that of system 2, whereas system 1 is already unstable. Similarly, in the last case where actual boom frequencies are 60% of the design boom frequencies, the peak LOS error for system 3 is at about 0.02°, and both system 1 and system 2 are unstable.

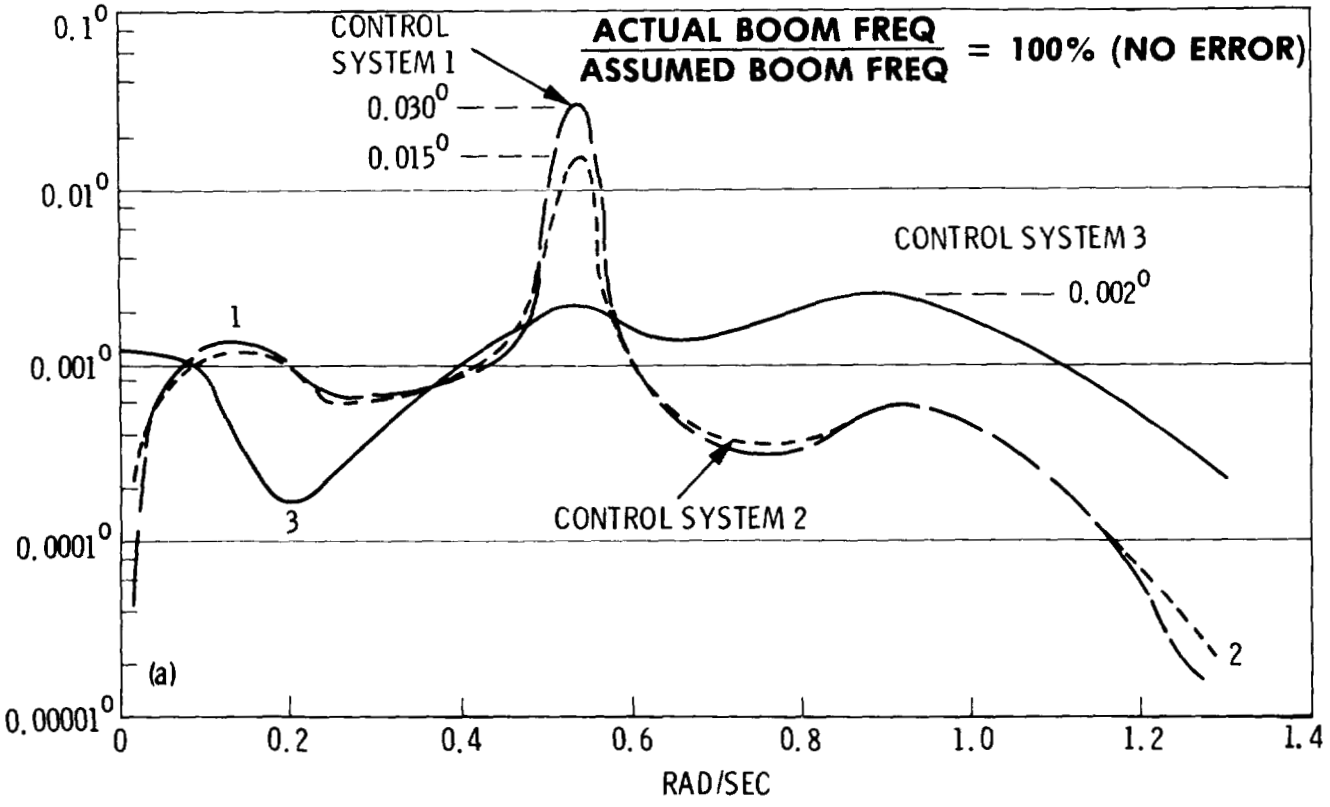

Figure 26

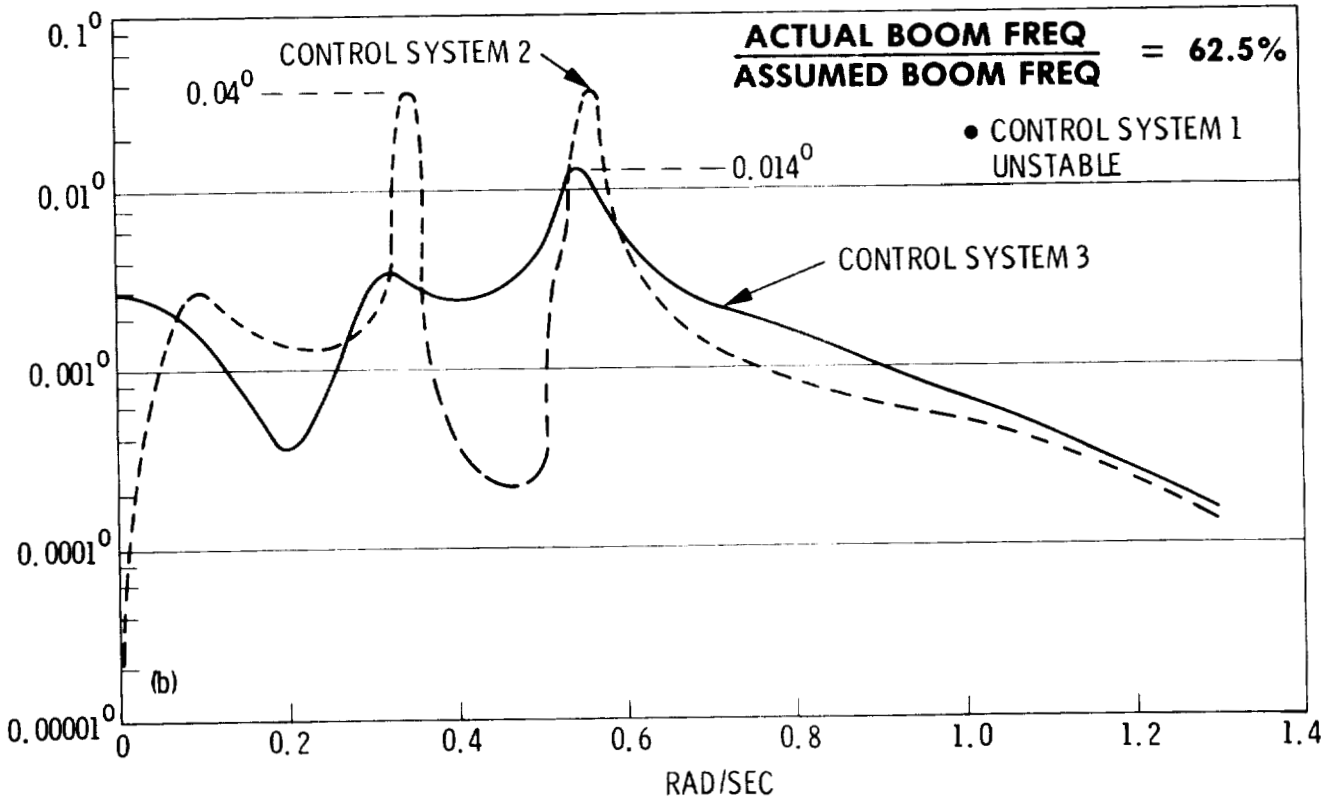

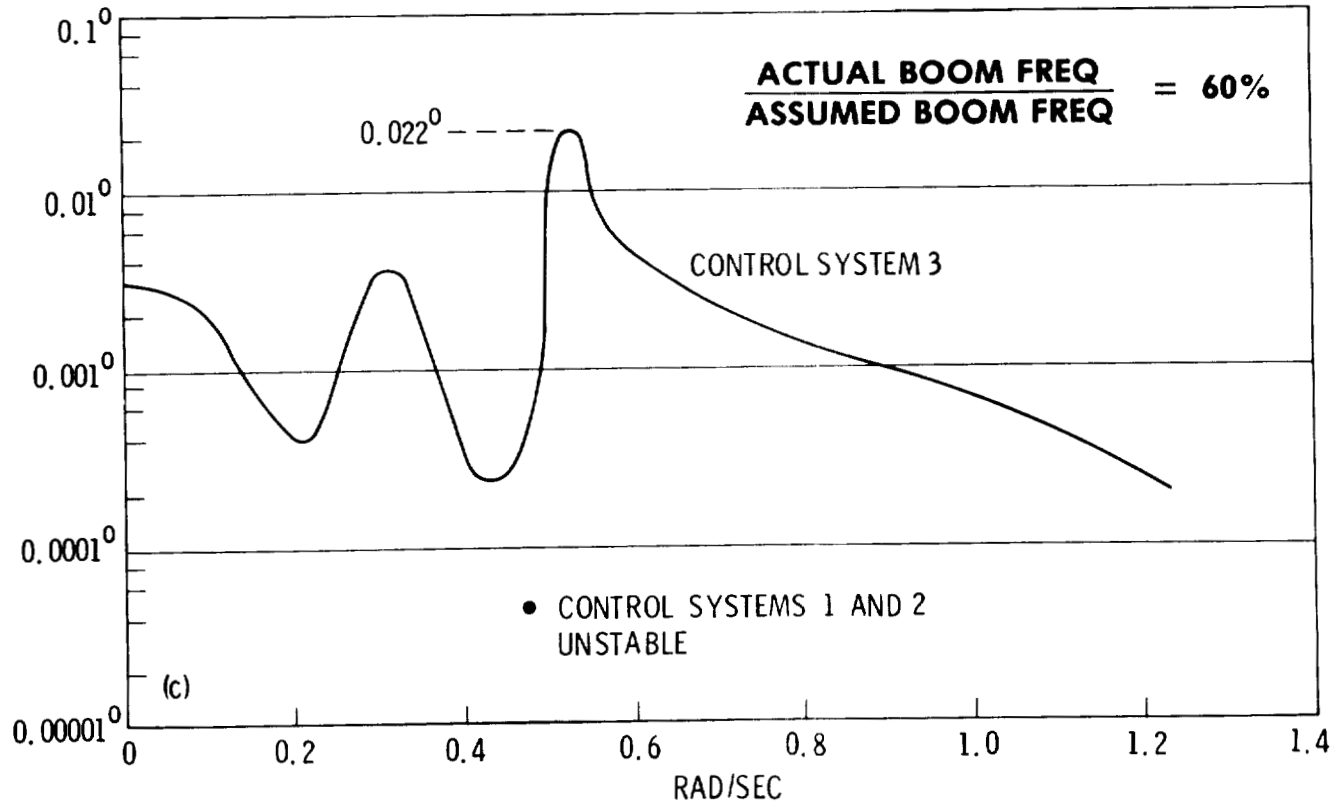

Figure 26.- Concluded.

SUMMARY OF RESULTS (DISH LINE-OF-SIGHT

STABILITY: PEAK ERROR)

(WRAP-RIB)

To summarize results obtained to date, dish LOS stability error is again used as an example in figure 27 to show performance and sensitivity results of three control designs. It is noted that performance of system 3 is much better than the performance of the other two systems as mentioned earlier. Furthermore, as boom frequency reduces, system 3 is more stable and robust than the other two systems.

From these results, it appears that uncertainties in boom dynamics and its stiffness (frequency) are very critical to the definition of control systems for the wrap-rib antenna systems.

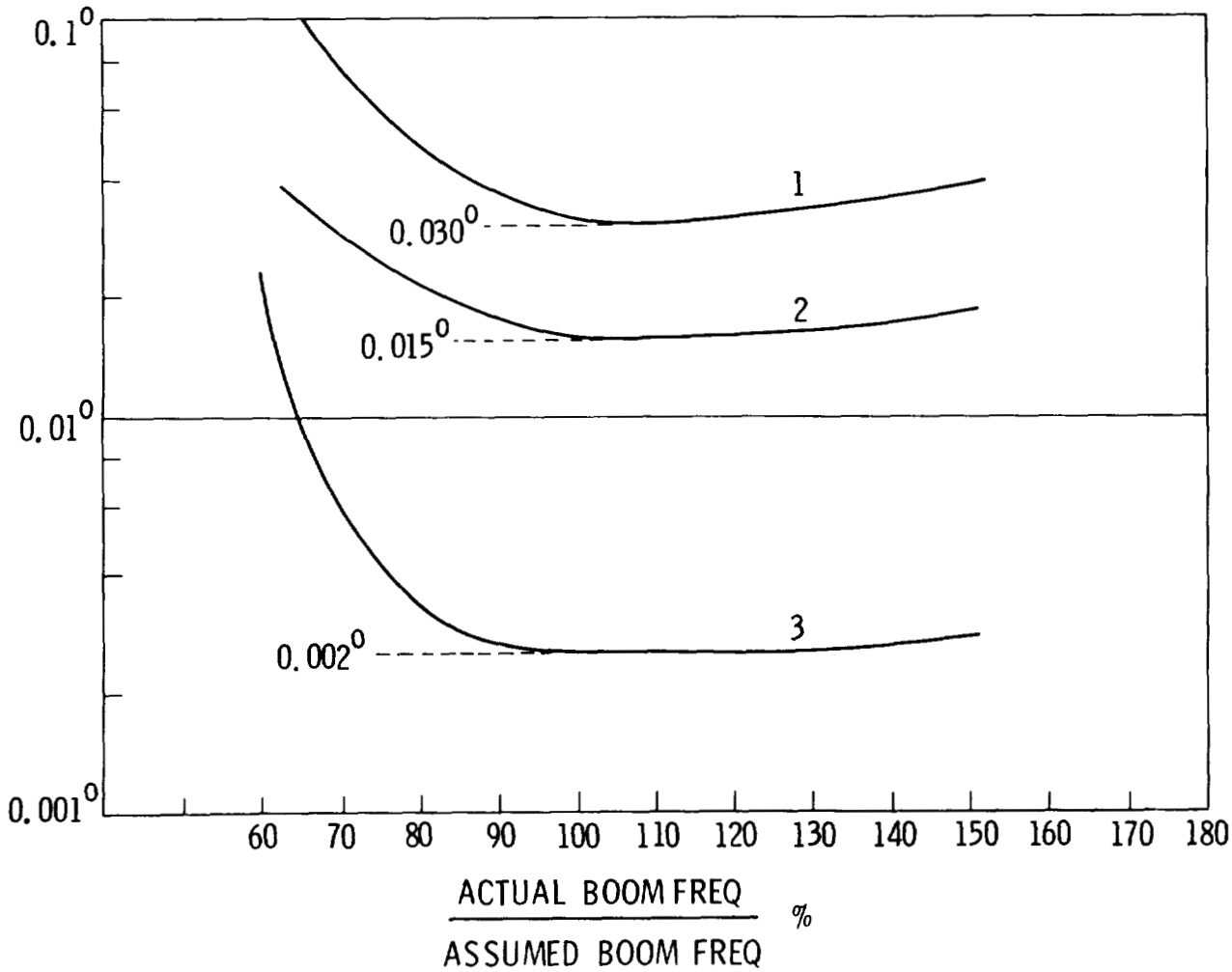

Figure 27

SUMMARY

(WRAP-RIB)

Figure 28 is a summary of what has been presented on the control of wrap-rib antenna systems:

1. First, the system drivers are the following:

The inevitable errors or discrepancies between the on-board controller design model and the real structure. The most critical vibration of the wrap-rib antenna appear to be the short boom twist and the torsion about antenna line of sight.

2. Control System 3 appears effective in stabilizing the short boom twist, which is the most critical of all vibrations. As system 3 is applied to the LMSS mission, it results in an average power requirement of 260 watts and ACS weight of about 1000 lb. which are considered very reasonable. Again, the details of this work will be presented as part of the LMSS control subsystem definition by A. F. Tolivar (ref. 3).

3. As in the hoop/column case, identification of critical modes can allow a control design to achieve its best performance possible.

- SYSTEM DRIVERS
  - STRUCTURAL UNCERTAINTIES/MODEL ERRORS
  - LOW FREQUENCIES OF BOOM
    - SHORT BOOM TWIST
    - TORSION ABOUT ANTENNA LINE-OF-SIGHT
- CONTROL SYSTEM 3
  - EFFECTIVE IN STABILIZING BOOM MOTIONS
  - RESULTING IN REASONABLE HARDWARE REQUIREMENTS WHEN APPLIED TO THE LMSS MISSION
    - AVG POWER 260 WATTS
    - ACS HARDWARE & PROPELLANT 1010 LB
- IN-ORBIT IDENTIFICATION OF CRITICAL MODES INSURES BEST CONTROL PERFORMANCE

Figure 28

CONCLUSIONS

Conclusions (fig. 29) that can be drawn for the control of large space antenna systems are the following:

1. Important control system drivers for the hoop/column configuration are dynamics associated with hoop rotations, and for the wrap-rib configuration are dynamics associated with the boom.

2. Model uncertainty as defined in this presentation results in control performance degradation. This has been established quantitatively for both antenna systems.

3. System instability can occur if uncertainties are sufficiently large.

4. Because flight data base for large space systems is nonexistent, large uncertainties will occur.

5. To demonstrate technology and to increase flight data base, in-flight experiments are necessary.

- BOOM AND HOOP DYNAMICS ARE IMPORTANT CONTROL SYSTEM DRIVERS
- UNCERTAINTY IN CONTROL/STRUCTURE INTERACTIONS RESULTS IN CONTROL PERFORMANCE DEGRADATION
- INSTABILITY OCCURS IF UNCERTAINTIES ARE SUFFICIENTLY LARGE
- LARGE UNCERTAINTIES WILL OCCUR BECAUSE FLIGHT DATA BASE IS NONEXISTENT
- IN-FLIGHT EXPERIMENTAL IDENTIFICATION OF CONTROL/STRUCTURE INTERACTIONS WILL DEMONSTRATE TECHNOLOGY AND INCREASE DATA BASE

Figure 29

PLANNED WORK

The planned work is summarized in figure 30 as follows:

1. Control Synthesis

Control design and evaluation for both antenna concepts are to be directed toward specific point designs in order to achieve maximum results. In particular, additional system drivers will be identified. Control performance sensitivity to uncertainties such as truncation errors, nonlinearities, and hardware constraints will also be determined.

2. Control Experiment Definition

Definition tasks for such a flight experiment involve the following areas. First, control goals and requirements must be defined. Then control hardware mechanization and requirements for the experiment are to be defined so that the experiment implementation can proceed.

The experiment can be designed to have its own control system or to utilize the reaction control system on board the shuttle. For either case, dynamics interactions between the shuttle and the experiment must be carefully examined to ensure the safety of shuttle/experiment.

Instrumentation for modal sensing and excitation is to be identified, selected, and integrated into the experiment. This will allow the proper implementation of sensing and actuation of experiments.

CONTROL SYNTHESIS

- COMPLETE EVALUATION OF SYSTEM DRIVERS
- DETERMINE SENSITIVITY TO UNCERTAINTIES
- ESTABLISH NEW CONTROL TECHNOLOGY PERFORMANCE BOUNDS

CONTROL EXPERIMENT DEFINITION

- DEFINE CONTROL GOALS AND REQUIREMENTS
- ESTABLISH MECHANIZATION APPROACHES
- DETERMINE EXPERIMENT/SHUTTLE CONTROL INTERACTIONS
- IDENTIFY INSTRUMENTATION FOR MODAL SENSING AND EXCITATION
- PERFORM PRELIMINARY DESIGN AND IMPLEMENTATION APPROACHES

Figure 30

REFERENCES

1. Freeland, R. E.: JPL Antenna Technology Development. Large Space Systems Technology - 1981, NASA CP-2215, Pt. 2, 1982, pp. 429-438.

2. El-Raheb, M.: Analytical Performance Prediction for Large Antennas. Large Space Systems Technology - 1981, NASA CP-2215, Pt. 2, 1982, pp. 471-477.

3. Tolivar, A. F.: LSS Control Technology. Large Space Systems Technology - 1981, NASA CP-2215, Pt. 1, 1982, pp. 241-247.

SPATIAL, HIGH-ACCURACY, POSITIONING-ENCODING SENSOR (SHAPES) FOR LARGE SPACE SYSTEM CONTROL APPLICATIONS

J.M. McLauchlan
Jet Propulsion Laboratory
Pasadena, California

Large Space Systems Technology - 1981
Third Annual Technical Review
November 16-19, 1981

INTRODUCTION

The Spatial, High-Accuracy, Position-Encoding Sensor (SHAPES) is a controls sensor suitable for the determination of the static shape and vibrational motion of large space structures and similar systems and for the determination of position and velocity in rendezvous and docking. It uses a combination of electro-optical techniques to measure the three-dimensional coordinates distributed over the structure at reading rates high compared to the rates at which the coordinates are changing. The technical approach is that of measuring the distance to and the direction of points on the structure from a single sensor head. Many points can be measured simultaneously from a single head without significantly increasing the complexity of the system. Figure 1 is a table giving an abbreviated summary of measurement performance requirements for flexible spacecraft control sensors. This table has been compiled from many sources but is generally characteristic of what would be required by large antennas requiring surface accuracies of 1/10 to 1/50 of the operating wavelength. The number of points on the structure which must be sensed for dynamic control is smaller than the entry given in the table for static shape determination by about five times.

	REQUIRED PRECISION	RANGE OF VARIABLE	NUMBER OF MEASURED POINTS	BANDWIDTH
RANGE	±0.2 mm TO ±0.03 mm	±0.1 m	50 TO 150 (STATIC SHAPE)	0.1 Hz TO 10 Hz
LATERAL DISTANCE				
ANGULAR DISPLACEMENT	±2 arc sec TO ±0.1 arc sec	±3 arc min		
ROTATION				
TWIST				

Figure 1

SHAPES -

SPATIAL, HIGH-ACCURACY, POSITION-ENCODING SENSOR

The basic components of the system are illustrated in figure 2. A pulsed light source floods the area containing the points to be measured with light. The points are designated by reflectors. The light returned to the sensor head from the reflectors is imaged on a streak tube. The tube can be operated in two modes: (1) a non-swept one which determines the location of the images on the face of the tube and (2) a swept mode which determines the time of arrival of the returned pulses. The first mode is used to determine the directions of the reflector from the sensor head while the second is used to determine their distances. The accuracy of the time-of-flight measurements is greatly increased by providing a fiber reference signal via a fiber-optics link and measuring the differences in the time of arrival of the pulses from the reflector and the reference pulses.

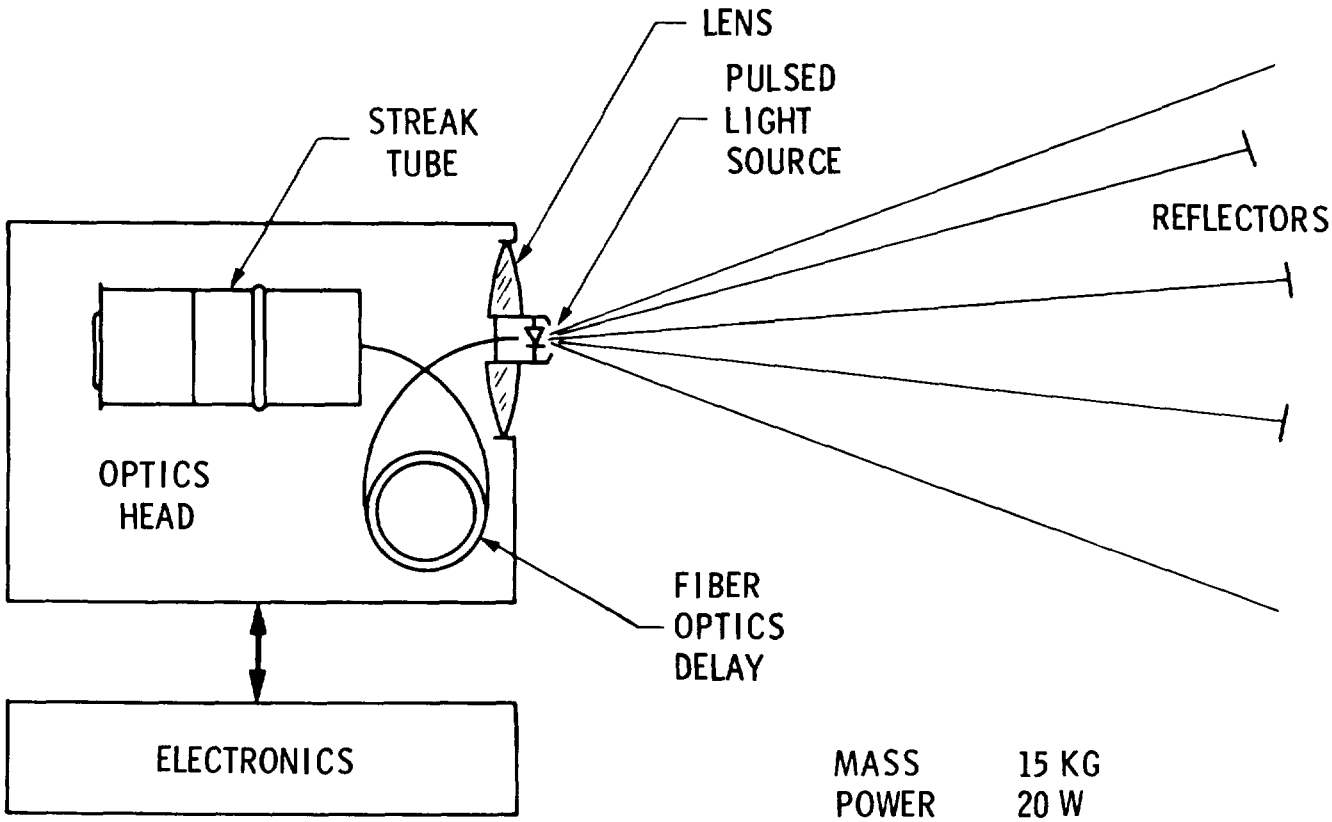

Figure 2

PICOSECOND PULSED LASER DIODES

There are two potential pulsed laser-diode light sources for SHAPES. One uses direct modulation of the diode current to obtain the short-pulse behavior. The other uses mode locking in an external cavity. The direct modulation allows a wide range of repetition frequencies but does not give as narrow a pulse as the mode-locking configuration. Mode locking is restricted by practical cavity lengths to high repetition frequencies, but gives pulses of shorter duration. The choice of one source or the other will be influenced by the particular requirements of a given situation. Figure 3 gives some results obtained at JPL in the two configurations with diodes operating at 0.82μm. The upper curve is for a direct-modulation diode and shows a width of 28 ps (full width at half maximum). The lower curve is the output of a synchronously pumped, mode locked laser and shown a 10 ps width.

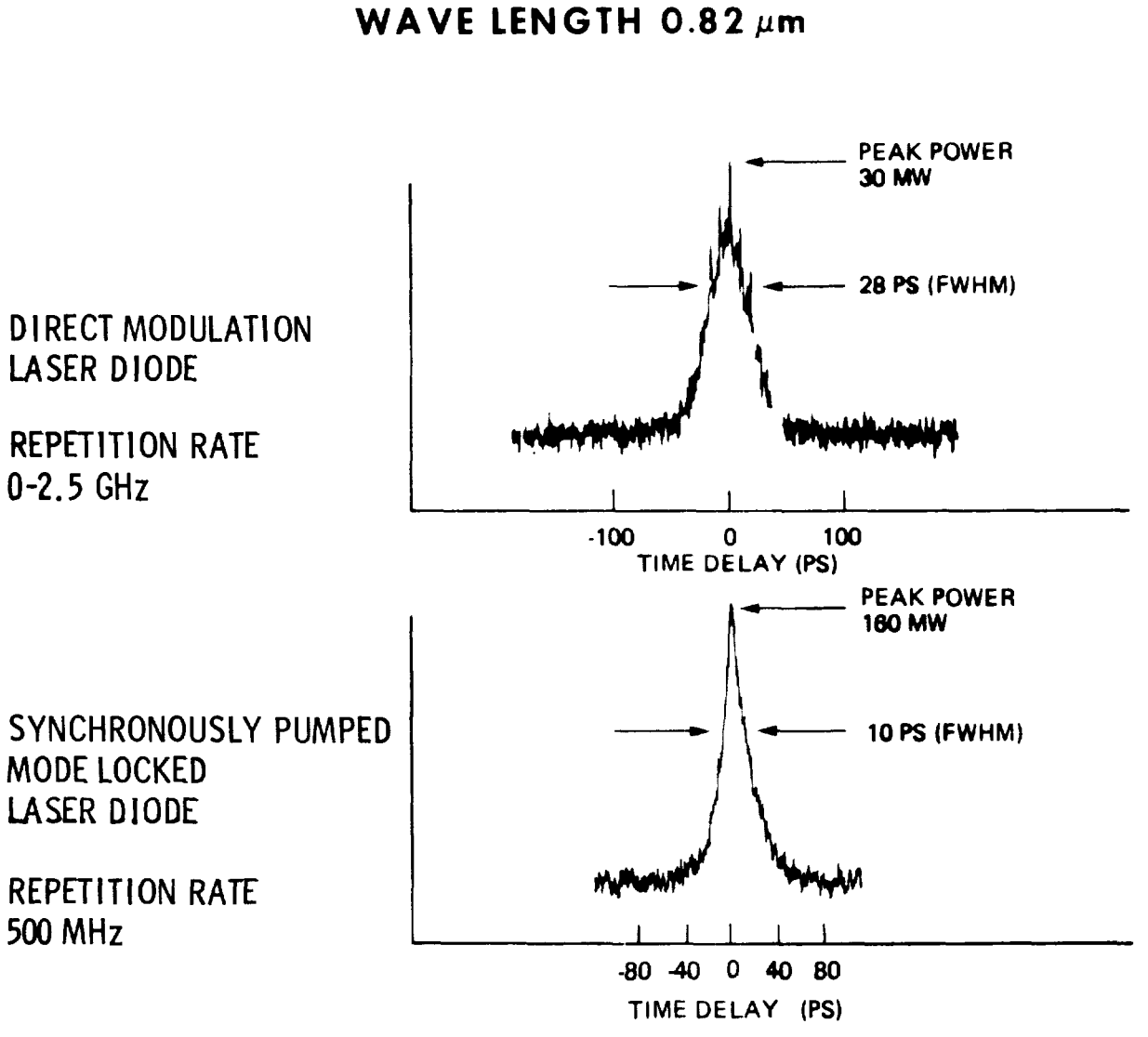

Figure 3

FIBER-OPTICS DELAY AND INTEGRATED-OPTICS WAVEGUIDE SWITCH

The fiber-optics delay which provides the reference pulse in SHAPES has two major components: the optical fibers and the integrated-optics waveguide switches. The propagation of the reference pulse through the fiber path provides the delay. The switches are used to insert or remove lengths of fiber from the path to adjust the delay to that required for the particular situation. The technology for the fibers is well developed. Fibers with losses of less than a db per kilometer are available. The temporal dispersion of the pulse as it propagates through the fiber is an important parameter, and this is of the order of 10 picoseconds per 100 kilometers.

Integrated-optics waveguide switches can be constructed using titanium-diffused lithium niobate technology. The waveguide structure is constructed by the deposition of Ti on $LiNbO_3$ through a mask. The Ti is diffused into the $LiNbO_3$ by heating in an oxidizing atmosphere changing the properties of the substrate and producing the waveguide. Metal electrodes are then deposited on the surface of the material producing a configuration as shown in figure 4. The application of a voltage to the electrodes changes the index of refraction of the $LiNbO_3$ between the waveguides thus changing the coupling between them. This technology is under development by JPL for high-data-rate communication and for the Fiber Optics Rotation Sensor (FORS). The experimental models have switching times of less than 100 ps and insertion losses of about 7 db. Improvements in the insertion loss are expected as the technology develops.

10% TO 90% RESPONSE LESS THAN 100 p sec

THIS COMPONENT IS UNDER DEVELOPMENT. PRESENT INSERTION LOSS IS 7 db. THIS IS EXPECTED TO SHOW SIGNIFICANT IMPROVEMENT WITH FURTHER WORK

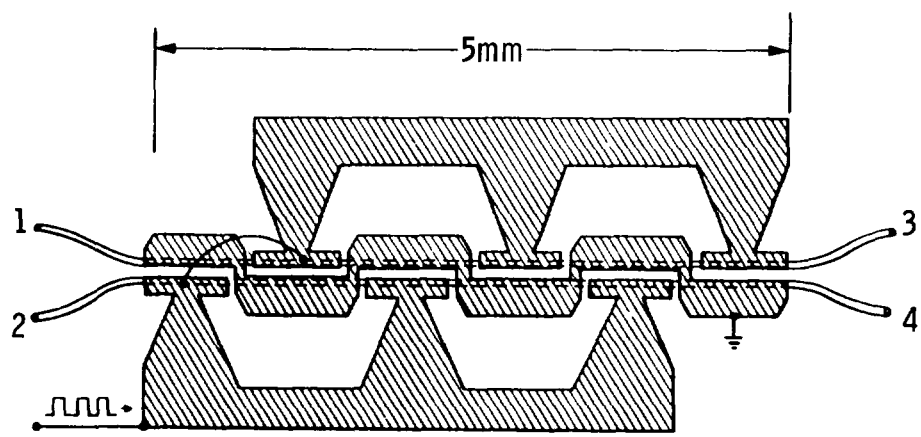

Figure 4

PICOSECOND STREAK TUBE

The streak tube which provides the fine time resolution draws on a well established technology. Streak tubes utilizing phosphor-screen output are widely used and offered by several manufacturers. CCD imaging devices are also widely used, and at least one manufacturer has produced a streak tube with a CCD output. This tube, shown in figure 5, has an S1 response photocathode (Ag-O-Cs) which has a peak close to the 0.82μm output of the laser-diode source. A typical gain (electrons out of the CCD per photon into the photocathode) is 10, and the transit-time spread is approximately 4 picoseconds. These parameters are sufficient for adequate performance of SHAPES in a number of situations. For other applications further development of the streak tube may be required.

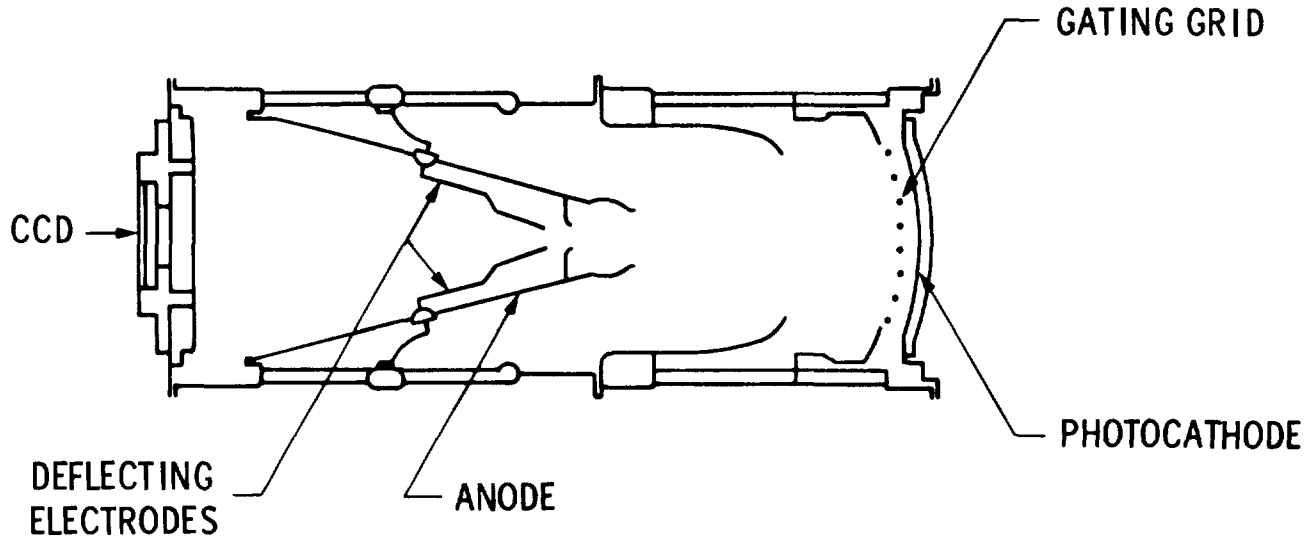

PHOTOCATHODE	S1 (Ag-O-Cs)
GAIN $\left(\frac{\text{CCD ELECTRONS}}{\text{PHOTON}}\right)$	~10
TRANSIT-TIME SPREAD	~4p sec

Figure 5

SHAPES RANGE MEASUREMENT

Figure 6 shows the SHAPES configuration for absolute range measurement. A diverging lens is used to control the spread of the illuminating beam. Retroreflectors are used to return the radiation to the sensor head efficiently. A beam splitter is used to couple the reference pulse into the fiber and to direct onto the photocathode after passing through the fiber delay. The integrated optics switches allow the switching of varying amounts of delay into the reference path, while the streak tube provides the fine resolution of range.

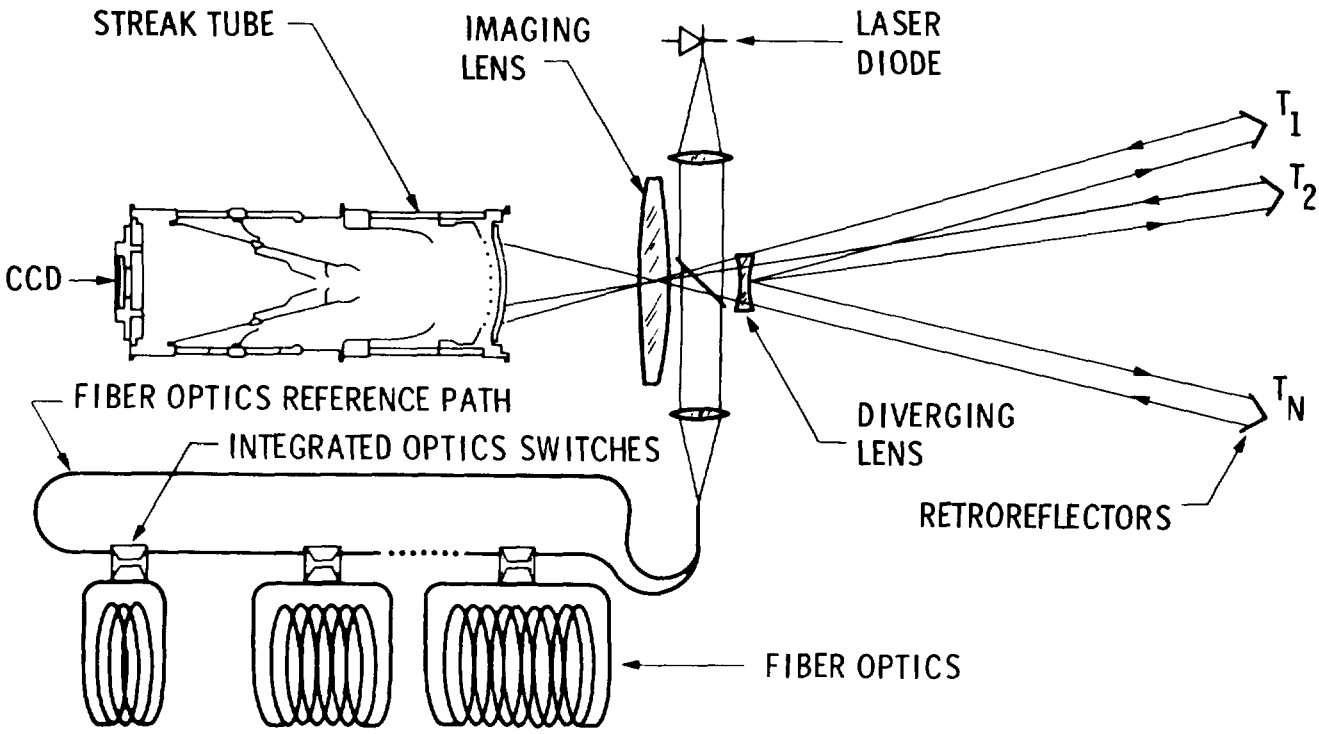

Figure 6

STREAK TUBE CCD DETECTOR

The images produced on the CCD detector by the electron optics of the streak tube are shown in figure 7. The circular spots are the direct images of the reflector as relayed by the electron optics with no sweep voltage applied to the deflection electrodes. The locations of these images measure the directions to the reflectors from the sensor head, and also provide the initial points for the time-delay measurements. The elongated spots are the images produced when the tube is sweeping. It is the displacement ΔZ_n of the two images (swept and unswept) of a point that is the measure of the time delay. The elongation of the swept spots is the result of the width of the pulse and the spread in electron transit time in the tube. The points in the center of the field separated by ΔZ_o are from the reference fiber.

Each point on the CCD image is the result of an accumulation of charge from many laser pulses. The readout of the CCD is controlled and the data processed by a microcomputer. The program interpolates to find the centroid of each spot. This can be done to an accuracy of 1/100 of the spot dimension.

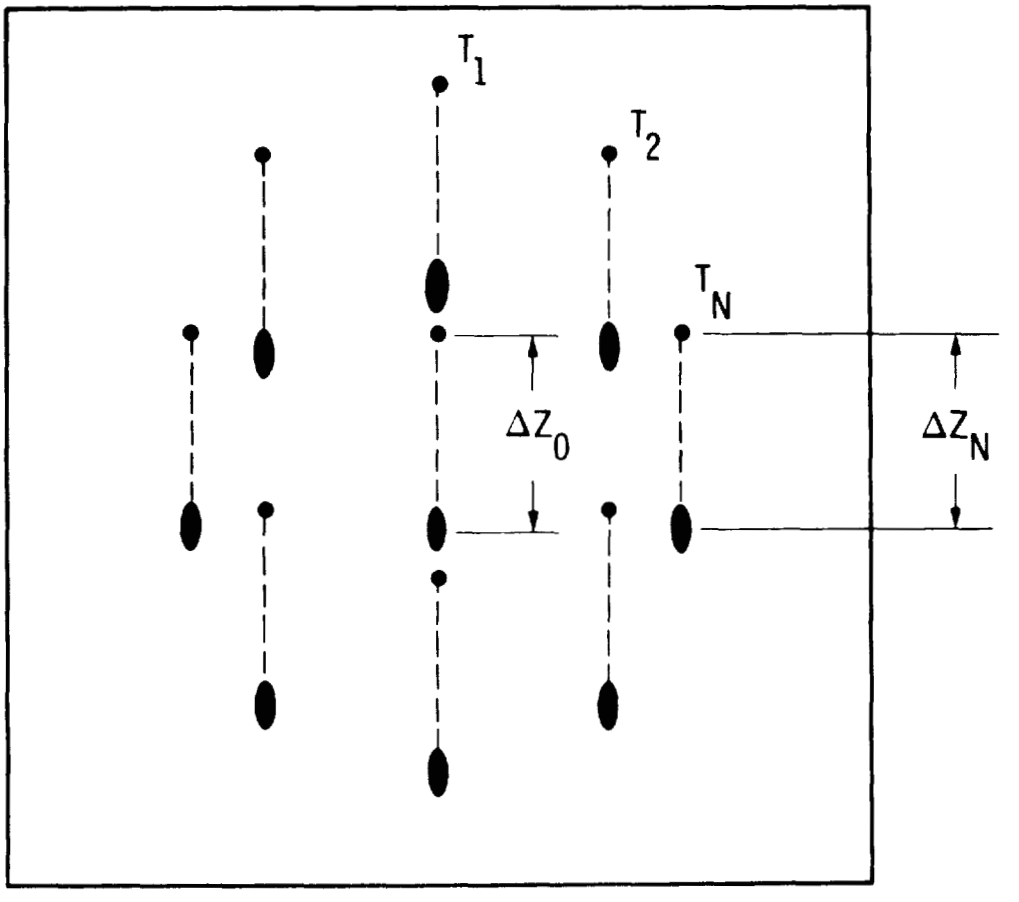

Figure 7

SHAPES RANGE MEASUREMENT

WITH HIGH-PRECISION CCD 2-AXIS ANGULAR MEASUREMENT

The precision with which the angular position of the reflector is determined can be improved by the addition of a beam splitter and second CCD as shown in figure 8. By taking the image locations from this second CCD the distortions of the electron optics of the streak tube are removed. Note that the losses of the beam splitter are partially offset because charge can be accumulated in both CCD simultaneously and only the readout needs to be time shared.

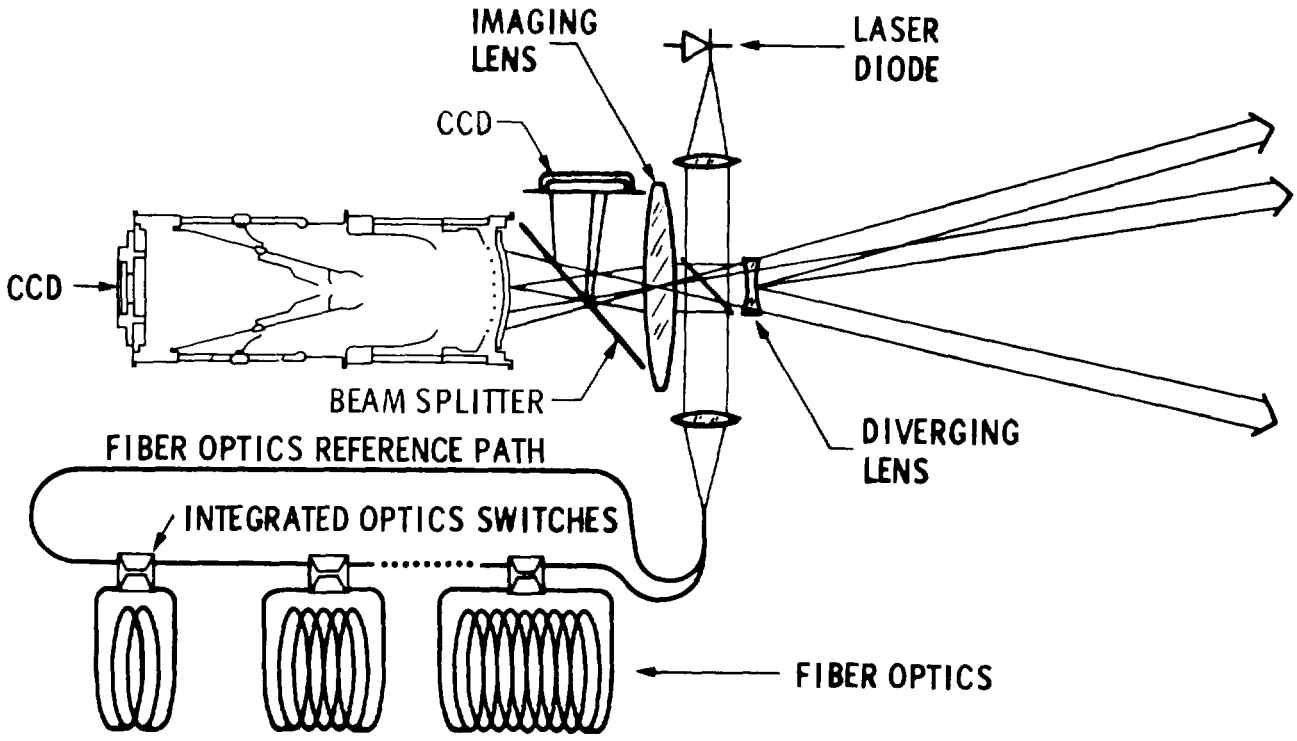

Figure 8

SHAPES RANGE MEASUREMENT WITH VERY HIGH PRECISION

CCD 2-AXIS ANGULAR MEASUREMENT

In some applications where the angular spread of the points is large, the system previously show in figure 8 reaches a limitation in that the angular motion of a given point moves the image over a very small portion of the CCD. This limitation can be overcome with the addition of image combining fiber optics and a relay lens as shown in figure 9. The image-combining optics is a set of coherent, i.e. imaging transmitting, fiber bundles. These rearrange the images of the sensed points into a more compact configuration for better utilization of the streak tube and the CCDs.

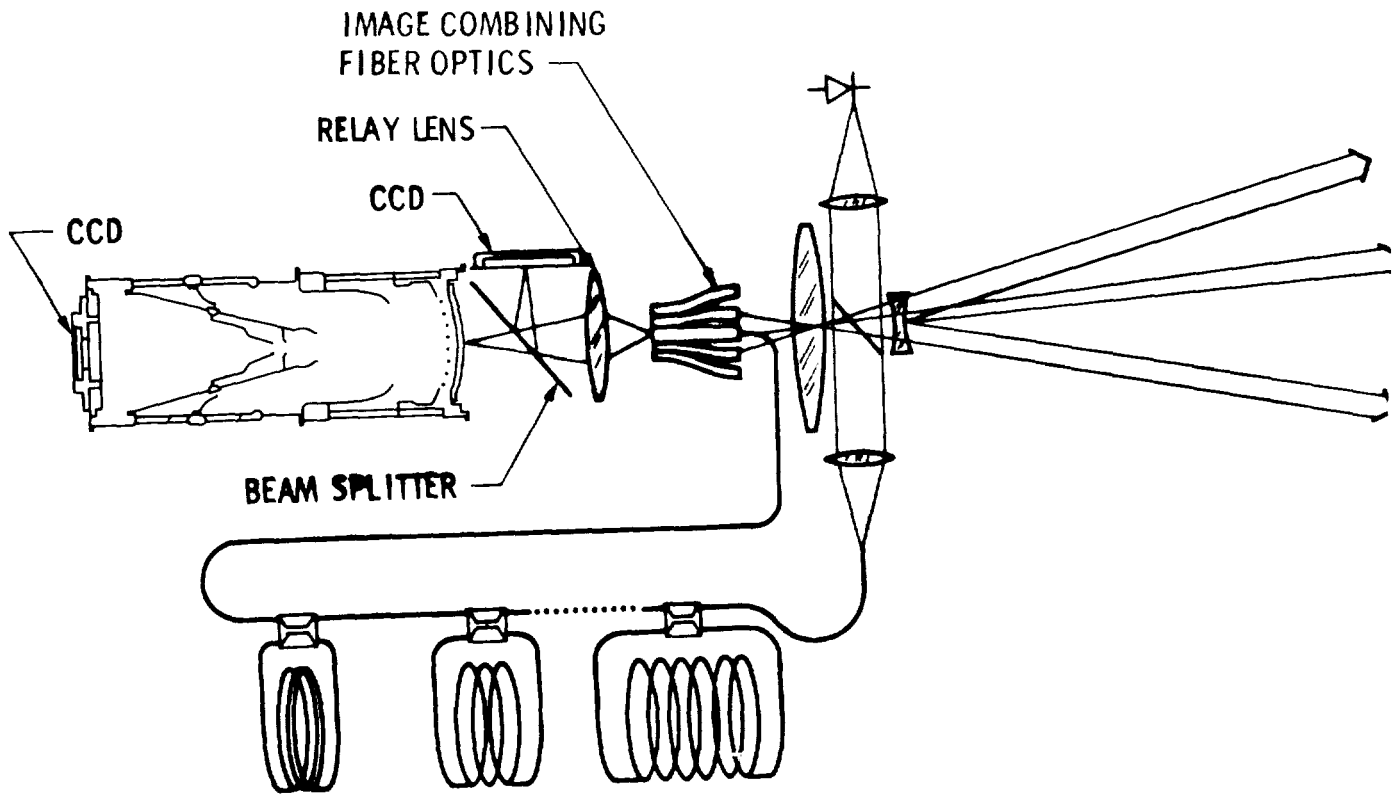

Figure 9

RANGE MEASUREMENT CCD WITH IMAGING FIBER OPTICS

The images which appear on the CCD of the streak tube when the image-combining optics are used are shown in figure 10. The principles of operation are the same as those shown in figure 7 except for the arrangement on the CCD. The interval designated ΔZ_o is that produced by the reference fiber.

The expected performance of the SHAPES system can be summarized as follows: The accuracy of the angular measurement with full field optics is one part in 10^4. With the field-compression field optics this becomes approximately one part in 10^5. The range measurement uncertainty is about 0.15 mm. The multiple targets can be of the order of 50 and the data range up to 10 target sets per second.

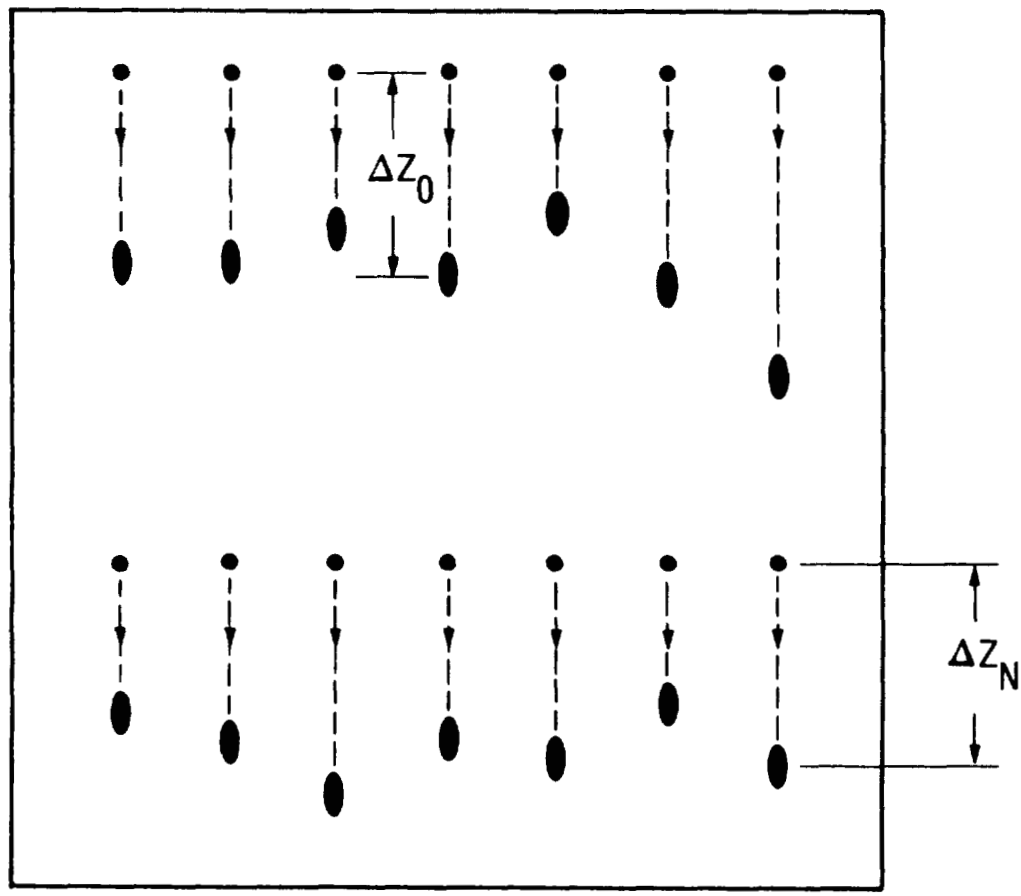

Figure 10

DEVELOPMENT STATUS OF SHAPES ENABLING NEW TECHNOLOGY

Figure 11 is a table showing the status of the various technologies re-required by SHAPES. Although they are in various states of development, all are sufficiently mature to allow work on shapes to go forward. The results for the picosecond laser diodes are ones obtained at JPL. Similar results have been obtained at other laboratories. The optical fiber used in the delay lines was developed for optical communication and is commercially available. The integrated-optics switches have been under development for some time, both high-speed data processing and transmission and for the Fiber Optics Rotation Sensor. Streak tubes with picosecond resolution are available with phosphor outputs from several manufacturers, and one manufacturer has demonstrated a tube with a CCD output. Finally, CCD's themselves have been a commercial item for several years and are available from several manufacturers.

TECHNOLOGY	STATUS
• PICOSECOND PULSED LASER DIODES	25 PS FWHM DEMONSTRATED 10 PS FWHM MODE LOCKED DEMONSTRATED
• FIBER OPTICS DELAY LINES	MATERIAL DISPERSION (@ 0.82 μm) ~10 PS/100 M
• INTEGRATED OPTICS SWITCHES	UNDER DEVELOPMENT 10 TO 90% RESPONSE < 100 PS
• PICOSECOND STREAK TUBE	• COMMERCIAL PRODUCT (PHOSPHOR OUTPUT) • CCD OUTPUT DEMONSTRATED 1979
• CCD IMAGING DETECTORS	• COMMERCIAL PRODUCT

Figure 11

SHAPES APPLICATION -

POINTING AND CONTROL OF A LARGE SPACE ANTENNA

The application of SHAPES to the pointing and control of a large space antenna is illustrated in figure 12. The particular antenna shown is a possible configuration for Land Mobile Satellite Service. The antenna is of wrap-rib construction and the spacecraft bus is located at the antenna feed. The particular advantages of SHAPES for this application are: (1) It can cover the entire antenna with a single sensor head, (2) It determines the location of many points simultaneously, (3) It operates from a central location on the bus and can be co-located with star trackers, earth sensors or other attitude sensing devices. When used in this way SHAPES provided information on static shape; vibration sensing; and, when combined with the attitude sensors, the information required for antenna pointing.

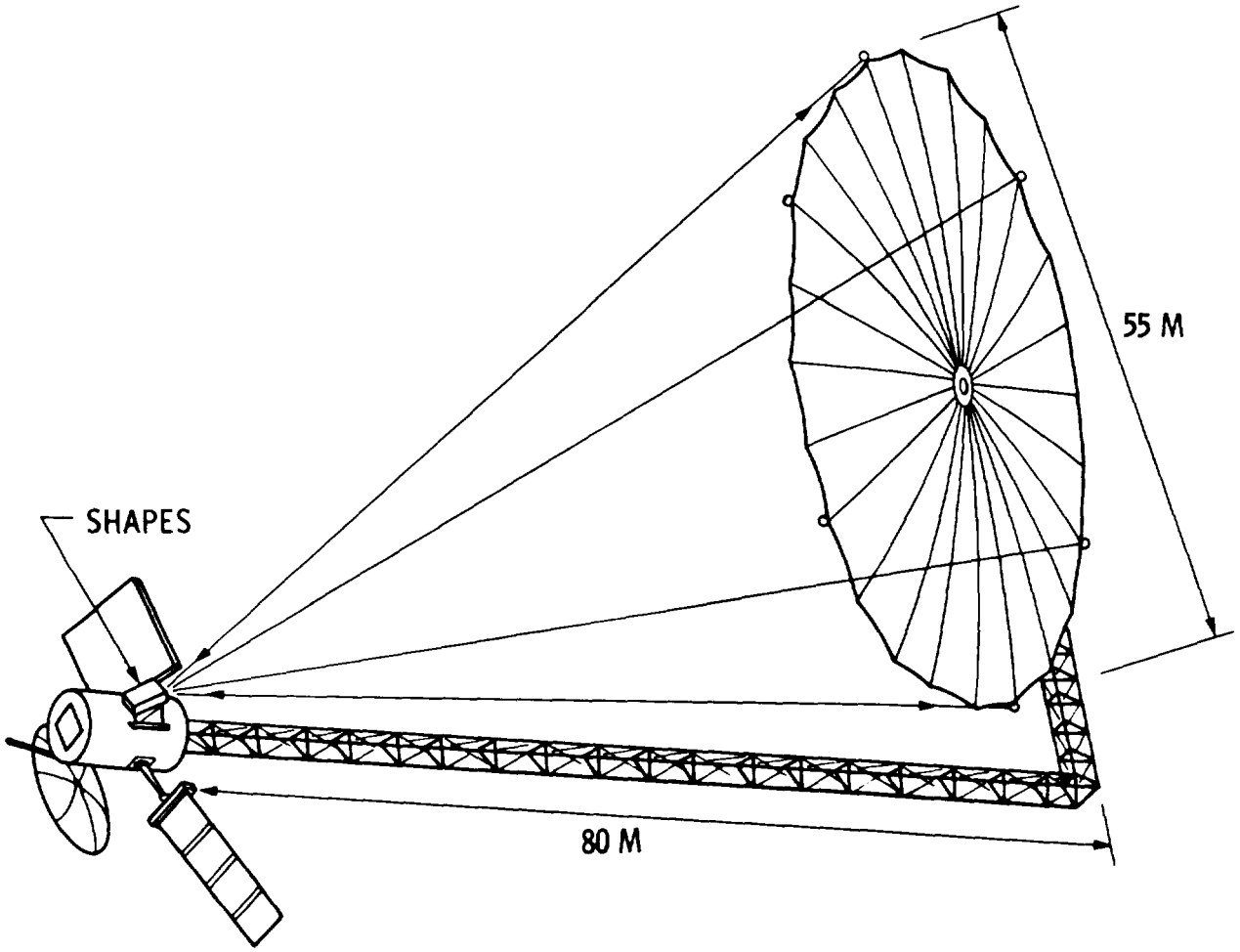

Figure 12

APPLICATION OF SHAPES TO RENDEZVOUS AND DOCKING

SHAPES can be used for the measurement of the three-dimensional position and the rotational and translational velocities in rendezvous and docking operations as shown in figure 13. The required modifications are an increased range of delays in the reference path and some autofocus capability both in the illuminating system and the imaging system.

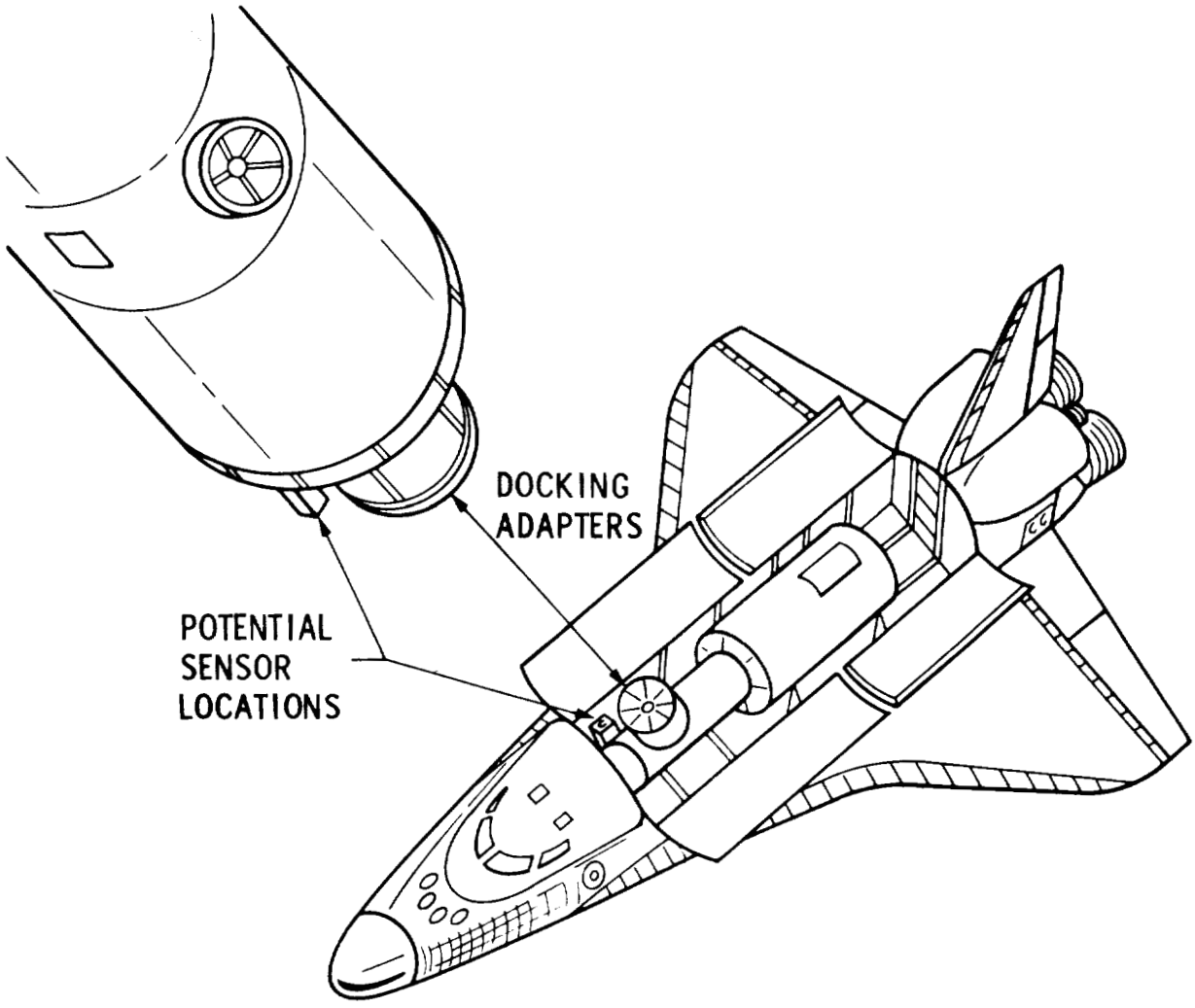

Figure 13

CONTROL TECHNOLOGY DEVELOPMENT

David B. Schaechter
Jet Propulsion Laboratory
Pasadena, California

Large Space Systems Technology - 1981
Third Annual Technical Review
November 16-19, 1981

CONTROL TECHNOLOGY DEVELOPMENT OBJECTIVES

The main objectives of the control technology development task are given in the slide below. The first objective is to develop control design techniques based on flexible structural models, rather than simple rigid-body models. Since large space structures are distributed parameter systems, a new degree of freedom, that of sensor/actuator placement, may be exercised for improving control system performance. Another characteristic of large space structures is numerous oscillatory modes within the control bandwidth. Reduced-order controller design models must be developed which produce stable closed-loop systems when combined with the full-order system. Since the date of an actual large-space-structure flight is rapidly approaching, it is vitally important that theoretical developments are tested in actual hardware. Experimental verification is a vital counterpart of all current theoretical developments.

- TO DEVELOP DYNAMIC AND SHAPE CONTROL DESIGN APPROACHES BASED ON FLEXIBLE MODELS
- TO MAXIMIZE CONTROLLER PERFORMANCE BY JUDICIOUS SENSOR/ACTUATOR PLACEMENT
- TO DEVELOP GENERALIZED MODEL REDUCTION TECHNIQUES
- TO DEMONSTRATE CONTROL TECHNOLOGY DEVELOPMENTS USING HARDWARE TEST FACILITY

MAJOR ACHIEVEMENTS

The chart below serves as an outline for the remainder of this presentation and lists the major achievements of the past year's work. Control-system design approaches based on distributed parameter (partial differential equation) systems have been developed. These control-system design approaches reduce control spillover. Analogous techniques have been applied to the figure-control problem, with shape control of a large flexible reflector yielding excellent results from a computer simulation. Stanford University developed control system designs for the case sensors and actuators are separated by a flexible member, an inherently difficult-to-control configuration. Purdue University has fully exploited the possibility of optimizing sensor and actuator locations in terms of overall system performance. A detailed finite-element model of our hardware verification facility was developed, and detailed calibrations of the associated instrumentation were made. Multivariable frequency domain control design approaches were developed primarily for the large-space-platform application.

- DEVELOPED DISTRIBUTED CONTROL-SYSTEM DESIGN APPROACHES FOR CONTROL SPILLOVER REDUCTION
- SIMULATED A FULL-UP SHAPE ESTIMATION AND SHAPE CONTROL SYSTEM
- DEVELOPED NON-COLOCATED SENSOR/ACTUATOR CONTROL-SYSTEM DESIGN TECHNIQUES
- OPTIMIZED SENSOR/ACTUATOR PLACEMENT FOR IMPROVED PERFORMANCE
- DEVELOPED A DETAILED EXPERIMENTAL FACILITY MODEL, INTERACTIVE CONTROL SOFTWARE, AND INITIATED A TESTING PROGRAM
- DEVELOPED MULTIVARIABLE FREQUENCY DOMAIN CONTROL DESIGN TECHNIQUES FOR BASE MOTION COMPENSATION

LARGE STRUCTURE CONTROL CONCEPT

Drawings of several spacecraft are shown below. Typical control objectives unique to large space structures are pointed out for some of these spacecraft. Although the control objectives of pointing control, attitude control, etc. may not at first seem to be unique to large space structures, the fact that these objectives are highly coupled with the structural vibrations resolves this discrepancy.

- NON-COLOCATION
- BASE MOTION COMPENSATION
- POINTING
- ATTITUDE

LSST PLATFORM CONFIGURATION

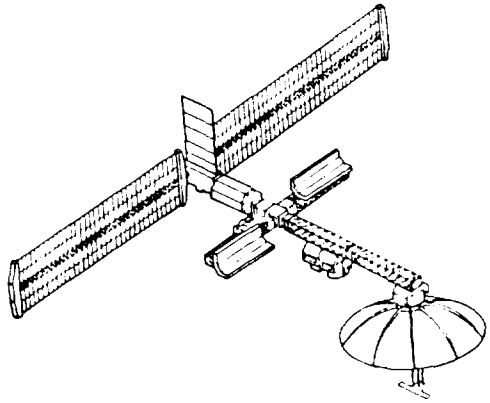

- NON-COLOCATION

GALILEO

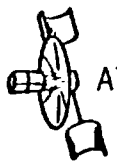

ATS-6

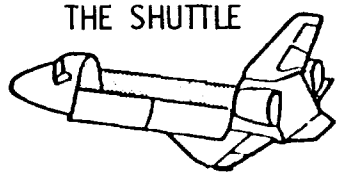

THE SHUTTLE

- SHAPE
- POINTING
- ATTITUDE
- STATION KEEPING
- DISTRIBUTED CONTROL

LAND MOBILE SATELLITE

THE DISTRIBUTED-SYSTEM CONTROL PROBLEM

There are distinct and major differences between past, lumped-parameter systems and future distributed systems. A lumped system whether it consists of a single rigid body, or even a rigid body with a finite number of spring hinged appendages, possesses a finite number of structural modes. A continuously distributed parameter system made up of beams, membranes, tethers, etc. possesses an infinite number of modes. The control problem emerges as a result of the on-board controller ability to handle a finite-order model. Yet with the infinite-order systems, sensors still measure the unmodeled modes and actuators still affect the unmodeled modes. This can lead to instabilities when the control loop is closed.

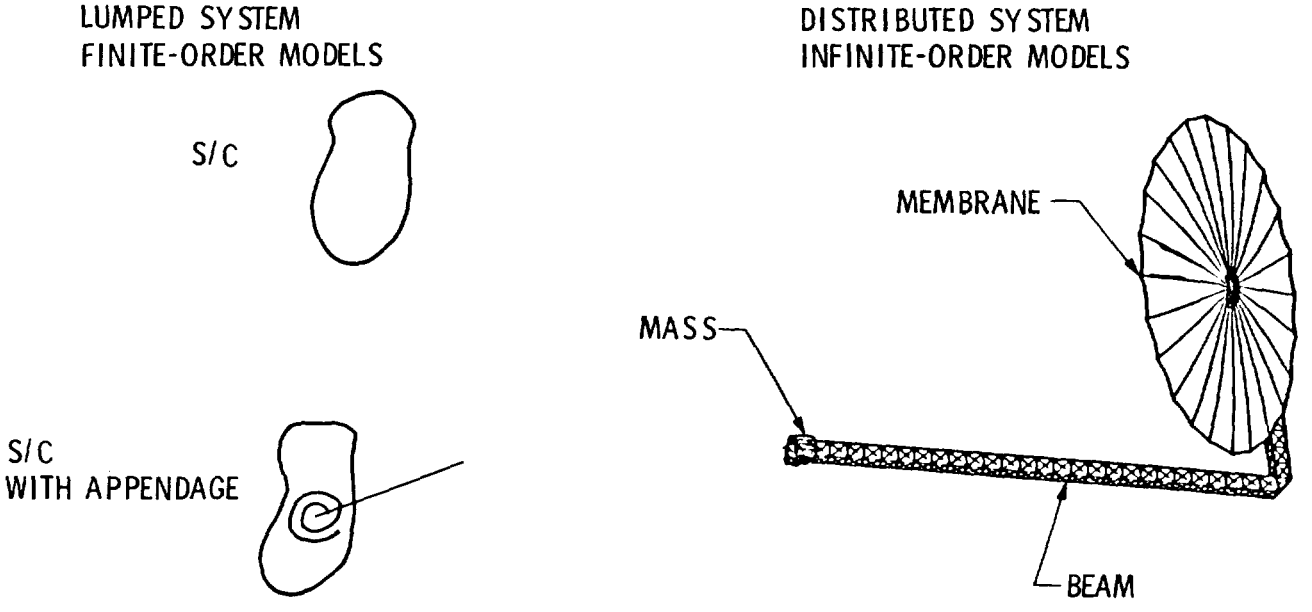

- EXISTING CONTROL-SYSTEM DESIGN PROCEDURES, WHEN APPLIED TO TRUNCATED DISTRIBUTED SYSTEMS MAY RESULT IN CLOSED-LOOP INSTABILITIES

THE SHAPE CONTROL PROBLEM

The shape control problem results from trying to estimate and control a continuous shape from a discrete set of sensors and actuators. The control process begins with the definition of a desired continuous shape. Discrete sensor measurements of the actual shape are combined with the structural model to yield a "best" estimated continuous shape. Subsequently, a set of controls are applied to return the shape as close as possible to the desired shape.

- CONTINUOUS STRUCTURE AND DESIRED CONTINUOUS SHAPE
- ONLY DISCRETE SENSOR OUTPUTS ARE AVAILABLE FOR RECONSTRUCTING ESTIMATED SHAPE
- ONLY DISCRETE ACTUATORS ARE AVAILABLE FOR CORRECTING THE SHAPE

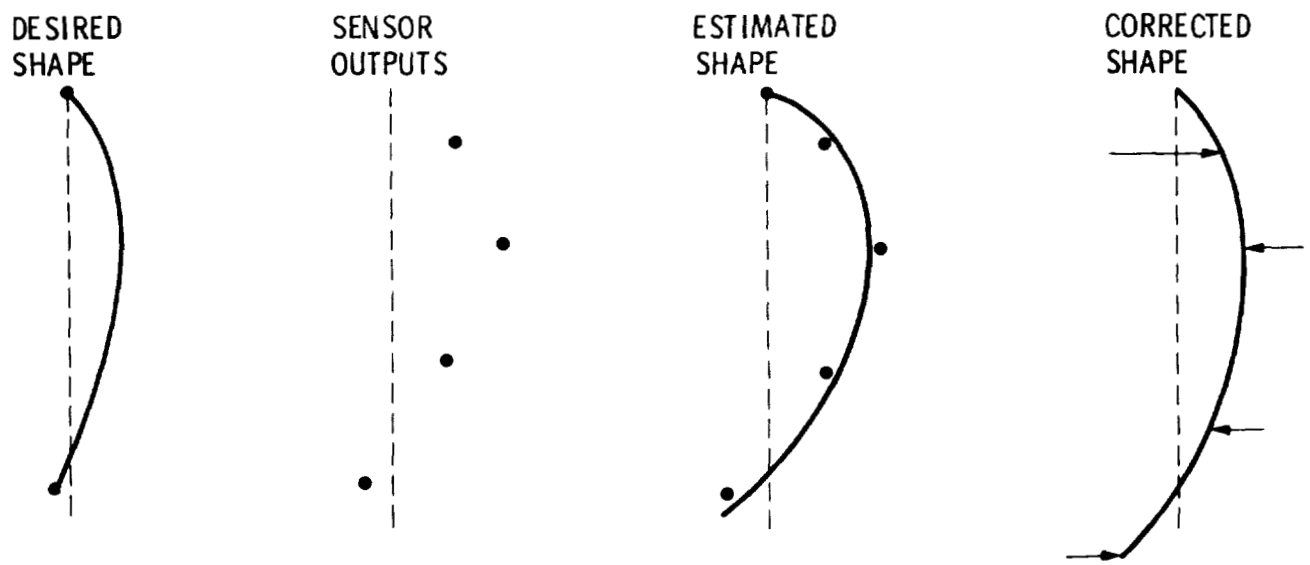

SCHEMATIC OF THE FLEXIBLE BEAM

Hardware verification of selected control concepts is performed in the JPL flexible-beam experimental facility. A schematic of this facility is shown below. It consists of a support tower, a pinned-free flexible beam hanging from the tower, and position sensors and force actuators located along the length of the beam. For evaluation of the distributed control system, an impulse is applied at the free end of the beam, and the resulting deflections at that point are observed. These results are shown on the following page.

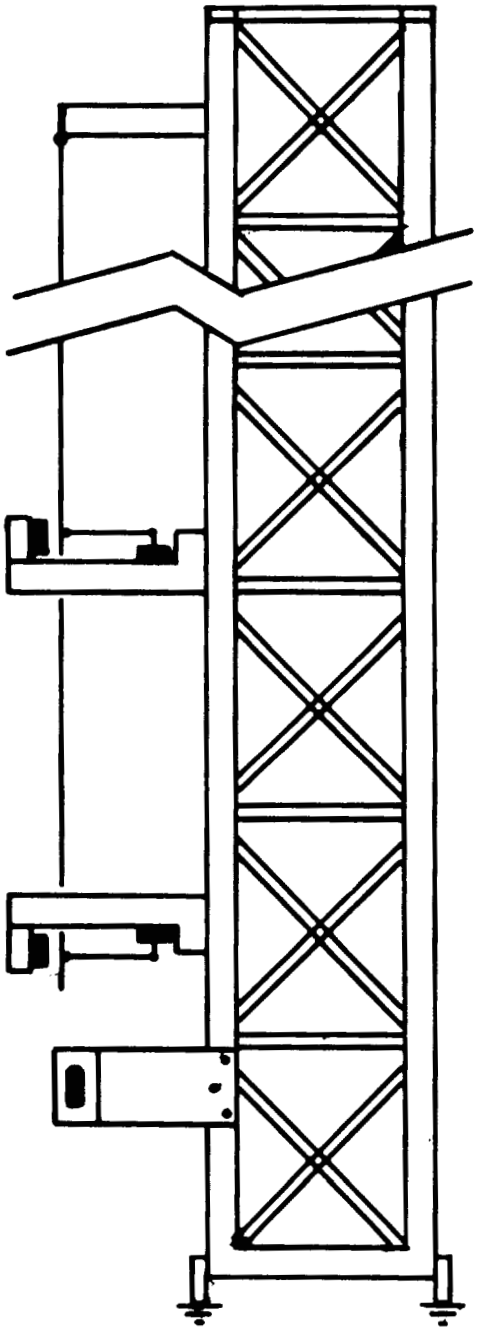

FLEXIBLE BEAM CONTROL

Control-system design approaches based on partial-differential-equation models have been verified on JPL's flexible-beam experimental facility (see previous page). The response of the free end of the flexible beam to an impulse applied at the free end is shown below. The first case is open loop. The damping is primarily due to the atmosphere. The second case shows the closed-loop response using a Kalman Filter controller based on the first three flexible modes. The rather persistent ringing occurs at the frequency of the first unmodeled mode, a classic case of spillover. The final chart shows the much improved response of the control system based on the partial-differential-equation model. The conclusion is that retaining the complete model throughout the control-system design process can greatly improve closed-loop performance.

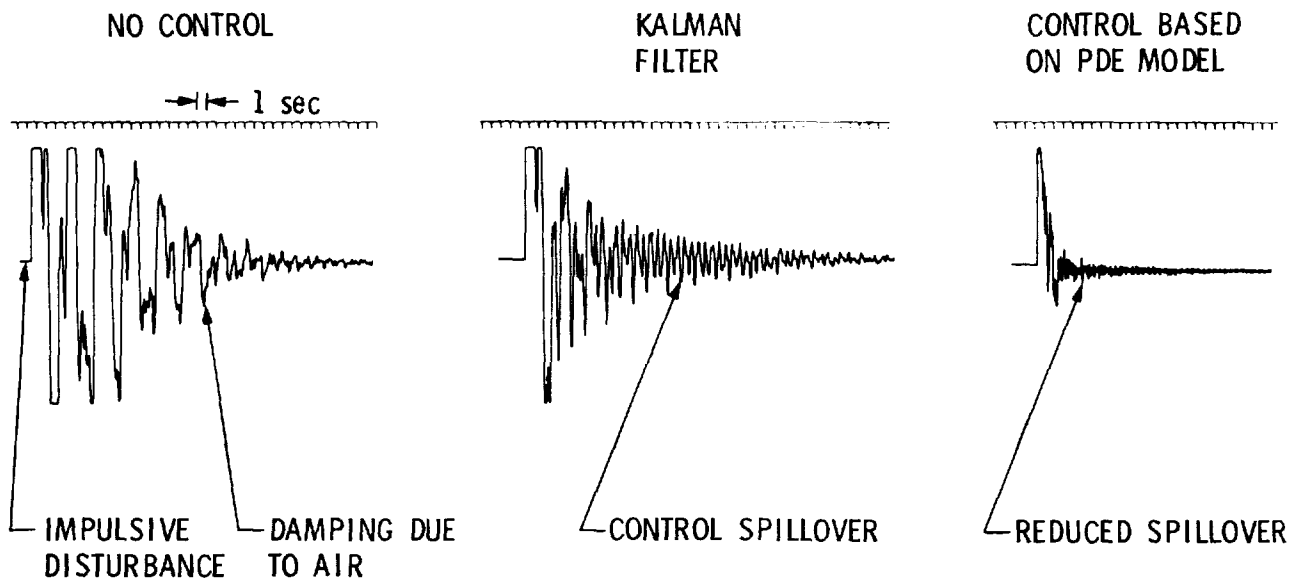

- CONTROLLER BASED ON PDE MODEL GREATLY REDUCES SPILLOVER

SHAPE CONTROL RESULTS

The figures below show the results of a shape estimation and control computer simulation. A known perturbation is first impressed upon the parabolic dish. This perturbation is a linear combination of the mode shapes for convenience. Eighteen sensor measurements are assumed along the periphery of the dish. From these discrete measurements, and a structural model, an estimated shape is computed. Note that it very closely matches the actual shape. Using nine actuators located at the hub of the dish, control forces are applied to return the dish as close as possible to the desired parabolic shape. The overall process yields excellent results.

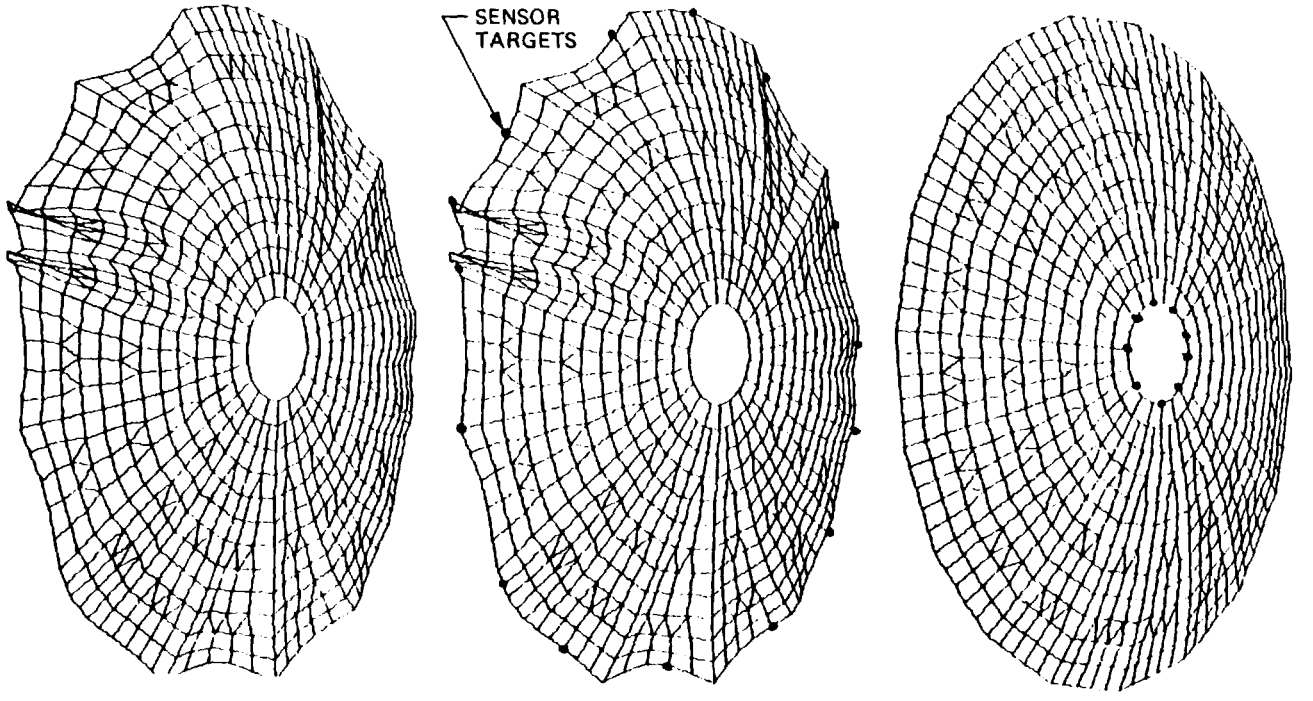

ACTUAL SHAPE $U^0 + 10\varphi_1 + 10\varphi_4 + 5\varphi_8 + 5\varphi_{10}$ ESTIMATED SHAPE CORRECTED SHAPE

CONTRACT ACTIVITIES

Stanford University has been studying control-system design techniques to overcome the destabilizing effects of sensor/actuator non-colocation. This problem is further complicated by uncertain knowledge of the flexibility separating the sensor and actuator. Adaptive control approaches using a phase-locked loop to track unknown or varying oscillation frequencies have been shown to be quite successful.

Purdue University is exploiting to full advantage the possibility of optimizing the sensor and actuator placement to achieve improved control performance. Purdue is also studying methods of reducing controller sensitivity to model errors. One very promising approach uses equivalent cost realizations to select good reduced-order controllers.

STANFORD UNIVERSITY

- SENSOR/ACTUATOR NON-COLOCATION
- ADAPTIVE CONTROL USING PLL

PURDUE UNIVERSITY

- OPTIMAL SENSOR/ACTUATOR PLACEMENT
- MODEL ERROR SENSITIVITY REDUCTION
- EQUIVALENT COST REALIZATIONS

HARDWARE VERIFICATION

A vitally important part of any theoretical control development for eventual spaceflight is hardware verification. Toward this end JPL has constructed a flexible-beam test facility for verifying many aspects of the control of large space structures. The facility has been augmented with a detailed finite-element model of the flexible beam, accurate calibrations of the sensors and actuators, a highly interactive software package for implementing various control systems, and a laser system for vivid visualization of the control-system objectives and performance. A movie demonstrating active shape control and active vibration suppression has been made which documents the excellent experimental results thus far obtained in these areas.

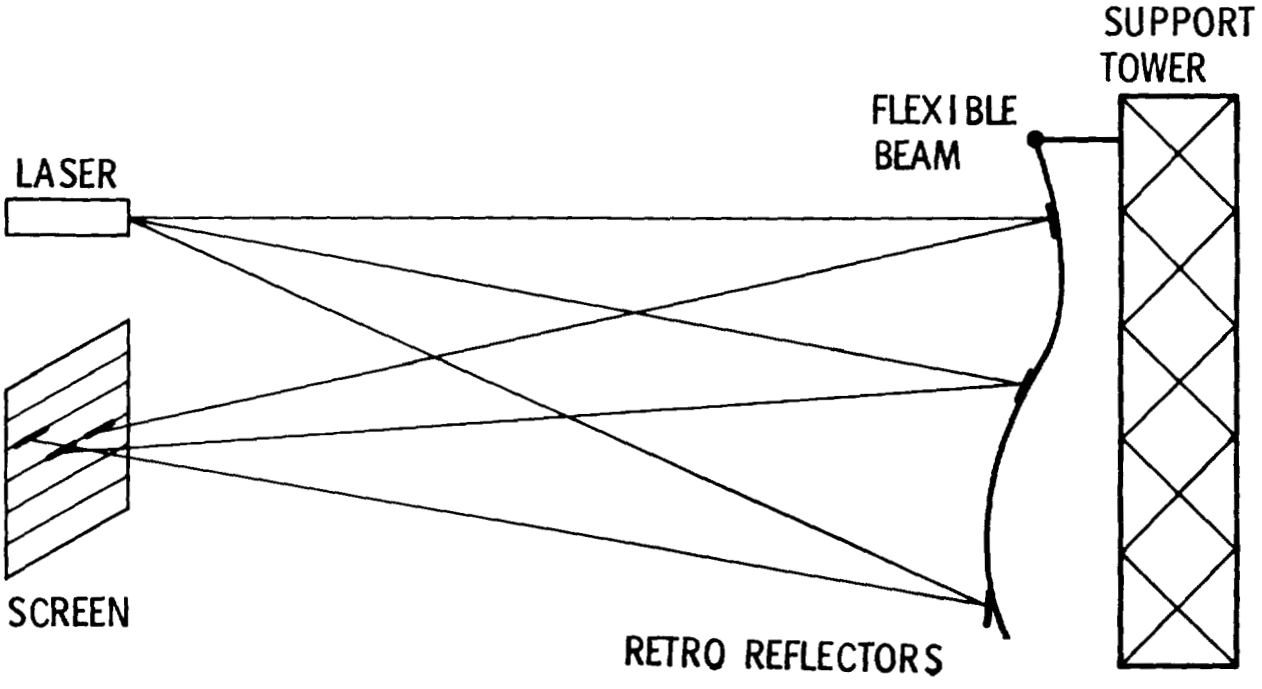

- SHAPE CONTROL
- DYNAMIC CONTROL

SUMMARY

The past year's work in the control of distributed parameter systems resulted in significant accomplishments. Prior to this year, all the results in this area had been based on partial-differential-equation models. These results have now been generalized to arbitrary finite-element models, with nice, closed-form analytical solutions resulting. It was also found that decentralized (or local) controllers are optimal in high-gain applications, i.e. in situations where the closed-loop dynamics are dominated by the feedback. The most impressive result in this area was the major reduction in control spillover obtained as a result of performing the design using a full-order model.

Shape estimation and control has been simulated on the computer using a finite element model of a large antenna. Excellent results were obtained. It was found that figure control performance is more often limited by the geometry of the sensor/actuator configuration than it was by the resolution of the sensor or the power of the actuator. In the laboratory, the continuous RMS shape error has been reduced to the theoretical limit, as governed by sensor/actuator geometry. It was also found that for economical design, there should be a specific balance between the number of shape sensors and the number of shape actuators.

CONTROL OF DISTRIBUTED SYSTEMS

- GENERALIZED PDE MODEL RESULTS TO FE MODELS
- OBTAINED CLOSED-FORM ANALYTICAL RESULTS
- DECENTRALIZED CONTROLLERS ARE OPTIMAL IN HIGH-GAIN APPLICATIONS
- OPERATOR TRUNCATION ALLEVIATES THE DESTABILIZING EFFECT OF MODEL TRUNCATION

SHAPE CONTROL

- SIMULATED STATIC SHAPE CONTROL OF A LARGE ANTENNA
- PERFORMANCE NOT ALWAYS CONTROL LIMITED, SOMETIMES GEOMETRY LIMITED
- RMS SHAPE ERROR REDUCED TO THEORETICAL LIMIT
- BALANCE MUST EXIST BETWEEN NUMBER OF SENSORS/ACTUATORS

SUMMARY (continued)

In the experimental validation area, a detailed facility model was made. This includes a finite element model of the beam in tension and an accurate calibration of the sensor/actuator scale factors. Interactive software has been developed for very fast implementation of a variety of control laws. Laser hardware, with beam-mounted retroreflectors, was installed for a vivid display of the beam's motion. Finally, as could only be found with actual hardware, nonlinearities, static friction, hysteresis, and unmodeled modes severely altered the control-system design process.

The area of platform control is discussed at length in a separate section.

Contractors have provided us with new insights into the control of systems where the sensor and actuator are separated by a flexible element. Phase-locked loops are employed to track changing or uncertain frequencies. Sensor and actuator placement is a new degree of freedom to be examined in the control-system design of distributed systems. Optimizing their location for improved control-system performance has been achieved under contract.

EXPERIMENTAL VALIDATION

- DEVELOPED A DETAILED FACILITY MODEL
- PRODUCED INTERACTIVE CONTROL-SYSTEM SOFTWARE
- SENSOR/ACTUATOR NONLINEARITIES, STATIC FRICTION, AND HYSTERESIS, NOT MODELED IN ADVANCE, SEVERELY ALTERED CONTROL DESIGN

PLATFORM CONTROL

- MULTIVARIABLE FREQUENCY DOMAIN DESIGN APPROACHES DEVELOPED

CONTRACT

- DEVELOPED NON-COLOCATED SENSOR/ACTUATOR DESIGN APPROACH
- OPTIMIZED SENSOR/ACTUATOR LOCATIONS FOR IMPROVED PERFORMANCE

FUTURE WORK

Further advances in control technology are required for successful application to large-space-structure control. A major thrust of future work will be to develop design techniques which can either adapt to changing or uncertain models or be insensitive to the model errors. In the past years, static shape control and vibration control have been independently demonstrated. Future work will be aimed at combining these distinct modes of operation. Control of distributed parameter systems based on continuum models will be investigated further to allow for generalized sensors (rate, acceleration, angular, strain etc.) and possibly generalized actuators. Shape control will be performed on more complex, multi-dimensional structures such as plate-like structures.

- IMPLEMENT MODEL ADAPTIVE AND INSENSITIVE CONTROL APPROACHES IN HARDWARE (FY 82)
- COMBINE STATIC SHAPE CONTROL WITH DYNAMIC CONTROL (FY 82)
- FORMULATE DISTRIBUTED CONTROL FOR GENERAL SENSOR/ACTUATOR TYPES (FY 82)
- SHAPE CONTROL FOR MULTIDIMENSIONAL CONFIGURATIONS (FY 83)

REFERENCES

A major output of a control technology development study is documentation. A partial list of publications from the past year is given below.

1. Weeks, C.: Shape Determination and Control for Large Space Structures. Jet Propulsion Laboratory Publication 81-71.

2. Edmunds, R.: Preliminary Control System Design for the Large Space Systems Technology (LSST) Reference Platform. Jet Propulsion Laboratory Publication 81-77.

3. Schaechter, D.B.: Estimation of Distributed Parameter Systems. AIAA Journal of Guidance and Control. 9/81.

4. Hamidi, M.: Optimal Control and Controller Location for Distributed Parameter Elastic Systems. IEEE 20th Conference on Decision and Control. 9/81.

5. Schaechter, D.B.: A Survey of Large Space Structure Control Approaches. IFAC, Kyoto, Japan. 4/81.

6. Rodriguez, G.: Model Error Estimation: S/C Control Applications of a Geometric Approach. IEEE, Workshop on Applications of Adaptive System Theory, New Haven, Conn. 5/81.

7. Hamidi, M.: On the Rigid Body Motion and Shape Distortion Evaluation for Large Flexible Spacecraft. Third VPI&SU/AIAA Symposium on Dynamics and Control of Large Flexible Spacecraft, 1981, pp. 191-202.

8. Rodriguez, G.: A Function Space Approach to Smoothing with Applications to Model Error Estimation for Flexible Spacecraft Control. IEEE Conference on Decision and Control, San Diego, CA. 7/81

9. Rodriguez, G.: Model Error Estimation for Large Flexible Spacecraft. AIAA Proceedings 3rd VPI Symposium on Dynamics and Control of Large Flexible Spacecraft. 7/81.

10. Eldred, D.: Experimental Demonstration of Static Shape Control. AIAA Guidance and Control Conference. 1/81.

11. Schaechter, D.B.: Distributed Control: Theory and Experiment. Purdue University Seminar. 4/81.

12. Schaechter, D.B.: Distributed Control of Large Space Structures. Jet Propulsion Laboratory Publication 81-15.

LSS REFERENCE PLATFORM CONTROL

Rance S. Edmunds
Jet Propulsion Laboratory
Pasadena, California

Large Space Systems Technology - 1981
Third Annual Technical Review
November 16-19, 1981

FY'81 LSS PLATFORM CONTROL OBJECTIVES

The long range objective of this task is to develop basic technology in the design, mechanization, and analysis of control systems for large flexible space structures. The focus of the FY'81 platform control effort was on the pointing control problems associated with multiple independently controlled experiment packages operating simultaneously on a single platform. All of the FY'81 objectives stated below were accomplished. Particular emphasis was placed on obtaining a quantitative comparison of controller performance with and without base motion compensation.

- DEVELOP FREQUENCY DOMAIN DESIGN CAPABILITY FOR MULTIVARIABLE SYSTEMS
- DEVELOP THREE DIMENSIONAL STRUCTURAL/CONTROL MODELS
- INCORPORATE BASE MOTION COMPENSATION INTO CONTROLLER DESIGN
- QUANTIFY CAPABILITIES AND LIMITATIONS OF CONTROLLERS

LSS PLATFORM CONFIGURATION

The LSS platform consists of solar panels, a central bus (with associated power, telemetry, and control systems), and platform arms with mounting pads on which various experiments can be attached. The actual configuration for the platform arms might vary widely depending on experiment requirements for physical separation and viewing angles. The tip to tip dimension of the solar panels is approximately 100 meters, and the total weight of the system is between 10 and 20,000 Kg.

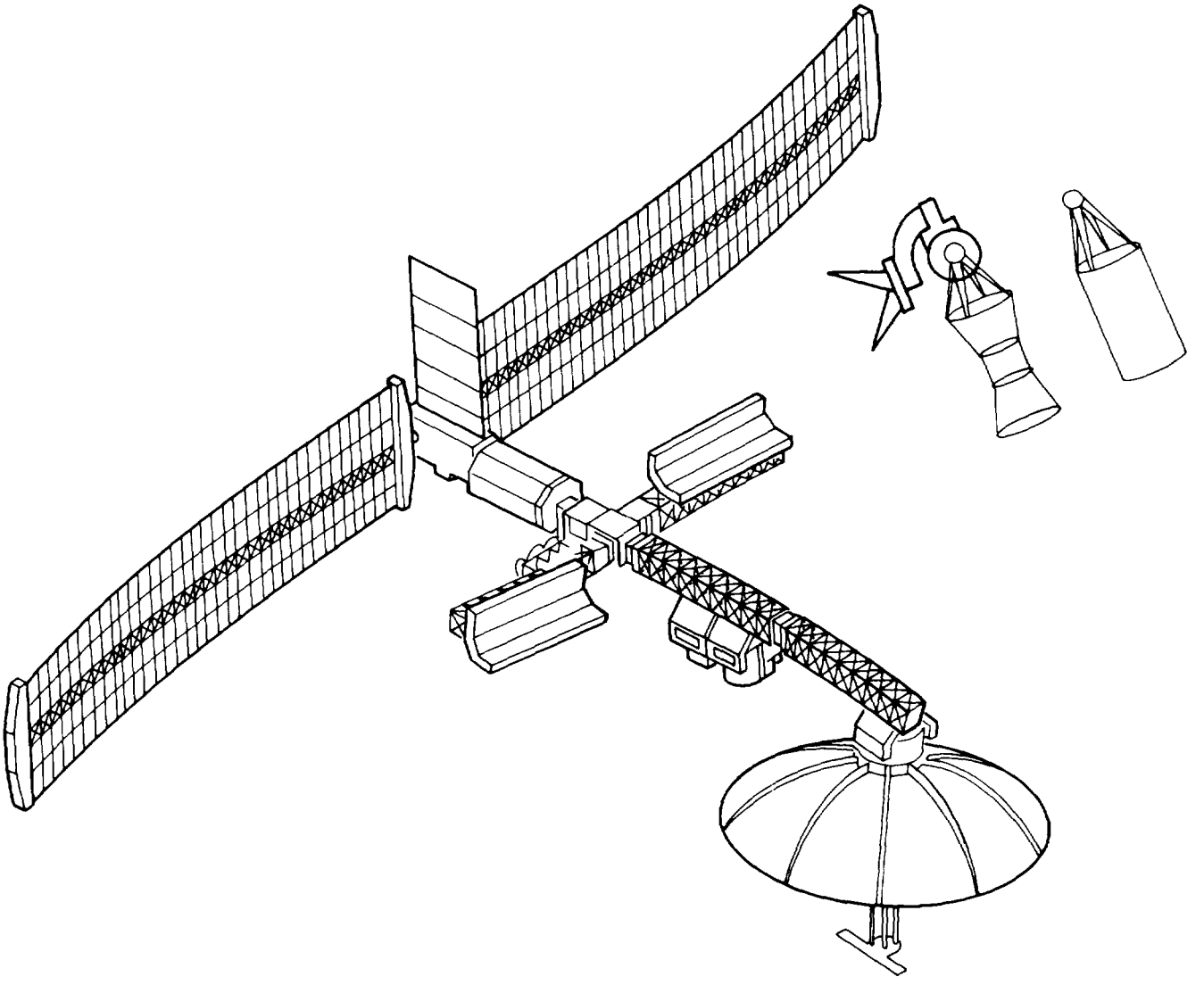

POINTING CONTROL PROBLEMS

Operation of multiple independent control systems on a single platform presents a major problem when high performance is required. The figure below illustrates the basic mechanism of payload controller interaction. A torque at payload 1 (PL No. 1) results in a rotation of the platform bus, which in turn causes a pointing error to result for payload 2. The magnitude of the disturbance caused by a torque applied by payload 1 depends primarily on the bus inertia and the geometry. It has been found from previous studies that conventional rate plus position control systems fail to meet performance requirements as a result of this interaction.

- PAYLOAD POINTING STABILITY IS DEGRADED BY CONTROLLER INTERACTION
- CONTROLLER INTERACTION EXISTS FOR RIGID SPACECRAFT AND IS AGGRAVATED BY FLEXIBILITY

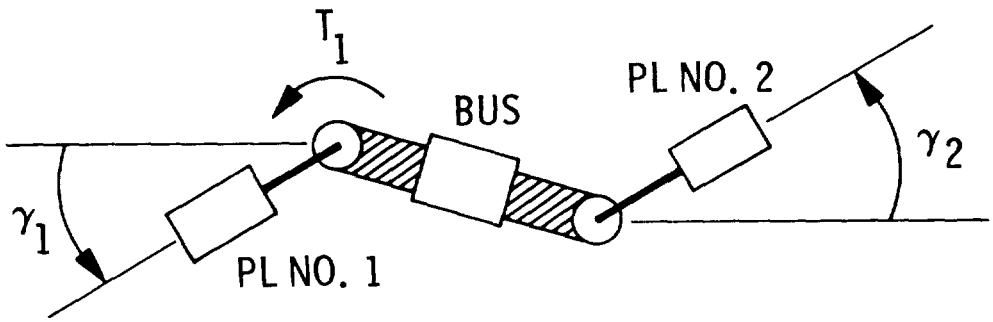

- CONVENTIONAL RATE PLUS POSITION CONTROLLERS DO NOT MEET PERFORMANCE REQUIREMENTS

POINTING CONTROL PROBLEMS (continued)

Control system design is complicated by large shifts in structural parameters which occur as a result of variations in the number and location of experiments mounted on the platform. Structural vibration frequencies in the controller bandwidth further complicate the design problem. The most difficult type of flexibility to design for is one which occurs between the gimbal actuator and the payload sensor. In this case, since the actuator and sensor are not colocated, phase shifts between an applied torque and the resulting angular acceleration at the sensor location can occur. These phase shifts can result in control system instabilities if not properly accounted for.

- CONTROLLER DESIGN IS COMPLICATED BY LARGE VARIATIONS OF STRUCTURAL PARAMETERS AND BY VIBRATION FREQUENCIES WITHIN THE CONTROLLER BANDWIDTH

- STRUCTURAL FLEXIBILITY BETWEEN ACTUATORS AND SENSORS PRESENTS SPECIAL DESIGN PROBLEMS AND MAY RESULT IN CONTROLLER INSTABILITY IF NOT PROPERLY ACCOUNTED FOR

LSS PLATFORM MODEL

The three-dimensional structural model used for this study is shown below. It's relative simplicity allows the effects of structural parameter variations to be investigated cost effectively, yet it has sufficient completeness to account for the generic characteristics of a platform. Payloads 1 and 2 are attached to their pallets with two-degree-of-freedom pointing mounts. Payloads 3 and 4 are rigidly attached to their pallets. Two variations of this basic configuration are considered. The first has a rigid element between the two axis hinge and the payload interface for payload 2, and the second has an elastic element in this same location. These variations will be called rigid pointing mount and elastic pointing mount configurations respectively.

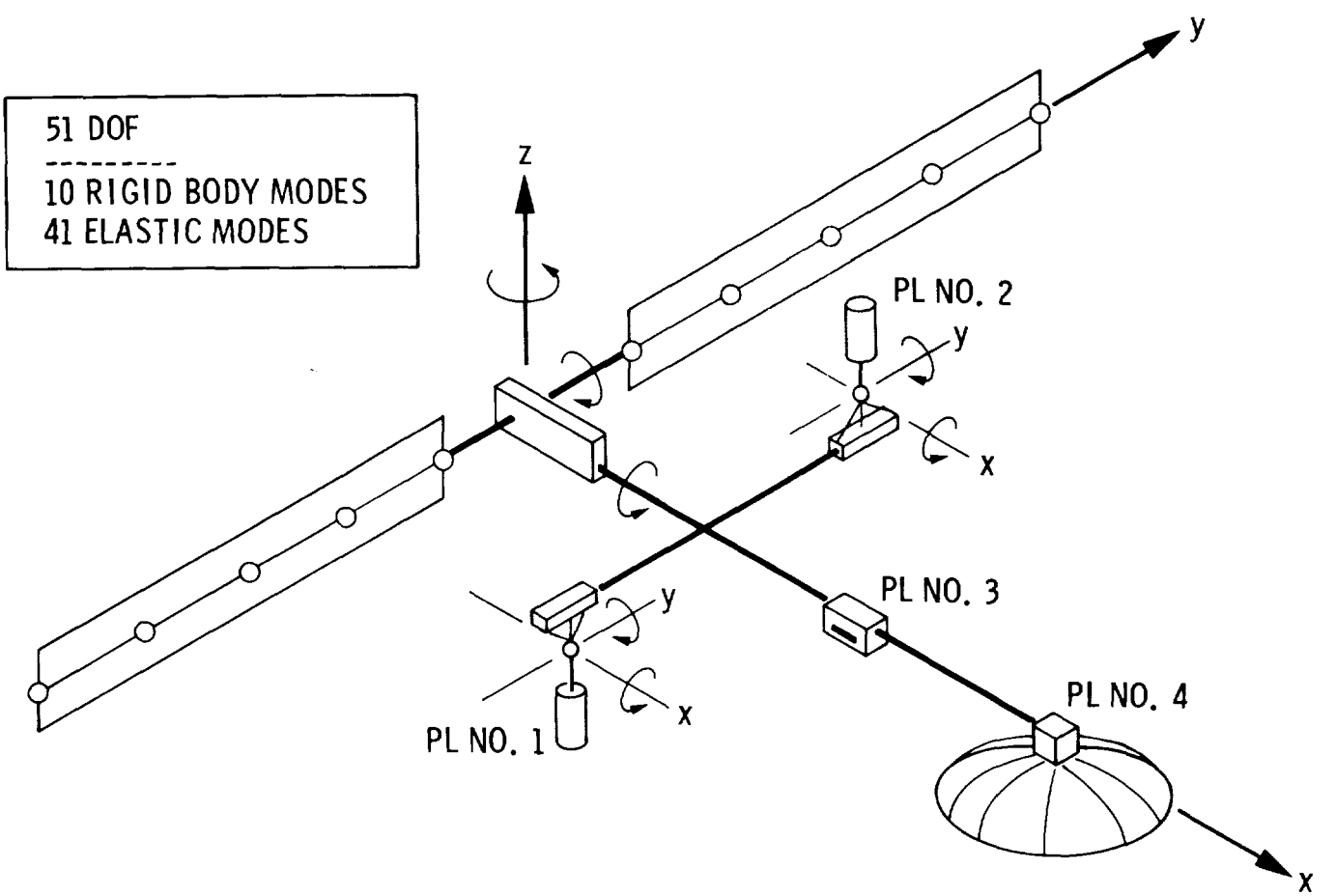

CONTROL SYSTEM DESIGN APPROACH

The control system design follows the steps outlined below. Once a controller configuration has been selected the most important modes of the structural model are selected. This selection takes into account the combined characteristics of the controller and structural model and is described later. Next, compensation and preliminary controller gains are selected based on Single-Input, Single-Output root locus design methods. The controller gains are adjusted using Multi-Input, Multi-Output root locus methods. Finally, performance is verified using dynamic simulations.

- SELECT CONTROLLER CONFIGURATION
- PERFORM MODEL REDUCTION TO SELECT MOST SIGNIFICANT STRUCTURAL MODES
- SELECT COMPENSATION TO STABILIZE SELECTED MODES USING SISO ROOT LOCUS METHODS
- SELECT CONTROLLER GAINS TO PROVIDE DESIRED BANDWITH USING MIMO ROOT LOCUS METHODS
- PERFORM SIMULATIONS TO DETERMINE SYSTEM PERFORMANCE

FREQUENCY DOMAIN DESIGN FEATURES

Single Input-Single Output (SISO) frequency domain approaches can be used to obtain controller designs which are relatively insensitive to parameter errors and model truncation. Also, many engineers prefer frequency domain approaches because of their directness and intuitive appeal. The Multi-Input, Multi-Output (MIMO) root locus approach developed for the LSS platform is robust and retains the appeal of SISO frequency domain approaches.

- STANDARD (SISO) FREQUENCY DOMAIN DESIGNS ARE ROBUST IN PRESENCE OF:
  - PARAMETER ERRORS
  - MODEL TRUNCATION
- SISO FREQUENCY DOMAIN APPROACHES HAVE DIRECTNESS AND INTUITIVE APPEAL
- MIMO FREQUENCY DOMAIN METHODS HAVE BEEN DEVELOPED FOR LSS PLATFORM WHICH RETAIN DESIRABLE FEATURES OF SISO DESIGNS

BASE MOTION COMPENSATION

This study investigates the use of base motion compensation to reduce the interaction between payloads. The basic operation may be explained with the help of the figure below. The acceleration of the payload hinge point (or base) is measured and used to apply a corrective torque (Tc). For an acceleration along the y axis, an x-axis torque is applied proportional to MLy. A similar y axis torque is applied for x axis accelerations.

Base motion compensation is being implemented on two major pointing systems under development for shuttle application. These are the Annular Suspension Pointing System (ASPS) under development by Sperry Flight Systems Division and the Instrument Pointing System (IPS) being developed by Dornier System. The study which follows is intended to identify generic limitations of pointing systems of this type, when operating in the LSS platform environment, without consideration of the detailed characteristics of a specific configuration.

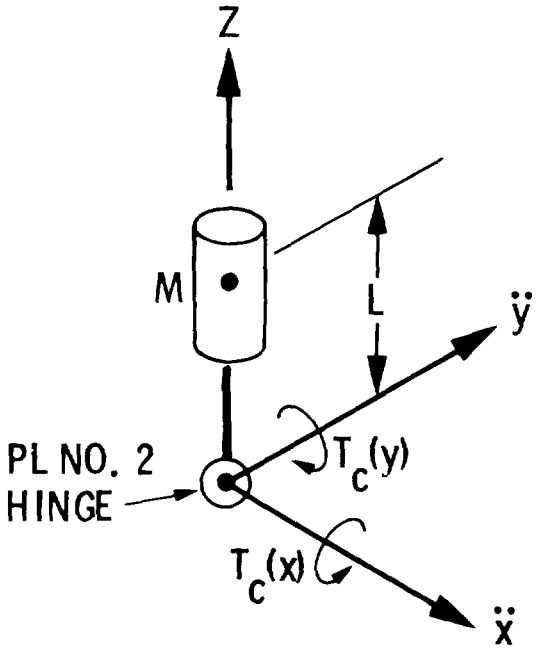

$$T_c(x) = -ML\ddot{y}$$

$$T_c(y) = ML\ddot{x}$$

MODEL REDUCTION METHOD

A reduced order model of the structure is desired for control system design. The method used for this study chooses those modes which have the greatest effect on sensor outputs based on step actuator inputs. Maximum actuator torques are used as determined from system specifications. The resulting open loop response of the sensors are normalized using specification values for these outputs. Modal influence coefficients are found for each mode which represent the maximum normalized responses over all actuator and sensor pairs.

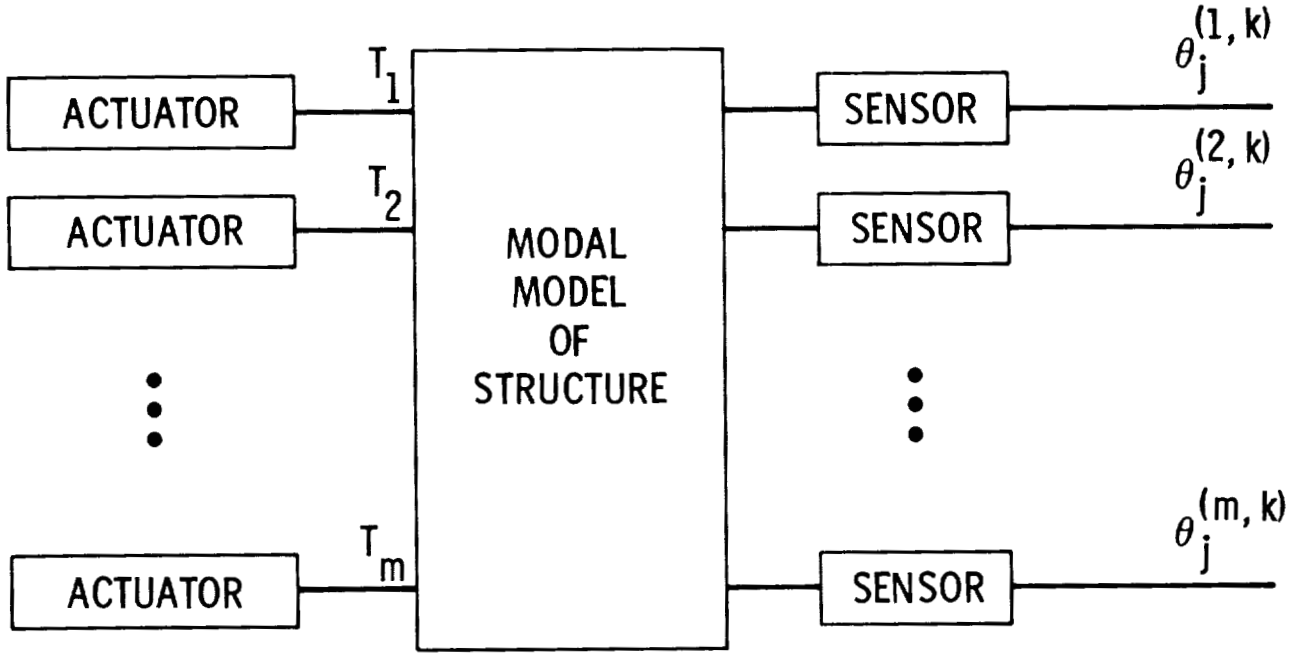

MODAL INFLUENCE COEFFICIENT

$$\overline{\theta}_j = \max_{i,k} \left[\theta_j^{(i,k)} / Q^{(i)} \right]$$

MODEL REDUCTION RESULTS
(Flexible Pointing Mount)

Model reduction results for the LSS platform are shown below. The model has 51 modes, 41 of which are elastic. Influence coefficients are shown for each of the elastic modes. The 12 most important elastic modes have frequencies between 0.06 and 2.3 Hz. The lower frequency modes (12 through 18) are dominated by solar panel bending. The intermediate frequency modes (22 through 32) include cross arm and trailing arm torsion and bending. The higher frequency modes (42 through 45) are associated with elasticity of the pointing mount.

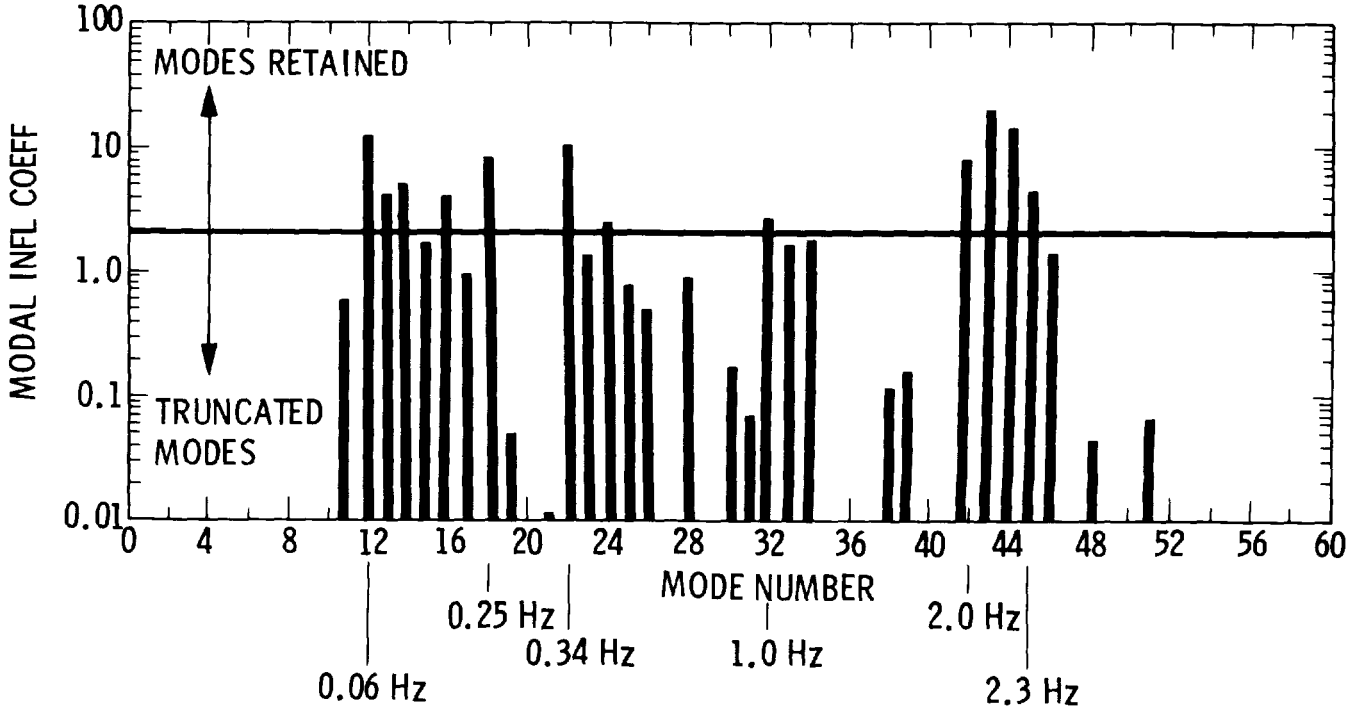

PAYLOAD CONTROLLER PERFORMANCE

Peak pointing errors for payload No. 2 as a result of a 5 degree slew by payload No. 1 are given in the figure below. The slew torque used was 20 N-m. For the rigid pointing mount a 0.25 Hz bandwidth controller was used. The range of pointing errors resulting from x and y axis slews was from 10 to 30 μrad for the rate plus position controller. Base motion compensation reduced these errors by more than an order of magnitude to between 0.3 and 1.0 μrad. A 16 Hz bandwidth accelerometer was used.

For the elastic pointing mount it was necessary to reduce controller bandwidth to 0.1 Hz to achieve stability. Pointing errors were between 50 and 150 μrad. Base motion compensation reduced the peak errors only slightly for this case.

Many user requirements are in the range of 0.05 to 5 μrad. Only the controller using base motion compensation and operating with a rigid pointing mount achieved performance in this range.

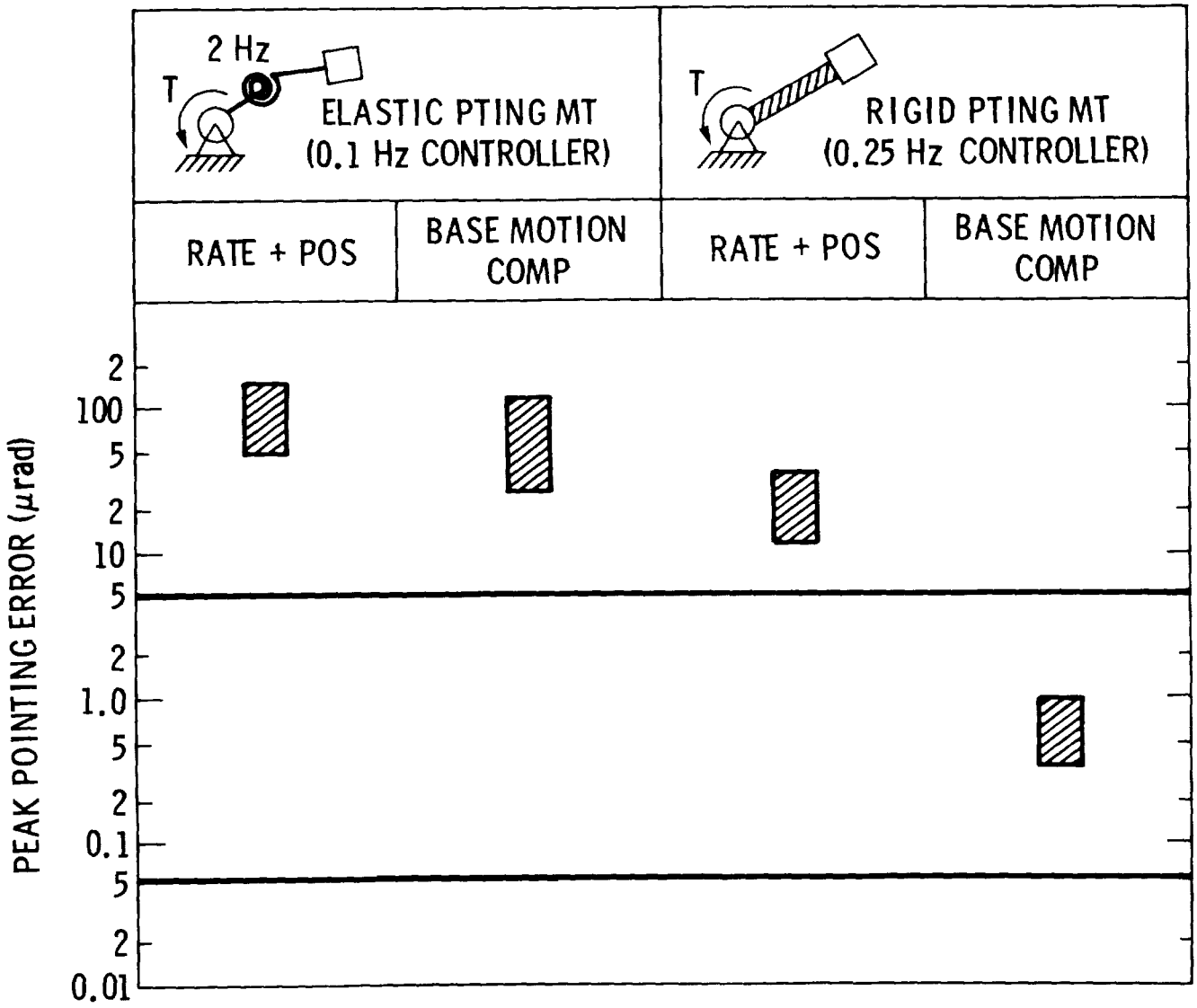

PAYLOAD CONTROLLER PERFORMANCE
(Elastic Pointing Mount)

Representative simulation results are shown below for the elastic pointing mount. Results shown are for a 5 degree y axis slew of payload No. 1. The slew torque profile was a +20 N-m step at time zero followed by -20 N-m at 20 seconds with the slew ending at 40 seconds. Although the peak errors for the rate plus position and base motion compensation controllers are fairly similar, the average pointing errors for the base motion compensation controller are less by a factor of 2 or 3 for the first 60 seconds. Notice, however, that low damping of the mode at 1.1 rad/s (.18 Hz) for the base motion compensation run results in poorer performance than the rate plus position controller after about 70 seconds.

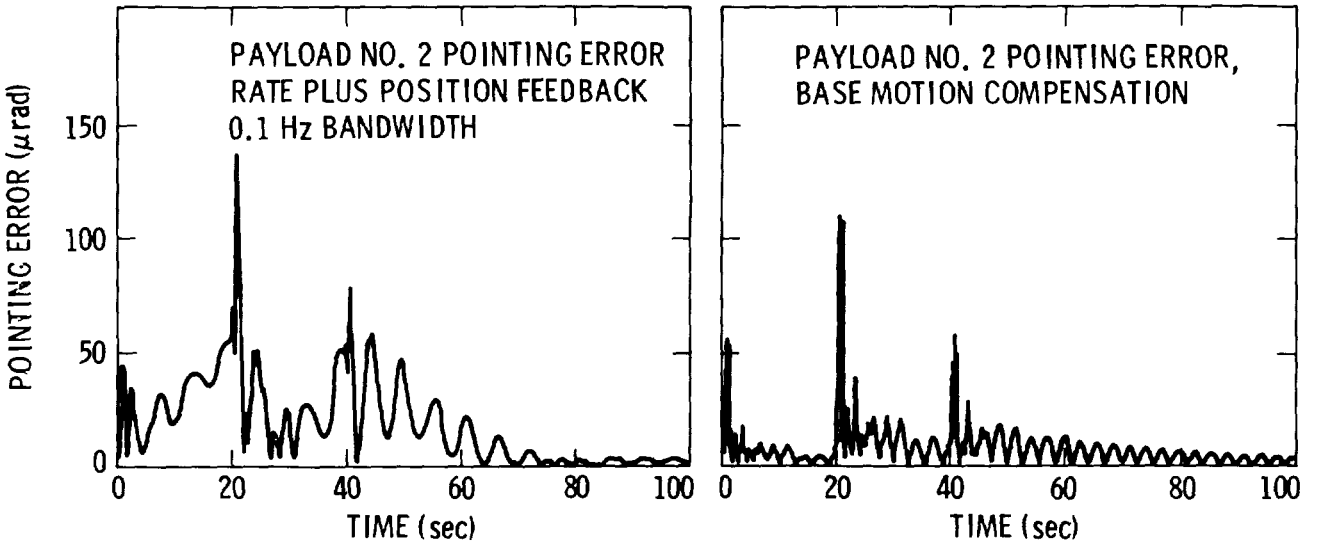

MIMO ROOT LOCUS RESULTS
RATE PLUS POSITION CONTROLLER

Multi-Input, Multi-Output (MIMO) root locus results are shown below for the rate plus position controller. These results include 7 rigid body (zero frequency) rotational modes and 12 elastic modes. In both cases, compensation consists of two-double notch filters one double notch set at 2.0 Hz the other at 2.3 Hz. These filters are used to prevent the elastic modes of the pointing mount from causing instability.

For nominal gain, the 3 rigid body rotational modes of the bus are placed at natural frequencies of .06 to .07 rad/s with damping near 0.7. The 4 rigid body rotational modes of the payloads are placed between 0.6 and 0.9 rad/s with similar damping. Damping for the 12 elastic modes is increased from 0.5% with zero gain to values between 1.5% and 24% at nominal gain.

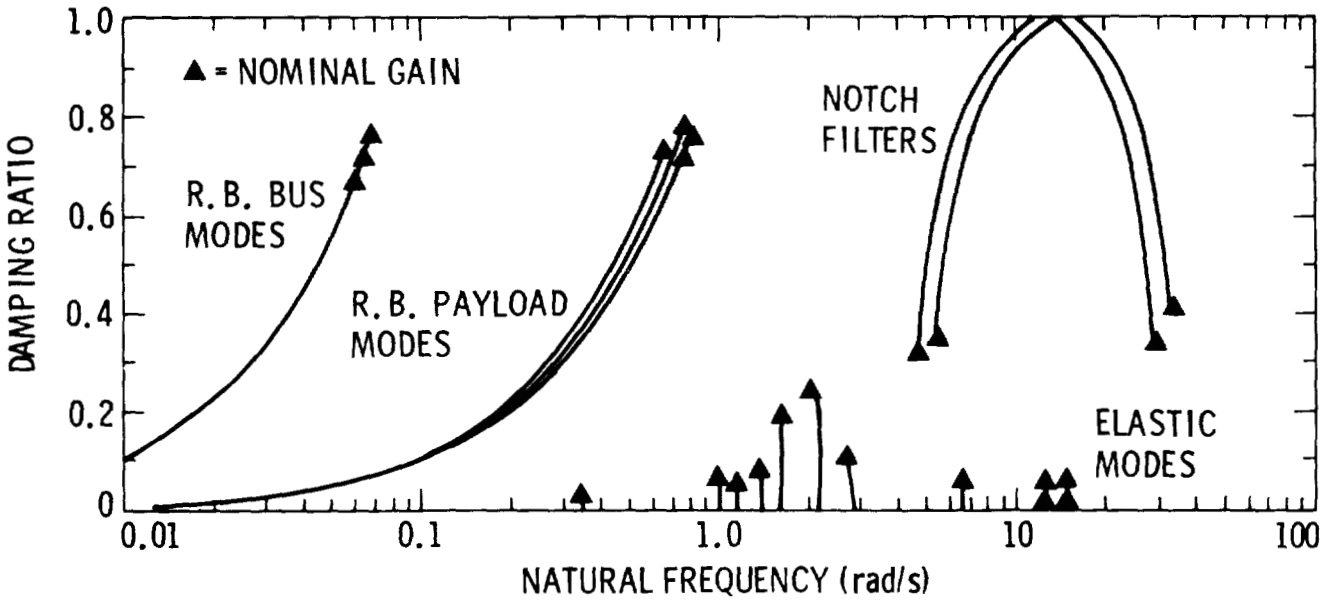

MIMO ROOT LOCUS RESULTS
BASE MOTION COMPENSATION CONTROLLER

MIMO root locus results for the controller using base motion compensation are similar to those for the rate plus position controller. Damping of the elastic modes is somewhat less however, especially at frequencies of 1.1 rad/s, 1.3 rad/s, and 1.9 rad/s where damping is reduced by a factor of 2. The loci associated with the notch filter poles exhibit less damping at nominal gain and this implies the system has a smaller stability margin since these loci are the first to go unstable as gain is increased. Another fact, not illustrated by these root loci, is that this controller is quite sensitive to errors in placement of the notch filter. The rate plus position controller is much more robust in this aspect.

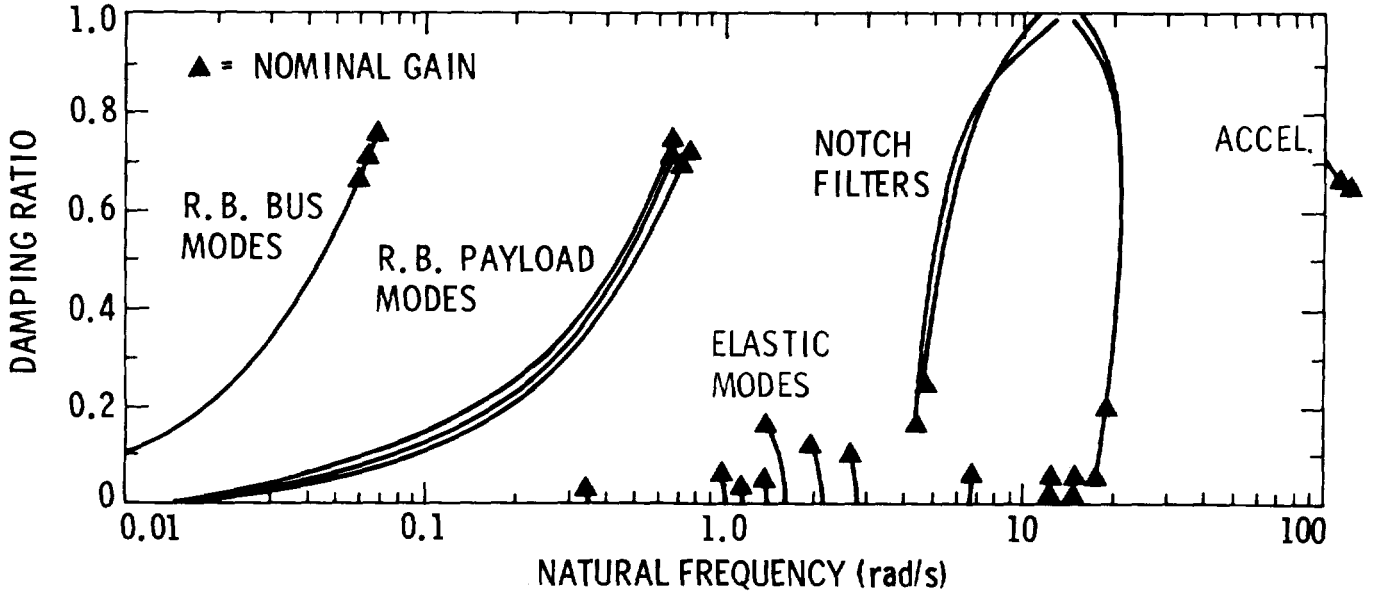

BUS CONTROLLER PERFORMANCE

Peak pointing errors for payload No. 4 as a result of a 5 degree slew by payload No. 1 are given in the figure below. The slew torque used was 20 N-m. For a bus controller bandwidth of 0.01 Hz, the range of pointing errors resulting from x and y axis slews was 350 to 1000 μrad. A 0.1 Hz bandwidth controller reduced this error by an order of magnitude, but further increases in bandwidth did not provide corresponding reductions in pointing error.

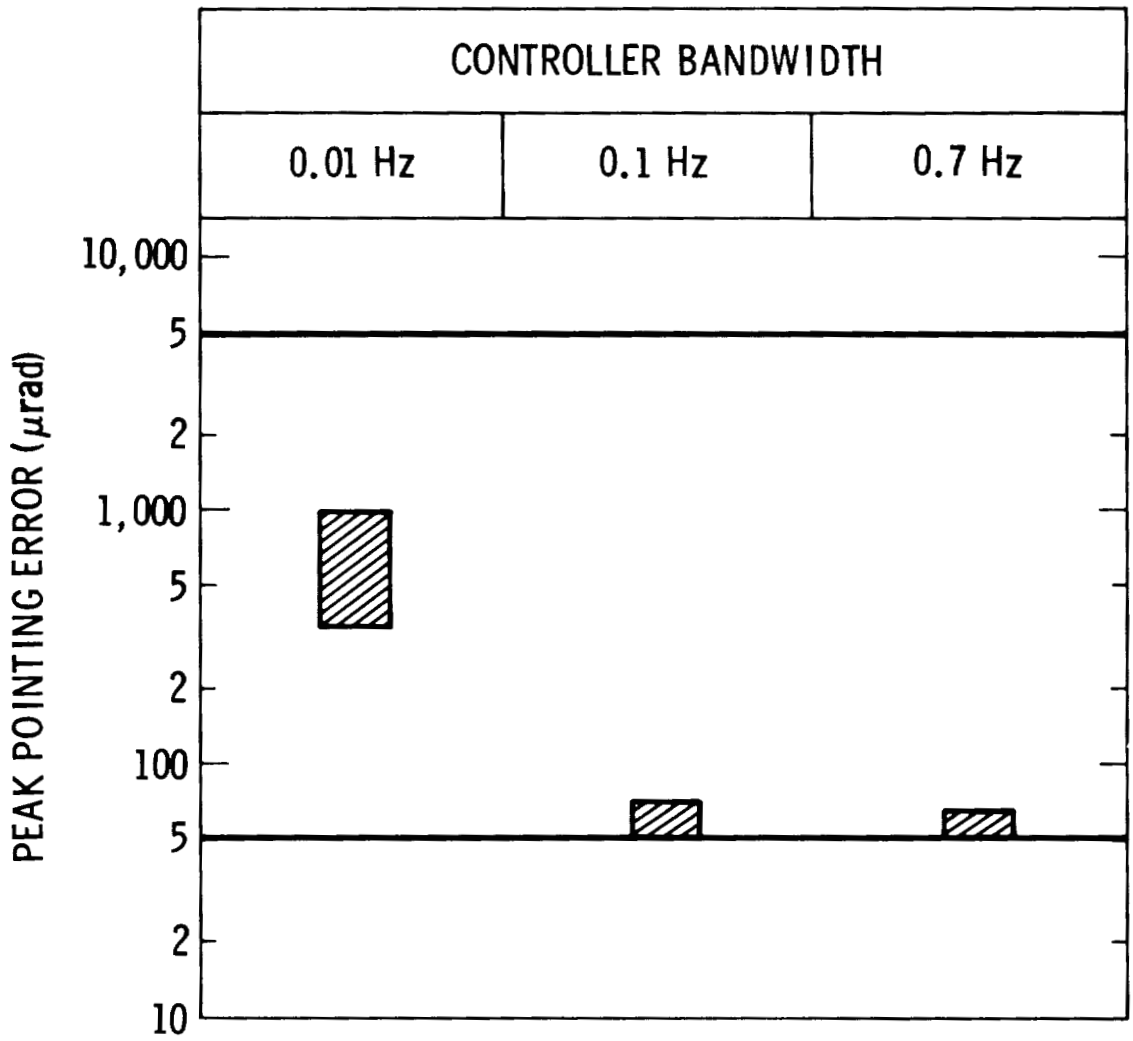

BUS CONTROLLER PERFORMANCE
(Rigid Pointing Mount)

Representative simulation results are shown below. Pointing errors are for payload No. 4. The slew profile for payload No. 1 was a +20 N-m step at time zero followed by -20 N-m at 20 seconds with the slew ending at 40 seconds. The peak errors for the 0.1 and 0.7 Hz controllers are similar, however, damping of the 0.1 Hz controller after the end of the slew is superior to the 0.7 Hz controller. These results show that spacecraft flexibility places a limit on the performance which can be expected from a bus controller.

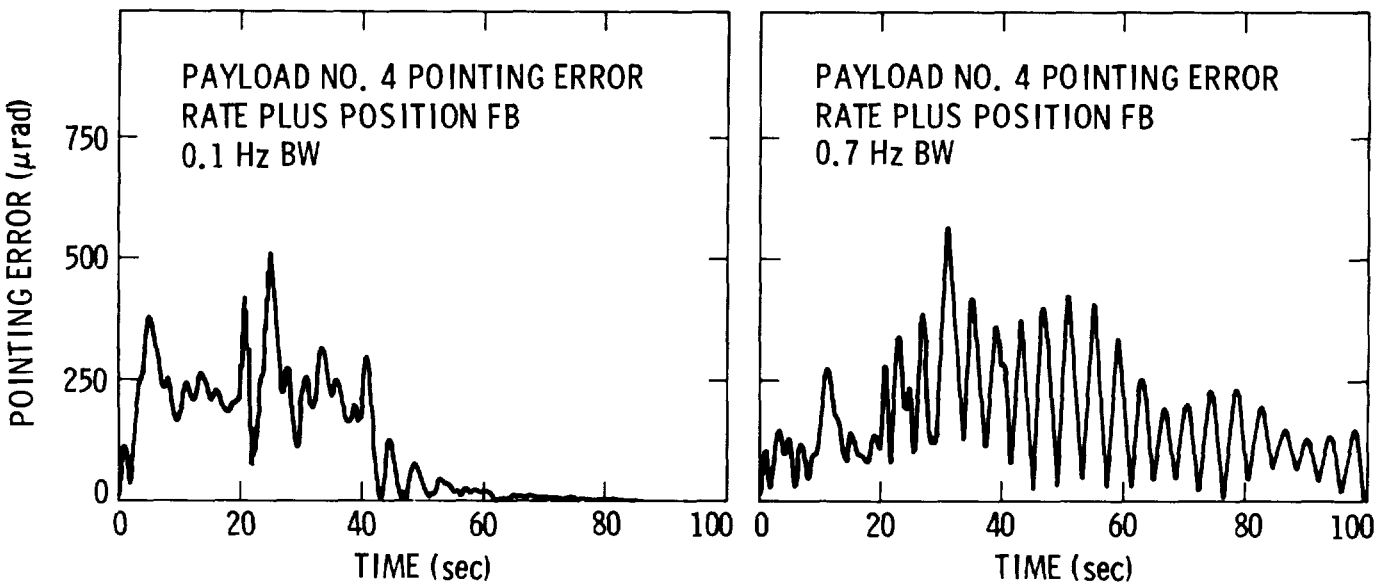

SUMMARY

In summary, it has been found that base motion compensation can be very effective when used with rigid pointing mounts. Pointing errors of less than 1 μrad/s can be achieved. However, the effectiveness of base motion compensation is severely limited when there are flexible elements between the pointing mount actuator and the payload sensor. Bus controller performance is also limited by spacecraft flexibility.

- BASE MOTION COMPENSATION IS EFFECTIVE WHEN USED WITH RIGID POINTING MOUNTS

  16 Hz ACCELEROMETER
  0.25 Hz CONTROLLER
  $>$
  0.3 TO 1.0 μrad POINTING ERROR

- FLEXIBILITY BETWEEN POINTING MOUNT ACTUATOR AND PAYLOAD SENSOR LIMITS EFFECTIVENESS OF BASE MOTION COMPENSATION

  2 Hz FLEXIBILITY
  0.1 Hz CONTROLLER
  $>$
  30 TO 150 μrad POINTING ERROR

- BUS CONTROLLER PERFORMANCE IS ALSO LIMITED BY SPACECRAFT FLEXIBILITY

  0.1 Hz CONTROLLER
  0.7 Hz CONTROLLER
  $>$
  50 TO 80 μrad POINTING ERROR

FUTURE WORK

Future work will be performed to determine the effect of man/shuttle disturbances on payload pointing. These disturbances will occur during periods of time when the shuttle is berthed to the LSS platform and will include man push off forces and shuttle thruster firings. Techniques for improving pointing mount disturbance isolation will be examined to include sensor output blending and optimized compensation parameters.

A variety of platform and payload configurations will be examined. These configurations will include advanced platforms having large flexible payloads (e.g. 100 meter antenna systems) and others intended for manned applications. Payload controller performance will be examined for each major configuration. Payload controller performance will also be determined as a function of platform and pointing mount stiffness.

- EXAMINE SENSITIVITY OF CONTROLLER PERFORMANCE TO DISTURBANCES CAUSED BY MAN/SHUTTLE INTERFACE
- DEVELOP IMPROVED METHODS FOR DISTURBANCE ISOLATION
- ESTABLISH CONTROLLER PERFORMANCE LIMITS FOR A VARIETY OF PLATFORM AND PAYLOAD CONFIGURATIONS
    - LARGE FLEXIBLE PAYLOADS
    - MANNED SPACE STATIONS
- DEVELOP CONTROLLERS TOLERANT OF CONFIGURATION CHANGES AND PARAMETER ERRORS

BERTHED ORBITING CONFIGURATION

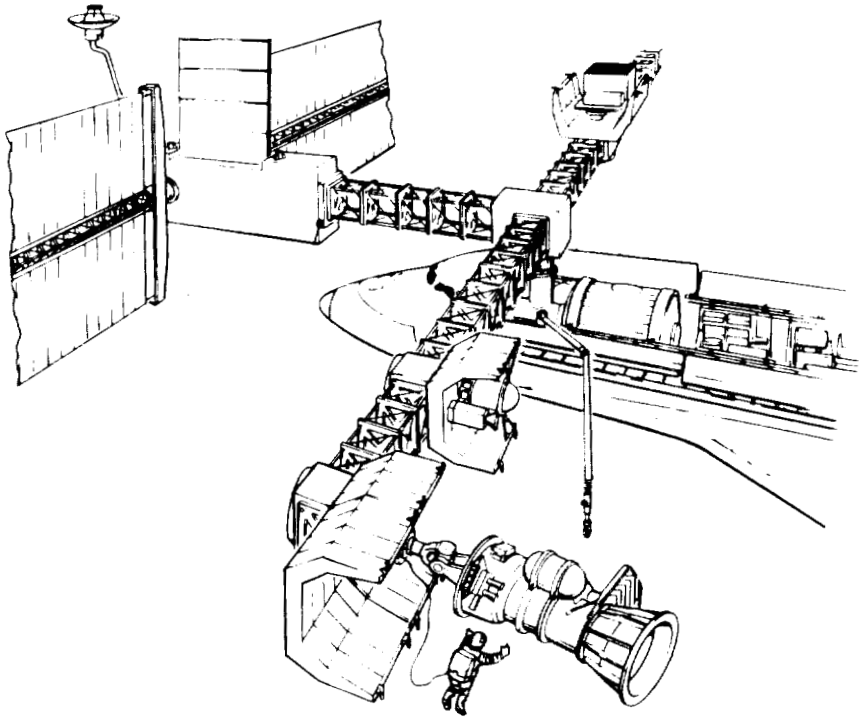

ADVANCED SCIENCE AND APPLICATIONS SPACE PLATFORM

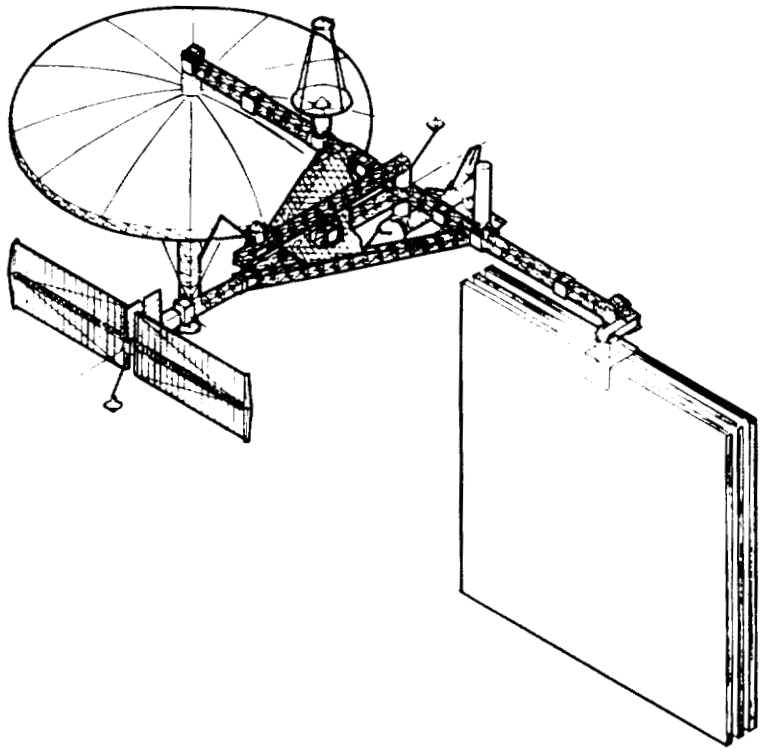

SPACE OPERATIONS CENTER

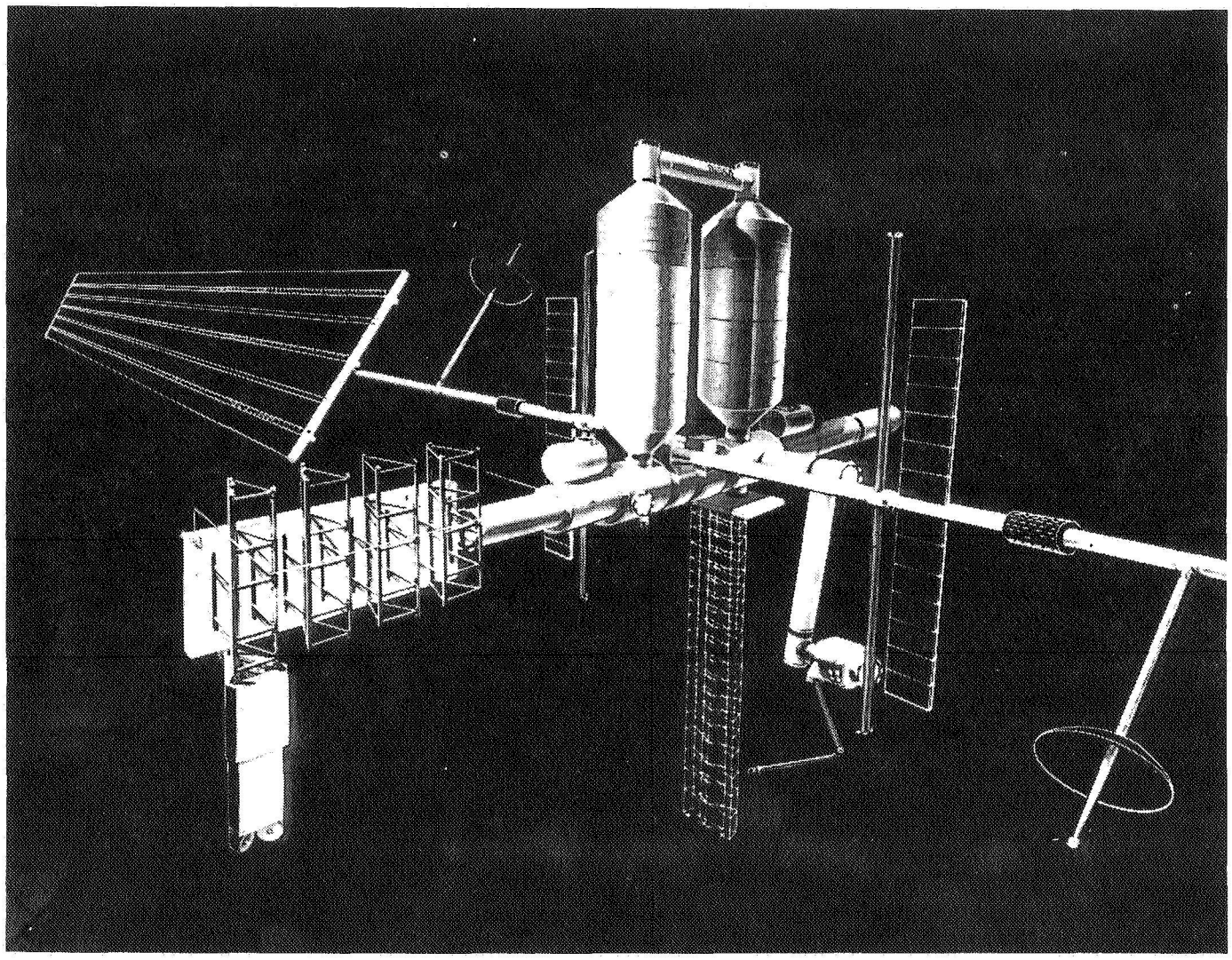

A STUDY OF AUTONOMOUS RENDEZVOUS AND DOCKING SYSTEMS

J. D. Micheal
Marshall Space Flight Center
Huntsville, AL

Large Space Systems Technology - 1981
Third Annual Technical Review
November 16-19, 1981

INTRODUCTION

The problem of automatically docking two spacecraft has received little attention in this country since a pilot has always been available. The Soviet Union has demonstrated a system for automatically docking two controlled, fully active vehicles (ref. 1). To date, no one has developed and flight-tested an automatic scheme in which one vehicle is completely inactive. There is a recognized need for this capability which is associated with satellite retrieval and space construction (ref. 2).

This paper presents an overview of our activities in the automatic rendezvous and docking area. Our interest first began as a result of our involvement with the Teleoperator Retrieval System (TRS) Project whose primary and initial mission was to reboost the Skylab to a higher orbit to extend its lifetime in space. During the course of our work on TRS, we conducted full six degree-of-freedom, man-in-the-loop, hybrid simulations of the TRS/Skylab docking problem. Witnessing the training time required along with the challenge this problem presented to experienced astronauts strongly influenced our decision to begin investigations of autonomous rendezvous and docking systems.

We will begin by covering briefly a representative mission scenario. We will continue our discussion with a statement of the problem which we have addressed and delineate the requirements for the extraction of relative attitude and position data. We have also included a systems block diagram and will describe the integral functions which go to make up an autonomous docking system. Such a system has been simulated, and the digital simulation will be described along with some representative results of a system based on a laser ranging device as the sensor. A television camera as the ranging sensor was also considered and we will discuss one such video based automatic docking scheme along with some representative results as well. Finally, we will briefly cover our current and ongoing efforts in the autonomous video rendezvous and docking area (fig. 1).

- MISSION SCENARIO
- STATEMENT OF PROBLEM
- SYSTEMS DESCRIPTION/BLOCK DIAGRAM
- SIMULATION RESULTS/RADAR
- VIDEO SYSTEMS DESCRIPTION
- CONCLUSION/PLANNED ACTIVITIES

FIGURE 1

MISSION SCENARIO

A typical mission scenario for an automatic rendezvous and docking mission is shown in figure 2. The chase vehicle will be launched from the ground into a coplanar parking orbit either just above and in front of the target vehicle or just below and trailing to minimize the plane change required to rendezvous. The long range rendezvous maneuvers will follow. The target and the chase vehicles have heretofore been tracked from the ground, but, with the advent of systems such as the Global Positioning System (GPS) and the Space Sextant, the tracking as well as the long range rendezvous in general may be done autonomously by the chase vehicle. During this phase, the chase vehicle is placed within the docking sensor's operational range and the target vehicle is acquired. In the approach phase, the chase vehicle's docking sensor output allows for the determination of relative attitude and position. These error signals input the chase vehicle control system which guides the chaser along a prescribed trajectory (one which would be optimized according to mission) to a predetermined standoff range. The station-keeping phase may call for the chase vehicle to circumnavigate the target vehicle for purposes of inspection or, in the event of a tumbling target, may require the chase vehicle to null the relative attitude rate errors in preparation for the docking phase. Final closure through the last 10-20 feet makes up the docking phase which will be the most critical time of the mission. Depending on the respective docking interfaces (chase to target), there may be a soft dock period where all systems are checked prior to rigidization of the docking hardware and completion of the task.

- LAUNCH
- LONG RANGE RENDEZVOUS
- TARGET ACQUISITION/APPROACH
- STATION KEEPING
- DOCK

FIGURE 2

STATEMENT OF PROBLEM

The primary focus of our studies has been on the last three phases of the mission scenario just described with emphasis on the approach phase. One of the first problems to be addressed in this study was deciding on the nature of the system to be studied and to baseline certain systems data such as chase and target vehicle configuration, reaction control system, sensor requirements, etc. Because of the available simulation data showing man's ability to pilot the Teleoperator Retrieval System (TRS) to a soft dock with the uncontrolled Skylab, this was the physical system selected for modeling.

The specific objectives of our studies have been to develop schemes for accomplishing automatic docking between two such spacecraft using a device on the chase vehicle to sense the relative position and attitude of the passive target. A number of devices are under development and one of the more promising ones is a laser ranging radar which we chose to model. In this technique (see fig. 3), the sensor scans a known pattern of reflectors on the target, thus generating a system of vectors between the two bodies which in turn is used to derive the chase to target vehicle relative position and attitude. A minimum of three measurements (reflectors) are required though additional measurements do provide a basis for manipulation to improve attitude position accuracy. In fact, the attitude/position error varies inversely with the square root of the number of reflectors and inversely with pattern size as well. However, assuming minimum requirements are met, the resulting relative position and attitude data would be used to drive a conventional reaction jet control system.

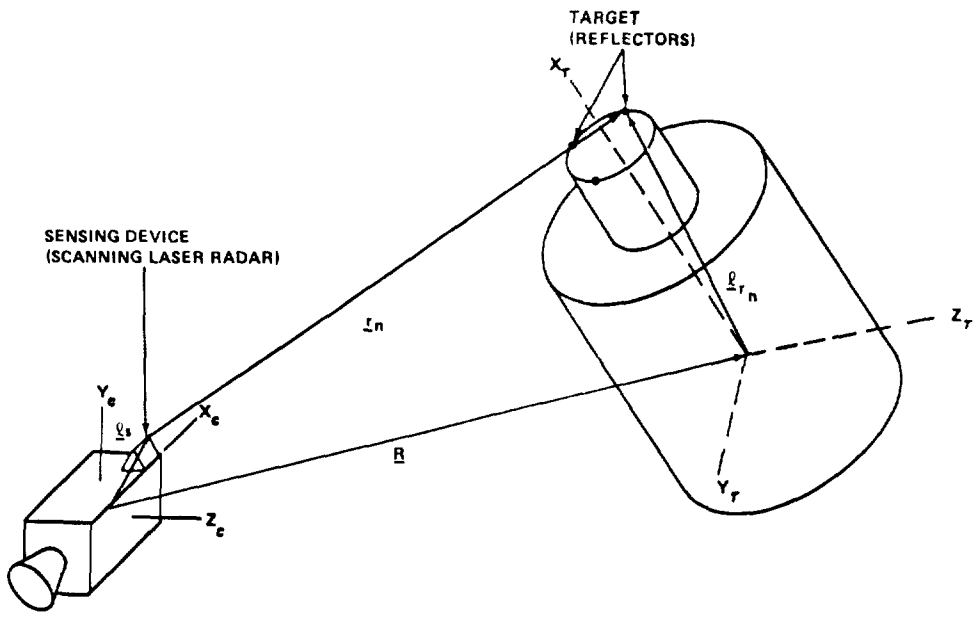

FIGURE 3

SYSTEM DESCRIPTION/BLOCK DIAGRAM

To evaluate the merits of this concept as well as others and to determine how inaccuracies in the data might degrade system performance, the dynamics of an active chase vehicle carrying the sensor and uncontrolled target vehicle carrying the reflector pattern were modeled using the data base described earlier.

A functional block diagram of the resulting digital simulation is presented in figure 4. The block labeled "Signal Processor" contains the algorithms for deriving relative position and attitude information from sensor output. A noise model for the sensor was derived based on sensor accuracies specified in reference 3. The vehicle dynamics block represents rigid body dynamic models of either the chase or target vehicles. The target vehicle motion is governed by orbital mechanics effects as well as being subject to programmed initial conditions which simulate a tumbling target. The chase vehicle motion is the result of orbital mechanics effects and firings from the Reaction Control System (RCS) engines. Signals to fire the RCS engines are generated within the Digital Auto Pilot (DAP), which uses quadratic switching lines determined by the rotational and translational acceleration capability of each chase vehicle axis. The manner in which the required commands are generated and nature of the commands themselves depend on the particular mission phase selected. The functional block(s) labeled mode/logic control contain the control laws for each of three mission phases: (1) Rendezvous Phase, (2) Station-keeping Phase, and (3) Closure and Dock Phase. This block represents the heart of the autonomous process where based on mission circumstance appropriate reference frames are selected and control priorities are set.

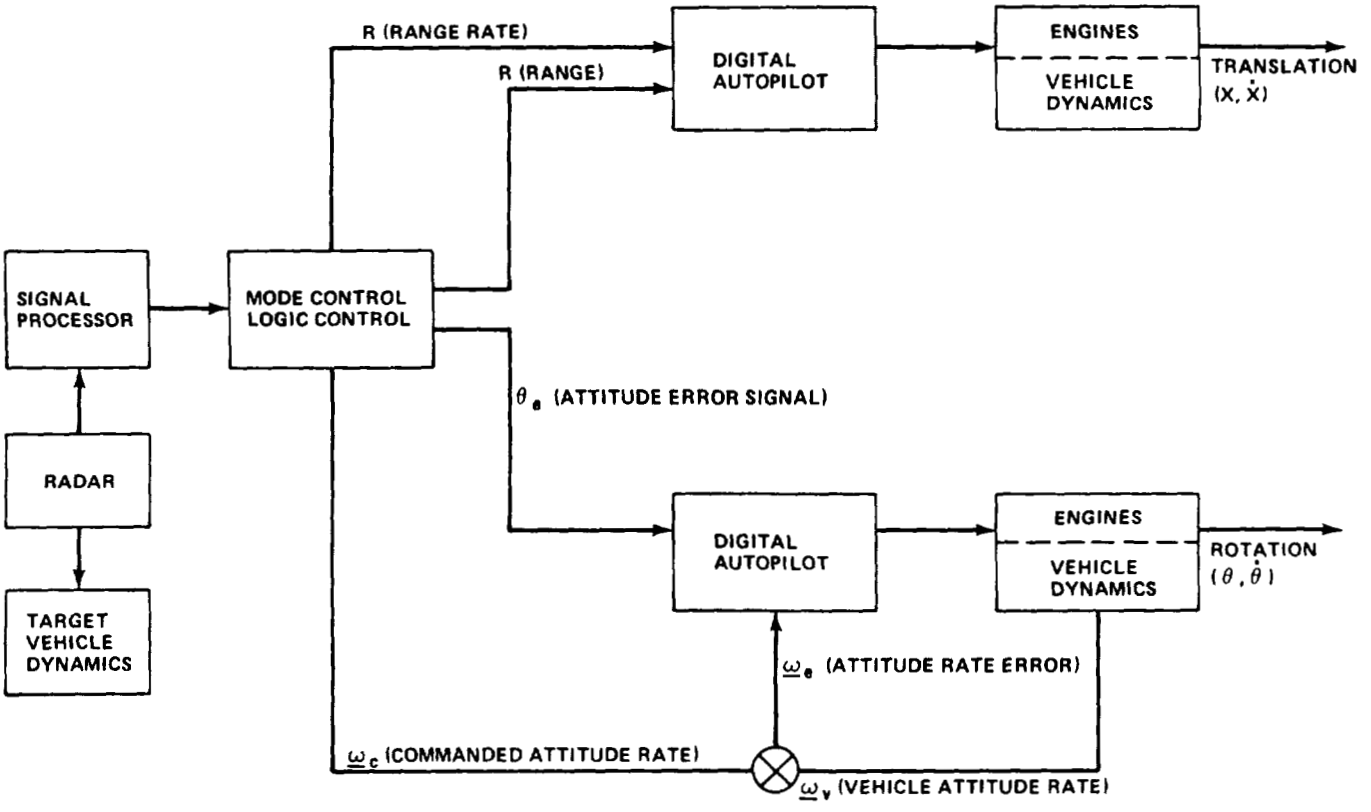

FIGURE 4

SIMULATION RESULTS

Results from the digital simulation program to date are encouraging and support the viability of an automatic rendezvous and docking concept based on the laser ranging radar. Production runs were chosen not only for their challenging nature (that is, high target tumbling rates) but also for initial conditions which would match those already investigated in our 6-DOF man-in-the-loop hybrid simulator. A typical run assumes the target vehicle to be in an arbitrary attitude with an initial angular rate. The chase vehicle begins its final approach from an arbitrary position on the order of 30 m distant.

The results from such runs do evidence a chaser vehicle capable of performing a rendezvous and soft dock with an uncontrolled target for a variety of initial conditions. Salient aspects of a representative case are revealed in the plot of range vs range rate (sensed data) in figure 5. The total target spin rate for the case was 1.7 deg/sec and the chaser vehicle was positioned initially at a probe to port range of 23 m and given a small initial closing velocity. The chaser vehicle accelerates to a closing velocity of .6 m/s at a range of 15 m and then decelerates to a velocity of .08 m/s at soft dock. Time of flight is specified at every 5 m range decrement with a total elapsed time for the flight of 56.3 secs. Characteristic data uncertainties (noise), such as those resulting from radar measurement errors, produce some degradations in results such as increased mission times and increased fuel requirements. Though the presence of noise, which can be seen in the comparison plots of range vs range rate in figure 5, does degrade system performance, the overall range/range rate profile remains essentially the same as the no noise case and similarly converges to the soft dock condition. A further example of this convergence is illustrated in figure 6 which is a plot of the root-sum squared (RSS) of the chase to target vehicle attitude errors vs time of flight. After 20 secs of elapsed time, a comparatively high attitude error has been nulled to within deadband limits and remains there for the duration of the flight.

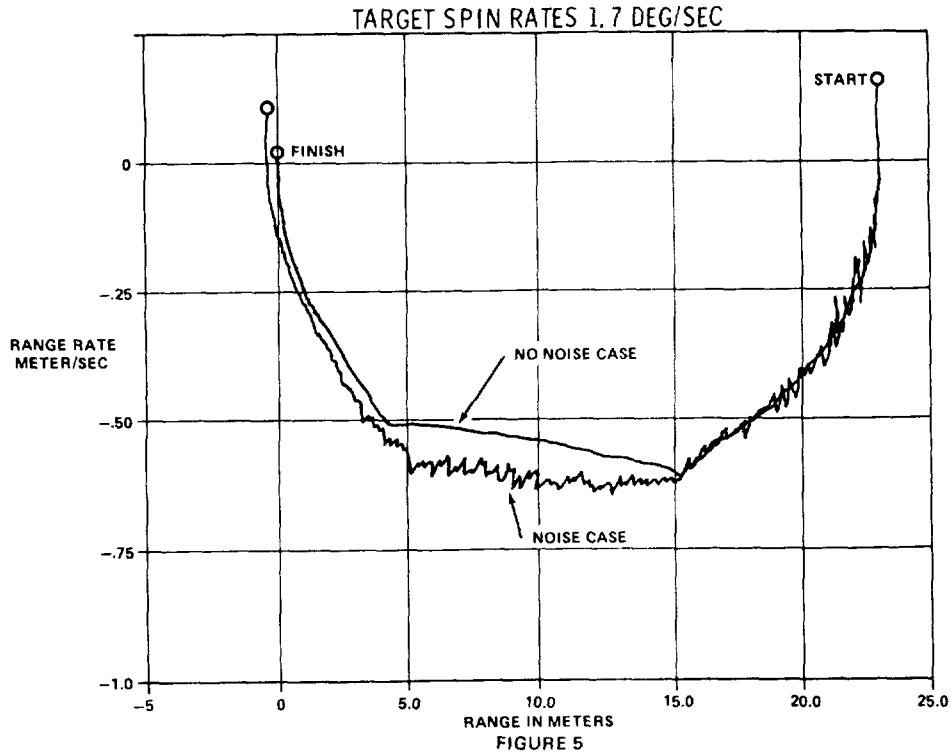

FIGURE 5

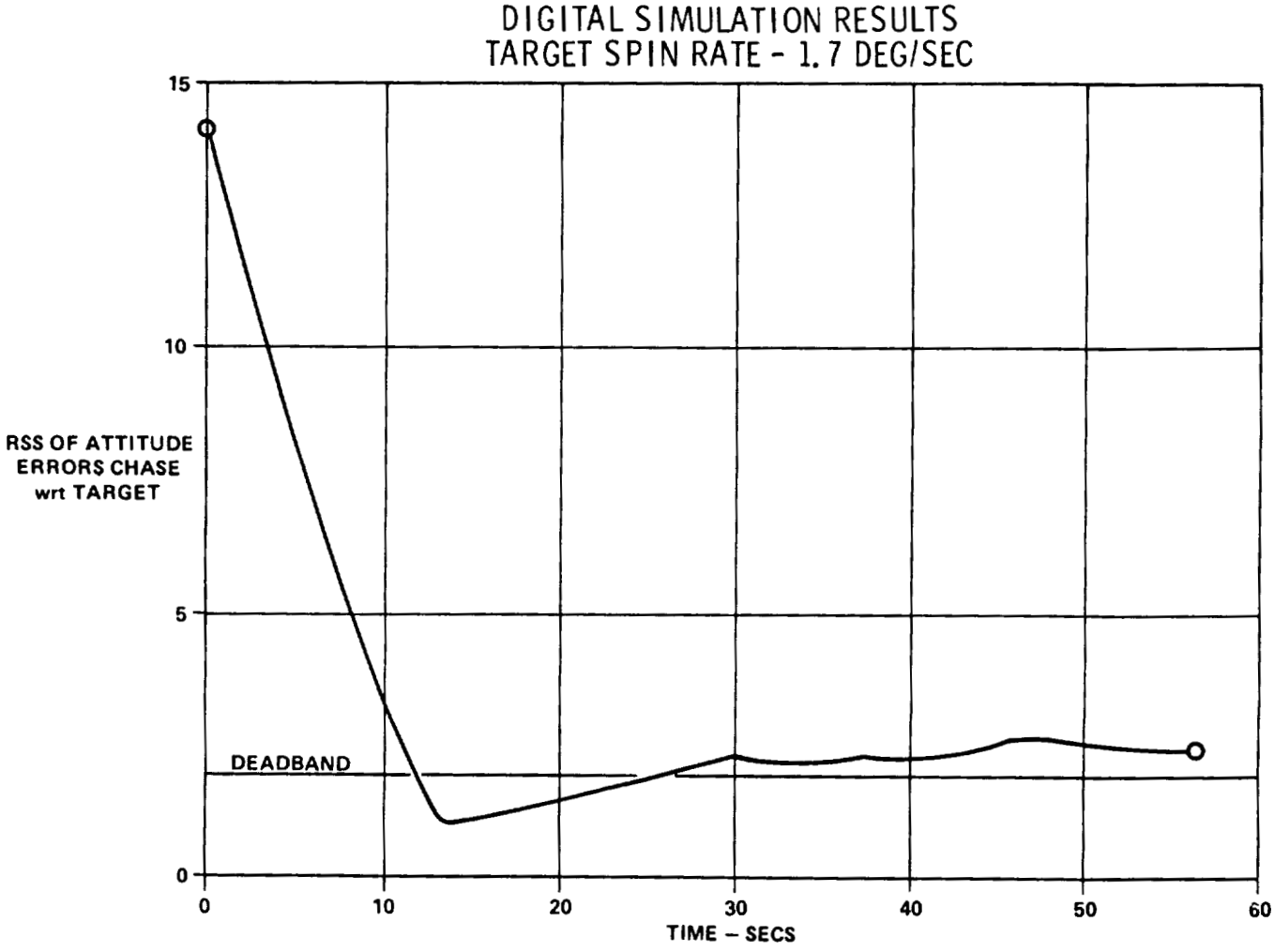
DIGITAL SIMULATION RESULTS
TARGET SPIN RATE - 1.7 DEG/SEC
RSS OF ATTITUDE ERRORS CHASE wrt TARGET
15
10
5
0
DEADBAND
0
10
20
30
40
50
60
TIME – SECS

FIGURE 6

VIDEO APPROACH

The large majority of missions dealing with spacecraft placement and retrieval or with space construction envisioned, thus far, involve a propulsive transfer stage equipped with a television system for providing visual feedback to a remote site. A visual system which could also provide tracking data for an autonomous docking system could prove to be quite an advantage to this category of mission. As a result, we have been investigating the feasibility of a video based autonomous rendezvous and docking system. Such a video system (see figure 7) would utilize a television camera that has the capability of digitizing the visual information and transferring this data to an image data processor in real time. Either through the knowledge of the target vehicle geometry or through the knowledge of a known pattern of reflectors on the target, the chase to target vehicle range and relative attitude may be derived. As with the lasar ranging technique, this data is used to drive the chase vehicle attitude control system. Since the practicability of automating the chaser vehicle control system, given the appropriate error signals, was established in our study of the laser ranging technique, the focus of our attention with the video system has been on the first four areas listed in figure 7.

The simulation program developed for these studies includes a model for the television camera which chooses the cluster of pixels to be turned on for each target pattern light or reflector as a function of camera parameters, target pattern, target orientation, and range. This data is the digitized representation of the visual image that is passed to the image data processor (IDP). The IDP in turn calculates the centroids of each of the pixel clusters and it is from the x-y coordinates of these light centroids that the relative attitude and position data may be derived. One target pattern which we have investigated is a circular pattern of eight lights or reflectors. Except when the line of sight is perpendicular or in the same plane of the pattern of reflectors, the pattern will appear as an ellipse to the computer. From the orientation of the ellipse and its eccentricity, relative attitude may be derived; and, from the semi-major axis length an estimation of range is made. This relative attitude and displacement data is less accurate than the technique based on the laser ranging device, but appears to be sufficient for the stable target case.

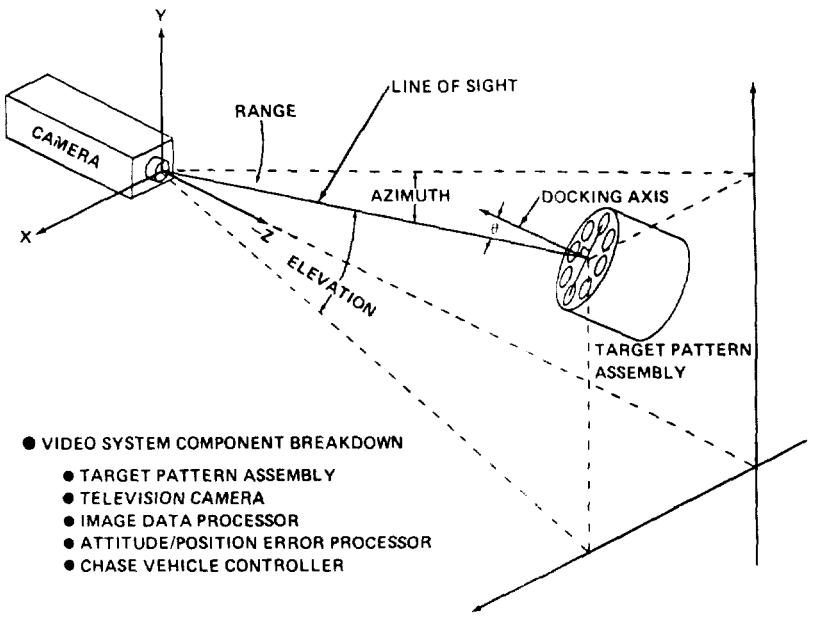

FIGURE 7

CONCLUSIONS/PLANNED ACTIVITIES

The results obtained thus far support the viability of both the laser ranging technique and the video technique as viable approaches for an autonomous docking system. Digital simulation results to date indicate areas of performance comparable to or exceeding that achieved by a trained pilot in our man-in-the-loop simulations. While no fundamental problems have been uncovered, additional work remains to be done, especially on the video system and more work is planned to improve this technique. In FY-82, we received support from OAST to continue this investigation, and a contract with Martin Marietta Corporation is just underway.

The contracted effort will include (see figure 8) the identification and functional description of video techniques, similar to the one described above, which offers a method for deriving relative position and attitude from video sensor output. The necessary extraction equations, algorithms, and associated computational operations will be outlined for each of the viable techniques discovered. Each of the above approaches will then be implemented in a simple docking simulation along with appropriate models for input data errors. Runs will be made against a series of test cases to provide a first level assessment of the approaches.

We will parallel this contracted effort with studies of our own enhanced by projected improvements in our simulation capability. We have recently obtained a television camera and associated interface hardware. This system, nearly complete, will operate in conjunction with a minicomputer to provide a new video system analysis and demonstration tool. This new system along with continuing improvements to our digital simulation programs will help in our efforts to improve on present video techniques and to explore new techniques with promising application to autonomous rendezvous and docking systems.

- STUDY CONTRACT PROGRAM MILESTONES
  - IDENTIFY/DESCRIBE VIDEO TECHNIQUES
  - DEFINE ALGORITHMS FOR DERIVING POSITION/ATTITUDE
  - IMPLEMENT/EXERCISE SIMULATION PROGRAMS
- MSFC'S PLANNED ACTIVITIES
  - HARDWARE DEMONSTRATION OF VIDEO SYSTEM
  - IMPROVE ON PRESENT VIDEO TECHNIQUES
  - EXPLORE NEW TECHNIQUES

FIGURE 8

REFERENCES

1. Legostayev, V. P. and Raushenbakh, B. V., "Automatic Assembly in Space," NASA Translation TT F-12, 113 presented at 19th Congress of the International Astronautics Federation, December 1968.

2. Schappell, R., et al, "Application of Advanced Technology to Space Automation," NASA CR-158350, 1979.

3. Flom, T., and Coombes, H. D., "Construction and Testing of a Scanning Laser Radar (SLR), Phase 2," NASA CR-123530, 1971.

A DISTURBANCE ISOLATION CONTROLLER FOR THE SOLAR ELECTRIC PROPULSION SYSTEM FLIGHT EXPERIMENT

H. B. Waites
Marshall Space Flight Center
Huntsville, AL

Large Space Systems Technology - 1981
Third Annual Technical Review
November 16-19, 1981

ABSTRACT

A disturbance isolation controller (DIC) is developed for a simplified model of the Solar Electric Propulsion System (SEPS) flight experiment which consists of a rigid Sperry gimbal torquer (AGS) mounted to a rigid Orbiter and the SEPS solar array (rigid) end mounted to the AGS. The main purpose of the DIC is to reduce the effects of Orbiter disturbances which are transmitted to the flight experiment. The DIC uses an observer, which does not require the direct measurement of the plant inputs, to obtain estimates of the plant states and the rate of the plant states.[1] The state and rate of state information is used to design a controller which isolates disturbances from specified segments of the plant, and for the flight experiment, the isolated segment is the SEPS solar array.

INTRODUCTION

The DIC design is an outgrowth of work form a dissertation[2] on model following controllers and from efforts to reduce the Orbiter acceleration disturbances for the European Instrument Pointing System (IPS) payloads. Model following controllers are required to have estimates of the plant states so that the plant can follow the model. If the inputs to the plant are not available for direct measurement, then the state estimator used in the model following controller can have biases; therefore, the model following controller performance is degraded. For the IPS controller, an accelerometer is mounted at the base of the IPS gimbals to measure accelerations caused by Orbiter disturbances. These disturbances are not available for direct measurement, so a state estimator, used in the IPS controller, would have biases and so would the rate of state information obtained by the estimator. With the apparent inability to estimate the states of the plant, an observer or filter is not useful for control of Orbiter disturbances.

An observer is developed for the flight experiment which does not require direct measurement of all the plant inputs. The observer's inputs are the output measurements of the states and the output measurements of the rate of the states. Using the output measurements of the AGS rate gyros and the AGS accelerometers, the observer converges to the plant states and the plant accelerations. This observer is a key ingredient in the DIC design.

The DIC is a force/torque feedback controller which uses the observer acceleration estimates and knowledge of the plant parameters to determine the appropriate torques for reducing the disturbance effects on certain segments of the plant. The reduction of acceleration effects not only decreases the loads on the payloads, but also improves payload pointing capability. The DIC can best be delineated by applying the control design to the simplified model of the flight experiment.

FLIGHT EXPERIMENT MODEL

The linear equations of motion for a rigid SEPS solar array connected to a rigid AGS which is connected to a rigid Orbiter are

$$\begin{bmatrix} m_{11} & m_{12} & m_{13} \\ m_{21} & m_{22} & m_{23} \\ m_{31} & m_{32} & m_{33} \end{bmatrix} \begin{bmatrix} \ddot{r}_o \\ \ddot{\Phi}_o \\ \ddot{\Phi}_i \end{bmatrix} = \begin{bmatrix} I_1 \\ \tilde{r}_d \\ 0_1 \end{bmatrix} F + \begin{bmatrix} 0_1 \\ 0_1 \\ I_1 \end{bmatrix} T_c, \tag{1}$$

$$\begin{bmatrix} \Phi_T \\ \dot{\Phi}_T \end{bmatrix} = \begin{bmatrix} 0_1 & 0_1 & T_G{}^t & 0_1 & I_1 & 0_1 \\ 0_1 & 0_1 & 0_1 & T_G{}^t & 0_1 & I_1 \end{bmatrix} \begin{bmatrix} r_o \\ \dot{r}_o \\ \Phi_o \\ \dot{\Phi}_o \\ \Phi_i \\ \dot{\Phi}_i \end{bmatrix}, \tag{2}$$

$$A_g = \begin{bmatrix} 0_1 & I_1 & 0_1 & \tilde{d}_{sm} & 0_1 & 0_1 \end{bmatrix} \begin{bmatrix} \dot{r}_o \\ \ddot{r}_o \\ \dot{\Phi}_o \\ \ddot{\Phi}_o \\ \dot{\Phi}_i \\ \ddot{\Phi}_i \end{bmatrix} \tag{3}$$

where

0_1 = 3x3 zero matrix,

I_1 = 3x3 identity matrix,

m_{ij} = 3x3 mass matrix, $(i,j) \in (1,2,3)$,

$\tilde{d}_{sm}$ = 3x3 tilde matrix representing a distance measurement from the Orbiter c.g. to the AGS gimbal torquers,

$T_G{}^t$ = 3x3 transpose of the AGS gimbal angles,

r_o, $\dot{r}_o$, $\ddot{r}_o$ = 3x1 vector position, velocity, and acceleration of the Orbiter c.g.,

Φ_o, $\dot{\Phi}_o$, $\ddot{\Phi}_o$ = 3x1 vector angular displacement, velocity, and acceleration of the Orbiter,

Φ_i, $\dot{\Phi}_i$, $\ddot{\Phi}_i$ = 3x1 vector angular displacement, velocity, and acceleration of the AGS payload,

Φ_T, $\dot{\Phi}_T$ = 3x1 vector measurement of the plant states provided by the AGS rate gyros,

A_g = 3x1 vector measurements of the rate of the plant states provided by the AGS accelerometers,

F = 3x1 vector Orbiter disturbance which cannot be measured directly,

r_d = vector from Orbiter c.g. to application of F, and

T_c = 3x1 vector control torque provided by the AGS gimbal torquers.

The Orbiter linear displacements are eliminated from (1) by the relationship

$$\ddot{r}_o = m_{11}^{-1} (F - m_{12}\ddot{\Phi}_o - m_{13}\ddot{\Phi}_i). \tag{4}$$

Substituting (4) into (1) and into (3) gives

$$\left[\begin{array}{c|c} n_{11} & n_{12} \\ \hline n_{21} & n_{22} \end{array}\right] \left[\begin{array}{c} \ddot{\Phi}_o \\ \hline \ddot{\Phi}_i \end{array}\right] = \left[\begin{array}{c} p_{11} \\ \hline p_{21} \end{array}\right] F + \left[\begin{array}{c} 0_1 \\ \hline I_1 \end{array}\right] T_c \text{ and} \tag{5}$$

$$A_g = [0_1 \mid V_{12} \mid 0_1 \mid V_{14}] \left[\begin{array}{c} \dot{\Phi}_o \\ \hline \ddot{\Phi}_o \\ \hline \dot{\Phi}_i \\ \hline \ddot{\Phi}_i \end{array}\right] + m_{11}^{-1} F \tag{6}$$

where

$$n_{11} = m_{22} - m_{21} m_{11}^{-1} m_{12},$$

$$n_{12} = m_{23} - m_{21} m_{11}^{-1} m_{13},$$

$$n_{21} = m_{32} - m_{31} m_{11}^{-1} m_{12},$$

$$n_{22} = m_{33} - m_{31} m_{11}^{-1} m_{13},$$

$$p_{11} = \tilde{r}_d \quad -m_{21} \quad m_{11}^{-1},$$

$$p_{21} = -m_{31} \quad m_{11}^{-1},$$

$$V_{12} = \tilde{d}_{sm} \quad -m_{11}^{-1} \quad m_{12}, \text{ and}$$

$$V_{14} = -m_{11}^{-1} \quad m_{13}$$

while the attitude measurement equation becomes

$$\begin{bmatrix} \Phi_T \\ \hline \dot{\Phi}_T \end{bmatrix} = \left[\begin{array}{c|c|c|c} T_G^t & 0_1 & I_1 & 0_1 \\ \hline 0_1 & T_G^t & 0_1 & I_1 \end{array}\right] \begin{bmatrix} \Phi_o \\ \dot{\Phi}_o \\ \Phi_i \\ \dot{\Phi}_i \end{bmatrix} \tag{7}$$

Writing equation (5) in state form gives

$$\begin{bmatrix} \dot{\Phi}_o \\ \hline \ddot{\Phi}_o \\ \hline \dot{\Phi}_i \\ \hline \ddot{\Phi}_i \end{bmatrix} = \left[\begin{array}{c|c|c|c} 0_1 & I_1 & 0_1 & 0_1 \\ \hline 0_1 & 0_1 & 0_1 & 0_1 \\ \hline 0_1 & 0_1 & 0_1 & I_1 \\ \hline 0_1 & 0_1 & 0_1 & 0_1 \end{array}\right] \begin{bmatrix} \Phi_o \\ \hline \dot{\Phi}_o \\ \hline \Phi_i \\ \hline \dot{\Phi}_i \end{bmatrix} + \begin{bmatrix} 0_1 \\ \hline q_{21} \\ \hline 0_1 \\ \hline q_{41} \end{bmatrix} F + \begin{bmatrix} 0_1 \\ \hline r_{21} \\ \hline 0_1 \\ \hline r_{42} \end{bmatrix} T_c \tag{8}$$

where

$$\begin{bmatrix} q_{21} \\ \hline q_{41} \end{bmatrix} = \left[\begin{array}{c|c} n_{11} & n_{12} \\ \hline n_{21} & n_{22} \end{array}\right]^{-1} \begin{bmatrix} p_{11} \\ \hline p_{21} \end{bmatrix} \quad \text{and}$$

$$\begin{bmatrix} r_{21} \\ \hline r_{42} \end{bmatrix} = \left[\begin{array}{c|c} n_{11} & n_{12} \\ \hline n_{21} & n_{22} \end{array}\right]^{-1} \begin{bmatrix} 0_1 \\ \hline I_1 \end{bmatrix}.$$

Alas! Upon examiniation of (7) and (8), it is found that the system is not observable. To remove this thorn from one's side, consider adding feedback to (1) by defining

$$T_c = T_o + T_{c1} \tag{9}$$

where

$$T_o = -K_1\dot{\Phi}_i - K_o\Phi_i \quad \text{and}$$

T_{c1} is unspecified.

Substituting (9) into (5) and rearranging yields

$$\left[\begin{array}{c|c} n_{11} & n_{12} \\ \hline n_{21} & n_{22} \end{array}\right]\left[\begin{array}{c} \ddot{\Phi}_o \\ \hline \ddot{\Phi}_i \end{array}\right] + \left[\begin{array}{c|c} 0_1 & 0_1 \\ \hline 0_1 & K_1 \end{array}\right]\left[\begin{array}{c} \dot{\Phi}_o \\ \hline \dot{\Phi}_i \end{array}\right] + \left[\begin{array}{c|c} 0_1 & 0_1 \\ \hline 0_1 & K_o \end{array}\right]\left[\begin{array}{c} \Phi_o \\ \hline \Phi_i \end{array}\right] = \left[\begin{array}{c} p_{11} \\ \hline p_{21} \end{array}\right] F + \left[\begin{array}{c} 0_1 \\ \hline I_1 \end{array}\right] T_{c1} \tag{10}$$

and writing (1) in state form gives

$$\left[\begin{array}{c} \dot{\Phi}_o \\ \hline \ddot{\Phi}_o \\ \hline \dot{\Phi}_i \\ \hline \ddot{\Phi}_i \end{array}\right] = \left[\begin{array}{c|c|c|c} 0_1 & I_1 & 0_1 & 0_1 \\ \hline k_{11} & d_{11} & k_{12} & d_{12} \\ \hline 0_1 & 0_1 & 0_1 & I_1 \\ \hline k_{21} & d_{21} & k_{22} & d_{22} \end{array}\right]\left[\begin{array}{c} \Phi_o \\ \hline \dot{\Phi}_o \\ \hline \Phi_i \\ \hline \dot{\Phi}_i \end{array}\right] + \left[\begin{array}{c} 0_1 \\ \hline q_{21} \\ \hline 0_1 \\ \hline q_{41} \end{array}\right] F + \left[\begin{array}{c} 0_1 \\ \hline r_{21} \\ \hline 0_1 \\ \hline r_{41} \end{array}\right] T_{c1} \tag{11}$$

where

$$\left[\begin{array}{c|c} d_{11} & d_{21} \\ \hline d_{21} & d_{22} \end{array}\right] = \left[\begin{array}{c|c} n_{11} & n_{12} \\ \hline n_{21} & n_{22} \end{array}\right]^{-1}\left[\begin{array}{c|c} 0_1 & 0_1 \\ \hline 0_1 & K_1 \end{array}\right], \text{ and}$$

$$\left[\begin{array}{c|c} k_{11} & k_{12} \\ \hline k_{21} & k_{22} \end{array}\right] = \left[\begin{array}{c|c} n_{11} & n_{12} \\ \hline n_{21} & n_{22} \end{array}\right]^{-1}\left[\begin{array}{c|c} 0_1 & 0_1 \\ \hline 0_1 & K_o \end{array}\right].$$

With a suitable selection of K_o and K_1, the system equations (11) and (7) are observable. Once the observability criterion is met, the observer and the DIC can be formulated.

OBSERVER AND DIC DESIGN

The key factor in the DIC is an observer which does not require direct measurement of the plant inputs. The observer for the flight experiment is derived by first rewriting (11), (7), and (6) into generic system equations. The system equations are

$$\dot{x} = Ax + B_c T_{c1} + B_D F, \tag{12}$$

$$y = Cx, \text{ and} \tag{13}$$

$$z = P\dot{x} + P_D F. \tag{14}$$

The full state observer [1] for (12), (13), and (14) is of the form

$$\dot{\alpha} = E\alpha + Gy + Hz + JT_{c1} \tag{15}$$

where

E = 12x12 observer dynamic matrix,

G = 12x6 matrix (unknown for present),

H = 12x3 matrix (unknown for present),

J = 12x3 matrix (unknown for present), and

α = 12x1 vector of the observer states.

Let α be a linear combination of x such that

$$\alpha = Tx. \tag{16}$$

Substituting (12)-(14) and (16) into (15) gives

$$T\dot{x} = ETx + GCx + H[P(Ax + B_cT_{c1} + B_DF) + P_DF] + JT_{c1} \tag{17}$$

Premultiplying (12) by T gives

$$T\dot{x} = TAx + TB_cT_{c1} + TB_DF. \tag{18}$$

Subtracting (17) from (18), collecting terms, and equating variables yields the matrix relations

$$TA - ET = GC + HPA, \tag{19}$$

$$TB_c = HPA + J, \text{ and} \tag{20}$$

$$TB_D = H(PB_D + P_D). \tag{21}$$

If $(PB_D + P_D)^{-1}$ exists, then

$$H = TB_D(PB_D + P_D)^{-1}. \tag{22}$$

Substituting (22) into (19) and collecting terms gives

$$T[I - B_D(PB_D + P_D)^{-1}P]A - ET = GC. \tag{23}$$

Letting

$$A_1 = [I - B_D(PB_D + P_D)^{-1}P]A \tag{24}$$

and using direct products[3] on (23) yields

$$(I \otimes A_1^t - E \otimes I)\hat{T} = \hat{GC} \tag{25}$$

where $\hat{T}$ and $\hat{GC}$ are 144x1 vectors of the form

$$\hat{T} = \begin{bmatrix} t_{1*}^t \\ \vdots \\ t_{12,*}^t \end{bmatrix} \quad \text{and} \quad \hat{GC} = \begin{bmatrix} (GC)_{1*}^t \\ \vdots \\ (GC)_{12,*}^t \end{bmatrix} .$$

If A_1 and E have no common eigenvalues, then

$$\hat{T} = (I \otimes A_1^t - E \otimes I)^{-1} \hat{GC}, \tag{26}$$

$$H = TB_D(PB_D + P_D)^{-1}, \text{ and} \tag{27}$$

$$J = TB_c - HPA. \tag{28}$$

If G is selected such that rank of C is equal to the rank of GC,[4] then T^{-1} exists.

For this paper, a reduced order observer is derived. The derivation is the same as the full state observer except that the dimension of T, E, and G are different. For the reduced order observer, the transformation is

$$\hat{T} = [I_6 \otimes A_1^t - E \otimes I_{12}]^{-1} \hat{GC} \tag{29}$$

where

I_6 = 6x6 identity matrix,

I_{12} = 12x12 identity matrix,

E = 6x6 stable matrix, and

G = 6x6 matrix.

For the simplified flight experiment model, the system parameters are shown in Table 1 and the observer parameters are shown in Table 2. Catenating the measurement equation (13) with the transformation obtained in (29) gives

$$\begin{bmatrix} y \\ \alpha \end{bmatrix} = \begin{bmatrix} C \\ T \end{bmatrix} x. \tag{30}$$

Since the rank of GC equals the rank of C, a solution for the plant states exists and it is

$$x = \left[\begin{array}{c} C \\ \hline T \end{array}\right]^{-1} \left[\begin{array}{c} y \\ \hline \alpha \end{array}\right]. \tag{31}$$

Table 3 shows the transformation and its inverse. This concludes the observer derivation for the flight experiment model.

To demonstrate the DIC design, consider the third vector equation in (1) which is

$$m_{31}\ddot{r}_o + m_{32}\ddot{\Phi}_o + m_{33}\ddot{\Phi}_i = T_o + T_{c1} = T_o + T_A + T_{DIC} \tag{32}$$

where

T_A = 3x1 attitude control torque and

T_{DIC} = 3x1 DIC torque.

Premultiplying A_g in (3) by m_{31} yields

$$m_{31}A_g = m_{31}\ddot{r}_o + m_{31}\tilde{d}_{sm}\ddot{\Phi}_o. \tag{33}$$

Using this result and the estimates of the plant states in (31), let

$$T_A = -L_1 x_4 - L_o x_3 + m_{31}A_g \tag{34}$$

where

$$\left[\begin{array}{c} x_1 \\ \hline x_2 \\ \hline x_3 \\ \hline x_4 \end{array}\right] \rightarrow \left[\begin{array}{c} \Phi_o \\ \hline \dot{\Phi}_o \\ \hline \Phi_i \\ \hline \dot{\Phi}_i \end{array}\right],$$

L_o = 3x3 attitude position gain, and

L_1 = 3x3 attitude rate gain.

Substituting (34) into (32) and collecting terms in the resulting equation gives

$$(m_{32} - m_{31}\tilde{d}_{sm})\ddot{\Phi}_o + m_{33}\ddot{\Phi}_i = -L_1 x_4 - L_o x_3 + T_o + T_{DIC} \tag{35}$$

Differentiating (31) yields

$$\dot{x} = \left[\begin{array}{c} C \\ \hline T \end{array}\right]^{-1} \left[\begin{array}{c} \dot{y} \\ \hline \dot{\alpha} \end{array}\right] \tag{36}$$

where

$$\begin{bmatrix} x_1 \\ \hline x_2 \\ \hline x_3 \\ \hline x_4 \end{bmatrix} \rightarrow \begin{bmatrix} \dot{\Phi}_o \\ \hline \Phi_o \\ \hline \dot{\Phi}_i \\ \hline \Phi_i \end{bmatrix}$$

Since $\dot{x}_2$ converges to $\ddot{\Phi}_o$, select

$$T_{DIC} = -T_o + (m_{32} - m_{31}d_{sm})\dot{x}_2. \tag{37}$$

Substituting (37) into (35) gives

$$m_{33}\ddot{\Phi}_i + L_1x_4 + L_ox_3 + (m_{32} - m_{31}\tilde{d}_{sm})(\ddot{\Phi}_o - \dot{x}_2)$$

$$= m_{33}\ddot{\Phi}_i + L_1\dot{\Phi}_i + L_o\Phi_i = 0 \tag{38}$$

which shows that the Φ_i variable is isolated from the dynamic variables r_o and Φ_o and the Orbiter disturbance F which is the goal of the DIC.

SUMMARY

This paper contains the development of a disturbance isolation controller for a simplified model of the SEPS flight experiment. The DIC design primarily consists of a method to obtain observer estimates which will converge to the plant states and the plant accelerations. Using the acceleration estimates, the DIC isolates the AGS payload from the Orbiter disturbances. Future considerations will include the effects of system noises, nonlinear plants and measurements, and a determination of the observer robustness.

REFERENCES

(1) Waites, H. B., "An Observer for a Deployable Antenna," AIAA 2nd Conference on Large Space Platforms, San Diego, CA., February 2-4, 1981.

(2) Waites, H. B., "Model Following Control With Applications," Ph.D. Dissertation, University of Alabama, 1978.

(3) Lancaster, Peter, "Theory of Matrices," Academic Press, Inc., New York, N. Y., 1969.

(4) Luenberger, David G., "State of Linear System," Ph.D. Dissertation, Stanford University, 1963.

A

0	0	0	1	0	0	0	0	0	0	0	0
0	0	0	0	1	0	0	0	0	0	0	0
0	0	0	0	0	1	0	0	0	0	0	0
0	0	0	0	0	0	1	0	0	0	0	0
0	0	0	0	0	0	0	1	0	0	0	0
0	0	0	0	0	0	0	0	1	0	0	0
0	0	0	0	0	0	0	0	0	1	0	0
0	0	0	0	0	0	0	0	0	0	1	0
0	0	0	0	0	0	0	0	0	0	0	1
0	0	0	0	0	0	1	0	0	3	0	0
0	0	0	0	0	0	0	2	0	0	6	0
0	0	0	0	0	0	0	0	3	0	0	9

BC

0.00E0	0.00E0	0.00E0
0.00E0	0.00E0	0.00E0
-0.00E0	0.00E0	-0.00E0
-6.19E 7	-0.00E0	-1.86E 11
-0.00E0	1.38E 7	-0.00E0
-2.70E 8	0.00E0	1.33E 7
0.00E0	0.00E0	0.00E0
0.00E0	0.00E0	0.00E0
0.00E0	0.00E0	0.00E0
1.43E 5	0.00E0	2.70E 8
0.00E0	1.38E 5	0.00E0
2.70E 8	0.00E0	4.95E 3

FD

0.00E0	0.00E0	0.00E0
0.00E0	0.00E0	0.00E0
0.00E0	-0.00E0	0.00E0
0.00E0	-5.99E 7	-0.00E0
1.34E 7	0.00E0	-6.80E 7
0.00E0	6.26E 7	0.00E0
0.00E0	0.00E0	0.00E0
0.00E0	0.00E0	0.00E0
0.00E0	0.00E0	0.00E0
-0.00E0	9.35E 7	0.00E0
-6.15E 7	-0.00E0	6.53E 7
0.00E0	-6.26E 7	0.00E0

C

1	0	0	0	0	0	1	0	0	0	0	0
0	1	0	0	0	0	0	1	0	0	0	0
0	0	1	0	0	0	0	0	1	0	0	0
0	0	0	1	0	0	0	0	0	1	0	0
0	0	0	0	1	0	0	0	0	0	1	0
0	0	0	0	0	1	0	0	0	0	0	1

P

0	0	0	0	-0.963	-0	0	0	0	0	-0.0356	0
0	0	0	0.963	0	-4.71	0	0	0	0.0356	0	0
0	0	0	0	4.71	0	0	0	0	0	0	0

PQ

1.13E 5	0.00E0	0.00E0
0.00E0	1.13E 5	0.00E0
0.00E0	0.00E0	1.13E 5

TABLE 1. SYSTEM PARAMETERS

E

-0	-1	0	0	0	0
-2	-2	0	0	0	0
0	0	-0	-1	0	0
0	0	-2	-2	0	0
0	0	0	0	-0	-1
0	0	0	0	-2	-2

G

1	0	0	0	0	0
0	1	0	0	0	0
0	0	1	0	0	0
0	0	0	1	0	0
0	0	0	0	1	0
0	0	0	0	0	1

H

0	0	0
0	0	0
0	0	0
-0	0.0431	0
-0.0431	0	0
-0	0	0
-0.00241	-0.00952	-0.0342
0.00541	-0.0357	0.0385
0	0.0578	0
0	0.066	-0
-0.00481	-0.0378	0.0685
-0.0108	-0.00621	0.077

J

0.00E0	0.00E0	0.00E0
0.00E0	0.00E0	0.00E0
0.00E0	0.00E0	0.00E0
1.36E-5	0.00E0	0.00E0
0.00E0	1.36E-5	0.00E0
-0.00E0	-0.00E0	-4.95E-3
-3.13E-6	1.29E-6	1.25E-8
4.29E-6	5.95E-7	-3.16E-8
1.16E-6	0.00E0	-5.36E-4
1.97E-6	0.00E0	6.94E-4
-6.73E-10	-2.58E-6	1.58E-4
-4.62E-9	1.19E-6	3.78E-4

TABLE 2. OBSERVER PARAMETERS

T

1	0	0	0	0	0	1	0	0	0	0	0
0	1	0	0	0	0	0	1	0	0	0	0
0	0	1	0	0	0	0	0	1	0	0	0
0	0	0	1	0	0	0	0	0	1	0	0
0	0	0	0	1	0	0	0	0	0	1	0
-1	-0.5	0	-0.5	-0.5	0	-1.07	-0.65	0	-0.241	-0.0939	0
1	0	0	1	0.5	0	-1.24	0.2	0	0.344	0.0499	0
0	0	-1	0.5	0	-0.5	0.173	0	-1.11	0.102	0	-0.109
0	0	-1	0	0	1	0.104	0	-1.32	0.14	0	0.14
0	0	0	0	-1	0.5	-0.000442	0.3	0.21	-0.00104	-0.2	0.0318
0	0	0	0	-1	0	0.000309	0.4	0.0955	0.000486	0.0997	0.0764

TI

14.3	12.6	4.99	4.01	0	0	25.3	9.98	2.67	7.66	12.6	4.99
1.34	5	10.7	0	2	0	12	10.7	9.33	1.34	12	10.7
9.14	0.864	9.9	0	0	1.33	1.73	10.9	20	9.1	0.864	5.43
6.66	4.66	1.33	2	0	0	9.32	2.66	2	3.33	4.66	1.33
1.33	2.67	4	0	1	0	5.33	4	2.67	1.33	5.33	4
2.68	1.1	4.89	0.00287	0	0.667	2.2	4.88	7.55	2.66	1.1	2.44
15.3	12.6	4.99	4.01	0	0	25.3	9.98	2.67	7.66	12.6	4.99
1.34	6	10.7	0	2	0	12	10.7	9.33	1.34	12	10.7
9.14	0.864	10.9	0	0	1.33	1.73	10.9	20	9.1	0.864	5.43
6.66	4.66	1.33	3	0	0	9.32	2.66	2	3.33	4.66	1.33
1.33	2.67	4	0	2	0	5.33	4	2.67	1.33	5.33	4
2.68	1.1	4.89	0.00287	0	1.67	2.2	4.88	7.55	2.66	1.1	2.44

TABLE 3. OBSERVER/STATE TRANSFORMATION AND ITS INVERSE

NOMENCLATURE

$M_{11}\ddot{r}_o + M_{12}\ddot{\Phi}_o + M_{13}\Phi_i = F$: ORBITER CG TRANSLATIONAL EQUATION
$M_{21}\ddot{r}_o + M_{22}\ddot{\Phi}_o + M\,23\ddot{\Phi}_i = \tilde{r}_d F$: ORBITER ROTATIONAL EQUATION
$M_{31}\ddot{r}_o + M_{32}\ddot{\Phi}_o + M_{33}\ddot{\Phi}_i = T_C + T_o$: PAYLOAD ATTITUDE EQUATION
F: FORCE WHICH IS NOT DIRECTLY MEASUREABLE i.e., CREW MOTION OR RCS
T_C: CONTROL TORQUE
T_o: OBSERVABILITY TORQUE (ADDED)
r_d: VECTOR FROM ORBITER CG TO FORCE (F) APPLICATION
M_{ij}: MASS MATRIX COMPONENTS

$\Phi_T = T_G^t\,\Phi_o + \Phi_i$: DIGITAL RATE GYRO MEASUREMENTS
$\dot{\Phi}_T = T_G^t\,\dot{\Phi}_o + \dot{\Phi}_i$: ANALOG RATE GYRO MEASUREMENTS
T_G^t : TRANSFORMATION FROM INERTIAL TO BODY FRAME

$A_g = \ddot{r}_o + \tilde{d}_{SM}\ddot{\Phi}_o$: AGS BASE ACCELEROMETER MEASUREMENTS
d_{SM} = VECTOR FROM ORBITER CG TO AGS ACCELEROMETERS

● FLIGHT EXPERIMENT CONFIGURATION

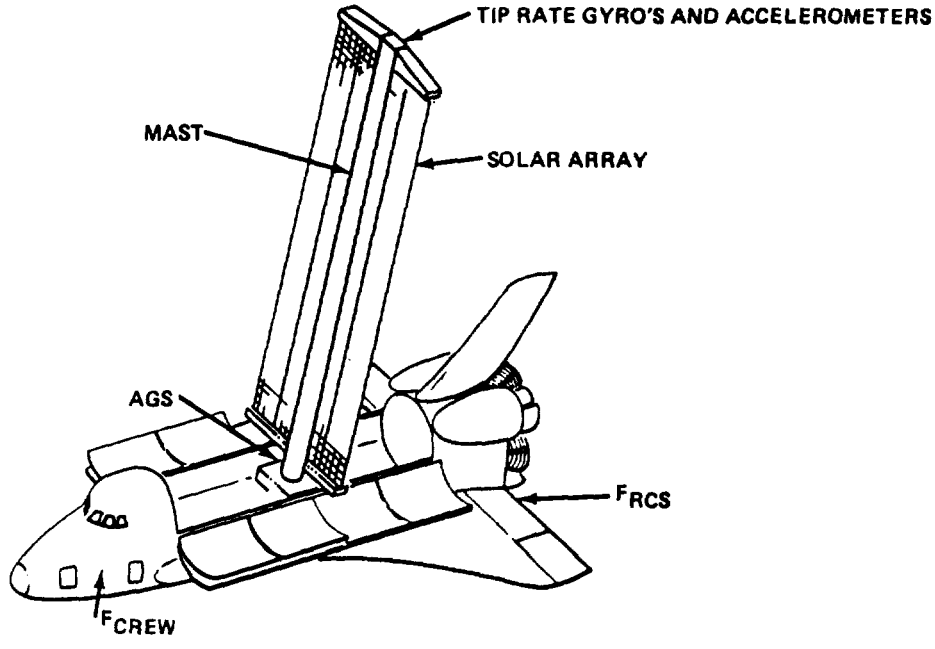

- EXPERIMENT OBJECTIVES
  - SUITABLE STRUCTURE
  - ASPECTS OF LSS CONTROL
- CONTROL OBJECTIVES
  - DISTRIBUTED SENSOR CONTROL
  - MODAL DAMPING
  - NESTED CONTROLLER
  - DISTURBANCE ISOLATION CONTROL
    - ORBITER DISTURBANCES
    - ACCELERATION REDUCTION

- SYSTEM EQUATION FOR SIMPLIFIED MODEL

$$\begin{bmatrix} m_{11} & m_{12} & m_{13} \\ m_{21} & m_{22} & m_{23} \\ m_{31} & m_{32} & m_{33} \end{bmatrix} \begin{bmatrix} \ddot{r}_o \\ \ddot{\Phi}_o \\ \ddot{\Phi}_i \end{bmatrix} = \begin{bmatrix} I_1 \\ \tilde{r}_d \\ 0_1 \end{bmatrix} F + \begin{bmatrix} 0_1 \\ 0_1 \\ I_1 \end{bmatrix} T_c + \begin{bmatrix} 0_1 \\ 0_1 \\ I_1 \end{bmatrix} T_o$$

$$\begin{bmatrix} \Phi_T \\ \dot{\Phi}_T \end{bmatrix} = \begin{bmatrix} 0_1 & 0_1 & T_G{}^t & 0_1 & I_1 & 0_1 \\ 0_1 & 0_1 & 0_1 & T_G{}^t & 0_1 & I_1 \end{bmatrix} \begin{bmatrix} r_o \\ \dot{r}_o \\ \Phi_o \\ \dot{\Phi}_o \\ \Phi_i \\ \dot{\Phi}_i \end{bmatrix}$$

$$A_g = \begin{bmatrix} 0_1 & I_1 & 0_1 & \tilde{d}_{sm} & 0_1 & 0_1 \end{bmatrix} \begin{bmatrix} \dot{r}_o \\ \ddot{r}_o \\ \dot{\Phi}_o \\ \ddot{\Phi}_o \\ \dot{\Phi}_i \\ \ddot{\Phi}_i \end{bmatrix}$$

SYSTEM BLOCK DIAGRAM

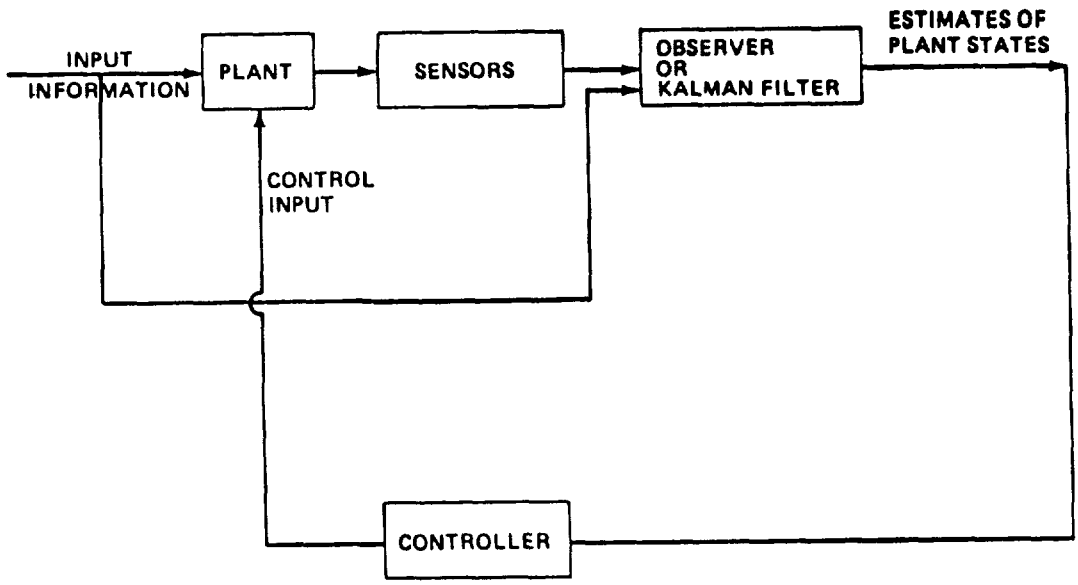

- GENERIC SYSTEM EQUATIONS

$$\dot{x} = Ax + B_c T_{c1} + B_D F$$

$$y = Cx$$

$$z = P\dot{x} + P_D F$$

- OBSERVER FORM

$$\dot{\alpha} = E\alpha + Gy + Hz + JT_{c1}$$

- OBSERVER CONSTRAINT EQUATIONS

$$TA - ET = GC + HPA$$

$$TB_c = HPB_c + J$$

$$TB_D = H(PB_D + P_D)$$

- CONSTRAINT EQUATION SOLUTIONS

$$\hat{T} = (I \oplus A)^{-1} \hat{GC}$$

$$H = TB_D (PB_D + P_D)^{-1}$$

$$J = TB_C - HPB_C$$

- ESTIMATOR EQUATIONS

$$\alpha = T x + e^{Et}\left(\alpha(0) - T x(0)\right)$$

$$\dot{\alpha} = T \dot{x} + E e^{Et}\left(\alpha(0) - T x(0)\right)$$

$$\begin{bmatrix}\alpha_1\\ \alpha_2\\ \alpha_3\\ \alpha_4\end{bmatrix} \rightarrow T \begin{bmatrix}\Phi_o\\ \Phi_o\\ \Phi_i\\ \Phi_i\end{bmatrix} \quad \text{AND} \quad \begin{bmatrix}\dot{\alpha}_1\\ \dot{\alpha}_2\\ \dot{\alpha}_3\\ \dot{\alpha}_4\end{bmatrix} \rightarrow T \begin{bmatrix}\dot{\Phi}_o\\ \ddot{\Phi}_o\\ \dot{\Phi}_i\\ \ddot{\Phi}_i\end{bmatrix}$$

- DISTURBANCE ISOLATION CONTROL TORQUE

$$m_{31}\,\ddot{r}_o + m_{32}\,\ddot{\Phi}_o + m_{33}\,\ddot{\Phi}_i = T_o + T_A + T_{DIC}$$

$$A_g = \ddot{r}_o + \tilde{d}_{sm}\,\ddot{\Phi}_o$$

$$T_A = -L_1\,\alpha_4 - L_o\,\alpha_3 + m_{31}\,A_g$$

$$T_{DIC} = -T_o + (m_{32} - m_{31}\,\tilde{d}_{sm})\,\dot{\alpha}_2$$

- FUTURE INVESTIGATION
  - COMPLEX SAFE MODEL
  - OBSERVER SENSITIVITY (PARAMETERS)
  - OBSERVER TRUNCATION
    - MODES
    - WORD LENGTH
  - NOISE

MODULAR ATTITUDE CONTROL

OF A LARGE SPACE PLATFORM

F. D. Chichester
The Bendix Corporation
Corporate Computer Center
Test Systems Division
Teterboro, New Jersey

Large Space Systems Technology - 1981
Third Annual Technical Review
November 16-19, 1981

MODULAR ATTITUDE CONTROL OF A LARGE SPACE PLATFORM

- o STATE VARIABLE MODEL
- o DECOMPOSED MODEL
- o DECOMPOSED PERFORMANCE INDEX
- o DECOMPOSED HAMILTONIAN
- o COSTATE EQUATIONS
- o CONTROL EQUATIONS
- o TPBV FORMULATION OF FIRST LEVEL SUBPROBLEMS
- o SECOND LEVEL COORDINATION SUBPROBLEMS
- o SUBPROBLEM HIERARCHY

THREE AXIS FIVE BODY MODEL OF A FLEXIBLE SPACECRAFT

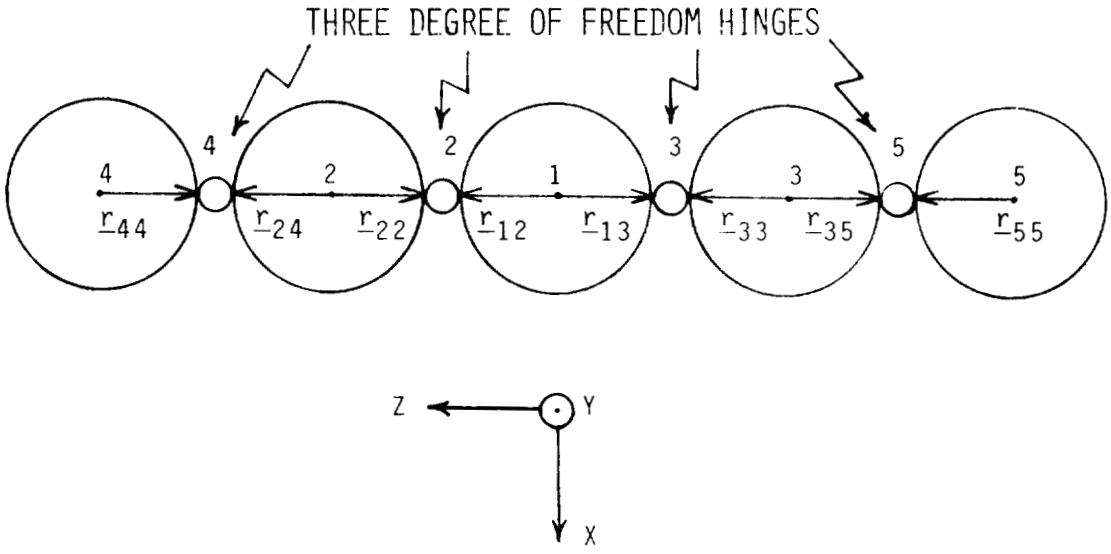

PERSPECTIVE VIEW OF HYBRID DEPLOYABLE TRUSS

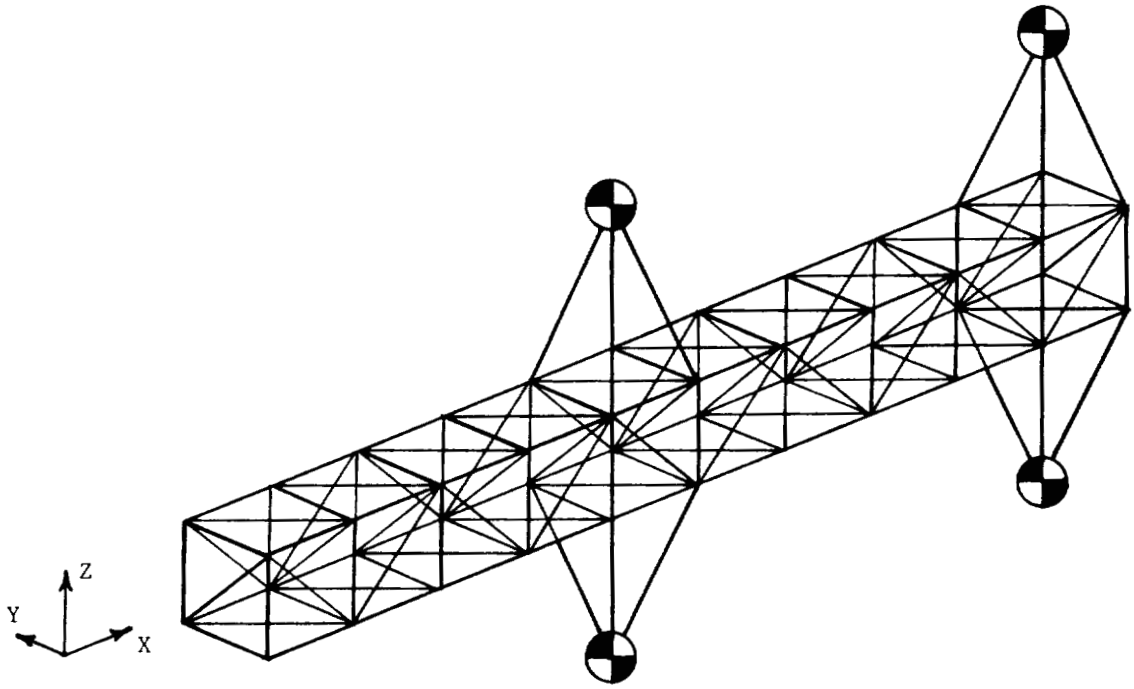

FIRST APPROXIMATION OF TRUSS

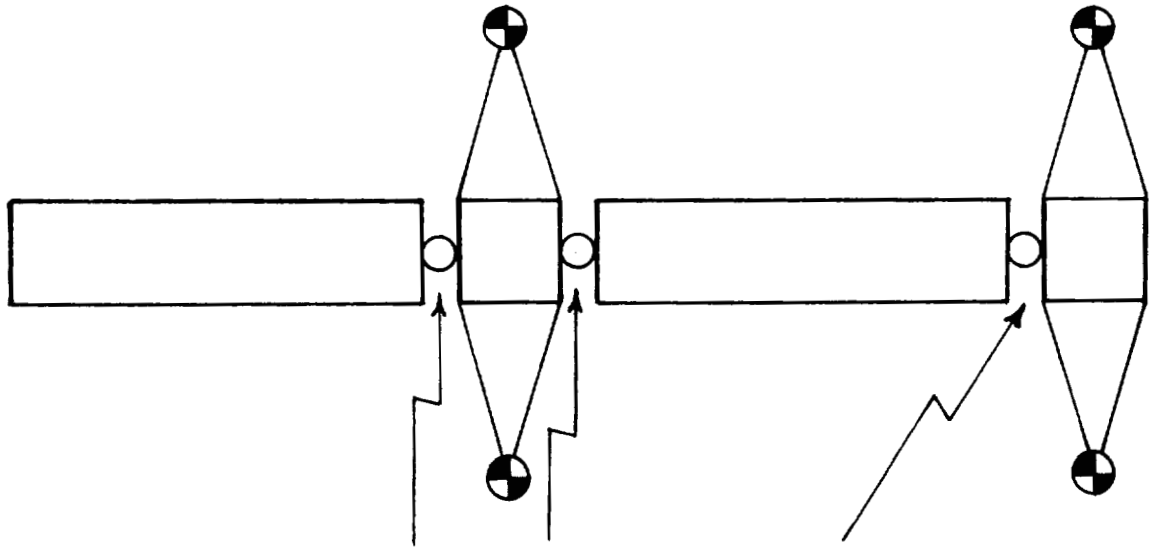

THREE DEGREE OF FREEDOM HINGES

THREE AXIS FOUR BODY MODEL OF TRUSS

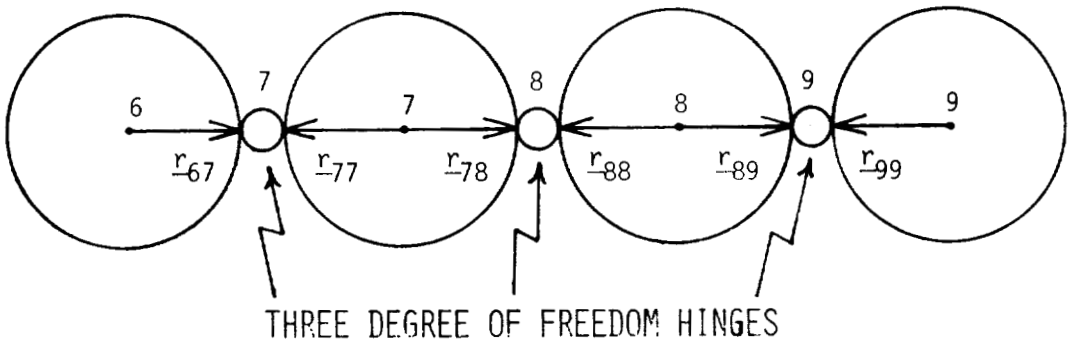

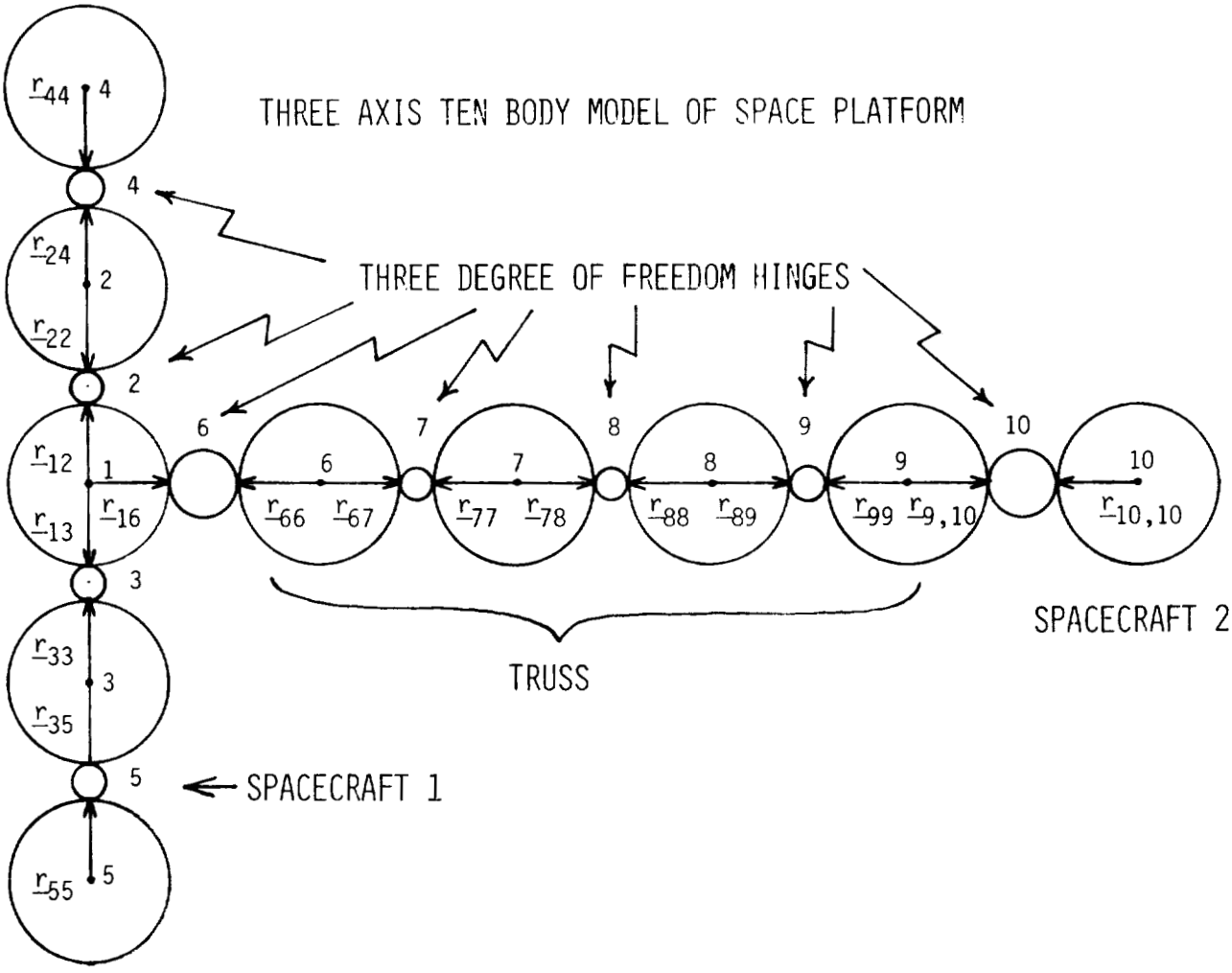

THE jTH TPBV SUBPROBLEM

$$\dot{\underline{x}}_j = A_{jj}\underline{x}_j + R_j\underline{\lambda}_j + \hat{\underline{a}}_j(t)$$

$$\dot{\underline{\lambda}}_j = -Q_j\underline{x}_j - A_{jj}^T\underline{\lambda}_j + \hat{\underline{b}}_j(t)$$

where:

$$\hat{\underline{a}}_j(t) = \sum_{\substack{k=1 \\ k\neq j}}^{3} (A_{jk}\underline{d}_j^k + B_{jk}\underline{s}_j^k - B_{jj}\underline{v}_j^k) \qquad \hat{\underline{b}}_j(t) = Q_j\underline{x}_{jd} - \sum_{\substack{k=1 \\ k\neq j}}^{3} \underline{\rho}_j^k \qquad R_j = -B_{jj}W_{ju}^{-1}B_{jj}^T$$

$\underline{x}_j(t_o) = \underline{x}_{j0}$ (initial boundary conditions)

$\underline{\lambda}_j(t_f) = 0$ (final boundary conditions)

$$\underline{\lambda}(t) = K(t)\underline{x}(t) + \underline{m}(t)$$

STATE VARIABLE ROTATIONAL DYNAMICS MODEL

$$\dot{\underline{x}}_j = \sum_{k=1}^{3} (A_{jk}\underline{x}_k + B_{jk}\underline{u}_k) \qquad j = 1, 2, 3 \qquad k = 1, 2, 3$$

where:

$$\underline{x}_k = (\underline{\omega}_k^T, \underline{\alpha}_k^T)^T$$

$$A_{jk} = \left[\begin{array}{c|c} \hat{G}_{jk}L_kC_{sk} & \hat{G}_{jk}L_kK_{sk} \\ \hline K_{jk} & [0] \end{array}\right] \qquad B_{jk} = \left[\begin{array}{c} \hat{G}_{jk} \\ \hline [0] \end{array}\right] \qquad [0] = 10 \times 10 \text{ zero matrix}$$

$$\underline{\omega}_1 = (\omega_{1x}, \omega_{2x}, \cdots, \omega_{10x})^T \qquad \underline{\omega}_2 = (\omega_{1y}, \omega_{2y}, \cdots, \omega_{10y})^T$$

$$\underline{\omega}_3 = (\omega_{1z}, \omega_{2z}, \cdots, \omega_{10z})^T$$

$\underline{u}_k$ (k = 1, 2, 3) has scalar expansion of the same form as $\underline{\omega}_k$.

$$\underline{\alpha}_1 = (\phi_1, \Delta\phi_{12}, \Delta\phi_{13}, \Delta\phi_{24}, \Delta\phi_{35}, \Delta\phi_{16}, \Delta\phi_{67}, \Delta\phi_{78}, \Delta\phi_{89}, \Delta\phi_{9,10})^T$$

$$\underline{\alpha}_2 = (\theta_1, \Delta\theta_{12}, \Delta\theta_{13}, \cdots, \Delta\theta_{9,10})^T$$

$$\underline{\alpha}_3 = (\psi_1, \Delta\psi_{12}, \Delta\psi_{13}, \cdots, \Delta\psi_{9,10})^T$$

MULTILEVEL STATE VARIABLE MODEL

$$\dot{\underline{x}}_j = A_{jj}\underline{x}_j + B_{jj}\underline{u}_j + \underline{a}_j(t) \qquad j = 1, 2, 3$$

$$\underline{a}_j = \sum_{\substack{k=1 \\ k\neq j}}^{3} (A_{jk}\underline{d}_j^k + B_{jk}\underline{s}_j^k) \qquad j = 1, 2, 3$$

$$\underline{d}_j^k = \underline{x}_k \qquad \underline{s}_j^k = \underline{u}_k \qquad k \neq j = 1, 2, 3$$

DECOMPOSED PERFORMANCE INDEX AND HAMILTONIAN

$$J = \sum_{j=1}^{3} \int_{t_o}^{t_f} P_j dt$$

where:

$P_j = \frac{1}{2}(\underline{x}_j - \underline{x}_{jd})^T Q_j (\underline{x}_j - \underline{x}_{jd}) + \frac{1}{2}\underline{u}_j^T W_{ju} \underline{u}_j$ $\qquad \underline{x}_{jd}$ = prespecified desired value of $\underline{x}_j$

Q_j = positive definite state variable error weighting coefficient matrix

W_{ju} = positive definite control energy weighting coefficient matrix

$$H = \sum_{j=1}^{3} H_j$$

where:

$$H_j = P_j + \underline{\lambda}_j^T \left[A_{jj}\underline{x}_j + B_{jj}\underline{u}_j + \sum_{\substack{k=1 \\ k\neq j}}^{3} (A_{jk}\underline{d}_j^k + B_{jk}\underline{s}_j^k) \right] + \sum_{\substack{k=1 \\ k\neq j}}^{3} (\underline{\rho}_j^k)^T (\underline{x}_j - \underline{d}_k^j) + (\underline{\upsilon}_j^k)^T (\underline{u}_j - \underline{s}_k^j)$$

COSTATE EQUATIONS

$$\dot{\underline{\lambda}}_j = -\frac{\partial H}{\partial \underline{x}_j} = -A_{jj}^T \underline{\lambda}_j - Q_j(\underline{x}_j - \underline{x}_{jd}) + \underline{b}_j(t)$$

where:

$$\underline{b}_j(t) = -\sum_{\substack{k=1 \\ k \neq j}}^{3} \underline{\rho}_j^k \qquad \underline{\lambda}_j(t_f) = 0 \quad \text{(final boundary conditions)}$$

CONTROL EQUATIONS

$$\frac{\partial H}{\partial \underline{u}_j} = 0 \rightarrow \qquad \underline{u}_j = -W_{ju}^{-1}\left(B_{jj}^T \underline{\lambda}_j + \sum_{\substack{k=1 \\ k \neq j}}^{3} \underline{v}_j^k\right)$$

SUBPROBLEM HIERARCHY FOR HYBRID MULTILEVEL-LQR ATTITUDE CONTROL OF THREE AXIS MODEL

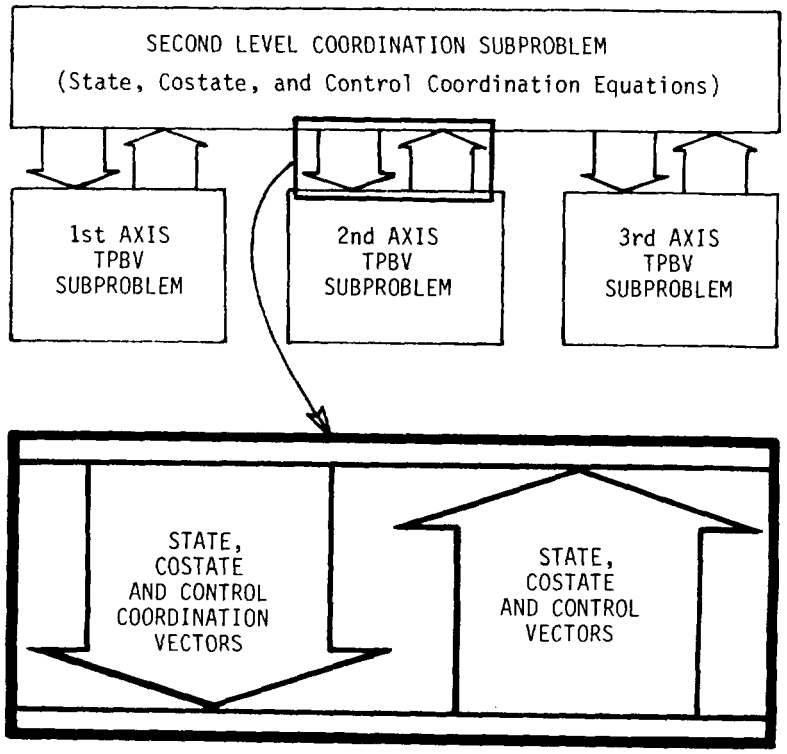

REFERENCES

1. Chichester, F.D., "Development of a Three Axis Gauss-Seidel Multilevel Model of a Flexible Space Vehicle," Proceedings of the Twelfth Annual Pittsburgh Conference on Modeling and Simulation, April 1981, University of Pittsburgh, Pittsburgh, Pennsylvania, pp. 1303-1308.

2. Chichester, F.D., "Application of Gauss-Seidel Multilevel and LQR Control to a Three Axis Rotational Model of a Flexible Space Vehicle," Proceedings of the Twelfth Annual Pittsburgh Conference on Modeling and Simulation, April 1981, University of Pittsburgh, Pittsburgh, Pennsylvania, pp. 1309-1315.

3. Chichester, F.D. and M.T. Borelli, "A Multilevel Control Approach for a Modular Structured Space Platform," Spacecraft Guidance and Control, AGARD. (To be published.)

SYSTEMS IDENTIFICATION TECHNOLOGY DEVELOPMENT FOR LARGE SPACE SYSTEMS

E. S. Armstrong
NASA Langley Research Center
Hampton, Virginia 23665

Large Space Systems Technology - 1981
Third Annual Technical Review
November 16-19, 1981

SYSTEMS IDENTIFICATION DEVELOPMENT

The need for systems identification in large aerospace structures arises because of ignorance of the structural parameters and changing control regimes. In particular, the dynamic characteristics of large, flexible spacecraft cannot be determined through ground tests and there is a basic need for a control system which can start with the best available system parameters and self-tune to a set which gives stable system response.

The objective of the research program established under RTOP 506-62-43 is to develop a methodology for synthesizing systems identification, both parameter and state, estimation and related control schemes for flexible aerospace structures with initial emphasis on the Maypole hoop-column antenna as a real world application. This important area of systems technology is an unsolved problem for large, flexible space structures with changes in configuration. The area intersects the disciplines of the mathematical theory of partial differential equations, lumped and distributed systems theory, adaptive control the high order systems, and structural dynamics mathematical modeling, to name a few, and requires a multi-disciplinary team of researchers to impact the foregoing objective.

The basic structure for such a team has been established through a university research grant (NAG-1-171) awarded April 1, 1981, to the Rensselaer Polytechnic Institute, Troy, NY, with Professor Mark Balas of the Computer and Systems Engineering Department as Principal Investigator. The personnel and expertise of the researchers supported under the grant are:

• Dr. Mark Balas, RPI	Nonadaptive control of large scale or distributed systems with mechanically flexible structures (ref. 1)
• Dr. Howard Kaufman, RPI	Adaptive control of multivariable systems (ref. 2)
• Dr. Alan Dearochers, RPI	Model order reduction techniques (ref. 3)
• Dr. Robert Loewy, RPI (added September 1, 1981)	Structural dynamics and modeling
• Dr. Thomas Banks, Brown University, Providence, Rhode Island	Consultant in mathematics and numerical methods

Since the grant effort began only recently, results to date are largely conceptual. Parameter estimation schemes for lumped multi-input multi-output systems will be extended to high order or distributed systems where possible and examined for sensitivity to spillover effects. The area of adaptive control is being surveyed for strengths and weaknesses in regard to Large Space Systems. At this writing the Luders-Narendra adaptive observer (ref. 4) and a modified auto-regressive moving average (ref. 5) method appear promising. Additionally, Dr. Loewy is developing a lumped parameter model of the hoop-column antenna which in complexity will lie somewhere between the finite-element and partial differential equation representations. The modeling approach proposed by Dr. Loewy is discussed

in the next section. It is felt that such a model will be more amenable to modern systems theory identification techniques than a finite-element model. Until this model is completed, techniques are being analyzed on a stretched membrane example which is felt to be generic to the hoop-column structure. Dr. Banks has developed a numerical approach (refs. 6 and 7) to system identification and control of distributed systems which appears promising for large space systems. It is intended that he apply his approach to a partial differential equation model of the hoop-column antenna.

In the future, the most promising control and identification techniques pinpointed in the first year of the grant will be applied to the lumped model developed by Dr. Loewy. It is expected that a separate grant will be awarded for the application of Dr. Bank's methodology.

A MODELING APPROACH FOR THE HOOP-COLUMN ANTENNA

Modeling studies of the "Maypole-cable-hoop-membrane" type antenna are being conducted using a transfer-matrix (ref. 8) numerical analysis approach. This methodology has been chosen as particularly well-suited for handling a large number of antenna configurations of a generic type. While not capable of providing, in principle, more information than a proper NASTRAN® formulation, a dedicated transfer matrix analysis, both by virtue of its specialization and the inherently easy compartmentalization of the formulation and numerical procedures, can be significantly more efficient not only in computer time required but, more importantly, in the time needed to review and interpret the results.

The analysis is seen as proceeding as follows: (1) state variable (bending, torsion, axial compression/tension) at the extremes of feed assembly and solar arrays will be "transferred" (by proper matrix transformations) inward; (2) wherever "branch points" occur (as at feed assembly to feed mast junctions, hoop support cable to upper mast assembly points, etc.), force and moment equilibrium and displacement compatibility conditions will be imposed, (3) the hoop-antenna-surface assembly will be modeled in pie-shaped segments, with transfers made azimuthally from one section to the next, and compatibility and equilibrium conditions imposed after state variables are transferred back onto themselves, that is, at 360° of azimuth. Stiffness transfer matrices, for example along the mast and around hoop segments, will probably be modeled as equivalent beams using subsidiary finite-element analyses to establish the beam-equivalent quantities. Mass transfer matrices will probably be formulated on a "lumped parameter" basis, using a small enough breakdown to reveal local flexibility effects if they are significant and such often-neglected terms as rotational mass moment of inertia in beam-bending.

Advantage will be taken of the polar symmetry of the structure as a whole. That is, aximuthal solutions will be satisfied by Fourier series representation, as in many problems involving polar symmetry; the vibrations of circular plates (ref. 9, e.g.) is one such case when the boundary conditions are also polar symmetric. In the analysis we propose, natural frequencies and modes are pictured as solved as separate cases for each Fourier harmonic using an azimuthal fraction of the total antenna with the proper boundary conditions. For the η^{th} Fourier series term, $\cos \eta\theta$, only a π/η sector of the antenna would need to be considered, with the

bending boundary conditions, for example, being transverse translation and bending moment equal to zero along the boundary of the pie-shaped element making up π/η sector of the full azimuth.

The numerical procedure for obtaining natural frequency and mode shape solutions would progress by trail and error, seeking values of ω that make an appropriate determinant zero. This would allow intermediate results (for a large number of particular values of trial frequency ω) for parts of the assembly (the mast, e.g.) to be stored for use in configurations with say, different antenna sizes if that's of interest, or different size solar arrays, and so forth. The numerical "assembly" of the various components in the transfer matrix approach can be held until the last steps of the numerical procedure, thus enhancing efficiency further, in studying a range of structures of a given generic type.

REFERENCES

1. Balas, M. J.: Toward a (More) Practical Control Theory for Distributed Parameter Systems. Control and Dynamic Systems: Theory and Applications, Volume 18, C. T. Leondes, ed., Academic Press, Inc., 1982. (To be published)

2. Kaufman, H.: and Berry P.: Adaptive Flight Control Using Optimal Linear Regulator Techniques. Automatica, vol. 12, no. 6, November 1976, pp. 565-576.

3. Desrochers, A. A.: On an Improved Model Reduction Technique for Nonlinear Systems. Automatica, vol. 17, no. 2, March 1981, pp. 407-409.

4. Balas, M. J.; and Lilly, J. H.: Adaptive Parameter Estimation of Large-Scale Systems by Reduced-Order Modeling. Proceedings of 20th IEEE Conference on Decision and Control, San Diego, CA, December 1981.

5. Balas, M. J.; and Johnson, C. R.: Adaptive Control of Distributed Parameter Systems: The Ultimate Reduced-Order Problem. Proceedings of 18th Conference on Decision and Control, Fort Lauderdale, Florida, December 1979.

6. Banks, H. T.: A Survey of Some Problems and Recent Results for Parameter Estimation and Optimal Control in Delay and Distributed Parameter Systems. Lefschetz Center for Dynamical Systems Report #81-19, Brown University, Providence, RI, July 1981.

7. Banks, H. T.; and Daniel, P. L.: Parameter Estimation of Nonlinear Nonautomous Distributed Systems. Proceedings of 20th IEEE Conference on Decision and Control, San Diego, CA, December 1981.

8. Pestel, E. C.; and Leckie, F. A.: Matrix Methods in Elastomechanics. McGraw-Hill Book Company, Inc., New York, 1963.

9. Leissa, A. W.: Vibration of Plates. NASA SP-160, 1969.

CONFIGURATIONAL AND SYSTEM REQUIREMENTS FOR CONTROL OF LARGE SPACE SYSTEMS

L. W. Taylor, Jr.
NASA Langley Research Center

Large Space Systems Technology-1981
Third Annual Technical Review
November 16-19, 1981

INTRODUCTION

An overview on the subject of control of large space systems is offered in which anticipated modeling and control difficulties are discussed. Particular emphasis is given to issues that have received little attention in the current literature on the control of large space structures. The status of the control work that has been done to date on large space systems could be pictured as being at "the back-of-the-envelope" stage in contrast to the detailed analytical effort that will be required to ensure future operational systems controlability.

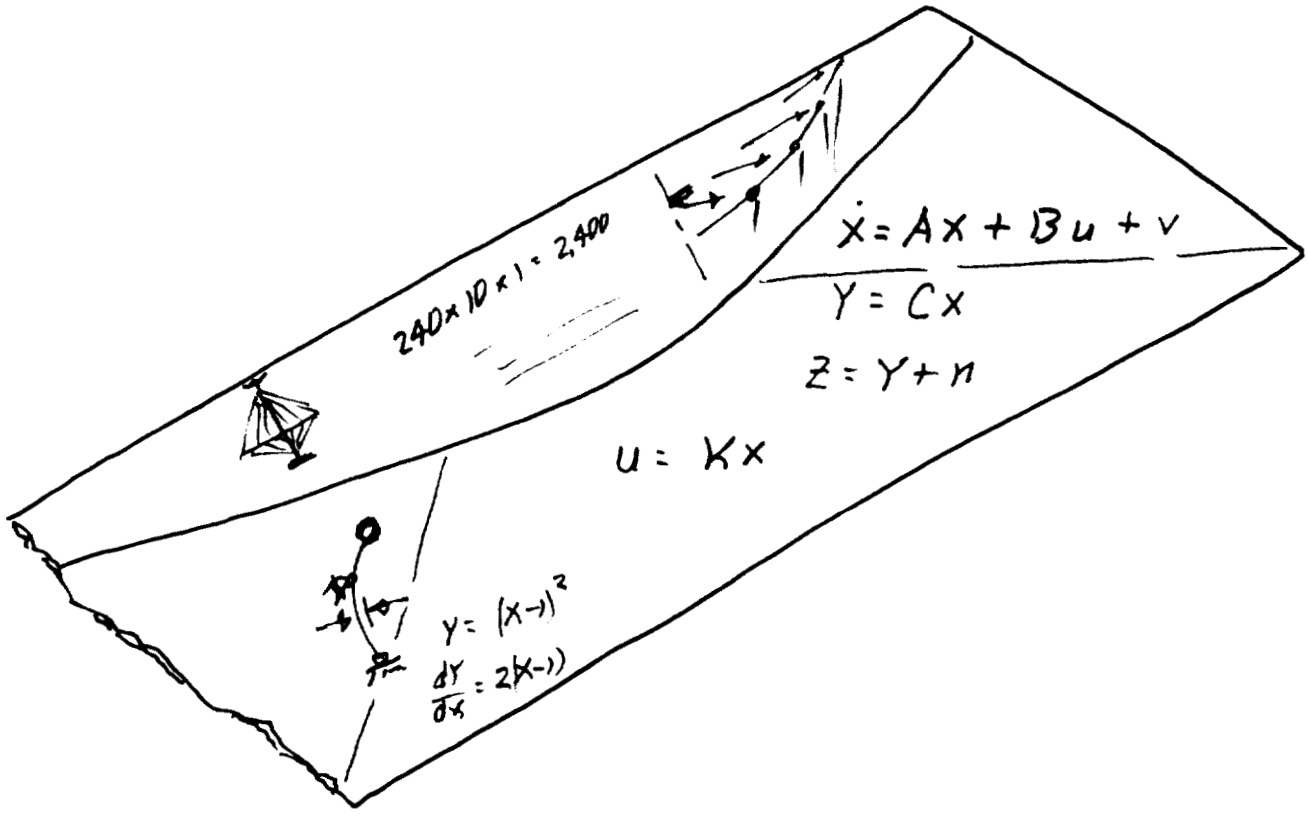

Figure 1

The discussion will be divided into two parts from the point of view of a specialist in systems identification. The first part of the discussion will deal with ground-based analysis of spaceflight data (1) to determine structural dynamics characteristics for the purpose of revising control laws, and (2) to trim the surface contour. The second part of the discussion is concerned with (1) systems identification for adaptive control and (2) auto-matic surface control.

SYSTEMS IDENTIFICATION FOR LARGE SPACE SYSTEMS

GROUND-BASED ANALYSIS OF SPACEFLIGHT DATA TO:

- DETERMINE STRUCTURAL DYNAMICS
- REVISE CONTROL LAW
- TRIM SURFACE CONTOUR

ON-LINE AND ON BOARD FOR:

- ADAPTIVE CONTROL
- AUTOMATIC SURFACE CONTROL

Figure 2

One might ask the questions "Why must structural dynamics be determined?" and "Why might pointing control involve structural dynamics?" The answers to these questions lie in the system requirements, structural dynamics characteristics, and the disturbance level. An example is offered in which an unacceptable 12-minutes settling time is required before a large flexible antenna meets its pointing requirement of .03° following a disturbance due to solar heating. For the example discussed, the effect of structural dynamics is crucial in the design of the pointing control system.

WHY MUST STRUCTURAL DYNAMICS BE DETERMINED?
WHY MIGHT "POINTING CONTROL" INVOLVE STRUCTURAL DYNAMICS?

A POINTING ACCURACY OF $.03^0$ REQUIRES THAT THE SUPPORTING MAST DEFLECT LESS THAN 1/10 OF AN INCH.

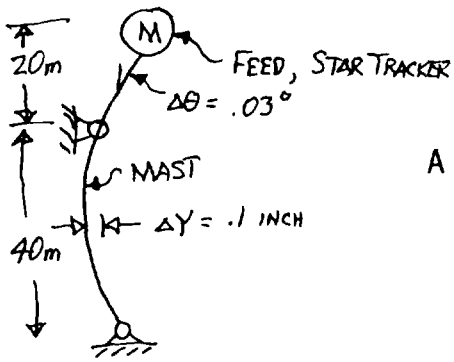

A STRUCTURAL FREQUENCY OF .1 HERTZ AND DAMPING RATIO OF .005 RESULTS IN A TIME TO HALF AMPLITUDE OF 221 SECONDS.

$$T_{1/2} = -\frac{\text{LOG } .5}{\zeta\omega_n} = 221 \text{ SECONDS}$$

SHOULD A SUDDEN DEFLECTION OF THE MAST OF 1 INCH OCCUR DUE TO SOLAR HEATING, THE POINTING ERROR WILL BE EXCESSIVE FOR 12 MINUTES.

Figure 3

In order to appreciate the importance of disturbances and noise, it is useful to observe that, for linear systems, its quasi-static error (no command input) is proportional to the amount of disturbance and noise. It behooves us then, to give these matters more attention. Sources of disturbances include solar (thermal and wind), on-board systems, and gravitational. Noise can come from sensors, actuators, and computers.

'LINEAR' SYSTEM PERFORMANCE IS PROPORTIONAL TO THE AMOUNT OF DISTURBANCE AND NOISE

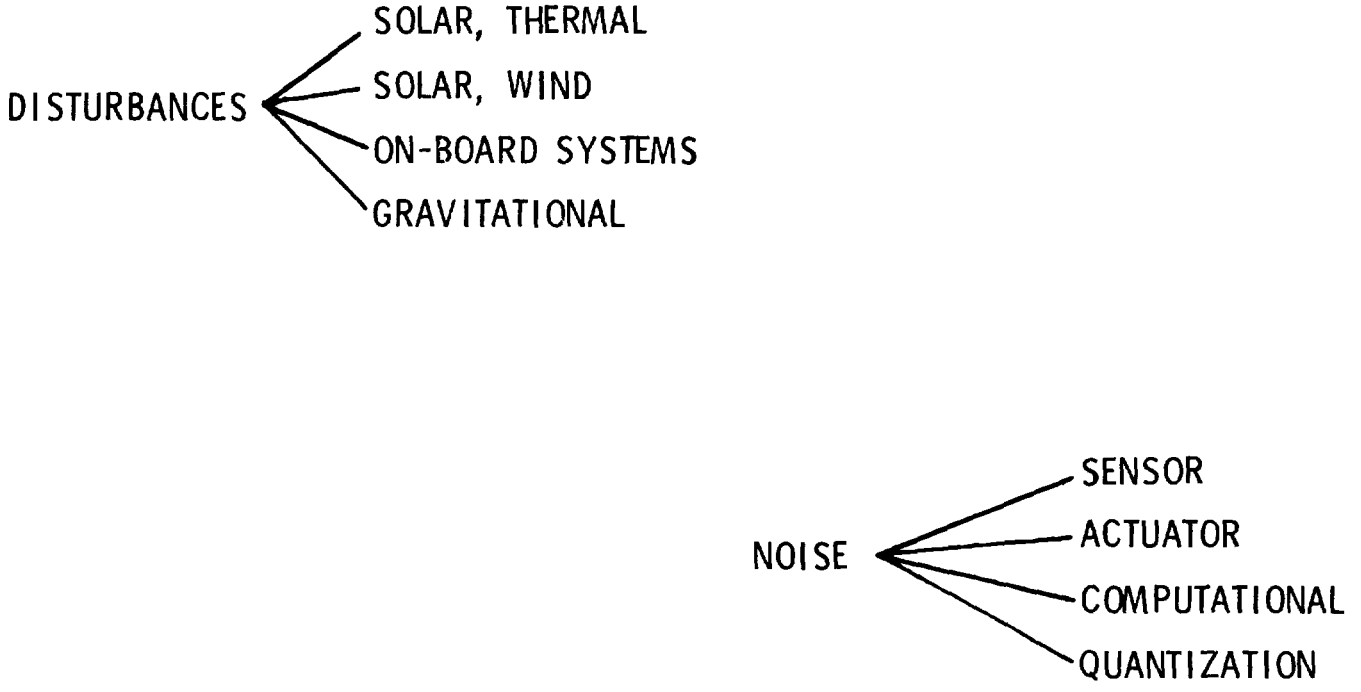

Figure 4

Because of the relative ease with which linear systems can be analyzed, nonlinearities are often neglected. Unfortunately, the nonlinearities can greatly affect system response, particularly at very large and very small amplitudes of motion. Nonlinear behavior generally comes from sensors, actuators and inertial coupling. It can be expected that system nonlinearities will result in limit cycles in pointing, in orbit maintenance, and probably at some structural modal frequencies.

SENSOR AND ACTUATOR NONLINEARITIES WILL RESULT IN LIMIT CYCLES IN POINTING, ORBIT MAINTENANCE, AND PROBABLY AT SOME STRUCTURAL MODAL FREQUENCIES

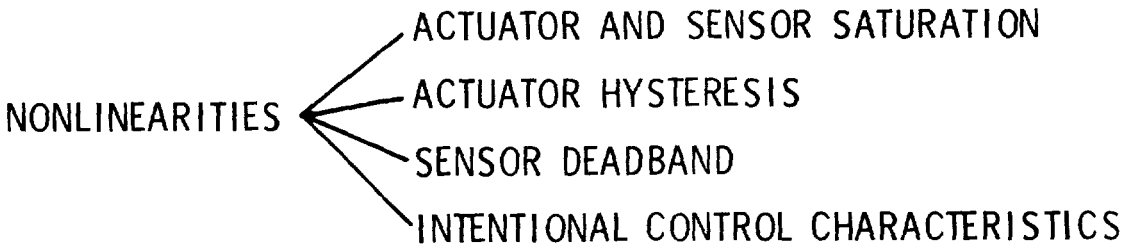

Figure 5

To close the first part of the discussion, we consider the computational aspects of ground-based analysis of spaceflight data. Transient analysis techniques will be required, either in the frequency or time domains. Attempts to determine the steady-state response to a sine-wave input, for example, are easily frustrated by lightly damped modes with little frequency separation. The instrumentation requirements are outlined and seen to be ordinary. Although the ground-based computer requirements are expected to be quite modest, the analysis techniques should first be tested using ground test data.

THE COMPUTATIONAL TASKS OF GROUND-BASED ANALYSIS OF SPACEFLIGHT DATA ARE ONLY MODERATELY DIFFICULT

STRUCTURAL DYNAMICS MODELING

- TRANSIENT ANALYSIS TO BE USED
- NO SPECIAL INSTRUMENTATION IS REQUIRED
- SPECIAL CONTROL INPUTS REQUIRED
- PERHAPS 10 MODES CAN BE MODELED
- NEED SAMPLE RATE OF 5 TO 10/SECOND
- NEED DATA LENGTH OF ABOUT 30 SECONDS
- GROUND-BASED COMPUTER REQUIREMENTS ARE INSIGNIFICANT
- SHOULD TEST ANALYSIS TECHNIQUE WITH GROUND TEST DATA

Figure 6

Turning to the problem of adjusting the surface contour of a large space system, we can expect that a static analysis will be sufficient, though extensive special instrumentation will be required. Repeated measurements serve to improve the accuracy in determining the surface contour and can detect surface motion. Analysis procedures should be tested using ground test data.

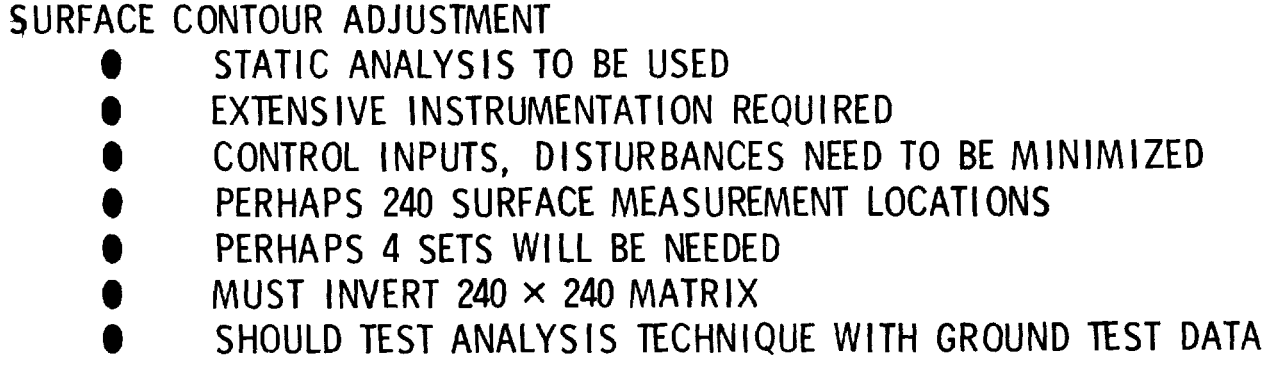

Figure 7

Examination of the distribution of modal frequencies reveals the difficulty in controlling large space systems at frequencies exceeding the first structural mode. A control bandwidth reaching a frequency ratio of 3.0 might become a typical limit. Difficulties arise in modeling, also the modes become packed. The particular dynamic characteristics must be examined, however, to make a meaningful assessment.

A SYSTEM HAVING A LARGE NUMBER OF CLOSELY SPACED MODES IS DIFFICULT TO MODEL

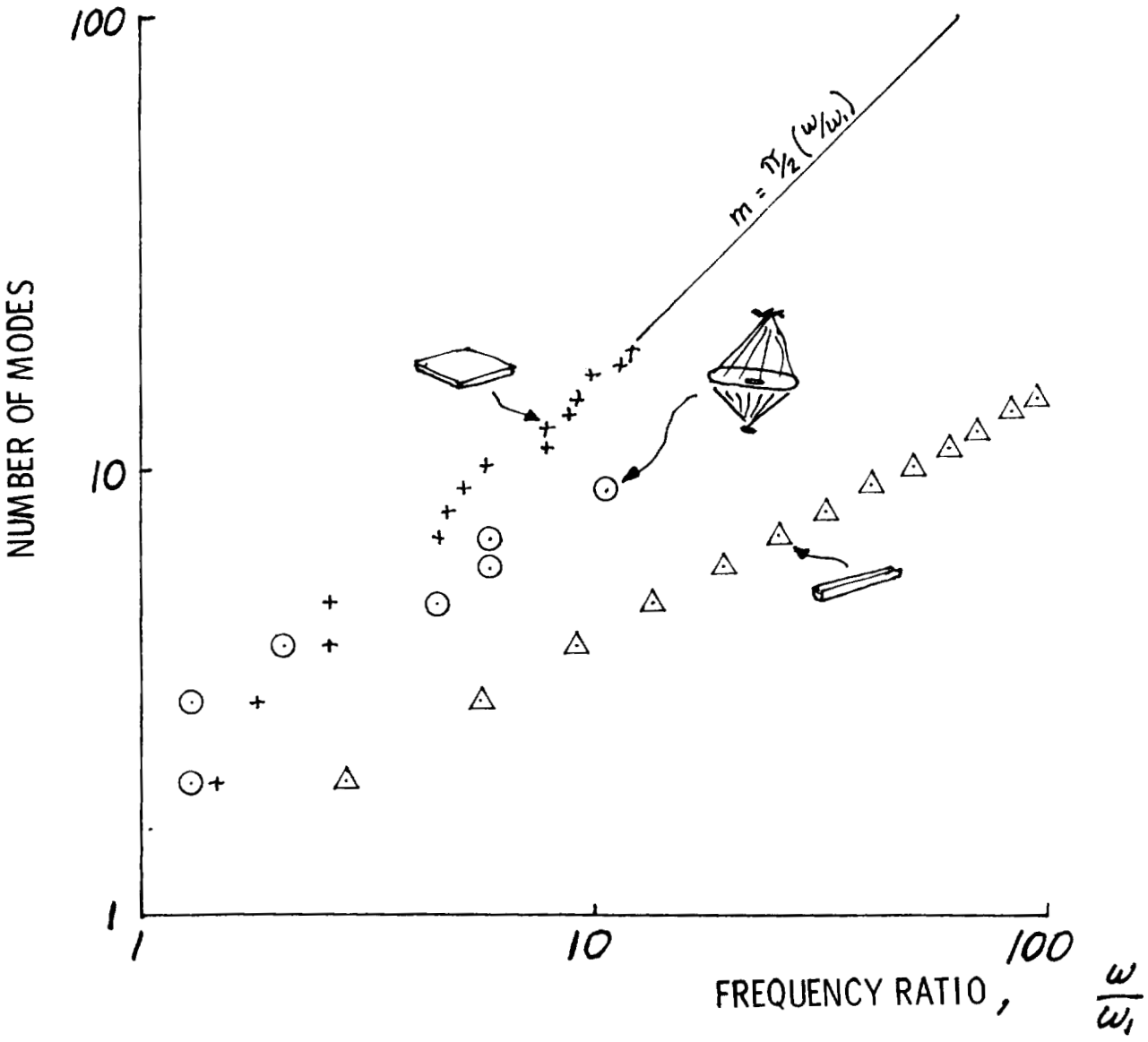

Figure 8

It should be noted that the limits to the effectiveness of control systems depends on the degree to which the control law can be adjusted. The bandwidth of a fixed control law will probably be limited to about the first structural mode of a large space system. If adjustment of the control law is possible after analyzing spaceflight data, then it should be possible to increase the control bandwidth, perhaps by a factor of two. Adaptive control would allow even tighter control by continually adjusting control in response changing conditions.

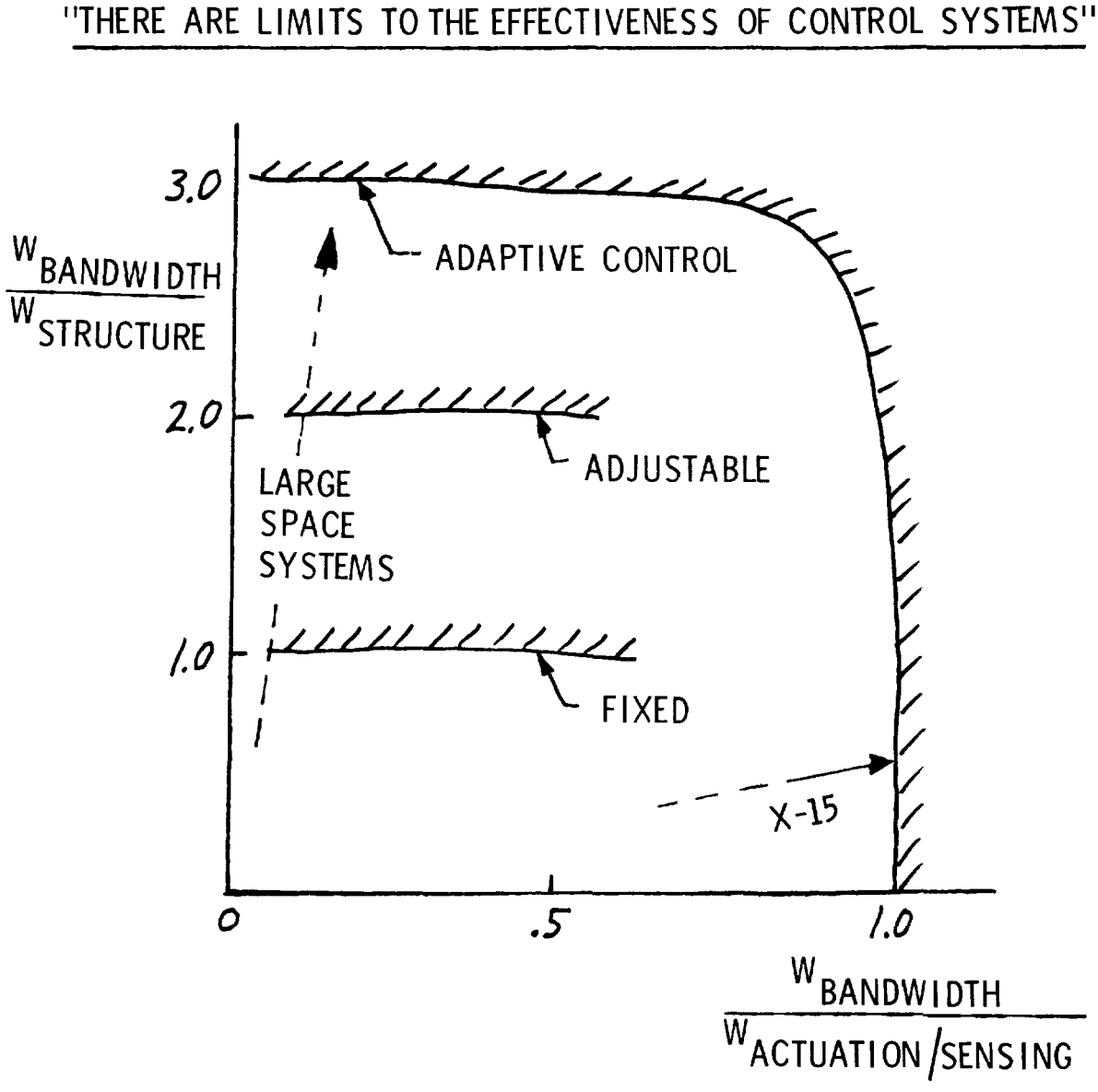

Figure 9

If the size of large space systems becomes bounded by control limitations, stiffer configurations will have an advantage. Their relatively higher structural frequencies enable control bandwidth requirements to be met for larger sized configurations. The hoop/column antenna, for example, is about four times as stiff as the offset wrap-rib configuration of the same diameter. For multi-frequency applications, this advantage narrows to a factor of two because of the lack of blocking for the offset configuration.

"IF THE SIZE OF LARGE SPACE SYSTEMS BECOMES BOUNDED BY CONTROL LIMITATIONS, STIFFER CONFIGURATIONS WILL HAVE AN ADVANTAGE"

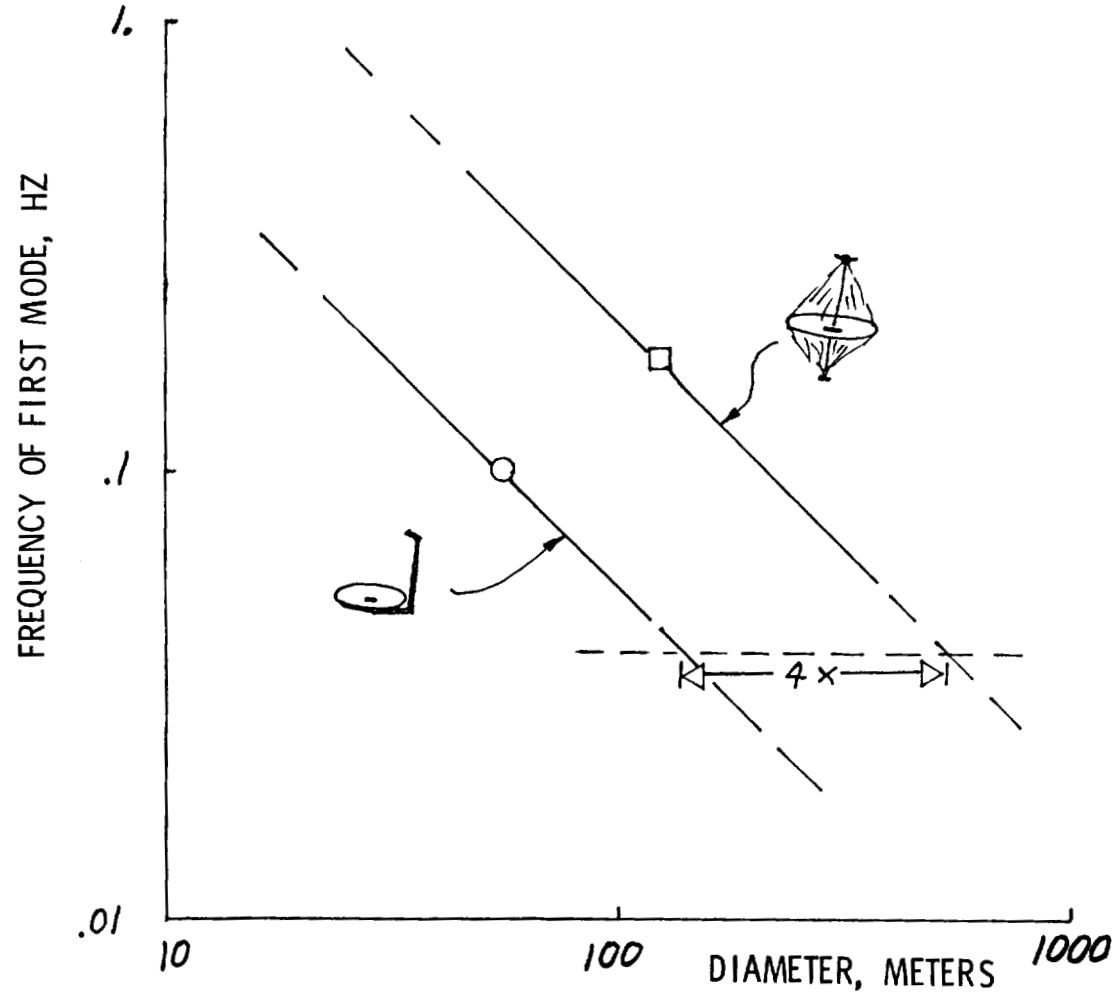

Figure 10

On-line systems identification for adaptive control of large space systems requires additional development, although simple forms of adaptive control would require less work. Practicalities are expected to limit the number of structural modes that can be modeled, on-line, to about four. Intentional disturbances will be required to produce response signals which can be separated from noise and unmodeled disturbances. The computational load is not insignificant, but lies within a practical range.

ON-LINE SYSTEMS IDENTIFICATION FOR ADAPTIVE CONTROL REQUIRES ADDITIONAL DEVELOPMENT

- SIMPLE FORMS OF ADAPTIVE CONTROL REQUIRE LESS DEVELOPMENT
- MAXIMUM LIKELIHOOD ESTIMATION WOULD BE USED
- NO SPECIAL INSTRUMENTATION IS REQUIRED
- SOMEWHAT OBTRUSIVE CONTROL INPUTS WOULD BE REQUIRED
- PERHAPS 4 STRUCTURAL MODES CAN BE MODELED, ON-LINE
- NEED SAMPLE RATE OF 10/SECOND
- UPDATE AFTER 30 SECONDS MIGHT BE POSSIBLE
- REQUIRES COMPUTATIONAL RATE ON THE ORDER OF 2.2 M OPS

$$\text{SENSITIVITY EQUATIONS} - MX^2 * NC * N = 14^2 \cdot 100 \cdot 300$$
$$\text{INFORMATION MATRIX} - MZ^2 * NC^2 * N = 20 \cdot 100^2 \cdot 300$$
$$\text{INVERSE} - NC^2/3 = 100^3/3$$

Figure 11

Automatic surface control of a large space structure is straightforward but is dependent on the accuracy and rapidity of surface measurements. The larger number of sensors and actuators involved in surface contour control will require fault management. The need for active surface control has not yet been established, but will depend on surface accuracy specifications, structural damping, and disturbance levels. Surface control at a particular point would need surface deflection information over a limited region.

AUTOMATIC SURFACE CONTROL IS STRAIGHTFORWARD

- BANDPASS OF SURFACE CONTROL IS PACED BY RATE OF MEASURING SURFACE DEFLECTION
- MUST ACCOUNT FOR FAILED SENSORS AND ACTUATORS
- PERHAPS 240 SURFACE MEASUREMENT LOCATIONS
- SIMPLE, CONSTANT GAIN, FEEDBACK CONTROL ADEQUATE
- COMPUTATIONAL REQUIREMENTS ARE MODEST ~ 50K OPS
  - CONTROL ⟶ $9 \cdot 240 \cdot 1 = 2160$
  - FILTER ⟶ $20 \cdot 240 \cdot 10 = 48{,}000$
  - REDUNDANCY ⟶ ?
- NEED FOR AUTOMATIC SURFACE CONTROL DEPENDS ON:
  - RF REQUIREMENTS
  - SURFACE RESPONSE TO DISTURBANCES, CONTROL, DEGREE OF STRUCTURAL DAMPING

$$u_{i,j} = \sum_{l=i-1}^{i+1} \sum_{m=j-1}^{j+1} k_{l,m} \, x_{l,m}$$

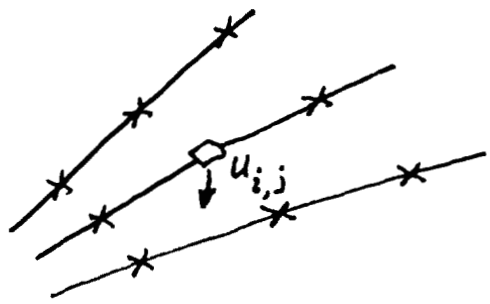

Figure 12

CONCLUDING REMARKS

- STRUCTURAL DYNAMICS MUST BE CONSIDERED IN DESIGNING EVEN POINTING CONTROL FOR LARGE SPACE SYSTEMS.
- DISTURBANCES, NOISE, AND NONLINEARITIES DRIVE THE CONTROL SYSTEM DESIGN.
- ADJUSTMENTS OF CONTROL GAINS AND SURFACE CONTOUR USING GROUND-BASED ANALYSIS ARE ONLY MODERATELY DIFFICULT.
- ADAPTIVE CONTROL PROMISES IMPROVED CONTROL BUT REQUIRES ADDITIONAL DEVELOPMENT.
- AUTOMATIC SURFACE CONTROL IS STRAIGHTFORWARD.
- CONTROL AND ANALYSIS TECHNIQUES NEED TO BE TESTED USING GROUND AND TEST-FLIGHT DATA.

Integrated Controls/Structures Study of Advanced Space Systems

C. S. Greene
T. B. Cunningham

Honeywell Systems & Research Center
Minneapolis, Minnesota

Large Space Systems Technology - 1981
Third Annual Technical Review
November 16-19, 1981.

PURPOSE OF STUDY

The integrated control/structures study was a task preformed jointly by the Martin Marietta Corporation and the Honeywell Systems and Research Center under a contract to the NASA Langley Research Center entitled "Advanced Space Systems Analysis" (Reference 1).

Figure 1 depicts the purpose of the study. For a given antenna mission one can postulate a cost tradeoff between a stiff structure utilizing minimal controls (and control expense) to point and stabilize the vehicle. Extra costs for a stiff structure would be caused by weight, packaging size, etc. Likewise, a more flexible vehicle should result in reduced structural costs but increased costs associated with additional control hardware and data processing required for vibration control of the structure. Figure 1 denotes that this tradeoff occurs as the ratio of the control bandwidth required for the mission to the lowest (significant) bending mode of the vehicle. The Honeywell portion consisted of establishing the cost of controlling a spacecraft for a specific mission and the same basic configuration but varying the flexibility.

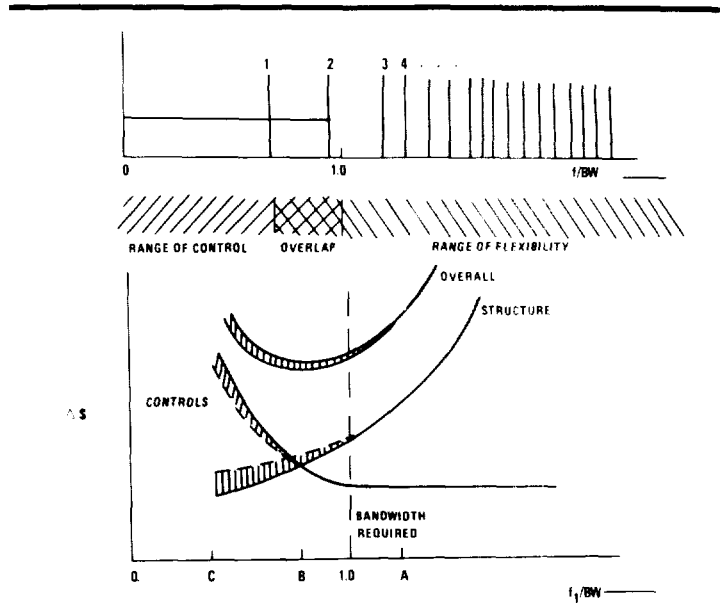

* EXAMINE TRADE-OFF OF CONTROL COST AND STRUCTURAL COST FOR LARGE ANTENNAS

APPROACH: DESIGN, "PRICE" AND COMPARE 4 SPACECRAFT FOR A TYPICAL ANTENNA MISSION

Figure 1

RADIOMETER CONCEPTUAL DESIGN

The study vehicle is shown in Figure 2. This is a conceptual design of a symmetric feed radiometer. The reflector is an electrostatically suspended membrane supported by a 170 meter (inside diameter) box truss ring. The feed is supported by two astromasts with two pairs of tension cables. The size used was determined to be the largest which could be packaged into one shuttle orbiter bay. The control design includes the effects of the astromast and hoop flexible modes, but does not include the electrostatic shape control.

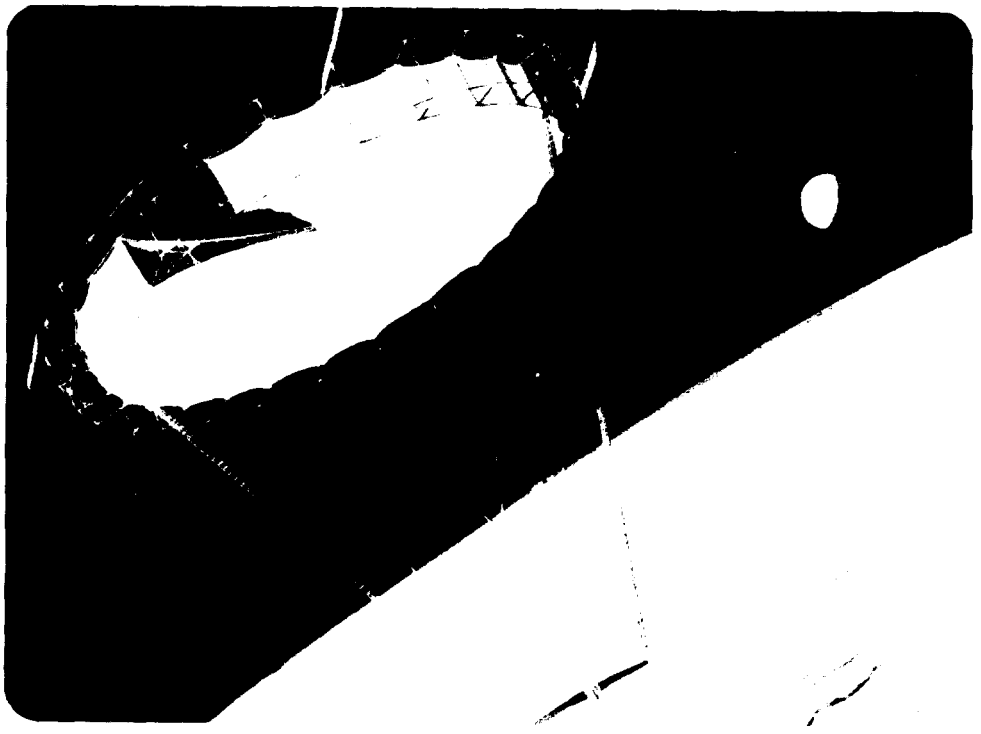

170 METER RADIOMETER

- **BOX TRUSS RING**
- **170 METER DIAMETER REFLECTOR (INNER DIAMETER)**
- **RADIOMETER CHARACTERISTICS**
  - **FREQUENCIES; 1.08, 2.03, 4.95 GHz**
  - **SPHERICAL SURFACE; F/D = 2**
  - **LINE FEED**
- **ELECTROSTATIC MEMBRANE**
  - **0.3 TO 0.5 mil POLYMER FILM SURFACE**
  - **50 m EFFECTIVE APERTURE**

Figure 2

STRUCTURAL OPTIONS

The Four structures were supplied by Martin Marietta to conduct the control design cost tradeoff analysis. Major characteristics are described in Figure 3. Early in the structural design phase it was discovered that aluminum elements could meet all the constraints of a single orbiter launch. Two of the designs, including the most flexible spacecraft, were developed assuming an aluminum structure. It should be noted, however, that none of the designs achieved the low first bending modes characteristic of other antenna concepts such as an offset feed wrap rib concept. Three factors contributed to this in varying degrees:

1). The box truss based concept is inherently stiff
2). Centerline feed concepts allow utilization of symmetry to achieve stiffness
3). Tension cables served to stiffen astromast feed supports

SPACECRAFT DESIGNATION	BOX CHARACTERISTIC DIMENSION	MATERIAL	1ST BENDING MODE
1. "RIGID"	14.00 m	GRAPHITE/EPOXY	3.9 v/s
2. "INTERMEDIATE #1"	8.65 m	GRAPHITE/EPOXY	.52 v/s
3. "INTERMEDIATE #2"	11.00 m	ALUMINUM	.53 v/s
4. "FLEXIBLE"	8.65 m	ALUMINUM	.291 v/s

Figure 3

STRAWMAN REQUIREMENTS

The mission requirements chosen for the study are shown in Figure 4. These are representative of an earth observation Radiometer; however, the slew requirement was set stringent to force the consideration of the effects of flexibility in the vehicle. In doing so, results were generated which provide guidelines for the design of many future large space structures and which indicate the value and future direction of LSS control.

MISSION: EARTH ORIENTED

ORBIT: 1000 km CIRCULAR INCLINED 60°

SLEW: 45° IN 5 MINUTES

POINTING ACCURACY: .005°

SURFACE ACCURACY: 1.5 mm (RIM AND FEED)

Figure 4

GENERAL CONTROL CONFIGURATION

Many aspects of a mission drive a control design. Since the purpose of this task was to examine the effects of flexibility, the bandwidth of a controller was of major concern. The slew command provides the most stringent of the control requirements and thus received the most attention in this study. In addition, the low amount of coupling between control axes permits one to consider each axis individually although the techniques extend to the highly coupled case. Figure 5 is a block diagram showing the structure of the controller used for analyzing the control requirements.

As in any physical system there are errors in disturbances which must be accomodated. The principal error source for the slew loop is the uncertainty between commanded and actual torque delivered by either jets or momentum exchange devices. For this study, we assumed that there was a 10% uncertainty in the control torque applied to the spacecraft. This uncertainty is modeled as an unknown disturbance torque, T_D. Note that this also accounts for center of gravity (CG) and inertia uncertainties.

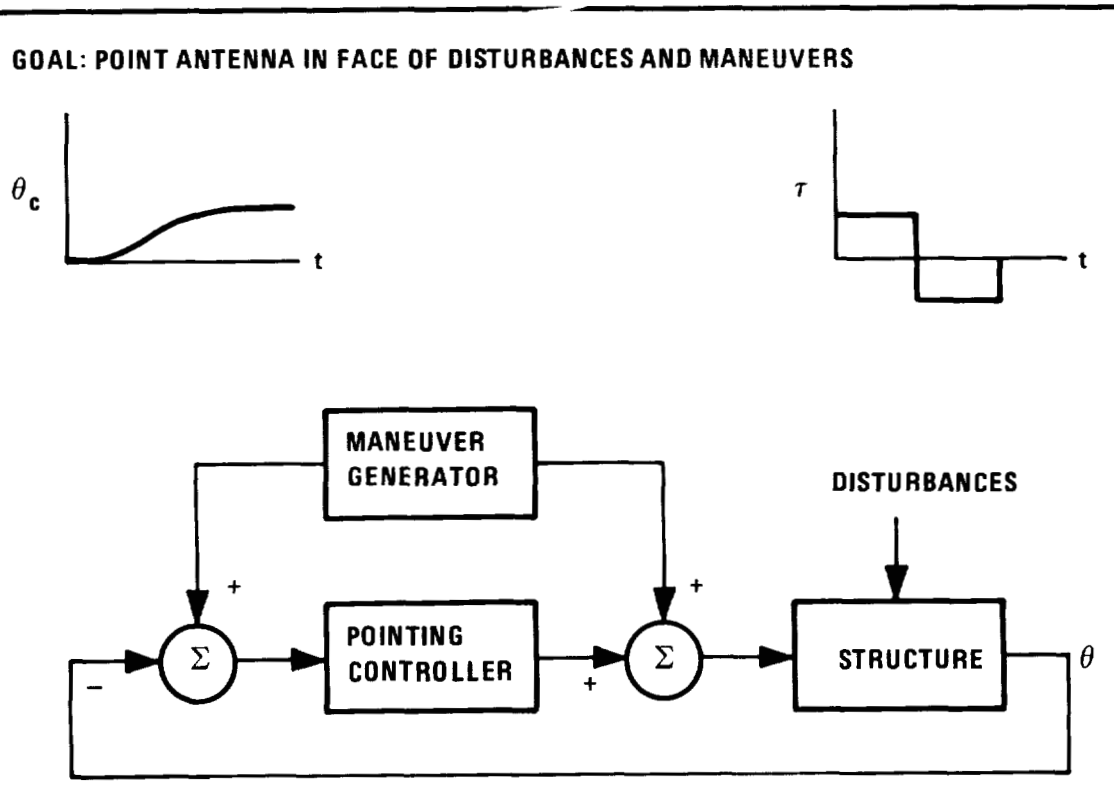

Figure 5

SLEW OPTION COMPARISON

There are many approaches available in the design of the nominal slew profile. For example, it is possible to design a slew which requires the bandwidth of the regulator to be minimized. An alternative is to minimize the energy (e.g. fuel) required to perform the maneuvers. The major characteristics of the minimal fuel and minimal bandwidth controls as applied to spacecraft are given in Figure 6. As can be seen the minimum bandwidth maneuver consists of performing the basic maneuver rapidly and then allow the structure to settle out. The minimum fuel maneuver is one in which the entire maneuver time is utilized. The minimum bandwidth maneuver requires roughly 17 times the torque and 4 times angular impulse (fuel) as the minimum fuel control but requires 1/5 the bandwidth. The decision as to which approach to use was based exclusively on fuel usage. A factor of 5 on bandwidth is very significant in terms of actuator and sensor capabilities but the cost associated with bandwidth must only be paid once. The fuel costs must be paid for on every slew maneuver and thus the minimum fuel approach was selected.

	MINIMUM BANDWIDTH CONTROL	MINIMUM FUEL CONTROL
TIME TO SLEW (T_3)	300 sec	300 sec
MANEUVER TIME (T_2)	74 sec	300 sec.
TORQUE REQUIRED	24,438 nt-m	1,468 nt-m
CONTROL BANDWIDTH (ω_b)	.04	.2 r/sec
IMPULSE REQUIRED	1.8×10^6 nt m-sec	$.44 \times 10^6$ nt-m-sec

Figure 6

OTHER BANDWIDTH REQUIREMENTS

Other disturbance sources for which we require feedback are summarized in Figure 7. These are aerodynamic torque, solar torque, and gravity gradient. Aerodynamic drag consists of a force exerted on a projected area of the spacecraft. Discussed in more detail in Reference 2, for a nominally local vertical orientation this results in a constant torque, a term at orbit rate, and a term at twice orbit rate. Solar torque has an effect on this spacecraft analogous to aero torque. At any point of interest in the orbit the angle of incidence of sunlight on each section of the spacecraft must be determined. Reference 3 contains the appropriate expressions for computing the total force resulting from solar torque. Because of the local vertical orientation of the spacecraft, however, solar torque does not contribute any net angular momentum to the spacecraft. However, large forces and torques do occur. A simple approximation to the torques includes both constant and orbit rate terms. In addition, shadowing of the spacecraft by the earth results in a nearly step change in the disturbance torque. Gravity gradient torques can cause a spacecraft to deviate from the desired attitude. Following a standard development of gravity gradient such as in Reference 4, conditions for the bandwidth of a controller can be determined.

- AERO TORQUE (TWO HARMONIC DIURNAL AIR DENSITY MODEL)
  - CONSTANT TORQUE
  - ORBIT RATE
  - 2x ORBIT RATE
- SOLAR TORQUE
  - CONSTANT
  - ORBIT RATE
  - STEP (SHADOWING) ← DOMINATES
- GRAVITY GRADIENT
  - MINIMUM B.W. FOR STABILITY
  - WIDER BANDWIDTH OFTEN PREFERRED
  - USUALLY SMALL

Figure 7

COMBINED AERO and SOLAR FORCING FUNCTIONS

The combined examination of aerodynamic and solar torques can be computed for various orbit and attitude parameters of the vehicle. As shown in Figure 8 for a given orbit these forces can be plotted. The altitude (ALT), orbit period (T), velocity (VEL), orbit inclination (INCL), and ascending node (PSIN) are all indicated in the graph. The attitude of the spacecraft (TH, PSI, PHI) of the earth pointing is also shown. The solid line refers to the x axis of the vehicle, the dash line to the y axis and the dot dash line to the z axis.

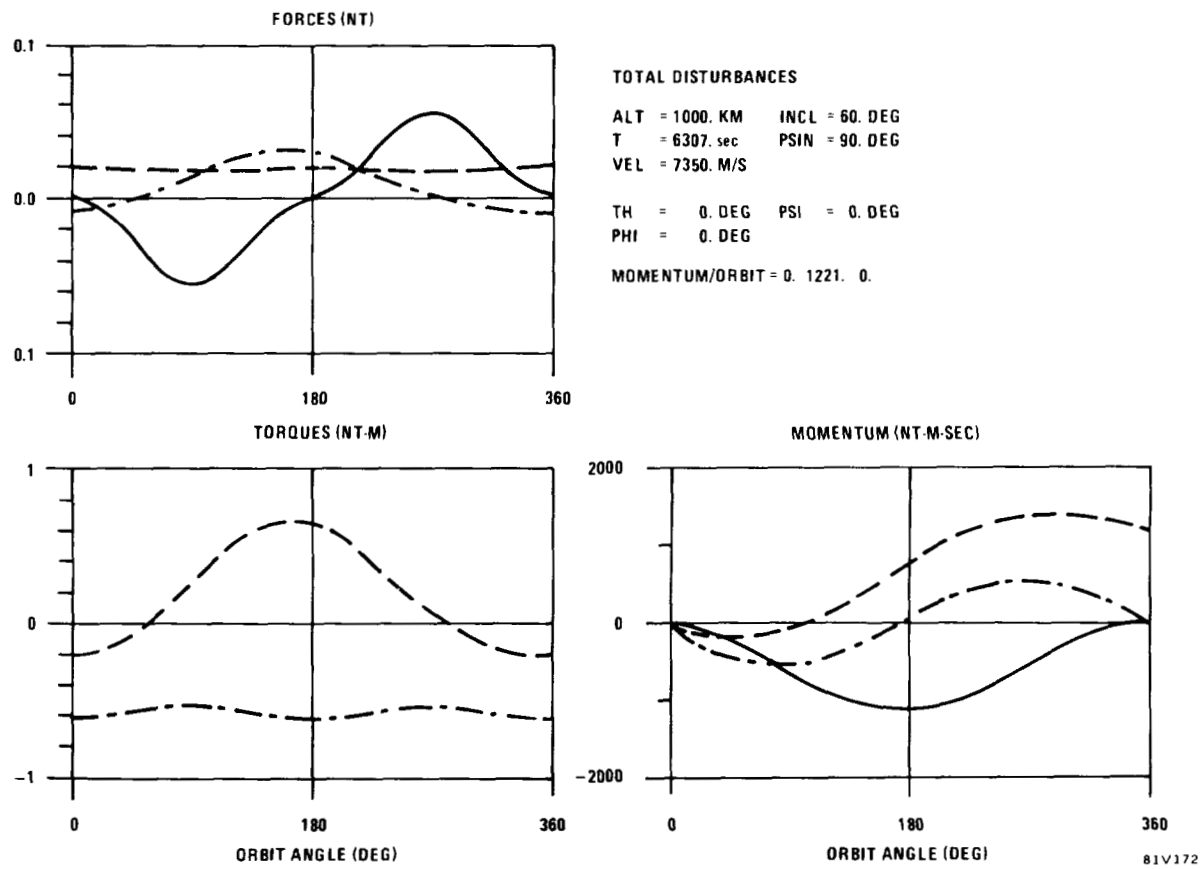

Figure 8

SUMMARY OF BANDWIDTH DRIVERS

A detailed analysis of all the disturbance sources (slew uncertainty, aerodynamic torque, solar torque, gravity gradient, and orbit maintenance) is provided in the final report of the ASSA contract (Reference 1). The bandwidth requirements to meet the mission goals stated earlier are summarized in Figure 9. Not shown are the gravity gradient and orbit maintenance bandwidth requirements which were negligible. Note that the significant bandwidth driver for this mission and spacecraft is the minimum energy slew bandwidth of .2 rad./sec. For comparison purposes the first bending modes of the four spacecraft are also shown. Only the flexible spacecraft with a first bending mode of .291 rad./sec. significantly interacts with the slew bandwidth. As will be discussed later the first bending mode, indeed the first few bending modes, of the spacecrafts are not significant and therefore the dynamic interaction we had searched for to provide the most challenging control problem did not occur for this type of structure.

- **SLEW BANDWIDTH (z)** .2 r/s
- **SOLAR STEP (y)** ≈ .01 r/s
- **SOLAR STEP (z)** ≈ .01 r/s
- **1ST BENDING MODE**

RIGID	3.9 r/s
FLEXIBLE	.291
INTER. 1	.52
INTER. 2	.53

Figure 9

CONTROL LAW DESIGN

As shown in Figure 10 two types of control laws or algorithms were designed for connecting the sensor outputs to the actuators. The first is for the low bandwidth control loops for which flexibility of the spacecraft is not an issue. These loops can be handled with standard lead compensators which involve achieving the appropriate phase margin during the cross-over region of the control loop through the use of lead compensators on the basic $1/s^2$ rigid body model of a spacecraft. This implies that all the bending modes of the vehicle are significantly higher than the desired cross-over point of the control loop. For the integrated control/structures study this included the required bandwidth for all disturbances sited earlier except the slew uncertainty bandwidth requirement.

The higher bandwidth control was required to meet the mission specifications in the face of the 10% uncertainty in the minimum energy slew maneuver. The effects of the flexibility of the vehicle must be considered. The most critical case in terms of driving the costs of control harware concerns the effects of the energy contained in the flexible modes violating the pointing and stabilization spec. Assuming that all passive damping and isolation techniques have been exhausted the use of dedicated vibration control to damp the structural modes to achieve a lower energy level for the structural modes. The implementation of this type of control would require the placement of actuators and sensors on various points along the flexible structure to implement dedicated damping of a particular structure. None of the four spacecraft studied exhibited enough bending mode energy to violate the pointing specifications and therefore none warranted this type of dedicated vibration control.

The other important effect of structural flexibility in control loop design concerns the stability of the control loop in the face of rapid changes of gain and phase caused by the bending modes of the vehicle. Control stability can be achieved by the proper placement of sensors and actuators (co-location is an important issue as discussed in Reference 5) and the proper attention to significant bending modes in the control law design. As we will see three of the four spacecraft examined in study required special attention to bending modes.

- **LOW BANDWIDTH CONTROL**
  - NO OVERLAP WITH BENDING MODES
  - INCLUDES ALL DISTURBANCES EXCEPT SLEW UNCERTAINTY
  - LEAD COMPENSATION AT CROSSOVER AND CMG'S ARE SUFFICIENT
- **HIGH BANDWIDTH CONTROL**
  - CASE 1: FLEXIBILITY EFFECTS VIOLATE POINTING SPEC.
    - REQUIRES DEDICATED VIBRATION CONTROL
    - NONE OF FOUR SPACECRAFT STUDIED EXHIBITED THIS PROBLEM
  - CASE 2: FLEXIBILITY AFFECTS ONLY STABILITY
    - CAN BE SOLVED BY PROPER SENSOR/ACTUATOR LOCATIONS AND CONTROL LAW DESIGN
    - 3 OF 4 SPACECRAFT AFFECTED

Figure 10

RIGID BODY CONTROL DESIGN

The generic form of the rigid body controller for spacecraft without attention to flexibility effects is shown in Figure 11. The $1/s^2$ term is essentially the rigid body motion of a torque input to an attitude output for a given spacecraft. The use of a lead compensator control law as shown in the figure provides lead at crossover with appropriate phase margin (approximately 45^o) and $1/s^3$ rolloff at high frequency to accommodate uncertainties.

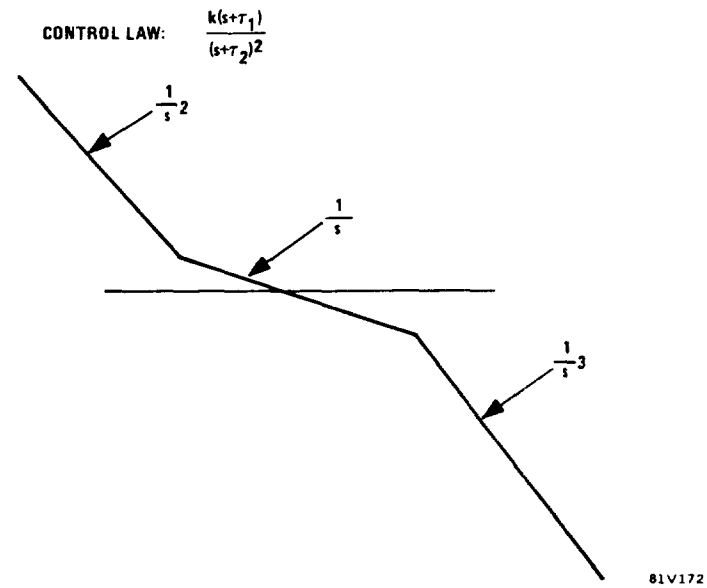

Figure 11

FLEXIBILITY EFFECTS OF RIGID BODY CONTROLLERS

Figures 12 through 15 show the effects of applying the rigid body control law designed to crossover at .2 rad/sec. to meet the slew uncertainty disturbance. Figure 12 shows the rigid body controller applied to the rigid body spacecraft. Note that none of the flexure modes (1/2 percent damping assumed for all bending modes) exceed the 0 db line in the gain plot. This means that the controller is gain stable and no specific attention to the additional compensation is necessary for this spacecraft design. Figures 13 and 14 show the rigid body control laws applied to the two intermediate spacecraft designs. In both cases one bending mode exceeds the 0 db line and other bending modes are close to the 0 db line. This means that the closed loop system would be unstable. Finally, in Figure 15 the rigid body controller is applied to the most flexible spacecraft examined in the study. Here we have a significant number of bending modes exceeding or near the 0 db line.

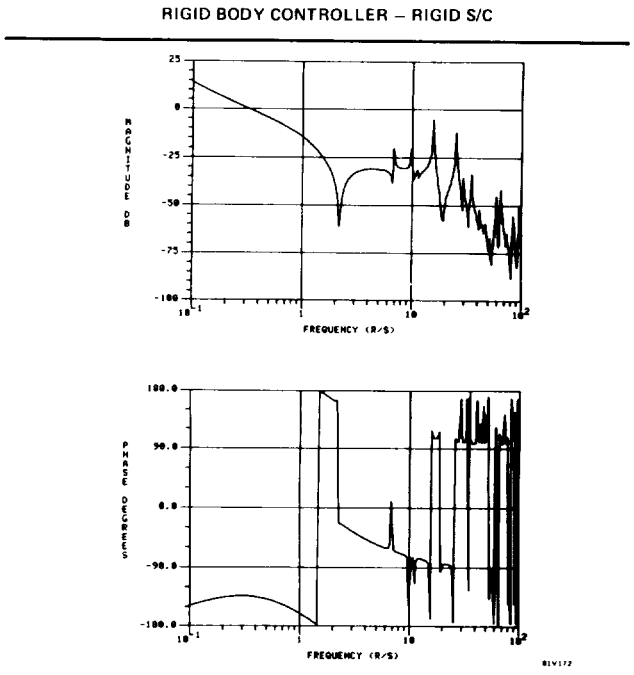

Figure 12

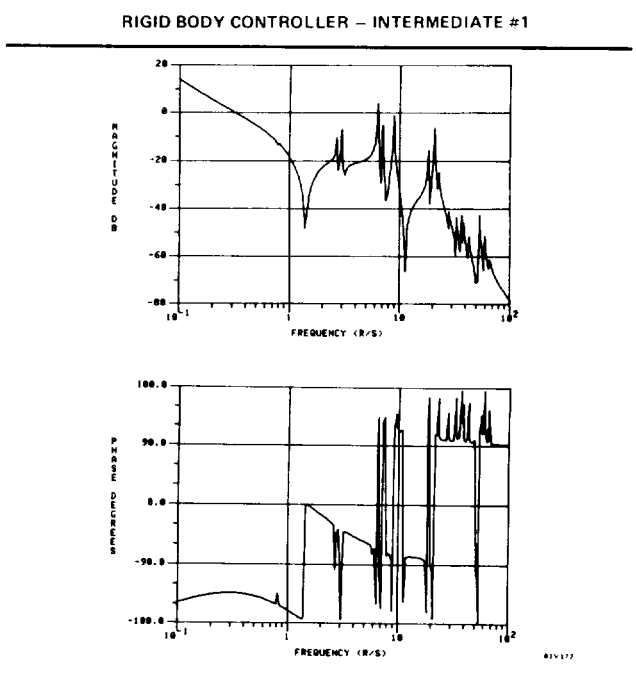

Figure 13

RIGID BODY CONTROLLER – INTERMEDIATE 2

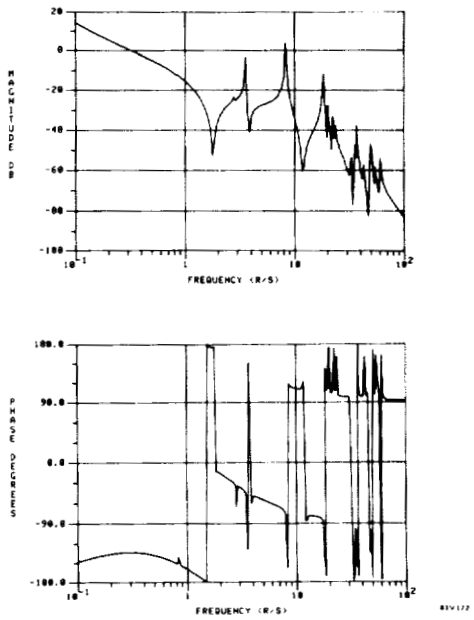

Figure 14

RIGID BODY CONTROLLER – FLEXIBLE S/C

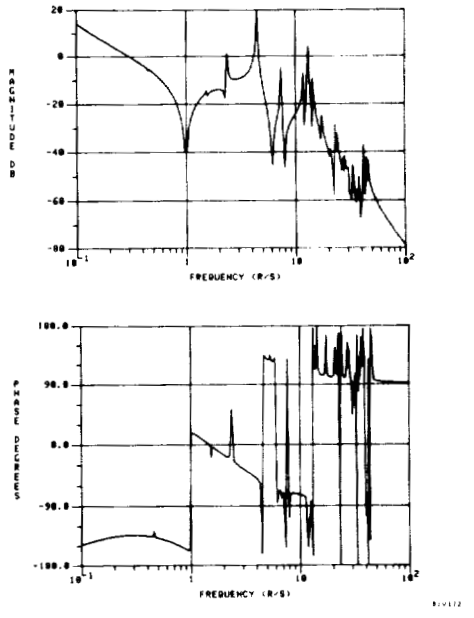

Figure 15

DEALING WITH FLEXIBILITY

It is obvious that the rigid body control law will not be appropriate for three of the four spacecraft designs. Figure 16 shows the numerous options one has at his disposal to attack the problems for all but the rigid spacecraft. One would be to modify the mission. This would result in a lower bandwidth requirement and essentially eliminate the overlap of bandwidth required to the flexure modes. This would be a last resort if other options were not available. The second option is to stiffen the structure to increase the bending modes and increase the damping. This of course is the objective of the rigid spacecraft. Option 3 is to utilize notch filters in the compensation path along with the rigid body control law. This indeed was the approach taken with the two intermediate spacecraft because both exhibited difficulties and only a few critical modes. Options 4 and 5 involve a change in the actuator type or to utilize distributed control. Both options were explored during the course of the study. Details of these options are discussed in Reference 1. The last option is to utilize a technique called slow roll-off. This is the solution chosen for the flexible spacecraft problem.

- **MODIFYING THE MISSION**
  - **CHANGE SLEW TIME TO 50 MINUTES**
- **STIFFEN STRUCTURE**
- **NOTCH FILTERS**
- **CHANGE ACTUATOR TYPE**
- **DISTRIBUTED CONTROL**
- **SLOW ROLL-OFF**

Figure 16

NOTCH FILTERS

The use of appropriately designed notch filters is a viable solution for the two intermediate spacecraft control law designs. Figure 17 shows a notch filter which can be utilized for both the intermediate spacecraft. Note that the 0 db exceedence of the flexure modes of the two spacecraft does not dictate a very deep notch in the filter, i.e., less than 10 db. This represents a very modest requirement in terms of assuring robustness. Also shown in Figure 17 is an attempt to design a notch filter which would be appropriate for the significant bending mode above the 0 db line for the flexible spacecraft. Note here that a very deep notch is required. A notch of such depth and the additional requirement for notch filters for the other unstable modes presents a critical robustness problem if the location of the frequency of the bending modes change. Another approach utilizing the slow roll-off technique was applied to the flexible spacecraft.

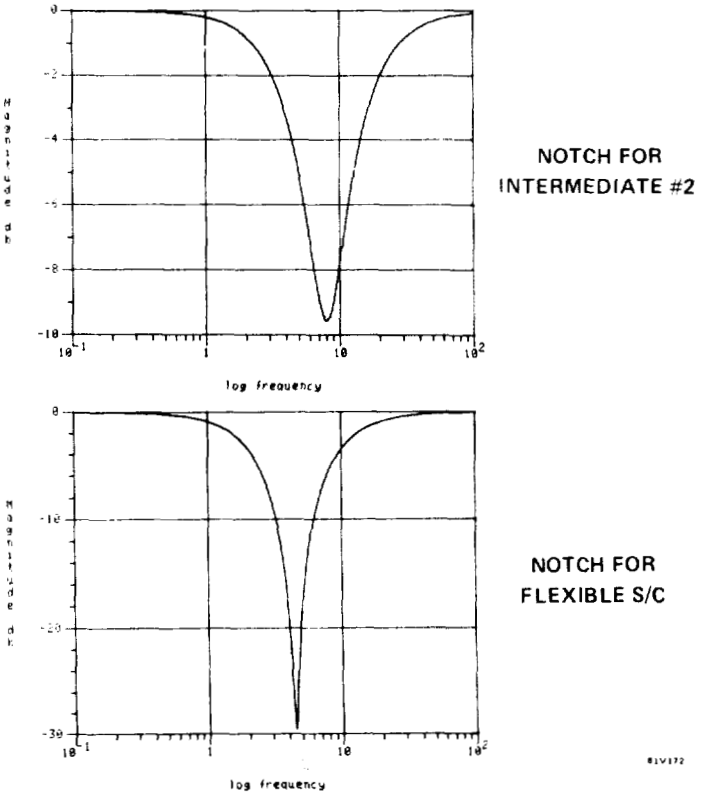

Figure 17

INTERMEDIATE SPACECRAFT CONTROL RESULTS

Using the notch filter shown in Figure 17a on the intermediate spacecraft number 1, the effect of the attenuation of the bending modes is shown in Figure 18. The notch filter has the effect of achieving gain stabilization and thereby solving the control problem.

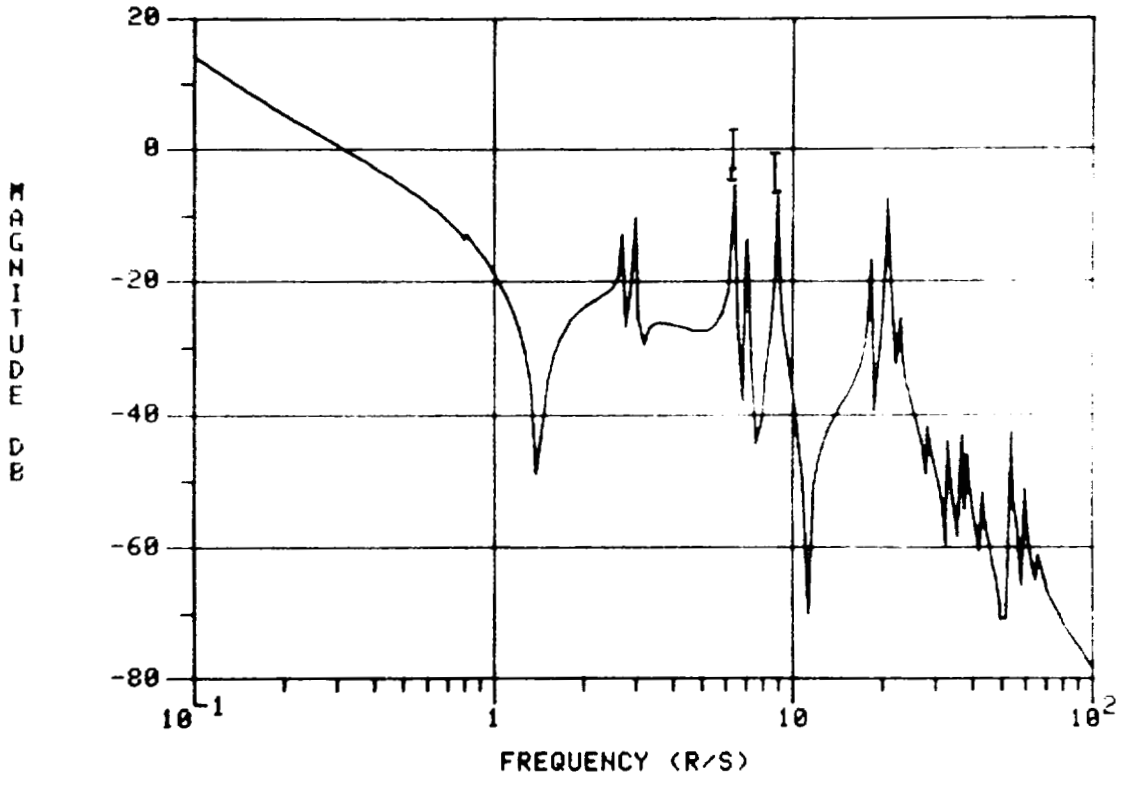

Figure 18

SLOW ROLL-OFF

The option to achieve robust control for the flexible spacecraft involves achieving phase stabilization, i.e., assuring that for every gain above 0 db we have adequate phase margin. Figure 19 describes the properties of a compensator used to achieve slow roll-off. As shown, the rigid body control law must be modified with the appropriate compensator, which consists of a cascaded set of lead-lags. Bending modes contain phase variations that basically oscillate between +90 degress and -90 degress (this assumes co-located sensors and actuators as discussed in Reference 5). In order to achieve a 45^{o} phase margin the compensator must achieve a roll-off less than first order. The appropriate gain roll-off to acnieve this through the use of the modified compensator would be approximately 13 db per decade for the region of the critical flexure modes. This is achieved by the cascading shown in the Figure 19. This type of compensation achieves a robust control for the envelope of transfer functions associated with these flexure modes. Slow roll-off requires much higher bandwidth (perhaps two orders of magnitude in frequency) than to implement either the rigid body controller or the rigid body with notch filtering. This requires higher bandwidth sensors and actuators plus an additional throughput requirement on digital processing.

It should be noted that this technique is not restricted to scalar or lightly coupled system. Reference 6 contains a version of these results for the multi-input spacecraft. The approach is similar in that one puts identical compensators of the form shown in Figure 19 into each input channel. In this case, additional design freedom provided by the multi-input problem can be used to increase damping on specified modes of the spacecraft.

- **MODIFY COMPENSATOR**

$$\frac{K(s+a)(s+10a)\cdots(s+10^{b}a)}{(s+3.6a)(s+3.6a)\cdots(s+3.6\times 10^{b}a)(S+C)}$$

- **GIVES $\approx 45^{\circ}$ MARGIN**
- **CONTROLS ENVELOPE OF TRANSFER FUNCTION $\Rightarrow$ ROBUST**
- **REQUIRES PHASE PROPERTY OF COLOCATION**
- **EXTENDS TO MIMO**

Figure 19

SLOW ROLL-OFF FOR THE FLEXIBLE SPACECRAFT

Results of utilizing the slow roll-off technique on the flexible spacecraft are shown in Figure 20. Note that by achieving a phase margin of 45^{o} up to a frequency of 11 rad./sec. there is no need to attenuate the bending modes below the 0 db line in the feedback control loop.

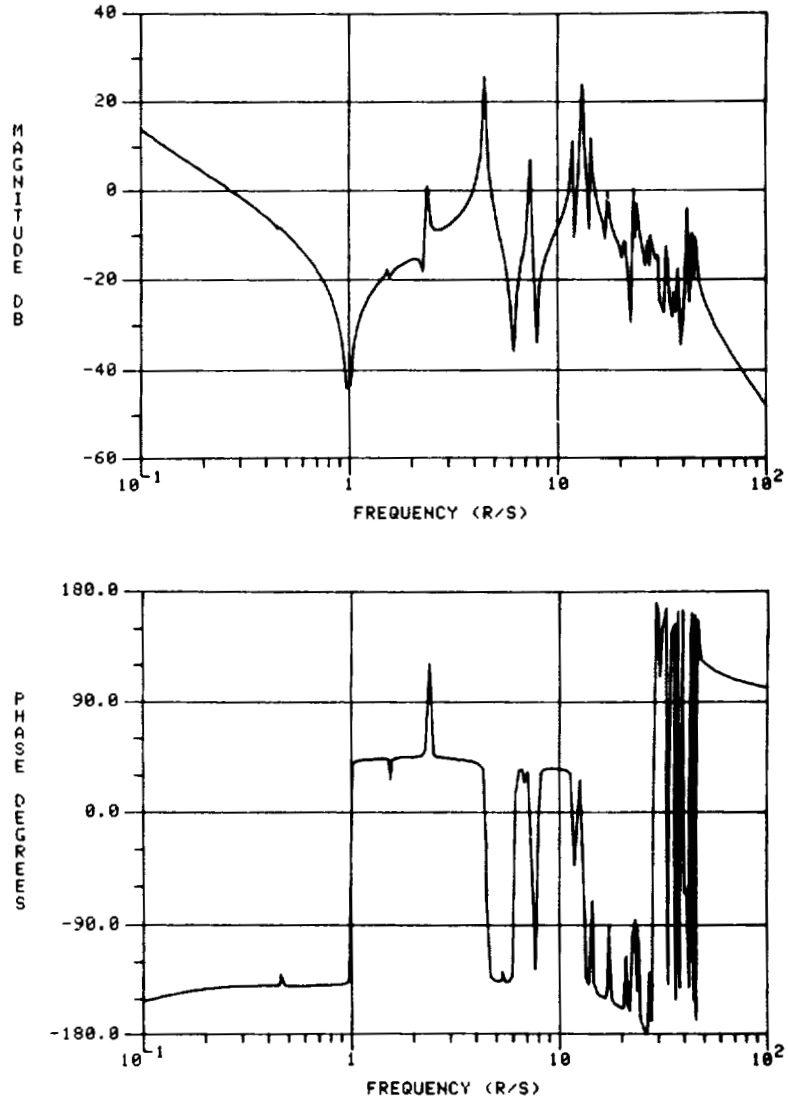

Figure 20

SENSORS AND ACTUATORS

The sensors and actuators required to implement the four control laws discussed are summarized in Figure 21.

Sensors - The primary sensors are gyros (co-located with CMG's and slew jets) on the rim of the spacecraft. For the y, z axis, two gyros are located to sense each axis and the outputs are then averaged to form the effective attitude measurement. This is done to take advantage of the co-location in the wide bandwidth cases. In order to provide an absolute reference one star sensor is required for each gyro.

Actuators - A combination of CMG's and jets are used to control all spacecraft versions. As indicated earlier the distinction between the various versions is in the bandwidth required of the components. The jets have the combined roles of the solar/aero drag makeup i.e., orbit maintenance, large slew maneuvering and CMG unloading. The CMG's are included for attitude maintenance during "normal" operation when the jets are not used.

- GYROS (6) } 4 ON RIM (±y, ±z)
- STAR SENSORS (6) } 2 ON FEED
- CMGS (RIGID REQUIRES 2x)
- SLEW JETS-HYDRAZINE (8) - ON RIM (± y)
- ORBIT MAINTENANCE JETS - ELECTRIC (24)

Figure 21

SENSOR/ACTUATOR PLACEMENT

Figure 22 shows the summary of the placement of the various sensors and actuators. Two gyros are located at (3) on the feed to provide the x axis reference. Note that due to low bandwidth requirement the position of these gyros is not critical. Also shown in Figure 22 is the placement of the jets and CMG's. Single axis devices have been selected and used in pairs, one pair to each axis. A total of six devices are required for redundancy. CMG's are placed as in Figure 22 at locations (1) to provide minimal momentum in the $\pm$ z and the $\pm$ x directions and at locations marked (2) with a nominal $\pm$ x orientation. These provide control torques about x, z, and y, respectively. A maximum torque capability of 2 nt-m is required.

In order to accomplish the 45^{o} slew in 300 seconds jets must be located to thrust is located in the $\pm$ x directions at points marked 1. Chemical (Hydrazine) engines are mounted in pairs. The jets, each with four to six Newtons (NT) of thrust, are located at the top and bottom edges of the rim (4 locations).

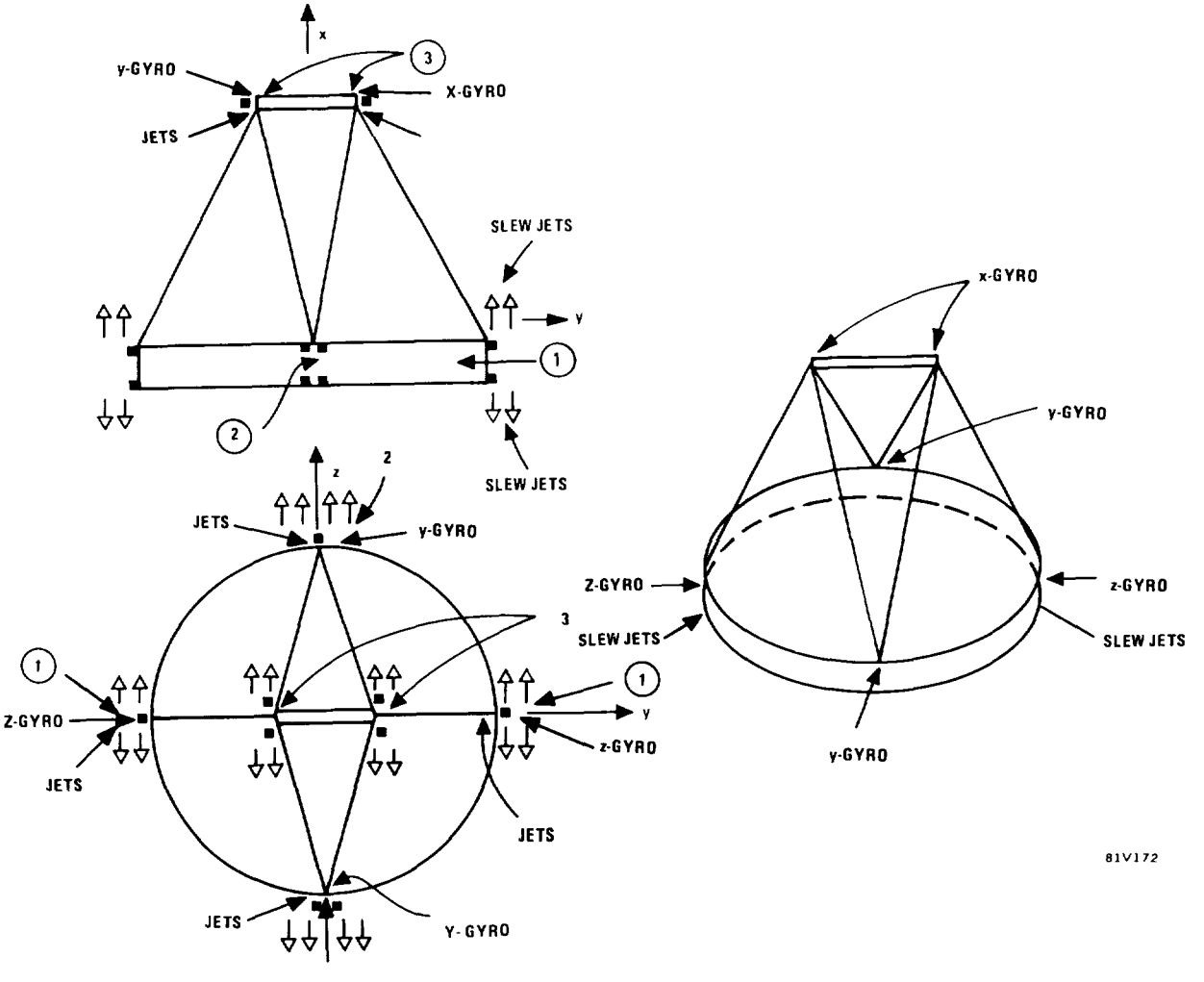

Figure 22

COST OF CONTROL

The purpose of costing each of the versions of the spacecraft is to determine the cost differential of each design. As such the relative prices and the reasons for the differences are far more important than the absolute cost estimates. In order to determine an overall control system cost the differences between each version are first highlighted. Following this, component costs were determined based on past history and taking into account the identified differences. Figure 23 briefly describes the results of the cost exercise. One should note that the rigid spacecraft had the highest control cost. This was because the stiffer heavier structure required larger CMG's than was required on the two intermediate spacecraft and the flexible spacecraft. The flexible spacecraft has a slightly larger increase in cost over the intermediate designs ($10,000). This is due to a requirement for higher throughput in the computations which dictates a more powerful digital computer. The higher throughtput is required because of the higher bandwidth dictated by the slow roll-off compensation design for the flexible spacecraft. It is estimated that the computations need to run at a 160 Hz for this design as opposed to approximately 10 Hz for the two intermediate spacecraft designs, and 3 Hz for the rigid body spacecraft design. One further note is that the impact of development costs for the respective systems and the cost of required testings (i.e., the flexible spacecraft design would require higher developmental costs) were not considered in this cost analysis.

- **EMPHASIS ON RELATIVE COST**
  - **LARGER CMG**
  - **WIDER B.W./COMPUTATION**

RIGID	**$12.98 M**
INTER.	**$12.38 M**
FLEXIBLE	**$12.39 M**

Figure 23

SUMMARY AND CONCLUSIONS

The major conclusions of this study were:

- For the type of spacecraft and missions studied the cost of the control system is a relatively weak function of the degree of frequency overlap. In fact, the control system for the rigid version was most expensive due to the larger CMG's required. It is important to note that the spacecraft studied in this development were stiff by nature due to the box truss design techniques used. A more flexible spacecraft, such as an off-set wrap rib, exhibits much lower frequencies for critical bending modes and therefore would require dedicated vibration control. This should be examined in terms of the cost impact of the control systems.

- There is a need for a control design methodology for spacecraft with overlaps between structural resonances and control system bandwidth. The solution of automatically stiffening the spacecraft, i.e., a "structural solution", does not result in a minimum cost design. Thus, there is validity for large space structures control.

- Structural uncertainties are a major driver in LSS control design. At least as important as initial uncertainties are ageing effects. Controllers must be either robust to this uncertainty or adapt to it. Robust controllers were used in this study; however, adaptive control should be explored where bandwidth requirements dictate.

REFERENCES

1. Park, A. Colton, and Greene, Christopher S., "Advanced Space Systems Analysis (ASSA)," NASA CR-165797, 1982 (to be published).

2. Large Advanced Space Systems Design Computer Program, Final Technical Report, NASA CR 15919-1, General Dynamics Convair Division, San Diego, California.

3. Spacecraft Radiation Torques, NASA Monograph, NASA SP-8027, October, 1969.

4. Kaplan, Marshall, Modern Spacecraft Dynamics and Control, John Wiley and Sons, 1976.

5. Greene, C. S., "Control of Large Space Structures: An Update," Honeywell SRC #MR12576, January 1980.

6. Greene, C. S., and Stein, G. "Inherent Damping, Solvability Conditions, and Solutions for Structural Vibration Control," 18th IEEE Conference on Decision and Control, Fort Lauderdale, FL, December 1979.

ACTIVE CONTROL OF SPACE STRUCTURES: PROOF OF CONCEPT EXPERIMENT

J. A. Breakwell
Lockheed Missiles and Space Company
Sunnyvale, California

Large Space Systems Technology - 1981
Third Annual Technical Review
Langley Research Center
Hampton, VA

November 17, 1981

MULTIPLE INPUT/MULTIPLE OUTPUT CONTROLS

One of the main advantages of modern control theory is its ability to deal easily with multiple input/multiple output systems. Two types of systems which fall into this category are flexible systems, where many measurements and several actuators may be necessary to provide control over bending behavior, and articulated systems which consist of several rigid bodies connected together by pivoting connections. In this latter case, multiple controls could be implemented, for instance, as torquers at the joints.

LMSC has conducted hardware tests of both types of systems and plans to do tests of a combined flexible/articulated system in the near future.

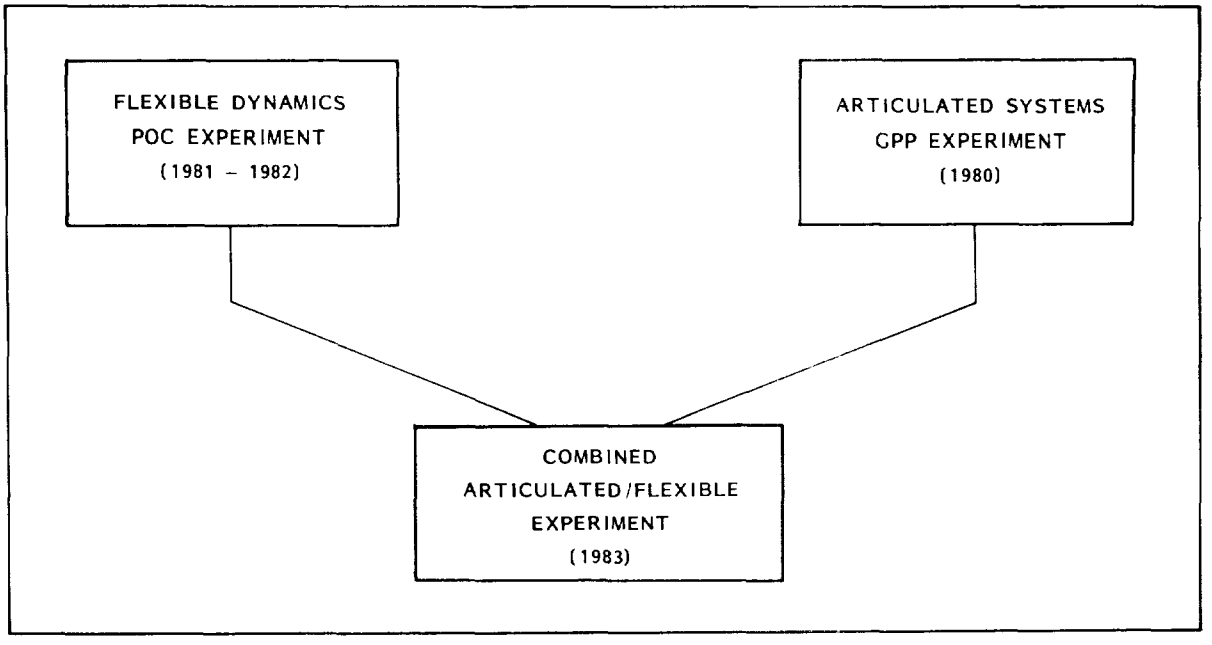

TYPICAL PERFORMANCE DEMONSTRATION

The test article consists of a payload (P/L) section and an equipment section (E/S) connected via three gimbals. The P/L, which performs large angle high rate maneuvers, is driven by four control moment gyros (CMGs) oriented so as to provide full three-dimensional torque capability. To minimize disturbances transmitted to the E/S, the axes of the three gimbals all intersect at the P/L center-of-mass. The E/S, which is to remain fixed in a laboratory reference frame, is controlled by torquers on the three gimbals. Attitude reference is provided by a rate gyro package and simulated star sensors mounted on the E/S plus optical encoders and resolvers on the gimbal axes. The total system weighs approximately 5,000 lbs and has maximum dimensions of approximately 10 feet in each direction.

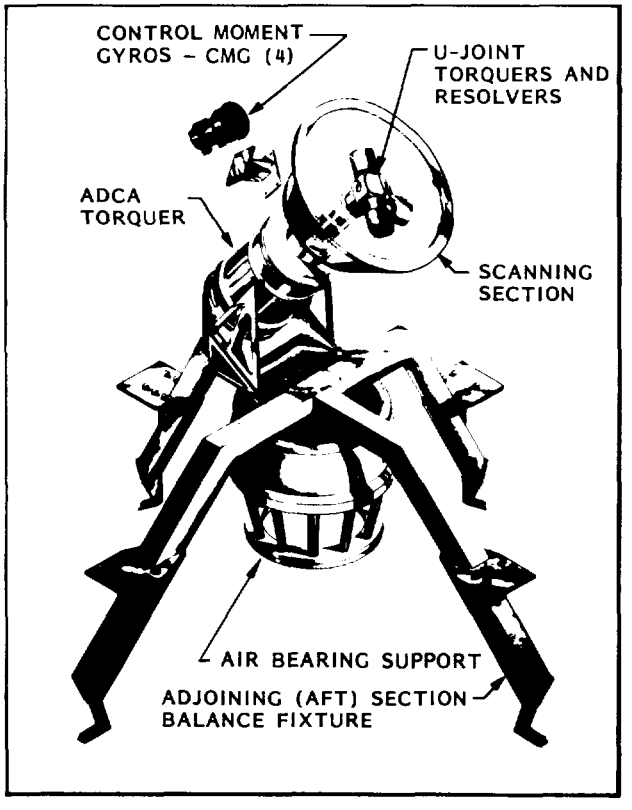

- **DEMONSTRATED MULTIBODY GIMBALLED SPACECRAFT MANEUVERING**
- **PERFORMED POINT-TO-POINT STEERING AND SYSTEMATIC SCANNING WHILE ADJOINED SECTION REMAINS FIXED IN ORBITAL COORDINATES**
- **DESIGNED, CONSTRUCTED AND FUNCTIONALLY TESTED AN AIR BEARING WORKING MODEL INCORPORATING MOMENT CONTROL TORQUERS**

MULTI-BODY MANEUVERING SYSTEM TEST

The test article is floated on a spherical air bearing (A/B) to allow for three rotational degrees of freedom with minimum environmental disturbance torques. The command/control computer and power supplies for sensors and actuators are located on the laboratory floor adjacent to the A/B. Power and data lines are connected to the floated test article via specially designed low friction mercury pool connectors. A laser beam is reflected off a mirror on the P/L to simulate the line-of-sight, and fixed laser detectors provide a measurement of pointing accuracy.

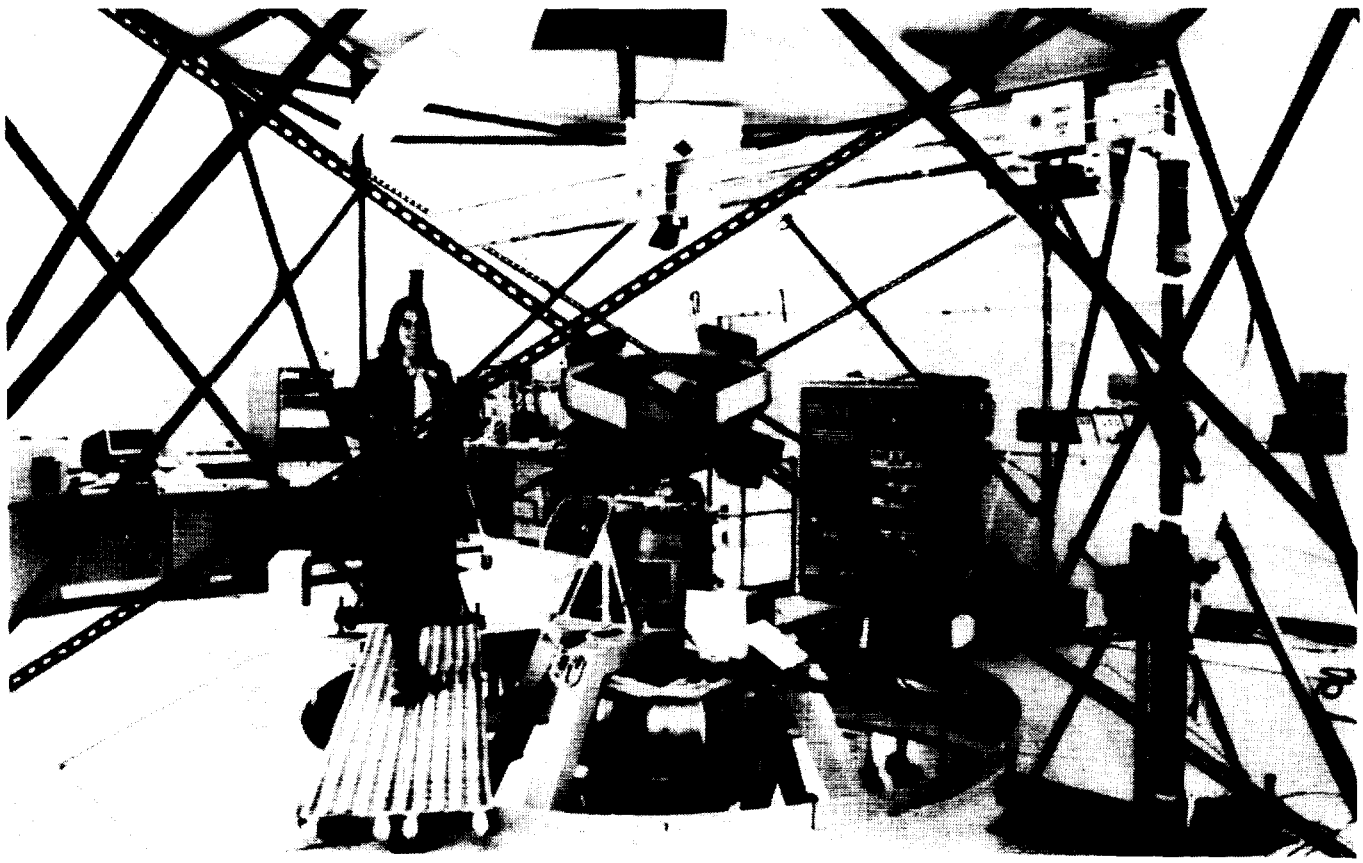

OBJECTIVES OF THE PROOF OF CONCEPT EXPERIMENT

The purpose of the ACOSS POC experiment is to demonstrate existing theories of LSS control on a realistic facsimile of a spacecraft, using sensors and actuators such as will actually be used in space. Beyond this goal, we will start work on establishing a testing procedure for these new control systems.

- EXPERIMENTALLY DEMONSTRATE ESTABLISHED THEORY
- ESTABLISH HARDWARE LIMITATIONS
- DEVELOP TECHNIQUES FOR TESTING CONTROL SYSTEMS

ARTIST'S CONCEPTION OF EXPERIMENT

The POC experimental specimen is a scaled down model of an offset fed RF antenna. An early goal is to control flexing of the specimen, using the CMG package, sufficiently to allow steady pointing of the line of sight (simulated by the laser path) at an inertial target. Later goals will be to control the dynamics of the entire antenna dish.

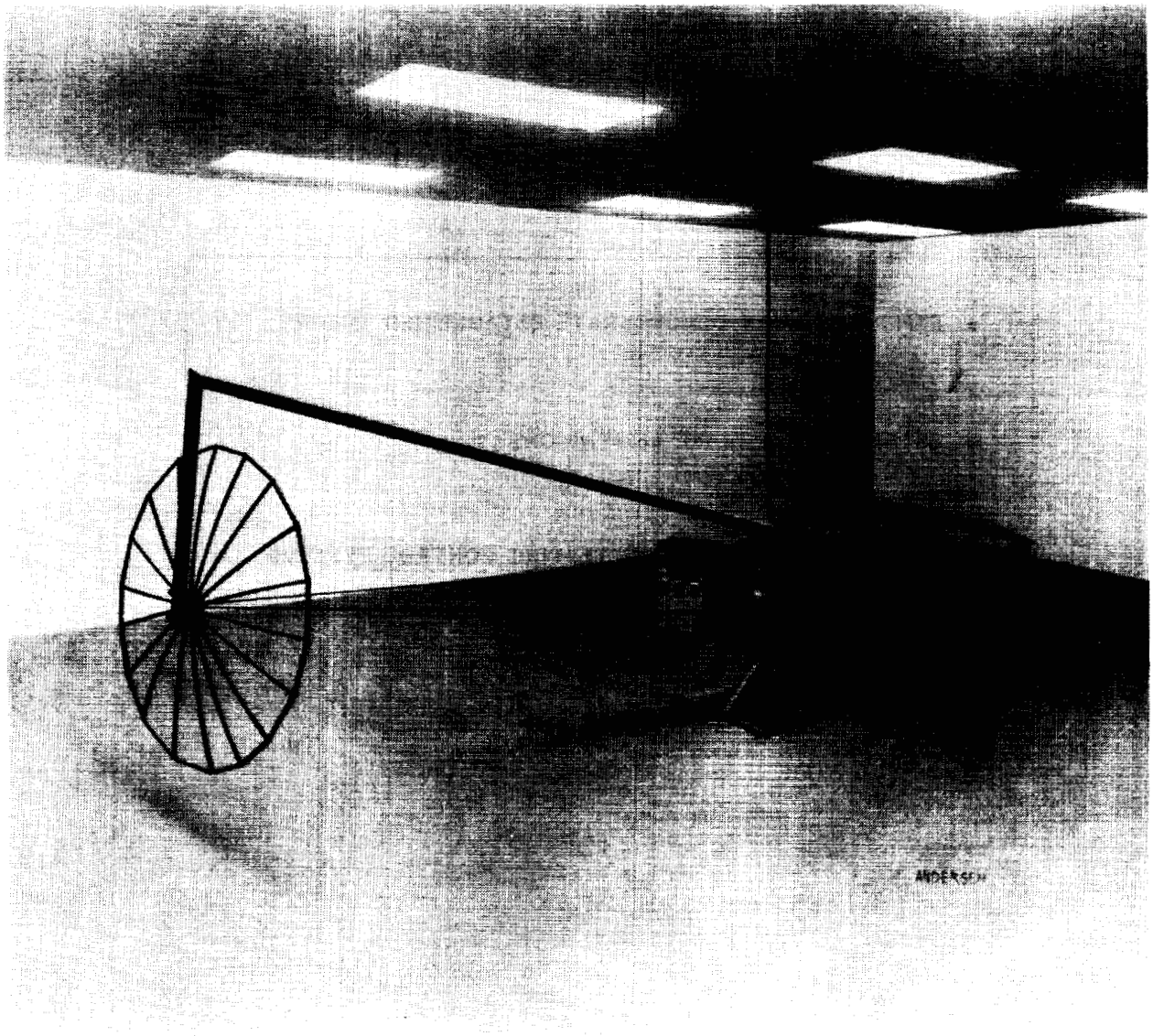

EXPERIMENT PHASES

Plans for 1982 are to complete the experiments which demonstrate line-of-sight (LOS) control capability with central actuators (CMGs) alone. Next, distributed actuation in the form of proof-mass actuators will be added to improve pointing performance. Eventually we will also demonstrate optimal slewing.

PHASE I OPEN LOOP MODAL CHARACTERIZATION
PHASE II DEMONSTRATION OF LINE OF SIGHT CONTROL WITH A SINGLE CENTRAL ACTUATOR; CONTROLS DESIGNED FOR TRANSIENT DISTURBANCE REJECTION
PHASE III DEMONSTRATION OF LINE OF SIGHT CONTROL WITH DISTRIBUTED ACTUATORS; CONTROLS DESIGNED FOR TRANSIENT DISTRUBANCE REJECTION
PHASE IV SAME AS PHASE III EXCEPT THAT CONTROLS DESIGNED FOR ON BOARD STEADY STATE DISTURBANCE REJECTION
PHASE V OPTIMAL SLEWING, CONTROL OF ANTENNA DISH DYNAMICS, ...

SCHEDULE OF EXPERIMENTAL PHASES

The schedule for carrying out the five phases described in the previous chart is shown below.

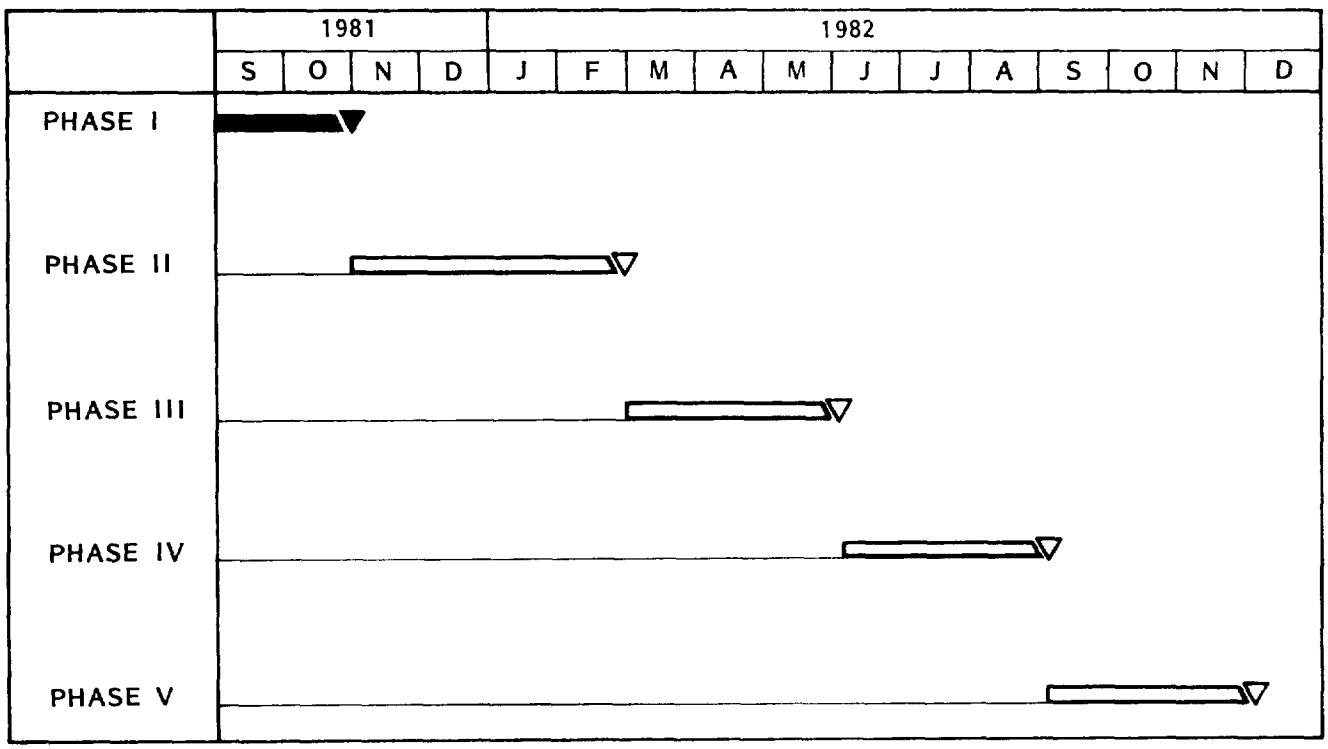

PHOTOGRAPH OF THE POC SPECIMEN

Some data on the POC experimental specimen:

Overall Length	29'
Antenna Dish Diameter	10'
Weight (Excluding Air Bearing)	590 lbs
Height	19'

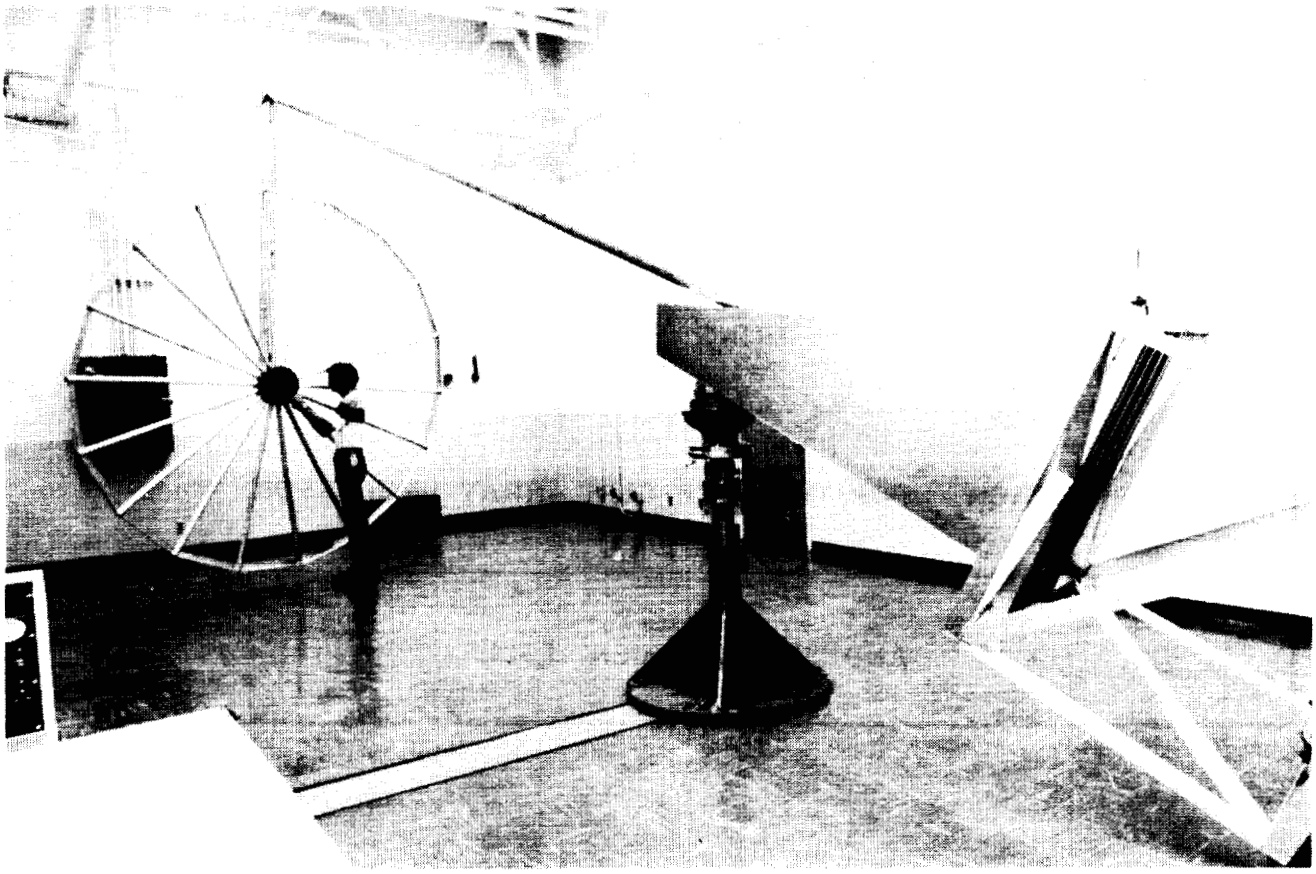

HARDWARE LIST

Shown here is a list of the major components used in the POC experiment. The computer plays a dual role; it both implements the control system, and monitors the testing procedures. The controls tests are modifications of standard modal testing procedures.

ACTUATORS:	C.M.G. CLUSTER, PROOF MASS ACTUATORS
SENSORS:	LASER ATTITUDE DETERMINATION RATE GYROS, ACCELEROMETERS
SUSPENSION:	AIR BEARING
COMPUTATION:	PDP 1145 WITH CSPI ARRAY PROCESSOR
	AND THE SPECIMEN ITSELF

PHOTOGRAPHS OF THE CMG CLUSTER

The next two pictures show the CMG cluster. Three CMGs are mounted such that the gimbal axes are symmetrically spaced on the surface of a 30° cone, and intersect at its apex. Each CMG can produce up to one hundred foot-pounds of torque, and has a momentum magnitude of five foot-lb-sec. Each unit weighs about forty pounds, and is approximately 1 1/2 feet long.

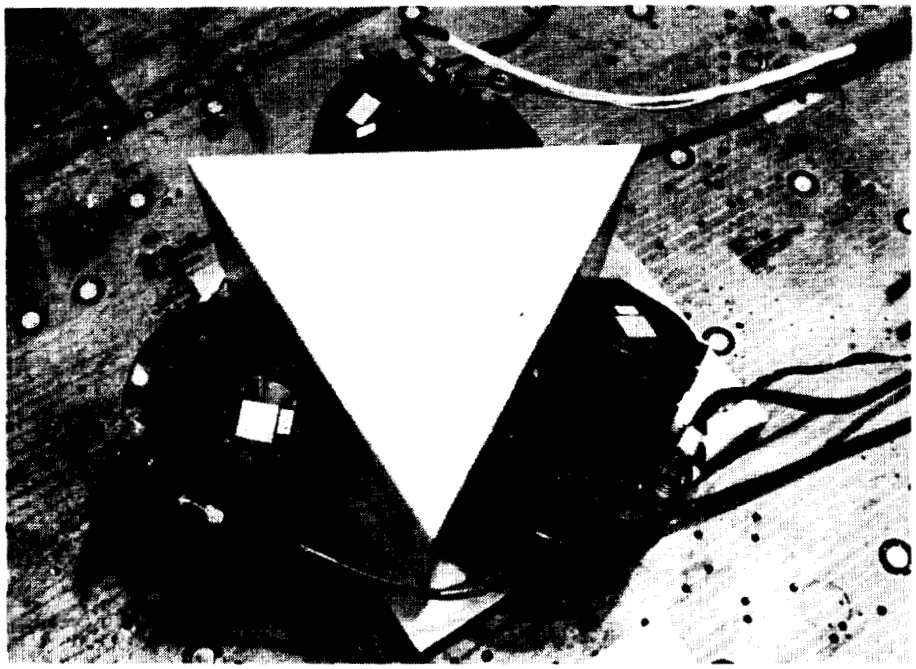

PHOTOGRAPH OF A PROOF-MASS ACTUATOR

Ten of these proof-mass actuators will be used to provide distributed actuation in Phases III and IV of the experiment. Each unit is capable of exerting a force of up to 1/2 lb. The force results from the proof-mass being accelerated by the magnetic coil. These devices can be used only for vibration suppression since they are not capable of producing a constant force.

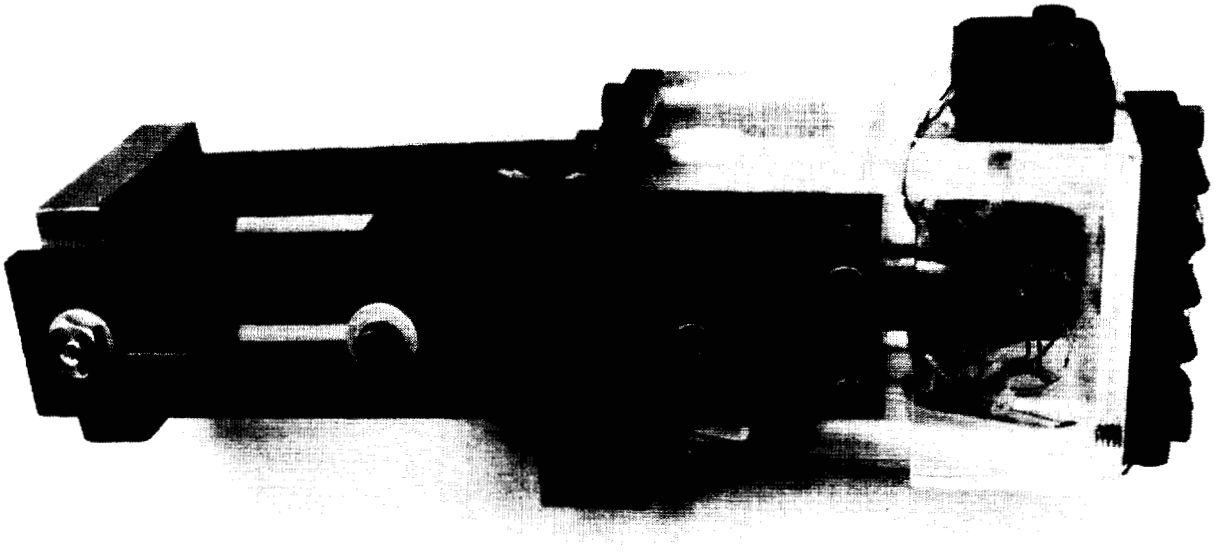

MODAL CHARACTERIZATION RESULTS

These data show how closely the finite element model was able to anticipate the modal frequencies of the specimen. Not shown is data on the agreement of the mode shapes; qualitatively agreement was good for the first five modes, but from then on analysis and experiment seemed to diverge. This uncertainty in the knowledge of the mode shapes could hamper design of the control system; maximum performance cannot be reached until the mode shapes are better determined.

	EXPERIMENTAL MODES	ANALYTICAL MODES (FINITE ELEMENT)
1.	1.50 Hz	1.67 Hz
2.	1.57	1.72
3.	3.01	3.28
4.	5.07	4.50
5.	6.91	6.23
6.	11.49	10.09 10.72
7.	13.02	12.11
8.	14.24	14.95
9.	15.33	15.44
10.	16.90	16.36
11.	16.98	17.29
12.	17.01	19.49
13.	17.61	20.50
14.	19.10	
15.	19.97	

CONTROL SYSTEM SCHEMATIC

Shown here is a schematic of the control system as it will be implemented on the POC experiment. The strategy is to estimate the modal amplitudes using a digital Kalman filter, and then to use these estimates, multiplied by the appropriate gains, to generate the actuator commands. The Kalman filter gains and the control gains are generated using conventional optimal control synthesis procedures.

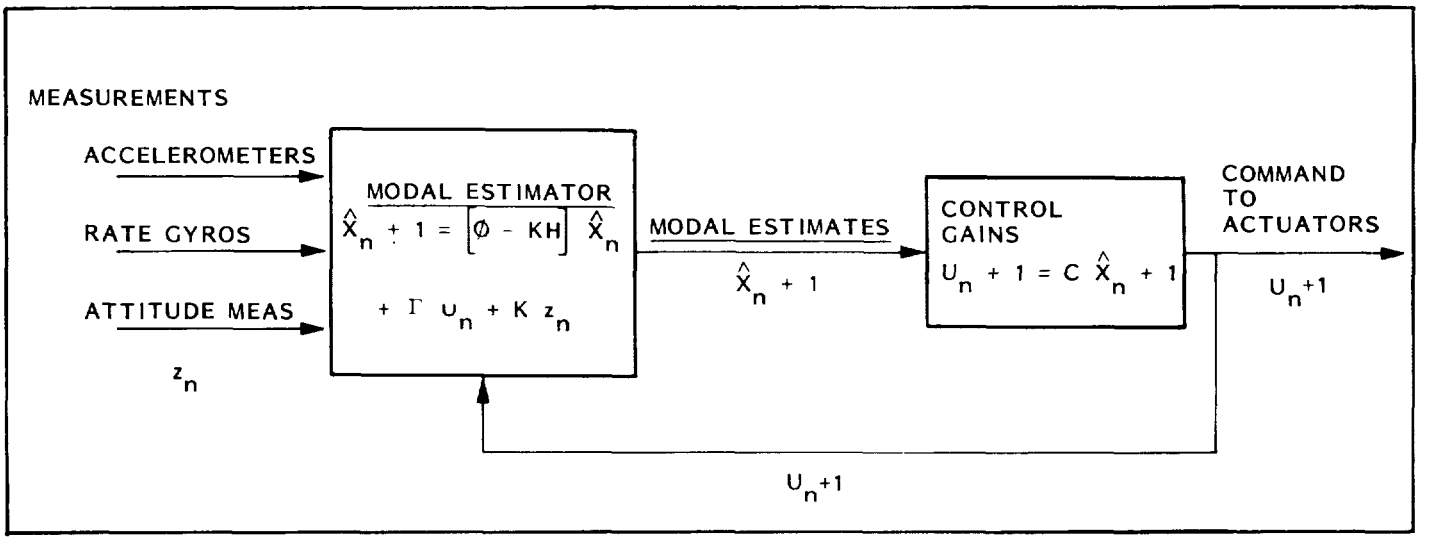

PHOTOGRAPH OF THE TOYSAT EXPERIMENT

The Toysat was an earlier experiment. We use it here to show the type of results we expect to obtain from the POC experiment. The Toysat consists of a 15 foot flexible beam fastened to the side of a 2 foot square block of aluminum. It is suspended from the ceiling in such a way as to allow free motion in the horizontal plane. Control of the motion of the specimen is provided by two linear actuators, and sensing is provided by accelerometers mounted at the ends of the beam, as well as linear position sensors mounted in tandem with the linear actuators. The control system used was a smaller version of that planned for the POC experiment.

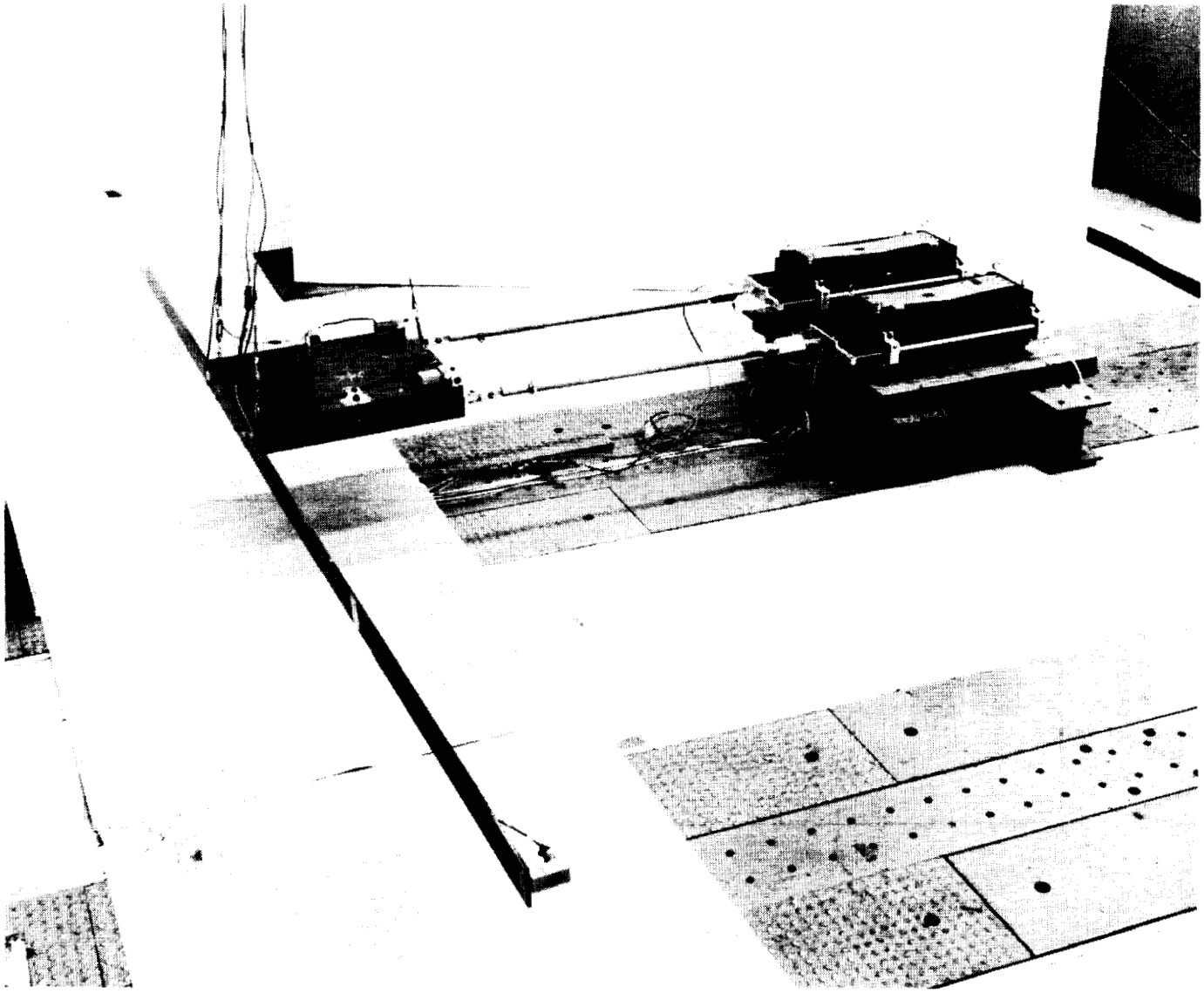

OPEN AND CLOSED LOOP BEHAVIOR

These time histories illustrate that the control system used was indeed able to significantly affect the flexible behavior of the Toysat. During the first four seconds of the test runs, a disturbance was input through the shakers. In the closed loop tests, the control system was on during the disturbance and for the next eight seconds. The control system reduced response during the disturbance, and greatly reduced the settling time after the disturbance was finished.

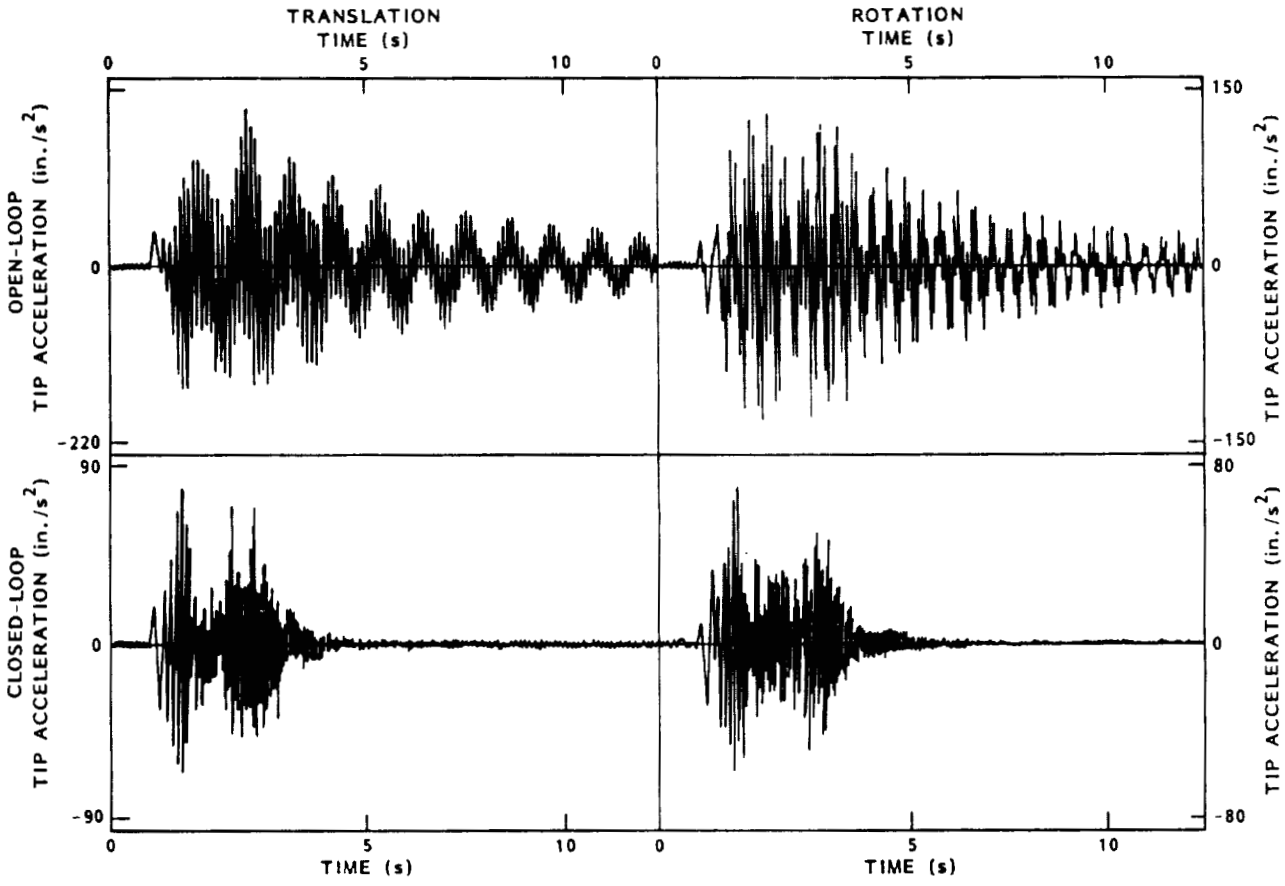

1. Report No.	2. Government Accession No.	3. Recipient's Catalog No.
NASA CP-2215, Part 1		

4. Title and Subtitle	5. Report Date
LARGE SPACE SYSTEMS TECHNOLOGY - 1981	March 1982
	6. Performing Organization Code: 506-62-43-05
7. Author(s)	8. Performing Organization Report No.: L-15096
William J. Boyer, compiler	10. Work Unit No.
9. Performing Organization Name and Address	11. Contract or Grant No.
NASA Langley Research Center Hampton, VA 23665	13. Type of Report and Period Covered: Conference Publication
12. Sponsoring Agency Name and Address	14. Sponsoring Agency Code
National Aeronautics and Space Administration Washington, DC 20546	

15. Supplementary Notes

16. Abstract

This document is a compilation of the papers presented at the Third Annual Large Space Systems Technology (LSST) Review at the Langley Research Center. The research was supported in Fiscal Year 1981 by the LSST Program Office and the Materials and Structures Section, Research and Technology Division, of the Office of Aeronautics and Space Technology. The review provided government, university, and industry personnel with an opportunity to exchange information, to assess the present status of technology development in large space systems, and to plan the development of new technology for large space systems. These papers were divided into four major areas of interest: (1) technology pertinent to large antenna systems, (2) technology related to the control of large space systems, (3) basic technology concerning structures, materials, and analyses, and (4) flight technology experiments. Part 1 contains information on program status; structures, materials, and analyses; and control of large space systems. Part 2 covers large antenna systems and flight technology experiments. Design studies, structural testing results, and theoretical applications are presented with accompanying validation data. These research studies represent state-of-the-art technology that is necessary for the development of large space systems. A total systems approach including structures, analyses, controls, and antennas is presented as a cohesive, programmatic plan for large space systems.

17. Key Words (Suggested by Author(s))	18. Distribution Statement
Large space systems Large antenna systems Structures, materials, and analyses Flight technology experiments	Unclassified - Unlimited Subject Category 15

19. Security Classif. (of this report)	20. Security Classif. (of this page)	21. No. of Pages	22. Price
Unclassified	Unclassified	444	A19

For sale by the National Technical Information Service, Springfield, Virginia 22161

NASA-Langley, 1982